Hydrogen Production by Low Temperature Steam Reforming of Ethanol Using Modified Ni-Sn/CeO_2 Catalysts

THESIS

Submitted in partial fulfilment of the requirements for the degree of

DOCTOR OF PHILOSOPHY

by

SERIYALA ANIL KUMAR

(2017PHXF0406P)

Under the Supervision of

Prof. BANASRI ROY

and

Co-supervision of

Dr. SRINIVAS APPARI

DEPARTMENT OF CHEMICAL ENGINEERING,
BIRLA INSTITUTE OF TECHNOLOGY AND SCIENCE,
PILANI.
2023

BIRLA INSTITUTE OF TECHNOLOGY AND SCIENCE, PILANI

CERTIFICATE

This is to certify that the thesis entitled **"Hydrogen Production by Low Temperature Steam Reforming of Ethanol Using Modified Ni-Sn/CeO_2 Catalyst"** and submitted by **Mr. Seriyala Anil Kumar** ID No **2017PHXF0406P** for award of Ph.D. of the Institute embodies original work done by him under my supervision.

Signature of the Supervisor

Name in capital letters: **Prof. BANASRI ROY**

Designation: **Professor, Department of Chemical Engineering**

Date:

Signature of the Co-Supervisor

Name in capital letters: **Dr. SRINIVAS APPARI**

Designation: **Assistant Professor, Department of Chemical Engineering**

Date:

Dedicated to…...

To my beloved family, "Mom", "Dad", "elder brother Naveen", "elder sister-in-law Swathi" "my wife Priyadarshini" and "younger brother Suresh"

To my positive energy & joy daughters "Sahasra" and "jyosmita"

ACKNOWLEDGEMENTS

Doing research on words requires searching, and it's impossible to search effectively without guidance. Therefore, I would like to express my deepest gratitude to my advisor, Prof. Banasri Roy, Associate Professor, Department of Chemical Engineering, BITS Pilani, for her consistent support throughout my project. I owe her a great amount of gratitude for all the ways in which she has educated me and guided me in my growth as a person and a professional like a true mentor. Her knowledge in the disciplines of nanomaterial fabrication, data analysis, and characterization appeared to have great impact on the learning process of my PhD study and pushed me to prepare better and better-organized research publications.

I would like to express my sincere thanks to my co-supervisor, Assistant Professor Dr. Srinivas Appari, for all his helpful advice and moral support over the course of this research work. It has been a pleasure for me to work with him and learn from him.

My deepest gratitude to my Doctoral Advisory Committee(DAC) members Dr. Bhanu Vardhan Reddy Kuncharam and Dr. Krishna C. Etika, for their insightful comments and suggestions.

I would like to thank Prof. Pratik N Sheth, HoD, Chemical Engineering Department. I would like to thank Prof. Ajaya Kumar Pani, Convener, Doctoral Research Committee for his support and suggestions.

I extend my sincere thanks to Prof. Souvik Bhattacharyya, Vice-Chancellor, BITS-Pilani for giving me the opportunity to carry out the Ph.D. work in BITS-Pilani, Pilani Campus. I would also extend thanks to Prof. Sudhirkumar Barai, Director, BITS Pilani, Pilani Campus. I am indebted to Dean, and Associate Dean, Academic - Graduate Studies & Research Division (AGSRD) (Ph.D programme), BITS- Pilani, Pilani Campus for providing the necessary research facilities required for my work.

My whole-hearted gratitude to Prof. Arvind Kumar Sharma and Prof. Hare Krishna Mohanta for their dynamic quality as a best teacher and valuable inspiring character. I extend my special thanks to all the respected faculty members of the Department of Chemical engineering, BITS Pilani, Prof. Pradipta Chattopadhyay, Prof. Smita Raghuvanshi, Prof. Suresh Gupta, Dr. Somak Chatterjee, Dr. Priya C Sande, Dr. Amit Jain, Dr. Jay Pandey, Dr. Mohit Garg, and Dr. Sarbani Ghosh for their encouragement throughout the work and fruitful discussions throughout the various stages of my doctoral study.

I would like to thank the Chemical Engineering Department's staff and lab assistants, Mr. Suresh Kumar Sharma, Mr. Jangvir, Mr. Kuldeep Kumar, Mr. Ashok Saini, Mr. Jeevan Lal Verma, and Mr. Sunder Lal Harijan, for helping me get things done on time in the department and in the lab.

I would like to extend my heartfelt thanks to all the research scholars of Chemical Engineering department, Ramakrishna, Rajesh, Dr. Raghavendra, Dr.Sudheer, Anand Reddy, Aditya, Dharmesh, Mannu, Shailee, Bharat, Mohan, Amir, Rachael, Soumya, Ipsita, Priya, Taniya and all other recent joiners.

My sincere gratitude to the special people in life, my parents Late. Arjun and Late. Shoba, they're my strength and my weakness, as well as to my younger brother, the late Suresh Kumar, who was my greatest friend. I would like to express my eternal thanks to Mr. Naveen Kumar, my elder brother, and to Dr. Swathi, my elder sister-in-law, who have been strong support and back bone to my entire life. I want to convey my eternal gratitude to my wife, Mrs. Priyadarshini, for all the love, support, and help she has given me throughout the years. Last but not least, I wish to thank my entire family, they have always motivated me to focus entirely on my academics.

SERIYALA ANIL KUMAR

ABSTRACT

Hydrogen is contemplated as an alternative clean fuel for the future. Ethanol steam reforming (ESR) is a carbon-neutral, sustainable, green hydrogen production method, while low temperature steam reforming may be more cost effective and favorable for hydrogen production (chapter 1). Low-cost Ni/CeO_2 powder catalysts demonstrate high ESR activity. However, acidic nature and instability of CeO_2 lead to the deactivation of the catalysts easily. Review of the literatures of last 20+ years (chapter 2) on ESR for hydrogen production over Ni/Al_2O_3 and Ni/CeO_2 based catalyst powders reveals that promoting the active metal phase Ni by other metals and/or modifying the CeO_2 support by other inorganic oxides could be a successful strategy to enhance active and stability of the Ni/CeO_2 based catalyst.

In this work three sets of bimetallic Ni-Sn catalysts supported on modified CeO_2 are considered for low temperature steam reforming of ethanol (LTSRE). Catalytic activity is studied at 25 °C interval from 200 to 400 °C, under atmospheric pressure, H_2O:EtOH = 12: 1 mole ratio, and feed flow rate 0.1 ml/min. GC and HS-GC instruments are used to evaluate the activity. The fresh, reduced and spent catalyst are characterized by FTIR, XRD, H_2-TPR, NH_3-TPD, Raman, FESEM, XPS, N_2 adsorption-desorption, and DTA/TGA techniques and these results are utilized to interpret the activity results. These are explained in detail in chapter 3.

The first study (Chapter 4.1) focuses on the development of Ni-Sn bimetallic catalysts supported on ZrO_2 modified CeO_2 powder. The catalyst powders are prepared by an ultrasonic-assisted solution combustion synthesis method. Addition of Zr and Sn decrease particle size and demonstrate a synergic effect for the increase of oxygen vacancies, enhance oxygen mobility in the catalyst lattice, and reduction of coke deposition. At 400 ℃, 100 % ethanol conversion and 68 % H_2 selectivity with least coke deposition is observed for the catalyst with 5 wt.% metal (Ni: Sn = 14:1 atomic ratio) loading on Ce:Zr = 1:2 mol ratio support, NiSn5/CZ12. Whereas, increasing metal loading demonstrates increase of the particle size & coke deposition and decrease of the oxygen vacancy. At 400 ℃, 58 % ethanol conversion and 42 % H_2 selectivity with highest coke deposition is observed for the catalyst with 20 wt.% metal loading on Ce:Zr = 1:1 mol ratio support, Ni20/CZ12.

The second work (Chapter 4.2) presents the effect of metal loading and support modification with MgO on LTSRE over Ni-Sn/CeO_2 catalysts prepared by a single-pot solution combustion synthesis (SCS) method. After 10 h time on stream (TOS) at 400 °C, NiSn(5)/CM12 catalyst with 5 wt.% total metal loading, optimal Sn (Ni:Sn = 14:1 atomic ratio), and Ce:Mg =1:2 mol ratio shows EtOH conversion 100% and H_2 selectivity 72% with low coke deposition. NiSn(20)/C catalyst with 20 wt.% total metal loading, optimal Sn (Ni:Sn = 14:1 atomic ratio) shows EtOH conversion 68% and H_2 selectivity 32% with high coke deposition. Physicochemical characterizations (XRD, Raman, FESEM, TEM, and N_2 adsorption-desorption) reveal that addition of MgO in CeO_2 and an optimal amount of Sn decrease both Ni and support particle sizes while oxygen storage capacity of the support increases (by

XPS). Alkaline characteristics of MgO reduces support's acidity and improves active metal-support interaction, as evaluated by NH_3-TPD and H_2-TPR.

The third study (Chapter 4.3) focuses on the effect of total metal loading and support modification with La_2O_3 (Ce:La = 2:1; 1:1, and 1:2 atomic ratios) on LTSRE over Ni-Sn/Ce-La-O catalysts prepared by a single-pot ultra-sonication assisted solution combustion method. Catalysts with total metal loading 5 wt.%, 33 and 67 at.% La, and optimum Sn (Ni:Sn = 14:1) demonstrate better efficiency compared to the Ni/CeO_2 catalyst. However, 50 at.% La addition degrades the activity of the catalyst. Higher metal loading (20 wt.%) and high Sn concentration (NiSn 1:1 atomic ratio) deteriorate the catalytic activity. The best activity and stability (EtOH conversion 100%, H_2 selectivity 60% with lowest coke deposition) are reveled for the N14S1(5)/CL21 catalyst with 5 wt.% total metal loading, Ni:Sn = 14:1, and Ce:La = 2:1 mol ratio at 400 ℃ after 20 hrs of time on stream. Physico-chemical characterizations (XRD, H_2 -TPR, NH_3 -TPD, Raman, FESEM, TEM, XPS, N_2 adsorption-desorption, DTA/TGA) are performed to understand the role of the Sn and La in the reaction and coke deposition behavior.

Comparison of the important catalytic activity results for all catalysts shows $Ni_{0.93}Sn_{0.07}(5)/Ce_{0.33}Mg_{0.67}O_{1.33}$ to be the best catalyst. The deactivation study and kinetic analysis would *be* performed by the researchers in future to evaluate the applicability of these catalysts for LTSRE.

***Keywords**: NiSn/CeO_2-ZrO_2, Ni-Sn/CeO_2-MgO, NiSn/CeO_2-La_2O_3 catalysts, Hydrogen, Support modification, Varying metal loading, Effect of tin composition, Solution combustion synthesis (SCS), Reaction mechanism.*

Table of Contents

List of Figures

List of Tables:

List of Abbreviations/symbols

AD: Acidity (μmol.NH_3/g)
ads: adsorbed on the surface
bcm: billion cubic meter
BM: Ball mill
BS: Boehmite synthesis
BET: Brunauer–Emmett–Teller
c: cube
CASG: citric acid assisted sol-gel method
CCM: Citrate complexing method
CD: Citrate decomposition
CI: Co-impregnation method
Comm.: Commercially procured
CP: Co-precipitation method
C rate : Carbon formation rate($mg_{coke}/mg_{cat.}h$)
CT: Calcination Temperature (°C)
D: Dual templated with P123 and ionic liquid as template
D_{CeO2}: Diameter of CeO_2 phase (nm)
D_{Ni} : Diameter of Ni in reduced catalyst (nm)
D_{NiO} : Diameter of NiO phase (nm)
D_p: Particle diameter (nm)
D_{pore}: Pore diameter (nm)
DE: Deposition method
DS: Dispersion (%)
DT: Drying Temperature (°C)
DTA: Differential thermal analysis
Ea: Activation energy kJ/mol
EDS: Energy dispersive spectrometer
EISA: Single-step evaporation-induced self-assembly
ESR: Ethanol steam reforming
EtOH: Ethanol
FESEM: Field emission scanning electron microscopy
FL: Flowerlike support morphology
FTIR: Fourier- transform infrared.
GHG: Greenhouse gases
GHSV: Gas hourly space velocity **(**h^{-1})
H_2O/EtOH: Water/Steam to Ethanol molar ratio
HT: Hydro-thermal method
IM: Wet impregnation method
IWI: Incipient wetness impregnation method
k : Rate constant (s^{-1})
LTSRE: Low-temperature steam reforming of ethanol
%M : Mole %,
mM: millimolar concentration.
MSI: Metal-support interaction
NC: Nanocube support morphology
NH_3-TPD: Ammonia- Temperature programmed desorption
nm: Nano meter
NP: Nano particles

NR: support morphology
O_a: 'a' is atomic fraction of oxygen in the compound.
OM: Oxygen mobility
ON: Over Night
OSC: oxygen storage capacity
p: particle
P3: P123 concentration (nM)
PI: P123 as templates
PM: Polymerization reaction
PT: Precipitation method
PYT: Pyrolyzation temperature
r: rod
RM: Reverse micro-emulsion
R: Reverse method in aqueous solution
RT: Reduction Temperature (°C)
%S: Percentage selectivity
S/C: Steam to carbon ratio
S_{BET}: BET surface area (m^2/g)
$S_{BET,Al2O3}$: BET surface area of Al_2O_3 support (m^2/g)
$S_{BET,support}$: BET surface area of support (m^2/g)
SG: Sol-Gel method
SR: Steam Reforming
TEM: Transmission electron microscopy
TGA: Thermogravimetric analyses
TOS: Time-on-Stream(h)
TPR: Temperature programmed reduction
V_p = Particle volume (cm^3g^{-1})
V_o & O_V: Oxygen vacancy
V_{pore}: Pore volume (cm^3g^{-1})
U- Urea method
USCS: Ultrasonication assisted with solution combustion synthesis
W_{pore}: Pore width (nm)
WGS : Water gas shift
WHO: World health organization
XPS: X-ray spectroscopy
XRD: X-Ray diffraction
%Y: Percentage yield
Y : Yield ($mmol/min.g_{cat}$)
Y_a : Yield (mol/mol.EtOH),
Y_b : Yield(μmol/min)

Chapter 1: Introduction

1.1 Energy scenario, supply and climate change

Energy is a basic need for the fundamental requirements of the human society and civilization including cooking, heating, cooling, lighting, transportation, operation of appliances, as well as information and communications technology and the manufacturing of every sector of a country. World population expected to reach 9.7 billion by 2050 from 7.3 billion in 2021 [1]. Accordingly, world energy production rate will increase 1 to 2% per year with current production rate 606 exajoules (EJ) to meet the energy requirement of the civilization. As per the world energy statistics-2021 (IEA), 80% of the energy is produced from fossil fuels [2,3] (**Fig. 1.1(a)**), and Russia, the United States, and the Arab countries of the Persian Gulf produce half of that (**Fig. 1.1(b)**). The Gulf countries and Russia export most of their energy to the European Union and China, where not enough energy is made to meet the demand [4].

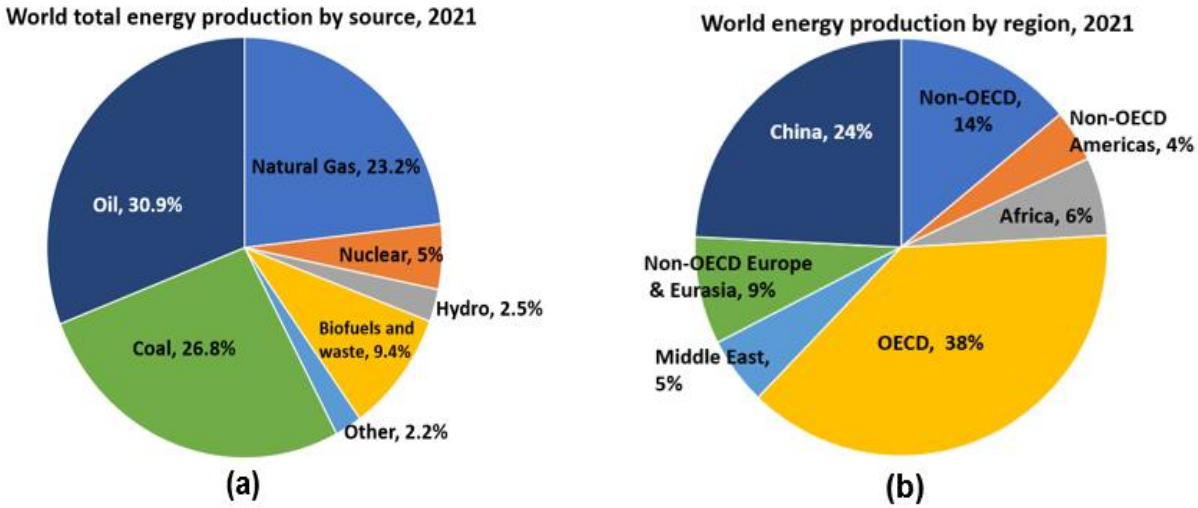

Figure 1. 1: World energy production by (a) different sources and (b) different countries [**Sources:** [2,3]].

Due to accelerated growth of global population, it is estimated that the worldwide energy consumption would increase nearly 50 % by 2050 from 595 EJ in 2021 (**Fig. 1.2 (a)**) (IEO 2021). At present world energy consumption in different sectors is as follows: industry 282 EJ, residential 80 EJ, commercial 60 EJ, and transportation 170 EJ [2,5]. Taking into account the consumption of petroleum and other liquid fuels estimated increase of the number of barrels would be from 77 million per day in 2021 to 115 million per day in 2050 [5]. The lion share of these consumption is by China and Organization for Economic Co-operation and Development (OECD) countries, such as USA, UK, etc (**Fig. 1.2(b)**). However, the average increased consumption of fossil fuels (by 1.3% every year) results in a significant increase in environmental pollution.

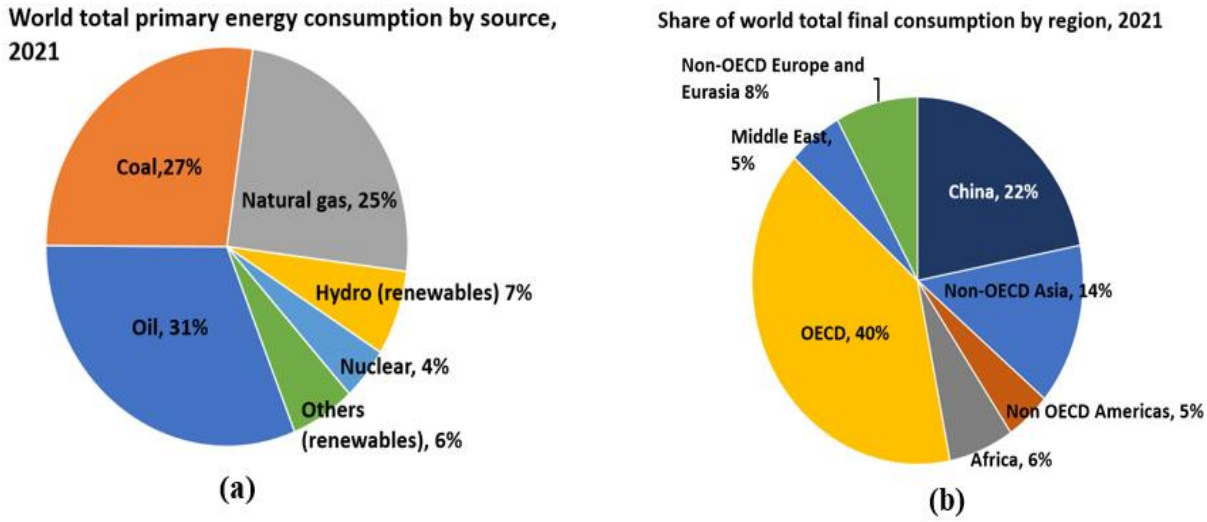

Figure 1. 2: World energy consumption by (a) different sources and (b) different countries [**Sources:** [2,3]].

World energy outlook (WEO)-2022 projects the total energy supply till 2050 (**Fig. 1.3**), with three different scenarios to minimize the carbon emissions based on the government policies [2]. The first one, the Stated Policies Scenario (STEPS) shows today's policy direction. Second one, the Announced Pledges Scenario (APS) assumes all government aspirational objectives to be completed on schedule. While the third one, Net Zero Emissions by 2050 (NZE) Scenario, aims to stabilize global average temperature. These scenarios are modelled for 26 countries and regions for the demand, electricity, and fuel transformations as well as for all the key producers on the supply side. As per the STEPS scenario the primary energy consumption is projected to rise by around 1% per year till 2030, due to greater usage of renewable energy sources (**Fig. 1.3**). Natural gas would see the largest slowdown with annual growth falling to around 0.4% from 2021 to 2030. Coal demand is expected to remain constant for the first half of the decade. However, the demand starts to fall in the second half of decade as the utilization of renewable energy grows. Additionally, it would decrease in industries, where green steel production is accelerating. APS scenario observes the same patterns, if governments, industries, and citizens take additional steps to follow the long-term climate goals. Natural gas expected to go down by 2030, due to considering the demand is less than 3,900 billion cubic meters (bcm) per year, which is 8% less than that of the current requirement. According to the NZE Scenario, it measures that natural gas to drop to less than 3,300 bcm by 2030 due to limiting the sale of fossil fuels. Nuclear power generation is expected to increase by 2030 in both the STEPS and APS. However, in the NZE Scenario the usage of low-emissions hydrogen and hydrogen-based fuels is three-times higher in 2030 than that in the APS. These trends are expected to increase energy-related CO_2 emissions in the STEPS. However, by 2030 emissions would fall to 36 Gt CO_2, 0.4 Gt lower than that of today. Whereas in APS, CO_2 emission rate will drop to 32 Gt CO_2 per year by 2030 [2].

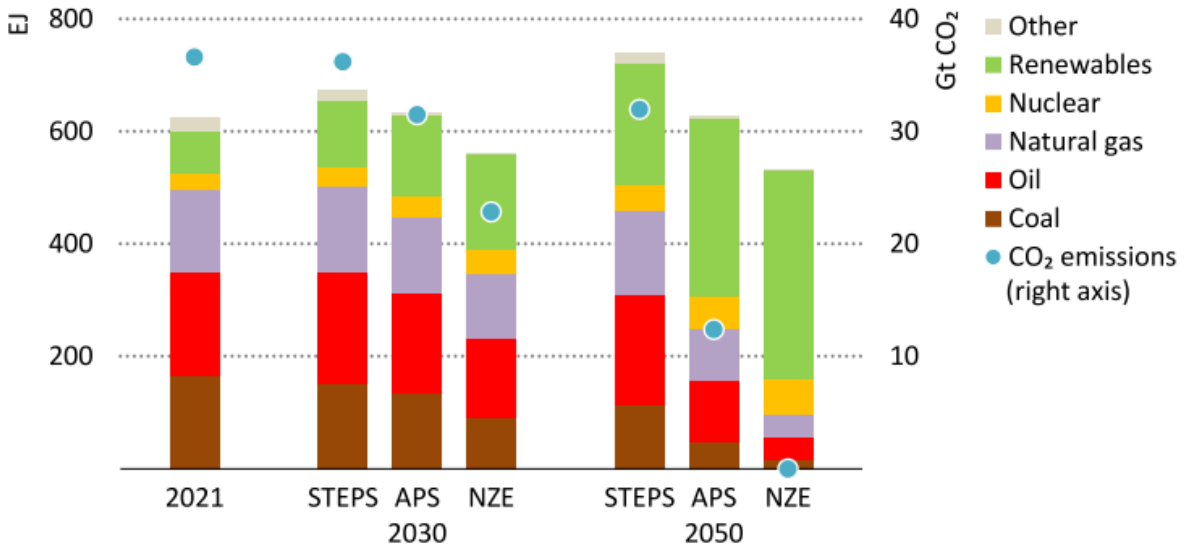

Figure 1. 3: Total energy supply by different fuels and CO_2 emission by three scenario [**Source:** [2]]
Notes: EJ = exajoule; Gt CO_2 = gigatonnes of carbon dioxide; STEPS = Stated Policies Scenario; APS = Announced Pledges Scenario; NZE = Net Zero Emissions by 2050 Scenario

India has one of the largest coal reserves in the world. In 2021, the total estimated reserve in India contains coal 352.13 billion tonnes, crude oil 587.33 million tonnes , and natural gas 1372.62 bcm (**Fig. 1.4(a)**). Based on the geographical distribution of crude oil the maximum reserves are in the western offshore (37%) followed by Assam (26%) [6]. The maximum reservoirs of natural gas are in the eastern offshore (40.6%) and western offshore (23.7%). The consumption of energy (**Fig. 1.4(b)**)from coal and lignite was highest which accounted for about 46.0% of the total consumption during 2020-21 followed by crude oil (31.0%) and electricity (Hydro, nuclear and others) (14.64%).

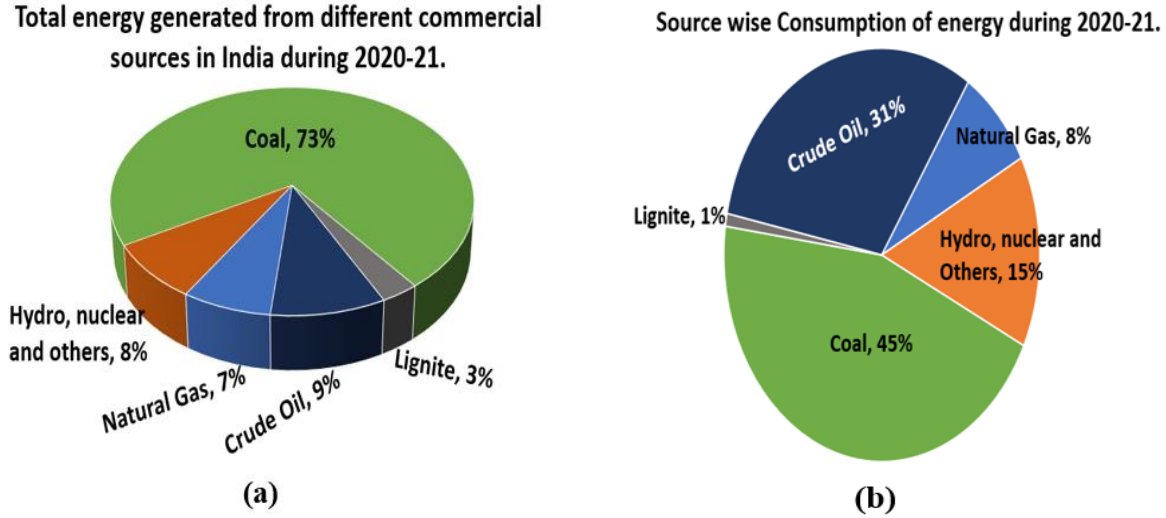

Figure 1. 4: In India total energy (a) generation and (b) consumption from different commercial sources during 2020-2021 period [**Sources:** [6]].

More than 15% of energy-related greenhouse gas (GHG) emissions occur from fossil fuel extraction, processing, and transport account which need to be minimized as quickly as possible. In

2021, indoor air pollution was responsible for around 3.6 million premature deaths, and outdoor air pollution caused 4.2 million. In recent years, air pollution has caused at least 19,000 additional deaths globally every day. 38,884.1 million tonnes of CO_2 emitted from energy utilization in 2021.

The total availability of crude oil has decreased by 11.78% over last year (from 259.12 MT in 2020 to 228.61 MT during 2021) [6]. Many companies and financial organizations have set goals and plans to invest less in fossil fuels and pay more attention to invest in clean energy technologies. **Table 1.1** lists the renewable and nonrenewable energy sources. Different renewable energy sources like biomass, solar energy, hydropower, wind energy, etc., and many more non-renewable energy sources which could be obtained by processing the fossil-fuels help in fulfilling the energy requirements. In India, the total estimated renewable energy generation is 163 gigawatts (GW) as on 31-08-2022. This consists of 59.34 GW of solar power (59.34 %), 41.2 GW of wind power (25.28 %) at a hub height of 120 meters, 51.7 GW of Hydro power (31.7 %), 10.2 GW of biomass/co-generation power (6.25%), and 0.47 GW of waste-to-energy (0.28%) [6,7] (**Fig. 1.5**).

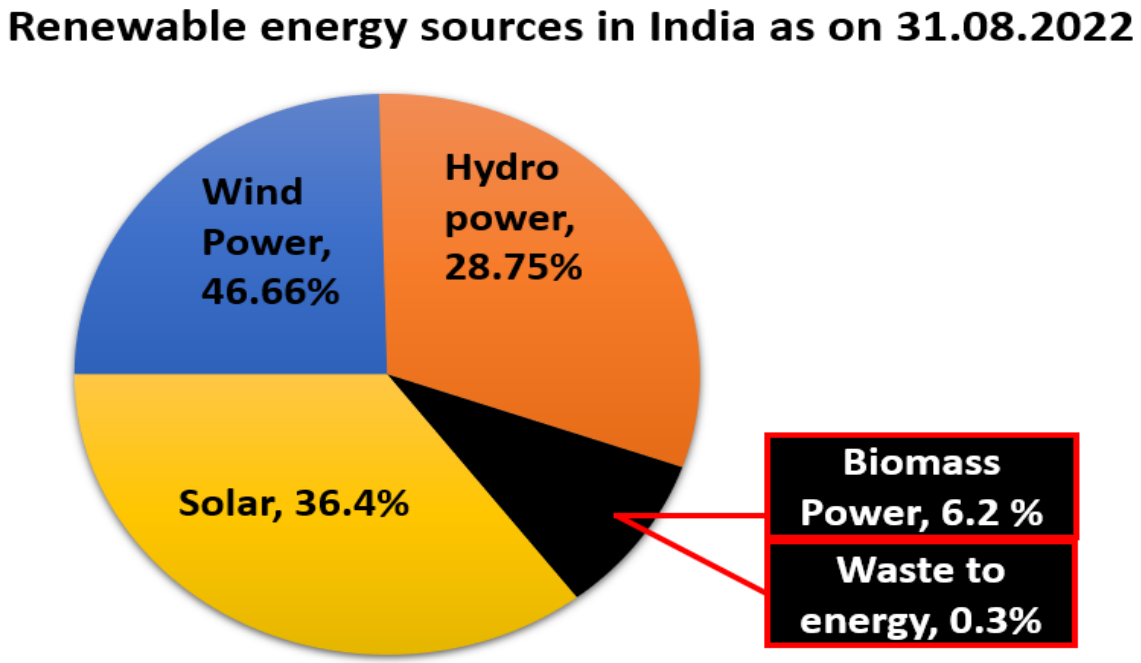

Figure 1. 5: Percentage of different renewable energy sources available in India [**Sources:** [6]].

Hydrogen is often described as a clean and sustainable energy vector and as the fuel of the future because it burns cleanly without releasing any kind of pollutants and has a very high heating value. **Table 1.2** summarizes the fuel properties of hydrogen.

Table 1. 1: Renewable and Nonrenewable energy sources

Energy sources	
Renewable	**Non-Renewable**
Energy generated from sun • Solar • Biomass • Biofuels • Wind	**Energy generated from fossil-fuels** • Coal • Crude oil/petroleum products • Natural gas
Energy generated from the interior of the earth • Geo-thermal	**Energy generated from atoms** • Nuclear
Energy generated from gravity • Hydropower • Tidal	

Table 1. 2: Properties of Hydrogen

Property	**Values/Description**
Melting Point	-259.2 ℃
Boiling Point	-252.9 ℃
Density	0.08375 kg/m³ (The lowest of any chemical element)
Octane number	> 130
Auto ignition temperature in air	585℃
Lower heating value (at 25℃ and 1 atm)	119.93 kJ/g
Higher heating value (at 25℃ and 1 atm)	141.86 kJ/g
Flash Point	<-253 ℃; $20K$
Flame Temperature	2,158℃
Air/fuel mass	34.2
Heat of Combustion	141.80 MJ/kg
Heat of vaporisation	446 kJ/kg
Odour	Odorless
Flammability	Highly Flammable
Combustion	When mixed with air and with chlorine it can spontaneously explode by spark, heat, or sunlight.

1.2 Hydrogen Economy

World market for the hydrogen as a fuel is steadily taking shape with the rise of stationary fuel cells which use hydrogen in home power systems, the development of fuel cell vehicle (FCV) technology, and the possible internal combustion engine automobiles. The market for generation of hydrogen is expected to grow from an estimated USD 142 billion in 2022 (**Fig. 1.6)** to USD 219.2

billion in 2030, which is 10.5% more than the amount produced presently [8] and it is projected to increase 1600 billion USD by 2050 [9].

Figure 1. 6: Hydrogen generation market by different industries and technology of forecast 2022-2030 [**Sources:** [9]].

As per hydrogen economy report, currently the major amount of hydrogen is utilized for infrastructure (120 billion USD) and hydrogen power generation industries with 25 billion USD and very less amount for FCVs [10]. However, as a result of the widespread use of FCVs, the market size of FCVs is projected to increase substantially and approach 1100 billion USD by 2050. The scale of infrastructures will rapidly increase to more than 300 billion USD in 2030 and then slowly increase to 400 billion USD until 2050 [10].

On the other hand, the market share per country demonstrates that Europe and North America are the major factors behind the promotion of the hydrogen economy. Europe set goals to reduce CO_2 emissions and invest more money into hydrogen infrastructure and renewable energy. Similarly, developing nations like China and India are actively involved in the research and development of hydrogen technology and aim to broadly implement hydrogen stations, which will result in a significant increase in market share by the year 2030 [11]. Japan, on the other hand, has the most popular hydrogen infrastructure, even though it has a small and stable market size of about $100 billion USD. Europe, North America, and China will be the three largest hydrogen markets by 2050, accounting for over 60% of the global market share, followed by India and Japan (**Fig. 1.7**). Currently, the primary industrial uses of hydrogen are in the production of ammonia (34 Mt of hydrogen), petroleum recovery and refining (43 Mt of hydrogen) methanol (15 Mt of hydrogen), and in direct reduction of iron in the steel industry (5 Mt of hydrogen) (**Fig. 1.8**). In the transportation sector, hydrogen is mostly used in fuel cell electric vehicles (FCEVs). In 2021, there were around 51,000 hydrogen FCEVs, a 55% increase from the end of 2020, and the major growth happened in South Korea. Over the duration of the year, more than 9,200 FCEVs were sold, which was more than 0.5% of total car sales. By the end of June 2022,

the world had more than 59,000 FCEVs, which was15% more than that at the end of 2021 (**Fig. 1.8**). The global number of hydrogen refueling stations were 700 by the end of 2021 and reached to 975 by the end of June 2022 [11].

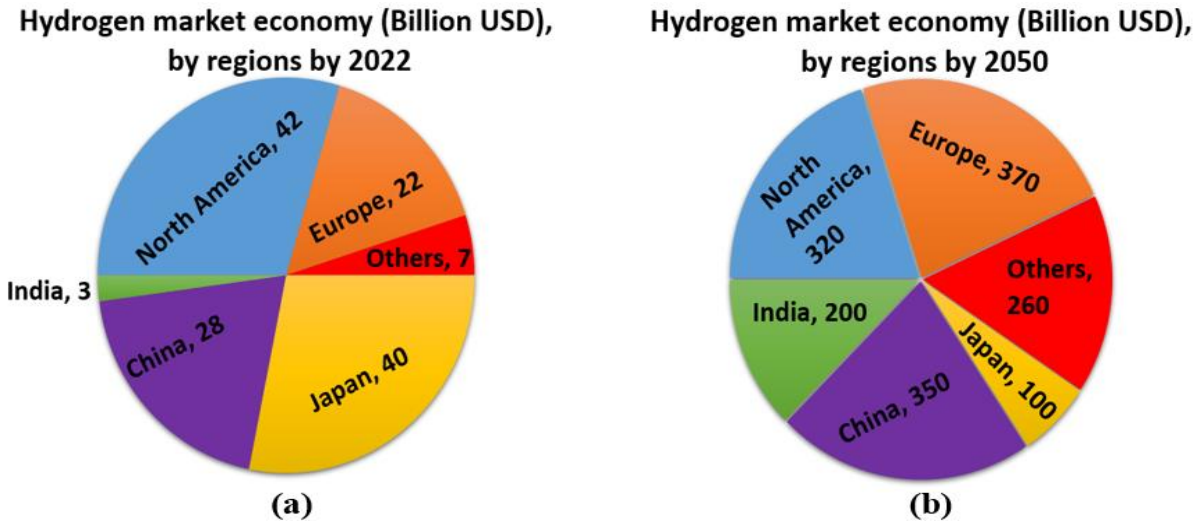

Figure 1. 7: Global hydrogen market economy country wise (a) at present in 2022 and (b) predicted to be by 2050 [**Sources:** [10,11]].

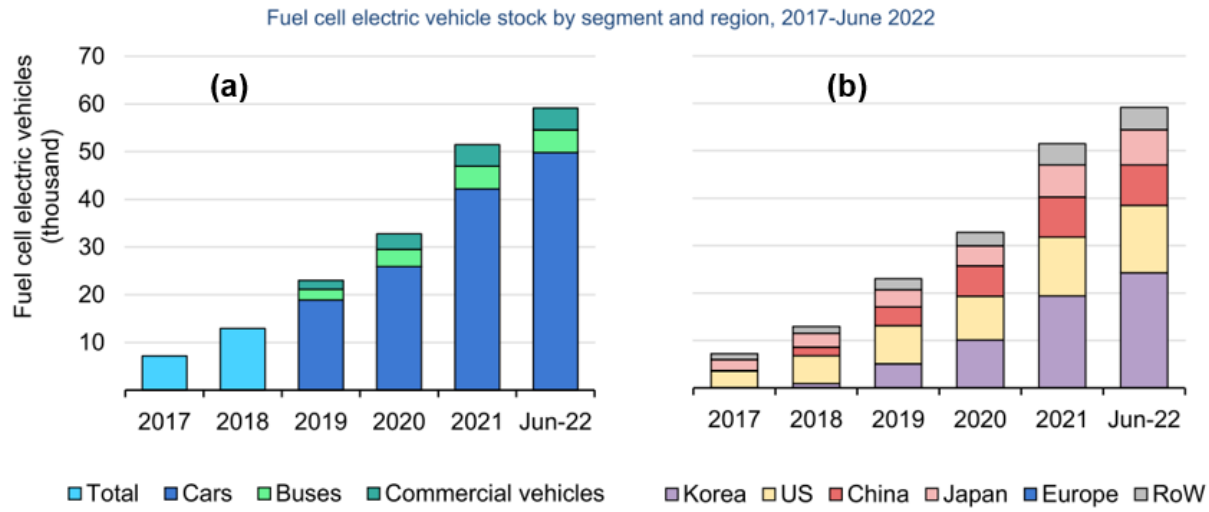

Figure 1. 8: World-wide fuel cell electric vehicles(FCEVs) production stock by (a) different segment and (b) region [**Sources:** [11]].

Hydrogen is not found in nature in its elemental form, so it must be taken out of chemical compounds using thermochemical, electrochemical, photochemical, and photobiological methods. Currently, non-renewable energy sources are used to make most of the hydrogen, and reforming technology (thermochemical) is used to make 85% of the hydrogen (thermochemical conversion method). However, the futuristic concept is to utilize renewable sources (such as biomass) to produce hydrogen. **Table 1.3** shows different types of hydrogen, related technology, cost, and CO_2 emissions. **Table 1.4** listed different hydrogen production methods with their advantages and disadvantages [12,13]. Clearly hydrogen from renewable sources is more favorable.

Table 1. 3: Different types of hydrogen, technology, cost and CO_2 emissions [**Sources:** [14]].

H_2 color	**Technology**	**Source**	**Products**	**Cost ($ kg/H_2)**	**CO_2 emissions**
Green H_2	Electrolysis	Water	$H_2 + O_2$	3.6 – 5.8	Minimal
Blue H_2	Reforming + Carbon capture	Natural gas	$H_2 + CO_2$ (Captured 85-95 %)	1.5 – 2.9	Low
Grey H_2	Reforming	Natural gas	$H_2 + CO_2$ (Released)	1 – 2.1	Medium
Black H_2	Gasification	Black coal (Bituminous)	$H_2 + CO_2$	1.1 – 2.1	High
Brown H_2	Gasification	Brown coal (Lignite)	$H_2 + CO_2$	1.1 – 2.1	High

Table 1. 4: Different hydrogen production methods with their advantages and disadvantages [**Sources:** [12,13]**]**.

Process	**Advantages**	**Disadvantages**	**Efficiency**
Steam Reforming (SR)	Most developed technology, carried at atmospheric pressure, high steam to glycerol ratio, high efficiency of its operation, low operational and production cost, less expensive catalysts are used, existing infrastructure.	Requires a raw material free of sulphur-containing compounds to avoid deactivation of the catalyst used, high production of carbon dioxide gas, depends on fossil fuels availability.	70-85%
Auto thermal reforming (ATR)	Novel technology, not requiring external heat, simpler and less expensive, Gasoline and other higher hydrocarbons may be converted into hydrogen on board for use in automobiles using suitable catalysts, shut down and started very rapidly.	It requires purified oxygen, carbon dioxide is produced as a by-product, depending on fossil fuels availability.	60-75%
Partial oxidation (PO)	Catalyst is added to lower the operating temperatures, high operating temperatures and safety concerns may make their use for practical and compact portable devices, proven technology	Difficult due to thermal management, CO_2 as a by-product depends on fossil fuels, produced heavy oils and petroleum coke along with hydrogen gas.	60-75%
Aqueous phase reforming (APR)	Aqueous phase reforming is advantages over steam reforming process since it has lower operating temperature, high density of the fluid reduces cost of reactors, high heat recovery efficiency, does not required steam feed system, takes place in liquid phase	Disadvantages compared to steam reforming process is lower selectivity of hydrogen due to low temperature. Formation of alkanes and carbon dioxide.	50%
Electrolysis	Well established technology, no pollution, abundant feed stock, and oxygen as by product, further conversion into electrical energy using fuel cells.	High capital cost, storage and transportation problems, high capital cost	60-80%
Thermolysis	Oxygen is the by-product, abundant feed stock, sustainable and clean	Cost involved is high, problems of corrosion, toxicity of elements.	20-45%

Dark fermentation	Simple method, no need of light, helps in waste recycling, no oxygen limitation, and CO_2 neutral.	Low yield of hydrogen, less conversion efficiency, huge volume of reactors required, removal of fatty acids.	60-80%
Photo fermentation	Uses different organic wastewater, recycling waste, CO_2 neutral.	Very low conversion efficiency, sunlight required, hydrogen yield and rate are low, oxygen sensitive.	0.1%
Bio photolysis	Operated at mild conditions, by product produced is oxygen, utilizes carbon dioxide	Raw material is costly, low yield of hydrogen, larger reactors required, sunlight needed	11%
Bio gasification	Feed stock available is more and cheap, neutral carbon dioxide	Feed stock impurities, sessional availability of raw materials, and formation of tar.	30-40%

In thermo-chemical conversion processes, heat and pressure are used to break down biomass into its parts, such as biofuels, gases, and chemicals. There are many kinds of thermochemical processes, such as combustion, gasification, pyrolysis, liquefaction, steam reforming, aqueous phase reforming, etc [14]. Steam reforming (SR) accounts for nearly half of the hydrogen produced worldwide (49%) (**Fig. 1.9**) [14,15]. The remaining contributions coming primarily from coal gasification (18%) and partial oxidation of refinery oil (30%) and 4% of H_2 is produced though other process [16].

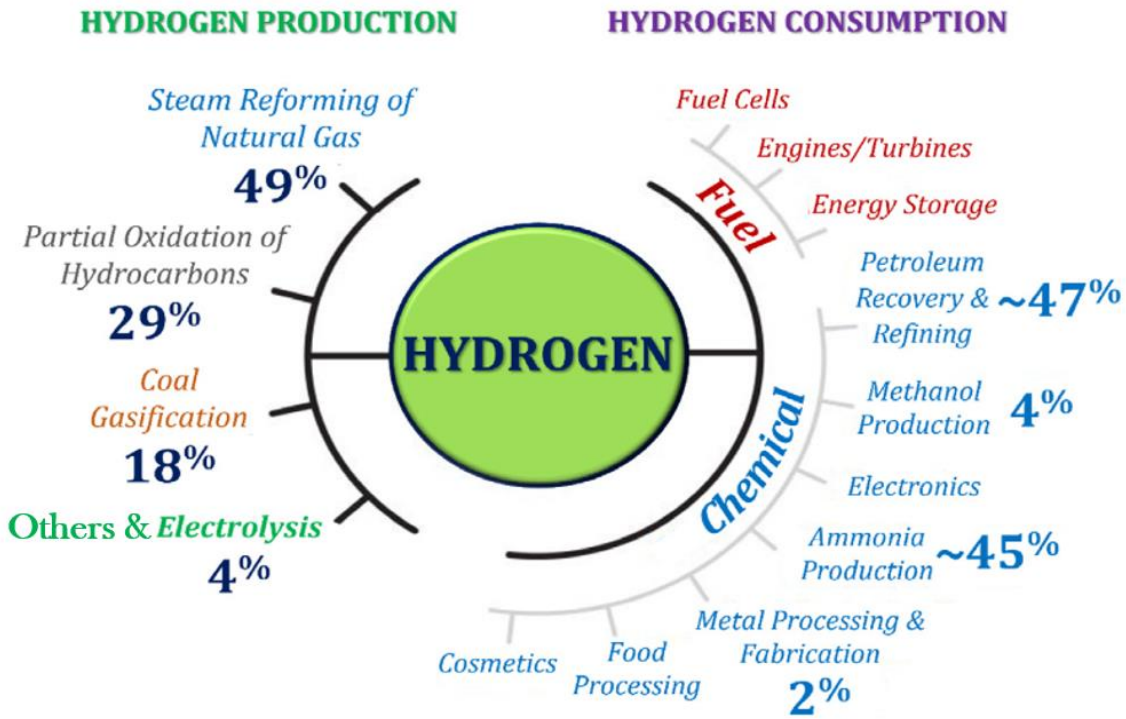

Figure 1. 9: World major hydrogen production methods and applications [**Sources:** [14,15]].

Currently, the significant resources of biomass as well as other renewable resources has attracted attention to produce renewable hydrogen. Scientists are extensively working on developing

technology to produce hydrogen from biomass and/or biomass derived hydrocarbons, including biodiesel, glycerol, ethane, propane, butane, and lesser alcohols like methanol and ethanol. One of the most important advantages of bioenergy utilization is that the biomass is capable of considering carbon sinks because it is CO_2-neutral.

1.3 Ethanol as a Feedstock for Hydrogen Production

Ethanol (C_2H_5OH) is considered as a good source for hydrogen production, because it has a high hydrogen content and low production costs, is commonly available, is non-toxic, and can be securely stored and handled. However, one of the most significant benefits of choosing ethanol is that it can be produced sustainably in large amounts from a different biomass source (energy plants, agro-industrial waste, or forestry residue materials) and minimizes the greenhouse gas emissions [17]. The boiling point of ethanol is 78.4 ℃, and its industrial manufacturing involves the hydration of ethylene between 250 and 300 ℃ and 5 to 8 MPa [18]. However, the reaction is reversible, thus it is possible to dehydrate ethanol and produce ethylene. In addition to being produced from fossil fuels, ethanol can be produced from the fermentation of biomass sources (known as "bio-ethanol") such agricultural wastes or municipal solid waste (MSW) [19]. Depending on the feedstock, ethanol (or bioethanol) could be considered as the first or second generation. **Figure 1.10** shows different routes for hydrogen production from biomass and ethanol [20].

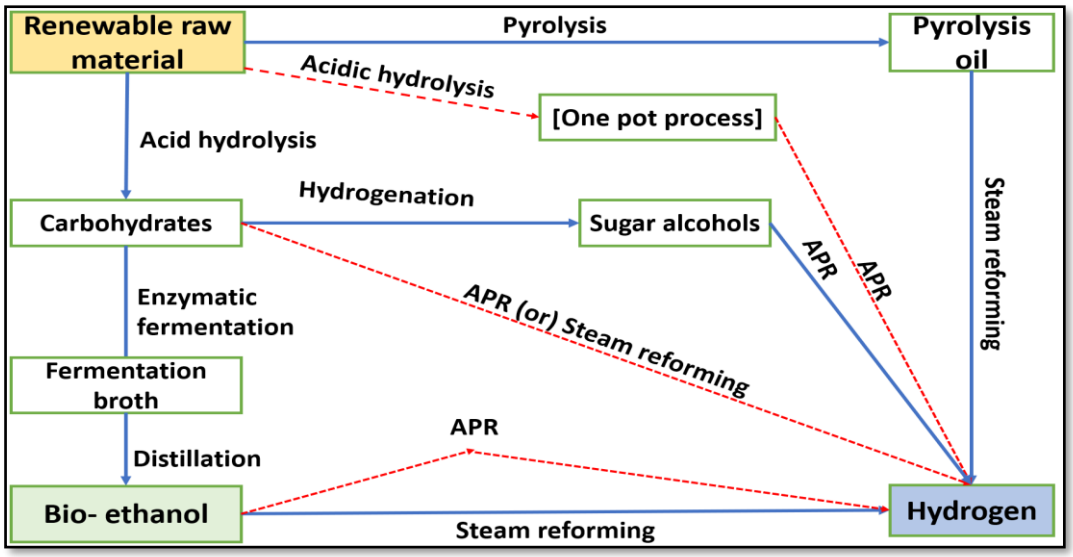

Figure 1. 10: Hyderogen prodcution from different routes [**Sources:** [20]].

The first generation of ethanol is made from foods that are high in sugar and starch, like sugarcane, corn, wheat, and potatoes. Although, there is a problem with using these substrates, which are meant to be food or feed. So, the price of 1st generation ethanol is relatively high. Since it is made from lignocellulosic biomass, 2nd generation ethanol is an alternative to 1st generation ethanol. This feedstock includes waste from the paper industry and wood processing, as well as waste from

agriculture and forestry. Researchers are looking into how to turn this lignocellulosic biomass into ethanol in an efficient way.

Potentially, the amount of ethanol that can be made from lignocellulosic biomass increases from 270 liters per tonne in 2010 to 400 liters per tonne in 2016 [21,22]. In the past ten years, ethanol production has increased in agriculture-based nations such as India, Brazil, and the United States. The ethanol production (million gallons) in major countries is depicted in **Fig. 1.11**. India has an abundance of inexpensive cellulosic biomass, which can be utilized for the manufacturing of ethanol to meet future energy demands [23].

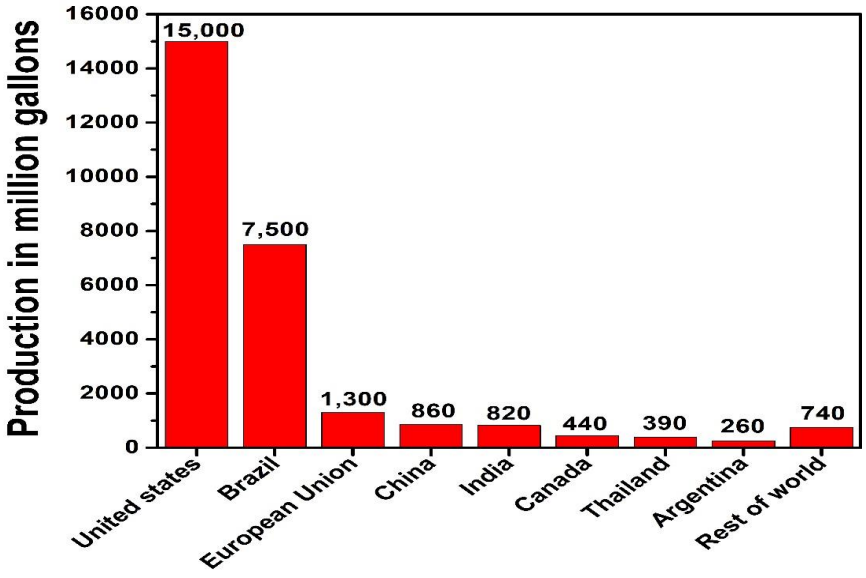

Figure 1. 11: Worldwide ethanol fuel production in major countries, 2022 [**Sources:** [23]].

1.4 Reforming Technology for the Production of Hydrogen

A well-developed technology called reforming pass the hydrocarbons over a catalyst at high temperature—typically between 400 and 800 ℃ and transform hydrocarbons into molecular hydrogen, carbon dioxide, or syngas (hydrogen and carbon monoxide). According to the Department of Energy (DOE) Office of Science Basic Energy Sciences program, USA, catalyst is a substance that speeds up a chemical reaction, or lowers the temperature or pressure needed to start one, without itself being consumed during the reaction. Catalysis is the process of adding a catalyst to facilitate a reaction [24]. Chemical reaction comprises breaking and forming of the bonds between the atoms in the molecules. At the same time reaction means that the atoms might be rearranged and recombined in the form of molecules. According to the collision theory the reacting molecules/atoms/ particles collide with each other in order to chemical reaction to happen. If a catalyst is involved in the reaction, then it would make this process more efficient by lowering the activation energy (**Fig. 1.12**). The activation energy is much higher for the reaction without catalyst, for example synthesis of ammonia. Without catalyst (Eq. 1.1) the required energy is high.

$$\frac{1}{2}N_2(g) + \frac{3}{2}H_2(g) \rightarrow NH_3(g) \qquad E_a = 200 \text{ kJ/mol} \qquad (1.1)$$

However, via Haber process by using iron catalysts, the reaction can go via multiple intermediates and the overall activation energy becomes less [25]. The reactions are as follows:

$$\frac{1}{2}N_2(g) + \frac{3}{2}H_2(g) \rightarrow N\ (ads) + 3H\ (ads) \qquad (1.2)$$

$$N\ (ads) + 3H\ (ads) \rightarrow NH(ads) + 2H\ (ads) \qquad (1.3)$$

$$NH\ (ads) + 2H\ (ads) \rightarrow NH_2(ads) + H\ (ads) \qquad (1.4)$$

$$NH_2(ads) + H\ (ads) \rightarrow NH_3(ads) \qquad (1.5)$$

$$NH_3(ads) \rightarrow NH_3(g) \qquad (1.6)$$

Overall equation

$$\frac{1}{2}N_2(g) + \frac{3}{2}H_2(g) \rightarrow NH_3(g) \qquad E_a = -46 \text{ kJ/mol} \qquad (1.7)$$

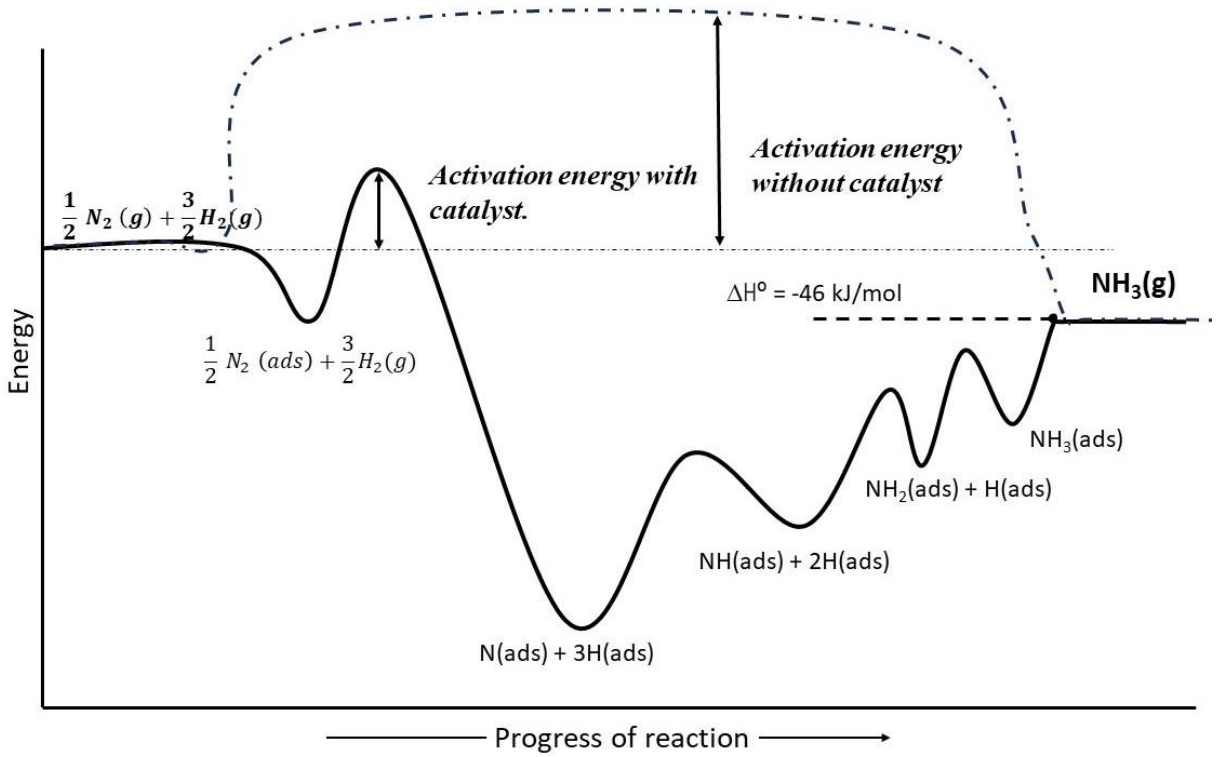

Figure 1. 12: The activation energy barriers for the reactions occurring during the synthesis of ammonia with catalyst (shown in solid line) and without catalyst (shown in dotted line) [**Sources:** [25]].

As a result, catalysts make it easier for atoms to break and form chemical bonds to produce new combinations and new substances. Using catalysts leads to faster, more energy-efficient chemical reactions.

Catalysts also have a key property called selectivity, by which they can direct a reaction to increase the amount of desired product and reduce the amount of unwanted byproducts. They can produce entirely new materials with entirely new potential uses. Over the past several decades, scientists

have developed increasingly specialized catalysts for essential real-world applications. In particular, powerful catalysts have transformed the chemical industry [26]. These advances have led to biodegradable plastics, new pharmaceuticals, and environmentally safer fuels and fertilizers [24].

The reforming process typically involves several major reactions. Most of the time, hydrogen (H_2) and carbon dioxide (CO_2) are the main products of a complete reaction. Carbon monoxide (CO) and methane (CH_4), on the other hand, may also be made during the process. There has been a lot of research and development on reforming to date. Some of these are steam reforming, dry gas reforming (also called CO_2 reforming), hydrothermal reforming (also called aqueous phase reforming), partial oxidation, and autothermal reforming.

1.4.1 Dry Reforming

Dry reforming, also referred to as carbon dioxide reforming, is a reforming reaction that produces syngas (includes hydrogen and carbon monoxide), from oxygenates and carbon dioxide. Most of the researchers has been studied ethanol so far in the context of dry reforming as compared to the other hydrocarbons [27,28]. In the early years dry reforming research was used to transform ethanol into carbon nanotubes with filaments while also making hydrogen [29]. As a catalyst, stainless steel 316 was used to make sure that the carbon deposits were easy to remove. For the best results, SS316 was heated to 800 ℃ before the experiment [29]. Dry reforming of ethanol (DRE) is a highly endothermic process. Following is the stoichiometric reaction of DRE:

$$C_2H_5OH + CO_2 \rightarrow 3CO + 3H_2 \qquad (\Delta H_{25}^{\circ} = 296.7 \text{ kJ/mol}) \qquad (1.8)$$

However, the above reaction needs to be carefully controlled since there are many competitive side reactions taking place, such as dehydrogenation of ethanol to acetaldehyde, dehydration of ethanol to ethylene or decomposition of ethanol into CO, CO_2 or acetone [30].

1.4.2 Aqueous Phase Reforming

Aqueous phase reforming (APR), commonly referred to as hydrothermal reforming, is a process of reforming in an aqueous phase (**Fig. 1.10**). This is a reforming technique that operates in the presence of excess water, at lower temperatures (usually 200 to 300 ℃), and high pressure up to 60 bars. The low temperature and high pressure make it easier to separate H_2 and CO_2 from other products that are volatile at atmospheric pressure [20]. The presence of oxygen, which weakens the C-C bond, enables easier splitting of hydrogen and CO. Then CO could be transformed to CO_2 via the water gas shift process. In addition, APR is advantageous for producing H_2 for a fuel cell with a negligible amount of CO in a single reactor, as the water gas shift (WGS) reaction is thermodynamically permitted at lower temperature reaction conditions [31].

1.4.3 Partial Oxidation

Partial oxidation is a reforming technique that converts oxygenated hydrocarbons into hydrogen and CO_2 or syngas in the presence of oxygen at temperatures and pressures between 1300 -1500 ℃ and 3 - 8 megapascals (MPa), respectively. The amount of air or oxygen needs to be regulated carefully to produce the best results, because complete oxidation (extra air supply) would entirely burn the fuel or reactant and lower the amount of hydrogen in final product [30]. The following stoichiometric equation of partial oxidation could be applied to all oxygenates:

$$C_aH_bO_c + \frac{(2a-c)}{2} O_2 \rightarrow aCO_2 + \frac{y}{2} H_2 \quad (1.9)$$

Catalytic partial oxidation is a low-cost alternative to syngas production. The exothermic nature of reaction is challenging to control reaction temperature [31]. It results in coke deposition and hot spot formation, which deactivates the catalysts over time. Extensive partial oxidation studies (thermodynamic research or experimental work) have been conducted on ethanol [32,33], but relatively few on glycol and glycerol [34,35]. Ethanol or propylene glycol would need an additional half mol of oxygen to produce syn gas (CO and H_2), which is less than what is needed to produce CO_2 and H_2. However, since the O/C ratios of ethylene glycol and glycerol are both 1, stoichiometrically these wouldn't need any additional air to break down into syngas.

1.4.4 Autothermal Reforming (ATR)

Autothermal reforming (ATR), also known as oxidative steam reforming (OSR), is a combination of a highly exothermic partial oxidation process and an endothermic steam reforming reaction [30]. A general stoichiometric reaction as follows:

$$C_aH_bO_c + [2a-(c+1)]H_2O + \frac{1}{2} O_2 \rightarrow aCO_2 + \frac{2[2a-(c+1)]+b}{2} H_2 \quad (1.10)$$

Considering ethanol as an example of a hydrocarbon undergoing autothermal reforming,

Partial oxidation reaction of ethanol is

$$C_2H_5OH + \frac{1}{2} O_2 \rightarrow 2CO + 3H_2 \quad (\Delta H^{\circ}_{25} = 54 \text{ kJ/mol}) \quad (1.11)$$

then the combination of partial oxidation and steam reforming of ethanol is as follows

$$C_2H_5OH + \frac{1}{2} O_2 + 2H_2O \rightarrow 2CO_2 + 5H_2 \quad (\Delta H^{\circ}_{25} = -28.4 \text{ kJ/mol}) \quad (1.12)$$

The autothermal reforming is usually operated between 500 – 800 ℃ under atmospheric pressure. Autothermal, which is based on the idea of self-sustained reforming, saves more energy, makes it easier to control the temperature of the system, and avoids catalyst deactivation by sintering or carbon deposition [36]. According to Aartun et al. [37], ATR or OSR has the main advantage of an extremely exothermic initial oxidation reaction which can produce heat for the succeeding endothermic reforming reactions. As a result, this method has tremendous potential for reducing heating costs while also increasing the amount of hydrogen produced. However, autothermal reforming is difficult to manage for a steady-state operation. Due to thermodynamic limitations, the efficiency of autothermal

reforming is always countered by a lower hydrogen yield compared to steam reforming. If air is used to separate, the process is expensive. However, if pure oxygen is utilized, it is necessary to build an extra plant for oxygen generation, resulting in extremely expensive costs [30]. Chen et al. [38] did a literature survey on OSR and autothermal reforming for different number of noble metal catalysts and oxide supports. They reported that OSR is applied when oxygen is supplied with external heating, whereas autothermal reforming operates simply on the amount of oxygen injected to increase the temperature.

1.4.5 Catalytic Reforming

Catalytic reforming is often used in oil refineries to change low-octane liquid hydrocarbons into more valuable high-octane components without making big changes to their carbon numbers [39]. Reactions like dehydrogenation, dehydro-isomerization, isomerization, dehydrocyclization, hydrocracking, hydrogenation, and carbon formation can happen in a catalytic reformer [39]. Hydrogen is mostly made as a byproduct of this technology, but it is also used in the hydrogenation and hydrogenolysis reactions [30]. In a petroleum refinery, catalytic reforming is usually done at temperatures around 500 °C, and the pressure inside the reactor changes depending on the quality of the feedstock [39]. High-pressure processes (20-50 bar), medium pressure (10-20 bar), and low-pressure (3-10 bar) are all possible. Although a significant amount of hydrogen may be produced as a byproduct of catalytic reforming of oxygenated hydrocarbons, this is greatly desired for hydrodeoxygenation in biofuel refineries [36].

1.4.6 Steam Reforming Process

Steam reforming has been known for more than 100 years. Probably it is the most well developed and established reforming technology applied in the petrochemical industries to convert natural gas (mainly methane) into hydrogen. For the past 50 years, its end products, has been used in the commercial production of fuels, various organic compounds, fuel cells and chemicals mainly in NH_3 industry [40]. Hence, currently a big portion of the research works is focused on applying steam reforming for converting biomass or biomass derived hydrocarbons, e.g. methanol, ethanol, glycerol, dimethyl ether or heavier hydrocarbons ($C_3 - C_{10}$ components) to energy sources. Challenges regarding hydrogen production technology are lowering the cost of production at least by a factor of 3-4 and improving production rates. The stoichiometric reaction for hydrocarbons are as follows [30,31]:

$$C_xH_yO_z + (2x - z)H_2O \rightarrow xCO_2 + \left(\frac{2(2x-z)+y}{2}\right)H_2 \quad (1.13)$$

$$C_xH_y + (2x)H_2O \rightarrow xCO_2 + \left(2x + \frac{y}{2}\right)H_2 \quad (1.14)$$

There are two steps to this process. In the first step, the raw hydrocarbons are mixed with steam and passed over the catalyst, generally takes place inside a tubular reactor. Here high CO syngas is

made [41]. Later in the second stage, the cooled product gas from step 1 is put into the CO catalytic converter, where steam is used to change most of the CO into carbon dioxide and hydrogen. Steam reforming reactions required high temperature (400 – 1000 ℃) but generally no atmospheric pressure, but, sometimes, elevated pressure is used in industrial practices. Additionally, the difficulties with this technology are generally attributed to coking, which is similarly related to thermodynamic constraints and catalyst activity at high temperatures, results the catalyst deactivation [42].

1.5 Steam Reforming of Ethanol for Hydrogen Production

Ethanol steam reforming (ESR) would be a great way to make hydrogen from ethanol with the current industrial infrastructure. In the past 20 years researchers have been working on low-temperature steam reforming to make H_2 from ethanol at mild operating conditions (≤ 500 °C). It has many advantages over high-temperature steam reforming, such as low operational and material costs and a small amount of CO in the product gas. Marino et al. reported for the first time in 1998 that low-temperature steam reforming of ethanol can be used to make hydrogen over a Cu-Ni supported catalyst [43]. Also, the temperature conditions used help the water-gas shift reaction, while CO and H_2 do not need to be separated, which lowers the capital cost. The temperature range for ESR is quite wide, ranging from 300 – 850 ℃ [44,45]**.** In the presence of a properly designed catalyst, it is possible to achieve complete conversion of ethanol at 350 ℃ under atmospheric pressure [46]. The theoretical steam reforming reaction of ethanol could be as follows:

$$C_2H_5OH\ (g) + 3H_2O(g) \leftrightarrow 2CO_2\ (g) + 6H_2\ (g) \qquad (\Delta H^{o}_{25} = +173\ kJ/mol) \qquad (1.15)$$

Although, like other reforming technologies, it is not a single step reaction, and several steps/intermediates are involved in the process depending on the catalytic system and reforming conditions used. Both thermodynamics and kinetics control the process and the end products. **Fig. 1.13** shows a flowchart with general **r**eaction pathways that can occur during ESR over metal catalysts [47]. In order to achieve high H_2 selectivity on a metallic catalyst low acidic nature supports are required. Other important beneficial factors are that the catalysts should have a high C-C bond breaking rate, a low C-O breaking rate, and a low methanation reaction rate. Monometallic noble catalysts, such as Pt, depending on the support could demonstrate high H_2 selectivity for ESR at low temperatures (200-500 C). However, the high cost of Pt makes it economically infeasible to use.

According to Sinfelt et al. [48], Grenoble et al. [49], and Vannice et al. [50] compared to Co, Pt, Pd, Fe, Ir, and Rh catalysts, Ni has higher rate of C-C bond breakage rate, reasonably good water gas shift activity, and moderate methanation reaction capacity. These traits make Ni a potential catalyst for ESR. Cerium oxide (CeO_2) a fluorite structured ceramic oxide either as a sole support or as an additive is well known to enhance the catalytic activity of metal-oxide catalyst systems. It increases oxygen storage capacity, buttresses the metal dispersion of the three way auto catalysts, and enhances

CO to CO_2 conversion as a consequence [51–56]. More regarding the Ni/CeO_2 catalyst and importance of the modification of this system is discussed in chapter 2: Literature review.

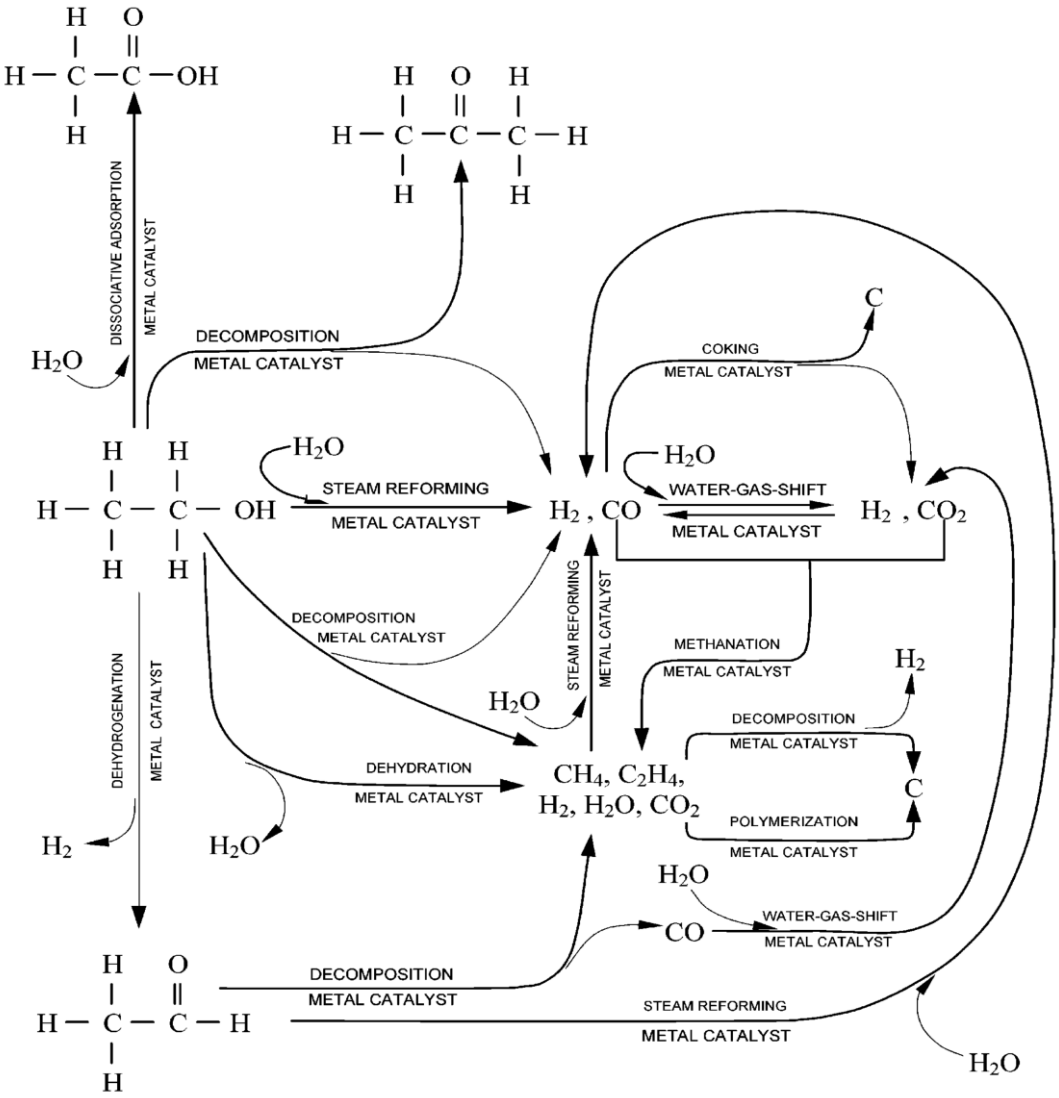

Figure 1. 13: General reaction pathways for ethanol steam reforming over metal catalysts [**Sources:** [47]].

1.6 Thesis organization

The thesis is organized in five chapter and purpose of those chapters are explained as follows:

Chapter 1: Introduction: This chapter opens with the idea of energy scenario, supply and climate change and the importance of renewable energy sources**.** Use of hydrogen in current and future market or hydrogen economy is discussed in short. Different techniques for hydrogen production, importance of Steam reforming of ethanol for hydrogen production**,** and catalysts for the purpose is addressed. At the end, the thesis organization is described.

Chapter 2- Literature review: This chapter examines the research articles published on the modification of Ni by various noble and non-noble metals and on alteration of the supports by different metal oxides in detail and their effect on ESR all through 2000-2023. Based on this literature review the research gap and the objective of the work is deduced. Slightly modified version of this review is published in an international journal on February 2022; https://doi.org/10.1016/j.ijhydene.2021.12.183

Chapter 3-Materials and methods: This chapter mentions the general methods to prepare heterogeneous nano catalysis, however emphasis is given on SCS and Ultra sonication assisted SCS techniques. Detailed information on the catalyst's preparation steps was provided. The physico-chemical characterization techniques used to understand the fresh, reduced and used catalysts are addressed. Finally, the experimental setup, procedure for catalytic activity study, and the equations applied to analyze the activity data are explained in detail.

Chapter 4-Results and Discussion: This chapter is a combination of several works and divided in three sub chapters as follows:

Section 4.1: This work focuses on the development of Ni-Sn bimetallic catalysts supported on ZrO_2 modified CeO_2 and their application for low temperature steam reforming of ethanol (LTSRE) at different temperature 200– 400 ℃. ZrO_2 observes to change the support chemistry and enhances the activity and stability of the catalyst. At 400 ℃, 100 % ethanol (EtOH) conversion, 68 % H_2 selectivity with least coke deposition is detected for the catalyst with 5 wt.% metal (Ni: Sn = 14:1) loading on Ce:Zr 1:2 mol ratio (NiSn5/CZ12) support. This work is published in an international journal in November 2022; https://doi.org/10.1016/j.matpr.2022.11.231

Section 4.2: This chapter presents the effect of metal loading and support modification of Ni-Sn/CeO_2 catalysts on low temperature steam reforming of ethanol (LTSRE). The catalyst with 5 wt.% total metal loading, Ni:Sn atomic ratio 14:1, and Ce:Mg mol ratio 1:2 observed to the best in terms of EtOH conversion, H_2 selectivity 72%, and with coke deposition. Various physicochemical properties of the Ni-Sn/Ce-Mg-O powders are inspected and correlated with the catalytic activities. This work is published in an international journal in January 2023; https://doi.org/10.1016/j.ijhydene.2023.01.039

Section 4.3: This study presents the effect of lanthanum (as support modifier) and tin (promoting the Ni) addition on Ni_YSn_{1-Y}(wt.%)/$Ce_{1-X}La_XO_2$ (X= 0.33, 0.5, 0.67 mole ratio and Y= 0.93, 0.87, 0.5 atomic ratio) catalysts for hydrogen synthesis by LTSRE. Various physicochemical characterization and activity results show that optimal amounts of lanthanum and tin help to enhance the catalytic performance. The $Ni_{0.93}Sn_{0.07}$(5)/$Ce_{0.67}La_{0.33}O_2$ catalyst demonstrates the maximum H_2 selectivity of 60% and 100 % EtOH conversion. This work is submitted in an international journal and under review.

Chapter 5: Conclusions and future scope: This chapter presents the overall conclusions of this work. Most important catalytic activity related results of the three groups of catalysts are presented in a tabular form and summarized. Finally, the scope of the future research is elaborated.

Chapter 2: Literature Review

The accelerated growth of the world population (at present around 7.3 billion and estimated to reach 9.7 billion by 2050) [57] and industrialization enhance the demand for energy, which is expected to increase by one-third of the present by 2040 as projected by the International Energy Agency (IEA) [58]. Currently, 84% of the total energy consumed worldwide is from fossil fuels, majority liquid fuels and petroleum. The average consumption of fossil fuels is increasing at a rate of 1.1% per year [3], leading to an accelerated increase of environmental pollution. The global mean concentration of CO_2 in the atmosphere is 410 ppm [59], rising at a rate of approximately 2 ppm/year, and predicted to exceed 450 ppm by 2050 [60]. The current atmospheric average concentration of methane (CH_4), nitrous oxide (N_2O), oxides of nitrogen (NOx), and sulphur (SO_X) are estimated to be 1870.5, 332, 60, and 20 ppb, respectively, with an average annual rate of increase 10.1, 0.9, 0.7 and 0.01 ppb, respectively [59]. These greenhouse gases (GHG) are considered the leading causes of climate change, global warming, health hazard, and agricultural damage. Worldwide roughly ten million health problem related cases (respiratory allergies, cardiovascular diseases and stroke, mental health and stress-related disorders, cancers, etc.) are caused by GHG emission annually. As per the report of WHO, globally 3 million air pollution and continual climate change related deaths are caused per year, and it is expected to increase at a rate of 0.25 million per year between 2030 and 2050. United Nations environment estimates an annual global crops loss of 30 million tons due to environmental pollution [61,62]. Owing to the setbacks of the conventional energy sources, alternative renewable clean energy sources are highly recommended, and hydrogen is one. It has a very high energy content per unit mass, almost three times higher than gasoline of about 121-142 kJ/gm [63].

In India, the national renewable energy act 2015 is drafted to promote renewable energy sources, reduce dependence on fossil fuels, ensure the security of energy supply, encourage macroeconomic development, and reduce emissions of CO_2 and other greenhouse gases with climate & environmental considerations [63]. National Hydrogen Energy Mission (NHM) initiative taken under the Ministry of New and Renewable Energy (MNRE); Government of India aims to produce hydrogen energy of 10 GW from bio-sources (part of India's ambitious goal of generating 175 GW Renewable energy) by 2022. The roadmap drawn under this mission would help India to meet the emission goals of the Paris Agreement [64–66].

The present use of industrial hydrogen is primarily for commercial chemical production, hydrocracking, and hydro-treatment in refineries. However, the upcoming applications are mainly targeted in replacing conventional energy sources in transportation, such as fuel-cell train (Alstom) [67], vehicles, internal combustion engine (ICE) (Alset Global GmbH, BMW), etc. Most of the major automobile manufacturers like Suzuki, Audi, Ford Motors, GM, Nissan, Kia, Toyota, Honda, Mercedes-

Benz, Hyundai, and Tesla, show interest in manufacturing of commercial hydrogen fuel-cell based vehicles [68,69].

Hydrogen is industrially manufactured by various processes like catalytic partial oxidation, steam reforming (SR), dry reforming, aqueous phase reforming, auto-thermal decomposition of hydrocarbons and coal, petroleum gasification, fermentation (biological ways), water electrolysis and solar thermochemical water splitting [70]. SR is a well-established, widely used, highly energy-efficient, and cost-effective process [71–76]. Various hydrocarbons in gas, solid, or liquid states are suitably used as feed for SR. Ethanol could be a potential commercial feedstock because of its wide availability, and India is the fourth-largest producer of ethanol in the world [77]. Also, Bio-ethanol is a renewable energy source produced from starch-rich substrates [19].

Several ceramic support (single or in combination; Al_2O_3, MgO, La_2O_3, SiO_2, TiO_2, CeO_2, activated C, ZrO_2, ZnO, zeolites-Y, hydrotalcite, etc.) based metallic (Pt, Ni, Ru, Rh, Pd, Ir, Co, Cu, Zn, Fe, etc., used as single or in alloy form) catalysts or metallic catalysts without any support (Raney NiSn) have been studied for hydrogen production from SR of ethanol (ESR). High hydrogen production rate and low production cost are desirable for the successful hydrogen economy, which require optimization of physicochemical properties of catalysts (controlled by chemistry and preparation conditions) and the reforming conditions (temperature, water/ethanol ratio, feed flow rate, contact time, environment, etc.). High reforming temperature ($T > 500\ ^{\circ}C$) and high water to ethanol ratio is more suitable for ESR. Ni, Co, and Cu are figured to be the best catalysts in the category of non-noble metals and Ni is the commonly used active metal because of its wide availability and low cost. Nickel also promotes favourable C-C and C-H bond breakage. In some cases, synergetic effect of Ni and the additives has proven to increase the selectivity of hydrogen and catalytic activity. The addition of additives and promoters together has also helped to stabilize the catalyst for a long time by reducing carbon deposition and nickel oxidation [70,78]. A number of Ni catalysts, supported on different inorganic oxides, such as Al_2O_3, CeO_2, ZnO, La_2O_3, SiO_2, MgO, ZrO_2, TiO_2, are studied for hydrogen production from steam reforming of several renewable feeds such as ethanol [79–81], acetic acid [82], biomass[83], methanol [84] and glycerol [85]. Al_2O_3 and CeO_2 based catalysts are considered effective in terms of high hydrogen production and less carbon formation. Sharma et al. (2017) compare the deactivation rate of the Al_2O_3, CeO_2, ZnO, MgO, ZrO_2 and SiO_2 supported Ni catalysts used for hydrogen production from low temperature ESR. The decreasing order of activity of these support systems is identified to be $CeO_2 > Al_2O_3 > ZrO_2$ [81]**.** According to a thorough Scopus database search on 'Ethanol Steam Reforming' and 'Ni' catalysts, the number of articles published on different ceramic supports are found to be as follows: Al_2O_3-56 articles, CeO_2- 43 articles, SiO_2-27 articles, ZrO_2-24 articles, ZnO-21 articles, La_2O_3-21 articles**,** MgO-13 articles, and TiO_2-5 articles. Based on the above discussion, Ni (as active metal) and CeO_2 & Al_2O_3 (as a support) could be considered as the potential candidates for hydrogen production using ESR.

According to Scopus database, 1460 research articles and 54 reviews have been published on 'Ethanol Steam Reforming' for 'hydrogen production' within the last two decades. The additional search words 'Ni' (580 research articles and 15 reviews), 'Al_2O_3' (56 research articles and 1 review), and 'CeO_2' (43 research articles and no review), are used to narrow down the set. Finally, the papers are verified manually to pick only the relevant publications (**Figs. 2.1(a)** and **(b)**). The cumulative numbers shown in Figs**. 2.1(a)** and **(b)** are the most relevant publications and are tabulated in **Tables 2.2** and **2.3**. **Figs. 2.1(a)** and **1(b)** disclose an interesting trend: the remarkable development of CeO_2 supported Ni-catalysts in 2015 is overtaken by Al_2O_3 supported Ni-catalysts in 2016 but sees a steady decline afterward. The ESR related review articles, which discussed hydrogen production and Ni catalysts, have been summarized in **Table 2.1**. Initially (2005-2011) the review papers mostly discuss & compare different hydrogen production processes, explored reaction pathways & mechanisms for ESR, cover thermodynamic approach for deciding reforming conditions, review different noble & non-noble metal catalysts in general for ESR, etc. In the next five years (2011-2016), review papers focus on the general combinations of the active metals and possible supports. They examine the effects of the physicochemical properties of the catalysts and the reforming conditions on the performance and stability of the catalysts. More in-depth thinking towards understanding the chemistry of the catalysts (such as importance of metal surface electronic properties and their modification via alloy formation, effect of the support oxygen mobility in the catalyst performance, etc.) is evident. In the last five years (2017-2020), review papers explore different modification strategies for the metal and support combinations, discuss performance of Ni- based Co- based, and Ni-Co based catalyst systems on different supports, etc. [19,47,92–97,78,81,86–91].

Vast amount of research articles are found on ESR over Ni/Al_2O_3 and Ni/CeO_2 based catalysts (**Figs. 2.1(a)** and **(b)**), but there is no in detail review article on those catalysts specifically. Hence, in this paper, a detailed investigation on Ni/Al_2O_3 and Ni/CeO_2 based catalysts is carried out. Various factors, such as modification of the active metal as well as support materials, metal loading, catalyst preparation methods, reforming conditions, and the effects of these parameters on catalyst performance are examined. Basic reaction mechanisms and involved thermodynamics are discussed for a better understanding.

2.1 Background of Ni Catalysts used in ESR

Sabatier's Nobel prize-winning work in the early 1900s could be considered as the starting point of Ni as a catalyst. Sabatier and Mailhe's research on the development of metallic oxide based catalysts for dehydrogenation, hydrogenation, dehydration, and hydration led to the application of Ni catalyst in the petroleum industry [98]. In 1913, Badische Anilin und Soda Fabrik (BASF, German multinational chemical company) patented Ni catalyst for SR. During World War I, the increased demand for explosives enhanced hydrogen consumption in ammonia production by Haber's process. This steered

to the commercialization of methane (sourced from coke gasification) SR in the 1930s to produce syngas using a Ni-based 'ICI catalyst 22-1', manufactured by Imperial Chemical Industries (ICI) London [99]. Until the 1955s, Ni catalysts were mostly applied on hydrogenation and methanation. After 1955, research focused on the commercialization of naphtha SR. In 1962, the birth year of the Journal of Catalysis (the first journal dedicated to catalysis), $NiK_2Al_2O_3$ complex oxide was introduced as a catalyst for the SR of naphtha and commercially sold under the tradename "KATALCO" [100].

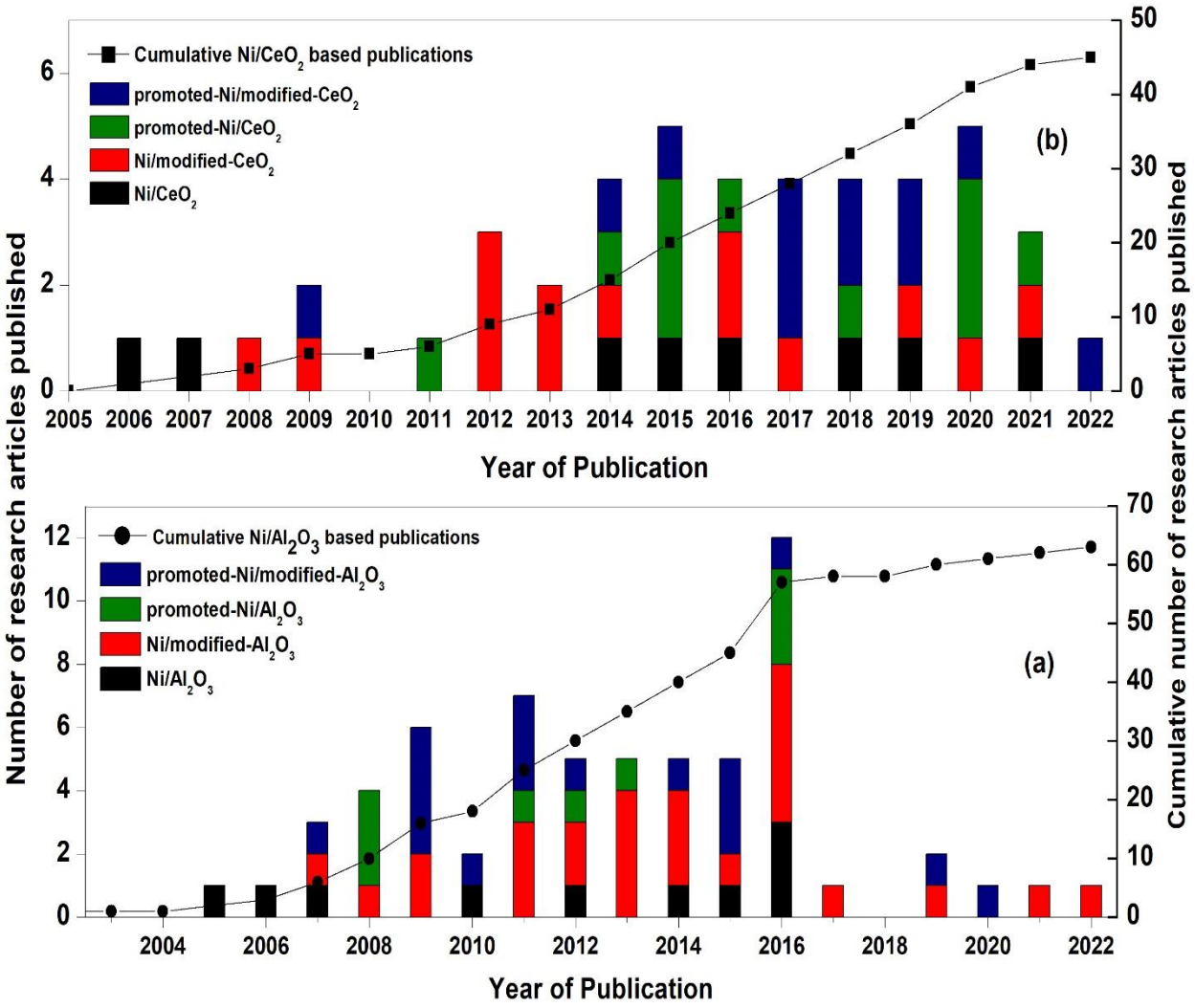

Figure 2. 1: Number of the articles published on ethanol steam reforming catalysts with year of publications for (a) Ni/Al_2O_3 based catalysts and (b) Ni/CeO_2 based catalysts. Data is collected from Scopus database.

The 1970's energy crisis led to the discovery of natural gas, and it eventually became the choice of feedstock for hydrogen production based on geographical availability [101]. Until 1970, research mainly focused on reforming reaction conditions, which affect the catalytic activity, and surface area of the supported Ni. The introduction of naphtha and natural gas as feedstock triggered studies focused on the change in catalyst support chemistry for reducing acidity.

Table 2. 1: Summary of review papers on ethanol steam reforming and hydrogen production 2000 – 2023.

SN	Article Title	Review Focus/ Review Aim/ Review Aim and Scope/ Review Objective	Ref
1.	A review on ethanol steam reforming for hydrogen production over Ni/Al_2O_3 and Ni/CeO_2 based catalyst powders.	• Detailed reaction mechanism on Ni/Al_2O_3 and Ni/CeO_2 based catalysts during ESR. • Ni/Al_2O_3 and Ni/CeO_2 based catalysts modification metal and support on SRE. • Thermodynamics and major ways for deactivation of the catalysts.	[45] 2022
2.	Modification strategies for enhancing anti-coking of Ni-, Co-based catalysts during ethanol steam reforming: A review	• Strategies for enhancing anti coking ability for modification of active metal and support. • Summary of carbon deposition during ESR over Ni-based catalysts.	[102] 2022
3.	Effect of Supports and Promoters on the Performance of Ni-Based Catalysts in Ethanol Steam Reforming	• Effect of Support Modifiers, active metal promoters, and Catalyst preparation method on catalysts performance	[93] 2020
4.	Recent progress in ethanol steam reforming using non-noble transition metal catalysts: A review	• General reaction mechanism proposed. • Performance of Co-, Ni- and Ni-Co based catalyst on different supports discussed.	[94] 2020
5.	Steam reforming of methanol, ethanol, and glycerol over nickel-based catalysts -A review	• Role and performance of Ni- (on different supports) catalysts for steam reforming of methanol, ethanol, and glycerol. • Effect of active metal and catalyst support on product distribution and conversion of alcohols. • Possible reaction pathways/mechanisms	[95] 2020
6.	Ethanol steam reforming for hydrogen production: Latest and effective catalyst modification strategies to minimize carbonaceous deactivation	• Possible Reaction mechanism and their effects on type of C deposition. • Effect of reforming conditions on C deposition. • Modification strategy of the metal and support. • Effect of preparation methods, precursor, and conditions on C deposition.	[81] 2017
7.	Catalytic steam reforming of Ethanol for hydrogen production: Brief status	• Reviewed different Noble metals & non- Noble metals catalysts in general. Not specific	[96] 2016
8.	Toward Understanding Metal-Catalysed Ethanol Reforming	• Reaction mechanism and pathways • Effect of the metal particle size on catalyst behaviours • Importance metal surface electronic properties and modification via alloy formation. • Effect of the Support Oxygen Mobility in the Catalyst Performance.	[88] 2015
9.	Hydrogen production from ethanol reforming: Catalysts and reaction mechanism	• Comparison of Noble metals & non- Noble metals in general • Performance of oxide supports especially CeO_2. • Reaction mechanisms based on catalysts. • Kinetic analysis • Catalyst deactivation aspects	[86] 2015
10.	Catalysts for H_2 production using the ethanol steam reforming (a review)	• overview the active metals and possible supports combinations in general.	[87] 2014

		• Examine physicochemical properties of the catalysts and reforming conditions for performance and stability of the catalysts	
11.	Advances in ethanol reforming for the production of hydrogen	• General aspects and Probable reaction mechanisms • Reviewed Noble metals & non- Noble metals catalysts in general. Not specific • Stability aspects of the catalysts • Addressed New technologies for H_2 production via ethanol reforming	[89] 2014
12.	Design of Nano catalysts for Green Hydrogen Production from Bioethanol	• Feedstocks, contaminant, and other general aspects of bioethanol • general features for designing of catalysts. • Performances of the Rh/Al_2O_3 based catalyst	[97] 2012
13.	Hydrogen via steam reforming of liquid bio feedstock	• Explored SR for ethanol and other bio-feedstock. • Discussed catalyst developments in general. • Examines Thermodynamic aspects of ESR	[90] 2012
14.	Production of Hydrogen from Ethanol: Review of Reaction Mechanism and Catalyst Deactivation	• Reaction Pathways • Catalyst Deactivation methods	[91] 2011
15.	Steam-reforming of ethanol for hydrogen production	• Reforming Conditions: Thermodynamic approach • Reviewed different Noble metals & non- Noble metals catalysts in general. Not specific • Discuss Effect of impurities in bioethanol on ESR • ESR mechanism	[92] 2011
16.	A review on reforming bioethanol for hydrogen production	• Reviewed different Noble metals & non- Noble metals catalysts in general for reforming of bioethanol. Not specific • Addressed autothermal reforming of bioethanol.	[19] 2007
17.	Current Status of Hydrogen Production Techniques by Steam Reforming of Ethanol: A Review	• Discuss & Compare different Hydrogen Production Processes • Explore Reaction pathways for ESR. • Examines different ESR catalysts in general. Not specific.	[47] 2005

The addition of potash and other alkali oxides helped reduce support's acidity but hindered catalyst activity. Some researchers examined the application of active magnesia and other supports instead of alkali oxides. In the 1990s, awareness about climate changes, global warming, and greenhouse gas effect led to the talks on alternative fuels and the hydrogen economy. The researchers showed interest in the production of hydrogen from renewable sources to reduce fossil fuel dependency. Methanol and ethanol were suggested as possible feedstocks for SR. Although methanol is highly abundant, ethanol is favored as it is less toxic and easily obtained from renewable sources like biomass [88].

2.2 Basic Mechanisms

Though noble precious metals show better performances than nickel in ESR activity and stability, nickel is economically more viable. The step edges of Ni particles exhibit high C-C bond breaking capacity and thus, hydrogenation and hydrogenolysis reactions of hydrocarbons occur on Ni catalyst. These step sites have very high site selectivity and play a role in determining catalytic activity [88]. Zanchet et al. and others discuss the ESR mechanism on the Ni/Al_2O_3 catalyst surface [88,103–106]. The ethanol hydroxyl group adsorbs on the nickel surface and forms $CH_3CH_2O^{ads}$ (superscript 'ads' indicates the species adsorbed on the catalyst) (E_a = 86.10 kJ/mol) intermediate by dehydrogenation process (**Fig. 2.2**, step 1). Due to the acidic nature of alumina support, the reaction may proceed in three directions. In one direction (step 2b), the $CH_3CH_2O^{ads}$ dehydrogenates to form acetaldehyde radical CH_3CHO^{ads} (E_a=207.9 kJ/mol and rate constant k= $1.93*10^{22}$ s^{-1} [107,108]). In the other two directions, steps 2a and 2c, the formation of ethylene (via dehydration reaction) and diethyl ether (via etherification) occurs, respectively.

The polymerization of ethane leads to the formation of polymeric carbonate species on the surface of the nickel [109]. The produced acetaldehyde (step 2b) gets dehydrogenated and produces CH_3CO^{ads} (E_a = 11.578 kJ/mol [107,108]) (step 3), which promotes production of CH_3^{ads} and CO^{ads} (step 4a) through the C-C bond scission. From here, reaction can proceed in two ways; one is the formation of surface carbon and hydrogen (step 5a) due to decomposition of methane at a higher temperature and the other is the formation of surface carbon and CO_2 by Boudouard reaction (step 5b). Both reactions further increase the formation of carbon on the surface of the catalyst, thus reducing its activity. From step 3, it is also possible for CH_3CO^{ads} to dehydrogenate to CH_2CO^{ads} (step 4b) followed by $CHCO^{ads}$ (step 5c). The $CHCO^{ads}$ (E_a=107.61 kJ/mol, k=$3.74*10^{12}$ s^{-1} [110]) (step 5c) may create CO^{ads} (and CH^{ads}) via C-C dissociation (step 6a), from which further activation of water leads the water gas shift (WGS) reaction resulting in H_2 and CO_2 production (step 7a). $CHCO^{ads}$ (step 5c) could be hydrogenated to form CH_4 (step 7b). Xu et al., Wang et al. and others elaborately address the ESR mechanism on the Ni/CeO_2 catalyst [111–114]. CeO_2, due to its high oxygen storage capacity (OSC) and oxygen mobility, promotes metal dispersion, enhances coke gasification and WGS reaction that has piqued the researcher's interest as support for ESR catalyst.

The ethanol hydroxyl group gets adsorbed on the nickel surface and forms $CH_3CH_2O^{ads}$ ethoxy specie (E_a=78.15 kJ/mol, and k=2.6*10^5 s^{-1} [115]) intermediate and H* (where * represents intermediates that are not adsorbed on the catalyst) by dehydrogenation process (**Fig. 2.3**, step 1) [115]. The dissociation of $CH_3CH_2O^{ads}$ can proceed in two ways: dehydrogenation (step 2a) and by deoxylation (step 2b). In deoxylation the cleavage of C-O bond in $CH_3CH_2O^{ads}$ occurs which results in the formation of $CH_3CH_2^{ads}$ [112]. Post deoxylation cleavage of C-H bond forms CH_3C^{ads} (step 3b) species followed by the C-C bond scission to form CH_3^{ads} (E_a=410.4 kJ/mol, k=2.10*10^{12} s^{-1} [110]) and carbon (step 4b) [81,89,91,116]. The carbon produced during this process results in the formation of carbon fibers over Ni's surface. The consequence of which the Ni begins to deactivate with time resulting in the loss in catalytic activity.

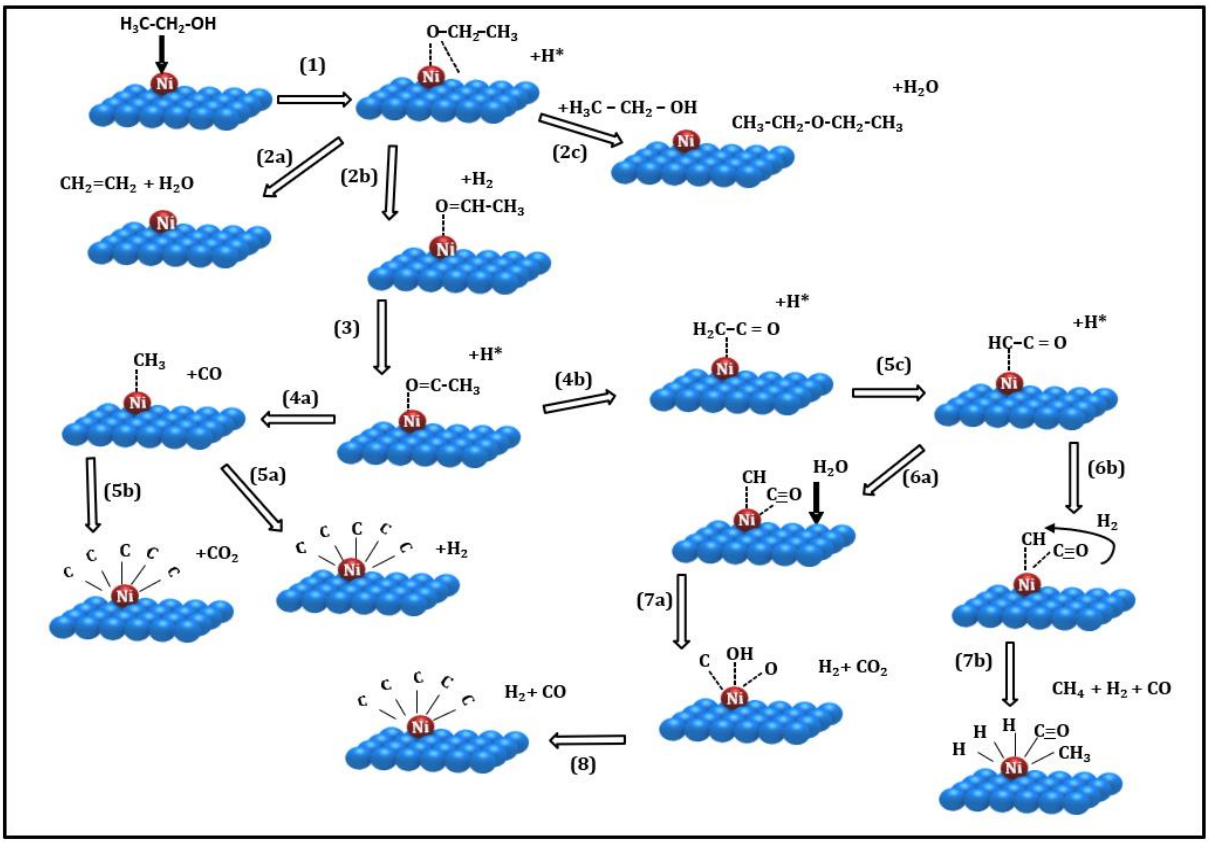

Figure 2. 3: Mechanism of the ethanol steam reforming on Ni/Al_2O_3 catalyst. The blue balls indicate the Al_2O_3 support, red balls are Ni particles, and * denotes free radicals. The solid lines indicate strong chemical bonding, while the dotted lines indicate interaction between catalyst and the intermediate species. The schematic is drawn by the authors based on the work of Zanchet et al. and others [81,89,91,116].

The reaction barrier for deoxylation process is lower (E_a=161.13 kJ/mol) than that of the dehydrogenation process (E_a=323.23 kJ/mol) [112]. When the reaction proceeds through the dehydrogenation of ethoxy (step 2a), the formed acetaldehyde CH_3CHO^{ads} further dehydrogenates to produce acetyl CH_3CO^{ads} (step 3a; E_a=53.73 kJ/mol, k=1.91*10^{11} s^{-1} [117]). Here, due to presence of

dual redox state (Ce^{4+} and Ce^{3+}) the CeO_2 support carries oxygen vacancies which in turn provides the necessary oxygen for the oxidation of acetyl to acetate (CH_3COO^{ads}) (E_a=290.42 kJ/mol [117]) intermediate (step 4a) [111]. The intermediate CH_3COO^{ads} go through C-C bond scission on the nickel surface to produce methyl CH_3^{ads} and carbonate CO_3^{ads} (steps 5a and 6a). The Ce^{3+} helps dissociating water and forms OH surface groups, which reacts with the methyl group and forms CO_2 and H_2 (step 7a), and thus suppresses the formation of CH_4. The hydroxyl group (OH) interacts with the deposited carbon on Ni surface and forms CO_2 and H_2 (step 6b-7b) similarly, thus helping in the catalyst's reactivation.

The critical differences between the mechanisms of these two types of catalysts could be summarized as follows: Two by- products ethylene (dehydration reaction, **Fig. 2.2**, step 2a) and diethyl ether (etherification reaction, **Fig. 2.2**, step 2c) could be observed in case of Ni/Al_2O_3 due to acidic nature of Al_2O_3 but not observed in CeO_2 system. In Ni/Al_2O_3 catalyst system, dehydrogenation is favoured, however deoxylation reaction (**Fig. 2.3**, step2b) is the favoured reaction pathway on Ni/CeO_2 surface due to lower reaction barrier. For Ni/Al_2O_3 catalyst system after CH_3CO^{ads} formation (step 3, **Fig. 2.2**), the reaction proceeds in two ways and both of them lead to carbon deposition and step 7b (**Fig. 2.2**) leads to methane formation. But in Ni/CeO_2 catalyst system after CH_3CO^{ads} formation (step 3a, **Fig. 2.3**), CeO_2 support may supply oxygen atom for oxidation of acetyl to acetate (CH_3COO^{ads}) and these intermediate formed paves way to the WGS reaction pathway. WGS may occur in Ni/Al_2O_3 catalyst system, if conditions are favourable to proceed in step 6a (**Fig. 2.2**) but it cannot result in incomplete catalyst reactivation as observed in Ni/CeO_2 catalyst system (step 7b, **Fig. 2.3**).

2.3 Basic Thermodynamics

Thermodynamic understanding regarding ESR helps to predict possible reaction pathways, yield, and selectivity of the final products. Equation (2.1) shows the overall ideal ESR reaction. Methane decomposition, Boudouard reaction and polymerization of ethylene are the major routes for carbon deposition. All these pathways are affected by the temperature. From the thermodynamic point of view, dehydrogenation (Eq. 2.2), the main step for producing H_2 is highly endothermic and favoured by an increase in temperature [115,117–119].

$$C_2H_5OH\,(g) + 3H_2O\,(g) \leftrightarrow 2CO_2\,(g) + 6H_2\,(g) \quad (\Delta H^0_{25} = +173\ kJ/mol) \qquad (2.1)$$

$$C_2H_5OH\,(g) \leftrightarrow CH_3CHO\,(g) + H_2\,(g) \quad (\Delta H^0_{25} = +68.9\ kJ/mol) \qquad (2.2)$$

Similarly, all reactions involving the production of CO such as ethanol decomposition (2.3), CH_4 SR (2.4) and CH_4 dry reforming (Eq. 2.5) are also favoured at increasing temperature due to their endothermic nature [120].

$$C_2H_5OH\,(g) \leftrightarrow CH_4\,(g) + CO\,(g) + H_2\,(g) \quad (\Delta H^0_{25} = +49\ kJ/mol) \qquad (2.3)$$

$$CH_4\,(g) + H_2O\,(g) \leftrightarrow CO\,(g) + 3H_2\,(g) \quad (\Delta H^0_{25} = +206.2\ kJ/mol) \qquad (2.4)$$

$CH_4\ (g) + CO_2\ (g) \leftrightarrow\ 2CO\ (g) + 2H_2\ (g)$ $(\Delta H^0_{25} = +54\ kJ/mol)$ (2.5)

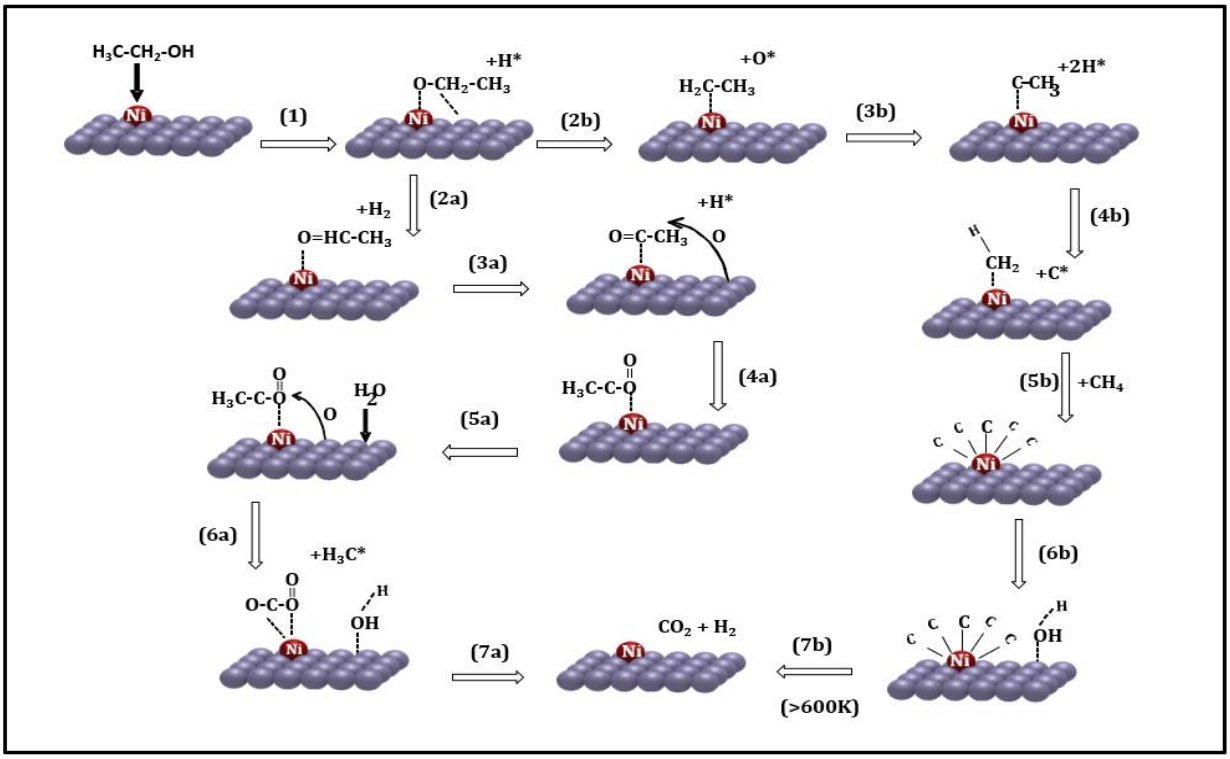

Figure 2. 4: Mechanism of the ethanol steam reforming on Ni/ CeO_2 catalyst. The violet balls indicate the CeO_2 support, red balls are Ni particles, and * denotes free radicals. The solid lines indicate strong chemical bonding, while the dotted lines indicate interaction between catalyst and the intermediate species. The schematic is drawn by the authors based on the work of Xu et al., Wang et al. and others [115,117–119].

Except for the case of ethanol decomposition (Eq. 2.3), all the reactions that lead to the formation of CH_4, such as ethanol hydrogenolysis (Eq. 2.6), acetaldehyde decomposition (Eq. 2.7), are exothermic and thus are favoured at the lower temperature. Moreover, the Boudouard reaction (Eq. 2.8), which is one of the main factors for forming carbon from CO, is disfavoured at the higher temperature [121].

$C_2H_5OH\ (g) + 2H_2\ (g) \leftrightarrow\ 2CH_4\ (g) + H_2O(g)$ $(\Delta H^0_{25} = -156\ kJ/mol)$ (2.6)

$C_2H_4O\ (g) \leftrightarrow\ CH_4\ (g) + CO(g)$ $(\Delta H^0_{25} = -55.8\ kJ/mol)$ (2.7)

$2CO\ (g) \leftrightarrow C\ (s) + CO_2\ (g)$ $(\Delta H^0_{25} = -171.5\ kJ/mol)$ (2.8)

Like most of the catalysts, the main problem with the Ni catalysts during ESR is deactivation. The major ways for the deactivation of the catalysts are as follows:

a) Coke deposition

b) Active metal sintering

c) Active metal oxidation

d) Poisoning

Secondary reactions of intermediates cause carbon deposition. Active metal composition and reforming conditions are determining factors in carbon formation rates. Below 400 ℃ reaction (8) and reverse carbon gasification and above 600 ℃ methane decomposition are the major sources for carbon deposition [122]. Diffusion of C and continuous precipitation on Ni particles leads to filamentous carbon formation. It is also reported that C dissolves into the Ni lattice to form nickel carbide (Ni_3C). Ni_3C enhances the nucleation and growth of filamentous carbon [123–125]. Filamentous carbon formed (especially whiskers) on migration to bulk metal phase does not lead to direct catalyst deactivation but blocks catalyst bed or breaks the pellet on continuous accumulation. It can also lift active metal off the catalyst support [126]. Ni, Co, and their alloys are more prone to carbon diffusion [70,127]. In the absence of diffusion, especially in noble metals, amorphous carbon encapsulates active metal resulting in direct catalyst deactivation [128]. Acetaldehyde and acetone are adsorbed on active sites preventing the adsorption of ethoxy species [129]. Acetaldehyde, ethylene, and other C2 intermediates polymerize and lead to amorphous carbon deposition [130]. The major drawback of Al_2O_3 is that the acid sites aid in ethanol's dehydration to form ethylene that further polymerizes to form coke [131]. If the Ni crystallite size is small, the carbon clusters formed on the step edges are not large enough to exceed the critical cluster size to form stable C nuclei [132]. Modifying the supports and /or promoting the Ni with other metals are known methods to decrease C deposition and enhance catalytic activity [126,133]. The active metal agglomeration at high temperatures, also known as sintering, an irreversible change reducing actives sites is another major cause for catalyst deactivation [134,135]. Steam can oxidize Ni active metal [136]. The large sintered Ni particles oxidize to form NiO and $NiAl_2O_4$, resulting in loss of catalytic activity [137]. While the coke deposition, sintering, and oxidation during reforming reaction could be the main causes for catalytic deactivation, poisoning of the Ni surface by the impurities (fusel alcohols, acetic acid, sulphur, and ethyl acetate) present in ethanol might be also possible [133,138–140].

Higher temperature can help in coping with carbon formation and improve overall ethanol conversion and H_2 selectivity. Although the reaction responsible to produce ethene by dehydration process (Eq. 2.9) is thermodynamically slightly endothermic and should be favoured at higher temperature, it has been found to decrease along with the increase in temperature.

$$C_2H_5OH\ (g) \leftrightarrow\ C_2H_4\ (g) + H_2O(g) \qquad (\Delta H^0_{25} = +45\ \text{kJ/mol}) \qquad (2.9)$$

Kinetically the rate of this reaction must have been decreasing along with the rise in the temperature. At low temperature the acidic nature of the Al_2O_3 support promotes ethylene production, which again can be coped up by increasing the reaction temperature [115]. The WGS reaction (Eq. 2.10) is exothermic and thus favours the production of CO_2 at the lower temperature. Since it is a reversible reaction, the CO_2 might undergo a reverse WGS reaction (2.11) at the higher temperature and contribute to CO production [141].

$$CO\ (g) + H_2O\ (g) \leftrightarrow\ CO_2\ (g) + H_2\ (g) \qquad (\Delta H^0_{25} = -41.2\ \text{kJ/mol}) \qquad (2.10)$$

CO_2 (g) + H_2 (g) ↔ CO (g) + H_2O (g) (ΔH^0_{25} = +41.2 kJ/mol) (2.11)

The low reaction temperature is preferred as it suppresses active metal sintering, favours WGS reaction and reduces energy consumption, although low H_2 yield is a drawback [142].

The ESR has been carried out with varying H_2O/EtOH ratio. A high H_2O/EtOH ratio causes an increase in ethanol conversion, H_2 production and CO_2 production while decreasing CO and CH_4 production, due to the simultaneous increase in the rate of CH_4 SR and WGS reaction. It also demotes the formation of C_2H_4 and promotes the acetaldehyde decomposition reaction. Some supports, such as CeO_2 show high WGS reaction and modifying the supports can enhance the WGS reaction rate as reported by many researchers [143,144]. Gas hourly space velocity (GHSV), inversely proportional to the contact time of reactant with the catalyst, affects the selectivity of products and ethanol conversion. Increased space velocity decreases H_2 selectivity, ethanol conversion, and CO selectivity while simultaneously increases CH_4 selectivity [145].

Tables 2.2 (Ni/Al_2O_3 based catalysts) and 2.3 (Ni/CeO_2 based catalysts) have tabulated the extensive literature published over the first two decades of the 21st century. The effects of catalyst modification strategies & preparation conditions (Method/DT/CT/RT), reforming reaction conditions (H_2O:EtOH/S:C/T(^oC)/TOS (h)/GHSV(h^{-1})), and their effect on physicochemical properties of the catalysts (particle size and surface area) and catalytic activity; mostly ethanol conversion and hydrogen productivity (yield & selectivity) are summarised. CO and CH_4 selectivity values are presented since they are important for carbon deposition. The C deposition rate on the spent catalyst is reported wherever data is available. Each table is classified into four groups based on their chemistry and this classification is used in this entire review to compare the catalysts. The four groups are as follows:

Group 1: Ni/Al_2O_3 or Ni/CeO_2 catalysts

Group 2: Ni/Modified support catalysts. Only support is modified using metal oxides.

Group 3 Promoted Ni/ Unmodified support catalysts: Active metal Ni is promoted using various noble and non-noble metals.

Group 4 Promoted Ni/ Modified support catalysts: Catalysts with promoted active metal and modified support to understand the synergy between bi/trimetallic catalysts and modified support. The abbreviations used in the tables are listed at the end of this paper.

2.4 Ni/Al_2O_3 Systems

2.4.1 Group 1: Ni/Al_2O_3

Al_2O_3 is a favoured support material due to its high surface area, good porosity and thermal stability [146]. In the first decade (2000-2010), research focuses on optimizing metal loading [147–150], reforming conditions [145,151,152], and catalyst preparation parameters in Ni/Al_2O_3 catalyst systems. Ni metal loading variation in Ni/Al_2O_3 catalysts ranges from 1 to as high as 78 wt.% and the

optimal amount is around 5-20 wt.% as seen in **Table 2.2**. Catalysts belonging to this group show a high hydrogen yield.

Controlling nucleation and grain growth, leading to the efficient catalysts of proper chemistry, high surface area, and particle dispersion of the active phase are the two main aspects of preparation processes. The morphology (pore geometry, size, and volume distribution, particle geometry and size distribution) of the ceramic oxide support substantially affects the overall physico-chemical characteristics of the catalyst. Most of the works report the one pot synthesis, in which both the support and the active phase is synthesized in a single step, however some try the loading of the metal on the pre-synthesized support powder.

For Ni/Al_2O_3 catalysts, the impregnation (IM) method is predominantly used in catalyst preparation. A single layer of active metal could be easily added on the catalyst surface in this method but cannot be used to synthesize catalysts with high metal loading. However, fine and uniform particle size with a homogeneous distribution of active components can be achieved in co-precipitation (CP) and precipitation (PT) methods even at high metal loading [153]. Higher H_2 yield has been reported in literature for the catalyst synthesised by a CP technique compared to that of the other two methods [150]. Researchers investigate different other methods, such as evaporation-induced self-assembly (EISA), non-thermal plasma treatment (NTP), etc., for the catalyst preparation [154,155]. In NTP treated catalyst, coke deposition reduces as ion bombardment induces metal redistribution resulting in smaller crystallites and higher metal dispersion on support surface.

Besides the preparation methods or precursors, calcination temperature has a huge effect on the physicochemical properties and activity of the catalysts. In general, high calcination temperature promotes agglomeration, reduces surface area and metallic dispersion, and increases particle size. In case of the Ni/Al_2O_3 system the elements gain higher diffusivity at high temperatures (≥ 600 °C) and complexed $NiAl_2O_4$ spinel may form. In spinel (AB_2O_4) structure, O^{2-} ions are arranged in an FCC lattice, the bivalent Ni^{2+} ions fill tetrahedral sites, whereas the Al^{3+} ions exist in the octahedral voids. At lower concentration of Ni, Ni/Al atomic ratio less than 16, Ni can occupy the octahedral position partially. The strong chemical bonding in the spinel inhibits the catalyst's reducibility, promotes metal dispersion and the formation of smaller Ni crystallites [148,156–159]. The strong metal support interaction (SMSI) may influence the morphology of metal nanoparticles (NP) such that the particles flatten. This flattening increases the contact area between support and metal NP, anchoring the particle to the support, thereby stabilizing the particles [160]. High adhesion energy of oxide support with the metal reduces mobility of the Ni particles and hinder their growth [161]. Due to SMSI oxide support encapsulates the metal NP blocking the access to metal NP under reducing conditions [162,163]. Besides Ni, other bivalent ions, such as Mg, Cr, Mn, Fe, Co, Cu, Zn, Cd, Sn, etc. take part in spinel formation with Al^{3+} ion. Similarly, some other trivalent ions, such as Ga, In, Ti, V, Cr, Mn, Fe, Co, Ni may form spinel. This is one of the causes of modifying the Al_2O_3 supports.

2.4.2 Group 2: Ni/Modified Al_2O_3

From the end of the first decade, the research works focus on reducing Al_2O_3 acidity. Basic oxides like MgO [164], ZnO [80,165–168], La_2O_3 [134,169,170] and Y_2O_3 [171] are used to modify alumina support (**Table 2.2**). The high number of articles reported in this group demonstrate the efficacy of Al_2O_3 support and the research interest in overcoming its drawbacks. Besides support modification, another interesting observation would be that both single and two step synthesis methods are applied for this group of catalysts and the extensive focus is on applying the sol-gel method (SG).

At the beginning of the last decade, CaO and ZrO_2 [172–175] are investigated as support modifiers. Apart from reducing acidity of alumina, CaO promotes ethanol and water adsorption on the support aiding in hydroxyl formation and C-C bond breaking. CaO also plays a prominent role in affecting Ni particle size and valence band of catalyst, and steam gasification of coke. CaO modified Ni/Al_2O_3 catalyst is commercially available as KATALCO-57-4 series by Johnson Matthey for SR. Choong et al. [2011] carry out the ESR over $Ni(1)/Al_{1-x}Ca_xO_a$ (x=0 to 0.06, Oa: stoichiometric amount (subscript a) of oxygen in the compound) catalyst system prepared by a two-step process and have found H_2 selectivity of 73.2 % at Ca atomic loading of x= 0.03 as oppose to 45.5% in the unmodified catalyst [103]. Choong et al. [2011] report reduction in surface area from 75.5 m^2/g at Ca atomic loading of 0.05 to 53.3 m^2/g at Ca atomic loading of 0.07. High carbon deposition due to the larger decomposition of CH_4 is observed at Ca atomic loading of 0.07 [176]. The inclusion of ZrO_2 also gives similar results, but it is expensive compared to abundantly available alkaline oxide CaO.

Denis et al.[2008] examine the effect of Na and Fe addition to $Ni(10)/Al_2O_3$ catalyst on ESR. Na modification of Al_2O_3 inhibits ethanol dehydration and helps the reduction of NiO, but no significant resistance to coking is created. Fe modification enhances WGS activity, although the surface area decreases [167]. Han et al. [2013] investigate the effect of different Zr/Al atomic ratio (0 to 0.41) in $Ni(10)/Al_{1-x}Zr_xO_a$ catalyst system (x=0 to 0.29) synthesized by sol-gel method. The catalyst acidity, surface area, and Ni-support interaction are found to be inversely related to the Zr/Al atomic ratio. Lattice contraction due to incorporation of Zr^{4+} into Al_2O_3 results in a decreased surface area from 339 m^2/g for unmodified catalyst to 214 m^2/g for $Ni(10)/Al_{0.71}Zr_{0.29}O_{1.64}$ powder. However, hydrogen yield increases with Zr/Al atomic ratio. A decrease in amount of coke deposited from 28.8 wt.% for $Ni(10)/Al_2O_3$ to 1.3 wt.% for $Ni(10)/Al_{0.71}Zr_{0.29}O_{1.64}$ is reported due to decrease in acidity. The same group reports the increase in H_2 yield from 54 to 124% on increasing the Ni loading from 5 to 20 wt.% for $Ni/Al_{0.83}Zr_{0.17}O_{1.58}$ catalyst and H_2 yield falls on further increase of Ni loading [175]. Han et al. [2014] use Pluronic P123 surfactant and soft templating technique for the synthesis of mesoporous $Ni(15)/Al_{0.83}Zr_{0.17}O_{1.58}$ catalysts by sol-gel method. Reportedly H_2 yield increases from 94 to 126% on increasing the P123 concentration from 0 to 12 mM [173].

Mg-Al mixed oxide forms $MgAl_2O_4$ spinel that promotes higher active metal dispersion and smaller Ni crystallite size. The basicity of this spinel prevents ethylene formation. Michele et al. [2019] report deposition of amorphous carbon (easily regenerated) on Ni(1.5)/$MgAl_2O_4$ and structured C nanotube formation at higher Ni loading (5 and 10 wt.%) leading to physical detachment of active metal. However, complete ethanol conversion and higher H_2 selectivity (79%) are achieved for Ni(5)/$MgAl_2O_4$ and Ni(10)/$MgAl_2O_4$ as opposed to 86 and 64%, respectively, for Ni(1.5)/$MgAl_2O_4$ [164].

The addition of ZnO to Ni/Al_2O_3 catalyst system reduces carbon formation and enhances ethanol conversion, although surface area decreases, and Ni particle size increases compared to that of the unmodified one. Anjaneyulu et al. [2016] prepare Ni(15)/$Al_{1-x}Zn_xO_a$ (x= 0.33, 0.67) catalyst by a two-step process. High carbon deposition of 14.7 $mg_{carbon}\ g_{cat}^{-1}\ h^{-1}$ for Ni(15)/$Al_{0.67}Zn_{0.33}O_{1.33}$ catalyst as opposed to 3.1 $mg_{carbon}\ g_{cat}^{-1}\ h^{-1}$ for the Ni(15)/$Al_{0.33}Zn_{0.67}O_{1.2}$ is reported. $ZnAl_2O_4$ inverse spinel is formed at Zn/Al = 0.5 and Ni-Zn tetragonal alloy is formed at Zn/Al = 2. This alloy formation decreases the amount of free active metal and number of large Ni particles, resulting in low carbon deposition [168].

Addition of a small amount of ZnO to Ni/MgO-Al_2O_3 improves H_2 selectivity and catalyst reducibility due to the weakening of NiO-MgO bond formation. Zeng et al. [2011] observe an increase in H_2 yield from 4.83 mol/mol_{EtOH} for the Ni(20)/$Al_{0.28}Mg_{0.72}O_{1.14}$ system to 4.94 mol/mol_{EtOH} for ZnO (atomic fraction of 0.14) loaded Ni(20)/$Al_{0.28}Mg_{0.72}O_{1.14}$ powder prepared by a two-step co-precipitation process despite of the reduction in catalyst surface area from 209.7 to 185.2 m^2/g [166].

Addition of CeO_2 to the Ni/Al_2O_3 catalyst modifies the Ni-O-Al bond to Ni-O-Ce interaction. The removal of atomic O from the Ni-O-Ce structure becomes easier than that from the Ni-O-Al interaction, which aids in decreasing Ni crystallite size of reduced catalyst. The high oxygen mobility of the CeO_2 lattice also facilitates the oxidation of carbon deposited on the catalyst surface, and increases metal reducibility and H_2 selectivity [177]. However, addition of both Zr and Ce with Al_2O_3 resulted in enhanced Ni crystallite size, increased coke deposition, and lower catalytic activity [178]. Shtyka et al. [2021] investigate ZnO and CeO_2 support modifiers separately at two different Ni loadings (5 and 20 wt%). Ni(20)/$Al_{0.88}Zn_{0.12}O_3$ demonstrates higher H_2 selectivity (78%) despite of the lower surface area (40 m^2/g) [80].

Magnetic inducement is used in catalyst synthesis to achieve homogeneity and high dispersion of metal ions. Vacharapong et al. [2020] apply a strong magnetic field during the preparation of the support (CP method) in order to control the Ce^{3+} ions dispersion. Somewhat improvement in H_2 yield is reported for the magnetically induced Ni(10)/$Al_{0.99}Ce_{0.01}O_{1.51}$ catalyst compared to the same catalyst synthesised without magnetic assistance [179].

In the last five years (2016-2021), research activities have been focused on La_2O_3 and Y_2O_3 as support modifiers. Y_2O_3 addition, along with lowering alumina acidity, enhances Ni reducibility, decreases Ni reduction temperature, prevents Ni sintering, and increases oxygen mobility [180].

Ramirez-Hernandez et al. [2016] examine ESR over Ni(10)/$Al_{1-x}Y_xO_{1.5}$ catalytic system (x= 0.03 to 0.08) prepared by a two-step process. Higher H_2 yield (5.55 mol/mol_{EtOH}) and lower carbon deposition (18.2 wt.%) are achieved at x = 0.08 as opposed to the H_2 yield of 5.36 mol/ mol_{EtOH} and 32.5 wt.% carbon deposition for the unmodified Ni(10)/Al_2O_3 catalyst [171].

Recent studies focus on La_2O_3 as a support modifier as it reacts with the by-product CO_2 to form lanthanum oxycarbonate ($La_2O_2CO_3$), which reacts with carbon deposited to form La_2O_3 and CO. La promotes structural and textural stabilization of the alumina support and enhances resistance to Ni sintering. Vicente et al. [2014] compare ESR over La_2O_3 modified (0.02 atomic fraction) and unmodified Ni(10)/Al_2O_3 catalyst systems synthesized by IWI method and reveal that La addition increase H_2 yield (0.5 mol/mol_{EtOH}) than that of the unmodified (0.45 mol/mol_{EtOH}) system [181]. Song et al. [2017] develop Ni(15)/$Al_{1-x}La_xO_a$ (x=0.05 to 0.17) catalysts by a two-step process (supported by SG and active metal loading by IM) and report a 24 % increase in H_2 yield at 0.09 La loading as compared to the unmodified catalyst. On increasing the La loading from 0.13 to 0.17, 80% decrease in the H_2 yield is observed due to partial coverage of the catalyst surface by larger La atoms [182]. Excess La atoms due to their size block access for ethanol to adsorb on Ni as seen in the EtOH-TPD analysis of the reduced catalysts [183]. Increase in Ni metal loading on La_2O_3 promoted Ni/Al_2O_3 catalyst decreases H_2 yield and increases production of CO and CH_4 [184]. Higher CT and reduction temperature (RT) of the Ni/ Al_2O_3-La_2O_3 catalysts results in larger Ni particles, enhances carbon whiskers' growth, decreases H_2 yield and ethanol conversion [185].

Addition of CeO_2 in Ni/Al_2O_3-La_2O_3 catalysts preferentially induces higher amount of lattice oxygen and observe to enhance the amount of $La_2O_2CO_3$ formation. It consequently promotes carbon gasification and improves H_2 selectivity. Osorio-Vargas et al. [2016] reported an increase in the hydrogen selectivity from 58 to 82% and coke formation 0.1 to 0.21 mg_{coke}/mg_{cat}.h due to the addition of 0.05 atomic loading of CeO_2 in Ni(10)/$Al_{0.94-x}La_{0.06}Ce_xO_{1.5}$ catalyst synthesized by a two-step IM method [186]. However, excess CeO_2 addition (beyond atomic loading 0.05) to Al_2O_3-La_2O_3 support might retard the WGS and CH_4 reforming activity and reduce H_2 selectivity [185,186]. Boudadi et al. [2021] investigate ESR over Ni catalysts supported on lanthanum-modified Al_2O_3, TiO_2, Al_2O_3-TiO_2 and Al-pillared bentonite (clay) prepared by a two-step process. The highest initial ethanol conversion (100) and H_2 yield (34%) are achieved on Ni(10)/La-Clay catalyst (despite low surface area of 36 m^2/g) due to high Ni dispersion caused by the textured clay. The Ti and La dual modification increases surface area (227 m^2/g) but decreases H_2 yield (12%) compared to the only La modified catalyst; surface area 209 m^2/g and H_2 yield 22%. However both catalysts show stability [119].

2.4.3 Group 3: Promoted Ni/ Al_2O_3

The third group in **Table 2.2** consists of promoted-Ni on unmodified alumina support catalysts. This kind of modification strategy seems to begin from the end of the first decade of the 21st century

and not much literature is found on this category. Nobel metal (Pt [187,188], Rh [189,190]) and transition metals (Cu [191,192], Co [193]) are mostly studied. Pt is chosen as a Ni promoter due to its WGS reaction capability and good thermal stability. The presence of noble metals such as Pd and Pt facilitates the reduction of NiO specie by hydrogen spill over phenomenon. Here the initially produced hydrogen dissociates to form active hydrogen on reduced noble metal clusters and then migrates and reduces the neighbouring NiO clusters [187,194,195]. Soyal-Baltacıoğlu et al. [2008] find an increase in the ethanol conversion from 42 to 74% at 550 °C on increasing the Pt loading from 0.001 to 0.004 atomic fraction in $Ni_{1-x}Pt_x(15+y)/Al_2O_3$ (where y is Pt metal loading wt.%) catalyst prepared by a two-step impregnation technique [188].

Researchers show interest in investigating Cu as a promoter for Ni because it helps fast dehydrogenation of ethanol to acetaldehyde and shows good WGS activity. However, Cu inclusion impairs the reforming activity, increases crystallite size, and decreases metal dispersion in Ni/ Al_2O_3 powder. De Rogatis et al. [2008] develop Cu promoted $Ni_{1-x}Cu_x(10)/Al_2O_3$ catalyst system and observe an increase in average crystallite size from 9 to 31 nm on increasing the Cu loading from 0.28 to 0.68 atomic fraction. Additionally, they report 4.1% less metal dispersion in catalyst with 0.68 Cu atomic loading compared to the unpromoted $Ni(10)/Al_2O_3$ catalyst [191]. Partial substitution of bigger Ni^{2+} ion by smaller Cu^{2+} ion results in lattice parameter reduction [192].

The recent emphasis is on Rh and Co as Ni promoters. Co is known to enhance WGS reaction and can cleave C-C bond like Ni. However, reduction in Ni incorporation into the alumina lattice due to Co assimilation in the structure (6 wt%) inhibits the strong interaction between the Ni and Al_2O_3 support. Zhao et al. [2016] report higher H_2 selectivity (88.9%) for the $Ni_{0.5}Co_{0.5}(15)/Al_2O_3$ catalyst prepare by a co-impregnation method compare to the same catalyst prepare by a sequential impregnating process during 100h reaction [193].

Rh addition reportedly decreases Ni particle size, improves metal dispersion, and enhances catalytic stability by increasing the carbon gasification rate as a result of augmenting basic nature of the catalyst. Gonzalez-Gil et al. [2015] witness a decrease in Ni particle size from 20 to 13 nm and carbon deposition from 17.2 to 5.8wt% on introducing 0.06 atomic % Rh in Ni/Al_2O_3 catalyst system prepared by a IWI technique [190]. The same group further investigate [2016] $Ni_{0.61}Rh_{0.06}Ce_{0.33}/Al_2O_3$ catalyst prepared on commercial alumina pellets by an IWI process. The stabilisation of Ni-Ce by Rh leads to a high yield of hydrogen (0.23 $Nm^3\ h^{-1}$) in the pilot studies [189].

2.4.4 Group 4: Promoted Ni/Modified Al_2O_3

Investigating the bimetallic catalysts are initiated to understand the effect of the synergistic chemistry between the noble and non-noble metals on ESR [196–198]. The last group in **Table 2.2** consists of promoted Ni/modified Al_2O_3 catalysts that focuses on exploring effect of synergistic interaction between bimetallic catalysts and modified support (with low acidity) on ESR [199,200].

Some works on this modification strategy are reported in the last decade and the catalysts in this group provide great stability. Other than the metal oxide modifiers mentioned in group 2, studies on CeO_2 as a support modifier are also reported [179,194,201,202]. The combination of La_2O_3 and CeO_2 has been the focus of this strategy. Campos et al. [2019] investigate synergistic interaction of a noble metal promoter (Rh) with a basic oxide (La_2O_3) and a reducible oxide (CeO_2) support modifier. Ni(10)-Rh(X)/$Al_{0.86}Ce_{0.08}La_{0.06}O_{1.54}$ (X = 0.25-1) catalyst synthesised by a two-step IM method is investigated for ESR reaction. Carbon deposition reduced by 70 times as compared to monometallic Rh based same catalyst and 560 times as compared to the monometallic Ni based same catalyst. Increased coke gasification capacity and enhanced WGS reaction rate are the reasons for the superior performance of the catalyst [194].

Wang et al. [2009] study ESR on the $Ni_{1-x}Cu_x/Al_{0.94}Mg_{0.06}O_{1.47}$ catalyst system (x=0.0 to 0.48) synthesized by a two-step method: support by IM and active metal loaded by IWI. Both amount and chemistry of the active metals are investigated. Addition of Cu, up to x= 0.32, improves catalytic activity and the further addition of Cu decreases H_2 yield [203].

The addition of Ni-Cu bimetallics on the Al_2O_3-MgO and Al_2O_3-ZnO support systems demonstrate higher dispersion and smaller particle size of the active phase due to formation of (Ni, Cu)(Al, Mg, Zn) O_3 spinel structures. Strong interaction of NiO with these complex spinel structures helps to prevent the growth of metallic Ni particles during reduction. Small Ni crystallite size coupled with the low acidity of the modified support help in less carbon deposition during reforming. Zhang et al. [2009] develop $Ni_{0.94}Cu_{0.06}(35)/Al_{1-x}M_xO_a$ (M= La, Si, Zn and Mg) catalyst systems by a two-step precipitation-impregnation method. The NiO particle size for the MgO or ZnO modified alumina support catalysts is reported to be much smaller than that of the SiO_2 promoted alumina catalyst. Less amount of carbon deposition on the $Ni_{0.94}Cu_{0.06}(35)/Al_{0.76}Mg_{0.24}O_{1.38}$ (0.5 g/g_{cat}) and $Ni_{0.94}Cu_{0.06}(35)/Al_{0.86}Zn_{0.14}O_{1.43}$ (0.2 g/g_{cat}) catalysts are reported as compare to the SiO_2 modified $Ni_{0.94}Cu_{0.06}(35)/Al_{0.94}Si_{0.06}O_{1.53}$ (2.2 g/g_{cat}) catalyst [204].

Zhang et al. [2009] study the effect of $Ni_{1-x}La_x/Al_{0.78}Si_{0.22}O_{1.61}$ (x=0.07, 0.12 and 0.17) catalyst on ESR. La in low amount (0.07 atomic fraction) reduces interaction between Ni and alumina support by forming $LaNiO_4$ perovskites, which is easier to reduce than the nickel aluminate spinel. H_2 selectivity improves from 85 to 100% by adding 0.12 atomic fraction La comparted to the unpromoted Ni/ $Al_{0.78}Si_{0.22}O_{1.61}$ catalyst [44].

The presence of noble metals, such as Pd and Pt, facilitate the reduction of NiO species by hydrogen spill over phenomenon. Profeti et al. [2009] investigate ESR over the $Ni_{1-x}Pd_x(15+y)/Al_{0.98}La_{0.02}O_{1.5}$ (x= 0.001, 0.0004; y is Pd wt.%) and $Ni_{1-x}Pt_x(15+y)/Al_{0.98}La_{0.02}O_{1.5}$ (x= 0.002, 0.006; y is Pt wt.%) catalyst system synthesized by a two-step impregnation method. The Pt promoted catalyst reveal higher H_2 yield (3.8 mol/mol_{EtOH}) and larger surface area (138 m^2/g) compare to the unpromoted catalyst with H_2 yield 3.44 mol/mol_{EtOH} and surface area 114 m^2/g [195].

Profeti et al. [2009] synthesize noble metal promoted Ni(5)-M(0.3)/$Ce_{0.03}Al_{0.97}O_{1.52}$ (M= Pd, Pt, Ir and Ru) catalyst system by a two-step process and study their activity for ESR. The Pd promoted catalyst shows the highest H_2 yield (4.43 mol/mol_{EtOH}) and lowest coke deposition (0.05 mmol/h) among all the catalysts with a high surface area of 163 m^2/g [202].

Ce support modifier performed better in Ni-Pt/Al_2O_3 catalyst system than the La, Mg and Zr support modifiers probably due to its higher OSC and WGS activity compared to the others. Navarro et al. [2015] synthesize $Ni_{0.95}Pt_{0.05}$(15.5)/$Al_{0.97}M_{0.03}O_{1.51}$ (M = Ce, La, Mg, Zr) catalyst by a two-step IM method and the highest H_2 selectivity of 18.8% is reported for the $Ni_{0.95}Pt_{0.05}$(15.5)/$Al_{0.97}Ce_{0.03}O_{1.51}$. Addition of Mg or Zr does not suppress ethylene formation but delays its production. La and Ce supported catalysts demonstrate the best catalytic stability due to enhancement of coke gasification [196].

The alkaline earth metal promoters are known to increase H_2 yield due to enhanced catalytic surface area and lower acidity induced. Song et al. [2016] prepare Ni(15)-M/$Al_{0.8}Zr_{0.2}O_{1.6}$ (M=Ca, Mg, Ba and Sr) catalysts by a two-step process (support by a SG method and active metal loading by a co-impregnation method). The $Ni_{0.83}Sr_{0.17}$(19.5)/$Al_{0.8}Zr_{0.2}O_{1.6}$ catalyst achieves the highest H_2 yield of 87.9%, highest Ni surface area (21.9 m^2/g-Ni) and low acidity (1.1 mmol-NH_3/g_{cat}) and the hydrogen yield decrease in the following order: Sr > Mg > Ba > Ca > unpromoted catalyst [205]. Co can increase WGS reaction and C-C bond breaking; however, Co addition (decreasing Ni) after certain threshold limit might promote coking. Chen et al. [2012] synthesize $Ni_{1-x}Co_x$(10)/$Al_{0.96}Ca_{0.04}O_{1.44}$ catalyst system by a two-step IM process, and figure that the coke deposition increases in the following order:

Ni(10)/$Al_{0.96}Ca_{0.04}O_{1.44}$ < $Ni_{0.67}Co_{0.33}$(10)/$Al_{0.96}Ca_{0.04}O_{1.44}$ < $Ni_{0.33}Co_{0.67}$(10)/ $Al_{0.96}Ca_{0.04}O_{1.44}$. $Ni_{0.67}Co_{0.33}$(10)/$Al_{0.96}Ca_{0.04}O_{1.44}$ catalyst achieves H_2 yield higher than that of the $Ni_{0.33}Co_{0.67}$(10)/$Al_{0.96}Ca_{0.04}O_{1.44}$ catalyst [206]. Contreras et al. [2021] investigate the influence of tungsten oxide as support stabiliser in $Ni_{1-x}Co_x$/$W_{0.001}Mg_{0.38}Al_{0.62}O_{1.31}$ catalyst system prepared by a two-step CP method for ESR. The bimetallic $Ni_{0.69}Co_{0.31}$(14.5)/$W_{0.001}Mg_{0.38}Al_{0.62}O_{1.31}$ power demonstrates the highest H_2 selectivity of 78% with low carbon formation rate 9.30 mg_{coke}/mg_{cat}.h among all the catalysts and high surface area 200 m^2/g. Further increase of Co deteriorates catalytic activity [207]. Liberatori et al., [2007] investigate the effect of Ag (as Ni promoter) and La_2O_3 (as support modifier) in Ni(15)/Al_2O_3 catalyst synthesized by a two-step process. Addition of 0.02 atomic fraction of Ag decreases H_2 selectivity from 75 to 50%, increases carbon deposition rate from 5.4 to 23.4 mg_{coke}/mg_{cat} h, and increases CH_4 selectivity. Whereas, addition of 0.03 atomic fraction of La_2O_3 decreases the carbon deposition rate from 5.4 to 4.6 mg_{coke}/mg_{cat} h [200].

Table 2. 2: Literature survey on steam reforming of ethanol on various Ni/Al_2O_3 based catalysts (2000-2023).

SN	Catalyst	Catalyst Properties	EtOH (%)	CO	H_2	CH_4	C rate	Reforming Conditions H_2O:EtOH/S:C/ T(°C)/ TOS (h)/GHSV(h^{-1})	Catalyst Preparation Method/ DT(h)/CT(h)/RT(h)	Ref & year
	Group 1: Ni/Al_2O_3									
1.	$Ni(15)/Al_2O_3$	S_{BET} = 168, D_{Ni} = 5.5	100	%S 10.5	%Y 90.3	%S 35.6	-	6/-/450/16.6/-	EISA(PI)/-/550(5h)/650(3h)	[155] 2016
		S_{BET} = 212, D_{Ni} = 5.3	100	8.1	94.2	35.4	-		EISA(D)/-/550(5h)/ 650(3h)	
2.	$Ni(20)/Al_2O_3$	S_{BET} = 289, D_{Ni} = 4.5	100	%S 5	%Y 40	%S 40	-	8/4/400/30/-	CP/80(24h)/450(4h)/-	[148] 2016
	$Ni(50)/Al_2O_3$	S_{BET} = 248, D_{Ni} = 3.7	100	0	40	4	-			
	$Ni(78)/Al_2O_3$	S_{BET} = 187, D_{Ni} = 6.0	100	0	40	30	-			
	$Ni(20)/Al_2O_3$	S_{BET} = 182, D_{Ni} = 7.1	100	5	31	20	-		IM/80(24h)/450(4h)/500(2h)	
	$Ni(50)/Al_2O_3$	S_{BET} = 115, D_{Ni} = 21	100	0	30	30	-			
	$Ni(78)/Al_2O_3$	S_{BET} = 71, D_{Ni} = 37	90	4	31	23	-			
3.	$Ni(5)/Al_2O_3$	S_{BET} = 225, D_{pore} = 12.1, D_{Ni} = 9.4	100	%S 8	%S 92.7	%S 2.1	-	3/-/437-737/-/ 10602	Support: Comm. γ-Al_2O_3 Metal loading: IWI/120(ON)/500(4h)/500(3h)	[154] 2015
4.	Ni Nanoparticles	-	100	%S 7	%Y 59	%S 26	-	3/-/250-500/-/51700	R/-/-/- ($NaBH_4$ reducing agent)	[145] 2014
	$Ni(55.6)/Al_2O_3$	-	100	0	70	21	-		Support: Comm. Al_2O_3 Metal loading: IM/90(24h)/700(5h)/700(3h)	
5.	$Ni(17.4)/Al_2O_3$	S_{BET} =164, V_p = 0.462	100	-	%S 19	-	-	3/-/400-500/4.2/-	Support: Comm. Al_2O_3 Metal loading: IM/120(12h)/700(2h)/ 600(2h)	[152] 2010
6.	$Ni(16)/Al_2O_3$	S_{BET} = 182, V_{pore}=0.57	88	%M 1	%M 32	%M 0	-	3/-/600/6/-	IM/125(ON)/550(3h)/700(1h)	[147] 2007
	$Ni(8)/Al_2O_3$	S_{BET} = 194, V_{pore}=0.78	80	6	62.5	1	-			
7.	$Ni(5)/Al_2O_3$	S_{BET} = 270, V_p = 0.560	100	-	%S 89.0	%S 0.5		3/-/450-600/-/-	IM/27(24h)/550(1h)/ 600(2h)	[151] 2006
		S_{BET} = 210, V_p = 0.430	100	-	87.4	0	-		IM/27(24h)/700(1h)/600(2h)	

8.	$Ni(10)/Al_2O_3$	D_{NiO}=26.5, S_{BET}=80	30	%S 4.2	%S 91	%S 6.1	-	3/-/400/4/-	CP/110(ON)/600(2h)/600(2h)	[150] 2005
	$Ni(15)/Al_2O_3$	D_{NiO} =29.8, S_{BET}=80	80	4.6	90	2.8	-			
	$Ni(20)/Al_2O_3$	D_{NiO} =38.5, S_{BET}=70	55	4.7	88	7.5	-			
	$Ni(25)/Al_2O_3$	V_{pore} = 0.19, S_{BET}=65	60	5.6	87	4.8	-			
	$Ni(10)/Al_2O_3$	D_{NiO} =15.3, S_{BET}=163	45	7	85	8.8	-		IM/110(ON)/600(2h)/600(2h)	
	$Ni(15)/Al_2O_3$	D_{NiO} =105.8, S_{BET}=158	45	6	87	11.3	-			
	$Ni(20)/Al_2O_3$	D_{NiO} =160.2, S_{BET}=157	42	5.4	85	12.9	-			
	$Ni(10)/Al_2O_3$	D_{NiO} =21.5, S_{BET}=170	45	14.9	86	4.9	-		PT/110(ON)/600(2h)/600(2h)	
	$Ni(15)/Al_2O_3$	D_{NiO} =20.8, S_{BET}=162	84	9.1	83	7.7	-			
	$Ni(20)/Al_2O_3$	D_{NiO} =39.6, S_{BET}=157	82	16.0	83	6.8	-			
	Group 2: Ni/modified Al_2O_3									
9.	$Ni(5)/Al_{0.4}Ce_{0.3}Zr_{0.3}O_4$	S_{BET} = 152.5, D_{Ni} = 2.4	100	39.7	60.0	2.4	3.7	6/-/550/-/10619	HT/70(24h)/600(6h)/-	[208] 2022
	$Ni(10)/Al_{0.4}Ce_{0.3}Zr_{0.3}O_4$	S_{BET} = 137.7, D_{Ni} = 5.6	100	28.4	82.7	13.3	5.0			
	$Ni(15)/Al_{0.4}Ce_{0.3}Zr_{0.3}O_4$	S_{BET} = 131.5, D_{Ni} = 9.4	93.6	36.1	74.0	11.1	15.9			
	$Ni(20)/Al_{0.4}Ce_{0.3}Zr_{0.3}O_4$	S_{BET} = 129.5, D_{Ni} = 8.9	91.7	23.9	66.3	10.9	19.1			
10.	$Ni(5)/Al_2O_3$	S_{BET} = 90, D_p = 5	100	%S 0	%S 72.6	-	-	6/-/300-600/-/-	Support: PT/120(ON)/400(4h)/-	[80] 2021
	$Ni(20)/Al_2O_3$	S_{BET} = 66, D_p = 55	100	0	72.6	-	-			
	$Ni(5)/Al_{0.9}Zn_{0.1}O_3$	S_{BET} = 55, D_p = 5	100	0	73.3	-	-		Support: CP/120(ON)/400(4h)/- Metal loading: Same for all 6 IM/110(4h)/400(4h)/900(2h)	
	$Ni(20)/ Al_{0.88}0Zn_{0.12}O_3$	S_{BET} = 40, D_p = 36	100	0	78.0	-	-			
	$Ni(5)/ Al_{0.87}Ce_{0.05}O_3$	S_{BET} = 68, D_p = 7	100	0	76.5	-	-			
	$Ni(20)/ Al_{0.94}Ce_{0.06}O_3$	S_{BET} = 54, D_p = 62	100	0	72.0	-	-			
11.	$Ni(10)/ Al_{0.97}\ La_{0.03}O_{1.5}$	S_{BET} = 209, V_{pore} = 0.5	80	-	%Y 22	-	-	6/-/500/5.8/-	Support: IWI/120(ON)/350(2h)/- Metal loading: (same for all 4) IWI/120(ON)/350(2h)/-	[119] 2021
	$Ni(10)/La_{0.97}Ti_{0.03}O_{1.52}$	S_{BET} = 42, V_{pore} = 0.3	50	0	17	12	-		Support: La - IWI/120(ON)/350(2h)/-	
	$Ni(10)/ Al_{0.84}Ti_{0.13}La_{0.03}O_{1.57}$	S_{BET} = 227, V_{pore} = 0.5	68	-	12	-	-			

									Ti + Al - MM/120(24h)/400(3h)/-	
	Ni(10)/La-Clay	S_{BET} = 36, V_{pore} = 0.05	100	-	34	-	-		Support: PLR&IWI/120(ON)/350(2h)/-	
12.	Ni(10)/–Al_2O_3 (No Magnet)	S_{BET} = 165.3 ,D_{pore} = 95.1	-	Y 37.9	Y 683.4	-	-	-/-/550-650/30/-	Support: CP/-/650(6h)/- Under the influence of magnetic field. Metal loading: IWI/110(12h)/500(4h)/600(1h)	[179] 2020
	Ni(10)/ $Al_{0.99}Ce_{0.01}O_{1.51}$ (No Magnet)	S_{BET} = 138.1, D_{pore} = 94.3	-	38.8	761.9	-	-			
	Ni(10)/ $Al_{0.99}Ce_{0.01}O_{1.51}$ (N–S pole arrangement)	S_{BET} = 142.2, D_{pore} = 91.2	-	32.8	727.7	-	-			
	Ni(10)/ $Al_{0.99}Ce_{0.01}O_{1.51}$ (N–N pole arrangement)	S_{BET} = 135.6, D_{pore} = 96.3	-	24.9	885.8	-	-			
	Ni(10)/ $Al_{0.99}Ce_{0.01}O_{1.51}$ (S–S pole arrangement)	S_{BET} = 135.6, D_{pore} = 94.2	-	28.3	813.6	-	-			
13.	Ni(1.5)/$MgAl_2O_4$	S_{BET} = 238, D_{Ni} = 24.9	86	-	%M 64	%S 0	-	3/-/400-625/8/2700	Support: CP/110/650(3h)/- Metal loading: CP/-/500(3h)/600(3h)	[164] 2019
	Ni(5)/Mg Al_2O_4	S_{BET} = 228 , D_{Ni} = 24.9	100	-	79	0	-			
	Ni(10)/Mg Al_2O_4	S_{BET} = 228, D_{Ni} = 33.2	100	-	79	0.79	-			
14.	Ni(15)/Al_2O_3	S_{BET} = 193, D_{Ni} = 8.1	100	%S 5.1	%Y 100.1	%S 28.5	-	-/-/450/15/-	Support: SG/80(120h)/550(5h)/- Metal loading: IM/80/550(2h)/700(1h)	[182] 2017
	Ni(15)/$Al_{0.95}La_{0.05}O_{1.5}$	S_{BET} = 154, D_{Ni} = 7.1	100	8.3	108.7	29.3	-			
	Ni(15)/$Al_{0.91}La_{0.09}O_{1.5}$	S_{BET} = 139, D_{Ni} = 6.7	100	8.9	124.3	27.2	-			
	Ni(15)/$Al_{0.87}La_{0.13}O_{1.5}$	S_{BET} = 133, D_{Ni} = 6.7	100	10.4	117.9	27.8	-			
	Ni(15)/$Al_{0.83}La_{0.17}O_{1.5}$	S_{BET} = 90, D_{Ni} = 5.7	98.9	12.3	64.1	28.8	-			
15.	Ni(7)/Al_2O_3	S_{BET}= 175, D_{Ni} = 9.6	100	%S 65	%S 35	%S 15	-	-/4/400-700/50/-	IWI/60(24h)/550(5h)/ 500(3h)	[170] 2016
	Meso-Ni(7)/Al_2O_3	S_{BET}= 280, D_{Ni} = 5.0	100	30	65	8	-		Support: La IWI/27(24h)/700(2h)/- Metal loading: meso-NiAl EISA/100(12h)/700(5h)/500(3h)	
	Ni(7)/$Al_{0.997}La_{0.003}O_{1.5}$	S_{BET}= 209, D_{Ni} = 5.4	100	28	68	7	-			
	Ni(7)/$Al_{0.995}La_{0.005}O_{1.5}$	S_{BET}= 202, D_{Ni} = 4.4	100	20	80	5	-			
	Ni(7)/$Al_{0.99}La_{0.01}O_{1.5}$	S_{BET}= 195, D_{Ni} = 4.7	100	20	65	6	-			
	Ni(7)/$Al_{0.98}La_{0.02}O_{1.5}$	S_{BET}= 167, D_{Ni} = 4.6	100	23	63	8	-			

16.	$Ni(10)/Al_2O_3$	S_{BET} = 189, D_{pore} = 10.0	49	%S 0	%S 28	%S 5.7	0.39	3/-/400-650/-/26000	Support: IM/100(0.5h)/700(6h)/- Metal loading: IM/-/500(4h)/650(1.5h)	[186] 2016
	$Ni(10)/Al_{0.94}La_{0.06}O_{1.5}$	S_{BET} = 134, D_{pore} = 9.1	89	7	58	14	0.10			
	$Ni(10)/Al_{0.9}La_{0.06}Ce_{0.05}O_{1.52}$	S_{BET} = 111, D_{pore} = 11.6	95	1.8	82	3.6	0.21			
	$Ni(10)/Al_{0.86}La_{0.06}Ce_{0.08}O_{1.54}$	S_{BET} = 99, D_{pore} = 12.9	98	3.9	76	8.9	0.11			
	$Ni(10)/Al_{0.82}La_{0.06}Ce_{0.12}O_{1.56}$	S_{BET} = 94, D_{pore} = 12	95	4.6	78	6.8	0.15			
17.	$Ni(15)/Al_{0.67}Zn_{0.33}O_{1.33}$	S_{BET} = 46, D_{Ni} = 11	100	%M 7	%M 68	%M 0	14.7	3/-/400-800/28/-	Support: CP/100(12h)/800(5h)/- Metal loading: IWI/100(12h)/250/750(1h)	[168] 2016
	$Ni(15)/Al_{0.33}Zn_{0.67}O_{1.2}$	S_{BET} = 61, D_{NiZn} = 16	100	19	68	1	3.1			
	$Ni(15)/Al_2O_3$	S_{BET} = 161, D_{Ni} = 4	85	8	71	6	2.3			
18.	$Ni(10)/Al_{0.97}La_{0.03}O_{1.5}$	S_{BET} = 35, D_{Ni} = 21.7	0.6	-	Y_a 0.3	-	-	6/-/550-700/3/-	Support: IM/110(24h)/900(3h)/- Metal loading: IWI/110(24h)/550(2h)/700(2h)	[134] 2016
19.	$Ni(10)/Al_2O_3$	S_{BET} = 245, D_{pore} = 12.4	100	Y_a 0.45	Y_a 5.36	Y_a 0.49	-	10/-/600/6/-	Support: SG/34(12h)/700(2h)/- Metal loading: IM/27(24h)/700(2h)/650(2h)	[171] 2016
	$Ni(10)/Al_{0.97}Y_{0.03}O_{1.5}$	S_{BET} = 240, D_{pore} = 7	100	0.41	5.20	0.89	-			
	$Ni(10)/Al_{0.95}Y_{0.05}O_{1.5}$	S_{BET} = 165, D_{pore} = 8.5	100	0.37	5.13	0.79	-			
	$Ni(10)/Al_{0.92}Y_{0.08}O_{1.5}$	S_{BET} = 148, D_{pore} = 9.6	100	0.36	5.55	1.48	-			
20.	$NiO(20)/Al_{0.96}La_{0.04}O_{1.5}$	S_{BET}= 131	100	Y_a 0	Y_a 0.78	Y_a 0	-	3/-/250-800/-/-	Support: Comm. Al_2O_3 -/-/750(5h)/- Metal loading: IWI/80(15h)/750(5h)/600(3h)	[169] 2015
	$NiO(20)/Al_2O_3$	S_{BET}= 148	100	0	0.82	0	-	4/-/500-750/-/-		
21.	$Ni(10)/Al_2O_3$	S_{BET} = 69, V_{pore} = 0.18, D_{pore} = 9.0	100	-	Y_a 0.45	-	-	6/-/500/20/-	Support: IM/110(24h)/650(3h)/- Metal loading: IWI/110(24h)/650(3h)/850(6h)	[181] 2014
	$Ni(10)/Al_{0.98}La_{0.02}O_{1.5}$	S_{BET} = 43, V_{pore} = 0.15,D_{pore} = 11.5	100	-	0.5	-	-			
22.	$Ni(10)/\alpha\text{-}Al_{0.97}La_{0.03}O_{1.5}$	S_{BET} = 33.9, V_{pore} = 0.167	100	%Y 10	%Y 94	%Y 0	-	-/6/700/4/13800	Support: (same for all 3) IM/100(12h)/600(3h)/- Metal loading: IWI/100(24h)/550(3h)/850(2h)	[185] 2014
		S_{BET} = 34.8, V_{pore} = 0.171	100	13	90	2	-		Metal loading: IWI/100(24h)/700(3h)/850(2h)	

		S_{BET} = 36.2, V_{pore} = 0.181	100	15	87	4	-		Metal loading: IWI/100(24h)/850(3h)/850(2h)	
23.	$Ni(15)/Al_{0.83}Zr_{0.17}O_{1.58}$ (P3: 0)	S_{BET} =388, D_{Ni} = 14.6	100	%S 2.6	%Y 94	%S 22.8	-	6/-/500/16.67/-	SG/80(12h)/550(5h)/600(3h)	[173] 2014
	$Ni(15)/Al_{0.83}Zr_{0.17}O_{1.58}$ (P3: 6)	S_{BET} =342, , D_{Ni} = 12.7	100	3.6	118	23.9	-			
	$Ni(15)/Al_{0.83}Zr_{0.17}O_{1.58}$ (P3: 12)	S_{BET} =322, , D_{Ni} = 9.3	100	2.5	126	24.5	-			
	$Ni(15)/Al_{0.83}Zr_{0.17}O_{1.58}$ (P3: 18)	S_{BET} =319, , D_{Ni} = 10.7	100	2.2	122	24.9	-			
	$Ni(15)/Al_{0.83}Zr_{0.17}O_{1.58}$ (P3: 24)	S_{BET} =317, , D_{Ni} = 11.3	100	2.0	120	27.7	-			
24.	$Ni(15)/Al_{0.83}Zr_{0.17}O_{1.58}$	S_{BET} =315, D_{Ni} = 4.5	-	%S 0	%Y 170	%S 0	-	3/-/400-700/33.34/-	SG/50(2h)/550(5h)/600(3h)	[118] 2013
	$Ni(15)/Al_{0.83}Zr_{0.17}O_{1.58}$	S_{BET} =222, D_{Ni} = 12.	-	7.5	165	0	-		Support: SG/-/550(5h)/- Metal loading: IWI/80(24h)/550(5h)/600(3h)	
25.	$Ni(10)/Al_2O_3$	S_{BET} = 339, AD = 131	100	-	%Y 104	-	-	6/-/500/15/-	SG/80(120h)/550(5h)/550(3h)	[175] 2013
	$Ni(10)/Al_{0.91}Zr_{0.09}O_{1.55}$	S_{BET} = 336, AD = 124	100	-	123	-	-			
	$Ni(10)/Al_{0.83}Zr_{0.17}O_{1.58}$	S_{BET} = 320, AD = 101	100	-	137	-	-			
	$Ni(10)/Al_{0.77}Zr_{0.23}O_{1.62}$	S_{BET} = 292, AD = 86	100	-	130	-	-			
	$Ni(10)/Al_{0.71}Zr_{0.29}O_{1.64}$	S_{BET} = 214, AD = 79	100	-	119	-	-			
26.	$Ni(5)/Al_{0.83}Zr_{0.17}O_{1.58}$	S_{BET} = 240, D_{pore}=7.5	72	%S 0	%Y 54	%S 11.6	-	6/-/500/35/-	SG/80(72h)/550(5h)/550(3h)	[172] 2013
	$Ni(10)/Al_{0.83}Zr_{0.17}O_{1.58}$	S_{BET} = 243, D_{pore}=7.2	100	10.6	120. 6	25.6	-			
	$Ni(15)/Al_{0.83}Zr_{0.17}O_{1.58}$	S_{BET} = 251, D_{pore}=7.4	100	10.5	124. 9	21.6	-			
	$Ni(20)/Al_{0.83}Zr_{0.17}O_{1.58}$	S_{BET} = 245, D_{pore}=6.9	100	6.5	120. 9	25.3	-			
	$Ni(25)/Al_{0.83}Zr_{0.17}O_{1.58}$	S_{BET} = 237, D_{pore}=7.6	100	5.3	110. 6	28.6	-			
27.	$Ni(10)/Al_2O_3$	S_{BET} = 191, D_p = 5.4	80	%M 5	%M 48	%M 2	-	3/-/500/5.8/-	Support: SG/110(10)/650(4h)/- Metal loading IWI/70(12h)/450(3h)/600(2h)	[183] 2013
	$Ni(10)/Al_{0.99}La_{0.01}O_{1.5}$	S_{BET} = 321, D_p = 5.8	83	5.5	60	2	-			
	$Ni(10)/Al_{0.97}La_{0.03}O_{1.5}$	S_{BET} = 298, D_p = 4.6	86	6	61	2	-			
	$Ni(10)/Al_{0.95}La_{0.05}O_{1.5}$	S_{BET} = 291, D_p = 4.0	75	6.5	2	2	-			
	$Ni(20)/Al_2O_3$	S_{BET} = 282, D_{Ni} =18.7	100	%S	%Y	%S	-	3/-/300-500/-/-	Support:	[180]

28.				3	28	64			CP/60(6h)/500(2h)/- Metal loading: IM/-/500(2h)/500(2h)	2012
	$Ni(20)/Al_{0.33}Y_{0.67}O_{1.5}$	S_{BET} = 18.7, D_{Ni} =12.5	100	0	36	32.5	-			
	$Ni(20)/Al_{0.5}Y_{0.5}O_{1.5}$	S_{BET} = 49.2, D_{Ni} =14.0	100	0	34	20	-			
	$Ni(20)/Al_{0.67}Y_{0.33}O_{1.5}$	S_{BET} = 109.3, D_{Ni} =14.3	100	0	33	27	-			
29.	$Ni(15)/Al_2O_3$	S_{BET} = 105, D_{Ni} = 2	99	%M 0	%M 65	%M 0	-	3/-/350-600/-/-	Support: CP/-/900(6h)/- Metal loading: IWI/-/450(4h)/500(3h)	[80] 2012
	$Ni(15)/Al_{0.91}Ce_{0.09}O_{1.55}$	-	100	0	67.5	5	-			
	$Ni(15)/Al_{0.9}Ce_{0.05}Zr_{0.05}O_{1.55}$	-	82	10	67.5	2.5	-			
30.	$Ni(1)/Al_2O_3$	-	83.9	%S 27.3	%S 45	%S 18.5	-	3/-/400/-/-	Support: IWI/-/850(8h)/- Metal loading: IM/100(2h)/450(5h)/600(2h)	[103] 2011
	$Ni(1)/Al_{0.97}Ca_{0.03}O_{1.49}$	-	100	6.21	73.2	33.5	-			
	$Ni(1)/Al_{0.94}Ca_{0.06}O_{1.47}$	-	97.9	13.3	67.3	32.8	-			
31.	$Ni(10)/Al_2O_3$	-	100	%S 2	%S 95	%S 5	-	3/-/400/24/-	Support: IWI/-/850(8h)/- Metal loading: IM/100(2h)/450(5h)/600(2h)	[176] 2011
	$Ni(10)/Al_{0.97}Ca_{0.03}O_{1.48}$	S_{BET} =75.5, D_{Ni} = 5.8	100	2	95	16	-			
	$Ni(10)/Al_{0.95}Ca_{0.05}O_{1.47}$	-	100	2	92	8	-			
	$Ni(10)/Al_{0.93}Ca_{0.07}O_{1.46}$	S_{BET} =53.3, D_{Ni} = 6.4	100	2	90	2	-			
32.	$Ni(20)/Al_{0.28}Mg_{0.72}O_{1.14}$	S_{BET} = 209.7, D_p = 8.79	100	Y_a 1	Y_a 4.83	Y_a 0.11	-	3/-/400-800/-/-	CP/120(ON)/600(6h)/700(2h)	[166] 2011
	$Ni(20)/Al_{0.29}Mg_{0.57}Zn_{0.14}O_{1.14}$	S_{BET} = 185.2, D_p = 8.7	100	1	4.94	0.1	-			
	$Ni(20)/Al_{0.3}Mg_{0.35}Zn_{0.35}O_{1.15}$	S_{BET} =185.9, D_p = 10.71	100	0.5	4.82	0.12	-			
	$Ni(20)/Al_{0.3}Mg_{0.14}Zn_{0.56}O_{1.15}$	S_{BET} = 121.3, D_p =11.69	100	0	4.84	0.12	-			
	$Ni(20)/Al_{0.31}Zn_{0.69}O_{1.16}$	S_{BET}=104.1, D_p = 12.24	100	0.5	4.86	0.11				
33.	$Ni/Al_{0.57}Zn_{0.43}O_{1.28}$	S_{BET} = 85.2	100	%S 0	%Y 96.1	%S 0	-	3/-/300-580/-/-	U/-/900(2h)/-	[165] 2009
34.	$Ni(10)/Al_2O_3$	S_{BET}=236.3, D_{pore}=4.8	-	-	%S 90	-	-	4/-/300-600/-/-	Support: Rest: IWI/-/850(6h)/- Fe: PT/110/400(6h) Metal loading: IM/110/400(6h)/400(1h)	[167] 2008
	$Ni(10)/Al_{0.99}Na_{0.01}O_{1.5}$	S_{BET}=226.1, D_{pore}=4.64	100	6	75	-	-			
	$Ni(10)/Al_{0.78}Fe_{0.22}O_{1.5}$	S_{BET}=6.4, D_{pore}=15.04	55	10	90	-	-			
35.	$Ni(15)/Al_{0.98}La_{0.02}O_{1.5}$	-	100	Y_a 0.5	Y_a 3	Y_a 0.4	-	4/-/400-500/-/-	Support: IM/105(24h)/900(30h)/-	[184] 2007

	$Ni(10)/Al_{0.98}La_{0.02}O_{1.5}$	-	100	0.2	3.3	0.2	-		Metal loading: IM/-/550(2h)/ 550(5h)	
36.	$Ni(9.7)/\gamma\text{-}Al_2O_3$	$S_{BET,\ support}$ = 130	-	% M 0	% M 76	% M 0.5	-	3/-/600-700/-/-	Support: Comm. Al_2O_3 Metal loading: Both same IM/120/500(5h)/500(3h)	[132] 2002
	$Ni(10)/Al_{0.93}Ce_{0.07}O_{1.53}$	-	-	3	65	3	-		Support: IM/120(ON)/500(3h)/-	
	Group 3: promoted Ni/ Al_2O_3									
37.	$Ni_{0.61}Rh_{0.06}Ce_{0.33}/Al_2O_3$	-	90	%M 0	%M 72	%M 0	-	4-10/-/150-700/-/-	Support: Comm. Al_2O_3 Metal loading: IWI/100/600(2h)/600(2h)	[189] 2016
38.	$Ni(15)/\ \gamma\text{-}Al_2O_3$	S_{BET} = 136.5, D_p = 9.0, V_{pore} = 0.32	100	%S 16	%S 88	%S 3	-	-/13/250-650/-/-	Support: Comm. Al_2O_3 -/-/600(6h)/- Metal loading: CI/110(24h)/600(3h)/600(2h)	[193] 2016
	$Ni_{0.5}Co_{0.5}(15)/\ \gamma\text{-}Al_2O_3$	S_{BET} = 142, D_p = 9.6, V_{pore} = 0.33	100	8	92	2	-		Support: IM/110(24h)/600(3h)/- Metal loading: CI/110(24h)/600(3h)/600(2h)	
39.	Ni/Al_2O_3	D_{Ni} = 20	90	%M 0	%M 70	%M 4	-	-/2/200-700/-/9000	Support: Comm. Al_2O_3 IWI/27(24h)/600(2h)/600(2h)	[190] 2015
	$Ni_{0.99}Rh_{0.01}/Al_2O_3$	D_{Ni} = 13	100	0	72	0	-			
40.	$Ni_{0.51}Cu_{0.47}K_{0.02}(12.15)/\gamma\text{-}Al_2O_3$	-	-	Y_a 0.80	Y_a 1.35	Y_a 0.81	-	2.5/300/-/-/-	Support: Comm. Al_2O_3 (for all) IM/50(ON)/550(2h)/- Metal loading CI/27(ON)/450(2h)/ 300	[192] 2013
		-	-	0.54	1.36	0.53	-		Metal loading CI/27(ON)/550(2h)/ 300	
		-	-	0.26	1.27	0.25	-		Metal loading CI/27(ON)/650(2h)/ 300	
		-	-	0.16	1.31	0.16	-		Metal loading CI/27(ON)/800(2h)/ 300	
41.	$Ni(10)/Al_2O_3$	S_{BET} = 84	100	Y_a 0.9	Y_a 4.6	Y_a 0	-	5/-/200-700/-/-	IM/120(ON)/600(5h)/750(4h)	[191] 2008
	$Ni_{0.72}Cu_{0.28}(10)/Al_2O_3$	S_{BET} = 78	100	0.2	4.9	0	-			
	$Ni_{0.32}Cu_{0.68}(10)/Al_2O_3$	S_{BET} = 78	100	0.2	4	0.1	-			
	$Ni_{0.52}Cu_{0.48}(10)/Al_2O_3$	S_{BET} = 82	100	0.4	4.7	0.4	-			

42.	$Ni_{0.996}Pt_{0.004}(15.3)/Al_2O_3$	-	74	-	%S 32	-	-	4/-/400-550/5/-	Support: IM/100(1h)/500(4h)/- Metal loading: IWI/150(2h)/600(2h)/500(4h)	[188] 2008
	$Ni_{0.999}Pt_{0.001}(15.2)/Al_2O_3$	-	42	-	38	-	-			
43.	$Ni_{0.996}Pt_{0.004}(15.2)/Al_2O_3$	-	95	%Y 0.5	%Y 182	%Y 4	-	3/-/350-550/1.5/-	Support: IM/200(1h)/900(1h)/- Metal loading: IWI/100(2h)/500(2h)/500(4h)	[187] 2008
	Group 4: Promoted Ni/modified Al_2O_3									
44.	$Ni(10)/Al_{0.62}Mg_{0.38}W_{0.001}O_{1.31}$	S_{BET}=152, D_{pore}=10.8	100	%S 1	%S 74	%S 4	11.3	4/-/450-600/3.367/1045	Support: CP/-/450-800(6h)/- Metal loading: CP/110(18h)/500(5h)/500(2h)	[207] 2021
	$Co(18)/Al_{0.62}Mg_{0.38}W_{0.001}O_{1.31}$	S_{BET}=220, D_{pore}=6.4	100	0.6	76	0.5	8.23			
	$Ni_{0.69}Co_{0.31}(14.5)/Al_{0.62}Mg_{0.38}W_{0.001}O_{1.31}$	S_{BET}=200, D_{pore}=8.4	100	1	78	2.2	9.30			
	$Ni_{0.46}Co_{0.54}(16.5)/Al_{0.62}Mg_{0.38}W_{0.001}O_{1.31}$	S_{BET}=160, D_{pore}=8.8	100	1.6	70	4.4	-			
	$Ni_{0.27}Co_{0.73}(18.5)/Al_{0.62}Mg_{0.38}W_{0.001}O_{1.31}$	S_{BET}=117, D_{pore}=10.7	100	2.6	66	8.2	-			
	$Ni_{0.12}Co_{0.88}(20.5)/Al_{0.62}Mg_{0.38}W_{0.001}O_{1.31}$	S_{BET}=142, D_{pore}=8.4	100	3.4	69	9	-			
45.	$Rh_{0.01}Ni_{0.99}(10.25)/Al_{0.86}Ce_{0.08}La_{0.06}O_{1.54}$	D_{Ni} = 10	100	%Y 0	%Y 68	%Y 1	30	3/-/500/24/26000	Support: IM/-/650(2h)/- Metal loading: IM/-/650(6h)/300(1.5h)/500(1h)	[194] 2019
	$Rh_{0.01}Ni_{0.99}(10.5)/Al_{0.86}Ce_{0.08}La_{0.06}O_{1.54}$	D_{Ni} = 10	100	1.9	70	2.4	0.86			
	$Rh_{0.02}Ni_{0.98}(10.75)/Al_{0.86}Ce_{0.08}La_{0.06}O_{1.54}$	D_{Ni} = 12	100	4.1	84	7.4	0.50			
	$Rh_{0.03}Ni_{0.97}(11)/Al_{0.86}Ce_{0.08}La_{0.06}O_{1.54}$	D_{Ni} = 11	100	4.9	69	17	0.01			
46.	$Ni(15)/Al_{0.8}Zr_{0.2}O_{1.6}$	S_{BET} =199, D_p = 10.6	100	%S 0	%Y 73.4	%S 40.5		3/-/450/16.67/-	Support: SG/80(120h)/550(5h)/- Metal loading: CI/80(12h)/550(5h)/650(3h)	[205] 2016
	$Ni_{0.83}Mg_{0.17}(16.24)/Al_{0.8}Zr_{0.2}O_{1.6}$	S_{BET} =185, D_p = 8.7	100	0	81.1	42.2				
	$Ni_{0.83}Ca_{0.17}(17)/Al_{0.8}Zr_{0.2}O_{1.6}$	S_{BET} = 181, D_p = 10	100	1.2	76.8	40.2	-			
	$Ni_{0.83}Sr_{0.17}(19.5)/Al_{0.8}Zr_{0.2}O_{1.6}$	S_{BET} =180, D_p = 8.6	100	0.4	87.9	39.8	-			
	$Ni_{0.83}Ba_{0.17}(22)/Al_{0.8}Zr_{0.2}O_{1.6}$	S_{BET} =175, D_p = 9.1	100	0.8	80.4	43.1	-			
47.	$Ni_{0.95}Pt_{0.05}(15.5)/Al_{0.97}Ce_{0.0.3}O_{1.51}$	$S_{BET,Al2O3}$=243, D_{Ni}=5	98.4	-	%S 18.8	-	-	3/-/500/24/24500	Support: IM/120(3h)/650(6h)/-	[196] 2015

	$Ni_{0.95}Pt_{0.05}(15.5)/Al_{0.97}La_{0.03}O_{1.5}$	$S_{BET,Al2O3}$=238, D_{Ni}=6	98.7	-	6.1	-	-		Metal loading: IM/110(2h)/-/550(1.5h)	
	$Ni_{0.95}Pt_{0.05}(15.5)/Al_{0.97}Mg_{0.03}O_{1.49}$	$S_{BET,Al2O3}$=224, D_{Ni}=5	99.8	-	2.0	-	-			
	$Ni_{0.95}Pt_{0.05}(15.5)/Al_{0.97}Zr_{0.0.3}O_{1.51}$	$S_{BET,Al2O3}$=244, D_{Ni}=6	100	-	2.3	-	-			
48.	$Ni(10)/\alpha\text{-}Al_2O_3$	DS=4.2, S_{BET} = 69	100	%S 20	Y_a 0.86	%S 1	-	6/-/300-700/-/-	Support: IM/126(ON)/550(5h)/- Metal loading: IWI/126(ON)/550(5h)/-	[199] 2014
	$Ni(20)/\alpha\text{-}Al_2O_3$	DS=1.3, S_{BET} = 63	100	-	0.75	-	-			
	$Ni(10)/Al_{0.5}La_{0.5}O_{1.5}$	DS=3.8, S_{BET} = 43	100	-	0.86	-	-			
	$Ni_{0.5}Co_{0.5}(10)/Al_{0.5}La_{0.5}O_{1.5}$	S_{BET} = 39	100	22	0.86	4	-			
49.	$Ni(10)/Al_{0.96}Ca_{0.04}O_{1.44}$	D_{Ni} = 10.6	100	%S 5	%S 100	%S 0	-	4/-/500-800/-/-	Support: IM/120(10h)/850(10h)/- Metal loading: IM/120(10h)/450)5h)/ 800(2h)	[206] 2012
	$Ni_{0.67}Co_{0.33}(10)/Al_{0.96}Ca_{0.04}O_{1.44}$	D_{Ni} = 9.6	100	6	100	0	-			
	$Ni_{0.33}Co_{0.67}(10)/Al_{0.96}Ca_{0.04}O_{1.44}$	D_{Ni} = 12.4	100	12	100	0	-			
	$Co(10)/Al_{0.96}Ca_{0.04}O_{1.44}$	D_{Ni} = 11.2	100	12	100	0				
50.	$Ni_{0.94}Cu_{0.06}(35)/Al_{0.76}Mg_{0.24}O_{1.38}$	D_{NiO} = 6.9	100	%S 15	%S 95.2	%S 10	0.25	3/-/250-600/-/-	Support: Si: SG/60(24h)/650(6h)/- Zn & Mg: PT/120(ON)/ 650(6h)/- Metal loading: IM/120(ON)/ 650(6h)/650(0.67h)	[204] 2011
	$Ni_{0.94}Cu_{0.06}(35)/Al_{0.86}Zn_{0.14}O_{1.43}$	D_{NiO} =20.1, D_{Ni} = 8.6	100	36.5	95.2	10	0.1			
	$Ni_{0.94}Cu_{0.06}(35)/Al_{0.94}Si_{0.06}O_{1.53}$	D_{NiO} =7.2, D_{Ni} = 18	100	29.6	92.0	7.2	1.1			
51.	$Ni_{0.84}Rh_{0.16}/Al_{0.92}Ce_{0.8}O_{1.53}$	-	80	%S 24	%S 85	%S 18		6/-/450-600/-/-	Support: Washcoating of Al_2O_3 on SS Plate Metal loading: IWI/120(3h)/600(3h)/500(2h)	[201] 2011
52.	$Ni_{0.94}Rh_{0.06}(6.94)/Al_{0.5}Y_{0.5}O_{1.5}$	S_{BET} = 110	98.2	Y_a 0.75	Y_a 3.84	Y_a 0.46	3.5	4/-/675/-/-	Support: IM/120(15h)/900(15h)/- Metal loading: CI/-/700(4h)/450(3h)	[198] 2010
	$Rh(0.94)/Al_{0.5}Y_{0.5}O_{1.5}$	S_{BET} = 133	97.2	0.7	3.53	0.55	12.4			
53.	$Ni_{0.68}(10)/Al_{0.94}Mg_{0.06}O_{1.47}$	-	-	%Y 15.1	%Y 88.3	%Y 24.8	-	10/-/550/-/-	Support: IM/110(4h)/650(6h)/- Metal loading: IWI/110(4h)/800(6h)/850(1h)	[203] 2009
	$Ni_{0.95}Cu_{0.05}(10.5)/Al_{0.94}Mg_{0.06}O_{1.47}$	-	-	12.5	73.5	23.9	-			
	$Ni_{0.92}Cu_{0.08}(11)/Al_{0.94}Mg_{0.06}O_{1.47}$	-	-	11	73.4	20.8	-			
	$Ni_{0.52}Cu_{0.48}(20)/Al_{0.94}Mg_{0.06}O_{1.47}$	-	-	8.2	59.6	10.9	-			
54.	$Ni(15)/Al_{0.98}La_{0.02}O_{1.5}$	S_{BET} = 114, D_{Ni} = 13	86	Y_a	Y_a 3.44	Y_a 0.52	-	4/-/450-600/-/-	Support: IM/90(ON)/550(5h)/-	[195] 2009

				0.094					Metal loading: IM/90(ON)/550(5h /700(1h)	
	$Ni_{0.996}Pd_{0.004}(15.1)/Al_{0.98}La_{0.02}O_{1.5}$	S_{BET} = 132, D_{Ni} = 24	99	0.08	3.78	0.52	-			
	$Ni_{0.99}Pd_{0.01}(15.3)/Al_{0.98}La_{0.02}O_{1.5}$	S_{BET} = 133, D_{Ni} = 26	99	0.1	3.71	0.59	-			
	$Ni_{0.998}Pt_{0.002}(15.1)/Al_{0.98}La_{0.02}O_{1.5}$	S_{BET} = 139, D_{Ni} = 17	99	0.1	3.79	0.62	-			
	$Ni_{0.994}Pt_{0.006}(15.3)/Al_{0.98}La_{0.02}O_{1.5}$	S_{BET} = 138, D_{Ni} = 19	97	0.08	3.80	0	-			
55.	$Ni_{0.86}Co_{0.14}(35)/Al_{0.78}Si_{0.22}O_{1.61}$	-	100	%S 6	%S 80	%S 30	-	3-12/-/400-600/-/-	Support: Al-Si: SG/-/-/- Rest: DE-PT/120(ON)/ 650(6h)/- Metal loading: Doping/-/-/-	[44] 2009
	$Ni_{0.93}La_{0.07}(35)/Al_{0.78}Si_{0.22}O_{1.61}$	-	100	1	92	10	-			
	$Ni_{0.88}La_{0.12}(40)/Al_{0.78}Si_{0.22}O_{1.61}$	-	100	7	100	1	-			
	$Ni_{0.83}La_{0.17}(45)/Al_{0.78}Si_{0.22}O_{1.61}$	-	100	5	94	7.5	-			
56.	$Ni(5)/Al_{0.97}Ce_{0.03}O_{1.52}$	S_{BET} = 185, D_{NiO} =7.50	98	Y_a 0.45	Y_a 2.75	Y_a 0.41	-	3/-/600/-/-	Support: IWI/80(10h)/550(3h)/- Metal loading: IWI/80(10h)/550(3h)/800(1h)	[202] 2009
	$Ni_{0.98}Ir_{0.02}(5.3)/Al_{0.97}Ce_{0.03}O_{1.52}$	S_{BET} = 154, D_{NiO} =8.80	99	0.55	3.01	0.48	-			
	$Ni_{0.97}Pd_{0.03}(5.3)/Al_{0.97}Ce_{0.03}O_{1.52}$	S_{BET} = 163, D_{NiO} =8.50	100	0.81	4.43	0.66	-			
	$Ni_{0.98}Pt_{0.02}(5.3)/Al_{0.97}Ce_{0.03}O_{1.52}$	S_{BET} = 156, D_{NiO} =7.90	100	0.55	3.22	0.88	-			
	$Ni_{0.96}Ru_{0.04}(5.3)/Al_{0.97}Ce_{0.03}O_{1.52}$	S_{BET} = 173, D_{NiO} =8.90	99	0.56	3.08	0.42	-			
57.	$Ni(15)/Al_2O_3$	S_{BET} = 67.1, V_P = 0.18	100	%S 0	%S 75	%S 20	5.4	3/-/600-800/-/-	Support: IM/-/900(8h)/- Metal loading: IWI/-/450(2h)/475(3h)	[200] 2007
	$Ni_{0.98}Ag_{0.02}(15.6)/Al_2O_3$	S_{BET} = 67, V_P = 0.17	100	15	50	20	23.4			
	$Ni(15)/Al_{0.97}La_{0.03}O_{1.5}$	S_{BET} = 71.8, V_P= 0.14	100	10	68	20	4.6			

2.5 Ni/CeO_2 Systems

CeO_2 was first identified in 1953 as a rare earth element through spectro-chemical method by U.S geological survey [209]. Observation on higher noble metal dispersion capability of CeO_2 compared to conventional Al_2O_3 led to the consideration of CeO_2 as an inert support to stabilize active metal nano particles for catalytic application in 1975 [210]. In 1976 Ford Motor Company employed cerium oxide as an oxygen storage component in the three-way catalyst of the car converter [211]. In 1977 for the first time CeO_2 was considered for production of hydrogen by using a thermochemical water splitting technique [212]. On the surface of non-stoichiometric CeO_2, Ce^{4+} ion can be reduced to Ce^{3+} easily and produce oxygen vacancy, which increases oxygen mobility in the CeO_2 support matrix as explained by Kröger-Vink Notation:

$$2CeO_2 \leftrightarrow Ce_2O_3 + V_o^{\cdot\cdot} + O_o^x + 2e'' \quad (2.12)$$

Addition of a divalent cation such as Ni can enhance the density of oxygen vacancy:

$$NiO \overset{CeO_2}{\longleftrightarrow} Ni''_{Ce} + V_o^{\cdot\cdot} + O_o^x \quad (2.13)$$

It also helps to enhance the reducibility of material. Polychronopoulou et al. [2020, 2021] study the design aspects of CeO_2 doped with transition metals (Cu, Co, Mn, Fe, Ni, Zr, and Zn) for low-temperature catalytic oxidation of CO by using transient DFT approach and kinetics study. These transition metals induce significant tensile lattice strain in the structure which also a cause of the oxygen vacancy formation. Ni Mn, Fe, and Zn dopants are observed to form segregated oxides within the matrix while presence of Ni enhances the catalytic activity compared with Mn, Fe, and Zn doped powders [213,214]. Because of its properties and emerging features, researchers emphasize to use CeO_2 in different industrial applications such as in photocatalysis, fuel cells, thermochemical water splitting's, organic reactions, and reforming processes. Most of the articles published on Ni/CeO_2 catalysts are after 2006, as observed in **Fig. 2.1(b)**. **Table 2.3**, also divided into four groups based on the catalyst modification strategy employed. For Ni/CeO_2 catalysts, researchers predominantly used IM and CP methods in catalyst preparation [122,215–219]

2.5.1 Group 1:Ni/CeO_2 Catalysts

Fajardo et al.[2007] compare the ESR performance of $Ni(17.3)/CeO_2$ catalysts prepared by bio-polymerization and impregnation methods. Catalyst prepared by polymerization method shows surface area of 36 m^2/g, 100% ethanol conversion, and 67.5% H_2 selectivity. However, the catalyst prepared by impregnation method exhibits much lower surface area (5 m^2/g) and ethanol conversion (30%) but H_2 selectivity improved to 77% [220]. General studies report that increase in metal loading increases particle size due to metal agglomeration/sintering and decreases the activity by coke formation on surface [122,215,217]. Jalowieki et al. [2010] study the effect of Ni/Ce atomic ratio (Ni/Ce = 0.073, 0.2, 0.4, 0.7, 0.9) on ESR over the Ni/CeO_2 catalysts prepared by co-precipitation method. The Ni

particle size as small as 8 nm and the highest H_2 selectivity of 65% are observed at Ni/Ce= 0.2 atomic ratio [217].

Moraes et al. [2015] synthesize CeO_2 support of nanocube (Ni(10)//CeO_2-NC), nanorod (Ni/CeO_2-NR) and flower-like (Ni(10)/CeO_2-FL) geometries by hydrothermal method and compare the effect of CeO_2 support morphology on carbon deposition on the spent catalysts during ESR. The amount of carbon deposition increase in the order Ni(10)/CeO_2-NR (0.23 $mg_c/(g_{cat}.h)$ < Ni(10)/CeO_2-FL (0.61 $mg_c/(g_{cat}.h)$ < Ni(10)/CeO_2-NC (1.05 $mg_c/(g_{cat}.h)$, but the H_2 yield is not affected by the morphology, as almost the same hydrogen yield (~ 48%) is reported for all the catalysts [221].

Seemingly, Greluk et al. [2021] compare Ni(10)/CeO_2 and Co(10)/CeO_2 catalysts synthesized by impregnation method. Strong metal support interaction between nickel metal and CeO_2 infer the redox property of the support and active metal particle size. Ni(10)/CeO_2 catalyst shows better activity compared to that of the Co(10)/CeO_2 powder [113].

2.5.2 Group 2: Ni/Modified CeO_2

In 2010s, the studies mainly focus on improving the thermal stability of CeO_2 at higher reaction temperatures. Investigators modify CeO_2 support with oxides of La [85,222,223], Mg [224,225], Ti [226], Pr [227,228], Gd [229] and Zr [115,230–232], as shown in the second catalyst group of **Table 2.3**. TiO_2 is considered as a support modifier because the substitution of Ce^{4+} ion by Ti^{4+} ion may enhance oxygen mobility and redox capacity of support, which leads to improved hydrogen selectivity and resistance to coke deposition for the catalyst. Ye et al. [2008] study the effect of Ti incorporation in the CeO_2 support in Ni (10)/$Ce_{1-x}Ti_xO_2$ (x = 0 to 1) catalyst system synthesized by a two-step process; support prepared by co-precipitation method and then followed by metal loading by IWI method. The XRD and TPR techniques show the presence of $NiTiO_3$ phase with CeO_2 as the Ti content increased. The mixed phase support obtains lower surface area and higher H_2 selectivity compared to those of the catalysts with pure CeO_2 and TiO_2 supports. Ni(10)/$Ce_{0.65}Ti_{0.35}O_2$ catalyst reveals the maximum H_2 selectivity of 64.6% with the lowest CH_4 selectivity of 2.4% [226]. Simultaneously, some research groups study MgO as support modifier.

The presence of MgO in Ni/CeO_2-MgO system forms $Ni_xMg_yO_2$ oxide solution and increases bonding force between Ni and support MgO most probably because of the fact that electronegativity of Mg (around 1.31) is higher than that of the Ce (1.12). This enhances the reduction temperature of the NiO phase for the MgO modified powder compared to that of the non-modified catalyst and decreases the particle size of the reduced metal for the MgO modified powder [225,233,234].

Praseodymium (Pr) mostly exists at 3+ oxidation state and expected to favor oxygen vacancy formation, improve ceria redox capability, and the anti-sintering ability of the catalyst. These prompt investigations of Pr-doped ceria as ESR catalyst in the early part of the second decade. The addition of Pr promoter to ceria improve the anti-sintering properties of the nickel particles by improving the

interaction between Ni and support and also improve OSC [228]. Xiao et al. [2019] synthesize Ni(10)/$Ce_{1-x}Pr_xO_2$ (x=0 to 0.30) catalysts by citric acid assisted sol-gel method. Pr doping modify the metal support interaction and control Ni particle size. The Ni(10)/$Ce_{0.8}Pr_{0.2}O_2$ catalyst shows the lowest Ni particle size 5.2 nm whereas the highest H_2 yield 7750 μmol/min is reported for the Ni(10)/$Ce_{0.7}Pr_{0.3}O_2$ catalyst [227].

Incorporating ZrO_2 into CeO_2 enhances the reducibility and thermal stability of ceria and also improves the metal dispersion [115,230–232]. Arslan et al. [2016] investigate the effect of varying calcination/reduction (400-650 ℃) temperature on Ni(3)/$Ce_{0.85}Zr_{0.15}O_2$ catalyst prepared by a two-step process. In comparison to the catalyst treated at 400 ℃, the support surface area decreases from 82.8 to 12.8 m^2/g and particle size increases from 4.2 to 13.0 nm for the catalysts treated at 650 ℃. The highest hydrogen selectivity 75% and negligible coke formation 1.9 % are reported for the catalyst calcined at 400 ℃ [235].

Recent studies investigate La_2O_3 and ZrO_2 as support modifiers. La^{3+} ion in La_2O_3 can increase oxygen vacancy in ceria lattice matrix, promote oxidation of carbon deposited on spent catalysts, and might be more effective than the $La_2O_2CO_3$ (mostly observes for the Al_2O_3-La_2O_3 system) for removing carbon. Zhurka et al. [2020] synthesize Ni(10)/$Ce_{0.15}La_{0.02}$ $Zr_{0.83}O_2$ system catalysts by impregnation method and study catalytic activity at different steam to carbon (S/C) ratios. H_2 yield increases from 20 to 82% and CO yield decreases from 50 to 20% with increasing S/C ratio 1 to 6 [222]. Xiao et al. [2021] study the effect of different support modifiers (La, Tb, Zr) on Ni(10)/CeO_2 catalyst prepared by a sol-gel method. The Ni(10)/$Ce_{0.8}La_{0.2}O_2$ catalyst shows the maximum H_2 yield of 8000 μmol/min, lowest carbon formation rate 100 μmol/min, 100% ethanol conversion, and the highest surface area 20.71 m^2/g. Comparatively, the surface area, metal-support interaction and activity of the same La modified catalyst reduce in case of the catalyst prepared by a IM method [224].

Trane-Restrup et al. [2013] study the effect of Zr and combination of Mg-Al-Zr oxides on the CeO_2 support. Ni(8)/CeO_2 based catalysts are prepared by a two-step IWI process. Both of the support modifiers decrease the surface area in comparison of the unmodified catalyst, but modification improves the EtOH conversion in general. Coke deposition is observed to reduce in case of the Ni(8)/$MgAl_2O_4$-$CeZrO_4$ catalyst (15 $mg_c/(g_{cat}.h)$) compared to that for the Ni(8)/$Ce_{0.6}Zr_{0.4}O_2$ catalyst (96 $mg_c/(g_{cat}.h)$) [234]. Li et al. [2019] study the effect of Ni addition on the $Ce_{0.7}BaZr_{0.1}Y_{0.1}Yb_{0.1}O_{3-\delta}$ for ESR. Addition of Ni metal increases the surface area of the support from 4.9 to 5.05 m^2/g, achieves 70 % H_2 selectivity with 100% ethanol conversion [236].

2.5.3 Group 3: Promoted Ni/ CeO_2

The third group in Table 2.3 consists of the promoted-Ni metal supported on the unmodified CeO_2. Physicochemical properties and ESR activities of the bimetallic (Ni-Cu [237–239], Ni-Co [240,241], Ni-Sn [242] and Ni-Pt [79]) catalysts on CeO_2 support are developed based on synergistic

interaction of transition and other metals with Ni and investigated in the first decade of 21st century. Qihai et al. [2011] prepare Cu promoted $Ni_{1-x}Cu_x(y)/CeO_2$ (x = 0-0.03 and y = 10 and 15 wt.%) catalysts by a two-step method.

The metal dispersion and H_2 selectivity increase from 5.56 to 14.88%, and from 45.05 to 70.74 %, respectively as the Cu atomic loading varied from 0 to 0.015 for the catalyst with total 10 wt.% metal loading [238]. Cobalt doping enhances the redox properties of cerium infer by metal support interaction [243]. Pinton et al. [2016] synthesize $Ni_{1-x}Co_x(22.5)/CeO_2$ (x=0, 0.5) catalysts by a two-step method. Compared to the unpromoted catalyst, addition of cobalt increases the surface area from 72 to 76 m^2/g, decreases the nickel crystal size from 8.0 to 7.5 nm, and increases the H_2 yield from 50 to 63%. For the same $Ni_{0.5}Co_{0.5}(22.5)/CeO_2$ catalyst, synthesizes by a reverse microemulsion method, the surface area observes to increase to 132 m^2/g and nickel crystallite size decreases to 3.9 nm, however catalytic properties does not improve [241].

Boron, with a stable 3+ oxidation state interacts with the CeO_2 support, promotes the formation of oxygen vacancies, and enhances the removal of deposited carbon. Huang et al. [2014] figures out an increase in the H_2 yield from 75 to 80% and a decrease in coke deposition from 9.5 to 1.7 mg_c/g_{cat} (by TG analysis) due to the introduction of 1.4 wt.% boron in $Ni(8.1)/CeO_2$ catalyst system [244].

Zahra et al. [2020] examine the effect of metal loading on $Ni(x)/CeO_2$ (x =10, 13, 15 wt.%) catalyst and the effect of secondary metal promoter on bimetallic $Ni(13)-Y(4)/CeO_2$ (Y=Cu, Mg, Co) catalysts prepared by a two-stage IM method. $Ni(13)-Mg(4)/CeO_2$ bimetallic catalyst demonstrates higher H_2 selectivity by enhancing the methane reforming compared to the Cu and Co promoted catalysts. Weak metal dispersion and larger crystalline size are observed with increasing metal loading in $Ni(x)/CeO_2$ catalyst [237]. Alkali promoter may enhance the electronic enrichment of Ni by altering the interaction between adsorbed intermediates and the active metal phase. Slowik et al. [2021] prepare $K_{0.14}Co_xNi_{0.86-x}(12)/CeO_2$ catalyst by a two-step process. Addition of cobalt reduces the CH_4 SR rate and Ni-Co interaction, which decreases the metal particle size and significantly improves the H_2 selectivity from 79 to 89% [240]. However, addition of excess potassium to Ni/CeO_2 catalyst decreases the reduction temperature, cause metallic agglomeration, and decreases metal dispersion which negatively affected the stability of the catalyst [245].

2.5.4 Group 4: Promoted Ni/ Modified CeO_2

The last group in **Table 2.3** consists of the works related to promoted Ni/modified CeO_2 catalysts that emphases on investigating synergistic interactions of bimetallic catalysts with modified support and their effects on ESR [85,246–250]. Most of the research works in this category are reported in the second decade of the 21st century. Addition of silica as support modifier enhances the metal dispersion and surface area leading to improve the catalytic behaviour [246,247]. In an initial paper Furtado et al. [2009] investigate $Ni_{0.92}Cu_{0.08}(11)$ bimetallic catalysts based on Al_2O_3, CeO_2-ZrO_2, Nb_2O_5

Table 2. 3: Literature survey on steam reforming of ethanol on various Ni/CeO_2 based catalysts (2000-2023).

SN	Catalyst	Catalyst Properties	EtOH (%)	CO	H_2	CH_4	C rate	Reforming Conditions H_2O:EtOH/S:C/ T(°C)/ TOS (h)/GHSV(h^{-1})	Catalyst Preparation Method/DT(h)/CT(h)/RT(h)	Ref & year
	Group 1: Ni/CeO_2									
1.	$Ni(10)/CeO_2$	D_{Ni} = 22.0	100	%S 3	%S 85	%S 18	-	12/-/420/21/-	Support: Comm.CeO_2 Metal loading: IM/110(12h)/500(1h)/ 500(1h)	[113] 2021
	$Co(10)/CeO_2$	D_{Co} = 22.5	100	6	82	3	-			
2.	$Ni(10)/CeO_2$	S_{BET} = 10, D_{Ni} = 5	100	-	%M 70.3	-	-	3/-/400-750/-/12000	CP/100(24h)/750(4h)/-	[215] 2019
	$Ni(20)/CeO_2$	S_{BET} = 30.5, D_{Ni} = 8	100	-	75.1	-	-			
	$Ni(30)/CeO_2$	S_{BET} = 35.8, D_{Ni} = 15	100	-	70.9	-	-			
3.	$Ni(10)/CeO_2$-p	S_{BET} = 3	100	%S 10	%S 64	%S 5	-	3/-/300-600/24/2700	Support: PT/65(12h)/600(4h)/ -Metal loading: IWI/50(1h)/450(3h)/550(1h)	[216] 2018
	$Ni(10)/CeO_2$-r	S_{BET} = 52	100	8	62	6	-			
	$Ni(10)/CeO_2$-c	S_{BET} = 16	100	6	65	7	-			
4.	$Ni(10)/CeO_2$	S_{BET} = 79, D_{CeO2} = 10	7	%S 5.6	%S 48.3	%S 18.2	0.63	3/-/300/-/-	Support: CP/110(2h)/500(5h)/- Metal loading: IWI/110(1h)/600(5h)/500(1h)	[221] 2015
	$Ni(10)/CeO_2$ (NC)	S_{BET} = 35, D_{CeO2} = 22	54	10.3	48	18	1.05			
	$Ni(10)/CeO_2$ (NR)	S_{BET} = 80, D_{CeO2} = 12	60	9.8	49.0	16.8	0.23			
	$Ni(10)/CeO_2$ (FL)	S_{BET} = 113, D_{CeO2}=10	54	6.6	47.6	19.1	0.61			
5.	$Ni(20)/CeO_2$	S_{BET} = 70.1, V_P = 0.22, D_p= 6	75	%S 23	%S 27	%S 31	-	6/3/350/-/-	Support: (same for all) SG/120(20h)/600(2h)/- Metal loading: BM/120(ON)/500(2h)/ 500(1h)	[219] 2014
	$Ni(20)/CeO_2$	S_{BET} = 41.9, V_P = 0.16, D_p= 18.7	30	%S 12	%S 24	%S 15	-		Metal loading: IM/120(ON)/500(2h)/ 500(1h)	
6.	$Ni_{0.07}Ce_{0.93}O_{1.93}$	S_{BET} = 92	-	%M -	%M -	%M -	-	3/-/400/-/-	CP/100/500(4h)/200(10h)	[217] 2010
	$Ni_{0.17}Ce_{0.83}O_{1.83}$	S_{BET} = 100	100	5	50.0	5	-			
	$Ni_{0.28}Ce_{0.72}O_{1.72}$	S_{BET} = 136, D_{NiO} = 8	100	7	65.0	7	-			
	$Ni_{0.42}Ce_{0.72}O_{1.72}$	S_{BET} = 91, D_{NiO} = 12	92	12	60.0	14	-			

	$Ni_{0.48}Ce_{0.52}O_{1.52}$	S_{BET} = 109, D_{NiO} = 11	95	4	62.0	4	-			
	$Ni_{0.83}Ce_{0.17}O_{1.17}$	S_{BET} = 84, D_{NiO} = 9.4	100	4	60.0	3	-			
7.	$Ni(17.3)/CeO_2$	S_{BET} = 5, V_{pore} = 0.004	30	-	%S 82	%S 0	-	3/-/325-500/4.7/-	Support: Comm. CeO_2 Metal loading: IM/200(24h)/650(2h)/-	[220] 2007
	$Ni(17.3)/CeO_2$	S_{BET} = 51, V_{pore} = 0.037	100	-	75	22.5	-		Support: BM/100(3h)/350/- Metal loading: PYT 500(1h)/-/-/500(2h)	
	$Ni(17.3)/CeO_2$	S_{BET} = 36, V_{pore} = 0.028	100	-	78	16	-		Metal loading: PYT 700(1h)/-/-/500(2h)	
8.	$Ni(30)/CeO_2$	S_{BET} = 28	100	%S 20	%S 96	%S 5	-	3/-/650/17.5/40000	Support: Comm. CeO_2 Metal loading: IWI/80(24h)/400(12h)/725(1h)	[122] 2006
	$Ni(21)/MgO$	S_{BET} = 45	100	24	98	2	-			
	Group 2: Ni/modified CeO_2									
9.	$Ni(10)/CeO_2$	S_{BET} = 29.37, D_p =3.98	85	Y_b 1460	Y_b 6000	Y_b 500	-	-/2/500-650/25/ 55920	SG/120(6h)/600(4h)/ 500(1h)	[224] 2021
	$NI(10)/Ce_{0.8}La_{0.2}O_2$	S_{BET} = 20.71, D_p =8.71	100	1500	8000	200	-			
	$NI(10)/Ce_{0.8}Tb_{0.2}O_2$	S_{BET} = 16.06, D_p =9.81	90	1550	7000	800	-			
	$NI(10)/Ce_{0.8}Zr_{0.2}O_2$	S_{BET} = 18.23, D_p =8.62	90	1860	7200	300	-			
	$NI(10)/Ce_{0.8}La_{0.2}O_2$(IMP)	S_{BET} = 16.63, D_p =16.44	60	1400	4500	600	-	-/2/500-650/2/ 55920	IM/120(24h)/600(4h)/500(1h)	
10.	$Ni(10)/Ce_{0.15}La_{0.02}Zr_{0.83}O_2$		60	% S 10	%Y 65	% S 0	-	-/3/300-600/-/-	Support: IM/120(ON)/800(5h)/- Metal loading: IM/120(ON)/800(4h)/ 550(1h)	[222] 2020
	$Rh(1)/ Ce_{0.13}La_{0.02}Zr_{0.85}O_2$	-	78	0	76	0	-			
	$Ni(10)/Ce_{0.15}La_{0.02}Zr_{0.83}O_2$	-	22	50	22	4	-	-/1/400/-/-		
	$Ni(10)/Ce_{0.15}La_{0.02}Zr_{0.83}O_2$	-	40	40	38	2	-	-/2/400/-/-		
	$Ni(10)/Ce_{0.15}La_{0.02}Zr_{0.83}O_2$	-	50	38	44	1	-	-/3/400/-/-		
	$Ni(10)/Ce_{0.15}La_{0.02}Zr_{0.83}O_2$	-	60	35	56	0	-	-/4/400/-/-		
	$Ni(10)/Ce_{0.15}La_{0.02}Zr_{0.83}O_2$	-	74	30	74	0	-	-/5/400/-/-		
	$Ni(10)/Ce_{0.15}La_{0.02}Zr_{0.83}O_2$	-	90	24	82	0	-	-/6/400/-/-		
11.	$Ni(10)/CeO_2$	D_{Ni} = 7.7	95.7	Y_b 1550	Y_b 7000	Y_b 500	-	4/-/600/50/44240	CASG/120(12h)/600(4h)/500(1h)	[227] 2019

	$Ni(10)/Ce_{0.95}Pr_{0.05}O_2$	D_{Ni} = 6.7	100	1480	7300	600	-			
	$Ni(10)/Ce_{0.9}Pr_{0.1}O_2$	D_{Ni} = 6.1	100	1760	7520	500	-			
	$Ni(10)/Ce_{0.8}Pr_{0.2}O_2$	D_{Ni} = 5.2	100	1700	7600	800	-			
	$Ni(10)/Ce_{0.7}Pr_{0.3}O_2$	D_{Ni} = 7	100	1820	7750	650	-			
	$Ni(10)/Ce_{0.8}Pr_{0.2}O_2$ -IMP	D_{Ni} = 12.5	91.9	800	6800	250	-		IM/120(24h)/600(4h)/500(1h)	
12.	$BaZr_{0.1}Ce_{0.7}Y_{0.1}Yb_{0.1}O_{3-\delta}$	S_{BET} = 4.91	-	%S -	%S -	%S -	-	5/-/500-750/24/-	Support: SG/200(10h)/900(2h)/- Metal loading: PT/-/900(2h)/650(3h)	[236] 2019
	$Ni/BaZr_{0.1}Ce_{0.7}Y_{0.1}Yb_{0.1}O_{3-\delta}$	S_{BET} = 5.05	100	%S 10	%S 70	%S 8	0.021			
13.	$Ni(7)/Ce_{0.85}Mg_{0.15}O_{1.85}$	S_{BET} = 28.21, D_p = 10-15	100	% S 10	% S 70	% S 4	-	6/3/400-600/4895	Support: CP/120(12h)/550(4h)/- Metal loading: IWI/-/-/600(1h)	[233] 2017
14.	$Ni(3)/Ce_{0.85}Zr_{0.15}O_2$	S_{BET} = 82.8, V_p = 0.10, D_p = 3.8, $D_{support}$ = 4.2	100	%S 1.9	%S 75	%S 4	-	3.2/-/400-650/-/-	Support: (same for all) HT/175(4h)/400(6h)/- Metal loading: IM/100(3h)/400(4h)/400(4h)	[235] 2016
	$Ni(3)/Ce_{0.85}Zr_{0.15}O_2$	S_{BET} = 61.0, V_p = 0.10, D_p = 3.8, , $D_{support}$ = 4.9	100	6.8	72	3.4	-		Metal loading: IM/100(3h)/450(4h)/450(4h)	
	$Ni(3)/Ce_{0.85}Zr_{0.15}O_2$	S_{BET} = 16.4, V_p = 0.08, D_p = 3.8, , $D_{support}$ = 7.1	100	8.8	73	5.1	-		Metal loading: IM/100(3h)/500(6h)/500(4h)	
	$Ni(3)/Ce_{0.85}Zr_{0.15}O_2$	S_{BET} = 12.8, V_p = 0.05, D_p = 1.6, , $D_{support}$ = 13	85.2	15	68.5	7.8	-		Metal loading: IM/100(3h)/650(6h)/650(4h)	
15.	$Ni(2)/Ce_{0.8}Zr_{0.2}O_2$	S_{BET} = 85	100	% S 9	% S 91	% S 0.5	-	5/-/300-600/10/-	Support: CP/120(3h)/600(5h)/- Metal loading: IM/120(ON)/600(0.5h)/600(1h)	[232] 2016
16.	NiO (12)/$Ce_{0.55}La_{0.45}O_{1.78}$	D_p = 20.5, D_{Ni} = 12.2, S_{BET} = 14.9	100	%S 13.6	%S 62.7	%S 0	-	3/-/350-650/-/40000	IM/120(24h)/300(2h) 800(5h)/ 650(1h)	[223] 2014
		D_p = 16.9, D_{Ni} = 11.9, S_{BET} = 18.7	100	14.7	65.9	0	-		CCM/120(24h)/300(2h) 800(5h)/650(1h)	
17.	$Ce_{0.42}Zr_{0.58}O_2$	S_{BET} = 31.2, D_{pore} = 15.9, V_{pore} = 0.109	-	%S -	%S -	%S -	-	3/-/600-700/-/-	Support: CP/110(ON)/750(6h)/-	[115] 2013

	$Ni(30)/Ce_{0.42}Zr_{0.58}O_2$	S_{BET} = 24.5, D_{pore} = 11.1, V_{pore} = 0.07	100	%S 5	%S 75	%S 0	-		Metal loading: IM/110(ON)/550(4h)/550(5h)	
18.	$Ni(8)/Ce_{0.6}Zr_{0.4}O_2$	S_{BET} = 90, D_p = 15	100	-	-	-	96	-/5.3-6/400-700/70/-	Support: IWI/110(2h)/900(8h)/- Metal loading: CI/110(ON)/800(2h)/600(1h)	[234] 2013
	$Ni(8)/CeO_2$	S_{BET} = 113, D_p =10	90	-	-	-	19			
	$Ni(8)/MgAl_2O_4$-$CeZrO_4$	S_{BET} = 53, D_p = 6	100	-	-	-	15			
19.	$Ni(2)/Ce_{0.74}Zr_{0.26}O_2$	S_{BET} = 82.9, V_P = 0.155, $D_{support}$ = 11.5	100	%S 0	%S 75.34	%S 0.4	-	8/-/200-600/-/-	Support: CP/120(ON)/600(5h)/- Metal loading: IWI/120(ON)/600(6h)/600(2h)	[231] 2012
	$Ni(10)/Ce_{0.74}Zr_{0.26}O_2$	S_{BET}=67.8, V_p=0.128, $D_{support}$ = 10.4, D_{Ni} = 24	100	5.28	70.32	0.6	-			
	$Ni(20)/Ce_{0.74}Zr_{0.26}O_2$	S_{BET}=42, V_P = 0.112, $D_{support}$ = 9.4, D_{Ni} = 26	100	8.8	71.74	3.1	-			
20.	$Ni(18)/Ce_{0.9}Gd_{0.1}O_2$	S_{BET} = 21, D_{Ni} = 32	30	%M 1	%M 50	%M 3	-	3/-/500/27/-	Support: (same for all) HT & CP/200(3h)/300(3h)/- Metal loading: IM/225(2h)/700(3h)750(1h)	[229] 2012
	$Ni(18)/Ce_{0.9}Gd_{0.1}O_2$	S_{BET} = 17, D_{Ni} = 33	40	1	48	3	-		Metal loading: IM/225(2h)/800(3h)/750(1h)	
	$Ni(18)/Ce_{0.9}Gd_{0.1}O_2$	S_{BET} = 1, D_{Ni} = 34	18	0	55	0	-		Metal loading: IM/225(2h)/1200(3h)/750(1h)	
21.	$NiO\ (15)/Ce_{0.7}Pr_{0.3}O_2$	-	100	%S 1	%S 68	%S 0	-	3/-/350-650/-/ 10000	PT/80(24h)/750(4h)/500(1h)	[228] 2012
22.	$Ni(10)/CeO_2$	$S_{BET, support}$: 30.4	100	%S 0	%S 87.4	%S 21.5	-	4/80(4h)/300-500/-/-	Support: IM/80(6h)/400(2h)/- Metal loading: IWI/(6h)/500(5h)/550(3h)	[225] 2009
	$Ni(10)/Ce_{0.67}Mg_{0.33}O_{1.67}$	$S_{BET, support}$: 33.2	100	2.5	90	13	-			
	$Ni(10)/Ce_{0.50}Mg_{0.50}O_{1.5}$	$S_{BET, support}$: 41.7	100	2.5	94	8.5	-			
	$Ni(10)/Ce_{0.33}Mg_{0.67}O_{1.33}$	$S_{BET, support}$: 55.0	100	5	94	7.5	-			
	$Ni(10)/MgO$	$S_{BET, support}$: 103.42	100	5	87.5	10	-			
23.	$Ni(10)/CeO_2$	S_{BET} = 39.1	97.1	%S 12.1	%S 61.1	%S 7.2	-	3/-/350-600/-/40000	Support: CP/80(20h)/700(1h)/- Metal loading: IWI/80(20h)/700(2h)/650(1h)	[226] 2008
	$Ni(10)/Ce_{0.85}Ti_{0.15}O_2$	S_{BET} = 36.1		16.9	64.0	2.8	-			
	$Ni(10)/Ce_{0.65}Ti_{0.35}O_2$	S_{BET} = 37.0		18.0	64.6	2.4	-			
	$Ni(10)/Ce_{0.5}Ti_{0.5}O_2$	S_{BET} = 37.3	100	0	64.1	5	-			
	$Ni(10)/Ce_{0.35}Ti_{0.65}O_2$	S_{BET} = 39.3		11.6	60.9	7.9	-			
	$Ni(10)/Ce_{0.15}Ti_{0.85}O_2$	S_{BET} = 39.7		12.1	62.7	6.2	-			

	$Ni(10)/TiO_2$		100	12.0	62.4	6.5	-			
	Group 3: Promoted Ni/CeO_2									
24.	$K_{0.14}Co_{0.86}(12)/CeO_2$	S_{BET} = 36.2, D_p =9.5	100	%S 6	%S 93	%S 10	-	12/-/420/24/-	Support: IM/110(1h)/ 420(1h)/- Metal loading: IM/110(12h)/420(1h)/420(1h)	[240] 2021
	$K_{0.14}Co_{0.21}Ni_{0.65}(12)/CeO_2$	S_{BET} = 28.4, D_p =8.8	100	0	79	20	-			
	$K_{0.14}Co_{0.43}Ni_{0.43}(12)/CeO_2$	S_{BET} = 25.4, D_p =7.9	100	0	81	30	-			
	$K_{0.14}Co_{0.65}Ni_{0.21}(12)/CeO_2$	S_{BET} = 24, D_p =6.8	100	4	89	25	-			
	$K_{0.14}Ni_{0.86}$ (12)/CeO_2	S_{BET} = 31.6, D_p =5.9	100	5	80	20	-			
25.	$Co(10)/CeO_2$	S_{BET} = 34.2, D_{pore} = 16.2	90	%S 6	%S 70	%S 10	6.6	12/-/420-500/-/-	Support: IM/110(12h)/650(1h)/ - Metal loading: CP/110(12h)/650(1h)/ 650(1h)	[243] 2020
	$Co_{0.91}La_{0.09}(10)/CeO_2$	S_{BET} = 38.9, D_{pore} = 16	60	8	78	8	1.8			
	$Ni(10)/CeO_2$	S_{BET} = 39.8, D_{pore} = 13.9	90	3	72	37	365.9			
	$Ni_{0.91}La_{0.09}(10)/CeO_2$	S_{BET} = 42, D_{pore} = 15.2	100	2	78	33	202.8			
26.	$Ni(10)/CeO_2$	S_{BET} = 66, D_{pore} = 8.5	83	%S 4	%S 69	%S 5	-	6/-/450-600/-/20000	Support: IM/80(18h)/400(4h)/ - Metal loading: IWI/100(4h)/500(4h)/50(3h)	[237] 2020
	$Ni(13)/CeO_2$	S_{BET} = 64, D_{pore} = 8.7	89	3	72	4	-			
	$Ni(15)/CeO_2$	S_{BET} = 62, D_{pore} = 9.4	88	2	70	5	-			
	$Ni_{0.77}$-$Cu_{0.22}(17)/CeO_2$	S_{BET} = 59, D_{pore} = 9.2	99	17	70	4	-			
	$N_{i0.7}$5-$Co_{0.24}(17)/CeO_2$	S_{BET} = 38, D_{pore} = 15.5	96	16	73	3	-			
	$Ni_{0.58}$-$Mg_{0.41}(17)/CeO_2$	S_{BET} = 48, D_{pore} = 9.5	91	17	74	1	-			
27.	$Co(10)/CeO_2$	S_{BET} = 47.6, D_{pore} = 13	%S 58	%S 76	%S 75	%S 5	32	12/-/420/21/-	Support: Comm. CeO_2 Metal loading: CI/110(12h)/500(1h)/ 550(1h)	[218] 2020
	$Co_{0.91}Ce_{0.09}(10)/CeO_2$	S_{BET} = 47, D_{pore} = 12.1	60	5	76	6	31			
	$Co_{0.67}Ce_{0.33}(10)/CeO_2$	S_{BET} = 52.1, D_{pore} = 11	55	5	75	5	29			
	$Co_{0.5}Ce_{0.5}(10)/CeO_2$	S_{BET} = 49.7, D_{pore} = 9.9	55	7	72	5	19			
	$Ni(10)/CeO_2$	S_{BET} = 52, D_{pore} = 10.9	48	7	75	20	152			
	$Ni_{0.91}Ce_{0.09}(10)/CeO_2$	S_{BET} = 52.8, D_{pore} = 10	50	7	81	24	52			

	$Ni_{0.67}Ce_{0.33}(10)/CeO_2$	S_{BET} = 64.8, D_{pore} = 8.5	46	8	84	18	15			
	$Ni_{0.5}Ce_{0.5}(10)/CeO_2$	S_{BET} = 46.9, D_{pore} = 9.6	42	15	84	16	13			
28.	$Ni_{0.77}K_{0.23}(12)/CeO_2$	S_{BET} = 31.6, D_{Ni} = 9.3	100	%S 2	%S 85	%S 11	-	12/-/420/100/-	Support: Comm. CeO_2 Metal loading: IM/110(12h)/420(1h)/ 420(1h)	[245] 2018
	$Ni(10)/CeO_2$	S_{BET} = 56.3, D_{Ni} = 5.8	100	2	75	35	-			
29.	$Ni(5)/CeO_2$	S_{BET} = 6.7, D_{Ni} = 20.1	98	%S 30	%S 70	%S 0	-	-/5/400-600/20/57000	CI/90(12h)/600(4h)/ 500(1h)	[242] 2016
	$Ni_{0.98}Sn_{0.02}(5.25)/CeO_2$	S_{BET} = 8.6, D_{Ni} = 20.2	98	28	68	0	-			
	$Ni_{0.91}Sn_{0.09}(6)/CeO_2$	S_{BET} = 7.3, D_{Ni} = 19.5	88	35	62	0	-			
	$Ni_{0.83}Sn_{0.17}(7)/CeO_2$	S_{BET} = 9, D_{Ni} = 21.8	78	42	50	2	-			
30.	$Ni(8.2)/CeO_2$	S_{BET} = 71, D_{Ni}=8.3	100	%S 0	%S 75	%S 10	-	13/-/250-500/-/-	CP/110(ON)/400(3h)/-	[244] 2014
	$Ni(9.2)/CeO_2$	S_{BET} = 60, D_{Ni}=18	100	0	72	8	-			
	$Ni_{0.54}B_{0.46}(9.5)/CeO_2$	S_{BET} = 26, D_{Ni}=8.0	100	0	80	0	-		Bi-metal loading: IM/110(ON)/400(3h)/-	
	$Ni_{0.5}B_{0.5}(10.3)/CeO_2$	S_{BET} = 9.7, D_{Ni}=18	100	0	76	0	-			
31.	$Ni_{0.54}Cu_{0.46}(10)/CeO_2$	-	-	%Y 18	%Y 78	%Y 5	0.04	3/-/300-600/-/-	Support: PT/110(12h)/500(5h)/- Metal loading: IM/210(12h)/500(3h)/400(1h)	[239] 2015
	Ni(10)/CeO2	-	-	21	49	24	0.21			
32.	$Ni_{0.5}Co_{0.5}(22.5)/CeO_2$	S_{BET}= 76, D_{Ni}=7.5	88	-	%Y 63	-	-	6/-/500/20/-	Support: CP/110(ON)/500(ON)/- Metal loading: IM/110(2h)/500(4h)/650(1h)	[241] 2015
	$Ni(22.5)/CeO_2$	S_{BET}= 72, D_{Ni}=8.0	100	-	50	-	-			
	$Ni_{0.5}Co_{0.5}(22.5)/CeO_2$	S_{BET}= 136, D_{Ni}=3.9	65	-	25	-	-		RM/120(2h)/500/650(1h)	
	$Ni(22.5)/CeO_2$	S_{BET}= 132, D_{Ni}=3.7	99	-	58	-	-			
33.	$Ni_{0.92}Pt_{0.08}(13)/CeO_2$	S_{BET} = 9.8, D_{NiO}= 23	100	%S 33	%Y 56	%S 2	0.045	3/-/238-574/-/ 15000	Support: Comm. CeO_2 Metal loading: IM/-/600/600(1h)	[79] 2014
34.	$Ni(10)/CeO_2$	S_{BET} = 79, D_{Ni} = 32.65, DS = 5.56	16.8	%S 9.5	%S 45.0	%S 12.1	-	7.6/-/300-600/3/-	Support: SG/80(48h)/600(3h)/- Metal loading: IWI/110(4h)/600(2h)/800(1h)	[238] 2011
	$Ni_{0.995}Cu_{0.005}(10)/CeO_2$	S_{BET} = 77, D_{Ni} = 20.77, DS = 8.93	28.2	8.8	48.5	11.7	-			

	$Ni_{0.99}Cu_{0.01}(10)/CeO_2$	S_{BET} = 75, D_{Ni} = 9.26, DS = 12.42	35.2	8.6	50.7	13.8	-			
	$Ni_{0.985}Cu_{0.015}(10)/CeO_2$	S_{BET} = 74, D_{Ni} = 10.64, DS = 14.88	97.3	5.5	70.7	12.6	-			
	$Ni_{0.97}Cu_{0.03}(10)/CeO_2$	S_{BET} = 72, D_{Ni} = 13.09, DS = 12.15	37.7	5.6	53.6	14.9	-			
	$Ni(15)/CeO_2$	S_{BET} = 64, D_{Ni} = 48.06, DS = 3.22	17.8	10.3	44.2	15.4	-			
	$Ni_{0.995}Cu_{0.005}(15)/CeO_2$	S_{BET} = 62, D_{Ni} = 30.94, DS = 5.98	27.6	7.8	50.4	12.6	-			
	$Ni_{0.99}Cu_{0.01}(15)/CeO_2$	S_{BET} = 63, D_{Ni} = 16.48, DS = 5.73	33.3	5.8	54.2	13.2	-			
	$Ni_{0.985}Cu_{0.015}(15)/CeO_2$	S_{BET} = 60, D_{Ni} = 10.92, DS = 7.12	97.6	3.4	70.6	12.3	-			
	$Ni_{0.97}Cu_{0.03}(15)/CeO_2$	S_{BET} = 57, D_{Ni} = 25.98, DS = 6.85	40.2	3.9	49.6	18.3	-			
	Group 4: Promoted Ni/modified CeO_2									
34.	$Ni_{0.93}Sn_{0.07}(5)/CeO_2$	D_{Ni} = 13, D_{CeO2} = 12	85	%S 14	%S 45	%S 27	-	12/-/200-400/10/7697	SCS/100(24)/-/500(3)	[251] 2023
	$Ni_{0.93}Sn_{0.07}(10)/CeO_2$	D_{Ni} = 21, D_{CeO2} = 16	81	17	41	31	-			
	$Ni_{0.93}Sn_{0.07}(20)/CeO_2$	D_{Ni} = 22, D_{CeO2} = 19	70	20	32	38	-			
	$Ni_{0.93}Sn_{0.07}(5)/Ce_{0.5}Mg_{0.5}O_2$	D_{CeO2} = 4	100	5	65	10	-			
	$Ni_{0.93}Sn_{0.07}(10)/Ce_{0.5}Mg_{0.5}O_2$	D_{Ni} = 10, D_{CeO2} = 9	99	9	57	17	-			
	$Ni_{0.93}Sn_{0.07}(20)/Ce_{0.5}Mg_{0.5}O_2$	D_{Ni} = 22, D_{CeO2} = 11	95	12	50	23	-			
	$Ni_{0.93}Sn_{0.07}(5)/Ce_{0.33}Mg_{0.67}O_{1.33}$	D_{CeO2} = 3	100	4	69	7	-			
	$Ni_{0.93}Sn_{0.07}(10)/Ce_{0.33}Mg_{0.67}O_{1.33}$	D_{Ni} = 20, D_{CeO2} = 4	100	8	59	15	-			
	$Ni_{0.93}Sn_{0.07}(20)/Ce_{0.33}Mg_{0.67}O_{1.33}$	D_{Ni} = 21, D_{CeO2} = 9	100	9	57	17	-			

	$Ni(5)/Ce_{0.33}Mg_{0.67}O_{1.33}$	D_{CeO2} = 4	98	12	51	22	-			
	$Ni_{0.88}Sn_{0.11}(5)/Ce_{0.33}Mg_{0.67}O_{1.33}$	D_{CeO2} = 4	85	17	40	31	-			
35.	$Ni(5)/Ce_{0.5}Zr_{0.5}O_2$	D_{NiO} = 18, D_{CeO2} = 11	90	%S 5	%S 59	%S 6	-	12/-/200-400/20/7697	USCS/100(24)/-/500(3)	[252] 2022
	$Ni(20)/Ce_{0.5}Zr_{0.5}O_2$	D_{NiO} = 39, D_{CeO2} = 25	64	14	45	21	-			
	$Ni(5)/Ce_{0.33}Zr_{0.67}O_{1.33}$	D_{NiO} = 18, D_{CeO2} = 8	95	2.5	62	4	-			
	$Ni(20)/Ce_{0.33}Zr_{0.67}O_{1.33}$	D_{NiO} = 37, D_{CeO2} = 21	72	12	49	16	-			
	$Ni_{0.93}Sn_{0.07}(5)/Ce_{0.5}Zr_{0.5}O_2$	D_{NiO} = 18, D_{CeO2} = 6	100	1	65	1	-			
	$Ni_{0.93}Sn_{0.07}(20)/Ce_{0.5}Zr_{0.5}O_2$	D_{NiO} = 27, D_{CeO2} = 16	76	9	52	13	-			
	$Ni_{0.93}Sn_{0.07}(5)/Ce_{0.33}Zr_{0.67}O_{1.33}$	D_{NiO} = 17, D_{CeO2} = 4	100	0	68	0	-			
	$Ni_{0.93}Sn_{0.07}(20)/Ce_{0.33}Zr_{0.67}O_{1.33}$	D_{NiO} = 19, D_{CeO2} = 14	82	7	56	9	-			
36.	$Ni/La_{0.8}Ce_{0.2}Mn_{0.6}Ni_{0.4}O_3$	S_{BET} = 7.82	100	%S 16.6	%S 67.1	%S 22.9	-	-/ 3/500-700/6/-	Support: SG/240(8h)/900(5h)/- Metal loading: PT/240(2h)/500(3h)/ 650(2h)	[253] 2020
	Ni-Cu/$La_{0.8}Ce_{0.2}Mn_{0.6}Ni_{0.4}O_3$	S_{BET} = 4.25	100	32.9	43.5	31.5	-			
	$La_{0.8}Ce_{0.2}Mn_{0.6}Ni_{0.4}O_3$	S_{BET} = 8.37	-	-	-	-	-			
37.	Pt(3)-Ni(10)/CeO_2-SiO_2	S_{BET} = 232	100	%S 10	%S 68	-	-	4/-/300-600/34/10000-30000	Support: IM/80(ON)/120(2h)/- Metal loading: IM/120(ON)/600(3h)/ 500(1.5h)	[247] 2018
38.	$Ni(8)/CeO_2$	S_{BET} = 106, D_{pore} = 6	33	%S 60	%Y 18	%Y 2	-	6/-/500/16/-	Support: IWI&CP/110(ON)/550(3h)/- Metal loading: IWI/110(18h)/550(4h)/550(1h)	[85] 2018
	$Ni(8)/Ce_{0.97}La_{0.03}O_{1.99}$	S_{BET} = 66, D_{pore} = 5	55	80	37	10	-			
	Co-Ni(8)/ $Ce_{0.97}La_{0.03}O_{1.99}$	S_{BET} = 76, D_{pore} = 4	100	100	70	3	-			
39.	$Ni_{0.7}Pt_{0.3}(13)/Ce_{0.25}Si_{0.75}O_2$	D_{NiO} = 114, D_{CeO2}= 68, S_{BET} = 232	100	%S 1	%Y 71.6	%S 0.1	-	4/-/300-600/70/10000-30000	Support: IM/80(2h)/600(3h)/- Metal loading: IM/150(2h)/600(2h)/600(3h)	[246] 2017
40.	$Ni_{0.92}Pt_{0.08}(13)/Ce_{0.1}Si_{0.9}O_2$	S_{BET} = 255	100	-	%Y 26.5	-	-	3/-/450/100/-	Support: IM/100(ON)/600(3h)/- Metal loading: IM/150(2h)/600(2h)/500(2h)	[249] 2017
	$Rh_{0.02}Ni_{0.9}Pt_{0.08}(13)/Ce_{0.1}Si_{0.9}O_2$	S_{BET} = 197	100	-	23.9	-	-			
	$Rh_{0.92}Ni_{0.08}(13)/Ce_{0.1}Si_{0.9}O_2$	S_{BET} = 223	100	-	23.2	-	-			
	$K_{0.02}Ni_{0.9}Pt_{0.08}(13)/Ce_{0.1}Si_{0.9}O_2$	S_{BET} = 105	100	-	20.1	-	-			

	$Cs_{0.02}Ni_{0.9}Pt_{0.08}(13)/Ce_{0.1}Si_{0.9}O_2$	S_{BET} = 203	100	-	24.7	-	-			
41.	$Ni_{0.92}Pt_{0.08}(13)/Ce_{0.5}Zr_{0.5}O_2$	S_{BET} = 49, D_{NiO} = 16.6	100	%S 15.6	%S 50	%S 29.3	-	3/-/300-600/-/114350	Support: IM/120(ON)/600(3h)/- Metal loading: IM/120(2h)/600(3h)/600	[248] 2015
	$Ni_{0.92}Pt_{0.08}(13)/CeO_2$	S_{BET} = 72, D_{NiO} = 16.6	100	-	60	-	-			
42.	$Ni(30)/Ce_{0.42}Zr_{0.58}O_2$	S_{BET} = 20.6, V_P = 0.048, D_{Ni} = 56.4	81.1	%S 10.6	%S 58.9	%S 6.3	-	13/-/600/-/-	Support: CP/110(ON)/750(5h)/- Metal loading: IM/-/-/550(6h)	[121] 2015
	$Ni_{0.98}Rh_{0.02}(31)/Ce_{0.42}Zr_{0.58}O_2$	S_{BET} = 14.9, V_P = 0.035, D_{Ni} = 47.6	86.0	3.0	72.8	3.2	-			
43.	$Ni_{0.88}Rh_{0.12}(1.24)/Ce_{0.5}Zr_{0.5}O_2$	S_{BET} = 6	100	%S 1	Y_a 5.5	%S 0	-	12/-/200-500/-/-	Support: CP/110(ON)/400(3h)/- Metal loading: CI/110(ON)/400(3h)/400(3h)	[250] 2014
	$Ni_{0.5}Co_{0.5}(2)/Ce_{0.5}Zr_{0.5}O_2$	S_{BET} = 11	100	0	5	0	-			
	$Ni_{0.58}Fe_{0.42}(1.7)/Ce_{0.5}Zr_{0.5}O_2$	S_{BET} = 10	100	0	5.7	0	-			
	$Ni(1)/Ce_{0.5}Zr_{0.5}O_2$	S_{BET} = 8	100	3	5	2	-			
44.	$Ni_{0.92}Cu_{0.08}(11)/\alpha\text{-}Al_2O_3$	S_{BET} = 39.2, D_{Ni} = 9.46	20	%M 10	%M 53	%M 10	-	10/-/400/-/-	Support: $Ce_{0.6}Zr_{0.4}O_2$ PT/110(2h)/500/- Support: Comm.ZnO and rest BS/-/1100(2h)/- Metal loading: IM/-/550(5h)/550(3h)	[254] 2009
	$Ni_{0.92}Cu_{0.08}(11)/Ce_{0.6}Zr_{0.4}O_2$	S_{BET} =54.2, D_{Ni} = 10.60	50	9	65	4	-			
	$Ni_{0.92}Cu_{0.08}(11)/Nb_2O_5$	S_{BET} = 32.0, D_{Ni} = 14.98	40	9	60	7	-			
	$Ni_{0.92}Cu_{0.08}(11)/ZnO$	S_{BET} = 6.4, D_{Ni} = 19.35	18	12	51	16	-			

and ZnO supports. The $Ce_{0.6}Zr_{0.4}O_2$ support demonstrates the lowest acidity, highest surface area, and highest H_2 selectivity 65 mol% [254]. Inclusion of Rh reveals less coke deposition and achieves higher stability than that of the other catalysts [250].

Recent year publications depict interest in Rh as Ni promoter and Zr as ceria modifier [250]. Mondal et al. [2015] promotes Rh on $Ni(30)/Ce_{0.42}Zr_{0.58}O_2$ catalyst prepared by a two-step process. Addition of 1 wt.% Rh with Ni helps to decrease the nickel particle size from 56.4 nm to 47.6 nm and increases H_2 selectivity from 58.9 to 72.8% [121]. Wang et al. [2020] study the effect of Cu on $Ni/La_{0.8}Ce_{0.2}Mn_{0.6}Ni_{0.4}O_3$ catalyst prepared by a two-step sol-gel method. Addition of Cu decreases surface area and H_2 selectivity of the catalysts which could be due to the fact that the Cu causes sintering of Ni particles [253].

2.6 Overview and outlook

The ESR is one of the promising routes for producing H_2 and reforming conditions such as reaction temperature, H_2O/EtOH ratio, feed flow rate, etc. are important parameters controlling the ESR process. The nature of the catalyst has significant influence on the mechanism and overall outcome of the ESR process. Ni/Al_2O_3 or Ni/CeO_2 based catalysts could be very effective for ESR. However, mechanistically Ni agglomerates easily and has a weak WGS reaction rate while Al_2O_3 is an acidic oxide, which reduces the activity of catalysts via coke deposition. On the other hand, CeO_2 is unstable in the long run at high reforming temperature. As for solutions, the research works conducted in the last two decades focus on manipulating the nature of the active metal, or the support oxide, or both in order to enhance catalytic activity and stability and to investigate the synergistic interactions of metal with support and their effects on ESR.

Different ceramic oxides, such as MgO, ZnO, La_2O_3, CaO, ZrO_2, CeO_2, Y_2O_3 etc. are used for reducing the acidity of Al_2O_3 support and coke deposition while metal-support interaction, surface area, metal particle size, and reducibility of metal increased leading to the overall activity and stability of the catalysts. Many researchers promote Ni metals mostly with noble (Pt, Rh, Pd) and transition (Cu, Co,) metals to enhance WGS reaction rate, reducibility, stability, and surface area of the active metals. CeO_2 support is modified with oxides of La, Mg, Ti, Pr, Gd, Zr, etc. While ZrO_2 improves reducibility and thermal stability of ceria and improves metal dispersion, the substitution of Ce^{4+} with the subvalent cations (La^{3+}, Pr^{3+}, Mg^{2+}, Gd^{3+}) help to increase oxygen mobility in the lattice via oxygen vacancy formation and enhance WGS reaction rate.

In addition to the reforming conditions and chemistry of the catalysts, particle size, porosity, surface area (governed by preparation method and catalyst chemistry) are the important factors that significantly dominate the activity of the catalysts. Different articles express H_2 production in different ways, such as yield (as %, mole H_2/min, mole $H_2/mole_{EtOH}$ converted, etc.) and selectivity (%). It is difficult to compare these results in a straight forward way. In order to see the catalytic activates on the

basis of a common platform important catalytic activity parameters; maximum H_2 yield (mole/min.gm catalyst) H_2 selectivity (%), and catalyst stability (h) have been plotted (**Fig. 2.4** for Ni/Al_2O_3 based catalysts and **Fig. 2.5** for Ni/CeO_2 based catalysts) as a function of the corresponding particle size in the articles. The effects of reforming reaction temperatures and catalyst chemistry of the catalysts on the activity are also illustrated. The H_2 yield ($F_{H2,out}$), values are calculated form the reported yield or selectivity values using the following formulae [181,255].

$$H_2 \text{ yield} = \frac{F_{H2,out}}{F_{EtOH,in} - F_{EtOH,out}} \quad (2.14)$$

$$H_2 \text{ selectivity} = \frac{F_{H2,out}}{6 * X * F_{EtOH,in}} \quad (2.15)$$

Where X is Ethanol conversion, $F_{EtOH,in}$ is inlet ethanol flowrate (molar), and $F_{EtOH,out}$ is outlet ethanol flowrate (molar). The stability values are collected from the ethanol conversion or H_2 selectivity/yield vs. time on stream (h) graphs and noted the point till which no falls in activity is observed. The H_2 selectivity values and particle size of active metallic phases are obtained from the articles reported in Tables 2.2 and 2.3.

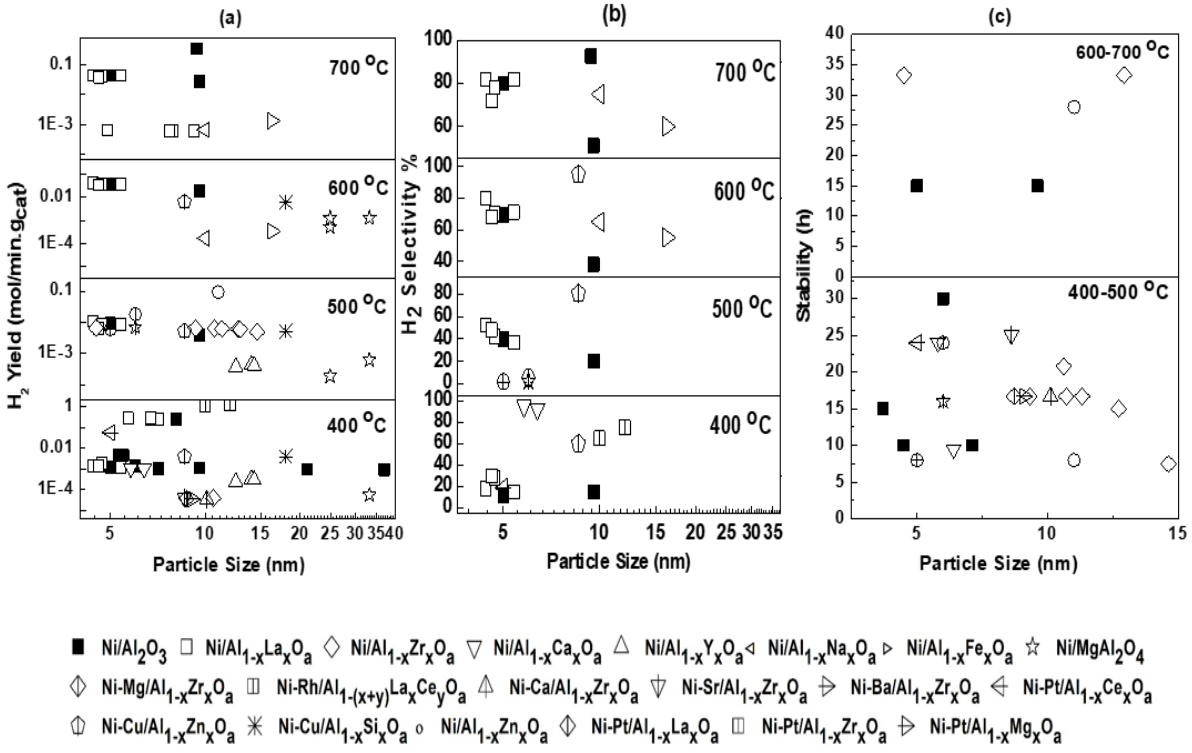

Figure 2. 6: Variation of catalytic activity of Ni/Al_2O_3 based catalysts with particles size at different temperatures for a) maximum H_2 yield (mol/min.g_{cat}), b) maximum H_2 selectivity (%), and c) maximum catalyst stability (h). The stability values are collected from the ethanol conversion or H_2 selectivity/yield vs. time on stream (h) graphs and noted the point till which no falls in activity is observed. The particle size of the active metallic phase and other data tabulated in Table 2.2 are used in the calculation.

In the case of the Ni/Al_2O_3 based catalysts, the support modification appears to be effective (**Figs 2.4(a)** and **(b)**) and Ni/Al_2O_3-La_2O_3 catalyst revealed to be most active among all. Reduction of

acidity of Al_2O_3 supported by basic oxides and catalysts modified by oxides of Zr seems to provide good stability even at larger particle size, as seen in **Fig. 2.4(c)**. For Ni/CeO_2 based catalysts, modification of the support by adding La_2O_3 and ZrO_2 appeared to increase the H_2 yield/selectivity, especially at a higher temperature, 500-600 °C (**Figs. 2.5(a)** and **(b)**). An increase in particle size reduces the stability of the catalysts in general, but Co might help stabilize Ni/CeO_2 at higher temperatures (**Fig. 2.5(c)**). The addition of K might be helpful both for increasing H_2 production and stability of the catalysts at low temperature applications. However, clearly there is the deficit of data points for such kinds of examination. A series of detailed and methodical long-term study of the most promising catalysts of different groups conducted by the same group under very similar conditions (both catalyst preparation and ESR) may help to realize the efficiency and stability of the catalysts more clearly.

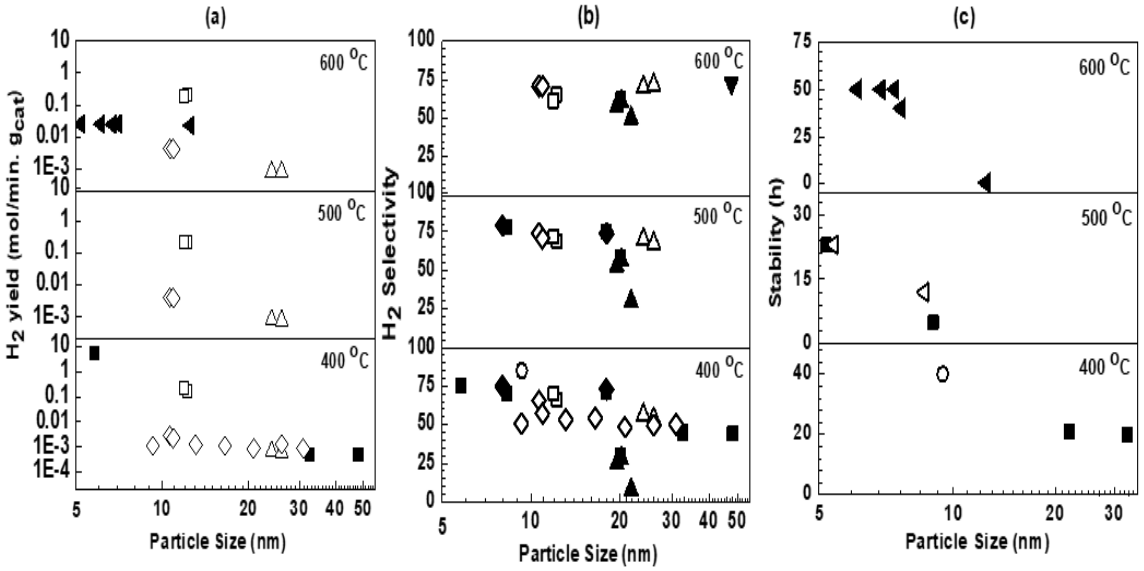

Figure 2. 8: Variation of catalytic activity of Ni/CeO_2 based catalysts with particles size at different temperatures for a) maximum H_2 yield (mol/min.g_{cat}), b) maximum H_2 selectivity (%), and c) maximum catalyst stability (h). The stability values are collected from the ethanol conversion or H_2 selectivity/yield vs. time on stream (h) graphs and noted the point till which no falls in activity is observed. The particle size of the active metallic phase and other data tabulated in Table 2.3 are used in the calculation.

Application of both two and single step processes for catalyst preparation is predominantly seen from group two onwards. Sol-gel and co-precipitation are the most used methods for support preparation and impregnation is the most common method for active metal loading. Other methods (such as reverse microemulsion, citrax complexing method, plasma treatment, etc.) are also examined to increase surface area, porosity, and metal dispersion. Very few articles explicitly compare the effect of two and single step processes on the catalytic activity and catalysts morphology. $Ni(15)/Al_{0.83}Zr_{0.17}O_{1.58}$ catalyst prepared by a two-step (support prepared by SG and then Ni loaded by IM method) and single step (SG)

processes show similar catalytic activity. However, the catalyst prepare by the single step SG method demonstrate a higher surface area (315 m^2/g) and smaller Ni crystallite size (4.5 nm) compared to the powder prepare by the two-step process (222 m^2/g, 12 nm) [174]. On the other hand, for Ni(10)/CeO_2 catalysts, results show the opposite trend; the two-step methods are more effective in obtaining higher surface area powders than the single step processes [215,219,221].

In the future, research needs to be focused on a sequence of thorough and systematic studies to realize the right preparation method to obtain the catalysts of optimum physicochemical properties. While most of the published articles are on the fundamental proof of concepts, very few reports are on the regeneration strategies and post regeneration activity study of the catalysts. Researches could be focused on how catalyst chemistry influences the mechanism and kinetics of the regeneration and the post regeneration activity.

2.7 Gaps in existing research

Review of the last 24 years research articles showed that relatively more ESR research is conducted over the Ni/Al_2O_3 rather than the Ni/CeO_2 related catalysts. Both Al_2O_3 and CeO_2 are known as good catalyst supports. However, Al_2O_3 behaves as a passive support and mostly provides stability to the catalysts, while CeO_2, due to its high oxygen storage capacity (OSC) and oxygen mobility could be an active part of the catalytic reactions. Additionally, it is possible to modify the shortcomings of the Ni/CeO_2 catalysts by promoting Ni and/or modifying CeO_2. Hence, LTSRE over the Ni/CeO_2 related catalysts is chosen as the topic of the present work. Below are the main points of the existing research gaps and later in the results & discussion section each of the gaps are elaborated further.

1. Detail experimental study of the effect of modification of CeO_2 (with La_2O_3, ZrO_2 and/or MgO) on physico-chemical properties of the Ni-Sn/CeO_2 catalysts and LTSRE are not reported yet.
2. Effects of variation of Sn in Ni-Sn/CeO_2 (and modified CeO_2) catalysts on physico-chemical properties of the catalysts and LTSRE are not studied elaborately.
3. It is important to study the effect of various composition of the support (Ce:La, Ce:Zr, Ce:Mg ratios) on catalytic activity.
4. Besides catalytic activity it is also important to examine the effect of total metal loading on catalysts surface chemistry, structure, phase composition, and how that affects the catalytic activity.

2.8 Research objectives

1. To study the effect of ZrO_2 as a support modifier and metal loading for Ni-Sn/CeO_2 catalysts on LTSRE. Catalytic activities will be correlated with the physicochemical properties of the catalysts.

2. To study the effect of MgO as a support modifier, metal loading, and variation of Sn concentration for Ni-Sn/CeO_2 catalyst on LTSRE. Catalytic activities will be correlated with the physicochemical properties of the catalysts.

3. To study the effect of La_2O_3 as a support modifier, metal loading, and variation of Sn concentration for Ni-Sn/CeO_2 catalyst on LTSRE. Catalytic activities will be correlated with the physicochemical properties of the catalysts.

2.9 Novelty of work

The previous discussion shows that Ni-Sn/Ce-Zr-O, Ni-Sn/Ce-Mg-O, and Ni-Sn/Ce-La-O catalysts could be effective for ethanol steam reforming. However, these systems are still unexplored, and accordingly the novelty of the work could be

1. Synthesizing the new catalytic systems; Ni-Sn/CeO_2 powders modified with MgO, ZrO_2, and La_2O_3 by SCS and ultrasonication assisted SCS methods. Application of these catalytic systems for hydrogen production by LTSRE never reported before.
2. Performing detailed experimental catalytic activity studies of these catalysts in relation to the varying Sn compositions, total metal loading, and various support ratios; (Ce:La, Ce:Zr, and Ce:Mg ratio). The LTSRE is performed between 200 to 400 °C, under atmospheric pressure, H_2O:EtOH = 12: 1 mole ratio, and feed flow rate 0.1 ml/min.
3. Investigating the physico-chemical characteristics of these catalysts in relation to the varying Sn compositions, total metal loading, and various support ratios; (Ce:La, Ce:Zr, and Ce:Mg ratio).
4. Correlating the catalytic activity and the physico-chemical properties of the fresh, reduced, and spent catalysts is very important new contribution of this work.
5. This complete technology is environmentally friendly (as ethanol produced from biomass) and also catalyst regeneration cost is less.
6. Catalyst stable for longer time will save the regeneration cost and metal cost.

Chapter 3: Materials and Methods

In this chapter, the general methods to prepare heterogeneous catalysis for synthesis are explained. These include co-precipitation, the sol-gel technique, hydrothermal, solution combustion synthesis (SCS), and ultrasonication combined with SCS. The emphasis was given for the SCS related methods. The physicochemical characterization methods for the fresh, reduced, and used catalysts, as well as a study of catalytic activity to produce hydrogen from ethanol using low temperature steam reforming technique is explained in detail.

3.1 Catalysts Preparation Methods

The preparation process of a catalyst would control its performance in specific reactions. The preparation design and process influence the features such as composition, surface structure, dispersion of the crystallinity, interfacial properties, and active phase. Finally, these factors influence the stability and activity of the catalyst. To get the desired qualities of the catalyst, an appropriate catalyst synthesis method must be used. In general, heterogeneous inorganic catalysts mean nano materials of high surface area, with nano particles and desired porosity. Several ways to make nanomaterials have been already developed and used. Most of the time, they fall into two groups: "top-down" and "bottom-up" methods (**Fig. 3.1**).

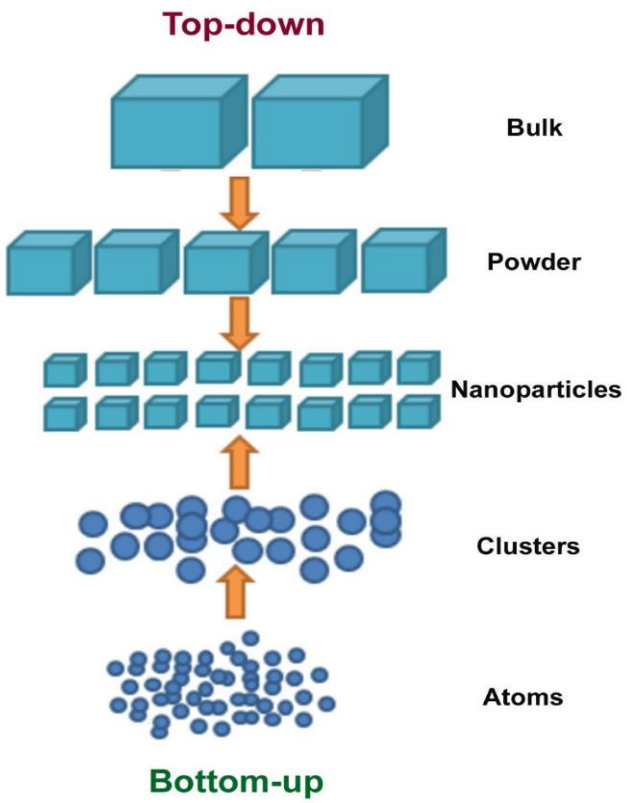

Figure 3. 1: Schematic diagram of bottom-up and top-down approaches [**Sources:** [257]].

In case of the top-down route, the bulk materials are broken up into nanoparticles using solid state routes, such as ball milling, or some other mechanical method [256]. It involves constantly breaking up coarse-grained solids into pieces that are smaller and smaller until they are only a few nanometers across. Wet chemical synthesis routes like sol-gel, hydrothermal, precipitation, co-precipitation, solution combustion synthesis, ultrasonication assisted synthesis, etc., belong to the bottom-up approach, which involves packing together atoms or molecules to make them smaller than a few nanometers. The bottom-up method is much more common and widely used to make nanomaterials, because it has a number of advantages [257]. In next subsections various catalyst preparation methods are discussed.

3.1.1 Impregnation Method

This is the most straightforward, economical, widely used, and well-known method of depositing catalyst's active phase on the support. In order to carry out this procedure, the active component precursor is dissolved in a solvent with sufficient solubility and volatility and added drop by drop to the support while being vigorously stirred. The resulting mixture is dried to get rid of extra solvent, and then it is reduced in an reducing atmosphere. The nature of the surface (permeability, porosity, area, etc.) and the reaction conditions affect the quality of the product (such as concentration, nature of dissolved substances, and pH, etc.). There were two possible impregnation processes steps: (i) Incipient wetness impregnation(IWI) followed by (ii) drying (equilibrium could not be reached) [258]. In IWI the volume of impregnated liquid (aqueous or organic solution) employed is equal to the support's pore volume (metal oxide or metal oxide precursor). The mass transfer within the pores during impregnation and drying controls the concentration profile of the compound that had been absorbed. When there is not much interaction between the active catalytic phase and the support, the dry or almost dry impregnation method is usually best.

The active catalytic phase and support interact strongly in the wet impregnation process. The main problem with impregnation method is keeping a high level of dispersion during the next steps of drying, calcining, and finally reduction [31]. Salinity solutions pH influences the surface charge, as well as the coordination state of the metal complex.

3.1.2 Hydrothermal Synthesis

Hydrothermal synthesis (**Fig. 3.2**) is becoming one of the most popular tools for processing advanced materials. This is especially true for nano structural materials, which could be used in a wide range of technologies, such as ceramics, electronics, catalysis, magnetic data storage, optoelectronics, biomedical, biophotonics, etc. Hydrothermal processing is one of the most effective methods for dealing with nanohybrid and nanocomposites, and it is also beneficial for processing nanoparticles with a uniform size and shape distribution. The word "hydrothermal" comes from the world of geology [259].

A British geologist, Sir Roderick Murchison et al. introduced the term. He thought that water at very high temperatures and pressures caused the changes in the earth's crust and the subsequent formation of rocks and minerals [260]. Different scientists have come up with different ways to describe the hydrothermal method. Hydrothermal synthesis, as described by Roy et al., involves the utilisation of water under extreme conditions of heat and pressure [261]. Byrappa et al. defines hydrothermal synthesis in 1992 as any heterogeneous reaction that takes place in an aqueous medium above room temperature and at a pressure of more than 1 atm [262]. Yoshimura et al. defines it as "reactions that happen in a closed system at high temperature and high pressure (>100°C and >1 atm) in aqueous solutions" [263]. The shape of the materials to be made could be controlled by high or low vapour pressure of the main component in the reaction. This method has been used to successfully make many different kinds of nanomaterials. There are many reasons why hydrothermal synthesis is better than other methods. Through hydrothermal synthesis, nanomaterials can be made that are not stable at high temperatures[259]. The main feature of hydrothermal method is used to make nanomaterials with high vapour pressures with little loss of materials [264].

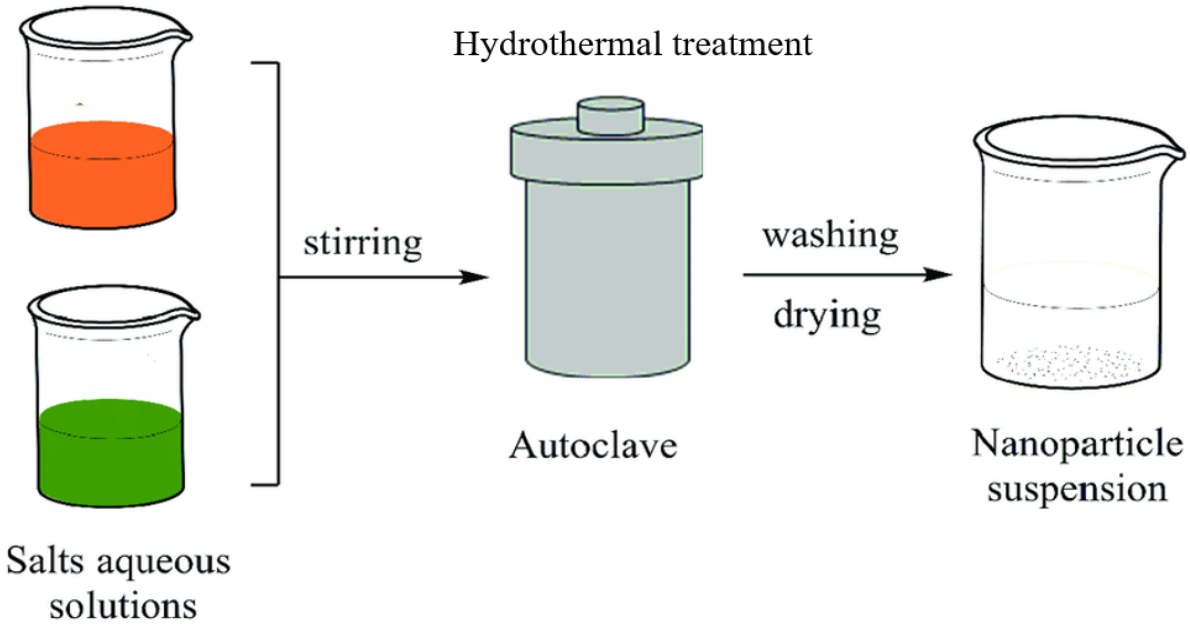

Figure 3. 2: Schematic diagram of hydrothermal synthesis [**Sources:** [264]].

3.1.3 Sol-Gel Method

The one-step sol-gel techniques are started to utilise in the late 1800s to manufacture metals. This technique is later rediscovered for glass manufacture without a high temperature melting procedure in early 1970. It is a common wet chemical method generally used to create glass materials and ceramic in a variety of forms, including powders, thin films, fibers, inorganic membranes, and aerogels, among others [265]. A sol is a mixture of solid particles that are suspended in a liquid and gel is a thick form of sols (solid encapsulating a liquid). High purity (99.99% purity) and extremely homogenous

composites may be created using the sol-gel process (**Fig. 3.3**). The cost-effectiveness as well as the lower process temperature of this technology in comparison to conventional technologies, make it conceivable to produce metal and ceramic nanomaterials using it at temperatures between 70 and 320 °C [31,265]. Additionally, it does not require specialized machinery or a unique setting. It is widely used in the production of nanoparticles and offers a number of benefits over co-precipitation or solid-state reactions. The reaction rate of salts relies on a number of variables, including pH, concentration, solvent type, and temperature. It's important to note that nano porosity in the final materials can be achieved by controlling the drying conditions. Catalytic material can be created using this approach as solids in bulk or powder form, or as metal nanoparticles scattered over a support or matrix [258]. However, it is difficult to produce xerogel or aerogel catalysts on a large scale in an appropriate form with significant mechanical strength and resistance to abrasion. The catalysts made using this technique may not have a perfectly uniform particle size distribution or shape because to agglomeration during the condensation process [265].

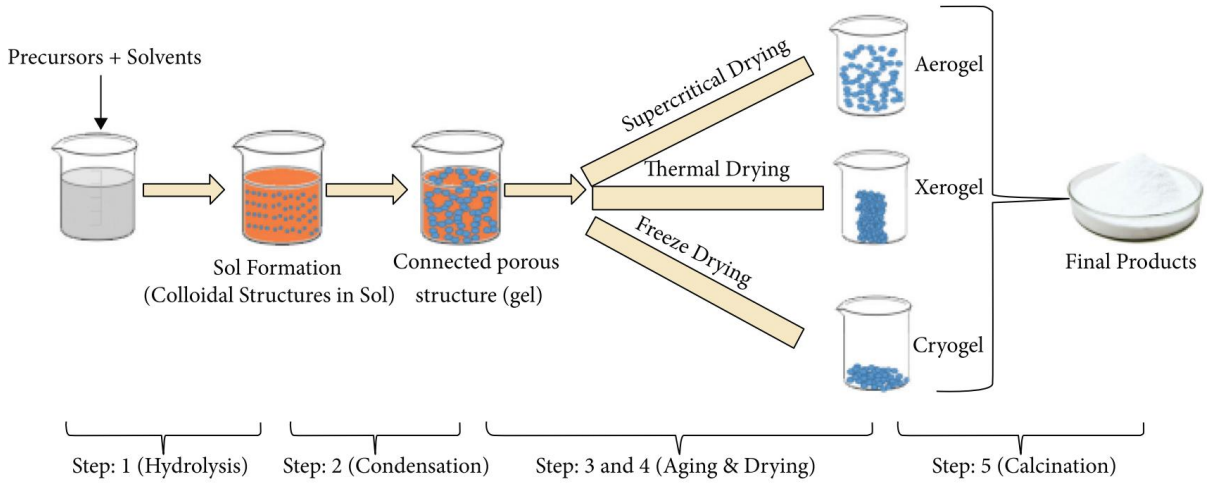

Figure 3. 3: Schematic diagram of sol-gel method at different stages from precursor to aerogel [**Sources:** [265]].

3.1.4 Precipitation and Coprecipitation Method

The required component is separated from the solution using this procedure. The term "co precipitation" refers to the simultaneous precipitation of multiple components. Precipitation is mostly utilised to prepare the active phase or single oxide support of bulk catalysts and support materials like Al_2O_3, SiO_2, TiO_2, ZrO_2, etc [258]. Co-precipitation is usually used to make catalysts with mixed oxide supports or active phase/oxide supports. The synthesis of precipitation and co-precipitation follow as; First, all precursors are mixed and make a solution using appropriate solvent. The precipitation process and hydroxide precipitation are then started by changes in the mixture's temperature and/or pH (such as the addition of NaOH). In the third stage, the precipitate is separated (either simply by filtration or centrifugation), washed with deionized water and/or ethanol, and dried at low temperatures. The oxide

is crystallized in the last phase, which involves heat treatment (calcination) at higher temperatures. Further, the final product can be ground in a crystal mortar and pestle (**Fig. 3.4**) [266].

The co-precipitation method has several advantages over other chemical methods, such as low price, low energy and time consumption, and the possibility of industrial-scale production. The control of particle size and content is comparatively easy with this approach. However, this method is not suitable for the formation of phase material with a high purity level [31]. Various factors, such as precipitation agent, pH, solution concentration, and temperature, influence the precipitation process. Furthermore, it is challenging to produce highly effective catalysts with this approach in terms of repeatability [266].

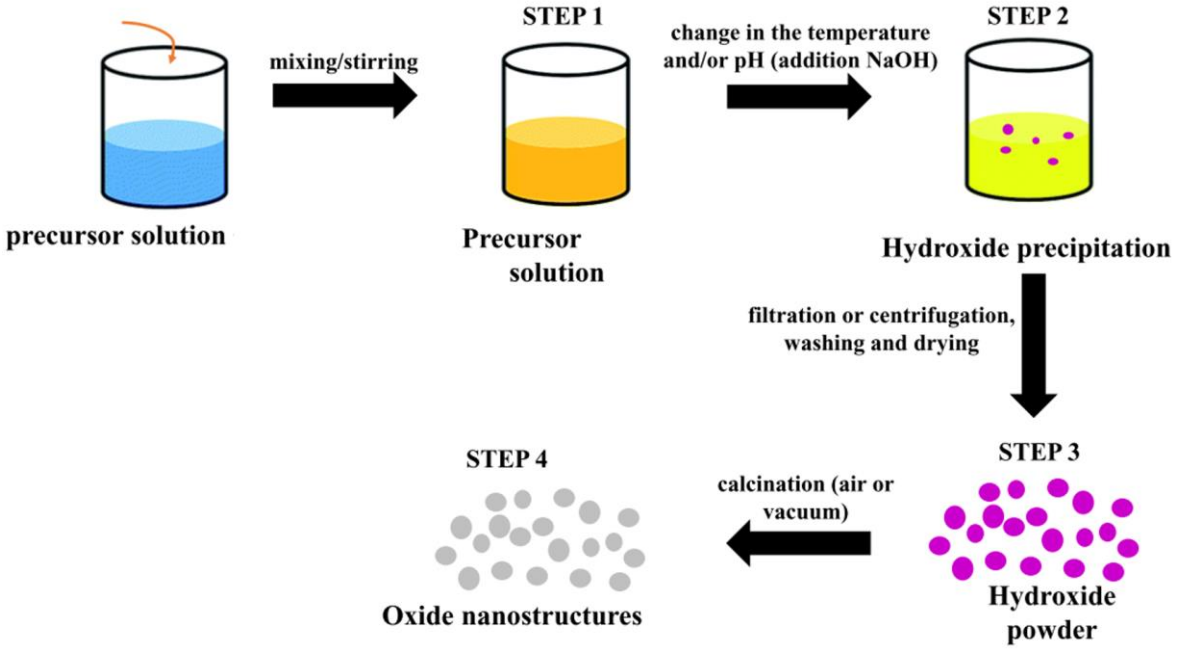

Figure 3. 4: The schematic diagram of precipitation and co-precipitation method [**Sources:** [266]].

3.1.5 Solution Combustion Synthesis (SCS) Method

Solution combustion synthesis (SCS), also known as liquid phase combustion synthesis was first used in 1981. In general, there are three stages to a solution combustion synthesis: i) the creation of the combustion mixture, ii) the formation of the gel, and iii) the combustion of the gel (**Fig. 3.5**) [267,268]. According to the principles of propellant chemistry, the combustion mixture in the SCS method consists of an oxidizer and a fuel in a stoichiometric ratio. This allows one to calculate the oxidizing/reducing valences (OV/RV) of a redox pair. Metal nitrates (oxidants) and organic fuels burnt together produce carbon dioxide (CO_2), water (H_2O), nitrogen oxide (N-O) gases, ammonia (NH_3), and other byproducts that can be used to generate heat. For the sake of clarity, SCS may be thought of as an energy-triggered, self-sustaining redox reaction between a fuel and an oxidant (often metal nitrates) in the presence of metal cations [268–270]. Because of its low cost, broad applicability, and convenience

of synthesising nano materials in the proper composition, allowing for diverse applications, SCS has become a standard approach for the synthesis of a wide variety of materials. SCS is being used in 65 different nations as a common method for producing nanomaterials. Extensive studies conducted over the past five years have shown SCS's strengths in the areas of material enhancement, energy savings, and environmental preservation [271]. Here different aspects of the SCS are discussed as follows.

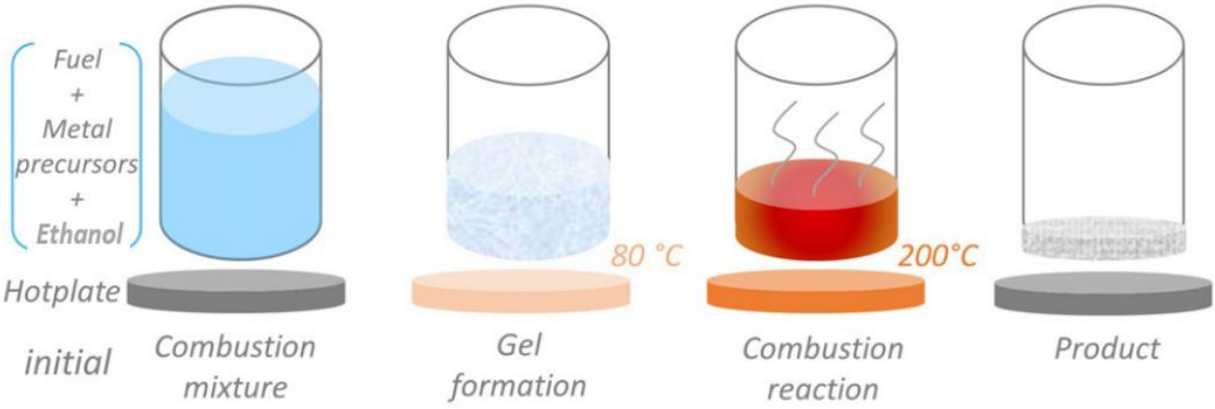

Figure 3. 5: Schematic representation of solution combustion synthesis (SCS) method [**Sources:** [268]].

3.1.6 Ultrasonication Assisted SCS Method

Ultrasound assisted SCS method has been shown to be a very helpful tool for making nanostructured materials and speeding up the rate of reaction in many systems that are reacting. Most of the chemical and mechanical effects of ultrasound come from its acoustic cavitation effects. This is when high-intensity ultrasound causes bubbles to form, grow, and explode in liquids [270]. When bubbles pop due to cavitation, the area gets very hot and has a lot of pressure for a very short time [272]. At the same time, cavitation causes local turbulence and small amounts of liquid to move around in the reactor, which can speed up the transport processes. Cavitation creates very unusual conditions that can lead to a wide range of chemical reactions. This is useful for making a wide range of nanostructured materials. Many research groups have found that ultrasonic-assisted processing is a good way to make metal oxides because it helps get a uniform size distribution, a high surface area, a short reaction time, and pure phases [270,273].

3.1.6.1 Significance of Fuel

The fuel not only acts as a reducer, but it may also serve as a microstructural template and complexing agent, all of which add considerably to the final product's qualities. It is made up of organic molecules, namely those containing carboxylate (glycine, urea, & citric acid) and aliphatic amine (hydrazides) groups that can combine with an oxidant to start combustion. [268]. Chelating agents in fuels stop metal ions from coagulating together and keep the composition of all elements the same. This makes it easier for strong coordinate bonds to form. A few fuels, including valine ($C_5H_{11}NO_2$),

acetylacetone ($C_5H_8O_2$), 2-methoxyethanol ($C_3H_8O_2$), phenyl alanine ($C_9H_{11}NO_2$), and glycine ($C_2H_5NO_2$), etc., are being considered for SCS (**Fig. 3.6**) [268,274].

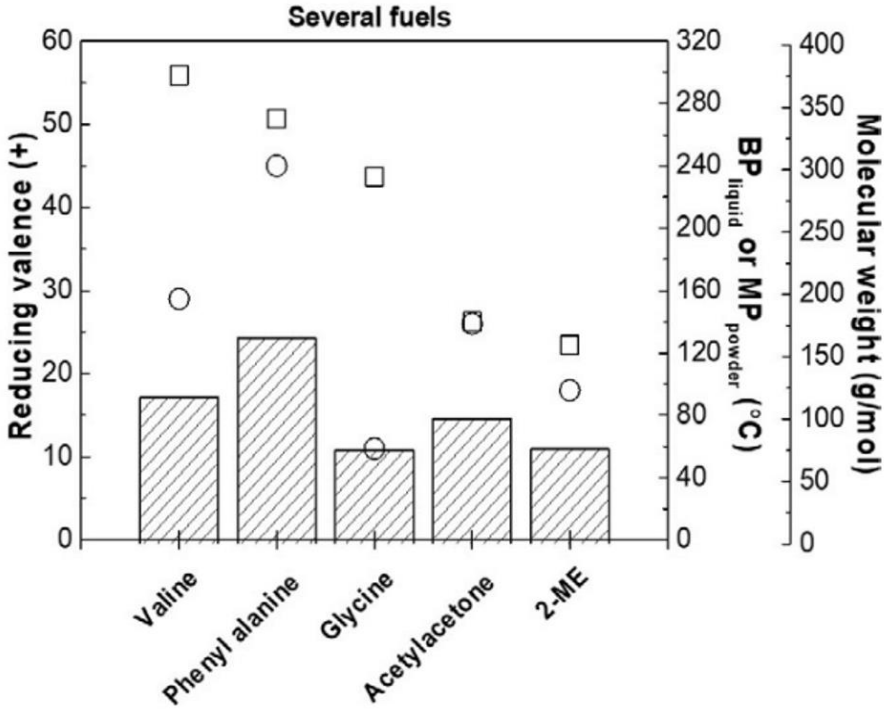

Figure 3. 6: Decomposition temperature [Melting point (MP) or Boiling point (BP)] and reducing valence (+) of most common fuels used in SCS [**Sources:** [268]].

Glycine, which has an amino group and a carboxylic group at the ends of its chemical structure, is a regularly employed fuel (**Table 3.1**) due to its strong coordination ability toward nitrates, low cost, and high exothermicity. Since glycine has carbon bonds, there might be high carbon impurities in the final product. However, glycine is an interesting molecule because it is zwitterionic [267,268]. It's electrically neutral because it contains many functional groups, each of which carries either a positive or a negative charge. This aids in maintaining a stable component composition and avoiding the occurrence of elective precipitation.

3.1.6.2 Oxidizer to Fuel Ratio

To determine the optimal stoichiometric ratio of oxidising (often nitrates) to reducing (fuel) elements in a combustion mixture (**Table 3.2**), Jain and co-authors describe a novel method in 1981. In this technique, oxygen (O) and nitrogen (N) are treated as oxidizers with valences of -2 and 0, respectively. Metal ions are regarded as reducing elements having final valences that match to the metal valence [268]. Carbon (C) and hydrogen (H) are considered reducing elements with respective valences of +4 and +1. The relationship between the quantity of reagents and their reducing and oxidising valences (RV/OV) could be express as follows [268,269].

$$\text{Fuel(reducer)/oxidizer ratio} = \frac{(-1)RV}{OV}n \quad (3.1)$$

n is the number of moles of fuel per mole of oxidizer.

Table 3. 1: List of various fuels used with metal oxides and achieved particle size [**Sources:** [268]].

Metal oxide	$T_{ignition}$ [°C]	Fuel(s)	Particle/crystallite size [nm]
$ZnO:Eu^{3+}$	400	TEA	50–300
$SrAl_2O_4:Eu^{2+}$, $SrAl_2O_4:Dy^{3+}$	300	TEA	<100
Fe_2O_3	300	Gly	17
$Ni_xZn_{1-x}O$ ($x=0.0-0.2$)	1000	U	33–44
CeO_2	400	Glu	35.5
V_2O_5	400	CA	37
NiO	800	Gly/U	10
MgO	400	VG	20–25
CuO	300	Gly	50
$Si:MnZnFe_2O_4$	350	Gly	10–40
ZnO	470	TEA/CA/EG	23
V_2O_5	900	EDTA	20
Bi_2MoO_6	300	U	90–500
NaV_6O_{15}	450	CA	width (100), length (400)
α-Fe_2O_3	500	Gly/Glu	18
α-Fe_2O_3/ Fe_3O_4	300	Gly	50–100

$T_{ignition}$: Ignition temperature for the combustion reaction, TEA: triethanolamine, Gly: Glycine, U: Urea, CA: Citric acid, EDTA: ethylenediamine tetraacetic acid, VG: Vetiver grass, Glu: Glucose, EG: ethylene glycol, CA: Citric acid

Table 3. 2: List of various oxidizers, fuels, and solvents used for SCS [**Sources:** [31]].

Oxidizer	**Fuel**	**Solvent**
Metal nitrates or nitrate hydrates: $Me^{\nu}(NO_3)_{\nu}\cdot nH_2O$	Urea (CH_4N_2O)	Water (H_2O)
ν - metal valence	Glycine ($C_2H_5NO_2$)	Hydrocarbons:
Ammonium nitrate (NH_4NO_3)	Sucrose ($C_{12}H_{22}O_{11}$)	Kerosene
	Glucose ($C_6H_{12}O_6$)	Benzene (C_6H_6)
	Citric acid ($C_6H_8O_7$)	Alcohols:
	Hydrazine-based fuels:	Ethanol (C_2H_6O)
	Carbohydrazide (CH_6N_4O)	Methanol (CH_4O)
	Oxalyldihydrazide ($C_2H_6N_4O_2$)	Furfuryl alcohol ($C_5H_6O_2$)
Nitric acid (HNO_3)	Hexamethylenetetramine ($C_6H_{12}N_4$)	2-Methoxyethanol ($C_3H_8O_2$)
	Acetylacetone ($C_5H_8O_2$)	Formaldehyde (CH_2O)

Figure 3.7 demonstrates the significance of the Fuel: Oxidizer ratio 1:1. The ratio of fuel to air in a SCS could be divided into five categories (**Fig. 3.7**). An external heat source is necessary to complete the combustion reaction in an extremely fuel deficient (EFA) state, when nearly no fuel is present. A little larger fuel quantity in fuel deficient (ED) combustion causes a slow combustion process that also requires extra heating to complete the reaction. Stoichiometric fuel/oxidizer ratios allow for self-combustion reactions and auto-ignition processes with very exothermic activity, producing

extremely high temperatures. Stoichiometric combustion, in which the perfect ratio of oxygen to fuel is achieved, is the most efficient and produces the greatest heat. To complete a reaction with a stoichiometric ratio of 1 (balanced reducing and oxidising species), ambient oxygen is not necessary for the reaction to occur. This stoichiometric condition denotes full combustion of the precursor components, resulting in the formation of metal oxide [31,267]. The probability of detecting impurities (carbon and carbonates) in the end product is increased under fuel rich situations, such as the fuel excess (FE) and extremely fuel excess combustion reaction (EFE). Since heat losses are not taken into account in the theoretical temperature (T_{th}), the experimental temperature of the reaction (T_{exp}) will always be lower than the theoretical temperature (T_{th}) in SCS [268].

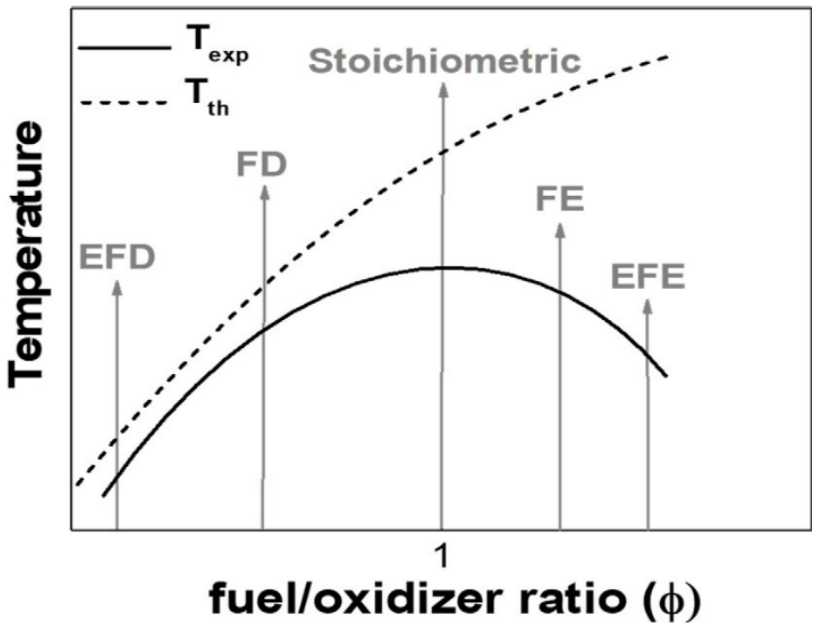

Figure 3. 7: Theoretical and experimental tread of temperature versus the fuel oxidizer ratio [**Sources:** [268]]. [EFD: extremely fuel deficient, FD: Fuel deficient, FE: Fuel excess, EFE: Extremely fuel excess.]

3.1.7 Experimental Method for the Synthesis of Catalysts by SCS and Ultrasonication Assisted SCS

For the present work glycine is used as the fuel as it is one of the cheapest and most cited fuels for SCS studies. The SCS processes used in this work are explained stepwise below.

3.1.7.1 Step Wise Procedure for Catalysts Preparation by SCS Method

Step 1: In this process, ethanol is used as an initial medium. Firstly, as per the stoichiometric all precursors added and well mixed through pestle mortar (**Table 3.3**). To obtain solution, metal precursor salts are dissolved in solvents like ethanol (20 ml) along with fuel glycine (H_2NCH_2COOH; Rankem, >

99% purity), then mixed thoroughly for 30 min to obtain a viscous solution. The mixture is transferred to a 500 cc beaker and dried overnight at room temperature.

Table 3. 3: List of the precursors used for preparation of Ni-Sn/CeO_2 catalyst with different precursors:

S.No	Catalyst	Precursors used	Manufacture company
1	$NiSn/CeO_2$	Nickel Nitrate hexahydrate $[Ni(NO_3)_2.6H_2O]$	Qualikems(QLS), 99%
		Tin Chloride $[SnCl_2.2H_2O]$	Molychem, 99%
		Cerium Nitrate hexahydrate $[Ce(NO_3)_2.6H_2O]$	Qualikems(QLS), 99.9%
2	$NiSn/Ce_{1-x}Mg_xO_2$	Nickel Nitrate hexahydrate $[Ni(NO_3)_2.6H_2O]$	Qualikems(QLS), 99%
		Tin Chloride $[SnCl_2.2H_2O]$	Molychem, 99%
		Cerium Nitrate hexahydrate $[Ce(NO_3)_2.6H_2O]$	Qualikems(QLS), 99.9%
		Magnesium Nitrate hexahydrate $(Mg(NO_3)_2.6H_2O)$	Molychem, 99%
3	$NiSn/Ce_{1-x}Zr_xO_2$	Nickel Nitrate hexahydrate $[Ni(NO_3)_2.6H_2O]$	Qualikems(QLS), 99%
		Tin Chloride $[SnCl_2.2H_2O]$	Molychem, 99%
		Cerium Nitrate hexahydrate $[Ce(NO_3)_2.6H_2O]$	Qualikems(QLS), 99.9%
		Zirconium Oxynitrate hydrate $(ZrO(NO_3)_2.xH_2O)$	Sigma-Aldirch, 99%
4	$NiSn/Ce_{1-x}La_xO_2$	Nickel Nitrate hexahydrate $[Ni(NO_3)_2.6H_2O]$	Qualikems(QLS), 99%
		Tin Chloride $[SnCl_2.2H_2O]$	Molychem, 99%
		Cerium Nitrate hexahydrate $[Ce(NO_3)_2.6H_2O]$	Qualikems(QLS), 99.9%
		Lanthanum Nitrate $(La(NO_3)_3.6H_2O)$	SRL chemicals (99%)

Step 2: Afterwards, the solution is heated to 300°C on a hot plate within a fume hood. In an attempt to monitor the temperature of the burning mixture over time, a type-K thermocouple with its tip covered is put on top of the components. This is the first of three steps in the procedure. Initially, the solution's viscosity rises as the solvent boils off and evaporates. As can be seen in **Figure 3.8**, the second phase involves foaming, followed by ignition at a single point, and the third phase involves the spread of the combustion front throughout the whole dish, resulting in a thick layer of black-brown foam. During this process, gases are formed and escape through the cluster of particles, due to which pores are formed between the particles. The generation of a lot of amount of gases during the combustion process dissipates the heat produced in the process, thereby limiting the temperature rise, which also helps in preventing the sintering of the particles.

Step 3: A total of four or five washes in DI water are performed on the resulting mass to flush out any remaining contaminants or unreacted compounds. Then wet paste is then dried in an oven (Macro scientific works: MSW-211)) at 60 °C for a period of 12 hrs. The dried sample is collected in a vile, named as fresh catalyst. **Figure 3.9** shows a general flow chart of solution combustion synthesis procedure for different catalysts preparation and the relative characterization techniques carried out.

Step 4: Before activity study, the catalysts are reduced with flowing hydrogen (15 ml/min) at 500 ^{o}C for 3 hours. The heating and cooling are performed at 2 ^{o}C/min under purging nitrogen at 10 ml/min.

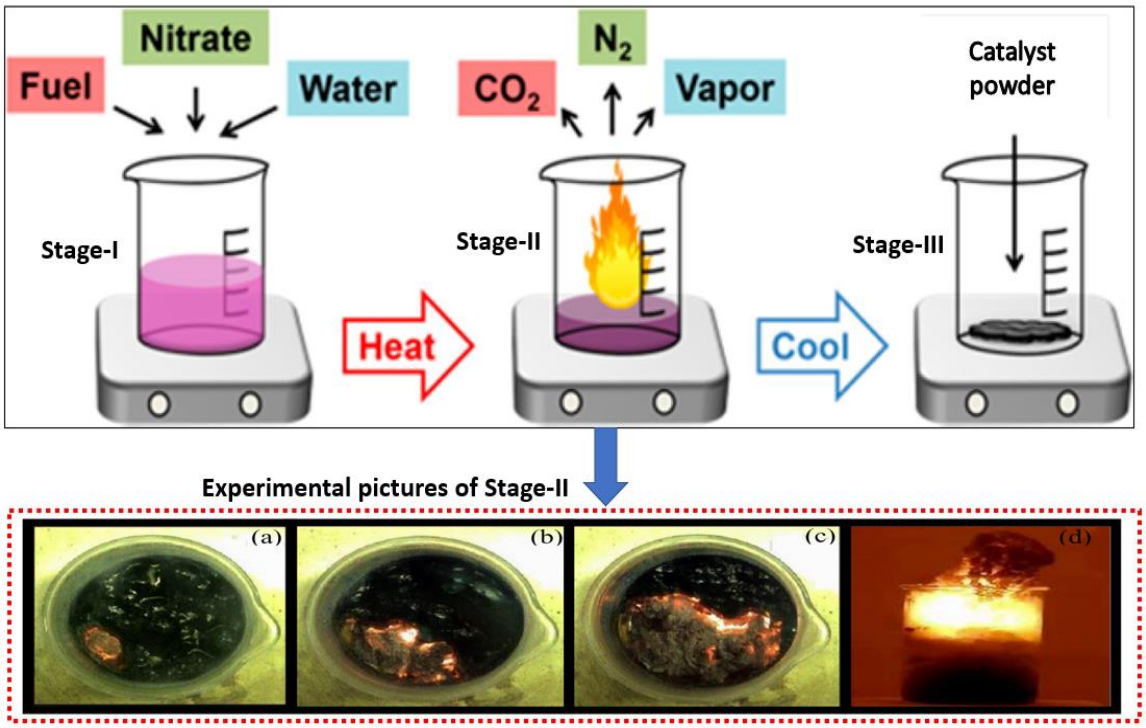

Figure 3. 8: Different stages of solution combustion synthesis [**Sources:** [31]].

3.1.7.2 Step Wise Procedure for Ultrasonication Assisted SCS Method

The preparation steps for the SCS and this method are also most similar. The minor difference between SCS and this method is, ultrasonication is used for the entire solution combustion synthesis process. Submerging the tip of an ultrasonic liquid processor (20 kHz, Sonics & materials, 8 cm horn diameter, 500 W) in the paste causes the mixture to vibrate. **Figure 3.10** shows the different stages of ultrasonication assisted SCS method.

The typical temperature-time profiles during the SCS process are recorded with the help of thermocouple (K-type), for $NiSn/CeO_2$, $NiSn/Ce_{1-x}Mg_xO_2$, $NiSn/Ce_{1-x}Zr_xO_2$, and $NiSn/Ce_{1-x}La_xO_2$ catalysts in a temperature data logger and shown in **Fig. 3.11**. It can be seen that at ignition (or) combustion starting temperature (T_{ig} ~ 150 °C), the reaction initiates and proceeds at extremely high rate reaching a maximum temperature value T_m ~ 650 °C. After that the temperature suddenly drops to ~ 250 °C within 25 seconds. The temperature profile depends on the experimental conditions (e.g.,

nature of the fuel, ratio between fuel and oxidizer, amount of catalyst, local mixture ignition etc.). The example physical appearance of catalysts shown in **figure 3.12**.

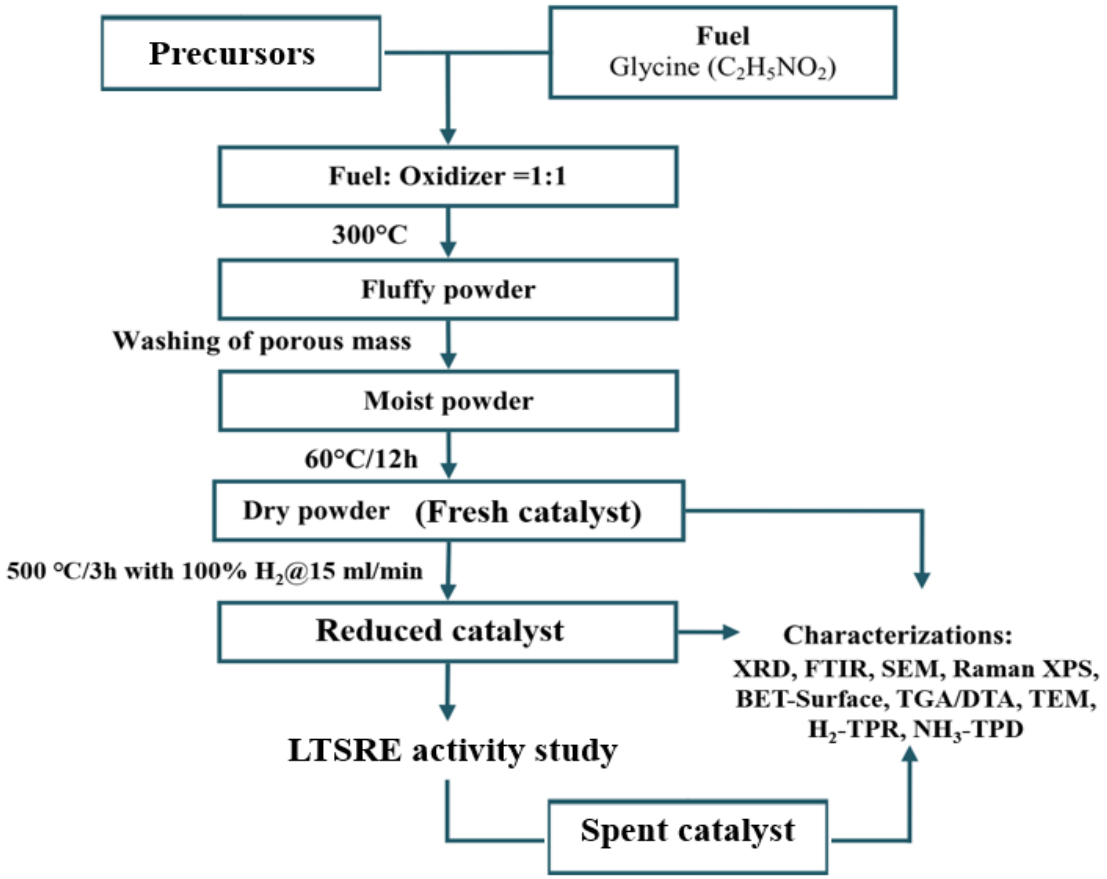

Figure 3. 9: General flow chart of solution combustion synthesis procedure for different catalysts preparation and the relative characterization techniques carried out.

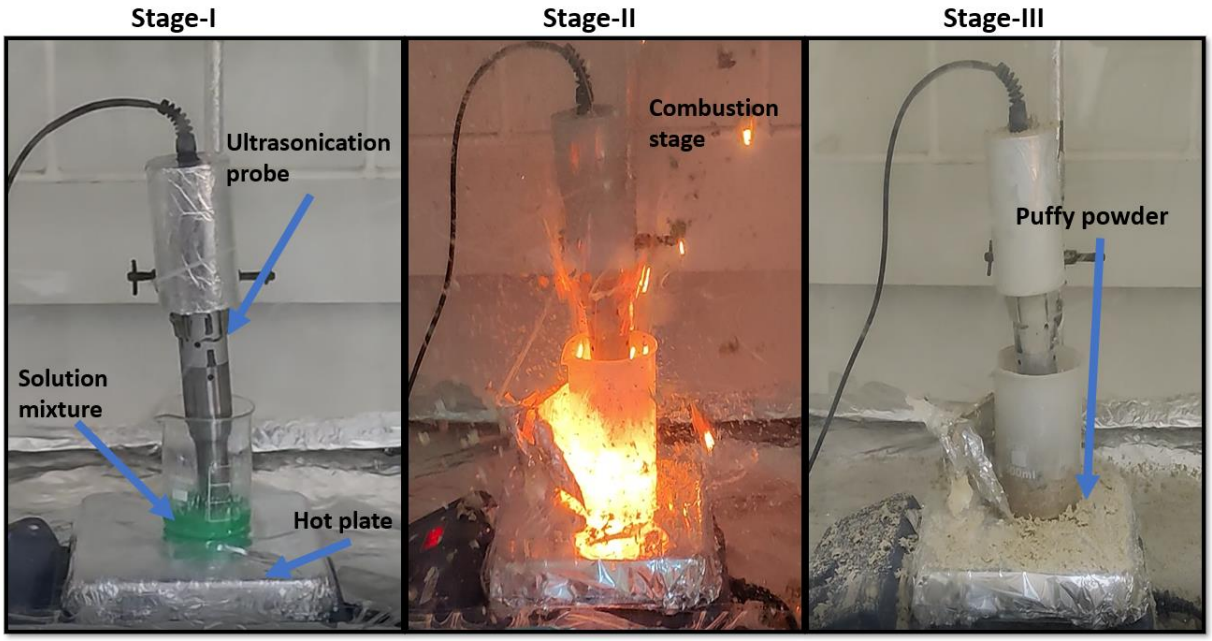

Figure 3. 10: Different stages of Ultrasonication assisted with solution combustion synthesis method.

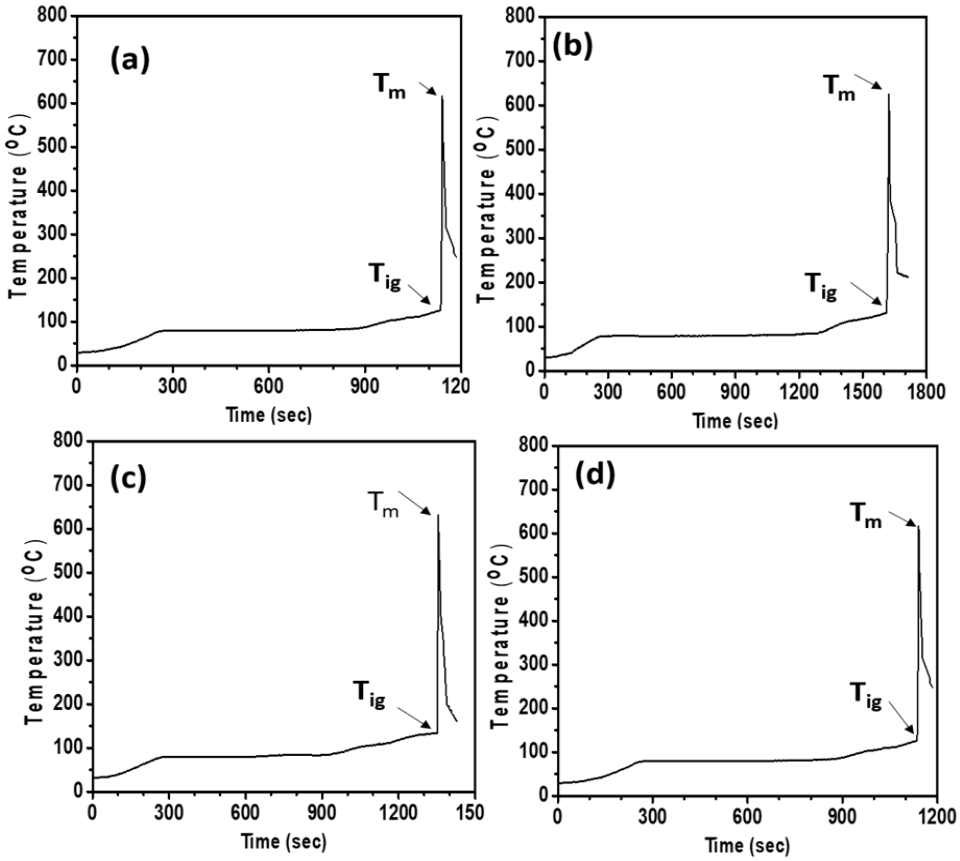

Figure 3. 11: Time (vs) temperature profile during solution combustion synthesis using thermocouple for (a) NiSn/CeO_2, (b) NiSn/$Ce_{1-x}Mg_xO_2$, (c) NiSn/$Ce_{1-x}Zr_xO_2$, (d) NiSn/$Ce_{1-x}La_xO_2$.

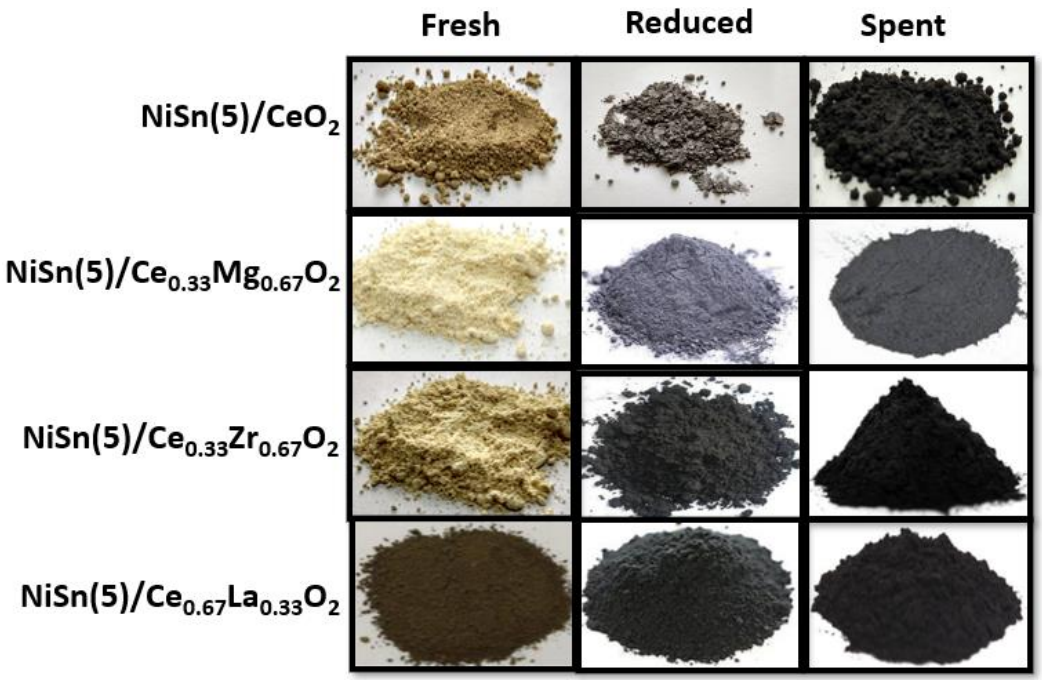

Figure 3. 12: Example physical appearance of NiSn(5)/CeO_2, NiSn(5)/$Ce_{0.33}Mg_{0.67}O_2$, NiSn(5)/$Ce_{0.33}Zr_{0.67}O_2$, , NiSn(5)/$Ce_{0.67}La_{0.33}O_2$ catalysts after preparation (fresh), reduction, and and spent.

3.2 Catalyst Characterizations

The primary objective of characterization is to understand the physical (microstructure, size, etc.) and chemical properties (chemical composition, phase composition, etc.) of the catalyst powders (fresh, reduced, and spent) and to understand the correlation of these properties with the catalytic activity variables (feed conversion, product selectivity, yield, etc.). This is important for the design and optimization of catalysts. The purpose of the characterization is to monitor the changes in the physical and chemical characteristics of the catalyst during the preparation and reaction phases for quality control. Determining the level of catalyst deactivation during the reaction phase is also crucial. It also helps to design procedures for catalysts regeneration. For the present study, catalysts has been examined by various characterizations techniques, such as X-ray diffraction (XRD), Fourier transform infrared spectroscopy (FTIR), Raman spectroscopy, Field emission scanning electron microscopy (FE-SEM), Transmission electron microscopy (TEM), X-ray photoelectron spectroscopy (XPS), Simultaneous Thermo gravimetric analysis (TGA) and differential thermal analysis (DTA) method, BET-Surface area, H_2-temperature programmed reduction (H_2-TPR), and temperature programmed desorption of ammonia (NH_3-TPD).

3.2.1 X-Ray Diffraction (XRD)

XRD technique is used to determine crystallinity, lattice parameters, unit cell dimension, cell volume, particle size, internal stress, etc. In this Θ-2Θ scan, the changes in the intensity of the scattered X-rays are measured or recorded and plotted against the angle of scattering (2Θ). Catalyst samples are prepared for XRD (-2 scan) utilising a Rigaku miniflex II machine and CuKα (λ = 1.54 nm) radiation (30 kV and 15 mA), 1.25° DS slit width, 150 mm goniometer radius under normal atmospheric condition. Equipment used during the XRD analysis is shown in figure 3.13. Catalyst is ground into fine powder with the help of a mortar and pestle so that it can adhere to the specimen holder, which is made of glass with a recess for powder (area: 2 cm *4 cm) and powder is pressed in it using a glass slide. The sample holder is mounted on the sample stage which keeps the sample aligned in the beam and controls the movement of the sample. Thus, the XRD run of the catalysts samples are carried under the following conditions: Sample Weight – 0.3-0.5 gm; 2Θ Range – 10 – 100°; Scan speed – 2 degrees per minute; Sampling acquiring rate –0.05°/sec.

3.2.2 Thermo Gravimetric Analysis (TGA) & Differential Thermal Analysis (DTA)

Thermo gravimetric analysis (TGA) is a thermal analytical technique which is used to identify the physical (gas adsorption & desorption) and/or chemical (decomposition due to loss of volatiles, chemisorption, reaction, etc) changes in sample with respect to temperature or time in terms of weight

loss or gain [275]. TGA instrument continuously records the change in weight of material during the heating/cooling. Results are plotted with temperature or time on the X-axis and weight loss in percentage on the Y-axis. Differential thermal analysis (DTA) is used to determine the physical (adsorption, desorption, crystallization, melting, vaporization, sublimation etc.) and chemical (oxidation, reduction, break down reactions, chemisorption etc.) phenomena which cause the change in heat energy (exothermic or endothermic) as a function of temperature or time [31,276].

Figure 3. 13: XRD equipment used in for catalyst characterization along with the catalyst placed over glass sample holder.

Results are plotted with temperature or time on the X-axis and heat flow in micro-volt on the Y-axis and by evaluating DTA curve, melting temperature and enthalpy data can be obtained. The equipment we have used for our characterization is DTG-60H, SHIMADZU, which simultaneously provide the thermo-gravimetric and differential thermal analysis data. Instrument consists of a furnace with sample and reference pans (made up of platinum as we are working up to 800 °C) placed inside and these are supported by a precision balance and a heat detector. The mass and heat energy change of the samples are monitored during the experiment. The TA-60WS thermal analysis (control the temperature) workstation connects the DTG-60 series and the computer. Intuitive data acquisition software controls the DTG-60 series and the FC-60A atmosphere control unit (to operate the gas flow). Equipment used during the analysis is shown in **Fig. 3.14**. The experimental conditions are: sample weight – (25-30) mg; temperature range (Heating) – 40 – 800 °C; scanning rate – 5 or 10°C /min, and gas –atmospheric air. During this process heating is controlled by keeping a constant heating rate however, cooling is not, it was a normal furnace cooling.

3.2.3 Fourier Transform Infrared Spectroscopy (FTIR)

Fourier-transform infrared spectroscopy (**Fig. 3.15**) is a vibrational spectroscopic technique, which takes advantage of asymmetric stretching, vibration and rotation of chemical bonds as they are exposed to designated wavelengths of electromagnetic spectra (Madejová 2003). Generally, molecules or material absorbs energy in the infrared (IR) region for molecular vibration. In the intensity (Y-axis) (vs) wavenumber (X-axis) graph the absorption/transmittance peaks correspond to the vibration of bonds between atoms of the particular groups.

FTIR spectra (Perkin Elmer Frontier^{TM}) performed by using KBr pellet procedure. Samples that were scanned between 400 and 4000 cm^{-1}. The average number of scans was 20.

Figure 3. 14: DTA/TGA equipment used for catalyst characterization.

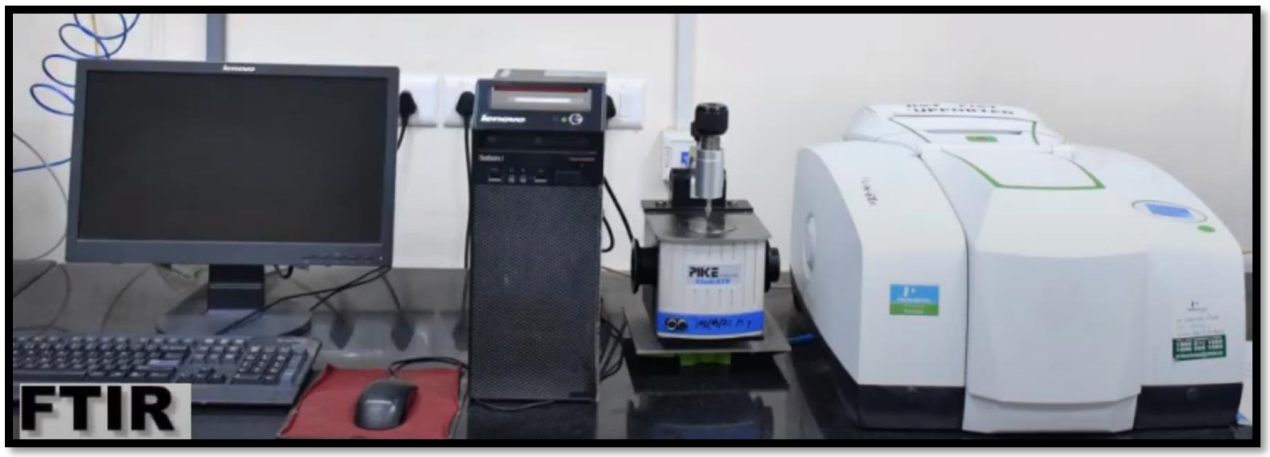

Figure 3. 15: FTIR equipment used for catalyst characterization.

3.2.4 Raman Spectroscopy

In this study, Raman spectroscopy characterization of the catalyst samples (Fresh, Reduced, and spent) is executed with the help of a Horiba LabRam HR pectrometer equipped with a confocal DM 2500 Leica optical microscope (equipped with 10x and 50x objectives) and multichannel detection (liquid nitrogen cooled CCD) over the range of 150-1400 cm^{-1}. A 532 nm argon laser (Model 171) is used as excitation source, with beam intensity not exceeding 10 mW on a sample. The incident beam is focused on the sample using a 50x objective lens. The diameter of the laser spot is kept ~2 µm. About 300-400 mg (about 1-mm thickness) of each catalyst is spread over a glass microscope slide. The Raman spectra are recorded at various spots on the surface of the sample as mapping, at room temperature and normal ambience. The Equipment set up used for the Raman data acquisition is shown in **Fig. 3.16**.

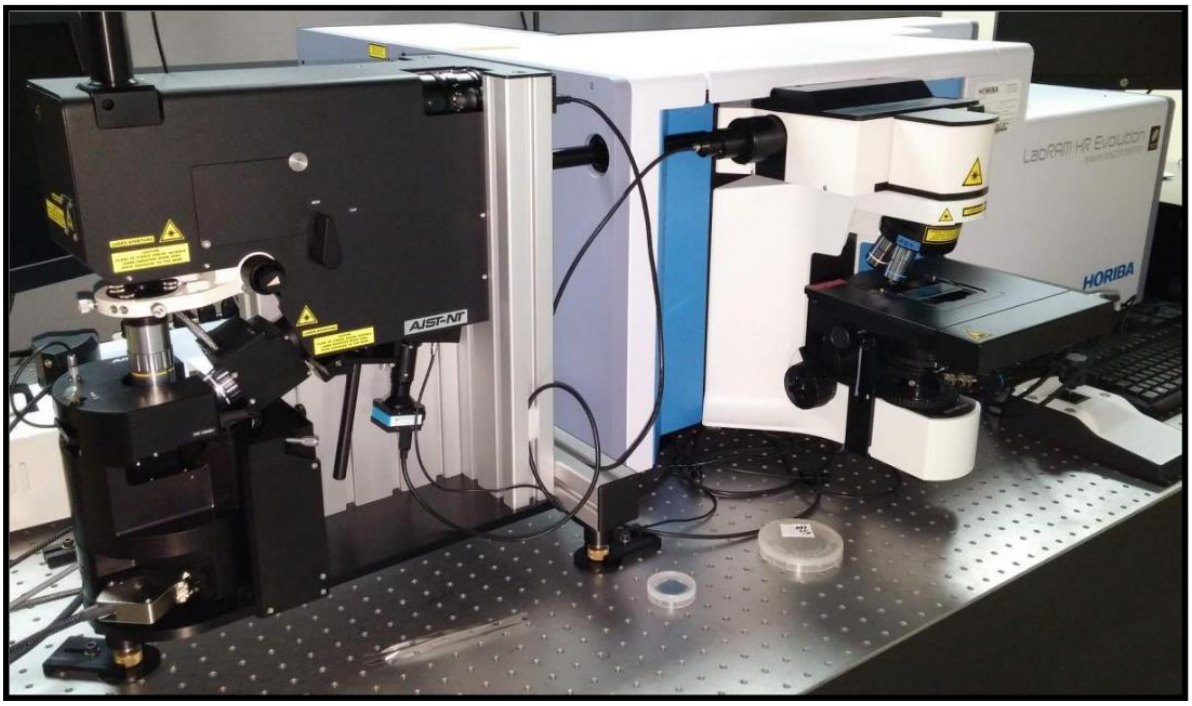

Figure 3. 16: Raman equipment used for catalyst characterization.

3.2.5 Field Emission Scanning Electron Microscope (FESEM)

The microstructures and particle size distribution of the catalysts are studied with a Nova Nano FE-SEM 450 (FEI) equipment with the specifications as: Beam landing energy 30 keV to 50 eV, resolution of 1.4 nm at 1 kV & 1nm at 10 kV, equipped with EDX spectroscopy system with 30º take-off angle for quantitative analysis, with digital imaging and X-ray mapping capability (**Fig. 3.17**). The EDX (SAPPHIRE SEM) detector has 128 eV resolutions, and 20,000:1 peak-to-background ratio maintained at high throughputs. The FE-SEM specimen is made by sprinkling powder on carbon tape mounted over aluminium stub. The images are acquired at different magnifications (500x-100000x) along with the EDX data.

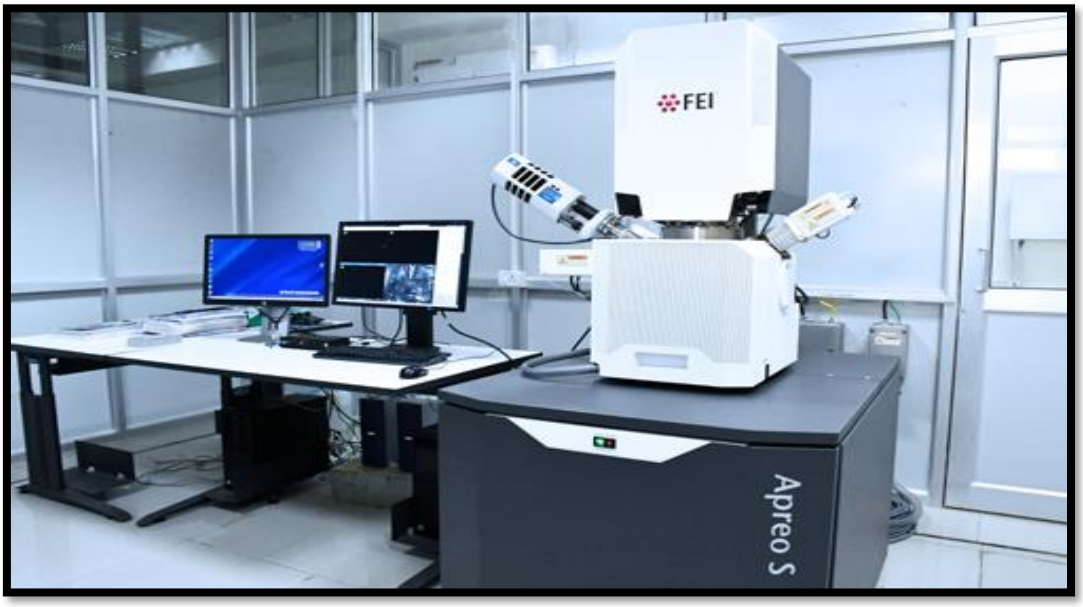

Figure 3. 17: FESEM equipment used for catalysts characterization.

3.2.6 X-Ray Photoelectron Spectroscopy (XPS)

In this study, X-ray photoelectron spectrometer (XPS, Thermo fisher scientific Pvt. Ltd, U.K), with a Al Kα monochromatic source, is used to acquire wide scan (0 – 1200 eV) and high resolution data. X-ray dual-beam monochromatic micro-focused with variable spot size (50 - 400 μm) in 5 μm steps. High-resolution spectra of each element are taken to measure how much coke has been deposited and to identify the chemical and electronic states of the different metals and metal oxides. For deconvolution of the XPS spectra, the XPSPeak4.1 software and the Shirley algorithm have been used. XPS is used to identify the chemical/electronic state of elements and elemental composition that exist within a material.

3.2.7 H_2-Temperature Programmed Reduction (H_2-TPR)

In this study, H_2-TPR samples are studied using a Micromeritics Autocheme II 2920 catalyst characterization system with a thermal conductivity detector (TCD). TPR is done with a flow rate of 25 ml/min of 10% H_2/Ar, and the sample is heated to 1050 °C at a rate of 10 °C/min. H_2 temperature programmed reduction (H_2-TPR) has been used to test the reducibility of various phases for catalyst samples. This technique is most often used for heterogeneous catalysts.

3.2.8 N_2-Absorption and Desorption

In order to estimate the catalyst surface area, pore diameter, and pore volume, a N_2-adsorption and desorption analyzer is utilised using Microtrac Bel, BEL SORP mini- II instrument. Samples are warmed for two hours at a temperature of 200 °C before being characterized.

3.2.9 Temperature Program Desorption of Ammonia (NH_3-TPD)

A Micromeritics Autocheme II 2920 system with a thermal conductivity detector is used to figure out the NH3-TPD of the samples. The NH_3-TPD is performed on our samples to determine the acidity of the supports. About 0.1 g of the sample is initially flushed with a He flow at 500 ℃ for 2 h, next cooled to 120 ℃ and then saturated with NH_3. After NH_3 is exposed, the sample is purged with He until the excess of physically adsorbed NH_3 is removed. Then this sample is heated to 500 ℃ at a heating rate of 10 ℃/min. The NH_3-desorption activation of activation energy calculated by using different heating rate of 10, 15, 20 ℃/min for $NiSn/CeO_2$ modified with La_2O_3 catalysts.

3.2.10 Transmission Electron Microscopy (TEM)

The transmission electron microscopy (TEM) was performed on an FEI titan instrument and operated at 80 kV using a focused ion beam (FIB) Helios G4-UX. TEM was done on the sample in a cross-sectional manner on the sample.

3.3 Catalytic Activity Measurements

3.3.1 Experimental Setup and Procedure

Low-temperature steam reforming of water-ethanol mixture is executed with a custom-designed continuous flow fixed bed stainless steel reactor (Diameter: 3/8"; Swagelok-SS-T6-S-049-20) located in a furnace (MAC-Muffle furnace; MAC-251) under atmospheric pressure. The reactor is filled with a 500 mg batch catalyst in between two layers of quartz wool. The catalysts are heated at 150 ºC for 30 minutes while 10 ml/min of nitrogen flows through the reactor to remove the moisture that has stuck to the surface. The liquid mixture of ethanol and water with a mole ratio of 1:12 is preheated at 110 ºC to form vapor, and N_2 gas (> 99.99%) is swept through the preheater to carry the vapour mixture to the reactor. The gas line (Diameter: 1/8"; Swagelok-SS-T2-S-028-20) connecting the pre-heater to the reactor is heated at 105-110 ºC to prevent condensation. GHSV (gas hourly space velocity) measured 7697 h^{-1} corresponding with feed flow rate 0.1 cc/min^{-1} at STP. Reaction temperature is maintained in between 200-400 °C. The product mixture from the reactor is passed through an ice cooled phase separator in order to condense the liquid in the product. The gaseous and liquid products from the phase separator are analyzed by using a gas chromatography. Schematic of low temperature steam reforming experimental set-up with picture of setup used in lab is shown in **Fig. 3.18 (a)** and **(b)**.

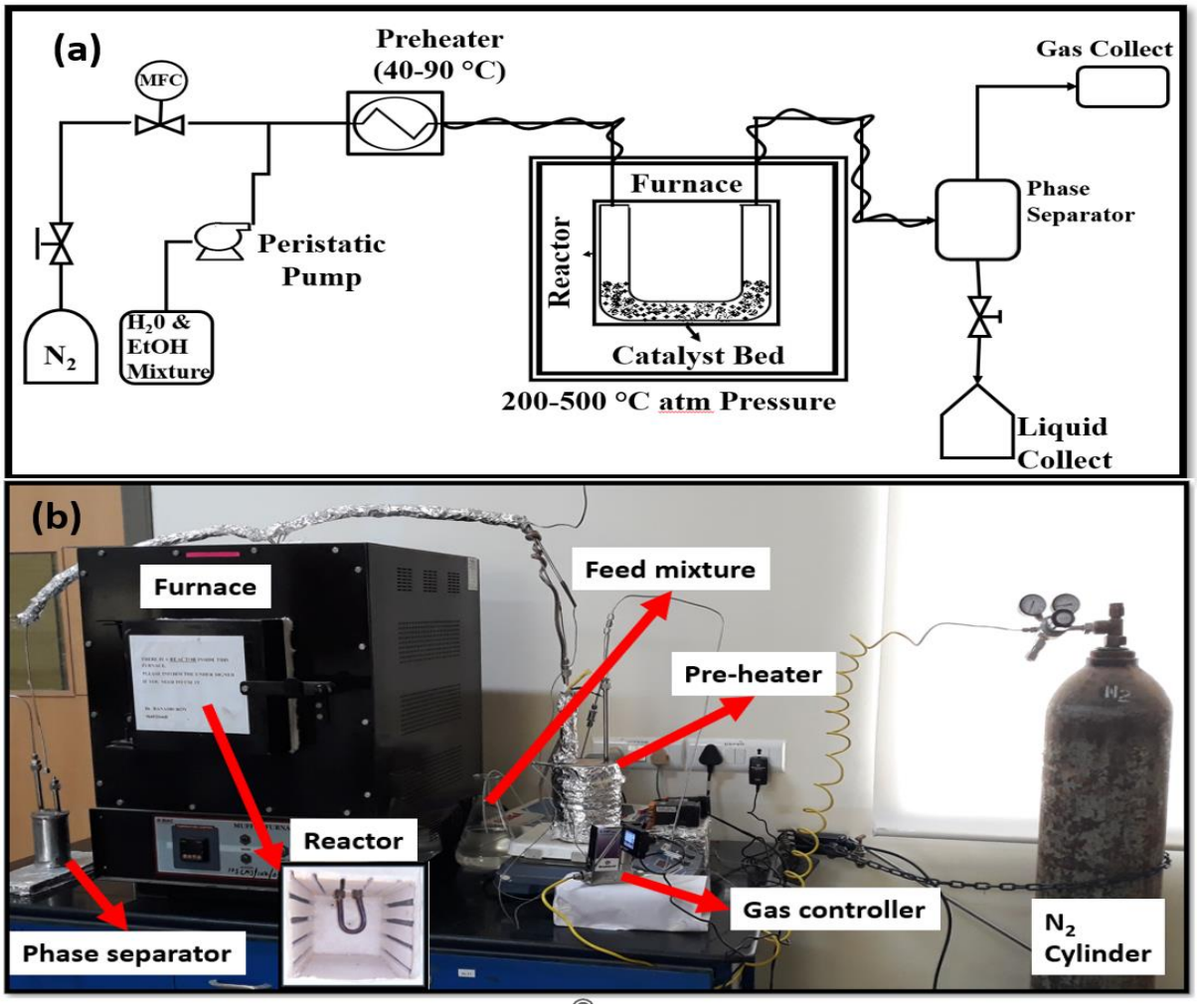

Figure 3. 18:(a) Schematic and (b) experimental setup used for low temperature steam reforming.

3.3.2 Gas samples Analysis Producer

The gaseous mixture is analyzed by using an offline gas chromatography instrument (GC; Shimadzu-2014) equipped with TCD (Thermal conductivity detector), where porapak (length 2 meter and 1/8 inch diameter SS column and 80/100 mesh with Adapter Shimadzu GC- 2014ATF) is the reference column and carbosphere is the sample column (length 2 meter and 1/8 inch diameter packed with carbo-sieve, 80/100 mesh with Adapter Shimadzu GC- 2014ATF). Basic working principle for GC, selection of carrier gas, operating parameters (oven temperature, carrier gas flow rate, etc.), and detail of the calibration technique are described in subsequent sections.

3.3.2.1 Working principle for GC

GC is a separation technique in which the components of a gas mixture are partitioned between two phases: the stationary and the mobile phase. Gas chromatography can be divided into two types based on the state of the stationary phase: gas-solid chromatography (GSC), where the stationary phase is a solid, and gas-liquid chromatography (GLC), where the stationary phase is a liquid [31]. The GC

schematic and equipment used in the study are shown in **Fig. 3.19 (a)** and **(b)**. The sample is injected at the entrance of the column called injection port with the help of a 500 microliter (µl) syringe. The sample is introduced into the carrier gas stream which carries the sample through the column. The carrier gas is an inert gas like helium or a non-reactive gas like nitrogen. Since the carrier gas doesn't react with the sample, the selectivity of GC separation can be attributed to the stationary phase alone. Columns are classified as either packed or capillary columns.

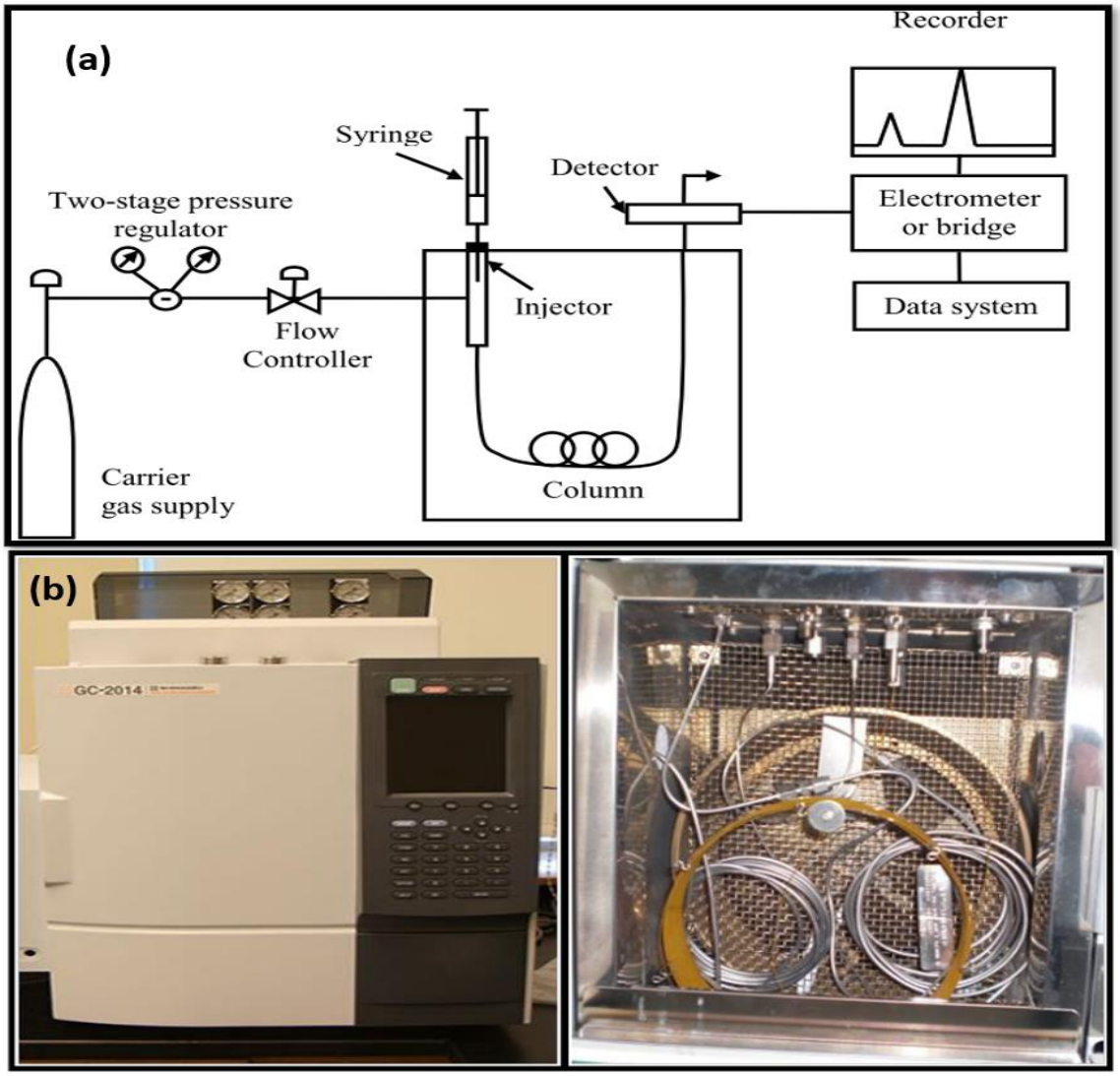

Figure 3. 19: (a) Schematic and (b) GC equipment used in the lab with insight of oven for gas product analysis.

Packed columns are coated with a microscopic layer of polymer (silica, alumina, carbon molecular sieve, calcium carbonate, calcium phosphate, magnesia, starch, etc. depending on applications) on an inert solid support inside glass or metal tubing [277]. Temperature in GC is controlled via a heated oven and column is fixed inside the oven. The injector and detector connections are also contained in the GC oven. The immobilized coated layer acts as the stationary phase which

obstructed the motion of sample components by adsorbing them at different regions depending on their ability for adsorption. Moving rate of molecules through the column depends on the strength of adsorption, which in turn depends on the nature (intermolecular and intra-molecular hydrogen bonding forces) of packing material and sample molecules. As the mixture moves down through the column, the component with greater adsorption power is absorbed in the starting of the column and the other is adsorbed at the end of the column. The weakly adsorbed component will be eluted more rapidly than the others which make each component eluted at different times, called retention time or residence time of that component. Most of the time, substances can be identified (qualitatively) by the order in which they come out of the column, which is called their "retention time." The detector picks up on a physical or chemical property of the analyte and gives a response. This response is amplified and turned into an electronic signal, which is then used to make a chromatogram.

The thermal conductivity detector (TCD) is a non-destructive universal detector. It is widely used in gas chromatography for its high reliability, simplicity, and ease of operation. The TCD measures the difference in thermal conductivity between the carrier gas flowing through a reference column and a sample component mixture flowing through a sample column [277].

3.3.2.1.1 Carrier Gas Selection

The selection of a carrier gas is an essential factor, and it depends on the products present in the sample and also on the detector. Typical carrier gases include helium, nitrogen, argon, hydrogen, and air. Our product gas sample contains mainly CO CO_2, CH_4, and H_2. Flame ionization detector (FID) cannot be used as H_2 is used to generate the flame in FID yet; H_2 is present in our product. Therefore, quantitative analysis of the producer gas is done with TCD. TCD senses the changes in the thermal conductivity of the product components and compares it to a reference flow of carrier gas and difference between these two should be large [31,278].

Most components have a thermal conductivity much less than that of the common carrier gas helium as shown in table 3.4. However, thermal conductivity of hydrogen (230.9 mW m^{-1} K^{-1} at 127˚C) is higher than helium (189.6 mW m^{-1} K^{-1} at 127 ˚C) and other components present in product such as N_2 (32.8 mW m^{-1} K^{-1} at 127 ˚C), CO_2 (25.2 mW m^{-1} K^{-1} at 127 ˚C) CO (32.3 mW m^{-1} K^{-1} at 127 ˚C) and CH_4 (50 mW m^{-1} K^{-1} at 127 ˚C) have lower thermal conductivity than helium (Tsederberg and Cess 1965).

Table 3. 4: The thermal conductivity of some gases as a function of temperature.

Gases	**Thermal conductivity in mW m^{-1} K^{-1} at various temperatures**				
	200K	300K	400K	500K	600K
Ar (Argon)	12.4	17.7	22.4	26.5	30.3
He (Helium)	118.3	155.7	189.6	221.4	251.6
H_2 (Hydrogen)	132.8	186.6	230.9	270.9	309.1
N_2 (Nitrogen)	18.3	26.0	32.08	39.0	44.8
CO(Carbon monoxide)	-	25.0	32.3	39.2	45.7
CO_2 (Carbon dioxide)	9.6	16.8	35.2	33.5	41.6
CH_4 (Methane)	21.8	34.4	50.0	68.4	88.6

Therefore, detection of hydrogen with helium results in a negative peak in comparison to other products consequently; we need another gas to quantify hydrogen. Nitrogen as a carrier gas cannot be used as it is already used as a carrier gas in catalytic activity. Hence, we have opted argon (22.4 mW m^{-1} K^{-1} at 27 ˚C) as the carrier gas which has the lowest thermal conductivity in comparison to all product components. Argon, all peaks come in negative and by changing the priority we get all the peaks in positive direction.

3.3.2.1.2 Operating Parameter Selection

The carrier gas flow rate and the oven temperature are the main parameters which are required to be controlled to achieve the separate peaks corresponding to different components of the gaseous product mixture. On keeping high carrier gas flow rate (≥ 10 ml/min), the analytes take less time in passing through the column which results in lower retention time for the components to be analyzed. Then, for a multicomponent system peak could be overlapped and difficult to analyze quantitatively at higher flow rate. However, low carrier gas flow rate (≤ 5 ml/min) increases the analysis time. The flow rate selection could be a compromise between the level of separation and analysis time. The optimum flow rate of carrier gas for the process is obtained to be 8 ml/min.

3.3.2.1.3 Calibration

Calibration is carried out in order to quantify the components present in the gaseous product. GC provides the response for every component present in the mixture in terms of peak intensity and retention time. Pure sample for each component is injected in the GC in order to determine the retention time for each component. Based on the retention time analysis of the pure components, each peak of the chromatograph corresponds to a particular component of gaseous mixture that can be identified. The number of peaks of chromatograph depends upon the number of components present in the gaseous mixture. The calibration (amount vs area) for the gaseous products is carried out by injecting a standard gaseous mixture (sigma gases & services, cylinder no: 74277) of different volume in the GC. The calibration curve is obtained by plotting the peak area of the standard component on the abscissa and the amounts of the standard component on the ordinate. **Figure 3.20** shows the calibration curves for

different components of the producer gas. The calibration Equations and R-square values are obtained by doing linear fitting of the data.

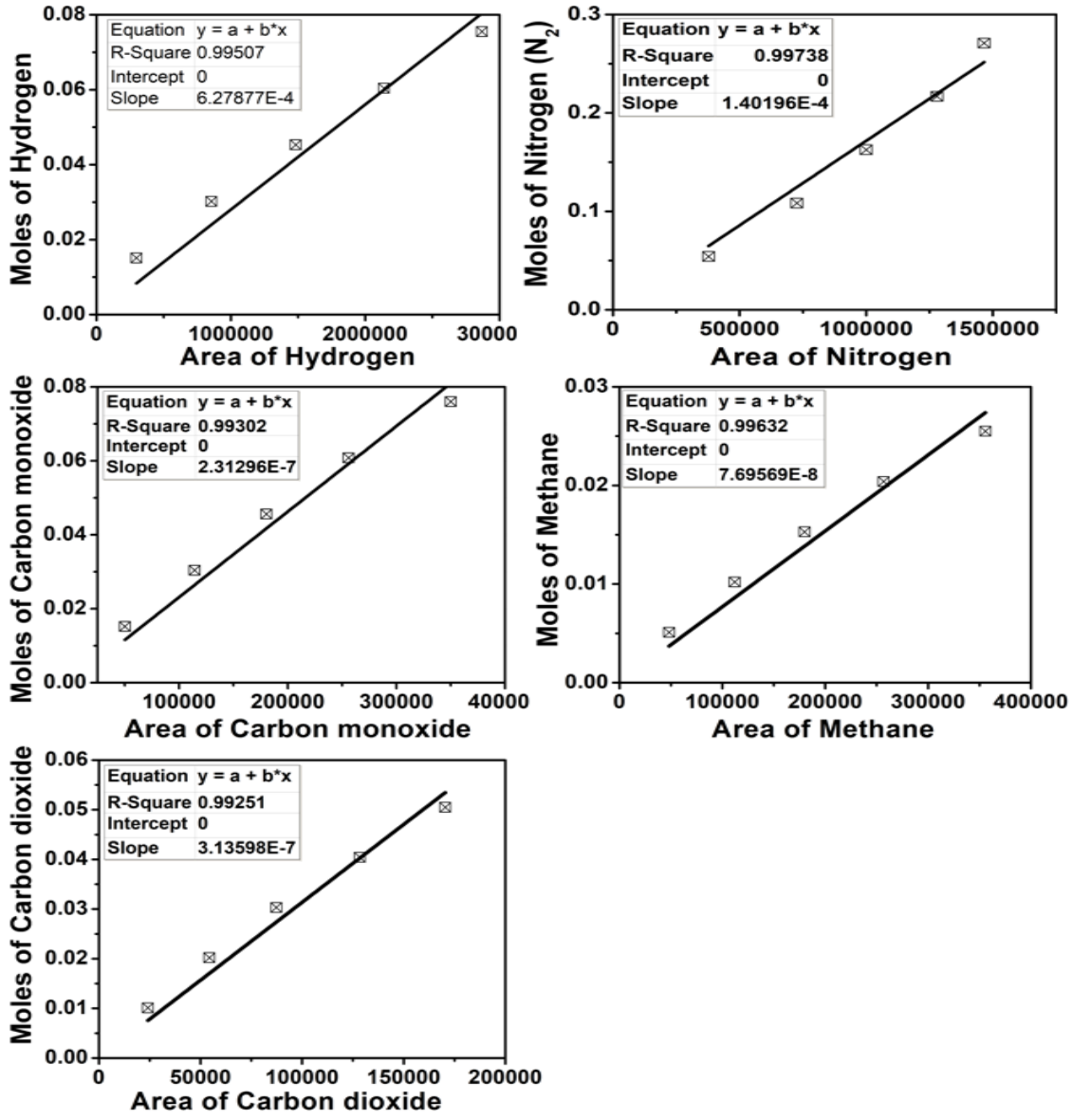

Figure 3. 20: Calibration curve for gaseous components.

3.3.2.2 Selectivity of Gaseous Components

Gaseous products are collected in the phase separator. To know the steady state time, gaseous products are analysed after every one hour. Moles of each component (H_2, CH_4, N_2, CO_2, and CO) present in the gaseous phase is calculated by using the area-amount calibration curves already prepared. This is further divided by the sum of amount of all components present in the mixture to get the mole fraction of each component. The following equation used to figure out the selective of gaseous products.

$$\text{Selectivity } (S_{gas}\ \%) = \frac{(Moles\ of\ gas)_{produced}}{(Total\ moles\ of\ gas)_{produced}} \times 100 \qquad (3.2)$$

Here, $Total\ moles\ of\ gas$ = Total moles sum of gaseous products (H_2, CO, CH_4, CO_2)

3.3.3 Liquid Sample Analysis

The liquid mixture is analyzed by using a head space gas chromatograph (HSGC, Shimadzu-HS10), equipped with FID (Flame ionization detector) and fused silica capillary column (with the industry standard polyimide outer coating, 0.10 mm in diameter, -60 °C - 330/350°C temperature, 10 m in length). The HSGC equipment used in the study is shown in **Fig. 3.21**. Working principle of HSGC, selection of carrier gas and operating parameters (temperature, pressure, carrier gas flow rate, etc) and detail of the calibration technique are described in subsequent sections.

Figure 3. 21: HSGC equipment used in the liquid analysis.

3.3.3.1 Working Principle of Headspace Gas Chromatography

Headspace with gas chromatography is a modified technique for separating the volatile components from the high molecular weight or unwanted compounds, which can contaminate the column if the mixture is directly injected into the gas chromatograph [279,280]. In general, a sample is prepared in a vial, containing the sample along with the dilutant with headspace (certain empty space within the vial). The vapor in the headspace is syringe out through transfer line to the GC system. The equations describing headspace theory are derived from three physical laws: 1) Dalton's law of partial pressures, 2) Henry's law for dilute solutions and 3) Raoult's law. The concentration of sample analyte in the headspace volume is given by mass balance: $C_O V_L = C_G V_G + C_L V_L$ (3.3)

Where C_G is the concentration of analyte in the headspace; C_O is the concentration of analyte in the original sample; V_G is the volume of gas in the sample vial; V_L is the volume of ingected sample;

K is the partition coefficient (or distribution coefficient) = C_L/C_G at equilibrium and β (phase ratio) = V_G/V_L. Rearranging provides [281]

$$C_G = \frac{C_o}{(K+\frac{V_G}{V_L})} = \frac{C_o}{(K+\beta)} \quad (3.4)$$

Our liquid product contains ethanol, methanol, acetone and acetaldehyde with water. High amount of water can contaminate the columns if the mixture is injected directly into the GC.

3.3.3.1.1 Operating Parameters Selection

N_2 is used as a carrier gas and H_2 and zero air is used for generating the flame. H_2 and zero air flow rate is set at 40 and 400 ml/min respectively, as the ratio of H_2: zero air should be 1:10 due to the safety concerns associated with hydrogen, while the N_2 flow rate is kept at 30 ml/min. Partition coefficient (K) and phase ratio (β) are the two important factors for the separation of volatiles from the mixture. For consistent results, the ratio V_G/V_L must remain constant. This means that the sample amount and vial size need to be kept the same [31,280]. Minimizing the partition coefficient provides a higher concentration of sample vapor in the headspace volume. However, K is temperature dependent for each component in air-water mixture. For ethanol, K at 40 °C is 1350, which can be reduced by increasing temperature as K= 330 at 75 °C [280]. Therefore, the oven temperature is fixed at 70 °C and sample is heated for 20 min. The vial is pressurized to 10 psi to avoid the loss of sample, [31,282]. After that, it is moved to the 10 µL of sample line to keep and then it goes through the transfer line. Sample line and transfer line temperature should be higher than the oven temperature to avoid the condensation, so it is fixed at 90 and 120 °C respectively.

Now, sample is injected into the column. However, there are two types of injection modes, split and split-less. Split mode is used if the mixture is concentrated, otherwise split- less mode is preferred. Our liquid sample is not very concentrated so split-less option is considered. Injection temperature and detector temperature is set at 200 and 250 °C respectively. The boiling temperature of methanol, ethanol, acetone and acetaldehyde is 64.7, 78.37, 56 and 20.2 °C, respectively. Therefore, initially the column temperature is maintained at 35 °C for 3 min, then increased at a rate of 10 °C/min up to 100 °C, and then to a final temperature of 240 °C at a rate of 20 °C/min and maintained for 2 min by considering the boiling temperature of each component present in the mixture.

3.3.3.1.2 Calibration

Calibration is carried out in order to quantify the liquid products. For calibration, five different concentration solutions, varied from 0.01 to 0.5 vol% are prepared for each component separately, using water as a dilution solvent. Later, concentration is calculated by using density and molecular weight of each component and expressed in terms of mol/10 µL as the sample line passes 10 µL of the mixture. The calibration curve is obtained by plotting the peak area of the standard component on abscissa and concentration of the standard component on ordinate. **Figure 3.22** shows the calibration curves for

different components of the liquid mixture. The calibration equations and R-squared values have been obtained through linear regression of data. Moles of each component present in the liquid product are calculated by using calibration equation from HSGC-FID in terms of mol/10 µL. Further, total concentration of each component in the liquid mixture is expressed in terms of mol.gm^{-1}cat.hr^{-1} by measuring the total volume of the liquid obtained after a single run (6-8 hrs) for 2 gm of catalyst. One of the gaseous and liquid sample scan from GC-TCD and HSGC are shown in **Fig. 3.23**.

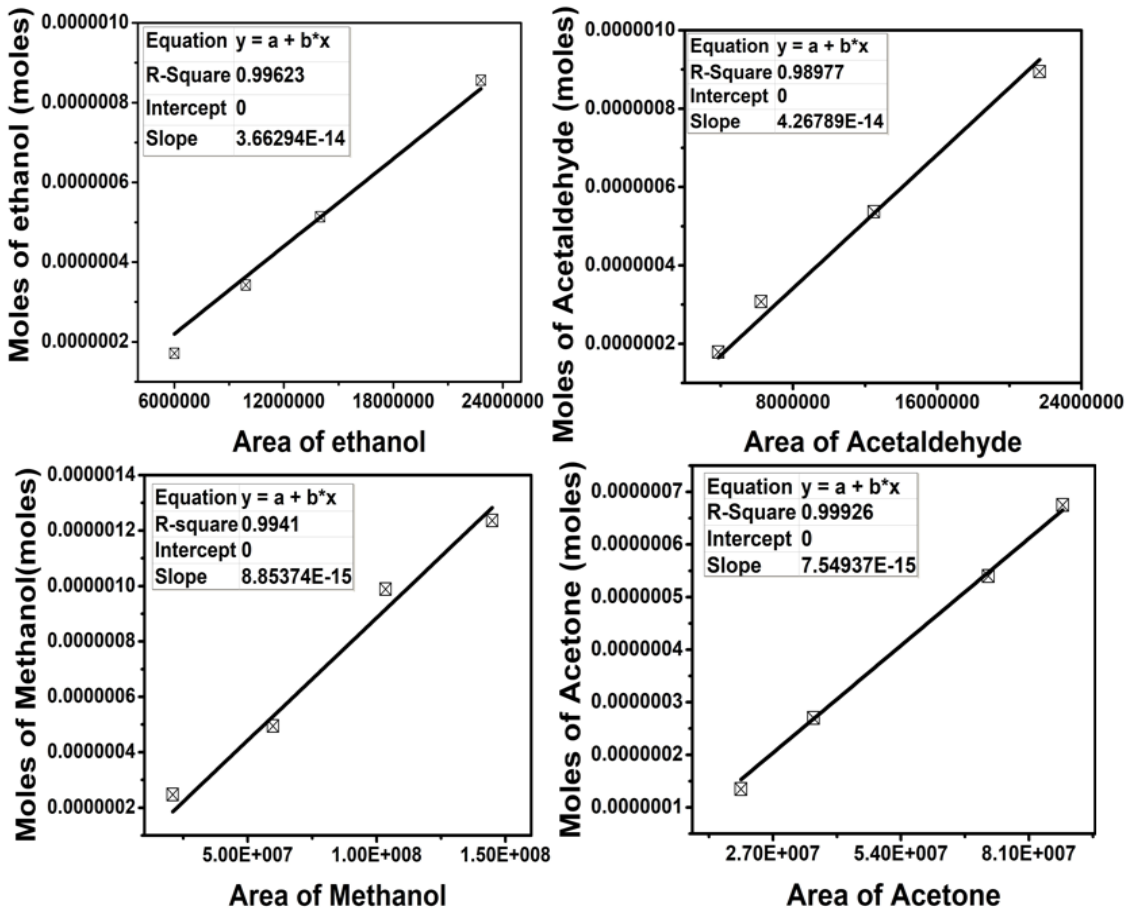

Figure 3. 22: Calibration curve for liquid components.

3.3.3.2 Flow rate

Flow rate (mole/min and ml/min) of the feed and product is calculated without or with the catalyst respectively by performing the same experiment (keeping the temperature of pre- heater and reactor, mole ratio, gas flow rate same) and collecting the liquid over six hrs. Flow rate (mol/min) for product stream we are calculating with the help of calibration curves. However, for feed stream this is calculated by measuring the collected liquid of ethanol-water in and we already know the ratio of ethanol and water so considering that and molecular weight of ethanol, flow rate of feed is calculated in mol/min.

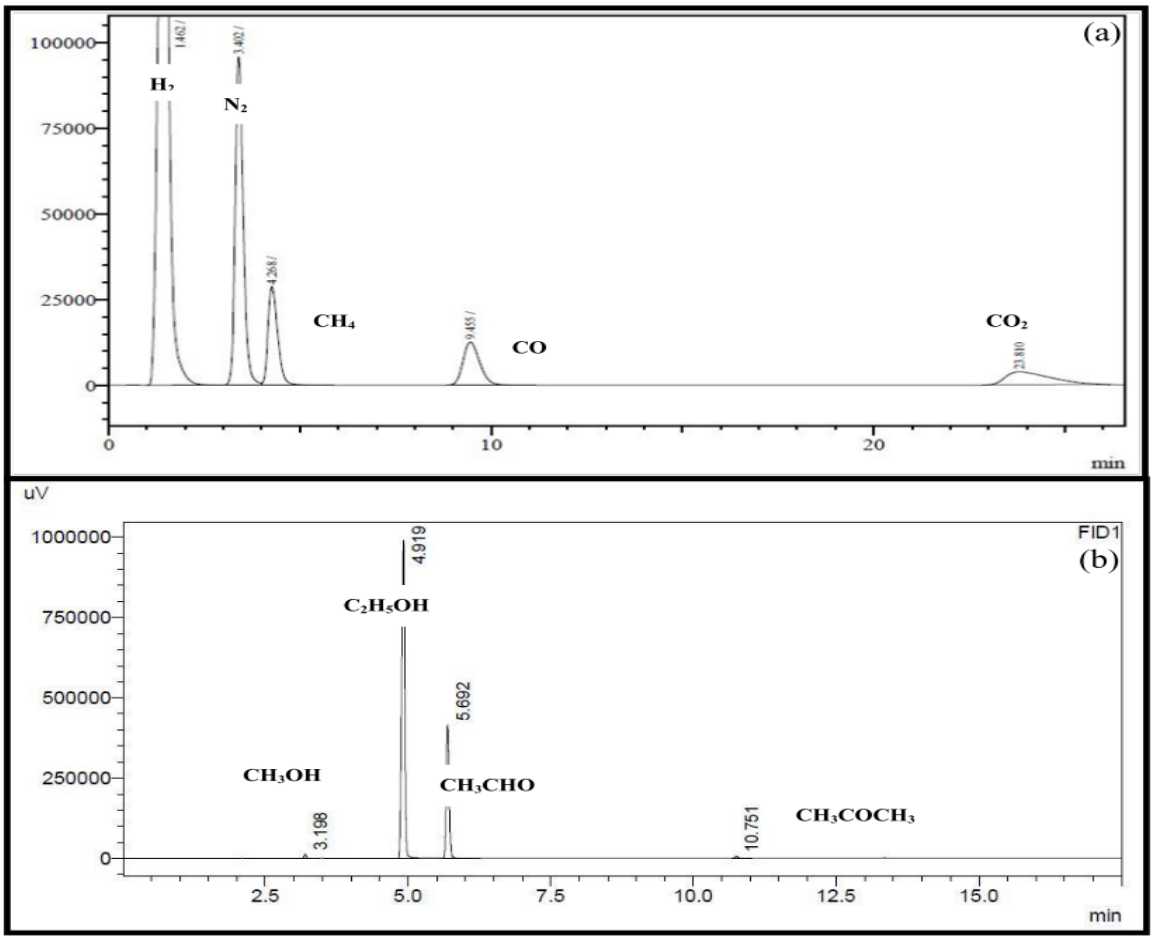

Figure 3. 23: Example of gaseous and liquid product sample scan from (a) GC-TCD and (b) HSGC.

3.3.3.3 Ethanol Conversion and Carbon in Gas and Liquid Phase

Consider, Ethanol (C_2H_5OH) feed flow rate (input) = x mol/min

Carbon in feed = 2 * x mol/min (3.5)

Liquid products are methanol (CH_3OH), acetone (CH_3COCH_3), acetaldehyde (CH_3CHO) and unconverted ethanol (C_2H_5OH). With the help of calibration curves obtained from HSGC and flow rate, concentration of each in product stream is determined in mol/min.

Consider that, the unconverted Ethanol (output) = y mol/min

Then, Ethanol conversion = Initial conc. of ethanol in the feed – unconverted ethanol conc.

= (x-y) mol/min (3.6)

Ethanol conversion (%) = [(Initial conc. of ethanol in the feed – uncovered ethanol conc.)/Initial conc. of ethanol in the feed] * 100 (3.7)

X_{EtOH} (%) = [(x-y)/x]*100 or [(mol $EtOH_{in}$- $EtOH_{out}$)/mol $EtOH_{in}$]*100 (3.8)

Methanol (CH_3OH) concentration = A mol/min;

Acetone (CH_3COCH_3) concentration = B mol/min;

Acetaldehyde (CH_3CHO) concentration = C mol/min;

Carbon in liquid = Carbon in Unconverted Ethanol +Carbon in Methanol +Carbon in Acetone +Carbon in Acetaldehyde

= (2*y+A+3*B+2*C) mol/min (3.9)

Carbon in gas = Carbon in feed – Carbon in liquid

= (2*x-2*y-A-3*B-2*C) mol/min (3.10)

Carbon (%) in gas = [(2*x-2*y-A-3*B-2*C)/ (2*x)]*100 (3.11)

Chapter 4:Results and Discussion

4.1 Steam Reforming of Ethanol for Hydrogen Production by Low-Temperature Steam Reforming Using Modified Ni-Sn/CeO_2 Catalyst

4.1.1 Highlights

- Effect of Sn & Zr addition and metal loading on LTSRE is investigated for NiSn/CeO_2 catalyst.
- Optimum Zr and Sn reduce particle size, enhance oxygen vacancies, and reduce carbon deposition.
- $Ni_{0.93}Sn_{0.07}(5)/Ce_{0.33}Zr_{0.67}O_{1.33}$ shows highest ethanol conversion & H_2 selectivity.

4.1.2 Introduction

Human civilization needs sustainable and environmentally friendly energy sources due to global warming and climate change, which would meet the global energy demand. There are different environmental-friendly energy sources such as wind, electrical, turbine, hydrogen, solar, etc. Among these, hydrogen energy may reveal an effective solution for our planet from environmental challenges [45,81]. Hydrogen can be produced from a variety of primary energy sources; such as methanol [95], ethanol [45], ammonia [283], gasoline, and natural gas [284], etc. Among these, ethanol could be considered as a stable renewable source for hydrogen production [45]. There are several pathways of hydrogen production, such as electrolysis, photolysis and thermolysis of water, biological reactions, gasification and pyrolysis of biomass, steam reforming, and partial oxidation of hydrocarbons. Among these ethanol steam reforming (ESR) using an appropriate catalyst shows a very efficient way of renewable hydrogen production as represented by the following overall stoichiometric equation 1.8 [247,285]:

Most of the time, ESR is performed between 600 and 1000 °C, where CO production is favoured by kinetics. The low temperature (< 450 °C) steam reforming (LTSR) reaction can decrease CO and methane (CH_4) production and increase H_2 selectivity at the end products[286].

Noble (Pt, Pd, Rh, Ir & Ru) as well as non-noble metals (Ni, Co, Cu, Fe, & Zn) are extensively reported as suitable active species for the ESR [287–289]. Among these Ni is the most commonly used active metal, because of its wide availability and low cost. Nickel also promotes favorable C-C and C-H bond breakage [45]. Due to its good redox properties and oxygen storage capacity (OSC), cerium oxide is extensively used in ESR as a support. Additionally, CeO_2 provides sites for separation of ethanol and water, leading to the formation of ethoxy and OH intermediates in ESR reaction [216]. Introduction of ZrO_2 into CeO_2 support may promote the formation of oxygen vacancies and facilitate adsorption and activation of the oxygen-containing groups such as OH, C–O–C, C═O, and −COOH on

the surface of the NiSn/ZrO_2−CeO_2 catalyst [290]. Thereby improves the ability of the catalyst to break the C−O bond, enhances resistance to carbon deposition on catalyst during the steam reforming process, and increase the activity and stability of the catalyst [291,292].

However, the main problem of the Ni/CeO_2 catalyst is the instability, Ni is known for carbon deposition and agglomeration during reforming reaction. Researchers study different Ni-bimetallic catalysts, Wang et al. (2022) investigate the effect of different metal loading on ethanol steam reforming over for Ni/$CeZrO_x$-Al_2O_3 catalysts [208]. Martínez et al. (2022) report on the application of bimetallic Rh-Ni catalysts obtained from $LaAl_{1-x-y}Rh_xNi_yO_3$ perovskites for ethanol steam reforming reaction [293] . Sohrabi and Irankhah (2021) study ethanol steam reforming on bimetallic Ni-X/$CeMnO_2$ (X= Cu, Co, K and Fe) catalyst. Ni-Cu demonstrates to be the best for ethanol conversion. But Ni-Fe shows high hydrogen yield and low coke deposition [294]. Xiao et al. (2021) examine the effect of La, Tb, and Zr support modifiers on Ni/CeO_2 catalysts for ethanol steam reforming [224]. Zhurka et al. (2020) investigate the effect of Ni/ZrO_2-La_2O_3 and Ni/CeO_2-ZrO_2-La_2O_3 catalysts on ethanol steam reforming reaction [222]. Campos et al (2019) compare the bimetallic Rh (x wt%)-Ni (10 wt%)/15 wt%La_2O_3-10wt%CeO_2-Al_2O_3 (x= 0.25, 0.5, 0.75, 1.0) with Ni(10wt.%)/La_2O_3(15wt.%)- CeO_2(10 wt.%)-Al_2O_3 for ethanol steam reforming. Addition of Rh (1.0 wt.%) to Ni (10 wt.%) enhances the activity and stability of the catalysts compared to the monometallic ones [295]. Reportedly, addition of tin(Sn) with Ni as a secondary metal increases the rate of C-C and C-H bond breakage, reduces the production rate CO and CH_4, and significantly increases the H_2 selectivity [296]. Tian et al. report application of NiSn/CeO_2 catalysts for ESR [242]. Mixing of CeO_2 with other oxides (e.g., ZrO_2, TiO_2, Al_2O_3) may form solid solution and enhances OSC [284,285,297].

In this paper the effect of varying metal loading, Ce: Zr mole ratio, and addition of Sn in Ni (Ni:Sn=14:1 atomic ratio) on LTSRE is explored. The catalysts are prepared by a ultra-sonication assisted solution combustion synthesis (SCS) method and the activity of the catalysts are examined at 200-400 °C, with ethanol to water mole ratio 1:12 and feed flow rate 0.1 ml/min. Various physicochemical properties of the Ni-Sn/Ce-Zr-O powders are inspected and correlated with the catalytic activities. The X-ray diffraction (XRD) analysis is used to identify the phase composition and calculate particle size of the catalysts. Raman spectroscopy data is used to estimate average particle size of CeO_2 phase and to understand the nature of the carbon deposited on the spent catalysts. Fourier-transform infrared (FTIR) spectroscopy identifiy different functional groups present in the powder samples. Simultaneous thermal analysis reveals the amount and nature of the carbon deposited on the spent catalysts. Scanning electron microscopy combined with energy dispersive spectrometer (EDX) depicts the surface morphology and elemental distribution.

4.1.3 Experimental

4.1.3.1 Catalyst preparation

The catalysts are prepared by a solution combustion synthesis (SCS) method assisted with ultra-sonication. Stoichiometric amount of nickel nitrate hexahydrate [$Ni(NO_3)_2.6H_2O$, qualikems(QLS), 98%)], tin chloride [$SnCl_2.2H_2O$, molychem, 97%)], cerium nitrate [$Ce(NO_3)_3.6H_2O$, QLS, 99.9%)], Zirconium(IV) oxynitrate hydrate [$ZrO(NO_3)_2.xH_2O$, Sigma-Aldirch, 99%)], and glycine [$C_2H_5NO_2$, molychem, 99%)] precursors as oxidizer to fuel ratio 1:1 are mixed thoroughly with ethanol in a 500 cc beaker. The transparent slurry mixture is left overnight for drying at room temperature. The homogenous paste is heated to 300 ^oC over a hot plate inside a fume hood to ensure security and avoid pollutant gases. Meanwhile, mixture is vibrated by submerging the tip of an ultrasonic liquid processor (Sonics & materials, 20 kHz, 500 W, 8 cm horn diameter) in the paste. The mixture is self-ignited in one place and spread throughout the beaker eventually. The obtained mass is washed with deionized water (DI) water to remove the unreacted salts and fuel and dried at 60 ^oC for 12 hours. Total 8 catalysts prepared, and the nomenclature of the catalysts are decided based on Ce:Zr molar ratio in support (CZ11 and CZ12 for the $Ce_{0.5}Zr_{0.5}O_2$ and $Ce_{0.33}Zr_{0.67}O_{1.33}$ supports, respectively) and total metal loading (5 and 20 wt.%). 4 catalysts are prepared with Ni only and 4 catalysts are prepared by maintaining Ni:Sn = 14:1 atomic ratio. The name and formula of the catalysts are mentioned in Table 4.1. Fresh, reduced and spent catalyst samples are characterized as follows.

4.1.3.2 Catalyst characterization

The phase composition and the crystallite size of the powders are identified by powder X-ray diffraction (Rigaku miniflex II, Cu-Kα (λ = 1.54 Å)) instrument. FTIR spectra (Perkin Elmer Frontier^{TM}) are collected by using KBr pellet procedure and the samples are scanned within the wavenumber range of 400 to 4000 cm^{-1}. Raman spectroscopy (Horiba LabRam HR spectrometer, Model 171) data are acquired by using 532 nm an Ar laser. Powder morphology, particle size, and elemental analysis are performed using a scanning electron microscope (FESEM; Nova Nano FE-SEM 450 (FEI), Oxford Instruments, UK) coupled with an X-ray energy dispersive spectrometer (EDS). An X-ray photoelectron spectrometer (XPS, Thermo fisher scientific Pvt. Ltd, U.K), with an Al Kα monochromatic source is used to acquire high-resolution Ni (2p), Sn (3d), Ce (3d), O (1s), and C (1s) spectra of the samples. XPS data are analysed by using XPSPeak 4.1 software and the Shirley algorithm is used for background correction. Simultaneous differential thermal and thermal gravity analysis (S-DTGA) (SHIMADZU, Model: DTG-60H) is performed from 30 to 800 °C, heating at 10 ^oC/min under flowing atmospheric air.

4.1.3.3 Catalyst activity test

The catalysts are reduced by treating with hydrogen at 10 ml/min and at 500 ^{o}C for 3 hours. The catalyst performance test is conducted in a custom-designed U-tube reactor loaded with a 500 mg powder catalyst and heated isothermally in a muffle furnace (MAC-Muffle furnace; MAC-251), the schematic diagram shown in **Fig. 3.18**. The water and ethanol (EtOH) mixture (mole ratio 12:1) is pumped (Athena technology, series-II) at the rate of 0.1 ml/min into a preheater at 120 ^{o}C and N_2 (>99.99%) gas is passed (10 ml/min) through the preheater to carry the vapor mixture to the reactor. The reforming occurs at a fixed temperature within 200-400 ^{o}C and under atmospheric pressure. Reaction products pass through an ice-cooled phase separator to separate gas and liquid. The gaseous products are analyzed at an interval of one hour for 20 h. A gas chromatography (SHIMADZU-2014) equipped with thermal conductivity detector (TCD) is used to quantify gas products and a head space-GC (Shimadzu model no.10) equipped with flow ionization detector (FID) is used to quantify liquid products. The mass balance was closed based on the carbon quantification measured in liquid and gaseous products.

The ethanol conversion and selectivity of the gaseous and liquid products are determined using the following equations [223,233,289].

$$\text{Conversion of ethanol } (X_{EtOH}\,\%) = \frac{(Moles\ of\ EtOH)_{feed} - (Moles\ of\ EtOH)_{exit}}{(Moles\ of\ EtOH)_{feed}} \times 100 \quad (4.1)$$

$$\text{Selectivity } (S_{gas}\,\%) = \frac{(Moles\ of\ gas)_{produced}}{(Total\ moles\ of\ gas)_{produced}} \times 100 \quad (4.2)$$

$$\text{Selectivity } (S_{liquid}\,\%) = \frac{(Moles\ of\ liquid)_{produced}}{(Total\ moles\ of\ liquid)_{produced}} \times 100 \quad (4.3)$$

$$\text{Carbon in gas products } (\%) = \frac{\text{Total carbon in CO, } CO_2\text{, and } CH_4}{Total\ C\ present\ in\ the\ out\ flow\ gas} \times 100 \quad (4.4)$$

4.1.4 Results

4.1.4.1 Physico-chemical Analysis

X-ray diffraction patterns of the samples are shown in Fig. 4.1(a) fresh, Fig. 4.1(b) reduced, and Fig. 4.1(c) spent catalysts**.** In fresh samples (**Fig. 4.1(a)**) NiO (PDF#1010095) and solid solution $Ce_{1-x}Zr_xO_2$ (PDF#2102839) are present [231,298,299] and no separate CeO_2 or ZrO_2 phase could be detected. Sn could not be detected as a separate phase probably due to low content or it incorporates into the Ni structure. At constant metal loading, some right shift of the $Ce_{1-x}Zr_xO_2$ 100% peak (111) is observed (**Fig. 4.1(d)**) as the amount of Zr increase in the support, which could be due to substitution of Ce^{4+} (ionic radii = 101 pm) by Zr^{4+} (ionic radii = 86 pm) into the CeO_2 lattice [300,301]. At the same time broadening of all $Ce_{1-x}Zr_xO_2$ and NiO phase peaks is noticed indicating the decrease of crystallite sizes [300]. At constant support composition, the $Ce_{1-x}Zr_xO_2$ and NiO peaks get narrower and crystallite sizes increase with increasing metal loading [298]. Addition of Sn leads to right shifting of the $Ce_{1-x}Zr_xO_2$ 100% peak (111) and broadening of the $Ce_{1-x}Zr_xO_2$ and NiO peaks in general. No significant

peak shift is observed for the NiO peaks with support modification and/or varying metal loading. In reduced catalysts, NiO converts into metallic Ni (PDF#9013034) (**Fig. 4.1(b)**) and crystallite size of nickel and $Ce_{1-x}Zr_xO_2$ support decrease compare with those of the fresh catalyst (**Table 4.1**). After steam reforming of ethanol (**Fig. 4.1(c)**) at 200-400 °C for 20 hr, $Ce_{1-x}Zr_xO_2$ and nickel crystallite size increase compared to that of the reduced samples, but the basic trend remains the same. All crystallite sizes are calculated using Scherer's formula from the 100% peaks of the compound and tabulated in Table 4.1.

In fresh catalysts, the FTIR band (**Fig. 4.2(a)**) at 1387 cm^{-1} belongs to the stretching vibration mode of Ni-O-Ni and/or Ni-O-Sn bond [302–304]. Intensity of this band enhances with the addition of Zr and/or Sn [299]. In reduced catalysts (**Fig. 4.2(b)**), the band at 1387 cm^{-1} disappeared, which indicates that NiO reduces into Ni^0. In spent catalysts (**Fig. 4.2(c)**), nickel peak (1387 cm^{-1}) could not be noticed due to the formation of carbon on surface during reforming process.

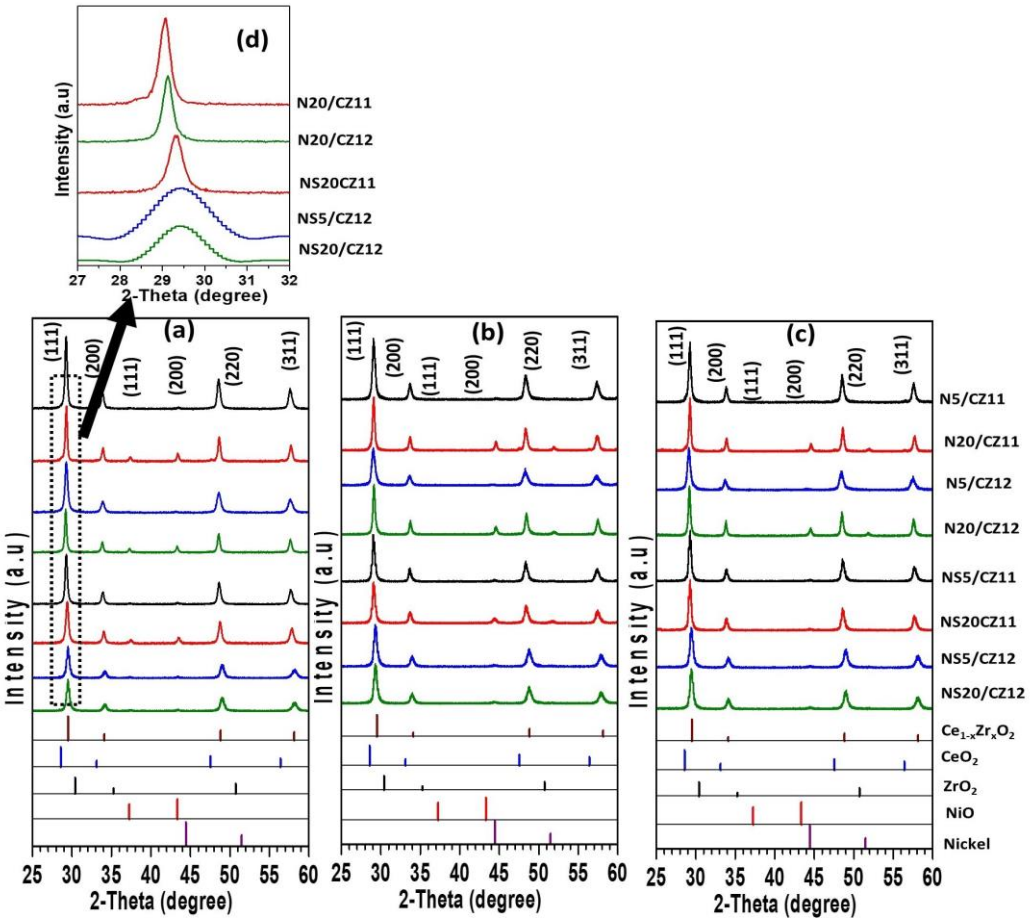

Figure 4. 1: XRD spectra for (a).Fresh, (b).Reduced, (c).Spent, samples and (d) Peak shift of fresh sample CeO_2 (111) Phase. And Phases identified with the reference PDF files of $Ce_{1-x}Zr_xO_2$ (PDF #2102839), CeO_2 (PDF #4343161), ZrO_2 (PDF #1521753), NiO (PDF #1010095), Nickel (PDF #9013034).

Fig 4.3(a), Fig 4.3(b), and **Fig 4.3(c)** depict the Raman spectra of the fresh, reduced, and spent catalysts, respectively. Three bands are observed for all samples. The most intense one peak at 465 cm^{-}

[1] corresponds to cubic fluorite (F_{2g}) structure of CeO_2 [305], whereas the peak at 310 and the shoulder at 620 cm^{-1} correspond to the highly sensitive oxygen disorder. The intensity of both peaks increases with increasing amount of Zr and/or addition of tin, indicating an increase in oxygen vacancies [306].

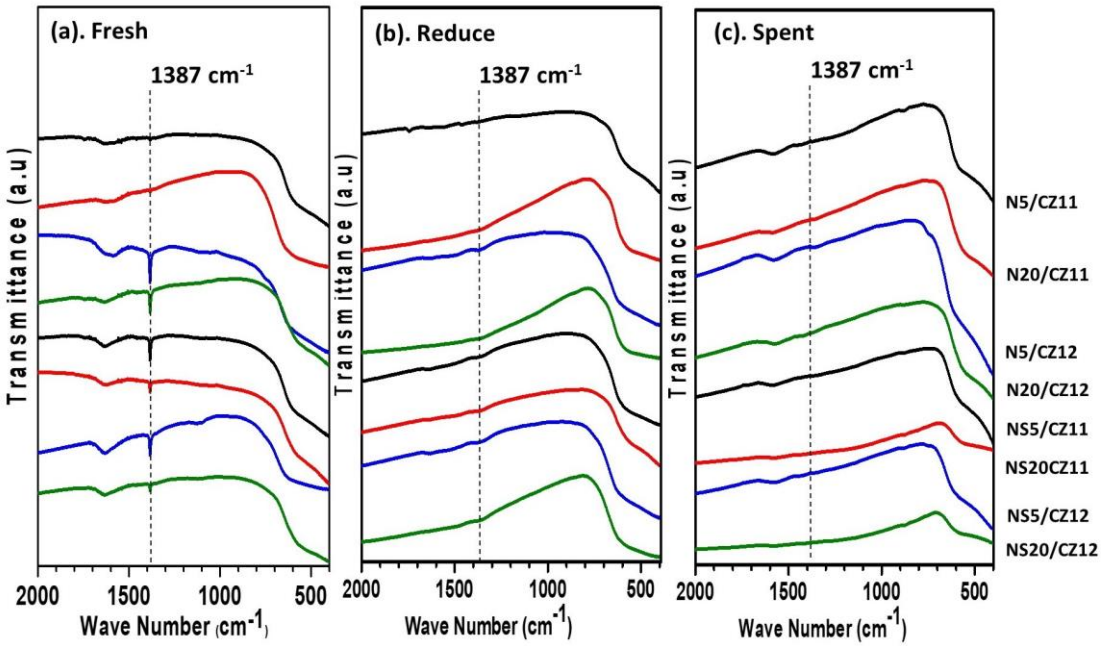

Figure 4. 2: FTIR spectra of (a) fresh, (b) reduce and (c) spent samples.

Table 4. 1: Average crystallize size from XRD, CeO_2 particle size from Raman for fresh(F), reduce(R), spent(S) samples and I_D/I_G ratio for carbon on spent sample from Raman.

Catalyst formula	Proposed Abbreviation of the catalyst	XRD Avg. crystalline size (nm)						Raman			
		Nickel			$Ce_{1-x}Zr_xO_2$			CeO_2 particle size (nm)			I_D/I_G for carbon on spent
		F NiO	R Ni	S Ni	F	R	S	F	R	S	
$Ni(5)/Ce_{0.5}Zr_{0.5}O_2$	N5/CZ11	18	14	17	26	21	24	11	9	15	1.00
$Ni(20)/Ce_{0.5}Zr_{0.5}O_2$	N20/CZ11	39	33	38	34	28	34	25	18	36	0.96
$Ni(5)/Ce_{0.33}Zr_{0.67}O_{1.33}$	N5/CZ12	18	14	16	22	17	20	8	7	11	1.02
$Ni(20)/Ce_{0.33}Zr_{0.67}O_{1.33}$	N20/CZ12	37	28	27	32	24	32	21	14	27	1.02
$Ni_{0.93}Sn_{0.07}(5)/Ce_{0.5}Zr_{0.5}O_2$	NS5/CZ11	18	14	17	25	18	21	6	3	10	1.03
$Ni_{0.93}Sn_{0.07}(20)/Ce_{0.5}Zr_{0.5}O_2$	NS20/CZ11	27	18	21	27	21	24	16	14	25	1.03
$Ni_{0.93}Sn_{0.07}(5)/Ce_{0.33}Zr_{0.67}O_{1.33}$	NS5/CZ12	17	12	14	20	14	18	4	1	6	1.40
$Ni_{0.93}Sn_{0.07}(20)/Ce_{0.33}Zr_{0.67}O_{1.33}$	NS20/CZ12	19	18	18	27	21	26	14	11	20	1.08

In fresh samples (**Fig. 4.3(a)**), the expected NiO peak at around 500 cm^{-1} could not be detected, due to shadowing effect of the high intensity peak at 465 cm^{-1} [307]. Not much noticeable changes are observed after reduction. However, in the spent catalysts (**Fig. 4.3(c)**) two new bands are observed at around 1350 and 1600 cm^{-1} corresponding to sp^3 hybridized disordered amorphous carbon (band D) and sp^2 hybridized graphitic carbon (band G), respectively [308]. The I_D/I_G ratio increases (inset image of **Fig. 4.3(d)**) with the decrease of metal loading, increase of Zr amount in $Ce_{1-x}Zr_xO_2$ support, and addition of tin in Ni (**Table 4.1**).

The grain size (d) of the CeO_2 powders is calculated from Raman frequency shift ($\Delta\omega$) of CeO_2 standard peak (465 cm^{-1}) by using the following equation [309–311]

$$d\ (nm) = 2\pi\ (\frac{B}{\Delta\omega}) \quad (4.5)$$

Here, B is the constant of CeO_2 with a value of 2.0.

Particle sizes for the catalysts are estimated to increase after reforming reaction compared to the same reduced samples. The increasing order of CeO_2 particle size commonly observed in fresh, reduced and spent (Table 4.1) is NiSn(5)/CZ12 < NiSn(5)/CZ11 < Ni(5)/CZ12 < Ni(5)/CZ11 < NiSn(20)/CZ12 < NiSn(20)/CZ11 < Ni(20)/CZ12 < Ni(20)/CZ11.

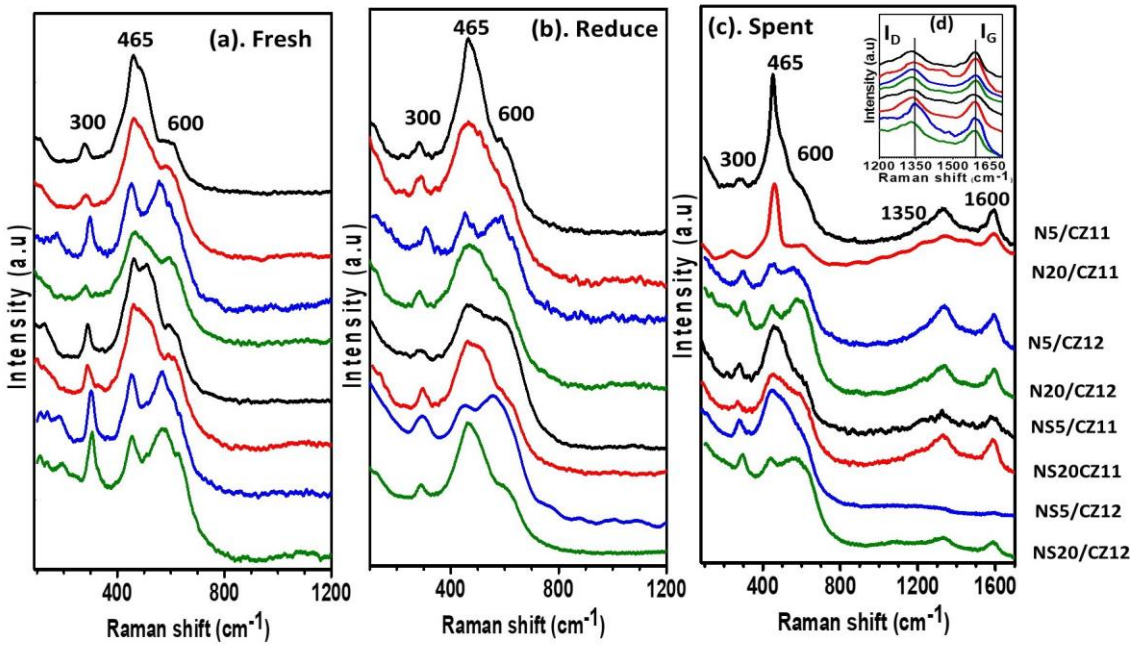

Figure 4. 3: Raman characterization for (a) fresh, (b) reduced, (c) spent catalysts, and (d)I_D & I_G peak of spent catalyst.

Figure 4.4 reveals the FESEM images along with EDS data of the best (NS5/CZ12) and worst (Ni20/CZ11) catalyst as decided based on the catalytic activity results. The fresh Ni20/CZ11 catalyst (**Fig. 4.4(a)**) is noticed to be made of lumped and agglomerated particles of average size 45 nm, whereas the NS5/CZ12 catalyst shows small particles of average size 36 nm (**Fig. 4.4(d)**) [299]. In reduced catalysts, morphology of the catalysts does not change much. But, for both Ni20/CZ11 (36 nm) (**Fig. 4.4(b)**) and NS5/CZ12 (24 nm) (**Fig. 4.4(e)**) catalysts average particle sizes decrease compared with the fresh catalysts. In spent catalysts (**Fig. 4.4(c)** and **4.4(f)**), particle size increases for both the N20/CZ11 (53 nm) and NS5/CZ12 (40 nm) catalysts. The elemental composition obtained from EDS is summarized in **Table 4.2.** Carbon deposition on spent Ni20/CZ11 and NS5/CZ12 catalysts are detected to be 48 and 29 %, respectively.

Figure 4.5 reveals the high resolution XPS spectra of the essential elements (Ni, Sn, Ce, O, and C) for the reduced and spent of the best (NS5/CZ12) and worst (Ni20/CZ11) catalysts; decide based on the catalytic activity results. Two peaks at ~855 and 857 eV corresponding to $Ni2p_{3/2}$ represent the Ni^{2+} and Ni^{3+} oxidative states which could be from NiO or $Ni(OH)_2$. The peak at 861.5 eV represents metallic nickel (Ni^0), and the $Ni2p_{3/2}$ satellite peak is noticed at 861.5 eV [312,313]. In reduce samples (**Fig. 4.5(a)**) only Ni^0 ($2p_{3/2}$) and Ni^{2+}($2p_{3/2}$) are noticed, while in the spent samples additional Ni^{3+} oxidation state is obtained. The calculated $Ni^0/(Ni^0+Ni^{2+})$ ratio obtain to be higher (0.38) for the reduced NS5/CZ12 catalyst compare to that (0.21) of the reduced N20/CZ11 catalyst indicates the presence of higher amount of the active phase on the NS5/CZ12 catalyst surface [312,313].

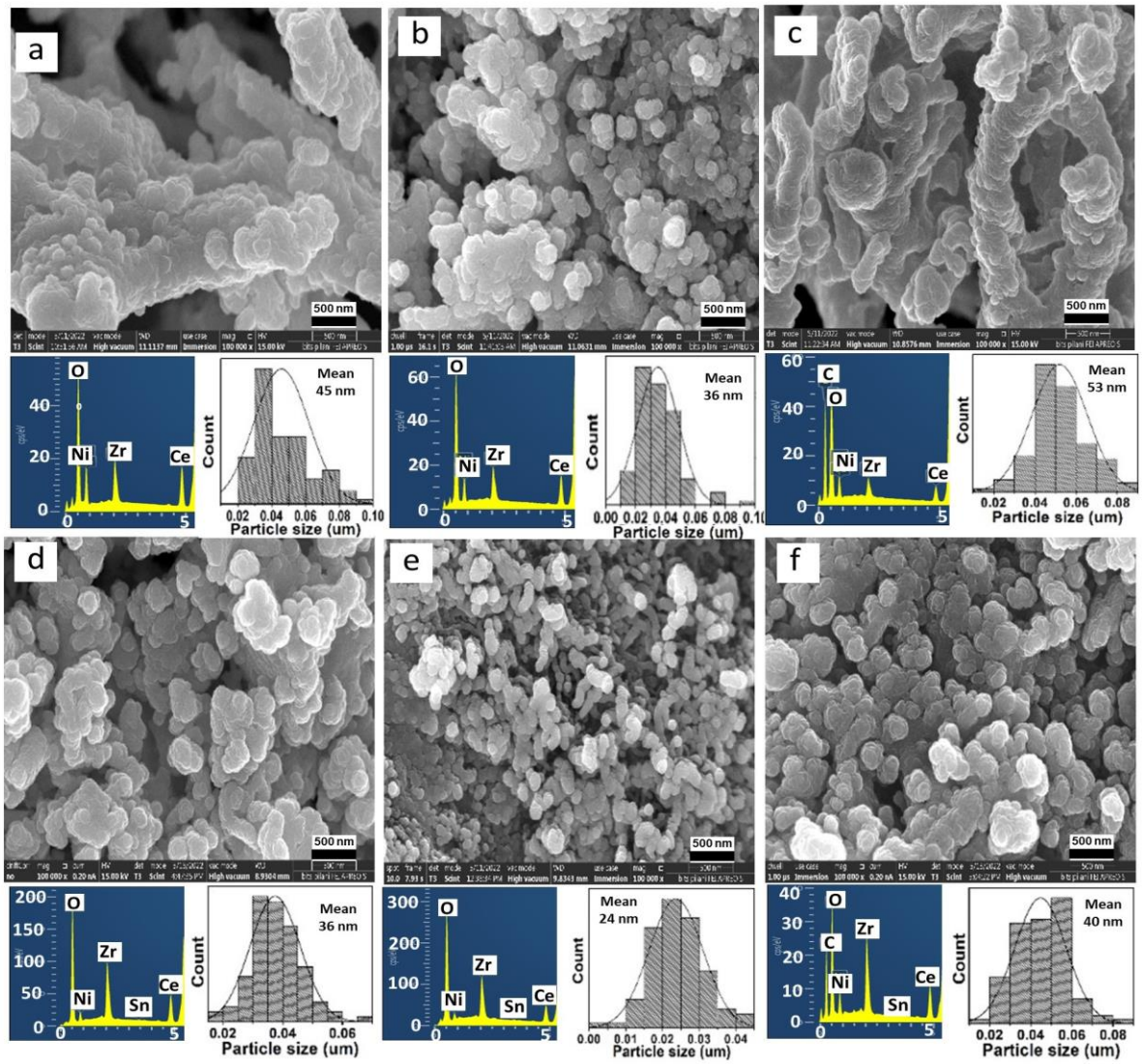

Figure 4. 4: FESEM images with particle size distribution and EDX spectrum for Ni20/CZ11 [(a) fresh, (b) reduce, (c) spent] and NS5/CZ12 [(d) fresh, (e) reduce, (f) spent] catalysts.

In high resolution XPS spectra of $Sn3d_{5/2}$ (**Fig. 4.5(b)**) two peaks at 486.2 and 494 eV indicate the presence of Sn^{2+} and Sn^{4+} oxidation states in the reduced and spent NS5/CZ12 catalyst [296]. For

the reduced NS5/CZ12 catalyst additional metallic tin(Sn^0) peak is also observed at 484.5 eV [296]. In the reduced sample, the $Sn^{2+}/(Sn^{2+}+Sn^{4+})$ ratio is calculated to be 0.75 and this ratio decreases to 0.49 in the spent sample. For both the catalysts (**Fig. 4.5(c)**) Ce^{3+} (corresponding to $Ce3d_{3/2}$ at 885 ± 0.2, 898 ± 0.2 eV and $Ce3d_{5/2}$ at 903± 0.2 eV) and Ce^{4+} (corresponding to $Ce3d_{3/2}$ at 883± 0.2, 890 ± 0.2 eV and $3d_{5/2}$ at 900 ± 0.2, 907± 0.2, and 917 ± 0.2 eV) oxidation states are observed in the reduced and spent samples. The higher $Ce^{3+}/(Ce^{3+}+Ce^{4+})$ ratio (0.34) in reduced NS5/CZ12 catalyst compared to that (0.28) in the reduced N20/CZ11 indicates higher oxygen mobility of the NS5/CZ12 catalyst.

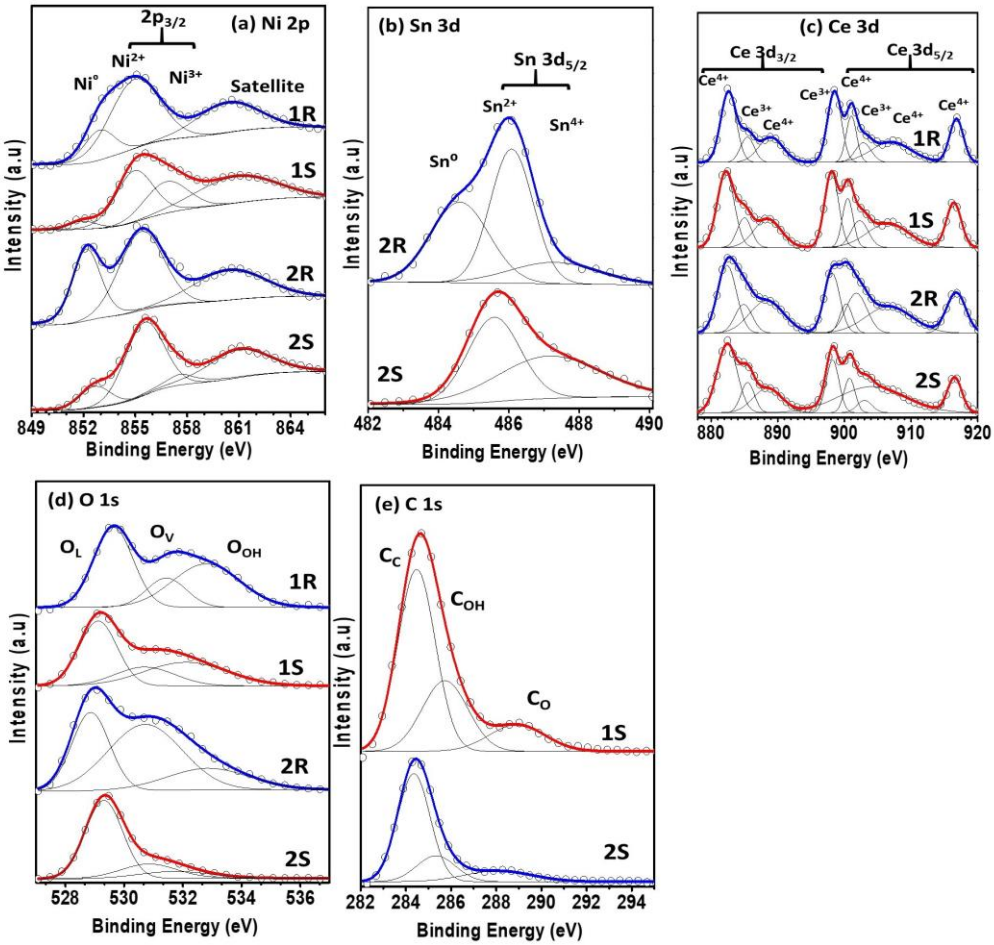

Figure 4. 5: High resolution XPS spectra of (a) Nickel, (b) Tin, (c) Cerium, (d) Oxygen, and (e) Spent catalyst of carbon elements for reduced (R) and Spent (S) sample of 1.N20/CZ11, & 2.NS5/CZ12 catalysts.

In spent samples, $Ce^{3+}/(Ce^{3+}+Ce^{4+})$ ratio values reduce to 0.31 and 0.24 for the NS5/CZ12 and N20/CZ11 catalysts, respectively. In high resolution O1s XPS spectra (**Fig. 4.5(d)**) the peaks at 529 ± 0.2 and 531 ± 0.2 eV correspond to the surface lattice oxygen (O_L) and oxygen vacancies (O_V), respectively in all catalysts [227]. The peak at 533 ± 0.2 eV corresponds to weakly bonded water molecule on the surface denoted by O_{OH}. The higher $O_V/(O_L+O_V+O_{OH})$ ratio (0.68) for the reduced NS5/CZ12 catalyst compared to that (0.44) of the reduced N20/CZ11 catalyst indicates better catalytic activity performance of the NS5/CZ12. In the spent samples the $O_V/(O_L+O_V+O_{OH})$ ratio values

decreased to 0.31 and 0.28 for the N20/CZ11 and NS5/CZ12 catalysts, respectively, as expected. High resolution C1s XPS spectra (**Fig. 4.5(e)**) is used to study the carbon deposition on the catalysts during reforming. In the spent catalysts the peak is at 284.8 eV corresponding to Sp^2 C=C bond, denoted by C_C. The peaks notice at 285.8± 0.2 and 289 ± 0.2 eV correspond to Sp^3 C-OH (C_{OH}) and O-C=O (C_O) carbon species, respectively [296,314]. The higher amount of total C deposition on the spent N20/CZ11 catalyst compared to the spent NS5/CZ12 is clear from the spectra. Additionally, the $(C_{OH}+C_O)/(C_C+C_{OH}+C_O)$ ratios calculated to be 0.6 and 0.4 for the NS5/CZ12 and N20/CZ11 catalysts, respectively, indicate that the C deposited on the NS5/CZ12 is easier to oxidize. These results are in the same line as the EDS, DTA-TGA, and Raman results.

DTA/TGA characterizations are performed to check the amount and nature of carbon deposited on the surface of the spent samples (**Fig. 4.6**). Generally, three exothermic DTA peaks could be observed for this type of analysis. An exothermic peak at lower temperature (200-400 ℃) due to decomposition of nickel hydroxide or oxidation of amorphous carbon as observed for the NS5/CZ12 catalysts. A middle temperature (400-600 ℃) exothermic peak corresponds to the filamentous carbon loss, whereas the high temperature (> 600 ℃) peak indicates the presence of graphitic carbon in the spent sample as shown in N20/CZ11 catalyst [315,316]. Accordingly, it could be concluded that the carbon on the spent N5/CZ11, N5/CZ12, and NS5/CZ11 catalysts are mixed amorphous and filamentous in nature. The order of TGA weight loss shows NS5/CZ12 (2.4 wt.%) < NS5/CZ11 (14.4 wt.%) < N5/CZ12 (16.34 wt.%) < N5/CZ11 (20 wt.%) < NS20/CZ12 (27.5 wt.%) < NS20/CZ11 (30.69 wt.%) < N20/CZ12 (31 wt.%) < N20/CZ11 (44.55 wt.%). Addition of Sn with Ni and modification of CeO_2 with ZrO_2 improves the carbon resistivity and stability of the catalysts. Increase in metal loading affects the catalyst in the opposite direction.

Table 4. 2: Elemental analysis (Wt.%) from EDS and XPS.

Elements	EDS						XPS			
	N20CZ11			NS5CZ12			N20CZ11		NS5CZ12	
	Fresh	Reduce	Spent	Fresh	Reduce	Spent	Reduce	Spent	Reduce	Spent
Ni	18	20	9	5	5	5	19	6	5	4
Sn	-	-	-	1	1	1	0	0	1	1
Ce	42	41	22	26	28	19	32	16	21	14
Zr	18	19	7	41	37	28	21	11	36	29
O	21	20	14	27	30	19	29	17	37	24
C	-	-	48	-	-	29	-	50	-	28

4.1.4.2 Catalytic Activity

Figure 4.7 shows the steady state catalytic activity in terms of ethanol conversion (%), C (%) in gas, selectivity (%) of the gaseous (H_2, CO_2, CO, CH_4), and liquid (CH_3CHO, CH_3OH, and CH_3COCH_3) products at feed concentration EtOH:H_2O 1:12 molar ratio, feed flow rate 0.1 ml/min and various reaction temperatures between 200-400 ℃. The ethanol conversion, C in the gas phase, and selectivity

of H_2 and CO_2 increase with the increasing in temperature, while CH_4 and CO followed opposite trend for all catalyst samples.

At 400 °C N5/CZ12 and N5/CZ11 catalysts (**Fig. 4.7(c)**) show the H_2 selectivity of 63 and 59%, respectively, CO selectivity 2.5 and 5% respectively, and CH_4 selectivity 4 and 6 %, respectively. Whereas N20/CZ12 and N20/CZ11 catalysts exhibit H_2 selectivity 46 and 42%, respectively, CO selectivity 11 and 15%, respectively and CH_4 selectivity 15 and 21%, respectively. Evidently, hydrogen selectivity increases with increasing zirconium concentration at constant metal loading and decreases with the increase of metal loading for a particular support composition.

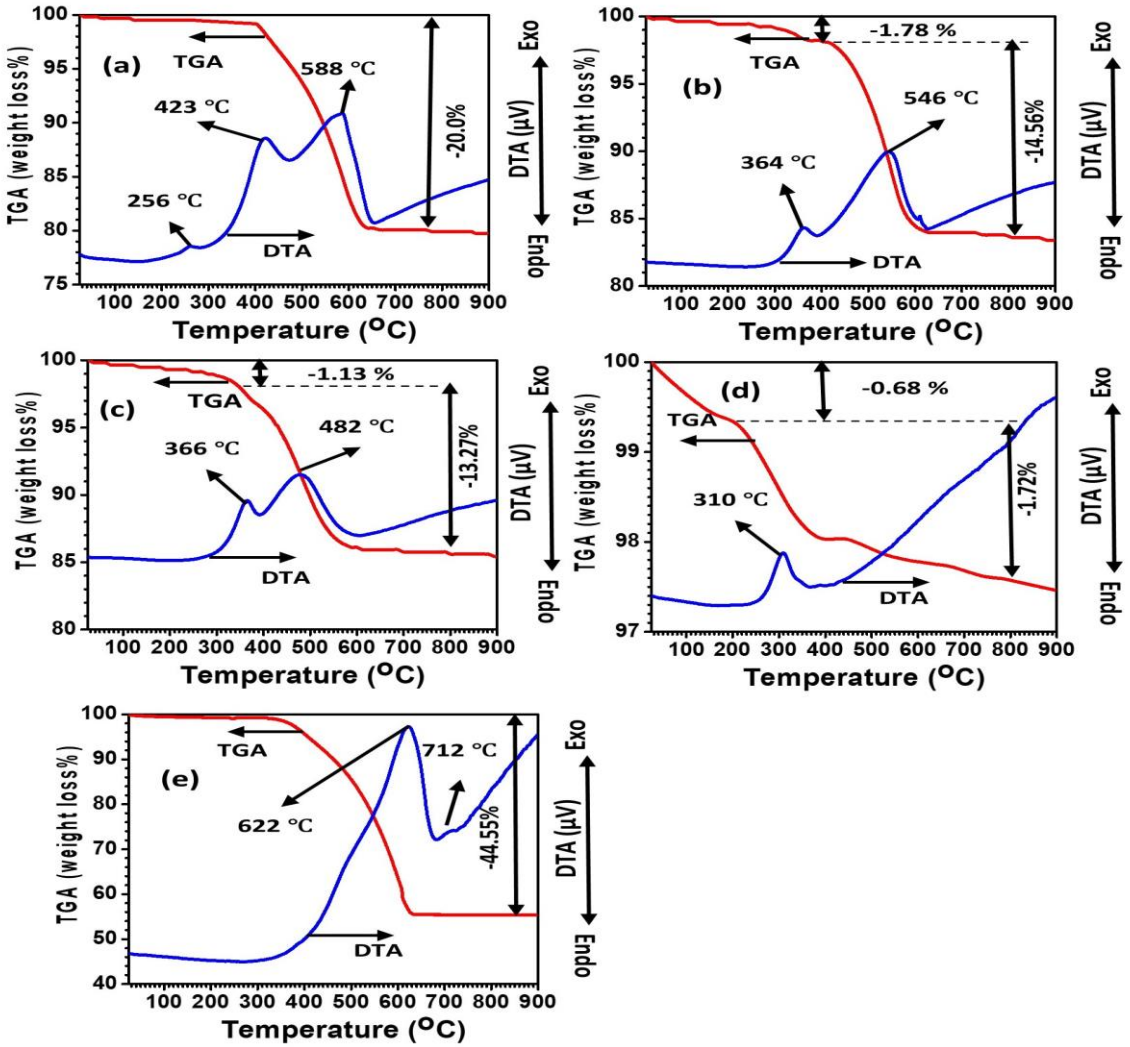

Figure 4. 6: DTA-TGA spectra for spent sample of (a) N5/CZ11, (b) N5/CZ12, (c) NS5/CZ11, (d) NS5/CZ12 and (e) N20/CZ11 catalysts in reactor 200-400 °C reaction temperature, EtOH : water 1:12 mole ratio and feed flow rate 0.1 ml/min.

The NS5/CZ12 and NS20/CZ12 catalyst show H_2 selectivity 69 and 55%, CO selectivity is 0 and 7 % and CH_4 selectivity is 0 and 9%, respectively at 400 °C. Which clearly indicates that the increase in Zr and addition of Sn lowers the CO and CH_4 selectivity and significantly enhances the H_2 & CO_2

selectivity. In liquid products, selectivity of acetaldehyde (CH_3CHO) (**Fig. 4.7(g)**) and acetone (CH_3COCH_3) (**Fig. 4.7(h)**) increase, while selectivity of methanol (CH_3OH) (**Fig. 4.7(i)**) decreases with increasing temperature for all catalysts. N5/CZ11 and N5/CZ12 catalysts show CH_3CHO selectivity of 52 and 56% at 400 °C, respectively, indicating that CH_3CHO selectivity increases with the increase of zirconium concentration. While CH_3OH and CH_3COCH_3 follow the reverse trend. However, CH_3CHO selectivity decrease with increasing metal loading as also observe by Slowik et al. [240]. Addition of tin shows similar selectivity trends as of zirconium and it may indicate that the addition of Zr^{4+} and tin enhances the ethanol dehydrogenation reaction (Eq. (2.2)).

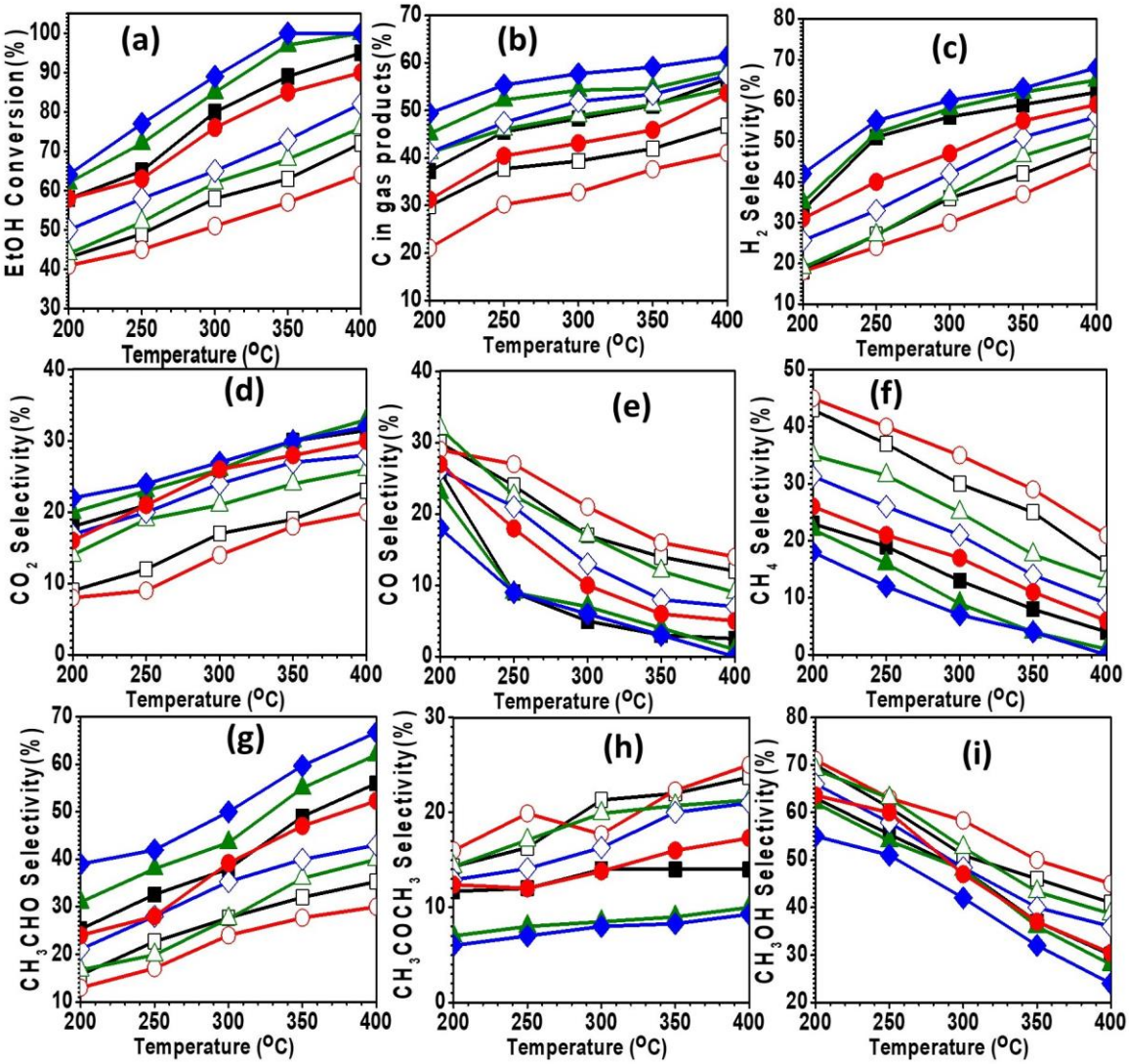

Figure 4. 7: Steady state variation of (a) EtOH conversion, (b) C in gaseous phase, selectivity of gaseous products (c) Hydrogen, (d) Carbon dioxide, (e) Carbon Monoxide, (f) Methane, and liquid products (g) Acetaldehyde, (h) Acetone, (i) Methanol as a function of temperature (200-400 ^{o}C), EtOH : water 1:12 mole ratio and feed flow rate 0.1 ml/min over N5/CZ11 (●), N20/CZ11 (◯), N5/CZ12 (■), N20/CZ12 (□), NS5/CZ11 (▲), NS20/CZ11 (△), NS5/CZ12 (♦), NS20/CZ12 (◇) catalysts.

4.1.5 Discussion

This work studies the LTSRE over Ni-Sn (14:1) bimetallic/CeO_2 catalyst and the effects of varying metal loading along with the support modification. The catalytic activity results obtained in this work are at the same level or better than that reported in the literature. Xiao et al. study on Ni(10 wt.%)/$Ce_{0.8}X_{0.2}O_2$ (X= La, Tb, Zr) catalysts prepared by two step impregnation method. The highest hydrogen selectivity 66% with 100% EtOH conversion is obtained for Ni(10 wt.%)/$Ce_{0.8}La_{0.2}O_2$ catalyst at 500 ℃ and EtOH: H_2O = 1/3 mole ratio [224]. Wu R-C et al. study ESR on Ni(10 wt.%)/$Ce_{0.5}Zr_{0.5}O_2$ catalyst prepared by co-precipitation and impregnation methods. The highest hydrogen selectivity of 65% and 100% EtOH conversion is obtained for the catalysts prepared by the co-precipitation method. By adding boron to the catalyst, the selectivity for hydrogen is slightly improved [285]. Arslan et al. study ESR on Ni(3 wt.%)/$Ce_XZr_{1-X}O_2$ (X= 0.5, 0.75, 0.83) catalysts prepared by impregnation method. The highest hydrogen selectivity (72%) and 100% ethanol conversion are obtained for the Ni(3 wt.%)/$Ce_{0.75}Zr_{0.25}O_2$ catalyst at 450 °C reaction temperature and H_2O/EtOH = 3.2:1 mole ratio, however catalyst show stability 5 h of reaction time [317].

It is demonstrated that Zr modification of CeO_2 support and Sn addition in Ni improves the stability and activity of the catalyst and increase in total metal loading deteriorates the quality of the catalysts. Physico-chemical characterizations (XRD, FESEM, EDS, DTG/TGA, Raman, and XPS) reveal that addition of tin and Zr support modification decrease the support and active phase particle sizes and reduce coke deposition on the catalysts during the reforming reaction. Raman and XPS data also validate that for the spent catalysts with Sn and higher Zr (CeO_2: ZrO_2 = 1: 2) nature of deposited carbon is more amorphous which could be oxidized easily. The particle size of the catalyst plays a major role in activity result. Incorporation of zirconium into ceria lattice produces $Ce_{1-x}Zr_xO_2$ solid solution and improves thermal stability. The $Ce_{1-x}Zr_xO_2$ solid solution enhances the metal-support interaction and could be responsible for smaller Ni particle size which as a result demonstrates high ethanol conversion, high hydrogen selectivity, and less coke deposition.

Non-stoichiometric nature of the Ce cation play important role in catalytic activity by formation of oxygen vacancies [307] as explained by Kröger-Vink notation [318].

$$2CeO_2 \leftrightarrow Ce_2O_3 + V_o^{\cdot\cdot} + O_o^x + 2e'' \quad (4.6)$$

XPS data shows that in case of the catalyst with Sn and higher Zr amount of Ce^{3+} and oxygen vacancies are also high. Technically substitution of Ce^{4+} (ionic radii = 101 pm) by Zr^{4+} (ionic radii = 86 pm) suppose not to create oxygen vacancies, however significant size difference of the ions may be responsible for the creation of additional oxygen vacancies in the lattice [319]. As observed from XPS

analysis presence of Sn^{2+} in the reduced NS5/CZ12 might be helpful for the formation of high concentration Ce^{3+} as follows [320]:

$$\boldsymbol{Sn^{2+} + 2Ce^{4+} \rightarrow Sn^{4+} + 2Ce^{3+}} \quad (4.7)$$

Thus both Zr and Sn addition may offer better catalysis activity with more hydrogen and less undesirable side-product synthesis in LTSRE [284,285,297,306]. Zr and Sn may promote the water gas shift reaction (Eq. 2.10) and also inhibits the carbon formation [320,321].

4.1.6 Conclusion

Ni-Sn/CeO_2-ZrO_2 catalysts show promising activity results and low coke deposition for LTSRE. Addition of Zr and Sn decrease particle size and demonstrate a synergic effect for the increase of oxygen vacancies, enhance oxygen mobility in the catalyst lattice, and reduction of coke deposition as divulge from the XRD, FESEM, XPS, DTA/TGA, and Raman spectroscope characterization. Accordingly, NS5/CZ12 catalyst leads to the best activity results maximum EtOH conversion of 100%, highest H_2 selectivity of 69% with lowest coke deposition 2.4 %. Higher metal loading causes agglomeration of the active metal and support particles which leads to the weakening of the metal-support interaction.

4.2 Effects of Metal Loading and Support Modification on the Low-Temperature Steam Reforming of Ethanol (LTSRE) Over Ni-Sn/CeO_2 Catalysts

4.2.1 Highlights

- Effect of metal loading, Sn, MgO on LTSRE is investigated for NiSn/CeO_2 catalysts.
- Ce-Mg-O support and optimum Sn reduce particle size and enhance oxygen vacancies.
- $Ni_{0.93}Sn_{0.07}(5)/Ce_{0.33}Mg_{0.67}O_{1.33}$ shows highest ethanol conversion & H_2 selectivity.
- Mg and optimum Sn help in reducing carbon deposition on spent catalysts.
- Lower metal loading (5 wt.%) enhances catalytic activity.

4.2.2 Introduction

According to recent data, the global consumption of fossil fuel is 13,685 million tons (Mt)/year, with an annual growth rate of 2.8%. It is 809 Mt/year in India, with a growth rate of 7% [4]. Currently, the global fossil fuel reserve contains 1,139 billion tons of coal, 187 trillion cubic meters of natural gas, and 1,707 billion barrels of crude oil. The current consumption rate will deplete within 80 years [322–324]. According to the United Nations Environmental Report 2019, the total amount of greenhouse gases in the atmosphere reached 55 gigatonnes (Gt) and global temperature increased by 3 °C [325]. Globally, the current amount of methane (CH_4), NO_x, carbon dioxide (CO_2) is 1849.9 ppb, 330.31 ppb, and 410 ppm, respectively [326,327], as a result of which it becomes pertinent to seek alternative clean-renewable energy sources like wind, solar, hydrogen, biomass [328].

H_2 can be produced from biomass or biomass-derived hydrocarbons using different methods like dry reforming (DR), steam reforming (SR), auto-thermal reforming (ATR), electrolysis, partial catalytic oxidation (PCOX), photocatalytic processes, etc. [273,329–331]. DR and SR typically require higher temperature (600 to 1200 °C), where carbon monoxide (CO) generation is kinetically favored [329,332]. ATR contains multiple step reactions and a highly exothermic process. It can generate heat for the subsequent endothermic reforming reactions. However, due to its thermodynamic restrictions, it is difficult to manage steady-state operation and the H_2 yield of ATR is always lower than that of SR [36,331]. PCOX converts oxygenated hydrocarbons into hydrogen (H_2) and CO_2 and needs to be operated at high temperature & low pressure to inhibit coke formation [331]. The photocatalytic process has benefits like being chemically and physically stable, cheap, and good for the environment. But it doesn't work very well, especially for their ability to be driven by invisible light [333]. Electrolysis can be used to make green hydrogen. However, this method is expensive and only makes up about 5% of all H_2 production, which uses a lot of energy [334]. The low temperature (< 450 °C) steam reforming

(LTSR) reaction decreases CO and CH_4 production and increases H_2 selectivity at the end products [286].

Researchers are trying to produce H_2 from different biomass derived feed sources, like glycerol, methane, bio-oil, ethanol, toluene, methanol, coal, acetic acid, etc. [95,329,335–338]. But steam reforming of ethanol (SRE) is promising because ethanol (EtOH) releases lower amount of toxic pollutants to the environment [339]. Additionally, India is the seventh largest producer (330 million gallons/year) of EtOH in the world [340].

Different noble (Pt, Pd, Ru, Cu, Ir, Rh) and transition metals (Ni, Co) based ceramic oxide catalysts are used for SRE [330]. In terms of C-C and C-H bond breaking as well as dehydrogenation reactions [216], non-precious nickel (Ni) is compatible with precious metals. In case of CeO_2 support, non-stoichiometric nature of the support cation (Ce) plays an important role in catalytic activity due to which the oxygen vacancies (V_O) formed [307] as explained by Kröger-Vink notation equation 4.6 [318].

The addition of Ni creates extra oxygen vacancy (V_O).

$$NiO \overset{CeO_2}{\longleftrightarrow} Ni''_{Ce} + V_o^{\cdot\cdot} + O_o^x \quad (4.8)$$

Metal-support interaction (MSI) plays a major role in catalyst stability and activity. The Ni^{2+} ion incorporated into the CeO_2 lattice creates the Ce-Ni-O phase, which may lead to the formation of smaller nickel particles, suppresses metal sintering, and resists coke formation [221,330,341]. Reportedly, better way to enhance the catalytic activity and stability is by modifying the support. The addition of basic nature MgO to the neutral or acidic oxides is observed to improve the activity, and the substitution of Ce^{4+} ions by Mg^{2+} ions lead to the formation of oxygen vacancy:

$$MgO \overset{CeO_2}{\longrightarrow} Mg''_{Ce} + O_O^{\times} + V_O^{\bullet\bullet} \quad (4.9)$$

Additionally, MgO may react with Ni to form a robust $Ni_xMg_{1-x}O$ solid solution due to the incorporation of Ni^{2+} into the MgO structure, which resists active phase sintering and enhances the activity [233,305,342]. Allowing secondary metals such as Sn, Pt, Co, and Cu would help to increase the catalyst's efficiency. Sn doping on nickel has improved the oxygen vacancies and helped in C-C and C-H bond breaking [296]. Shabaker et al. [343] worked on Sn modified Ni-catalyst with different atomic ratios Ni_4Sn, $Ni_{270}Sn$, $Ni_{14}Sn$, and NiSn. Among these, $Ni_{14}Sn$ catalyst achieved higher H_2 selectivity at low temperatures.

A significant amount of research articles (170) has been published on Ni modification and CeO_2 support modification in the field of steam reforming of ethanol within the last 10 years and out of those, 45 articles were published on Ni (or modified Ni)/$Ce_xMg_{1-x}O_2$. Among these 8 papers discussed on low-temperature steam reforming (≤ 500 °C) of ethanol. Sohrabi et al. [344] studied LTSRE on bimetallic Ni(10 wt.%)-x (4wt.%)/$Ce_{0.6}Mn_{0.4}O_2$ (x = Cu, Co, K and Fe) catalysts prepared by co-precipitation method. Ishihara et al. [345] prepared Ni(16 wt.%)/$C_{0.6}Al_{0.4}O_2$, Ni(16 wt.%)/Al_2O_3 and Ni(32

wt.%)/$C_{0.3}A_{0.7}O_2$, catalysts using sol-gel method. Substitution of 40 at. % Al in Ni(16 wt.%)/$C_{0.6}A_{0.4}O_2$ improved the H_2 yield from 20 to 40% and EtOH conversion from 70 to 95% at 500 ℃ and EtOH:H_2O = 1/12 mole ratio. Increased Ni loading 16 to 32 wt.% enhanced H_2 yield slightly with 100% ethanol conversion at the same reactor conditions. Niazi et al. [237] studied LTSRE on Ni (13 wt.%)-Mg (4 wt.%)/CeO_2 and Ni(x)/CeO_2 (x=10, 13, 15 wt.%) catalysts prepared by impregnation method. Rodrigues et al. [346] studied LTSRE over Ni/$Ce_{0.9}Sm_{0.1}O_2$ synthesized by hydrothermal method followed by wet impregnation of Ni. Reforming occurred at 500 ºC and H_2O/ EtOH mole ratio 3. Matus et. al. [347] investigated ESR on Ni (2 wt.%)/$Ce_{1-x}M_xO_2$ (M = Mg, Gd, La; x = 0.2, 0.5 mole fraction) catalysts prepared by sol-gel method with EtOH:H_2O molar ratio of 1:3 and temperature 200-600 ℃. Reportedly, the Mg interacted with nickel to form Ni-Mg-O solid solution and helped to stabilise metallic nickel through sintering resistance, indicating an improvement in metal support interaction strength. Luo et al. [348] studied LTSRE over Ni(10 wt.%)/$Mg_{0.99}Ce_{0.01}O_2$ catalyst prepared by impregnation method. The H_2 yield and ethanol conversion at 500 ℃ and steam/ethanol molar ratio = 6 were increased due to CeO_2 addition. Campos et al. [194] studied LTSRE on bimetallic Rh(X)-Ni(10)/$Ce_{0.6}La_{0.4}O_2$ (X=0.25, 0.5, 0.75, 1.0 wt.%) catalysts synthesized by impregnation method. The 1%Rh-Ni(10) catalyst performed the best with 100% EtOH conversion at 400 ℃. Tian et al. [242] studied LTSRE (at 400 ºC) on Ni-Sn(X)/CeO_2 (X=0, 0.25, 1, 2 wt.%) catalyst prepared by co-impregnation method. Santander et al. [233] synthesized the Ni(7 wt.%)/$Ce_{0.85}Mg_{0.15}O_2$ catalyst using a dip-coating method. The addition of Mg boosted OM and OSC of the support and helped in decreasing nickel particle size. Strong interactions between nickel and CeO_2-MgO support inhibit the sintering of nickel particles during the reduction process. Bepari et al. [349] worked on $Ni_{0.25}Mg_{0.5}Al_{0.25}$(1-X)/(X)$CeO_2$ (X=5, 10 wt.%) catalysts prepared by wet impregnation method. Shabaker and Dumesic et al. [84,343] examined the aqueous phase reforming of ethanol on Al_2O_3 supported Raney Ni catalyst modified by different amounts of Sn. The $Ni_{14}Sn/Al_2O_3$ catalyst demonstrated higher H_2 selectivity at 210 ℃ and 51.3 bar.

These literatures show that modification of CeO_2 and Ni active phase might enhance the surface oxygen mobility and stabilize the active metal and support nanoparticles. However, almost no research articles reported the combined effects of varying bimetal (NiSn) loading and support (Ce-Mg-O) modification on LTSRE. The novelty of this paper focused on LTSRE over Ni-Sn/Ce-Mg-O bimetallic powders for hydrogen production.

The effects of varying metal (Ni: Sn =14:1) loading, Ce: Mg mole ratio, and Ni: Sn atomic ratio on LTSRE were explored. The catalysts were prepared by a solution combustion synthesis (SCS) method, and the activities of the catalysts were examined at 200-400 °C, with ethanol to water mole ratio of 1:12 and a feed flow rate of 0.1 ml/min. Various physicochemical properties of the Ni-Sn/Ce-Mg-O powders were inspected and correlated with the catalytic activities. The X-ray diffraction (XRD) analysis was used to identify the phase composition and calculate the catalysts' particle size. Raman

spectroscopy data was used to estimate the average particle size of the CeO_2 phase and to understand the nature of the carbon deposited on the spent catalysts. Fourier- transform infrared (FTIR) spectroscopy identified different functional groups were present in the powder samples. Simultaneous thermal analysis revealed the amount and nature of the carbon deposited on the spent catalysts. X-ray spectroscopy (XPS) was used to identify the oxidative state of different metals/mixed oxides and the nature and amount of the carbon present in the spent catalysts. Temperature programmed reduction (TPR) was performed to study the metal support interaction. NH_3-TPD was used to study the acidity of the supports. N_2 adsorption/desorption study was used to measure surface area and pore size distribution for the samples. Electron microscopy combined with an energy dispersive spectrometer (EDS) depicted the surface morphology and elemental distribution.

4.2.3 Experimental

4.2.3.1 Catalyst Preparation

The catalysts were prepared by a single pot solution combustion synthesis (SCS) method (Fig. 3.9) already applied elsewhere [350–354]. Stoichiometric amount of precursors; nickel nitrate hexahydrate [$Ni(NO_3)_2.6H_2O$, qualikems(QLS), 98%)], tin chloride [$SnCl_2.2H_2O$, molychem, 97%)], cerium nitrate [$Ce(NO_3)_3.6H_2O$, QLS, 99.9%)], magnesium nitrate [$Mg(NO_3)_2.6H_2O$, molychem, 99%)], and glycine [$C_2H_5NO_2$, molychem, 99%)], as an oxidizer to fuel ratio 1:1 were mixed thoroughly with ethanol in a 500 ml beaker. The transparent slurry mixture was dried overnight at room temperature and then heated at 300 ^oC over a hot plate inside a fume hood to avoid pollutants and ensured security. The mixture was self-ignited in one place and spreaded throughout the beaker eventually. The obtained mass was washed with DI water to remove the unreacted salts and fuel and dried at 60 ^oC for 12 hours. Consequently, the powder that has been dried is called a "fresh catalyst".

Total 11 catalysts were prepared, and the nomenclature for 9 of those catalysts were decided based on Ce:Mg molar ratio in support (C, CM11 and CM12 for the CeO_2, $Ce_{0.5}Mg_{0.5}O_2$ and $Ce_{0.33}Mg_{0.67}O_{1.33}$ supports, respectively) and total metal (constant metal composition Ni:Sn =14:1 atomic ratio was maintained) wt.% loading (5, 10, and 20). Hence the $NiSn(10)/Ce_{0.5}Mg_{0.5}O_2$ sample was named NiSn(10)/CM11. The remaining two catalysts; one without Sn ($Ni(5)/Ce_{0.33}Mg_{0.67}O_{1.33}$ or Ni(5)/CM12) and the other one Ni:Sn= 8:1 atomic ratio ($Ni8Sn(5)/Ce_{0.33}Mg_{0.67}O_{1.33}$ or Ni8Sn(5)/CM12) were prepared to study the effect on Sn. The name and formula of the catalysts were mentioned in **Table 4.3**.

Fresh, reduced and spent catalyst samples were characterized as follows.

4.2.3.2 Catalyst Characterization

Powder X-ray diffraction (Rigaku miniflex II, Cu-Kα ($\lambda = 1.54$ Å); 30 kV and 15 mA) technique was used for identifying the phase composition and crystallize size. Samples were scanned within the

2 theta (2Θ) range of 20 - 80^{o} at a rate 2^{o}/min. FTIR (Perkin Elmer Frontier^{TM}) data were procured using KBr pellet procedure within the wavenumber range of 400 to 4000 cm^{-1} and the data averaged over 20 scans [355]. Raman spectroscopy (Horiba LabRam HR spectrometer, Model 171) data was acquired by using 532 nm Argon laser.

Powder morphology, particle size and elemental analysis were performed using a FESEM (Nova Nano FE-SEM 450 (FEI), Oxford Instruments, UK) coupled with an X-ray energy dispersive spectrometer (EDS) and Transmission electron microscopy (FEI Titan Themis 60-300 keV) instruments. X-ray photoelectron spectrometer (XPS, Thermo fisher scientific Pvt. Ltd, U.K), with a Al Kα monochromatic source, was used to acquire wide scan data within the range 0 – 1200 eV. High-resolution spectra of the C (1s), Ce (3d), Mg (1s), Ni (2p), Sn(3d) and O (1s) elements were collected to quantify the deposited coke and to identify the chemical/electronic states of the different metal/metal-oxides, qualitatively and quantitatively. XPSPeak4.1 software and the Shirley algorithm were used for the deconvolution of the XPS spectra [289,356].

Temperature programmed reduction (TPR), and temperature program desorption of ammonia (NH_3-TPD), samples were characterized by using a Micromeritics Autocheme II 2920 catalyst characterization system with a thermal conductivity detector (TCD). TPR was carried out under flowing 10% H_2/Ar of 25 ml/min, and the sample was heated up to 1050 ℃ at 10 ℃/m rate. The NH_3-TPD was performed on our samples to determine the acidity of the supports. About 0.1 g of the sample was initially flushed with a He flow at 500 ℃ for 2 hrs, next cooled to 120 ℃ and then saturated with ammonia (NH_3). After NH_3 was exposed, the sample was purged with He until the excess of physically adsorbed NH_3 was removed. Then this sample was heated to 500 ℃ at a heating rate of 10 ℃/min [357].

A gas adsorption analyzer (Microtrac Bel, BEL SORP mini- II) was used to determine the catalyst surface area, pore diameter and pore volume. Before characterization samples were preheated at 200 ℃ for 2 hrs. Simultaneous differential thermal and thermal gravimetric analysis (S-DTGA) (SHIMADZU, Model: DTG-60H) was performed from 30 to 800 ℃, heating at 10 ℃/min under flowing atmospheric air [289,355,358].

The catalyst activity test was conducted for 10 h TOS at each temperature from 200 – 400 ℃ with interval of 25 ℃ and the catalytic activity procedure discussed in section 4.1.3.3.

4.2.4 Results

4.2.4.1 Physico-Chemical Characterizations

Here, we have discussed the most efficient and inefficient catalysts in terms of activity and modification. NiSn(5)/CM12 catalyst was shown to be most efficient, whereas NiSn(20)/C catalyst was the most inefficient. The effects of support modification at constant metal loading were explained for NiSn(20)/CM12, NiSn(20)/CM11, and NiSn(20)/C catalysts. The NiSn(5)/CM12 and NiSn(20)/CM12

catalysts explained the metal loading effect. The effect of tin composition can be understood by NiSn(5)/CM12, Ni8Sn(5)/CM12, Ni(5)/CM12 catalysts.

X-ray diffraction patterns of the samples were shown in Fig. 4.8(a) fresh, Fig. 4.8(b) reduced, and Fig. 4.8(c) spent catalysts. The phases present were identified as cubic CeO_2 (PDF#4343161), NiO (PDF#1010095), $Ni_{1-x}Mg_xO_2$ (PDF#240712), and Ni (PDF#9013034). Sn was not detected as a separate phase due to low content or incorporated into the Ni structure.

In a fresh CeO_2 catalyst, only CeO_2 and NiO phases were observed (**Fig. 4.8(a)**). However, no separate MgO phase was detected with Ni/Mg atomic ratios of 0.13, 0.28, 0.63 and 0.08, 0.17, 0.37 for NiSn(X)/CM11 and NiSn(X)/CM12 (X=5, 10, & 20 wt.%), respectively. This can be explained by the identical ionic radii of Mg^{2+} (0.065 nm) and Ni^{2+} (0.070 nm) ions, which result in the formation of $Ni_xMg_{1-x}O_2$ solid solution from any proportion of NiO and MgO [233,359]. Changes in metal loading and the incorporation of MgO with CeO_2 influenced the morphology of both the support matrix and the active metal phase (**Fig. 4.8 (a)** & Supplementary Fig. **4.18 (a)**). At constant metal loading, an increase in MgO amount resulted in a broadening of the XRD peaks, which decreased the support and $Ni_{1-x}Mg_xO_2$ particle size. A lower angle shift of the 100% CeO_2 peak (111) was clear for the catalysts NiSn(20)/CM12 and NiSn(20)/C (**Fig. 4.8(d)**). Overall, the support particle size increased with the metal loading for all the fresh, reduced, and spent catalysts (**Table 4.3**).

In the case of fresh NiSn(X)/C (X=5, 10, 20 wt.%) catalysts, the NiO particle size remained almost the same for both the 10 and 20 wt.% metal loading. The NiO peak was not visible in 5 wt.% of all catalysts due to the high dispersion effect [149,193]. CeO_2 particle size followed common trend as NiSn(5)/CM12 < NiSn(5)/CM11 < NiSn(10)/CM12 < NiSn(10)/CM11 < NiSn(20)/CM12 < NiSn(20)/CM11 < NiSn(5)/C < NiSn(10)/C < NiSn(20)/C (**Table 4.3**). Addition of a small quantity of Sn (14:1 Ni:Sn atomic ratio) initially decreased the support and Ni-phase particle size, while an excess of Sn increased particle sizes for both the support and Ni-phase, with a common trend as NiSn(5)/CM12 < Ni8Sn(5)/CM12 < Ni(5)/CM12 [360].

After reduction, the nickel oxide (NiO) phase converted to a metallic Ni phase for CeO_2 supported catalysts (**Fig. 4.8(b)**). However, in the case of CM11 and CM12 supported catalysts, complete conversion was not observed due to strong interaction between NiO and MgO (**Fig. 4.8(e)**) [233,329]. Rather, Ce-Mg intermetallic and $Ni_{1-x}Mg_xO_2$ complex oxide phases have been noticed to appear with the addition of Mg, and the intensity of these phases increased as Mg addition was increased (**Fig. 4.8(e)**). The particle size of the catalyst's support and active phase followed the similar trend as the fresh catalyst, but slight increase was observed due to sintering effect. However, for the 5wt.% metal-loaded catalysts, Ni peaks could not be detected.

After 10 hours of steam reforming ethanol at 200-400 °C, the CeO_2 particle size increased significantly compared to the reduced catalyst particle size, but the basic trend remained consistent. For catalysts supported by CeO_2, metallic Ni was partly oxidised into NiO phase [356,357,361]. In the case

of NiSn(X)/CM11 and NiSn(X)/CM12 catalysts, the $Ni_{1-x}Mg_xO_2$ solid phase was unaffected (**Fig. 4.8(c)**). Using Scherer's formula, all particle sizes were calculated and summarized in **Table 4.3**. CeO_2 lattice strain was calculated for all catalysts using XRD data by the Williamson-hall method (Supplementary data, **Table 4.7**), and it was observed that the particle size decreased with the increased lattice strain [362]. The effect of metal loading and Mg on the size of metal particles is the same as in other research articles. Matus et al. [347] reported that when Mg^{2+} concentration increased by Ni(2 wt.%)/$Ce_{1-x}Mg_xO_2$ (X= 0, 0.1, 0.2, 0.5 mole fraction) and CeO_2 particle size decreased from 18 to 9 nm.

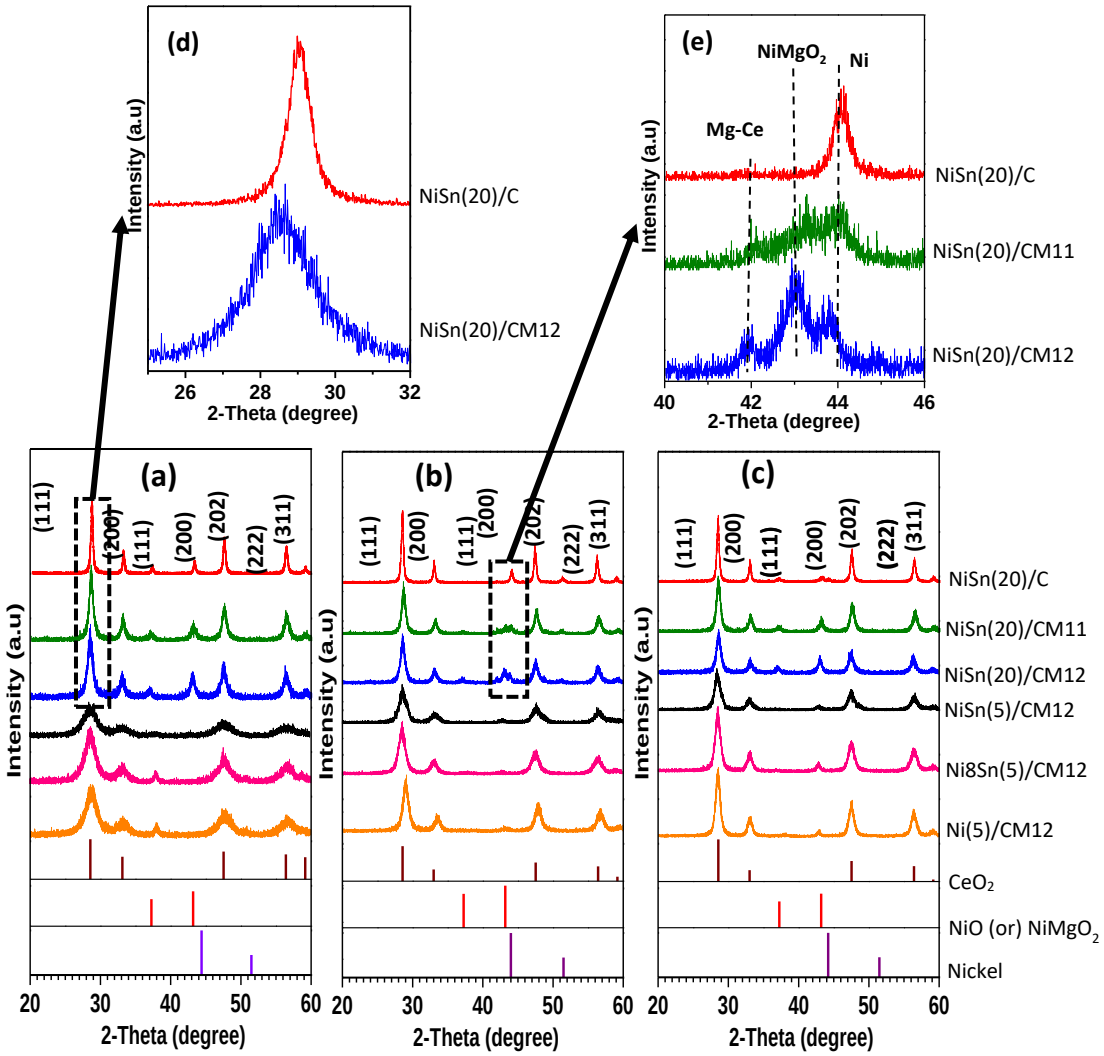

Figure 4. 8: XRD spectra for (a). Fresh, (b). Reduced, (c).Spent, (d)peak shift and (e) Peak split of phases identified with the reference PDF files of CeO_2 (PDF #4343161), NiO(PDF #1010095) (or) $NiMgO_2$ (PDF#240712), Nickel (PDF #9013034).

Tian et al. [242] studied Ni(5 wt.%)-Sn(X)/CeO_2 (X= 0, 0.25, 1, 2 wt.%) catalyst. They found that adding tin up to 0 to 1 wt.% initially decreased nickel particle size from 20.2 to 19.5 nm, then abruptly increased from 19.5 to 21.8 nm with an increase from 1 to 2 wt.%. Santander et al. [233] reported that the size of support particles went up by 10 to 15 nm as the metal loading went from Ni(7 wt.%)/$Ce_{0.85}Mg_{0.15}O_2$ to Ni(10 wt.%)/$Ce_{0.92}Mg_{0.08}O_2$.

FTIR spectra showed the presence of several vibrational bands in all samples, as shown in Fig. 4.9(a) fresh, Fig. 4.9(b) reduced, and Fig. 4.9(c) spent catalysts. The cerium (Ce) vibrational band commonly observed in all catalysts at 800 and 1100 cm^{-1} belongs to Ce-OH and Ce-O, respectively. In the fresh (**Fig. 4.9(a)**) catalyst, the peaks were observed around 1400 cm^{-1} and 1600 cm^{-1}, corresponding to Mg-O stretching [363]. The peak intensity slightly increased with increasing Mg^{2+} concentration at constant metal loading [302]. According to reports, the Ni-O-Sn stretch band peak would occur at 1400 cm^{-1}. However, it was difficult to identify due to its very weak nature and its overlap with the Mg-O stretching band (**Fig. 4.9 (a)** & Supplementary data, **Fig. 4.19**) [302–304]. The water absorption band commonly observed in all catalysts around ~3400 cm^{-1}, 3600 cm^{-1} belongs to the O-H group [364–366].

Due to the reduction of NiO to Ni metal, the intensity of Mg-O stretching was decreased in reduced catalyst (**Fig. 4.9 (b)**) and appeared as a small peak in the case of NiSn(X)/CM11 and NiSn(X)/CM12 catalysts. Due to reoxidation of the active phase, the Ni-O-Sn/ Mg-O band at 1400 cm^{-1} reappeared in spent catalyst (**Fig. 4.9 (c)**). Clearly, the intensity of the band was maximum for CM12 supported catalysts, whereas it was much lower for CM11 and CeO_2 supported samples. This could be related to the formation of carbon on the surface during the reforming process, which indicates that CM12 support catalysts have less carbon deposition and more stable than other catalysts. Bobadilla et al. [367] prepared Ni(17 wt.%)-Sn(9 wt.%)/$Ce_{0.75}Al_{0.15}Mg_{0.1}$ catalyst by using impregnation method. Mg^{2+} interaction was observed around 1643 cm^{-1}, and the vibrational peak of Ni-Sn at 1480 cm^{-1}. It has been reported that Mg^{2+} and Ni-Sn peak intensity was increased with addition of Mg^{2+}.

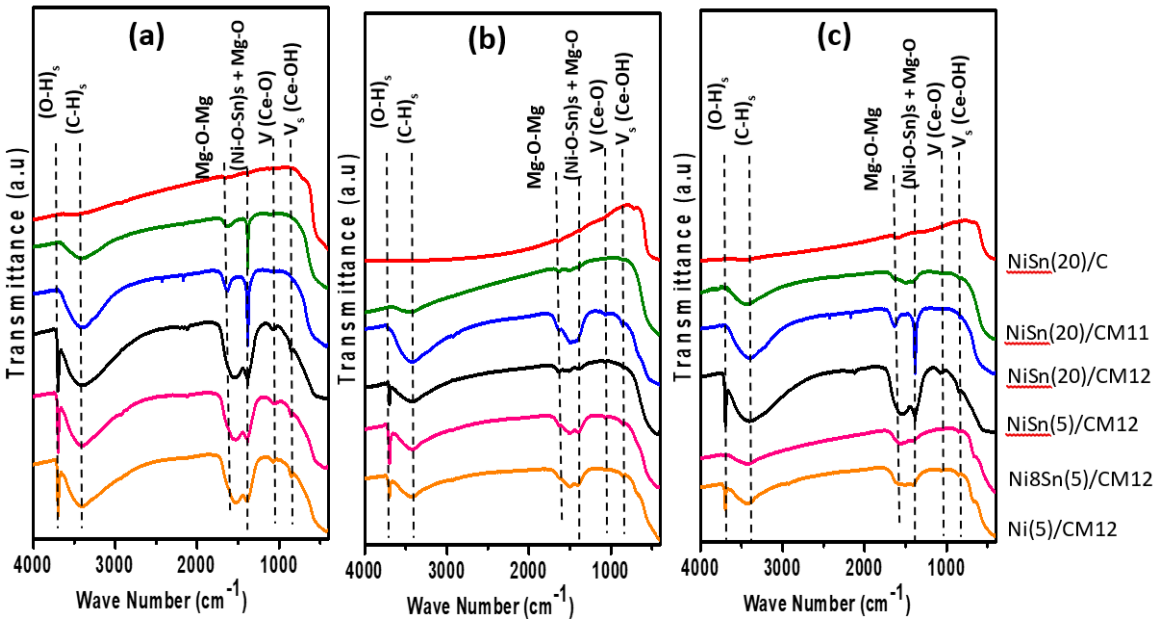

Figure 4. 9:FTIR characterization for (a) Fresh, (b) Reduced, and (c) Spent catalyst.

Table 4. 3: Fresh (F), Reduce (R) and Spent (S) catalyst samples average crystalline size of CeO_2, Ni, and $Ni_{1-x}Mg_xO_2$ as calculated by XRD, CeO_2 particle size and I_D/I_G ratio for carbon on spent sample measured by Raman and average particle size calculated by FESEM. Reduce and spent nickel particle size determined by transmission electron microscopy.

Catalyst formula	Proposed Abbreviation of the catalyst	XRD Avg. Crystalline Size (nm)								Raman				FESEM		
		CeO_2			Nickel					CeO_2 particle size (nm)			I_D/I_G for carbon on spent	Average particle size(nm)		
		F	R	S	F	R		S		F	R	S		F	R	S
					NiO/ $Ni_{1-x}Mg_xO_2$	Ni	NiO/ $Ni_{1-x}Mg_xO_2$	Ni	NiO/ $Ni_{1-x}Mg_xO_2$							
$Ni_{0.93}Sn_{0.07}(5)$-CeO_2	NiSn(5)/C	12	15	18		13				9	13	17	0.97	32	42	51
$Ni_{0.93}Sn_{0.07}(10)$-CeO_2	NiSn(10)/C	16	21	25	22	21		14	10	11	15	22	0.94	35	43	52
$Ni_{0.93}Sn_{0.07}(20)$-CeO_2	NiSn(20)/C	19	24	27	22	22		18	10	15	18	25	0.93	36	45	53
$Ni_{0.93}Sn_{0.07}(5)$-$Ce_{0.5}Mg_{0.5}O_2$	NiSn(5)/CM11	4	7	9					11	4	5	7	1.14	26	37	46
$Ni_{0.93}Sn_{0.07}(10)$-$Ce_{0.5}Mg_{0.5}O_2$	NiSn(10)/CM11	9	10	10	9	10		15	9	5	7	9	0.99	29	39	48
$Ni_{0.93}Sn_{0.07}(20)$-$Ce_{0.5}Mg_{0.5}O_2$	NiSn(20)/CM11	11	12	13	12	22	5		13	7	9	13	0.99	31	40	49
$Ni_{0.93}Sn_{0.07}(5)$-$Ce_{0.33}Mg_{0.67}O_{1.33}$	NiSn(5)/CM12	3	6	8			8		11	2	3	6	1.21	24	37	42
$Ni_{0.93}Sn_{0.07}(10)$-$Ce_{0.33}Mg_{0.67}O_{1.33}$	NiSn(10)/CM12	4	9	10		20	14		14	4	5	8	1.10	29	37	47
$Ni_{0.93}Sn_{0.07}(20)$-$Ce_{0.33}Mg_{0.67}O_{1.33}$	NiSn(20)/CM12	9	11	11	12	21	17		14	6	8	11	1.00	29	39	49
$Ni(5)$-$Ce_{0.33}Mg_{0.67}O_{1.33}$	Ni(5)/CM12	4	8	10			13		16	4	6	10	0.97	39	42	49
$Ni_{0.88}Sn_{0.11}(5)$-$Ce_{0.33}Mg_{0.67}O_{1.33}$	Ni8Sn(5)/CM12	4	7	9			11		14	3	5	8	0.99	32	37	46

Raman spectra was depicted in Fig. 4.10(a) for fresh, Fig. 4.10(b) for reduced, and Fig. 10(c) for spent catalysts. Three bands were observed commonly for all fresh, reduced, and spent samples. The strongest one, centered at around 450 cm^{-1}, corresponds to the first order (F_{2g}) vibration mode of the Ce^{4+} fluorite unit cell, which corresponds to CeO_2 [305]. The peak width increased as the intensity decreased, at constant metal loading and support modification (**Fig. 4.10**). However, peak width and intensity were reduced as the metal loading and tin concentration increased while the support composition remained constant (**Fig. 4.10** & Supplementary data, **Fig. 4.20**) [342]. The presence of peaks at 230 and 600 cm^{-1} indicated that a highly sensitive oxygen disorder was related with Ce-O stretching vibration. As the amount of Mg^{2+} increased, the intensity of 600 cm^{-1} weak shoulder was increased, indicating an increased oxygen vacancy [368]. A very weak vibrational peak was observed at 1160 cm^{-1}, corresponding to the sp^3 amorphous carbon present only for fresh and reduced catalysts.

In fresh samples(**Fig. 4.10 (a)**), NiO peak was expected at around 500 cm^{-1} and could not be well detected, probably due to the shadow effect of the long tail of the first-order CeO_2 peak at 450 cm^{-1} [307]. However, the Ni peak was not visible even after the reduction of catalyst, due to the long tail of the first order peak.

Feeble changes were observed between fresh and reduced samples. However, after the reforming reaction (**Fig. 4.10 (c)**), two additional bands were identified at approximately 1350 and 1600 cm^{-1}, corresponding to sp^3 hybridized disordered amorphous carbon (band D) and sp^2 hybridized graphite (band G), respectively. The I_D/I_G ratio increased with the decrease in metal loading and the addition of Mg^{2+} to the CeO_2 support, which corresponded well with the trend of particle size (**Table 4.3**).

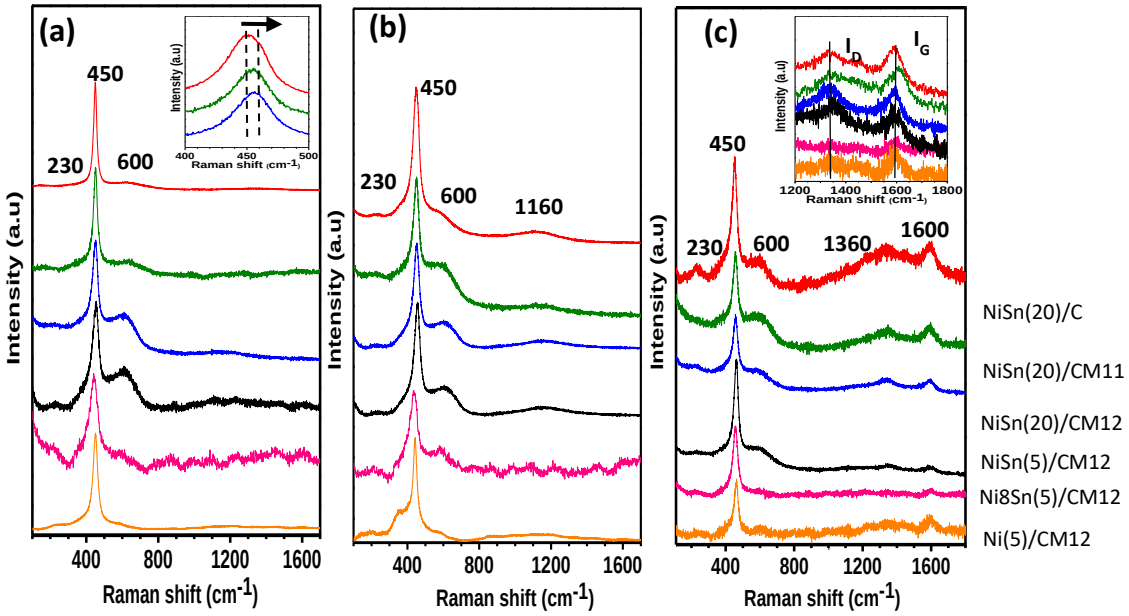

Figure 4. 10: Raman Characterization of for (a) Fresh, (b) Reduced, (c) Spent catalysts.

The CeO_2 grain size (d) was calculated from the Raman frequency shift ($\Delta\omega$) of cerium with respect to the CeO_2 standard peak (450 cm^{-1}) by using the following equation 4.5 [309–311]. Particle size for the catalysts were estimated to increase after reforming reaction compared to the same reduced sample. However, the dependency of the particle size on metal loading and support modification remained the same. The increasing order of CeO_2 particle size commonly observed in fresh, reduced and spent (**Table 4.3**) is NiSn(5)/CM12 < NiSn(5)/CM11 < NiSn(10)/CM12 < NiSn(10)/CM11 < NiSn(20)/CM12 < NiSn(20)/CM11 < NiSn(5)/C < NiSn(10)/C < NiSn(20)/C. Tin variation observed in particle size as NiSn(5)/CM12 < Ni8Sn(5)/CM12 < Ni(5)/CM12. Fang et al. [369] studied Ni (12 wt.%)/$Mg_{0.71}Al_{0.29}O_2$ catalyst and reported I_D/I_G value was increased from 0.5 to 1.02 with the addition of Ce 5 wt.% in spent catalyst after 20 hrs stability test at 400 ℃.

Electron microscopy (FESEM & TEM) along with X-ray Energy Dispersive Spectroscopy (EDS) measurements were performed to observe the micro-structural surface morphology and elemental composition of the samples shown in Fig. 4.11 & 4.12.

SEM images of fresh NiSn(5)/CM12 catalysts showed the finest particles on the surface morphology (**Fig. 4.11 (a)**). The NiSn(20)/C catalyst exhibited (**Fig. 4.11 (d)**) a structure resembling large lumps. Typically, adding Mg^{2+} to the catalyst showed small particles on the sheet layer under constant metal loading. Whereas, increasing metal loading at constant supported catalyst showed asymmetric structure variation lumps with foam like structure. Tin composition modified catalyst showed changes in morphology, with Ni(5)/CM12 exhibiting a foam-like structure, and Ni8Sn(5)/CM12 displaying a sheet-like structure with larger particles than NiSn(5)/CM12 supplementary data Fig. 4.21.

Typically, particle size increased for the same catalyst after reduction due to agglomeration, but the basic catalytic structure stays unchanged. Carbon deposition was identified over the surface of the spent catalysts. However, NiSn(20)/C spent catalyst surface observed (**Fig. 4.11 (f)**) carbon nanotubes followed a tip-growth mechanism as seen in TEM (**Fig. 4.12 (f)**), and this would immobilise nickel catalytic activity with particle agglomeration [81,370–372]. Carbon whisker increased as the metal loading increased, similar results were reported by Rajib et al. [373]. EDS analysis showed the elemental weight percentage of different catalysts shown in Table 4.4. Support modified catalyst showed less carbon percentage compared with unmodified catalyst samples, similar observation by Fang et al. [369]. NiSn(20)/C spent catalyst showed a high amount of 51 wt.% of carbon, whereas NiSn(5)/CM12 spent catalyst showed a low amount of 16 wt.% of carbon, practically TEM also followed the same trend.Average particle size (**Table 4.3**) was calculated for fresh, reduced and spent catalysts based on SEM images through ImageJ software. After the steam reforming process, particle size increased with the effect of temperature and carbon.

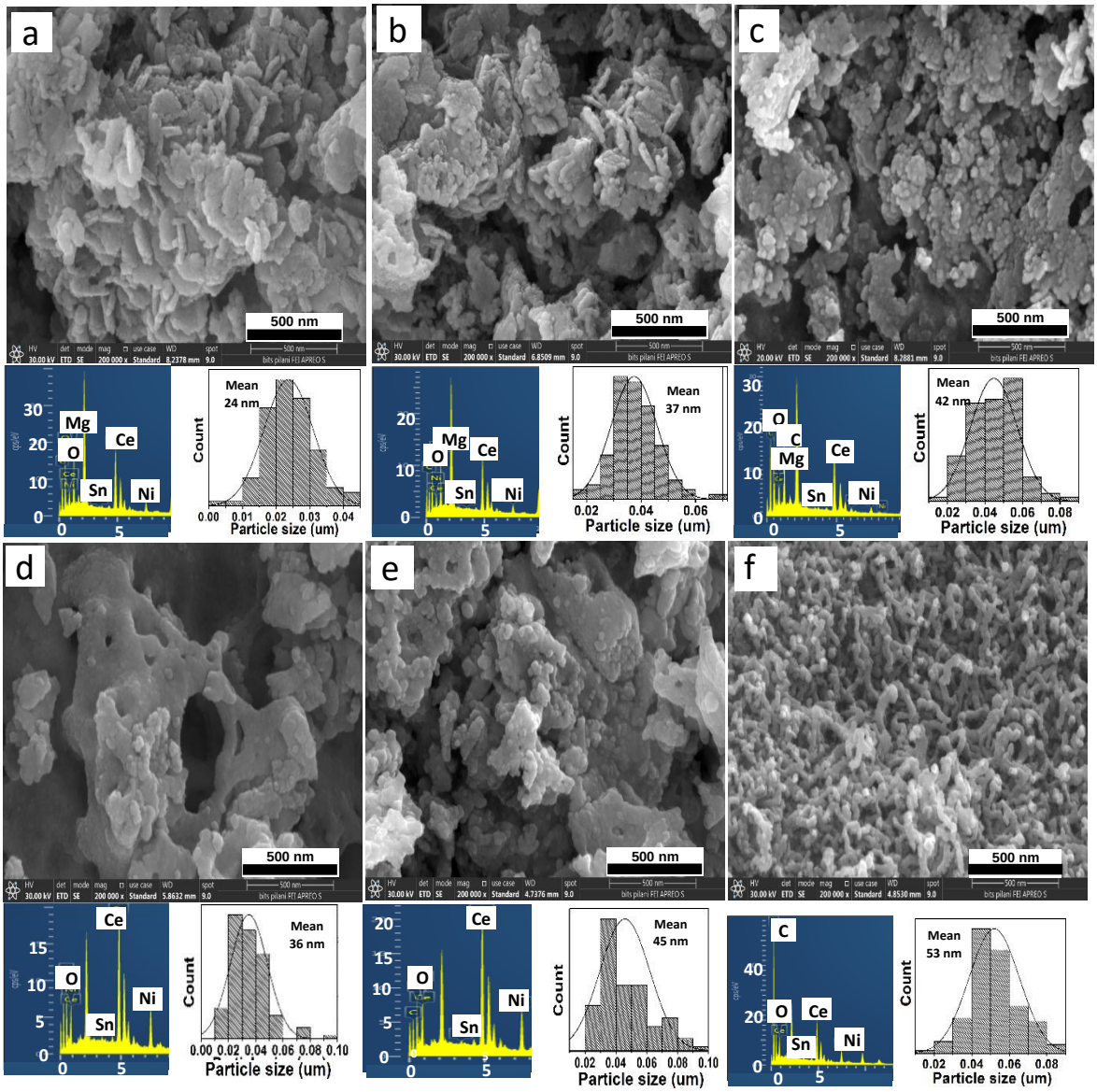

Figure 4. 11: FESEM images with particle size distribution and EDS spectrum for NiSn(5)/CM12 [(a) fresh, (b) reduce, (c) spent] and NiSn(20)/C [(d) fresh, (e) reduce, (f) spent] catalysts .

Common trend noticed as NiSn(5)/CM12 < NiSn(5)/CM11 < NiSn(10)/CM12 < NiSn(10)/CM11 < NiSn(20)/CM12 < NiSn(20)/CM11 < NiSn(5)/C < NiSn(10)/C < NiSn(20)/C. Tin variation observed in particle size as NiSn(5)/CM12 < Ni8Sn(5)/CM12 < Ni(5)/CM12. Ni particle size was measured for reduced and spent samples through TEM images for NiSn(20)/C, NiSn(5)/CM11, NiSn(5)/CM12 catalysts is 18, 10, 6 and 19, 11, 9 nm, respectively.

Wide scan XPS spectra showed the presence of essential elements Ni, Sn, Ce, Mg, O, and C in all catalyst samples (Supplementary data **Fig. 4.22**). In all fresh catalysts (Supplementary data, **Fig. 4.24 (a)**), $Ni2p_{3/2}$ corresponding to Ni^{2+} present at B.E ~855 eV and Ni^{3+} 857 eV could be observed, which attributed to NiO and $Ni(OH)_2$, respectively. $Ni2p_{3/2}$ satellite peak noticed at 861.5 eV [312,313].

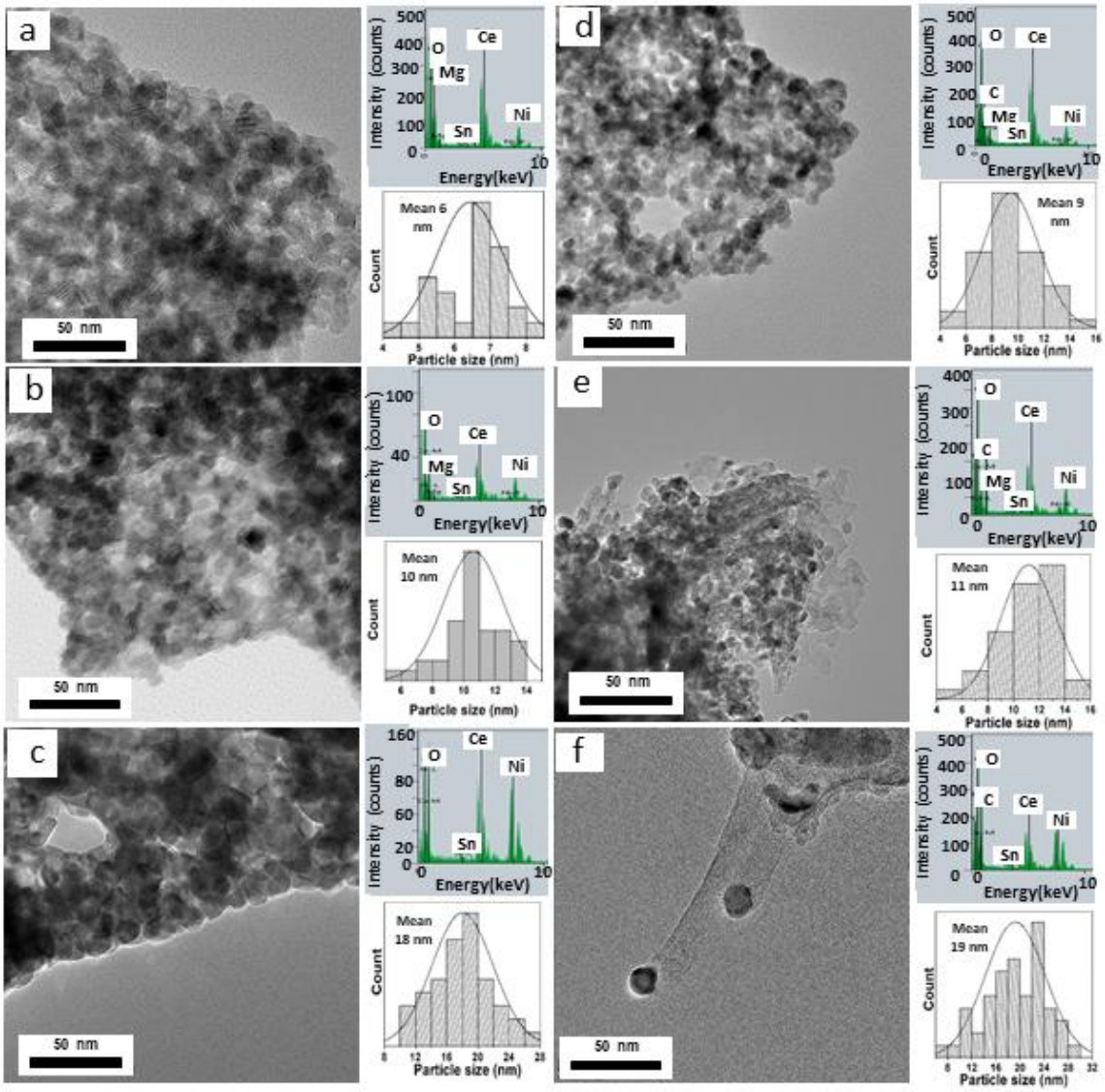

Figure 4. 12: TEM images with particle size distribution and EDS spectrum for NiSn(5)/CM12 [(a) reduced, (d) spent], NiSn(5)/CM11 [(b) reduced, (e) spent] and NiSn(20)/C [(c) reduced, (f) spent] catalysts.

At constant metal loading with the addition of Mg, the Ni $2p_{3/2}$ peaks were noticeably larger and narrower than NiSn(X)/C. According to Zhang et al. [374], the higher intensity and narrower peak indicated more favourable for the formation of metallic nickel (Ni^0) during reduction and also decreased the reduction temperature studied by Shi et al. [225]. However, Ni $2p_{3/2}$ peaks shifted towards lower B.E with increasing metal loading at constant support in fresh and spent catalyst samples. Whereas reverse trend noticed in reduced samples, due to effect of reduction [312]. It has been indicated that MSI getting weaker with an increase in metal loading. Ni^{2+} peak shift was slightly higher at B.E 856 eV for Ni8Sn(5)/CM12 and Ni(5)/CM12 catalysts compared to NiSn(5)/CM12 catalyst at B.E 855 eV.

In the reduced sample with the addition of Ni^{2+}, metallic nickel (Ni^0) was also observed at ~853 eV, corresponding to $2p_{3/2}$ (**Fig. 4.13 (a)**). At constant metal loading, $Ni^0/(Ni^0 + Ni^{2+})$ ratio increased as

Mg^{2+} was added to CeO_2 support (**Table 4.5**). It has been suggested that incorporating Mg^{2+} into CeO_2 support might reduce the diffusion of Ni^0 into the support and allow it to remain on the sample surface, as observed by other mixed support oxides [374–376].

And the ratio of $Ni^0/(Ni^0 + Ni^{2+})$ increased commonly as metal loading increased at constant support. It indicated a larger dispersion at lower (5 wt.%) metal loading and a weaker MSI as the metal loading increased due to sintering or particle agglomeration. The ratio of $Ni^0/(Ni^0 + Ni^{2+})$ order followed as NiSn(20)/CM12 > NiSn(10)/CM12 > NiSn(5)/CM12 > NiSn(20)/CM11 > NiSn(10)/CM11 > NiSn(5)/CM11 > NiSn(20)/C > NiSn(10)/C > NiSn(5)/C. Order followed for variation of tin composition as Ni(5)/CM12 < Ni8Sn(5)/CM12 < NiSn(5)/CM12 (Table 4.5).

It is understood that adding a small amount of tin to nickel enhances nickel reducibility and leads to increasing the $Ni^0/(Ni^0 + Ni^{2+})$ ratio. Nickel reducibility decreased with further increasing tin, and similar phenomenon was observed in pastor et al. [360]. After catalytic reforming (Supplementary data, **Fig. 4.23 (c)**), no peak corresponding Ni^0 was observed, only Ni^{2+} ($2p_{3/2}$) and Ni^{3+} ($2p_{3/2}$) were noticed. XPS analysis (**Table 4.4**) revealed that weight (%) of Ni commonly increased with metal loading.

Tin(Sn) was characterized by two spin-orbit groups between the range of 486 ± 1 and 494 ± 1.5 eV. For all catalysts both Sn^{2+} (corresponding to Sn $3d_{5/2}$ at 486 and Sn $3d_{3/2}$ 494 eV) and Sn^{4+} (corresponding to Sn $3d_{5/2}$ at 487 and Sn $3d_{3/2}$ 495.4 eV) oxidation states were observed [296]. In fresh samples (Supplementary data, **Fig. 4.24(a)**) at constant metal loading, $Sn^{4+}/(Sn^{2+} + Sn^{4+})$ ratio values increased with the incorporation of MgO into support. In comparison, $Sn^{4+}/(Sn^{2+} + Sn^{4+})$ ratio values decreased with increasing metal loading. It means the addition of nickel increased the relative number of electrons in the external shell of Sn. Since the electronegativity of Sn (1.96) was slightly high compared with the nickel (1.90) [377]. No significant peak shift was observed with changing metal loading and support modification for fresh, reduced, and spent samples. But $3d_{5/2}$ and Sn $3d_{3/2}$ peaks were shifted towards higher B.E with increasing tin composition Ni:Sn 14:1 to 8:1.

In reduced sample (**Fig. 4.13 (b)**), in addition to Sn^{2+} and Sn^{4+}, the metallic tin(Sn^0) was also observed at 485 eV [296]. $Sn^{4+}/(Sn^{2+}+Sn^{4+})$ ratio values increased for the same sample (Eq. 4.11), but the trend remained same in comparison to the fresh sample. Due to the fact that reduction might occur in two steps, Sn^{2+} was reduced to tin metal (Sn^0) or Sn^{2+} was converted to Sn^{4+} by electron loss during Ce^{4+} ion reduction. [378].

$$Sn^{2+} \rightarrow Sn^{o} + 2e^{-} \quad (4.10)$$

$$Sn^{2+} + 2Ce^{4+} \rightarrow Sn^{4+} + 2Ce^{3+} \quad (4.11)$$

Table 4. 4: Elemental analysis (%) from EDS (FESEM & TEM) and XPS.

Name of the catalyst	FESEM elemental analysis (wt.%)													XPS elemental analysis (wt.%)												TEM elemental analysis (wt.%)								
	Fresh				Reduced				Spent					Fresh				Reduced				Spent					Reduced				Spent				
	Ni	Sn	Ce	Mg	Ni	Sn	Ce	Mg	Ni	Sn	Ce	Mg	C	Ni	Sn	Ce	Mg	Ni	Sn	Ce	Mg	Ni	Sn	Ce	Mg	C	Ni	Sn	Ce	Mg	Ni	Sn	Ce	Mg	C
NiSn(5)/C	3	0.4	42.6	0	4	0.4	48.6	0	2.1	0.2	30.9	0	42	3.7	0.3	64.6	0	4.1	0.59	68.7	0	2.6	0.2	33.1	0	39.1									
NiSn(10)/C	7.2	1	38	0	8	1	42.2	0	5	0.8	26.1	0	46	7.6	1.1	61.6	0	8	1	63.7	0	4.4	0.4	23.1	0	48.7									
NiSn(20)/C	16	2	30.3	0	16.1	2.2	35	0	11	1.4	19.6	0	50.5	16.8	2.3	52.4	0	17.1	2.2	53.7	0	8.3	0.8	20.2	0	53.3	16.8	2.3	55.3	0	9.8	1.2	19.6	0	52.4
NiSn(5)/CM11	3.7	0.4	28.6	10.5	4	0.4	31	11	3.1	0.2	29	10.8	19	3.8	0.4	37.8	9.7	4.3	0.6	46.7	11.7	3	0.3	28.7	11	19	4	0.4	46.8	11.9	3	0.3	29	11	18.9
NiSn(10)/CM11	8	1.1	27	8.5	8.2	1.2	28	8.2	7.3	1.2	27	8	25.2	7.4	1.2	35.9	8.2	8.2	1.1	44	11.1	7	0.9	27	8	26									
NiSn(20)/CM11	16.5	2.1	25.1	6.1	17	2.3	25	6.3	12	1.8	20.1	5.2	34.8	16.9	2	31	6.1	17.2	2.4	39.1	7.6	12	1.1	19.2	4.3	37									
NiSn(5)/CM12	4	0.4	26.4	12.6	4.2	0.6	28	16	3.6	0.4	27	12.6	16	3.9	0.4	27.7	13.6	4.3	0.63	39.7	15.6	3.9	0.3	28	13.4	15.8	4.2	0.5	39.6	15.7	3.3	0.3	27.8	13.7	15.9
NiSn(10)/CM12	8.1	1.2	26	12.4	8.5	1.3	26	13.1	7.3	1	26.6	12.7	18.6	8.1	1.3	24.9	13.4	8.6	1.4	37.4	14.6	7.8	1	26	12	21									
NiSn(20)/CM12	17.1	2.3	23	9.7	17.2	2.6	24	10	15.3	2	23.2	10.3	25.2	17	2.3	22.1	10.3	17.3	2.6	33.5	12.4	16.1	1.7	23.2	10	27									
Ni(5)/CM12	4.6	0	28.6	13	4.9	0	31	14.5	3.3	0	24.8	11	23	4.3	0	29.3	14.7	4.8	0	40.8	16.7	3	0	25.6	12.6	21	4.6	0	40.7	17					
Ni8Sn(5)/CM12	3.7	1	26.6	13	3.8	1	28	16.1	3	0.6	26	11.2	21.2	3.9	0.5	28.6	14.5	4	1	39.5	16	3.4	0.5	27	13	18	3.9	0.8	40.2	16					

Because Ce and Sn were group-IV elements, they tend to create stable oxidation states during reduction because Sn^{4+} oxidation state is more stable than its Sn^{2+} state. Similarly, Ce^{3+} oxidation state is more stable than its Ce^{4+} oxidation state [320]. Increasing Sn^{4+} concentration helped to enhance the activity by improving OSC (Eq. 4.11). $Sn^0/(Sn^0+Sn^{2+}+Sn^{4+})$ ratio values exhibited a similar trend as $Ni^0/(Ni^0 + Ni^{2+})$ ratio with respective metal loading and support modification. But, increasing Sn composition followed the reverse phenomenon (**Table 4.5**), a similar observation was noticed by Xie et al.[379] and Fan et al. [377].

In spent catalysts (Supplementary data **Fig. 4.24(c)**), metallic Sn disappeared, and the ratio of $Sn^{4+}/(Sn^{2+}+Sn^{4+})$ decreased, similarly to the trend observed in fresh catalysts. Because Sn inhibits the carbon formation by promoting water gas shift reaction [320,321].

$$CO + H_2O \rightarrow CO_2 + 2H^+ + 2e^- \quad (4.12)$$

$$Sn^{4+} + 2e^- \rightarrow Sn^{2+} \quad (4.13)$$

CeO_2 has two oxidation states, i.e., Ce^{3+} and Ce^{4+}. Ce^{3+} (corresponding to Ce $3d_{3/2}$ at 885 ± 0.2, 898 ± 0.2 eV and Ce $3d_{5/2}$ at 903 ± 0.2 eV) and Ce^{4+} (corresponding to Ce $3d_{3/2}$ at 883± 0.2, 890 ± 0.2 eV and $3d_{5/2}$ at 900± 0.2, 907± 0.2, 917 ± 0.2 eV) were present in all catalysts. $Ce^{3+}/(Ce^{3+}+Ce^{4+})$ ratio (**Table 4.5**) values in fresh catalysts increased with Mg^{2+} support modification at constant metal loading (Supplementary data, **Fig. 4.25**). This indicated that mixed oxides enhanced the OSC, which is related to oxygen vacancy (Eq. 4.9). With increasing metal loading, the ratio $Ce^{3+}/(Ce^{3+}+Ce^{4+})$ values decreased, indicating a reduction in OSC as a result of a weak MSI between nickel and cerium. Increasing the Sn composition (Ni8Sn(5)/CM12) (or) the absence of Sn (Ni(5)/CM12) decreased the $Ce^{3+}/(Ce^{3+}+Ce^{4+})$ values compared with NiSn(5)/CM12 catalyst. No significant peak shift was observed with changing metal loading, support modification and Sn composition. Min et al. [380] explained that Ce^{4+} partially substituted by Sn^{4+} forms the Ce-O-Sn bond, which increases the OSC with a moderate amount of Sn. However, a higher amount of Sn weakens the reducibility of SnO_2 phase and the Ce-O-Sn bond, resulting in a drop in OSC.

In reduced catalyst (**Fig. 4.13 (c)**), Ce^{3+} ratio values increased for the same sample (Eq. 4.27), trend followed the same as fresh catalyst. In spent catalysts, $Ce^{3+}/(Ce^{3+}+Ce^{4+})$ ratio decreased with an increase in Ce^{4+} due to the absorption of oxygen (Eq. 4.14) during the reforming process explained by Kroger-Vink equation 4.6 [381].

$Ce^{3+}/(Ce^{3+}+Ce^{4+})$ ratio followed order commonly for fresh, reduced and spent is NiSn(5)/CM12 > NiSn(5)/CM11 > NiSn(10)/CM12 > NiSn(10)/CM11 > NiSn(20)/CM12 > NiSn(20)/CM11 > NiSn(5)/C > NiSn(10)/C > NiSn(20)/C. The order followed for varying Sn composition NiSn(5)/CM12 > Ni8Sn(5)/CM12 > Ni(5)/CM12.

Surface lattice oxygen (O_L) has B.E at 529 ± 0.2 eV and oxygen vacancies (O_V) has B.E at 531 ± 0.2 eV [227]. The presence of weakly bonded water molecules of oxygen has a B.E at 533 ± 0.2 eV denoted

by O_{OH}. In fresh catalysts, $O_V/(O_L+O_V+O_{OH})$ ratio has increased with the addition of Mg^{2+} at constant metal loading without a significant peak shift (Eq. 4.9) (**Table 4.5**). However, the $O_V/(O_L+O_V+O_{OH})$ ratio decreased, and O_L peak slightly shifted towards the higher B.E with increasing metal loading at constant support, as O_V originated from O-Ce^{3+} (Supplementary data **Fig. 4.26**). $O_V/(O_L+O_V+O_{OH})$ ratio values increased when a small amount of tin was added to Ni(5)/CM12 at a ratio of Ni:Sn 14:1. However, $O_V/(O_L+O_V+O_{OH})$ values decreased with increasing Sn composition Ni:Sn 8:1 (Eq. 4.8) [382].

Table 4. 5: XPS oxidative state ratio of Ni^0, Sn^0, Sn^{4+}, Ce^{3+}, O_V, C_{OH} for fresh (F), reduce (R) and spent (S) catalyst samples.

Catalyst Name	$Ni^0/(Ni^0+Ni^{2+})$ for reduced	$Sn^0/(Sn^0+Sn^{2+}+Sn^{4+})$ for reduced	$Sn^{4+}/(Sn^{2+}+Sn^{4+})$			$Ce^{3+}/(Ce^{3+}+Ce^{4+})$			$O_V/(O_L+O_V+O_{OH})$			$C_{OH}/(C_C+C_{OH}+C_O)$
			F	R	S	F	R	S	F	R	S	
NiSn(5)/C	0.03	0.05	0.3	0.4	0.0	0.3	0.4	0.2	0.4	0.6	0.5	0.25
NiSn(10)/C	0.04	0.06	0.2	0.4	0.0	0.2	0.3	0.1	0.3	0.5	0.4	0.14
NiSn(20)/C	0.06	0.05	0.2	0.4	0.0	0.2	0.2	0.1	0.3	0.5	0.4	0.12
NiSn(5)/CM11	0.10	0.04	0.4	0.5	0.4	0.4	0.4	0.3	0.7	0.8	0.7	0.36
NiSn(10)/CM11	0.12	0.05	0.4	0.4	0.4	0.3	0.4	0.2	0.6	0.6	0.6	0.32
NiSn(20)/CM11	0.15	0.05	0.3	0.4	0.2	0.3	0.3	0.2	0.5	0.5	0.5	0.28
NiSn(5)/CM12	0.17	0.03	0.5	0.6	0.5	0.4	0.5	0.3	0.7	0.8	0.7	0.59
NiSn(10)/CM12	0.18	0.03	0.4	0.5	0.4	0.4	0.4	0.3	0.6	0.7	0.6	0.34
NiSn(20)/CM12	0.19	0.03	0.3	0.4	0.3	0.3	0.3	0.2	0.5	0.7	0.4	0.30
Ni(5)/CM12	0.11	-	-	-	-	0.4	0.4	0.3	0.5	0.7	0.6	0.42
Ni8Sn(5)/CM12	0.15	0.04	0.5	0.5	0.4	0.4	0.4	0.3	0.6	0.7	0.6	0.48

In reduced (**Fig. 4.13(d)**) catalysts, oxygen vacancy increased for the same sample (**Table 4.5**), due to the effect of increased Ce^{3+} [227]. $O_V/(O_L+O_V+O_{OH})$ ratio trend was same as fresh catalyst, but no significant peak shift was noticed with metal loading and support modification. But Ni8Sn(5)/CM12 catalyst for both O_L and O_V were shifted towards higher B.E compared with NiSn(5)/CM12 in reduced and spent samples.

In spent catalyst (Supplementary data **Fig. 4.27 (c)**), $O_V/(O_L+O_V+O_{OH})$ ratio values decreased for the same sample, because of increasing O_L which was originated from O-Ce^{4+} [227], Commonly $O_V/(O_L+O_V+O_{OH})$ order followed in fresh, reduced and spent catalyst as NiSn(5)/CM12 > NiSn(5)/CM11 > NiSn(10)/CM12 > NiSn(10)/CM11 > NiSn(20)/CM12 > NiSn(20)/CM11 > NiSn(5)/C > NiSn(10)/C > NiSn(20)/C. Varying Sn composition the order followed as NiSn(5)/CM12 > Ni8Sn(5)/CM12 > Ni(5)/CM12.

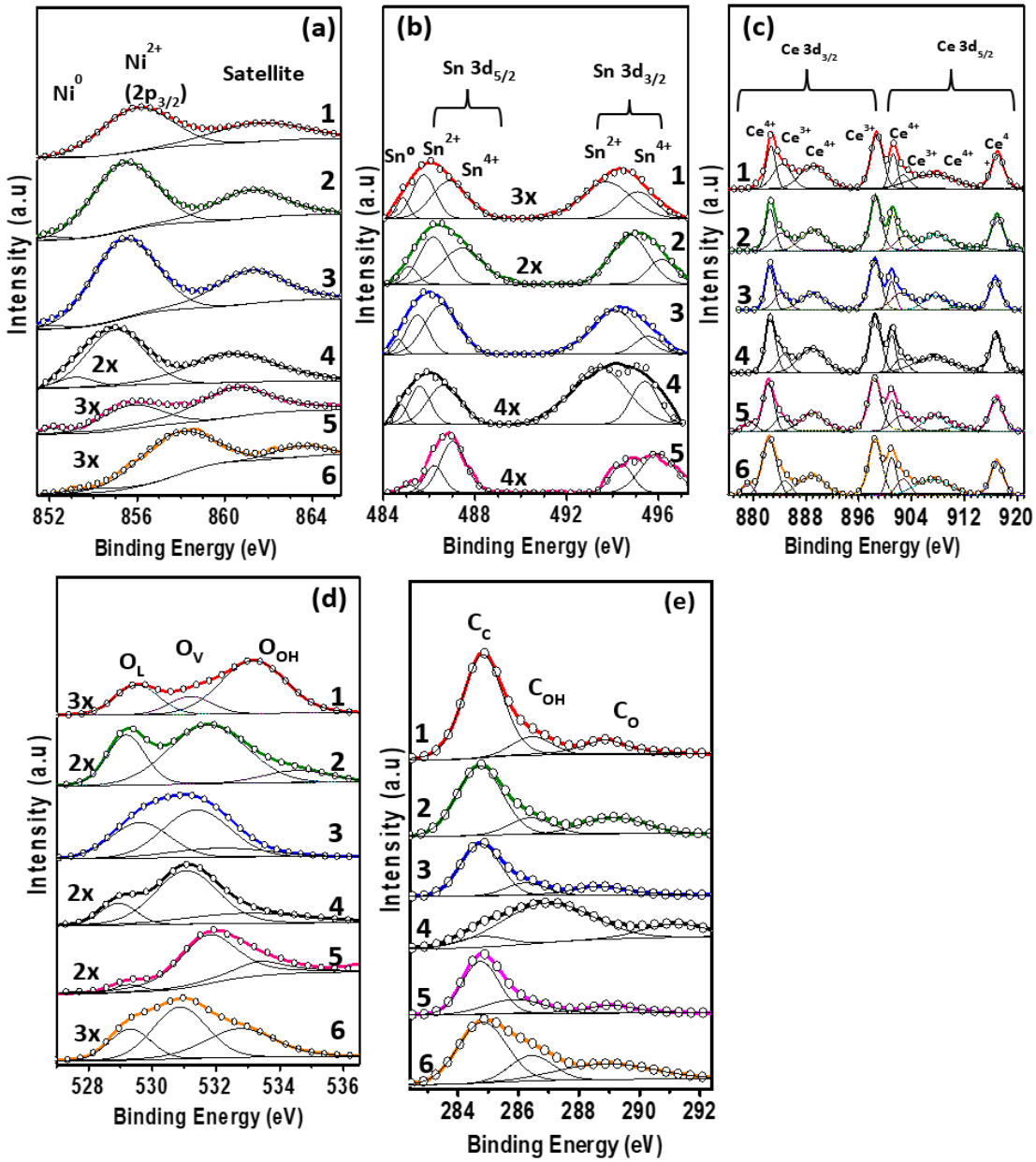

Figure 4. 13: High resolution XPS spectra of (a) Nickel, (b) Tin, (c) Cerium, (d) oxygen and (e) Spent catalyst of carbon elements for reduced catalyst samples of 1.NiSn(20)/C, 2.NiSn(20)/CM11, 3.NiSn(20)CM12, 4.NiSn(5)/CM12, 5.Ni8Sn(5)/CM12 and 6.Ni(5)/CM12 catalyst.

XPS data was used to study the adventitious carbon contamination. In spent catalysts, C=C peak at 284.8 eV corresponding to sp^2 carbon, denoted by C_C (**Fig. 4.13 (e)**). C-OH & O-C=O peaks noticed at 286 ± 0.2 & 289 ± 0.2 eV corresponding to sp^3 carbon, which was favorable for reforming activity denoted by C_{OH} &C_O, respectively [296,314]. At constant metal loading, the addition of Mg to Ce reduces the C=C peak area and increases the $C_{OH}/(C_C+C_{OH}+C_O)$ ratio (**Table 4.5**). which indicated that mixed oxide helped to oxidize the sp^2 carbon on catalyst surface during steam reforming process. However, an opposite trend

was noticed with increasing metal loading at constant support (Supplementary data, **Fig. 4.27**). It has been indicated that increasing metal loading was not favorable to oxidize the sp^2 carbon.

XPS elemental analysis (**Table 4.4**) tells order of carbon wt.%, follows NiSn(5)/CM12 < NiSn(5)/CM11 < NiSn(10)/CM12 < NiSn(10)/CM11 < NiSn(20)/CM12 < NiSn(20)/CM11 < NiSn(5)/C < NiSn(10)/C < NiSn(20)/C. NiSn(5)/CM12 > Ni8Sn(5)/CM12 > Ni(5)/CM12 was the order of the $C_{OH}/(C_C+C_{OH}+C_O)$ ratio when Sn composition varied. This indicates that the addition of Sn at a ratio of Ni:Sn 14:1 atomic ratio helped to increase the oxidation of carbon on the catalyst surface (**Figure 4.13 (e)**), whereas further increasing Sn composition at a ratio of Ni:Sn 8:1 atomic ratio decreased the oxidation of carbon compared with Ni(5)/CM12. It has been suggested that the small amount of tin atoms reduced coke formation by promoting the WGS reaction. However, the large amount of tin weakens the performance by covering Ni active sites and adsorption of CO [321,382,383].

Figure 4.14(a) depicts the NH_3-TPD profiles of the CeO_2 (C), CeO_2:MgO mole ratio 1:1 (CM11) and 1:2 (CM12) support materials. Weak acidic peaks with high intensity were observed at 77, 72, and 64 °C in C, CM11, and CM12, respectively. Strong acidic peaks were only observed at 235 and 165 °C for C and CM11 support, which was not as strong as the strong acidic peak. The CM12 support showed no prominent strong acidity peak. This showed that the addition of Mg^{2+} made the support less acidic [384]. Due to its low acidity, CM12 support was more favorable for reforming processes than C and CM11 support.

H_2 temperature programmed reduction (H_2-TPR) has been used to test the reducibility of various phases for fresh catalysts (**Fig. 4.14(b)**). The reduction peaks between 200 - 400 °C could be attributed to the reduction of relatively large NiO particles, which are not strongly anchored on the support, to metallic nickel (Ni^0) [329]. The peaks between 400 and 600 °C were attributed to smaller Ni-species interacting more strongly with CeO_2 and/or MgO. The reduction peaks observed above 600 °C are attributed to bulk CeO_2 and/or strong interaction compound created between Ni^{2+} and MgO [329,385]. In comparison to NiSn(X)/C (X = 5, 10, 20 wt.%) catalysts, the TPR profiles of NiSn(X)/CM11 and NiSn(X)/CM12 catalysts exhibited low peak intensity, indicating that difficult reduction was probably due to NiO and MgO interaction [237]. In addition, TPR profiles revealed that the addition of Mg^{2+} to the support at constant metal loading resulted the low intensity peak shifting towards higher temperature, but the opposite trend was observed with increasing metal loading at constant support. This indicates that the addition of Mg^{2+} strengthened the interaction between metal and support, whereas increasing metal loading weakens the interaction [386–388]. The total H_2 consumption (calculated from the area of the peaks) was seen to increase with increasing Mg^{2+} concentration at constant metal loading and decrease with increasing metal loading at constant support composition. The maximum and minimum H_2 consumption values, 4216 and 269 $\mu mol/g_{cat}$, are calculated for the NiSn(5)/CM12 and NiSn(20)/C catalysts, respectively. It shows that stronger metal support interaction results in higher hydrogen consumption [237].

Figure 4.15 reveals the N_2 adsorption-desorption isotherms and pore size distribution for the fresh and reduced catalysts of NiSn(20)/C, NiSn(5)/CM12, respectively. Type-IV mesoporous nature was noticed in both the catalysts [389–391]. Hysteresis was small in NiSn(20)/C compared with NiSn(5)/CM12 catalyst. This was due to the pore blockage, which resulted in decreasing pore volume of fresh catalysts such as 0.06626, 0.331 and for reduced 0.05368, 0.2775 cm^3/g for NiSn(20)/C, NiSn(5)/CM12, respectively.

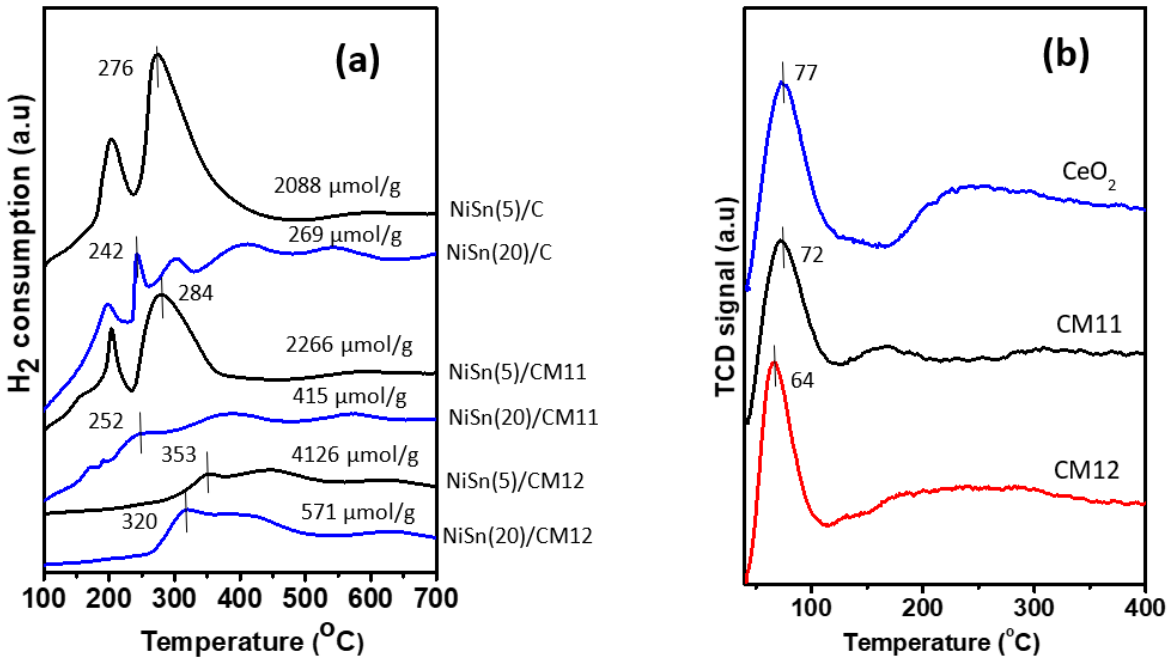

Figure 4. 14: (a) H_2 temperature programmed reduction (H_2-TPR) along with H_2 consumption values for fresh catalysts, (b) NH_3-TPD profiles for CeO_2 and CeO_2 modified with MgO supports.

The mean pore diameter for NiSn(20)/C, NiSn(5)/CM12 fresh catalysts were 28.7, 10.1 nm and for reduced samples were 28.57, 17.73 nm. The BET surface of fresh catalysts was 9.2326, 131.42 m^2/g, and for reduced catalysts such as 7.5143, 62.61 m^2/g of NiSn(20)/C, NiSn(5)/CM12, respectively.

Based on the observed results, the addition of Mg^{2+} ion catalyst increased surface area by 17 times. Particle size was calculated by using surface area through the following equation.

$$\text{Particle diameter (nm)} = \frac{6000}{\left(BET\ surface\ area\ \left(^{m^2}/_{g}\right)\right)\times\left(bulk\ density\ \left(^{g}/_{cm^3}\right)\right)} \qquad (4.14)$$

Particle size (Eq. 4.14) calculated for a fresh catalyst is 90.7, 8.3 nm and 108.5, 17.6 nm for reduced NiSn (20)/C, NiSn(5)/CM12, respectively.

DTA/TGA characterization was performed for the spent catalysts to check the amount of carbon deposited on the surface shown in **Fig. 4.16** and supplementary **Fig. 4.28**. DTA analysis showed one exothermic peak commonly in catalysts around 350 °C for NiSn(X)/CM11, and NiSn(X)/CM12 (X=5, 10, 20 wt.%) catalysts. Generally, DTA exothermic peaks below 400 ºC could be attributed to the

decomposition of nickel hydroxide (or) amorphous carbon. However, the NiSn(X)/C catalyst observed two distinct temperature peaks at 500-600 °C related to filamentous carbon and peaks over 600 °C associated with graphitic peaks [369,392].

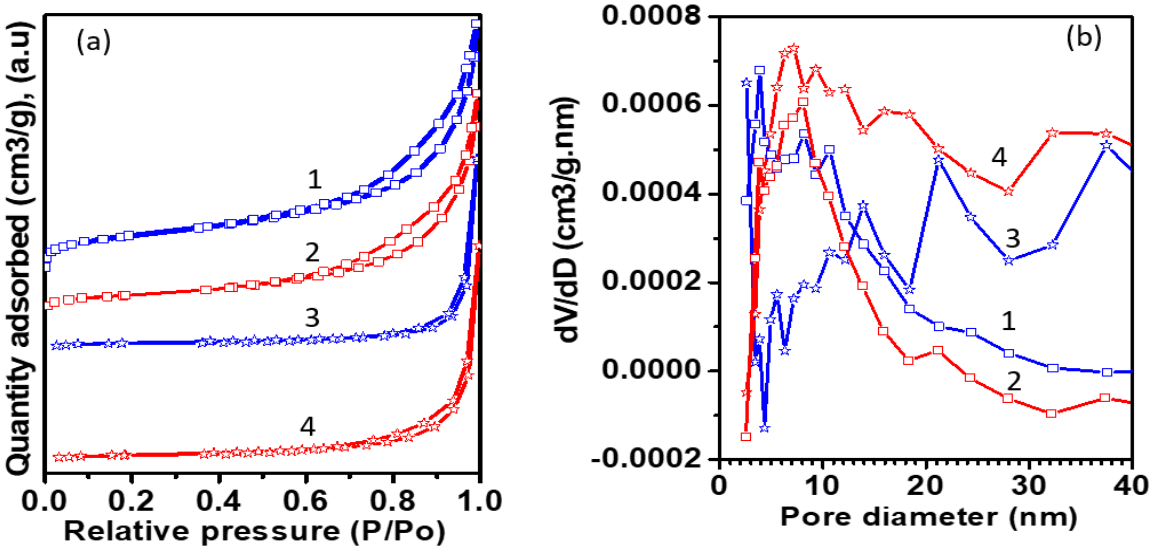

Figure 4. 15:(a) N_2 adsorption-desorption isotherm and (b) Pore diameter distribution for (1) Fresh, (2) Reduce NiSn(5)/CM12 and (3) Fresh, (4) Reduced of NiSn(20)/C catalyst samples.

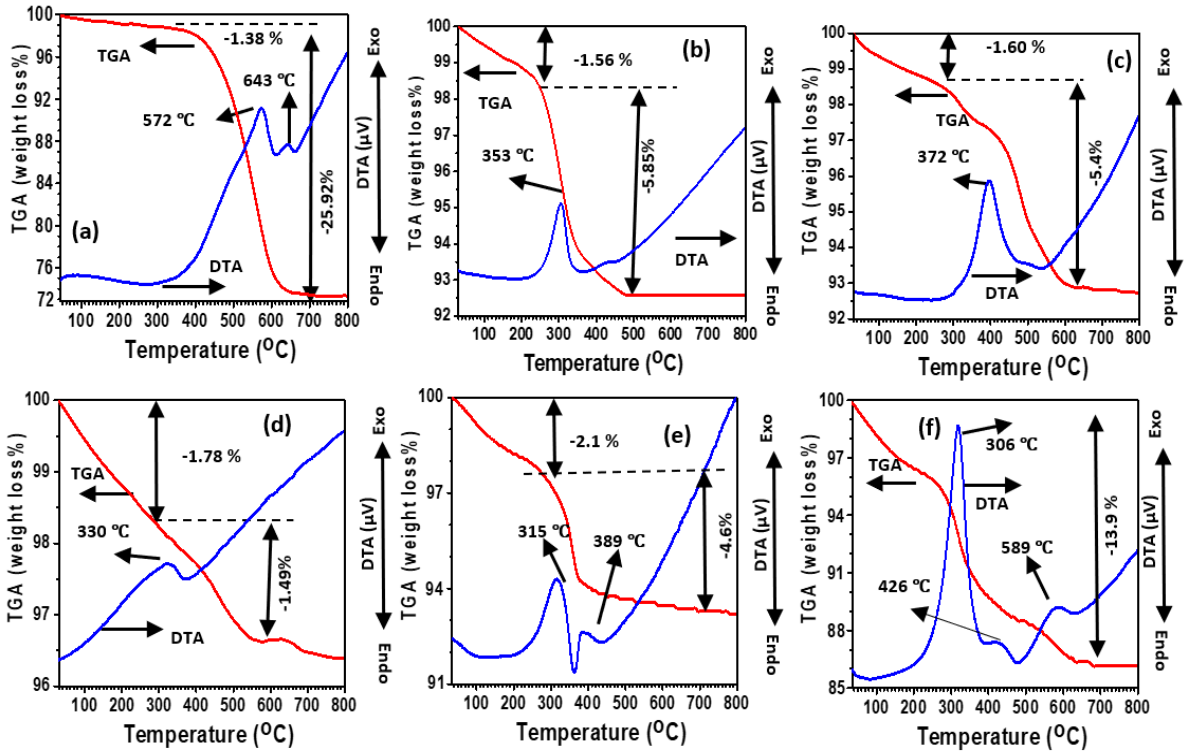

Figure 4. 16: DTA/TGA for (a) NiSn(20)/C, (b) NiSn(20)/CM11, (c) NiSn(20)/CM12, (d) NiSn(5)/CM12, (e) Ni8Sn(5)/CM12, (f) Ni(5)/CM12 of used catalysts.

The order of TGA weight loss showed as NiSn(5)/CM12 (3.2%) < NiSn(5)/CM11 (4.9%)< NiSn(10)/CM12 (5.57%) < NiSn(20)/CM12 (7%) < NiSn(10)/CM11 (7.4%) ≤ NiSn(20)/CM11 (7.41%) < NiSn(5)/C (11.00%) < NiSn(10)/C (17.76%) < NiSn(20)/C (27.3%). Tin composition varied (Fig. 4.16) catalyst showed weight loss order as NiSn(5)/CM12 (3.2%) < Ni8Sn(5)/CM12 (6.6%) < Ni(5)/CM12 (13.6%). It was understood that tiny amount of Sn addition to nickel helped to reduce the carbon formation and further increasing the amount of Sn increased carbon formation.

4.2.4.2 Catalytic Activity Study

Figure 4.17 illustrates the steady state catalytic activity in terms of ethanol conversion (%), selectivity (%) of the gaseous (H_2, CO_2, CO, CH_4) and liquid (CH_3CHO, CH_3OH, and CH_3COCH_3) products at feed concentration of EtOH:H_2O at 1:12 molar ratio, feed flow rate 0.1 ml/min and various reaction temperatures between 200-400 ℃. In all catalyst samples, ethanol conversion and selectivity of H_2 and CO_2 was consistently improved with temperature (200-400 °C).

At 400 °C, NiSn(5)/CM12 catalyst exhibited the maximum hydrogen selectivity of 71% with 100% EtOH conversion. However, the H_2 selectivity of NiSn(10)/CM12 and NiSn(20)/CM12 was 59 and 56 %, respectively. Notably, the hydrogen selectivity decreased with increasing metal loading for all catalyst samples (**Fig. 4.17(a)** & Supplementary **Fig. 4.29**). NiSn(20)/C, NiSn(20)/CM11, and NiSn(20)/CM12 exhibited H_2 selectivity of 32, 50, and 56 % and CO selectivity of 20, 12, and 9 %, respectively, at 400 °C. This clearly demonstrated that adding Mg^{2+} into the cerium lattice enhanced the hydrogen production by reducing coke formation. The addition of a minute amount of tin (Ni:Sn 14:1 atomic ratio) as a bimetallic to NiSn(5)/CM12 increased the H_2 selectivity from 50% to 71%, while decreased the CH_4 and CO selectivity from 31% to 7% and 17% to 4%, respectively, at 400 °C (**Fig. 4.17**). In addition, with increased Sn composition (Ni:Sn 8:1 atomic ratio), H_2 selectivity decreased from 71 to 51% and increased CH_4 and CO selectivity from 7% to 22% and 4% to 13%, respectively. This implied that adding a little amount of tin improved H_2 selectivity by limiting carbon formation, whereas increasing the Sn content weakens CO adsorption and decreases catalyst activity [360,382].

In liquid products, the selectivity of acetaldehyde (CH_3CHO) (**Fig. 4.17 (f)**) and acetone (CH_3COCH_3) (**Fig. 4.17 (g)**) increased, while the selectivity of methanol (CH_3OH) (**Fig. 4.17 (h)**) decreased with increasing temperature. At 400 °C, NiSn(5)/CM12, NiSn(10)/CM12, and NiSn(20)/CM12 showed CH_3CHO selectivity of 89, 77, and 71 %, respectively, while CH_3OH and CH_3COCH_3 showed selectivity of 6, 12, and 16 %, respectively. Although the selectivity of the NiSn(20)/CM11 and NiSn(20)/C catalysts for CH_3CHO was 69 and 46 %, respectively. And for CH_3OH and CH_3COCH_3, the percentages were 14%, 27%, and 17%, 27%, respectively. The results showed that CH_3CHO selectivity increased as the Mg^{2+} concentration increased and decreased as the metal loading was increased. While the trends for CH_3OH and

CH_3COCH_3 showed opposite direction. The decreasing order of activity performance with regard to hydrogen selectivity and ethanol conversion demonstrated NiSn(5)/CM12 > NiSn(5)/CM11 > NiSn(10)/CM12 > NiSn(10)/CM11 > NiSn(20)/CM12 > NiSn(20)/CM11 > NiSn(5)/C > NiSn(10)/C > NiSn(20)/C. The composition of Sn varied as follows: NiSn(5)/CM12 > Ni8Sn(5)/CM12 > Ni(5)/CM12.

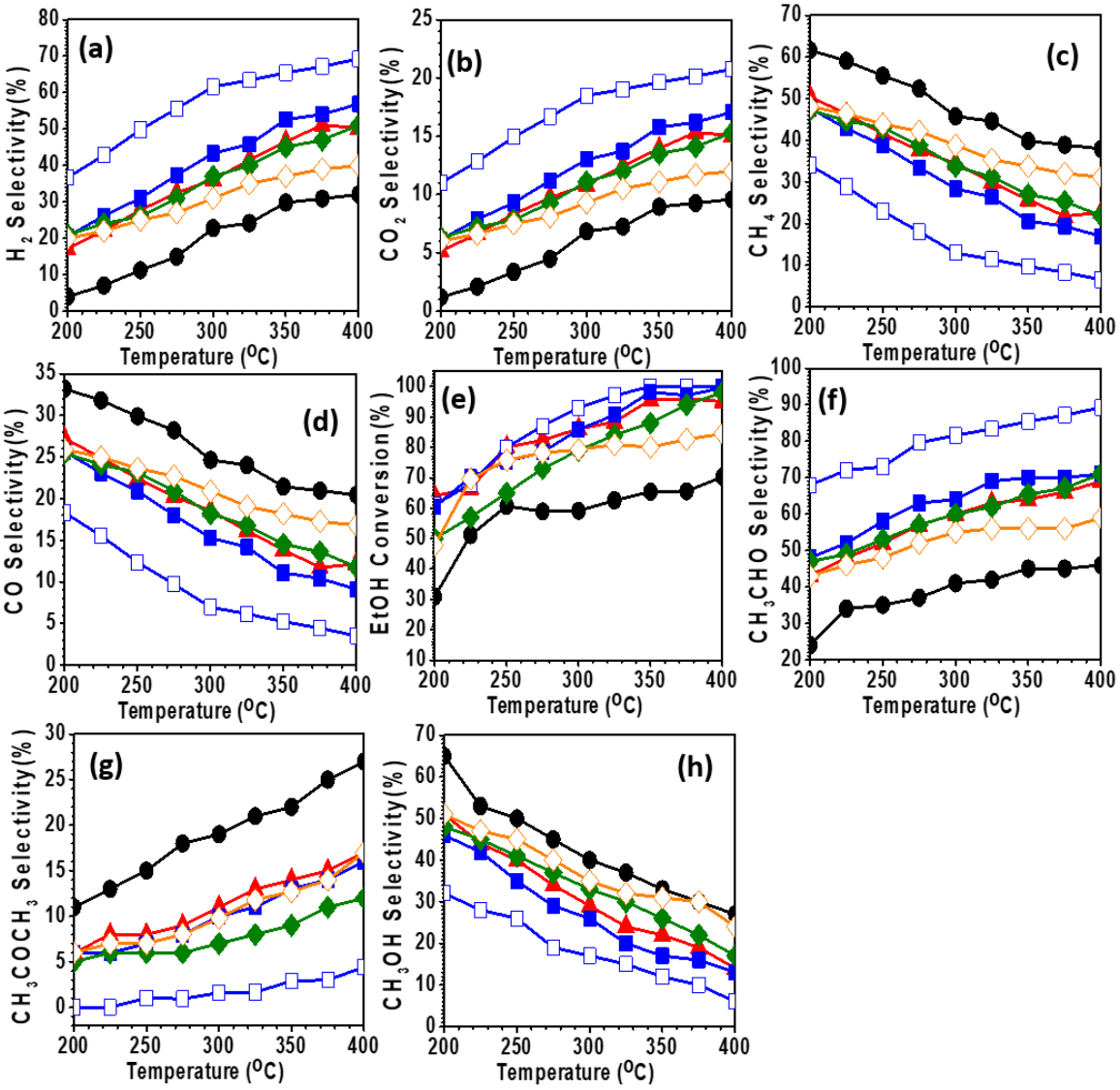

Figure 4. 17: Catalytic activity as a function of temperature (200-400 °C) for NiSn(5)/CM12 (□) , NiSn(20)/CM12 (■), NiSn(20)/CM11 (▲), NiSn(20)/C (●), Ni8Sn(5)/CM12 (♦), Ni(5)/CM12(◊) catalysts low temperature steam reforming of EtOH : water 1:12 mole ratio.

4.2.5 Discussion

The ESR mechanism on the Ni/CeO_2 and related catalyst is discussed elaborately in previous publication [45]. Based on the gaseous and liquid state products it could be believed that the same mechanism is applicable for the present case also.

This study demonstrated the function of Sn-doped bimetals on the surface of nickel, as well as the effect of varying bimetal loading and support modification. At 500 °C, the physicochemical characteristics of the Ni/CeO_2 catalyst revealed that NiO was easily reduced to Ni^0. But, only a small fraction of nickel was reduced in the NiSn(X)/CM11 and NiSn(X)/CM12 catalysts (observed at X=10 and 20 Wt.%) were attributed to the presence of a strong $Ni_xMg_{1-x}O_2$ solid phase, as determined by XRD. Shi et al. [225] reported that NiO interaction with support was higher in Ni/CeO_2-MgO than Ni/CeO_2. Due to the high dispersion of Ni inside the support, the Ni peak was not visible for metal loadings below 10 wt. %. This would result the reduction of Ni-metal particles and increased in the metal's active surface area [392].

It has been demonstrated that adding Mg^{2+} to the CeO_2 support supported and the optimal quantity of Sn as a bimetallic on the Ni surface enhances the stability and activity of the catalyst. Whereas there was an increase in the overall metal loading and degraded the quality of the catalysts. Physico-chemical characterizations (XRD, Raman, SEM, and TEM) showed that adding Mg^{2+} significantly decreased the Ni and CeO_2 particle size. Because the ionic radii of Mg (0.065 nm) were smaller than Ni (0.075 nm), Ce (0.102 nm), and Sn (0.118 nm). This led to a mild variation in lattice strain, which modified the surface morphology of the catalyst. The NiSn(5)CM12 catalyst showed the best H_2 selectivity of 71% and the lowest CO selectivity of 4% and CH_4 selectivity of 7%. According to DTA-TGA, NiSn(5)CM12 catalyst showed the least amount of carbon weight loss (3.2 %), whereas the NiSn(20)/C catalyst showed the highest amount of carbon weight loss 27.3 %. Clearly, the modification of CeO_2 support with Mg controlled the coke deposition on the surface of the catalyst during the reforming process. FESEM surface morphology revealed two forms of fibrous carbon deposited on the catalyst's surface during the SRE. The first type, tiny and less intense, was carbon with an amorphous (disordered) structure. The second type, longer and more intense was graphitic structure fibrous carbon. NiSn(5)/CM12 contained a greater quantity of amorphous (disordered) carbon, as shown by Raman spectroscopy. FESEM detected a greater proportion of graphitic carbon in NiSn(20)/C, which resembles carbon nanotubes/rods with agglomeration particles. Helveg et al. [393] explained that nickel crystal size influences carbon nucleation. Increasing nickel crystal size eventually resulted in an increased graphene layer on the surface of Ni. XPS investigation demonstrated that adding Mg^{2+} to CeO_2 support as a mixed oxide enhanced the concentration of Ce^{3+}, which can be attributed to greater oxygen vacancy (or) OSC. Due to the fact that Mg^{2+} ions accepted the nearby O^{2-} valance bond. Due to the mixed oxide support, the NiSn(5)/CM12 catalyst had a greater ratio of $Ce^{3+}/(Ce^{3+}+Ce^{4+})$ and metallic nickel, which increased the catalytic activity. According to Chengxi et al. [394], the addition of Mg^{2+} reduces nickel particle size and increases OSC. In addition, the strong interaction between nickel and CeO_2-MgO support inhibited the sintering of nickel particles during the reduction process.

Increasing metal loading led to agglomeration of the crystal structure studied by XRD, Raman, and FESEM as the active metal and support particle sizes increases. Increasing NiO particle size weakens the metal-support interaction [233]. Wang et al. [215] reported that higher metal loading cause Ni sintering, which resulted in less active sites on the support surface. Adding a small quantity (Ni:Sn 14:1 atomic ratio) of tin to nickel-metal enhanced H_2 selectivity and reduced carbon formation significantly in the NiSn(5)/CM12 catalyst. Sn helped to minimize the formation of carbon by promoting the water gas shift process. Because group-IV elements Sn and carbon share a tetravalent electronic structure and carbon (2.56), which has a stronger electronegativity than tin (1.96). According to Hengne et al. [395], Sn reduces the methane formation by enhancing methane reforming and also water gas shift reactions, considerably boosts the H_2 selectivity, and reduces carbon production. Pastor et al. [360] reported that Sn makes Ni-Sn alloys, which makes Ni more stable and resistant to sintering.

Increasing Sn content (Ni:Sn 8:1 atomic ratio) affected the textural characteristics and particle size of a nickel and CeO_2 support in a Ni8Sn(5)/CM12 catalyst. Raman analysis showed that the carbon on the catalyst surface was more graphitic as compared to NiSn(5)/CM12; consequently, the weight loss of the catalyst increased, as observed by DTA-TGA. Tian et al. [242] reported that Sn significantly reduces coke deposition, however the addition of more Sn reduces the oxygen storage capacity (OSC). Stroud et al. [383] reported that Sn could probably be found in Ni_3Sn or any other form of Ni-Sn alloy. A large amount of tin would combine with CeO_2 to make a complex form, which could weaken the bond between the nickel and the support. Effect of this rapid sintering made the particles bigger and could also block the active sites of nickel [360] because the higher ionic radii of tin (0.118 nm) than nickel (0.07 nm). Shabaker et al. [343] demonstrated increasing Sn content results decrease Ni active surface area due to geometric effect.

Similar kind of results were reported on Villagran et al. [385] studied Ni(8 wt.%)/$Ce_{0.05}MgAl_2O_4$ catalyst prepared by wet impregnation. After 7 hours of SRE at 600 ℃ temperature with H_2O/EtOH = 2 mole ratio, the catalyst showed H_2 selectivity of 69% with 95% EtOH conversion. However, Ni(8 wt.%)/$Ce_{0.05}MgAl_2O_4$ catalyst showed H_2 selectivity as stable for 4hrs of reaction time before deactivating. Xiao et al. [224] studied Ni(10 wt.%)/$Ce_{0.8}X_{0.2}O_2$ (X= La, Tb, Zr) catalysts prepared by two step impregnation method. The highest hydrogen selectivity of 66% with 100% EtOH conversion was obtained for Ni(10 wt.%)/$Ce_{0.8}La_{0.2}O_2$ catalyst at 500 ℃ reaction temperature and EtOH: H_2O = 1/3 mole ratio. Niazi et al. [237] studied on Ni(X)/CeO_2 (X= 10, 13, 15 wt.%) and Ni(13 wt.%)-Mg(4 wt.%)/CeO_2 catalyst, prepared by simultaneous wet impregnation method. Maximum H_2 selectivity 65% with 80% EtOH conversion has been noticed for Ni(15 wt.%)/CeO_2 with increasing metal loading at 450 ℃, feed H_2O/EtOH 6 mole ratio. At same reaction conditions, Ni(13 wt.%)-Mg(4 wt.%)/CeO_2 showed 70% H_2 selectivity and 83% EtOH conversion. Araiza et al. [216] reported that Ni(10 wt.%)/CeO_2 catalyst prepared by precipitation followed by wet impregnation method. At 400 ℃ temperature, selectivity of H_2, CH_3CHO,

and C_3H_6O was noticed 58, 2, and 5, respectively, at 50% EtOH conversion after 10 hrs reaction. Santander et al. [233] explained Ni(7 wt.%)/$Ce_{0.85}Mg_{0.15}O_2$ catalyst showed the H_2 selectivity 60% with 80% EtOH conversion at 450 ℃ temperature after 16 hrs reaction. Zhang et al. [394] studied on Ni(10 wt.%)/$Ce_{1-x}Mg_xO_2$ (X=0, 0.03, 0.05, 0.07, 0.1, 0.5 mole) catalysts, prepared by citric acid sol-gel method. At 400 ℃ temperature, increasing mole of Mg 0 to 0.1, H_2 selectivity increased 50 to 60% with 100% EtOH. At same reaction conditions, CH_3CHO and CH_3COCH_3 selectivity observed 5, 10% and 10, 30 % for Ni(10)/$Ce_{0.93}Mg_{0.07}O_2$, Ni(10)/$Ce_{0.9}Mg_{0.1}O_2$ catalysts, respectively. These literature results for ethanol steam reforming over different catalysts are summarized in Table 4.6 in terms of selectivity (S) and ethanol conversion (X). Combination of NiSn bimetallic and MgO modified CeO_2 support might have potential as a LTSRE catalysts.

Table 4. 6: Literature data for ethanol steam reforming over different catalysts reported in terms of selectivity (S) and ethanol conversion (X).

Catalyst name	EtOH/ H_2O ratio	Reaction temperature (℃)	H_2 selectivity (X)	Conversion (X)	Ref.
Ni(10 wt.%)/$Ce_{0.8}La_{0.2}O_2$	1/3	500	66	100	[224]
Ni(8 wt.%)/$Ce_{0.05}MgAl_2O_4$	1/2	600	69	95	[385]
Ni(15 wt.%)/CeO_2	1/6	450	65	80	[237]
Ni(13 wt.%)-Mg(4 wt.%)/CeO_2	1/6	450	70	83	
Ni(10 wt.%)/CeO_2	1/3	400	58	50	[216]
Ni(7 wt.%)/$Ce_{0.85}Mg_{0.15}O_2$	1/3	450	60	80	[233]
Ni(10 wt.%)/$Ce_{0.9}Mg_{0.1}O_2$	1/8	400	60	100	[394]
NiSn(5)/CM12	1/12	400	71	100	This work

4.2.6 Conclusions

Ni-Sn/CeO_2-MgO catalysts showed promising results for catalyst activity and low coke deposition for LTSRE. NiSn(5)/CM12 catalyst exhibited the maximum H_2 selectivity of 71% with 100% EtOH conversion and NiSn(20)/C exhibited the lowest H_2 selectivity of 32% with 68% EtOH conversion at 400 ℃ . The addition of Mg^{2+} creates a solid solution $Ni_{1-X}Mg_xO_2$ with Ni as detected by XRD and a stronger metal-support interaction generated as shown by TPR. Thus, Ni particle size reduced, and dispersion improved. MgO in CeO_2 and an optimal amount of Sn probably enhance the oxygen mobility and oxygen storing capacity of the support. MgO also helped to introduce a basic nature (NH_3-TPD showed) in the support. The combination of these increased both catalytic stability and activity. FESEM and DTA-TGA analysis showed deposition of smaller and amorphous nature carbon on NiSn(5)/CM12 catalyst while longer and more intense graphitic fibers were noticed on NiSn(20)/C. Higher metal loading causes active metal and support particle agglomeration, which lead to the weakening of the metal-support interaction, reduced activity, and increases coke deposition.

4.2.7 Supplementary data

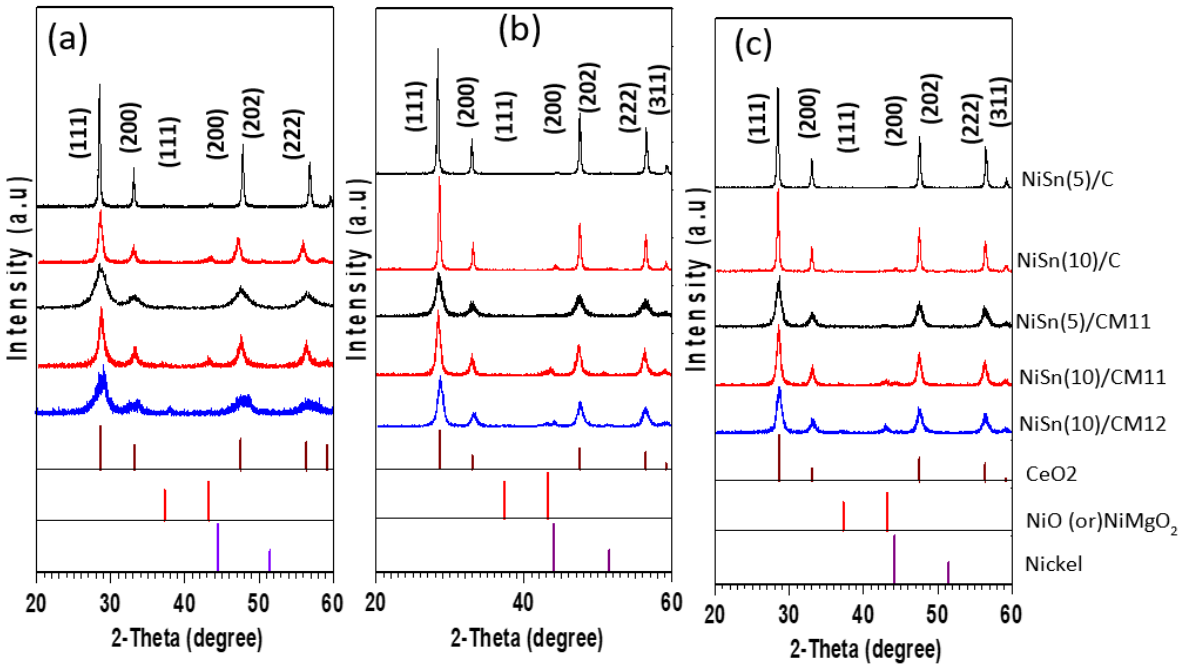

Figure 4. 18: XRD spectra for (a) Fresh(F), (b) Reduced(R), and (c) Spent (S) catalyst, phases identified with the reference PDF files of CeO_2 (PDF#4343161), NiO (PDF#1010095), $NiMgO_2$ (PDF#240712), Nickel (PDF#9013034).

Table 4. 7: CeO_2 lattice strain (Williamson-hall method) through XRD data.

	CeO_2 strain (10^{-3})		
Catalyst Name	**Fresh**	**Reduce**	Spent
NiSn(5)/C	12	10	8
NiSn(10)/C	9	7	6
NiSn(20)/C	8	6	5
NiSn(5)/CM11	35	20	16
NiSn(10)/CM11	17	15	15
NiSn(20)/CM11	14	12	11
NiSn(5)/CM12	45	24	19
NiSn(10)/CM12	33	16	15
NiSn(20)/CM12	17	13	13
Ni(5)/CM12	34	18	14
Ni8Sn(5)/CM12	36	21	17

We used the Williamson-Hall (W-H) plot method [396] given by the relation to calculate CeO_2 lattice strain

$$\beta \cos\theta = 0.89\,\lambda/d + 4\varepsilon \sin\theta \qquad (4.15)$$

where, λ is the wavelength of the X-ray radiation used (λ = 1.5406Å), θ is Bragg angle, d is crystallite size, β is the full width at half-maximum (FWHM) of the Bragg peak and ε is the lattice strain.

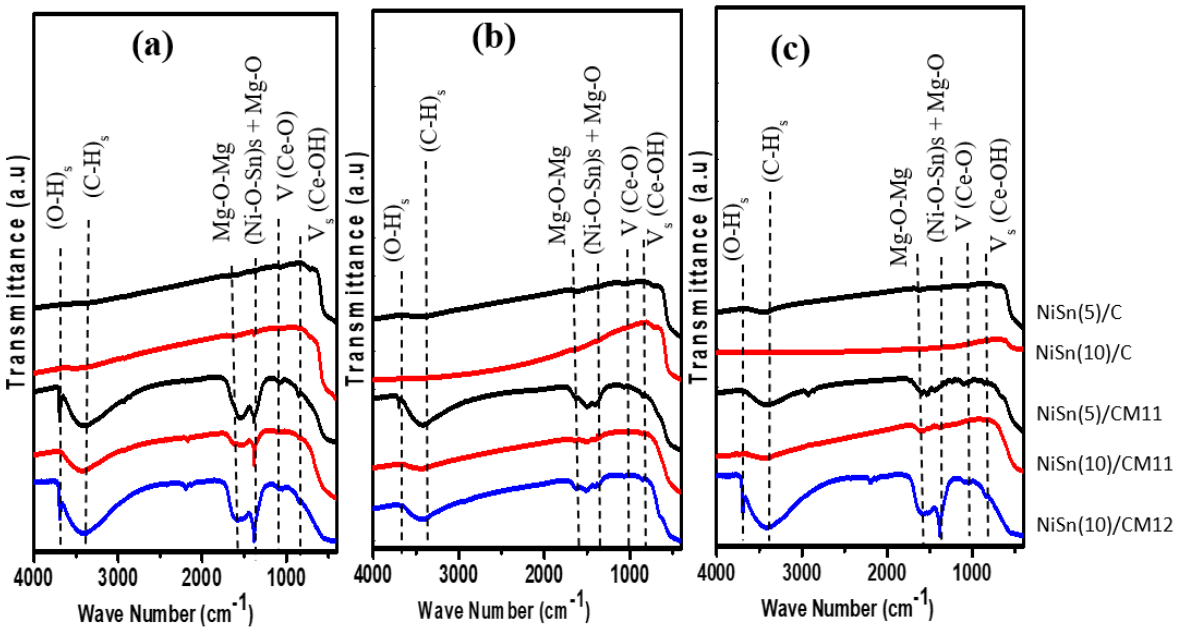

Figure 4. 19: FTIR characterization for (a) Fresh, (b) Reduced, (c) Spent catalyst.

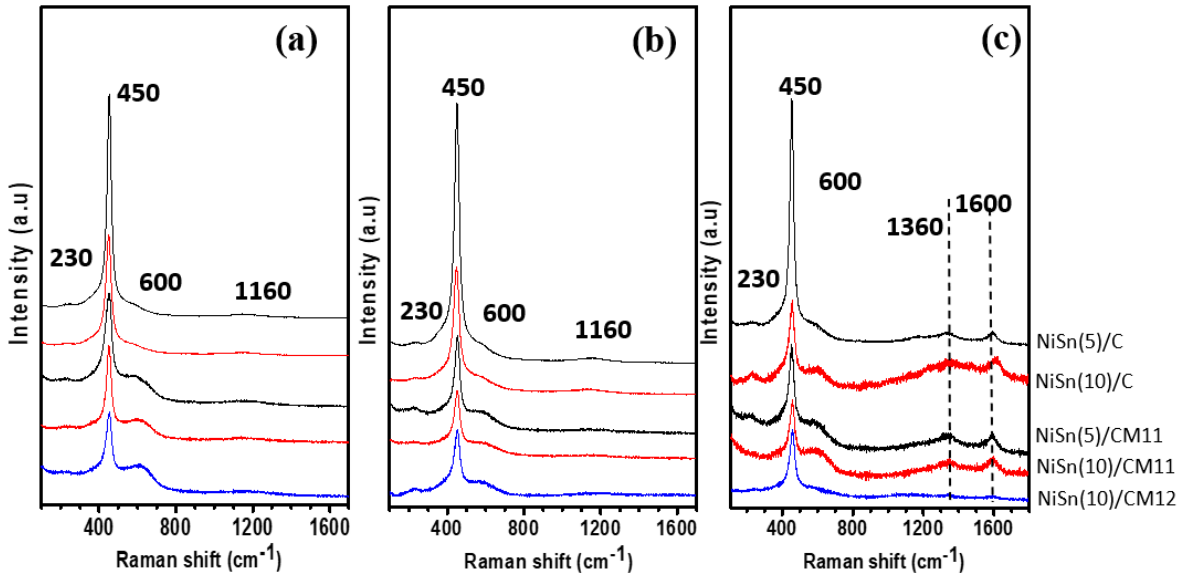

Figure 4. 20: Raman characterization for (a) Fresh, (b) Reduced, (c) Spent catalyst.

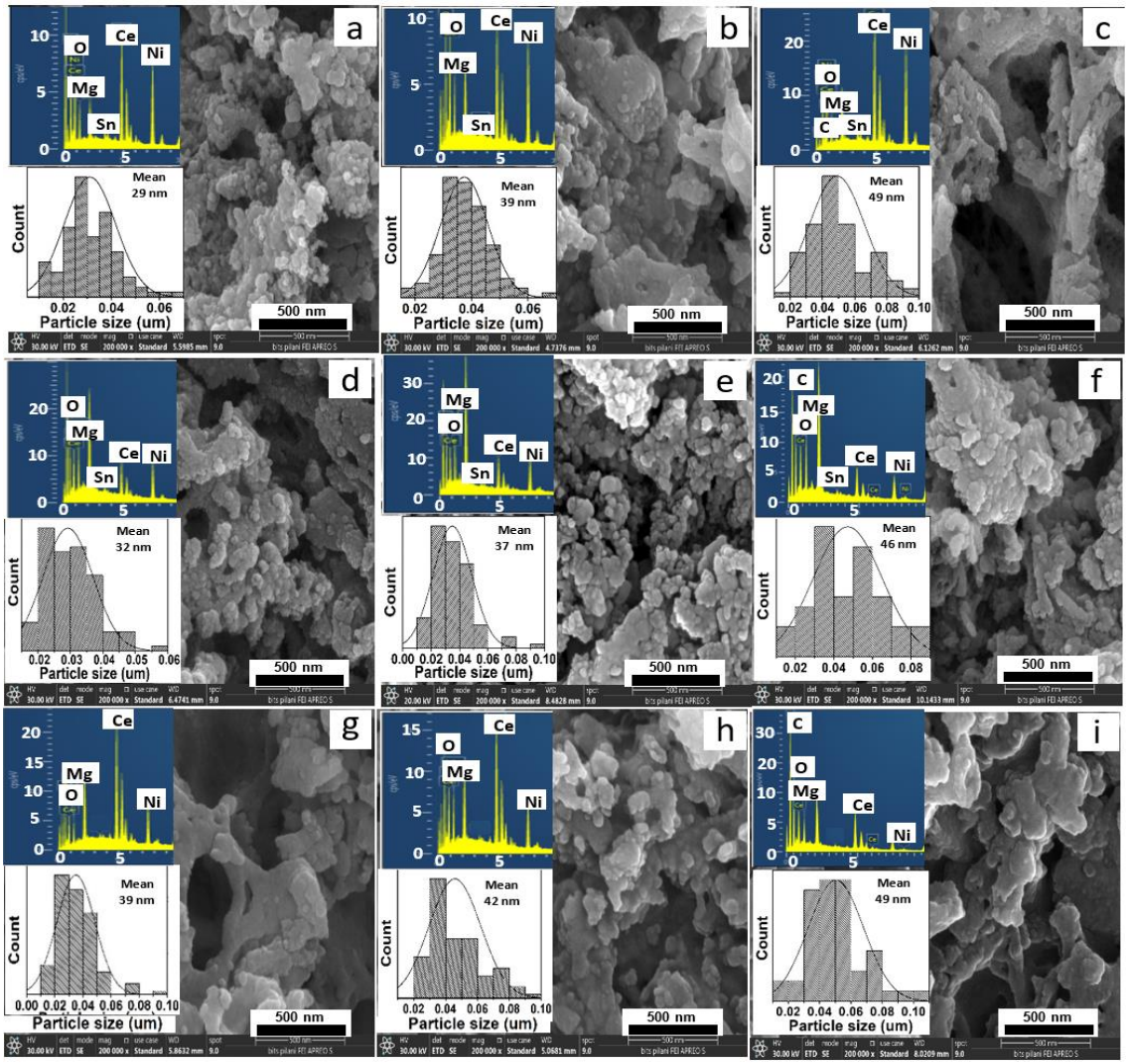

Figure 4. 21: FESEM images with particle size distribution and EDX spectrum for NiSn(20)/CM12 [(a) fresh, (b) reduce, (c) spent], Ni8Sn(5)/CM12 [(d) fresh, (e) reduce, (f) spent] and Ni(5)/CM12 [(g) fresh, (h) reduce, (i) spent] catalysts **.**

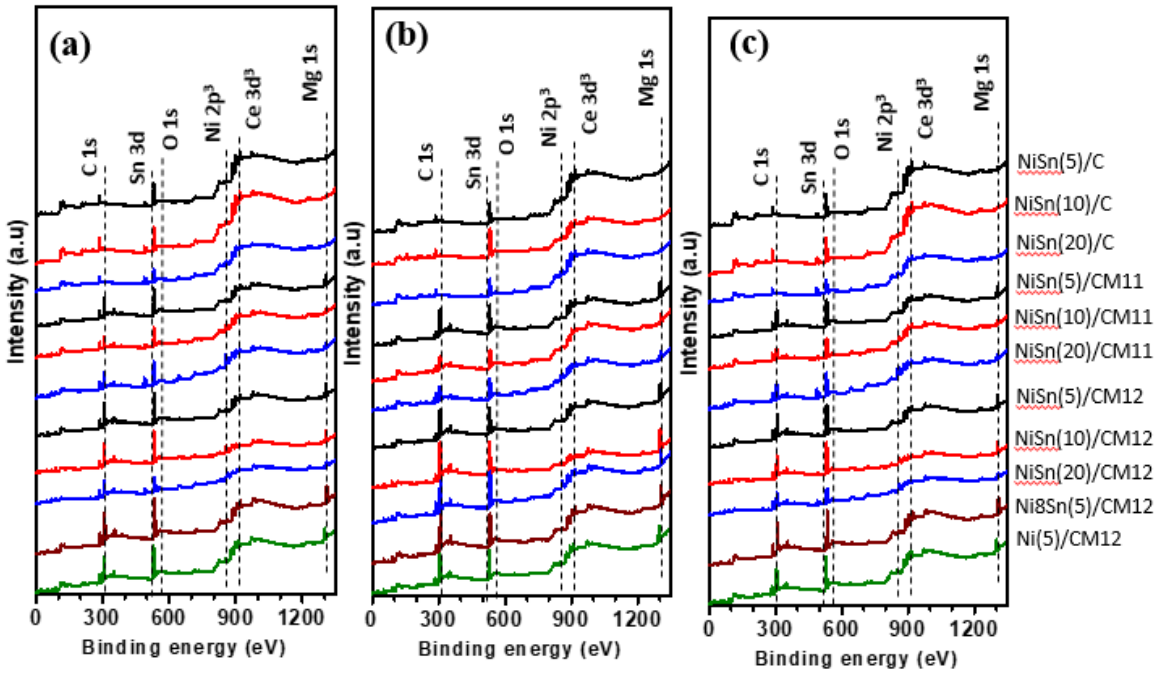

Figure 4. 22: Wide scan XPS spectra of a) Fresh, b) Reduce, c) Spent samples.

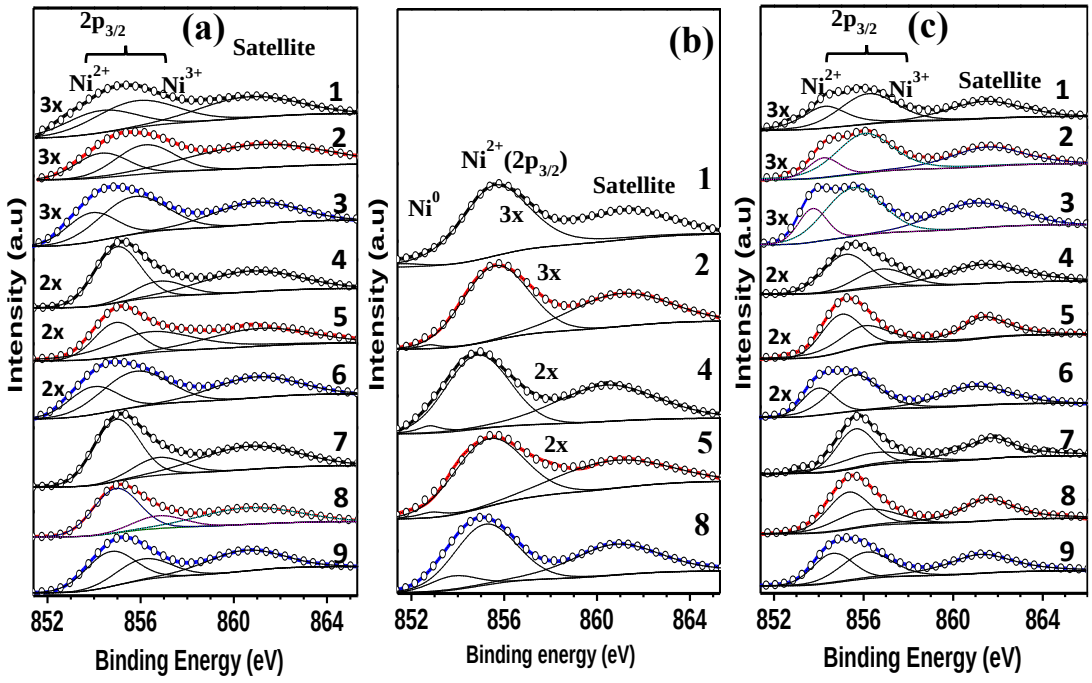

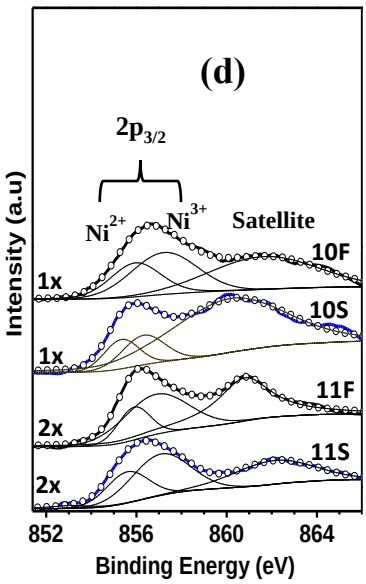

Figure 4. 23: High resolution XPS spectra of nickel a) fresh (F), b) reduce (R), c) spent (S) samples for 1. NiSn(5)/C, 2. NiSn(10)/C, 3. NiSn(20)/C, 4. NiSn(5)/CM11, 5. NiSn(10)/CM11, 6. NiSn(20)/CM11, 7. NiSn(5)/CM12, 8. NiSn(10)/CM12, 9. NiSn(20)/CM12 catalysts and d) fresh (F) and spent (S) of 10. Ni(5)/CM12 and 11.Ni8Sn(5)/CM12 catalysts.

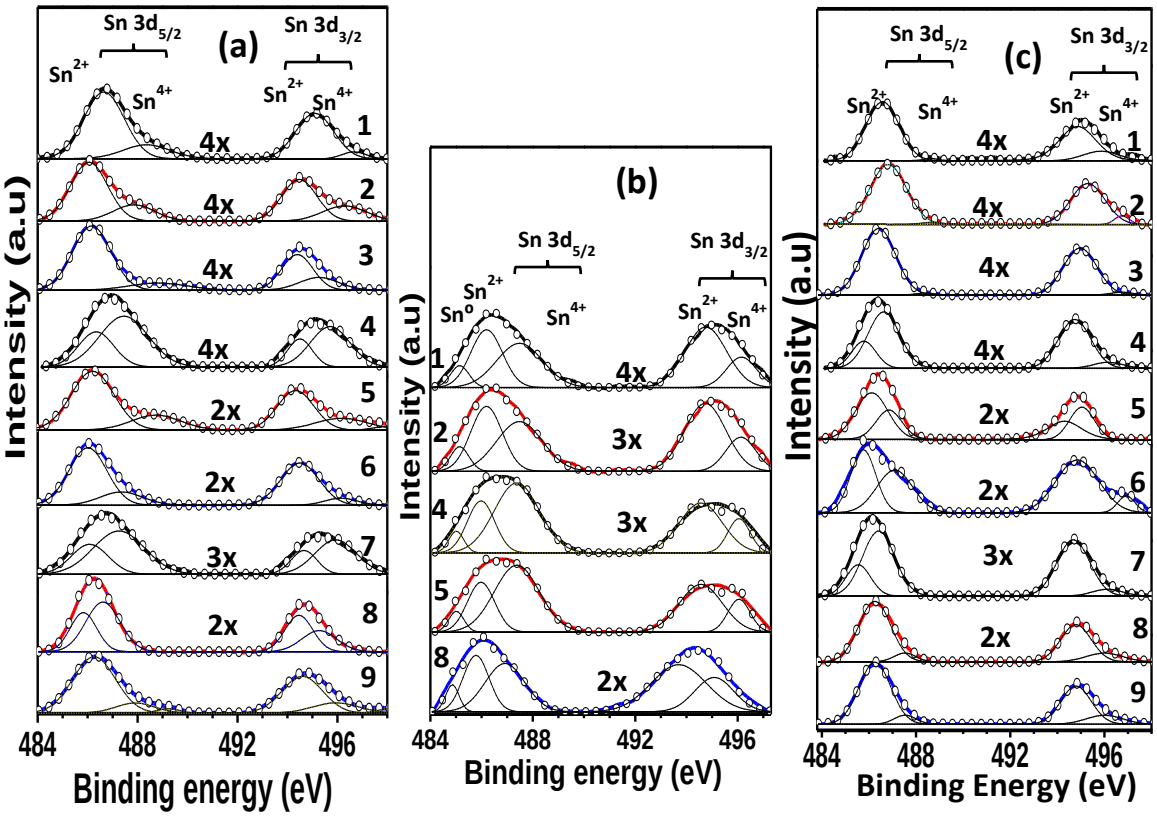

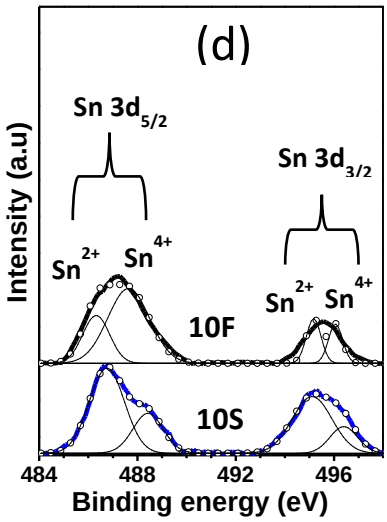

Figure 4. 24: High resolution XPS spectra of tin a) fresh (F), b) reduce (R), c) spent (S) samples for 1. NiSn(5)/C, 2. NiSn(10)/C, 3. NiSn(20)/C, 4. NiSn(5)/CM11, 5. NiSn(10)/CM11, 6. NiSn(20)/CM11, 7. NiSn(5)/CM12, 8. NiSn(10)/CM12, 9. NiSn(20)/CM12 catalysts and d) fresh (F) and spent (S) of 10. Ni(5)/CM12 catalyst.

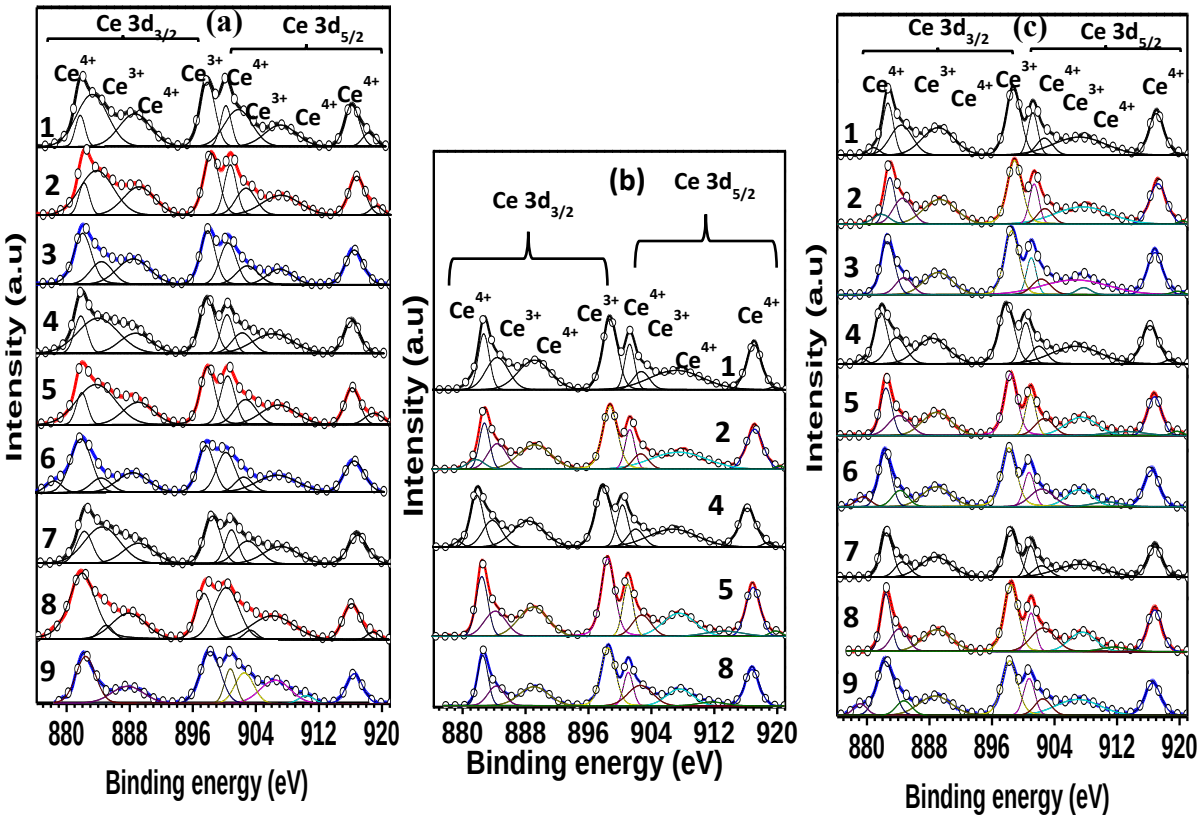

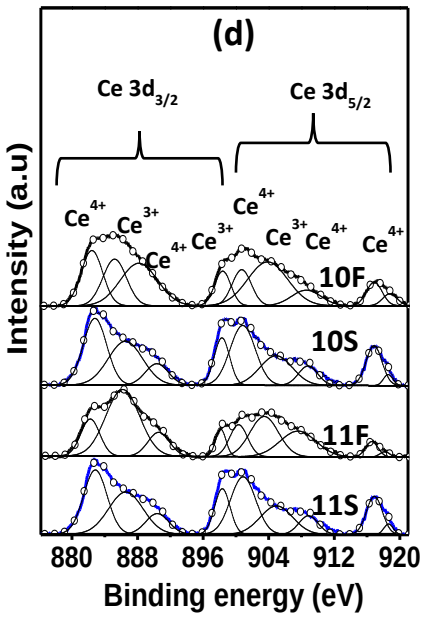

Figure 4. 25: High resolution XPS spectra of Cerium a) fresh (F), b) reduce (R), c) spent (S) samples for 1. NiSn(5)/C, 2. NiSn(10)/C, 3. NiSn(20)/C, 4. NiSn(5)/CM11, 5. NiSn(10)/CM11, 6. NiSn(20)/CM11, 7. NiSn(5)/CM12, 8. NiSn(10)/CM12, 9. NiSn(20)/CM12 catalysts and d) fresh (F) and spent (S) of 10. Ni(5)/CM12 and 11.Ni8Sn(5)/CM12 catalysts.

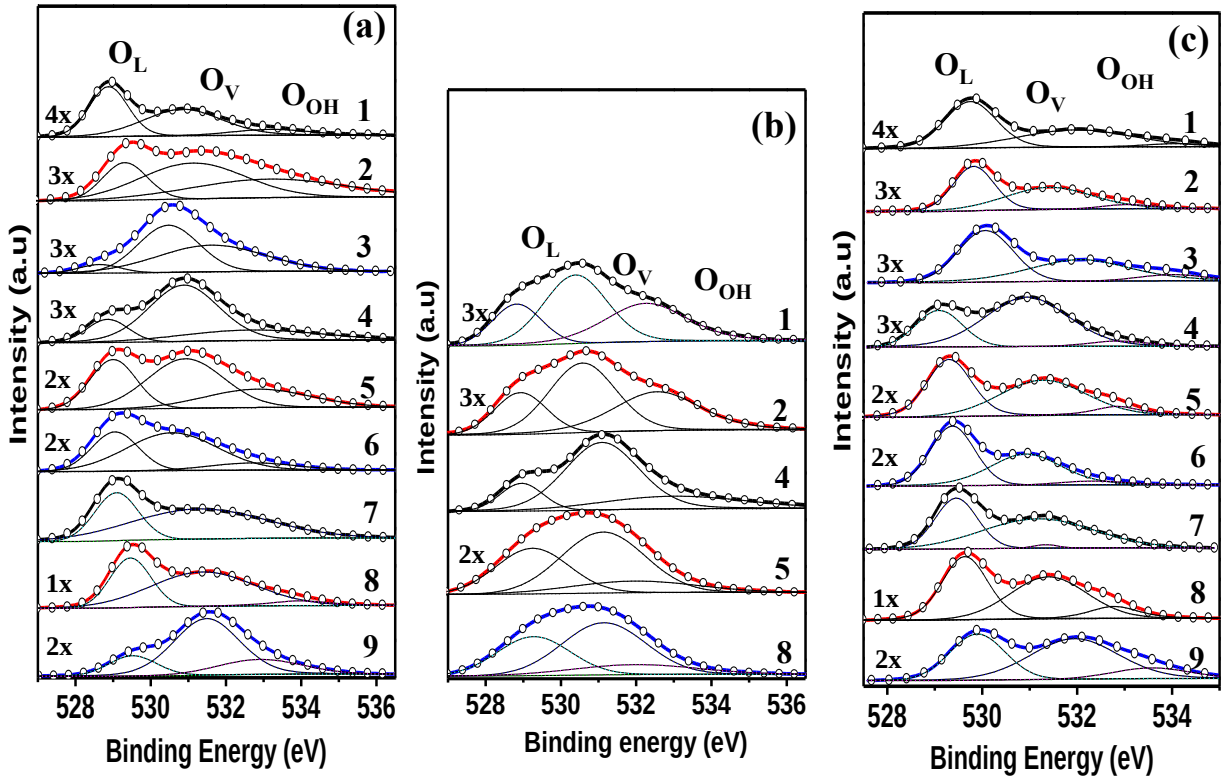

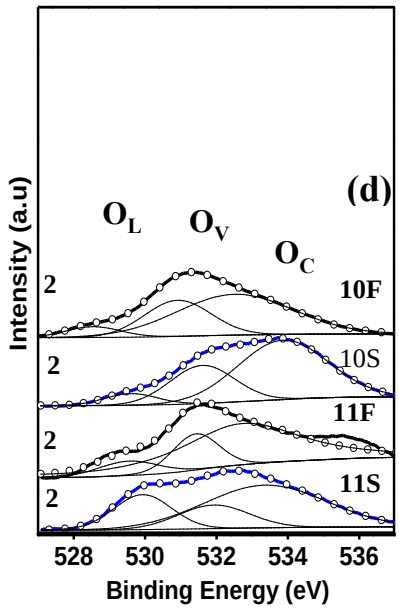

Figure 4. 26: High resolution XPS spectra of oxygen a) fresh (F), b) reduce (R), c) spent (S) samples for 1) NiSn(5)/C, 2) NiSn(10)/C, 3) NiSn(20)/C, 4) NiSn(5)/CM11, 5) NiSn(10)/CM11, 6) NiSn(20)/CM11, 7) NiSn(5)/CM12, 8) NiSn(10)/CM12, 9) NiSn(20)/CM12 catalysts and d) fresh (F) and spent (S) of 10) Ni(5)/CM12 and 11) Ni8Sn(5)/CM12 catalysts.

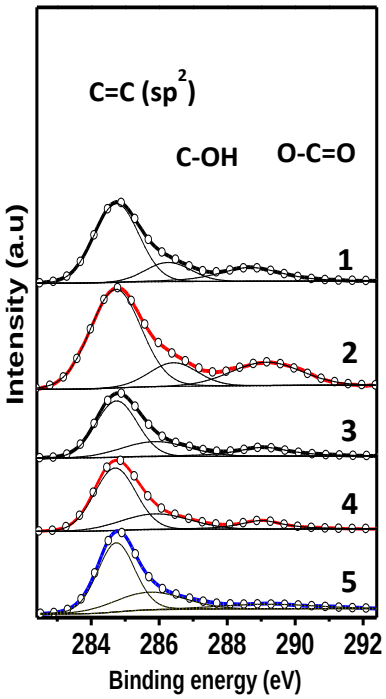

Figure 4. 27: High resolution XPS spectra for carbon Spent catalyst of 1) NiSn(5)/C, 2) NiSn(10)/C, 3) NiSn(5)CM11, 4) NiSn(10)/CM11, and 5) Ni8Sn(10)/CM12 catalyst.

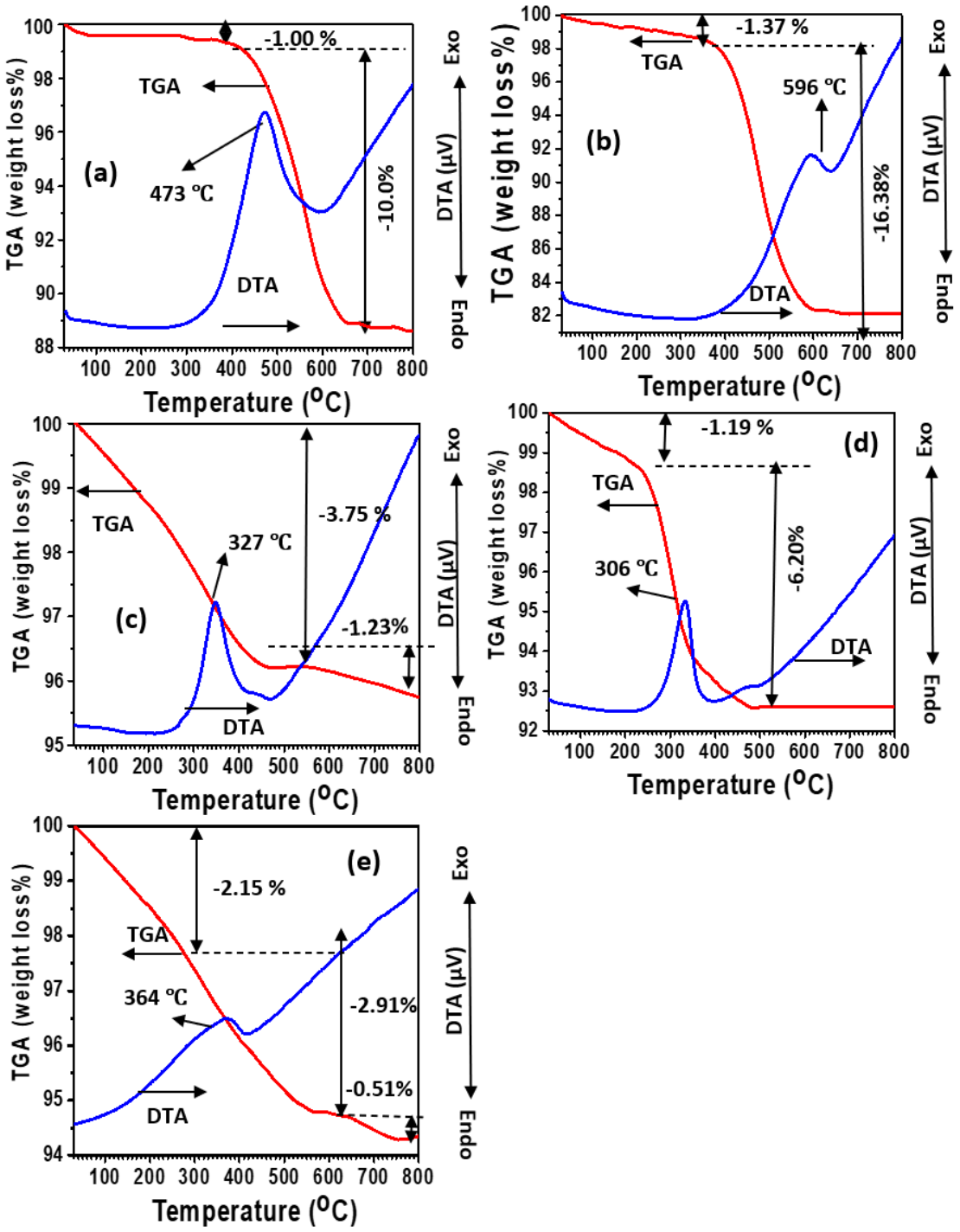

Figure 4. 28: DTA/TGA for (a) NiSn(5)/C, (b) NiSn(10)/C, (c) NiSn(5)/CM11, (d) NiSn(10)/CM11 and (e) NiSn(10)/CM12 catalyst.

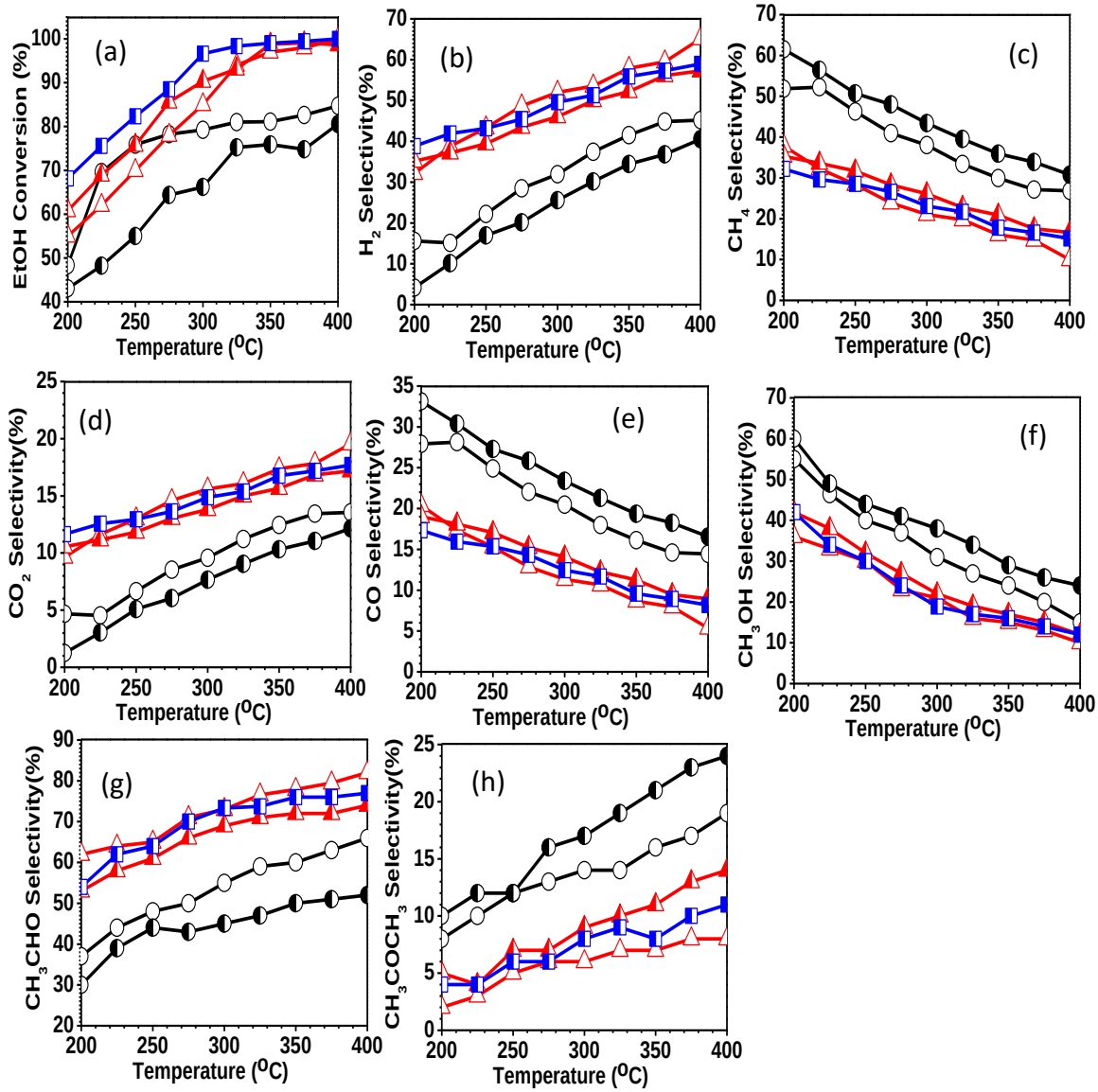

Figure 4. 29: Catalytic activity as a function of temperature (200-400 ^{o}C) of (a). Ethanol conversion, (b).Hydrogen (H_2), (c). Methane (d). Carbon dioxide, (e).Carbon monoxide, (f).Methanol, (g).Acetaldehyde, (h).Acetone, for NiSn(5)/C (◯), NiSn(10)/C (◐), NiSn(5)/CM11 (△), NiSn(10)/CM11(◭), NiSn(10)/CM12 (◧) catalysts low temperature steam reforming of EtOH : water 1:12 mole ratio.

4.3 Tin and Lanthanum Modified Ni/CeO_2 Catalyst Systems for Low Temperature Steam Reforming of Ethanol

4.3.1 Highlights

- Effect of Sn, metal loading, La_2O_3 on NiSn/CeO_2 catalysts is investigated for LTSRE.
- Ce-La-O support and optimum Sn reduce particle size and enhance oxygen vacancies.
- $Ni_{0.93}Sn_{0.07}(5)/Ce_{0.67}La_{0.33}O_2$ shows highest ethanol conversion & H_2 selectivity.
- La and optimum Sn help in reducing carbon deposition on spent catalysts.
- High metal loading (20 wt.%) reduces catalytic activity & stability.

4.3.2 Introduction

The world population is projected to increase from 7.3 billion in 2021 to 9.7 billion by 2050 [1]. According to the world energy statistics report-2022, 80% of the current energy demand is produced from fossil fuels [2]. The International Energy Outlook 2021 (IEO 2021) anticipates that the global energy consumption will increase nearly 50% by 2050 from 595 exajoules (EJ) utilization in 2021, as a result of the accelerated growth of the world's population [5]. Per day consumption rate of petroleum and other liquid fuels, in terms of million barrels is estimated to increase from 77 in 2021 to 115 in 2050 [5]. However, the average consumption of fossil fuels increases by 1.3% every year, resulting in a significant increase in environmental pollution. According to the United Nations Environmental Report of 2022, the amount of greenhouse gases (GHG) in the atmosphere has reached 54 gigatonnes (Gt), which has resulted the global temperature increase by 2.8 ℃ [397]. The international energy agency (IEA) designs a polices to reduce 50% of the GHG emissions by 2050 and mitigate global warming [398]. This can be possible with the usage of renewable energy sources like wind, solar, hydrogen (H_2), biomass, etc.

H_2, with energy density (120 MJ/kg) three times higher than the gasoline (43 MJ/Kg) has potential to satisfy the current energy demand [399]. Many thermochemical processes, like combustion, gasification, pyrolysis, liquefaction, steam reforming, aqueous phase reforming, etc., could be used to produce hydrogen from biomass derived hydrocarbons. In comparison to other processes, steam reforming (SR) accounts for almost half (48%) of the world's hydrogen production [16]. Numerous researches explore various resources, including biodiesel, glycerol, ethane, propane, butane, natural gas, and alcohols, for H_2 production [252,361,372,392,400–402]. Ethanol (EtOH) could be considered a good renewable resource for H_2 production, because it has relatively high hydrogen content (C:H =1:3), non-toxicity, low production cost, good availability, and easy of handling [45]. Currently, India is the fifth largest EtOH producer in the world with production rate 830 million gallons per year [23]. Compared to standard high temperature (500 - 1000

℃) steam reforming, low temperature (200-450 ℃) steam reforming of ethanol (LTSRE) is highly favorable for increasing H_2 selectivity by reducing CO and methane (CH_4) production [286].

Nickel is an abundant and inexpensive metal and several studies have found that, Ni could be an active catalyst for H_2 production by LTSRE, due to its great capability of C-C and C-H bonds breakage [32,45,107,353,355]. However, the Ni catalysts are heavily prone to deactivation.

Catalyst deactivation can occur through four mechanisms [45]: carbon deposition, active metal sintering, metal oxidation, and catalyst poisoning. Secondary reactions of the intermediates, such as Boudouard reaction (Supplementary Eq. (4.40)) & reverse carbon gasification below 400 ℃, and methane decomposition (Supplementary Eq. (4.39)) above 600 ℃ are the major contributors for carbon deposition [45,403]. High temperature conditions may cause active metal agglomeration or sintering, which irreversibly reduces active sites. Nickel catalysts are susceptible to both carbon deposition (various forms: amorphous, filamentous, and graphitic) and sintering during reforming reaction. Amorphous carbon encases the active metal and indirectly deactivates the catalyst. Filamentous carbon is formed through continuous precipitation of carbon on Ni particles. Eventually this carbon diffuses and dissolutes in the Ni lattice leading to the formation of nickel carbide (Ni_3C) [392,404]. Ni_3C promotes the nucleation and growth of filamentous carbon. While filamentous carbon migration may not directly cause catalyst deactivation, it can block the catalyst bed due to continuous accumulation [45,405]. The build-up of graphitic carbon can completely deactivate the catalyst, necessitating replacement or regeneration to restore activity [406,407]. Sintered Ni particles can be oxidized to form NiO and diminishes catalytic activity [226,251]. The Ni surface can also be poisoned by impurities present in ethanol, such as fusel alcohols, acetic acid, sulfur, and ethyl acetate, resulting in catalytic deactivation. These processes collectively contribute to the loss of catalyst performance [45,406,408].

The addition of Sn in Ni reported to augment the catalytic performance of Ni [45,242,382,409]. According to pastor et al. [360] the elements of period V (Sn, Pb, etc.) may interact with period IV elements (such as Ni) and improve their catalytic activity. According to the research articles published by Dumesic's group, addition of Sn in Ni improves the H_2 selectivity of catalyst by lowering the alkanes selectivity (precursors of the coke formation) [84,382,410]. Shabaker & Dumesic et al. [343] modify Ni/Al_2O_3 catalyst with different atomic ratios of Sn (Ni_4Sn, $Ni_{270}Sn$, $Ni_{14}Sn$, and NiSn) and study those for the aqueous phase reforming of ethylene glycol. $Ni_{14}Sn$ catalyst demonstrates the highest H_2 selectivity. In a previous publication the effect of CeO_2 support modification with basic nature MgO on LTSRE over $Ni\text{-}Sn/CeO_2$ catalysts has been deliberated [251].

Proper selection of the support may further enhances its catalytic activity & coke resistance capacity, and reduces sintering tendency [411–413]. Ceria has been widely used as a support due to several reasons. The foremost reason is that the transition between Ce^{3+} and Ce^{4+} ions is fast and easy, which

increases oxygen storage/release capacity (OSC) of CeO_2 [414,415]. This OSC of CeO_2 leads to high water gas shift reaction rate of the catalyst [415], and boosts catalytic activity in ethanol reforming. Addition of Ni in CeO_2 may create extra oxygen vacancy ($V_o^{\cdot\cdot}$), as explained by Kröger-Vink notation equation 4.8 [318].

But, CeO_2 has low thermal stability [411,416]. Modification of CeO_2 by other metal oxide such as ZrO_2, La_2O_3, Pr_2O_3, Mn_2O_3, Al_2O_3 or MnO_2 forms solid solution, inhibits sintering of CeO_2, and improves catalytic activity [45,226,408,411,415]. Chen et al. apply clay supported Ni(2.5 wt.%)-Ce(2.5 wt.%)-Zr/attapulgite catalysts for ESR [417,418]. Additionally, lanthanum oxide in Ni/CeO_2 enhances metal-support interaction, nickel dispersion, and catalyst basicity [406,407,414,415,419]. However, excess amounts of La^{3+} may decrease the active surface area and oxygen mobility through the support lattice [408,419].

Greluk et al. [243] compared the ethanol steam reforming activity of the Ni(10 wt.%)-La(2 wt.%)/CeO_2 & Ni((10 wt.%)/CeO_2 catalysts synthesized by co-impregnation method. Addition of 2 wt.% La in Ni(10 wt.%)-La(2 wt.%)/CeO_2 catalyst decreased the nickel particle size from 12 to 9 nm, & carbon formation rate from 366 to 203 mg/$g_{cat.}$h, however both the catalysts showed the same H_2 selectivity (78%) and ethanol conversion (100%) at 420 ℃ and H_2O:EtOH molar ratio 12:1.

Liu et al. [223] compared the activity of the Ni(10 wt.%)/$Ce_{0.55}La_{0.45}O_2$ catalysts prepared by two different procedures; citrate complexing and impregnation methods. The Ni(10 wt.%)/$Ce_{0.55}La_{0.45}O_2$ catalyst prepared by citrate complexing method show better activity in terms of H_2 selectivity 66% and EtOH conversion 84% at 400 ℃.

According to the knowledge of the authors, no article has been published on the LTSRE study over the Ni-Sn/Ce-La-O catalysts so far. The present paper focuses on the application of Ni-Sn/Ce-La-O catalysts, prepared by ultrasonication assisted solution combustion synthesis (SCS) method, for H_2 production by LTSRE. The effects of varying total metal loading, Ce: La mole ratio, and Ni:Sn ratio on LTSRE is investigated. The catalytic activities are investigated between 200 and 400 °C, at a feed flow rate of 0.1 ml/min, and an ethanol to water mole ratio of 1:12. The catalytic activity results are correlated with the physicochemical characteristics of the Ni-Sn/Ce-La-O powders.

4.3.3 Experimental

The methods for catalyst preparation, characterization, and the catalytic activity study were explained in a previous publication [251].

4.3.3.1 Catalyst preparation

Single pot ultrasonication assisted solution combustion synthesis (SCS) method was used to synthesize the catalysts (**Fig. 3.9 & 3.10**). Stoichiometric amounts of the precursors; nickel nitrate hexahydrate [$Ni(NO_3)_2.6H_2O$, qualikems(QLS), 98%], tin chloride [$SnCl_2.2H_2O$, molychem, 97%], cerium nitrate [$Ce(NO_3)_3.6H_2O$, QLS, 99.9%], lanthanum nitrate [$La(NO_3)_3.6H_2O$, SRL chemicals, 99%], and glycine [$C_2H_5NO_2$, molychem, 99%], as an oxidizer to fuel ratio 1:1 were mixed thoroughly with ethanol in a 500 ml beaker. The translucent slurry mixture was air-dried at ambient temperature for 24 hrs, followed by heated to 300 ℃ on a hot plate in a fume hood. The mixture ignited on its own in one spot and quickly spread throughout the beaker. The resulting material was washed with DI water to remove unreacted salts and fuel before drying at 60 ℃ for 12 hrs. The dry powders were referred to as the "fresh catalysts." Total 10 catalysts were prepared, and the nomenclature of those catalysts were decided based on Ce:La molar ratio in support (C, CL21, CL11 and CL12 for the CeO_2, $Ce_{0.67}La_{0.33}O_2$, $Ce_{0.5}La_{0.5}O_2$ and $Ce_{0.33}La_{0.67}O_{1.33}$ supports, respectively), metal composition (N14S1, N7S1, N1S1 for the metal composition Ni:Sn =14:1, 7:1, & 1:1 atomic ratio, respectively), and total metal loading (5, and 20 wt.%). Hence the Ni14Sn1(5)/$Ce_{0.5}La_{0.5}O_2$ sample was named N14S1(5)/CL11. The name and formula of the catalysts are mentioned in **Table 4.8.**

4.3.3.2 Catalyst characterization

To determine the phase composition and crystalline size, the X-ray diffraction (XRD) analysis of the powders was executed using a Rigaku miniflex-II (λ = 1.54 Å, 30 kV and 15 mA) diffractometer. The samples were scanned throughout the 2 theta (2Θ) range of 20-60º at a rate of 2º/min. Quantitative elemental analysis of the fresh catalysts was carried by using an inductively coupled plasma optical emission spectroscopy (ICP-OES) instrument (Perkin Elmer Optima 7000 DV with Auto sampler S10 Series) under nebulizer pressure 2.4 bar, sample flow rate 1.0 mL min^{-1}, and flushing time of 15 s. The calibration charts for Ni, Sn, Ce, and La elements were constructed using 1, 5, 10, 15, and 20 ppm solutions of $Ni(NO_3)_2.6H_2O$, $SnCl_2.2H_2O$, $Ce(NO_3)_3.6H_2O$, $La(NO_3)_3.6H_2O$ precursors, respectively in 5% aqueous solution of HNO_3. Approximately 2 mg of each catalyst was ground and dissolved in 5% HNO_3, making up the volume to 100 ml.

The H_2-temperature-programmed reduction (TPR) and temperature-programmed desorption of ammonia (NH_3-TPD) and carbon dioxide (CO_2-TPD) of the samples were studied using a Micromeritics Autocheme II 2920 system with a thermal conductivity detector (TCD). TPR was performed with 15 Vol% H_2/Ar mixture, at a flow rate of 50 cc/min, and increasing the temperature of the linearly at a constant heating rate of 10 ℃ per minute up to 700 ℃. A thermocouple placed in the bed monitors the temperature For NH_3-TPD or CO_2-TPD 40-120 mg sample was degassed at 500ºC with a ramp rate of 10ºC/min in 50

cm^3/min He flow. It was then cooled down to 80°C under the same flow rate of He. The absorption of ammonia was carried out with 10% ammonia in helium at a flow rate of 50 cm^3/min for 1 hour. Similarly for CO_2-TPD 15 cm^3/min of pure CO_2 mixed in 25 cm^3/min pure helium was flown over the sample for 1 hour. TPD analysis was then performed by heating the sample to 600 °C using ramp rate of 15 °C/min.

Raman spectroscopy (Horiba LabRam HR spectrometer, Model 171) data was acquired using an Argon laser at 532 nm. Surface morphology, particle size, and elemental analysis were carried out with the help of a FESEM (Nova Nano FE-SEM 450 (FEI), Oxford Equipment, UK) instrument combined with an X-ray energy dispersive spectrometer (EDX). A tiny amount of sample was sprinkled on the double-sided carbon tape pasted on a FESEM sample mount and coated by using gold to improve sample electrical conductivity and prevent charging during imaging. Transmission electron microscopy analysis was carried out by using a Talos Arctica Cryo, 200 keV instrument. A pinch of powder was homogeneously dispersed in ethanol by ultrasonication, and one or two drops of this suspension was placed on a copper grid.

Wide scan X-ray photoelectron spectroscopy data (between 0 – 1200 eV) was collected using an Al Kα monochromatic source (XPS, Thermo fisher scientific Pvt. Ltd, U.K.). The high-resolution spectra of the elements C(1s), Ce(3d), La(3d), Ni(2p), Sn(3d), and O(1s) were acquired for qualitative and quantitative analysis of the various metals/metal-oxides. For deconvolution of the XPS spectra, XPSPeak4.1 software and the Shirley method were used.

Microtrac Bel, BEL SORP mini-II instrument was used for measuring surface area, pore diameter, and pore volume in catalysts by N_2 gas adsorption-desorption method. Samples were heat treated at 200 °C for 2 hrs in order to clean the surface before characterization. S-DTGA (SHIMADZU, Model: DTG-60H) was carried out between 30 and 800 °C with a heating and cooling rate of 10 °C/min under air flow rate 10 ml/min.

The catalyst activity test was conducted for 20 h TOS at each temperature from 200 – 400 °C with interval of 50 °C and the catalytic activity procedure discussed in section 4.1.3.3.

4.3.4 Results

Here, we have discussed the most efficient and inefficient catalysts in terms of activity and modification. N14S1(5)/CL21 catalyst was shown to be most efficient, whereas N14S1(20)/CL11 catalyst was the most inefficient. The effects of support modification at constant metal loading were explained for N(5)/C, N(5)/CL21, N14S1(5)/CL11, N14S1(5)/CL12 catalysts. The N14S1(5)/CL11 and N14S1(20)/CL11 catalysts explained the metal loading effect. The effect of tin composition can be understood by N(5)/CL21, N14S1(5)/CL21, N7S1(5)/CL21, N1S1(5)/CL21 catalysts.

4.3.4.1 Catalytic Activity Study

Figure 4.30 and supplementary **Fig. 4.40** illustrates the steady state catalytic activity at various reaction temperatures between 200-400 ℃ in terms of ethanol conversion (%), selectivity (%) of the gaseous (H_2, CO_2, CO, CH_4) and liquid (CH_3CHO, CH_3OH, and CH_3COCH_3) products at feed concentration of EtOH:H_2O molar ratio 1:12, and feed flow rate 0.1 ml/min.

Low-temperature steam reforming (200-400 ℃) (LTSR) has a high selectivity towards hydrogen. WGS (Supplementary Eq. (4.31)) and boudouard reactions (Supplementary Eq. (4.40)) are thermodynamically more favorable at low temperature, which reduce production of carbon monoxide [45,231,420]. With increasing temperature conversion of ethanol and selectivity of H_2 and CO_2 increase, while selectivity of CO and CH_4 decrease, which could be possible due to favorable ethanol dehydration (Supplementary Eq. (4.27)) and methane steam reforming (Supplementary Eq. (4.29, & 4.30)) [45,231]. Addition of La upto 33% in cerium support (Ce:La mole ratio 2:1) enhances the ethanol conversion and selectivity of H_2 and CO_2, but further increasing La^{3+} concentration initially decreased and then increased the ethanol conversion and selectivity of H_2 and CO_2 [85,182]. Adding small amount of tin (Ni:Sn atomic ratio = 14:1) improved the ethanol conversion and selectivity of H_2 and CO_2, however ethanol conversion and selectivity of H_2 and CO_2 decreased with further increasing tin composition [360,382,410].

The substitution of 33 atomic % of cerium by La in the N(5)/C catalyst increased the H_2 and CO_2 selectivity from 32 to 36% and 7 to 8%, lowered the CO selectivity from 21 to 19%, and increased the EtOH conversion from 68 to 86%, at 400 ℃. Furthermore, by adding a little quantity of tin in nickel (Ni:Sn atomic ratio = 14:1) into N(5)/CL21 catalyst, the selectivity of H_2 and CO_2 increased significantly from 36 to 60 % and 8 to 14%, selectivity of CO was massively reduced from 19 to 8% and EtOH conversion increased from 86 to 100%. Addition of 50 atomic% La in ceria support at constant metal (5 wt.%) loading, reduce the H_2 and CO_2 selectivity from 60 to 48%, and 14 to 10% , respectively while the selectivity of CO raised from 9 to 15%, and the EtOH conversion reduced from 100 to 87%. Further increase of La to 67 atomic % in N14S1(5)/CL11, the selectivity of H_2 and CO_2 selectivity increased from 48 to 58%, and 10 to 13% respectively, and CO decreased from 15 to 11% and EtOH conversion increased 87 to 100%, respectively. As the metal loading increased from 5 to 20 wt.%, conversion of ethanol, and H_2 and CO_2 selectivity decreased, and CO selectivity increased at constant support and metal (Ni:Sn atomic ratio 14:1) composition.

Based on the activity results, we have chosen N14S1(5)/CL21 catalyst to study the effect of nickel tin composition. The H_2 and CO_2 selectivity dropped from 60 to 46% and 14 to 9% respectively, CO selectivity increased from 9 to 16% and EtOH conversion decreased 100 to 85 % with increased Sn composition from Ni:Sn 14:1 [N14S1(5)/CL21] to 1:1 [N1S1(5)/CL21] atomic ratio.

In liquid products, increasing temperature enhanced the selectivity of acetaldehyde (CH_3CHO) **(Fig. 4.30 (f))** and acetone (CH_3COCH_3) (**Fig. 4.30 (g)**), whereas methanol (CH_3OH) followed the opposite trend (**Fig. 4.30 (h)**), this could be possible due to ethanol dehydrogenation (supplementary Eq. (4.27)) and condensation (supplementary Eq. (4.36)) [189,403,421,422]. CH_3CHO selectivity increased from 40 to 46% and CH_3COCH_3 decreased from 35 to 32% with incorporation of 33 atomic% La into N(5)/C catalyst and CH_3CHO selectivity further increased from 46 to 74% and CH_3COCH_3 decreased from 32 to 17% with addition of tin (Ni:Sn 14:1) into N(5)/CL21 catalyst.

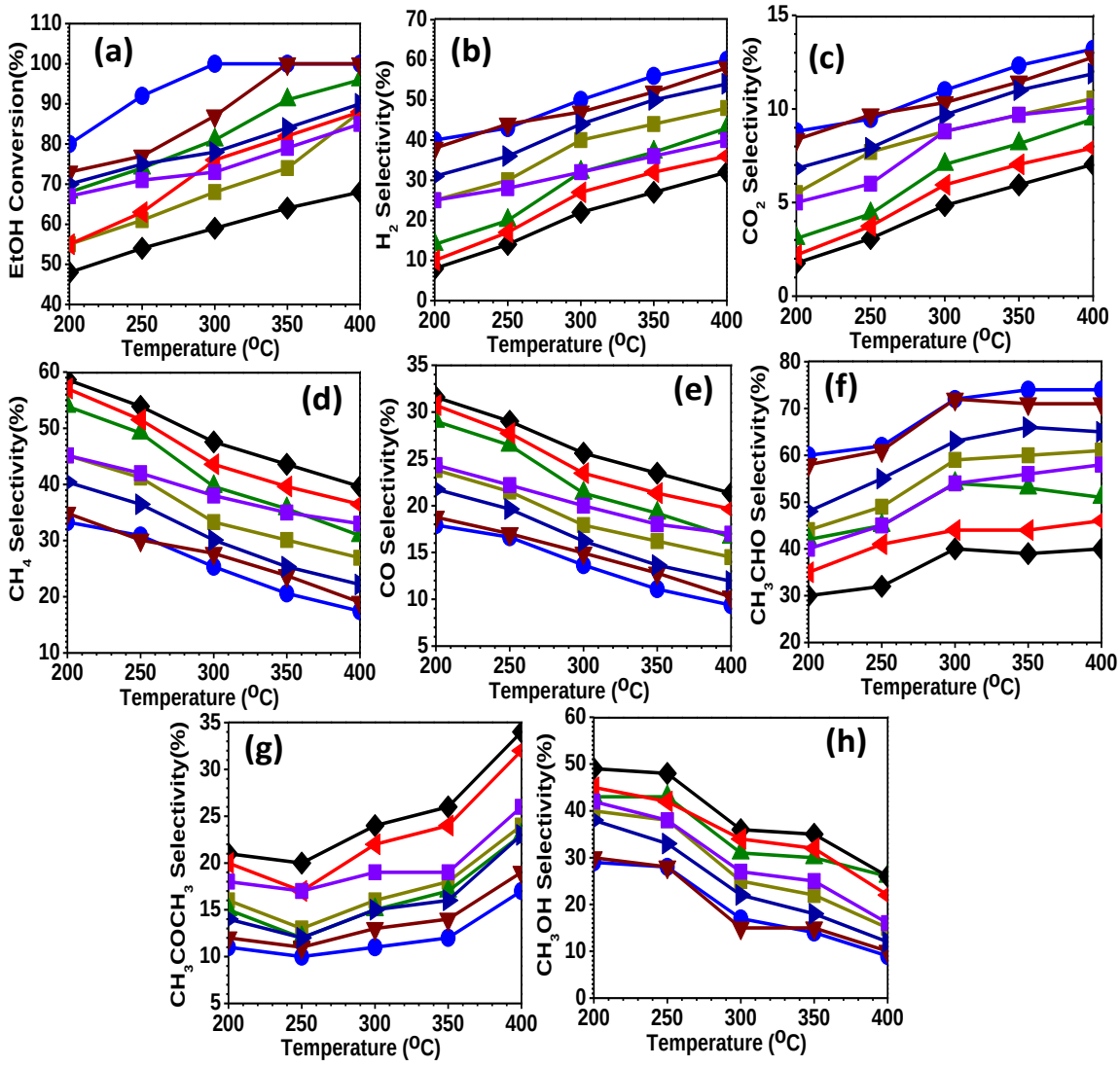

Figure 4. 30: Steady state variation of (a) EtOH conversion, selectivity of gaseous products (b) hydrogen, (c) carbon dioxide, (d) methane, (e) carbon monoxide, and liquid products (f) acetaldehyde, (g) acetone, (h) methanol as a function of temperature (200-400 °C), EtOH :H_2O 1:12 mole ratio and feed flow rate 0.1 ml/min over N14S1(5)/CL21 (●) , N14S1(5)/CL11 (■), N14S1(20)/CL11 (▲), N14S1(5)/CL12 (▼), N7S1(5)/CL21 (▶), N1S1(5)/CL21 (■), N(5)/CL21(◀), and N(5)/C(◆) catalysts.

CH_3CHO selectivity decreased from 74 to 61% and CH_3COCH_3 increased from 17 to 24% with increasing La to 50 atomic% in N14S1(5)/CL21 catalyst and further increase of La to 67 atomic % showed the opposite effect. CH_3CHO selectivity decreased from 74 to 58% and CH_3COCH_3 increased from 17 to 26% with increasing Ni:Sn atomic ratio from 14:1 to 1:1 at constant support composition. The increasing order of catalyst performance in terms of H_2 selectivity and EtOH conversion could be express as N(5)/C < N(5)/CL21 < N14S1(20)/CL11 < N14S1(5)/CL11 < N14S1(20)/CL12 < N14S1(20)/CL21 < N14S1(5)/CL12 < N14S1(5)/CL21. Effect of tin composition varied as N1S1(5)/CL21 < N7S1(5)/CL21 < N14S1(5)/CL21.

Similar study results are reported by other researchers, Zhurka et al. [222] investigated ethanol steam reforming over Ni(10 wt.%)/(CeO_2)-ZrO_2-La_2O_3 and Ni(10 wt.%)/ZrO_2-La_2O_3 catalysts prepared by wet impregnation method. The CeO_2 modified Ni(10 wt.%)/(CeO_2)-ZrO_2-La_2O_3 sample exhibited lower carbon formation rate (0.25 $mg_{carbon}/g_{cat}.h$) and higher H_2 selectivity (58%) compared to Ni(10 wt.%)/ZrO_2-La_2O_3 (carbon deposition rate 0.63 $mg_{carbon}/g_{cat}.h$ and H_2 selectivity 42%) at 400 ℃ and H_2O:EtOH molar ratio 3:1. Xiao et al. [224] examine the effect of La (20 atomic%) doping on Ni(10 wt.%)/CeO_2 catalyst for steam reforming of ethanol and reported that the La modification of the support increases the H_2 selectivity from 47 to 58% with ethanol conversion from 80 to 87% and decrease the carbon deposition from 2.60 to 0.48 $mg_{carbon}/g_{cat}.h$ at 500 ℃ and H_2O:EtOH mole ratio 3:1. Campos et al. [194] investigate LTSRE on bimetallic Rh(X)-Ni(10 wt.%)/$Ce_{0.6}La_{0.4}O_2$ (X=0.25, 0.5, 0.75, 1.0 wt.%) catalysts prepared by impregnation method. At 400 ℃, the Rh(wt. 1%)-Ni(10 wt.%) catalyst shows the best H_2 selectivity of 70% with 100% EtOH conversion at 400 ℃ and H_2O:EtOH molar ratio 3. Moogi et al. [423] synthesized Ni(10 wt.%)-La(5 wt.%)-Ce(5 wt.%)/SBA-15 & Ni(10 wt.%)/SBA-15 catalysts by modified triblock copolymer method and compared their activity for the ethanol steam reforming. Metal sintering and coke formation were observed for the Ni/SBA-15 catalysts without and with La_2O_3 promoter, whereas the catalytic activity of both La_2O_3 and CeO_2 promoted Ni/SBA-15 catalyst (Ni-La_2O_3-CeO_2/SBA-15) remained stable (in terms of gas production rate and hydrogen selectivity) with time on stream.

4.3.4.2 Physico-Chemical Characterizations

X-ray diffraction patterns of the samples are shown in fresh (**Fig. 4.31(a)**), reduced (**Fig. 4.31(b)**), and spent (**Fig. 4.31(c)**) catalysts. The phases present are identified as cubic CeO_2 (PDF (#075-7750), NiO (PDF #44-1159), La(NiO_3) (#79-2451), La_2O_3 (#40-1281), $Ce_{0.5}La_{0.5}O_2$(#84-4175), $Ce_{0.8}La_{0.2}O_2$(#80-5544), and Ni (PDF#04-0850). Sn related phases couldn't be noticed for any catalyst at any stage probably due to low concentration of tin or tin incorporated in the nickel structure as a solid solution.

In fresh N(5)/C sample (**Fig. 4.31(a)** & supplementary **Fig 4.41**), only CeO_2 and NiO phases were identified. No distinct CeO_2 or La_2O_3 phases could be identified till 50 atomic% substitution of Ce by La, however $Ce_{0.8}La_{0.2}O_2$ phase was observed for N14S1(5)/CL21 and $Ce_{0.5}La_{0.5}O_2$ phase was observed for N14S1(5)/CL11 and N14S1(5)/CL12 catalysts in addition with NiO. Additionally, $LaNiO_3$ and La_2O_3 phases could be identified for N14S1(5)/CL12 fresh catalyst. Xue et al. [424] synthesized $Ni_2La_2(10)/CeO_2$ catalyst and reported the formation of $LaNiO_3$ phase due to interaction between La_2O_3 and NiO. Increasing metal loading from 5 to 20 wt.%, didn't change phase composition with respect to the 5 wt.% metal loaded respective catalysts till 50 atomic% La substitution. Further increasing La to 67 atomic%, $Ce_{1-x}La_xO_2$ solid solution peak shift was noticed towards lower 2-theta in N14S1(20)/CL12 catalyst. Increasing tin from Ni:Sn 14:1 to 1:1 atomic ratio at constant support composition, phase compositions didn't change. After reduction nickel oxide (NiO) changes to nickel metal (Ni^0) phase for all catalyst samples (**Fig. 4.31(b)** & **Fig. 4.41**). However, due to the significant interaction between the La and CeO_2, the $Ce_{1-x}La_xO_2$ solid phase is stable even after reduction at 500 °C for 3 h with H_2.

After 20 hrs LTSRE at 200-400 °C, partial amount of metallic nickel oxidized to nickel oxide phase for N(5)/C and Ni(5)/CL21 catalysts (**Fig. 4.31 (c)**). However, for both the NiSn 14:1 and 7:1 atomic ratio catalyst samples, metallic nickel phase remained unaffected as was observed by Xiao et al. [224]. The crystalline size of $Ce_{1-x}La_xO_2$ support solid solution decreased and NiO or Ni phase increased with addition of La into cerium support at constant metal loading and Ni:Sn atomic ratio 14:1 for all fresh, reduce and spent catalysts. Increasing meal loading from 5 to 20 wt.%, $Ce_{1-x}La_xO_2$ support solid solution crystalline size decreased and NiO or Ni phase increased at constant support composition and Ni:Sn atomic ratio 14:1 for all fresh, reduce and spent catalysts. However, both $Ce_{1-x}La_xO_2$ support solid solution and NiO or Ni phase crystalline size increased with increasing Ni:Sn atomic ratio from 14:1 to 1:1 at constant metal loading and support composition for all fresh, reduce and spent catalysts. Crystalline size was calculated by using Scherrer equation and summarized in **Table 4.8**.

$Ce_{1-x}La_xO_2$ support crystalline size for the best (N14S1(5)/CL21) and worst (N14S1(20)/CL11) catalysts (according to the activity results) was calculated to be 28, 29, & 30 nm, and 24, 27, & 31 nm in fresh, reduce and spent samples, respectively. Active phase crystalline size was calculated to be 15 (NiO), 17 (Ni), & 18 (Ni) nm, and 23 (NiO), 25 (Ni), & 28 (Ni) nm in fresh, reduce and spent samples of the same best and worst catalysts, respectively. The La_2O_3 and $LaNiO_3$ crystalline size was calculated to be 38, 22, & 31 nm, and 18, 23, & 24 nm, in N14S1(5)/CL12 catalyst fresh, reduce and spent samples, respectively. Greluk et al. [243] reported that addition of 0.1 wt.% La as promoter in Ni-0.1La/CeO_2 catalyst decreased both CeO_2 support and NiO particle size from 24 to 22 nm & 16 to 9 nm, respectively, in fresh catalyst. Lima et al. [425] reported that Ni particle size increased by increasing the nickel content in $Ce_{1-3x}La_{2x}Ni_xO_2$ catalyst (x= 0.1, 0.2, 0.25).

The decreasing order of NiO particle size followed common trend as N(5)/C > N(5)/CL21 > N14S1(20)/CL11 > N14S1(5)/CL11 > N14S1(20)/CL12 > N14S1(5)/CL12 = N14S1(20)/CL21 > N14S1(5)/CL21. Effect of tin followed common trend for $Ce_{1-x}La_xO_2$ and Ni particles as N1S1(5)/CL21 > N7S1(5)/CL21 > N14S1(5)/CL21. Grabcheno et al. [426] studied the effect of La/Ce ratio on Ni(10 wt.%)/$Ce_{1-x}La_xO_2$ (x = 0, 0.25, 0.5, 0.75) catalyst. CeO_2 (or) $Ce_{1-x}La_xO_2$ crystalline size showed the trend as Ni(10 wt.%)/CeO_2 (55 nm) > Ni(10 wt.%)/$Ce_{0.5}La_{0.5}O_2$ (27 nm) > Ni(10 wt.%)/$Ce_{0.25}La_{0.75}O_2$ (25 nm) > Ni(10 wt.%)/$Ce_{0.75}La_{0.25}O_2$ (24 nm).

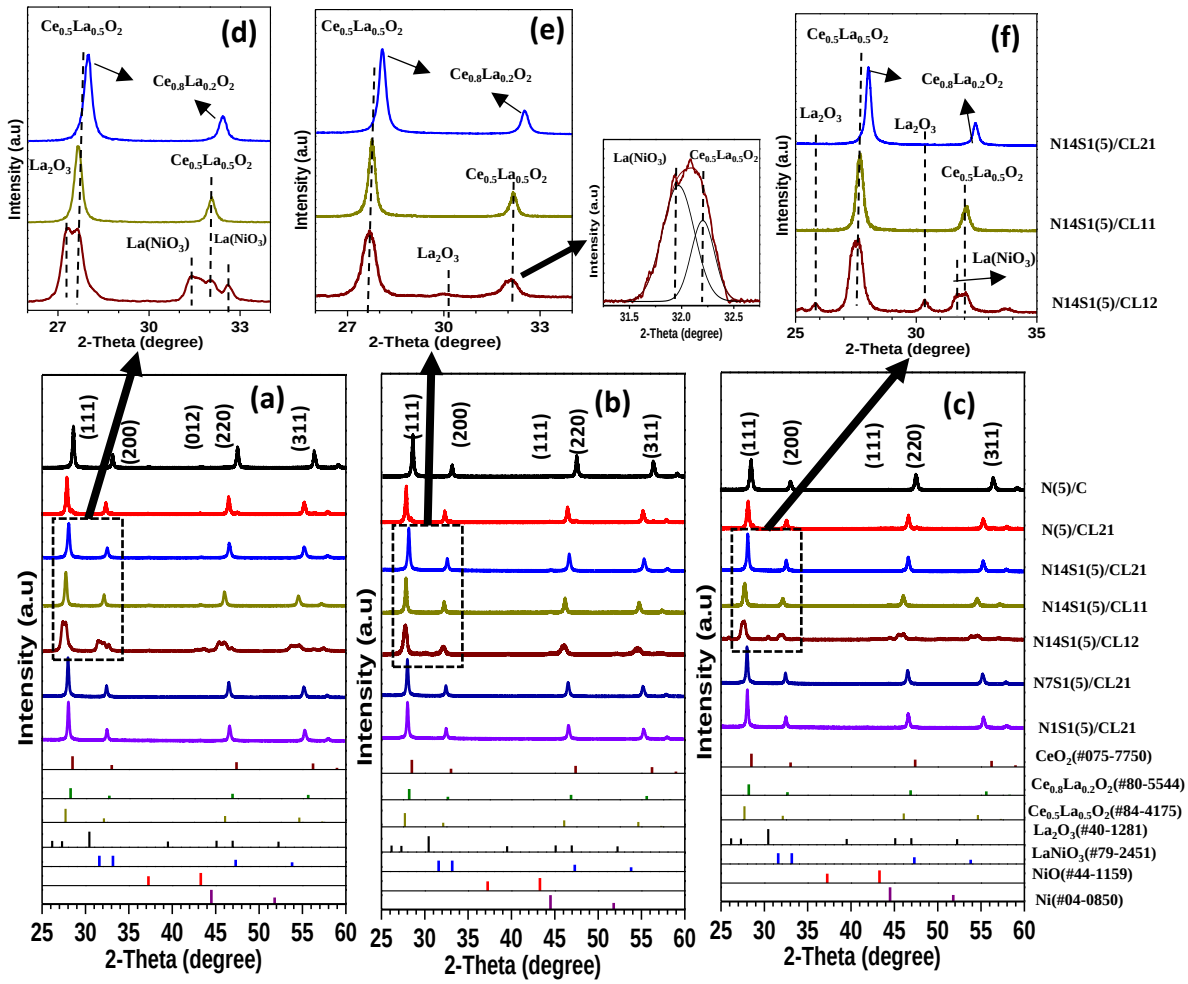

Figure 4. 31: XRD spectra for (a) Fresh, (b).Reduced, (c) Spent of phases identified with the reference powder diffraction file (PDF) of Ni(PDF# 04-0850), CeO_2(PDF#75-7750), NiO(PDF#44-1159), $Ce_{0.5}La_{0.5}O_2$(PDF#84-4175), $Ce_{0.8}La_{0.2}O_2$(PDF#80-5544), $NiLaO_3$(PDF#79-2451), La_2O_3(PDF#40-1281). The inset images show the peak shifting and phase separation for the (d) fresh, (e) reduce, and (f) spent catalysts, respectively.

Table 4. 8: Average crystalline sizes of CeO_2, $Ce_{1-x}La_xO_2$, Ni, and NiO phases calculated from XRD spectra, and textural properties calculated from N_2 adsorption-desorption isotherm for the fresh (F), reduce (R) and spent (S) catalyst samples.

S.NO	Catalyst formula	Proposed Abbreviation of the catalyst	XRD Avg. Crystalline Size (nm)								N_2 adsorption-desorption			
			Oxide support				Nickel/Nickel related phases				S_{BET} (m^2/g)		D_p (nm)	
			Phases	F	R	S	F	R	S		R	S	R	S
							NiO	Ni	Ni	NiO				
1	$Ni(5)/CeO_2$	N(5)/C	CeO_2	37	38	40	25	27	19	16				
2	$Ni(5)/Ce_{0.67}La_{0.33}O_2$	N(5)/CL21	$Ce_{0.8}La_{0.2}O_2$	36	37	38	22	24	13	19				
3	$Ni_{0.93}Sn_{0.07}(5)/Ce_{0.67}La_{0.33}O_2$	N14S1(5)/CL21	$Ce_{0.5}La_{0.5}O_2$	28	29	30	15	17	18		132	8	6	19
4	$Ni_{0.93}Sn_{0.07}(20)/Ce_{0.67}La_{0.33}O_2$	N14S1(20)/CL21	$Ce_{0.5}La_{0.5}O_2$	23	23	25	18	19	22					
5	$Ni_{0.93}Sn_{0.07}(5)/Ce_{0.5}La_{0.5}O_2$	N14S1(5)/CL11	$Ce_{0.5}La_{0.5}O_2$	31	33	37	20	23	25		82	5	13	30
6	$Ni_{0.93}Sn_{0.07}(20)/Ce_{0.5}La_{0.5}O_2$	N14S1(20)/CL11	$Ce_{0.5}La_{0.5}O_2$	24	27	31	23	25	28		31	3	22	34
7	$Ni_{0.93}Sn_{0.07}(5)/Ce_{0.33}La_{0.67}O_2$	N14S1(5)/CL12	$Ce_{0.5}La_{0.5}O_2$	32	18	20	18	19	20		87	9	10	21
			La_2O_3	38	20	31								
8	$Ni_{0.93}Sn_{0.07}(20)/Ce_{0.33}La_{0.67}O_2$	N14S1(20)/CL12	$Ce_{1-x}La_xO_2$	17	20	21	19	20	23					
9	$Ni_{0.87}Sn_{0.13}(5)/Ce_{0.67}La_{0.33}O_2$	N7S1(5)/CL21	$Ce_{0.5}La_{0.5}O_2$	33	33	34	18	20	24					
10	$Ni_{0.5}Sn_{0.5}(5)/Ce_{0.67}La_{0.33}O_2$	N1S1(5)/CL21	$Ce_{0.5}La_{0.5}O_2$	36	36	37	21	23						

**S_{BET}= Surface area, V_P= pore volume, D_{Pore} = pore diameter, D_p = particle size.

Metal support interaction was analyzed by using H_2 temperature-programmed reduction (H_2-TPR) technique (**Fig. 4.32**). The peak between 230 to 280 °C corresponds to the reduction of the NiO phase [251], and between 320 to 340°C is attributed to reduction of Ce^{4+} to Ce^{3+} [415].

At constant metal loading, adding 33 atomic% of La and little Sn (Ni:Sn atomic ratio 14:1) in N(5)/C catalyst showed significant improvement in NiO reduction temperature from 238 to 276 °C & a second peak appeared at 330 °C, while total H_2 consumption value increased from 220 to 1353 µmol/$g_{cat.}$ Increasing La to 50 atomic% in N14S1(5)/CL21 catalyst decreased NiO reduction peak temperature from 276 to 245 °C and H_2 consumption value from 1353 to 456 µmol/$g_{cat.}$ [424]. Further increasing La to 67 atomic% in N14S1(5)/CL21 catalyst shifted the NiO reduction peak to 261 °C, & two new peaks appeared at 336 & 455 °C corresponding to Ce^{4+} and $LaNiO_3$ reduction, respectively [427].

Increasing metal loading from 5 to 20 wt.% (at constant support and Ni:Sn atomic ratio 14:1) and increasing Ni:Sn atomic ratio from 14:1 to 1:1 (at constant support and metal loading), decreased the NiO reduction peak temperature and H_2 consumption value [395].

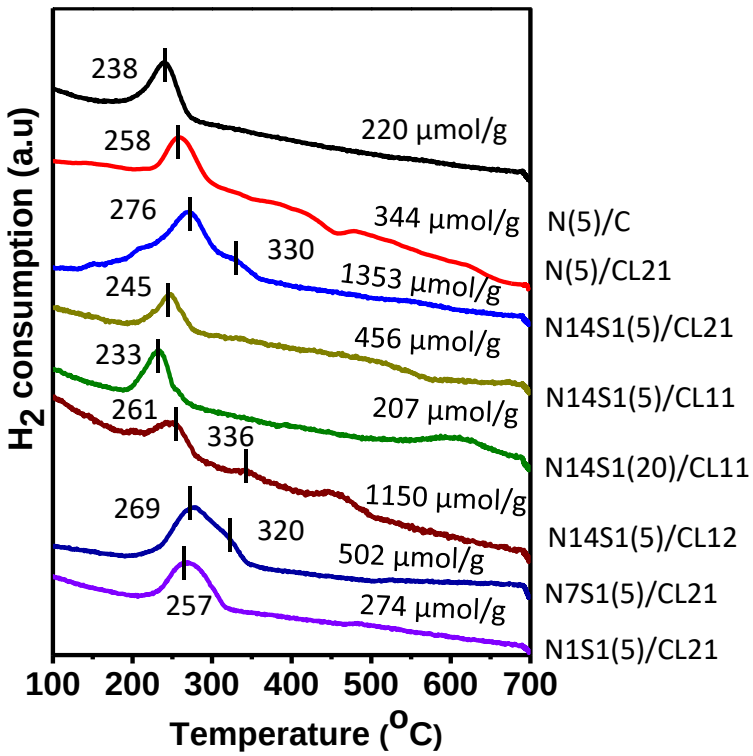

Figure 4. 32: H_2 temperature programmed reduction (H_2-TPR) profiles along with H_2 consumption values for the fresh catalysts.

Greluk et al. [243] reported that addition of 0.1 wt.% La in Ni-0.1La/CeO_2 catalyst increased the NiO reduction peak temperature by ~40 °C, indicating better nickel dispersion and improved metal-support interaction. Grabcheno et al. [426] reported the shifting of the NiO reduction peak from 350 to 392 °C due to addition of 0.75 at.% La in Ni/CeO_2 catalyst. Lima et al. [428] reported that increasing ceria content in $La_{1-x}Ce_xNiO_3$ (x=0, 0.05, 0.1, 0.4, 0.7, 1) catalyst increased the NiO reduction temperature. Xue et al. [429] reported the order of H_2 consumption as Rh/CL0.3 > Rh/CL0.4 >

Rh/CL0.5 > Rh/CL0.2 > Rh/CL0.1 > Rh/C obtained from the H_2-TPR study of the Rh(1 wt.%)/$Ce_{1-x}La_xO_2$ (x = 0, 0.1, 0.2, 0.3, 0.4, 0.5) catalysts. Wang et al. [430] reported that for the Au/$La_xCe_{1-x}O_2$ (x=0.1, 0.25, 0.5, 0.75, 1 at.%) catalysts NiO reduction temperature increased with addition of La upto 0.25 at.% and then dropped drastically with further increasing La.

The acidic/basic nature of the fresh CeO_2, & CeO_2 modified with La_2O_3 supports are investigated by NH_3-TPD and CO_2-TPD (**Fig. 4.33**). In NH_3- TPD (**Fig. 4.33(a)**) peaks at 110 to 158 °C correspond to weak acidic site, while 270 to 310 °C correspond to strong acidic site. It is clear that incorporating 33 atomic% of La into Ce support lowers the total number of acid sites. The increasing order of acidic nature noticed as CL21 (18 µmol/g) > CL11 (34 µmol/g) > CL12 (45 µmol/g) < C (55 µmol/g). Weak acid (strong base) centers on the support enhances catalytic activity and selectivity. Weak acid sites converts the CH_3CHO to CH_4 formation via Eq. (4.16) & (4.17) [103]. This CH_4 converts to CO_2 and CO via WGS (Supplementary Eq. (4.31)) and methane reforming reactions (Supplementary Eq. (4.29, & 4.30)) [431], contributing to improving H_2 and catalytic performance [432,433]. However, strong acidity catalysts can generate coke on the catalysts via decomposition of ethanol (Supplementary Eq. (4.37, & 4.38)) and methane (Supplementary Eq. (4.39)) [103].

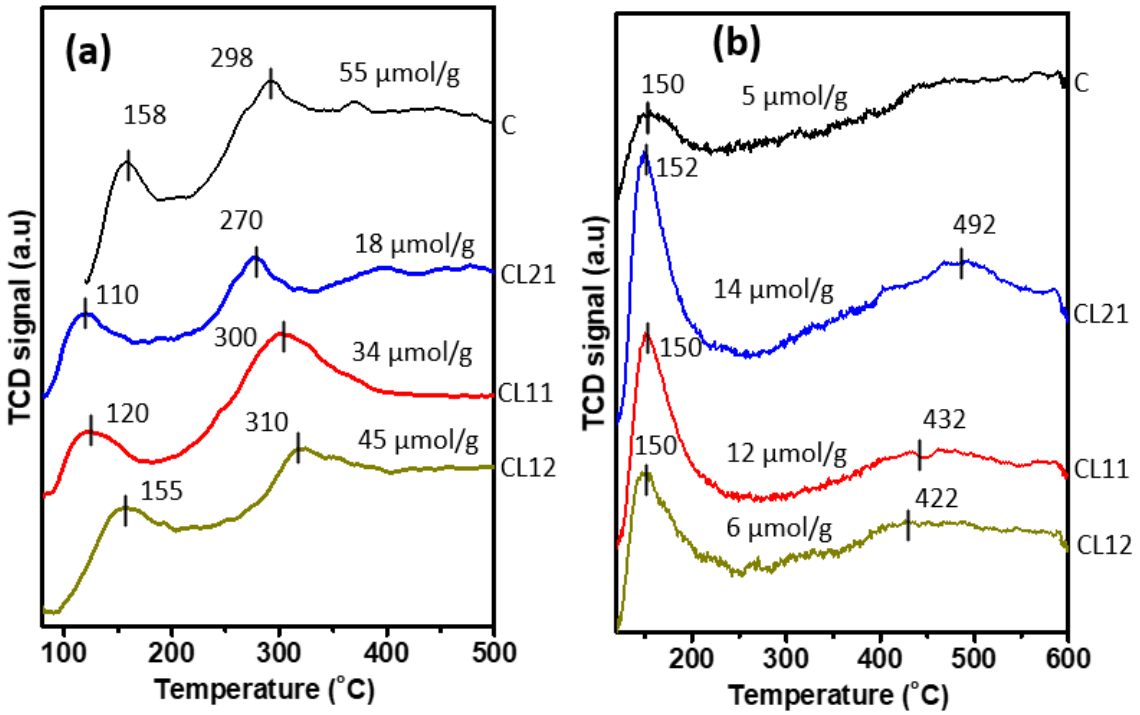

Figure 4. 33: (a) NH_3-TPD & (b) CO_2-TPD profiles of the fresh CeO_2 and CeO_2 modified with La_2O_3 supports along with gas adsorption amounts.

$$CH_3CHO + OH \rightarrow CH_3COO + H_2 \quad (4.16)$$

$$CH_3COO + OH \rightarrow OCOO + CH_4 \quad (4.17)$$

In the CO_2-TPD profiles (**Fig. 4.33(b)**), peaks below 200 °C indicate bicarbonate formation by reaction between gaseous CO_2 and the surface OH^- species, linked to weak basicity sites. The peaks appear in range of 200-450 °C represent surface basic sites with moderate strength generated

due to metal-oxygen interactions. Peaks above 450 °C are attributed to strong basic sites derived from lattice oxygen species [387,434]. The $Ce_{0.75}La_{0.25}O_2$ support exhibits the highest density of basic sites (14 µmol/g) and the decreasing order of basicity could be observed as CL21 (14 µmol/g) > CL11 (12 µmol/g) > CL12 (6 µmol/g) > C (5 µmol/g).

Raman spectroscopy (**Fig. 4.34** and supplementary **Fig. 4.42**) was chosen to acquire insight into oxygen vacancies in all catalysts and types of carbon formation in spent catalysts. The first order band at 465 cm^{-1} (F_{2g}) corresponding to CeO_2 [305]. The peak at 240 cm^{-1} belongs to less stable oxygen disorder and the peak shoulder at 590 cm^{-1} is combination of oxygen vacancy (Ov) at 560 cm^{-1}, intrinsic defects of oxygen vacancy (O_{ID}) at 600 cm^{-1} & extrinsic defects of oxygen vacancy (O_{ED}) at 640 cm^{-1} created from $Ce^{4+} \rightarrow Ce^{3+}$ transition and incorporation of La_2O_3 into CeO_2 [224,415,435].

In fresh samples, 33 atomic% La addition in N(5)/C catalyst caused F_{2g} peak intensity decrease and width increase, which could be due to $Ce_{1-x}La_xO_2$ solid oxide phase formation (**Fig. 4.34 (a)**) [224]. Also, the intensity of the 580 cm^{-1} peak increased compared to that of N(5)/C catalyst. The NiO peak (500 cm^{-1}) could not be identified, most likely as a result of the shadowing effect of F_{2g} peak [251,307]. In case of 50 atomic% La in N14Sn1(5)/CL21 catalyst, the F_{2g} band intensity reduced [415,436], whereas increasing La to 67 atomic%, the F_{2g} band intensity increased compared to 50 atomic% La. Increasing metal loading from 5 to 20 wt.% (at constant support and Ni:Sn atomic ratio 14:1) and increasing Ni:Sn atomic ratio from 14:1 to 1:1 (at constant support and metal loading), show red Raman shift of the F_{2g} peak. No distinct difference was observed in the reduced samples (**Fig. 4.34 (b**)) compared with the corresponding fresh once [415,436].

Two additional bands, corresponding to sp^3 hybridized disordered amorphous carbon (band D) and sp^2 hybridised graphite (band G), were found in the spent samples (**Fig. 4.34 (c)**) at around 1350 and 1600 cm^{-1}. Incorporating La into N(5)/C catalyst slightly increased the I_D/I_G ratio from 0.97 to 0.98, while additional tin (Ni:Sn atomic ratio 14:1) significantly increased the I_D/I_G ratio further from 0.98 to 1.12. Increasing metal loading from 5 to 20 wt.% decreased I_D/I_G ratio in N14S1(5)/CL11 catalyst from 0.99 to 0.95 and changing Ni:Sn atomic ratio from 14:1 to 1:1 in N14S1(5)/CL21 catalyst decreased I_D/I_G ratio from 1.12 to 0.95. The decreasing order of I_D/I_G ratio followed as N14S1(5)/CL21 (1.12) > N14S1(5)/CL12 (1.02) > N14S1(20)/CL21 (1.01) > > N7S1(5)/CL21 (1.0) > N14S1(20)/CL12 (0.99) = N14S1(5)/CL11 (0.99) > N(5)/CL21 (0.98) > N(5)/C (0.97) > N14S1(20)/CL11 (0.95) = N1S1(5)/CL21 (0.95).

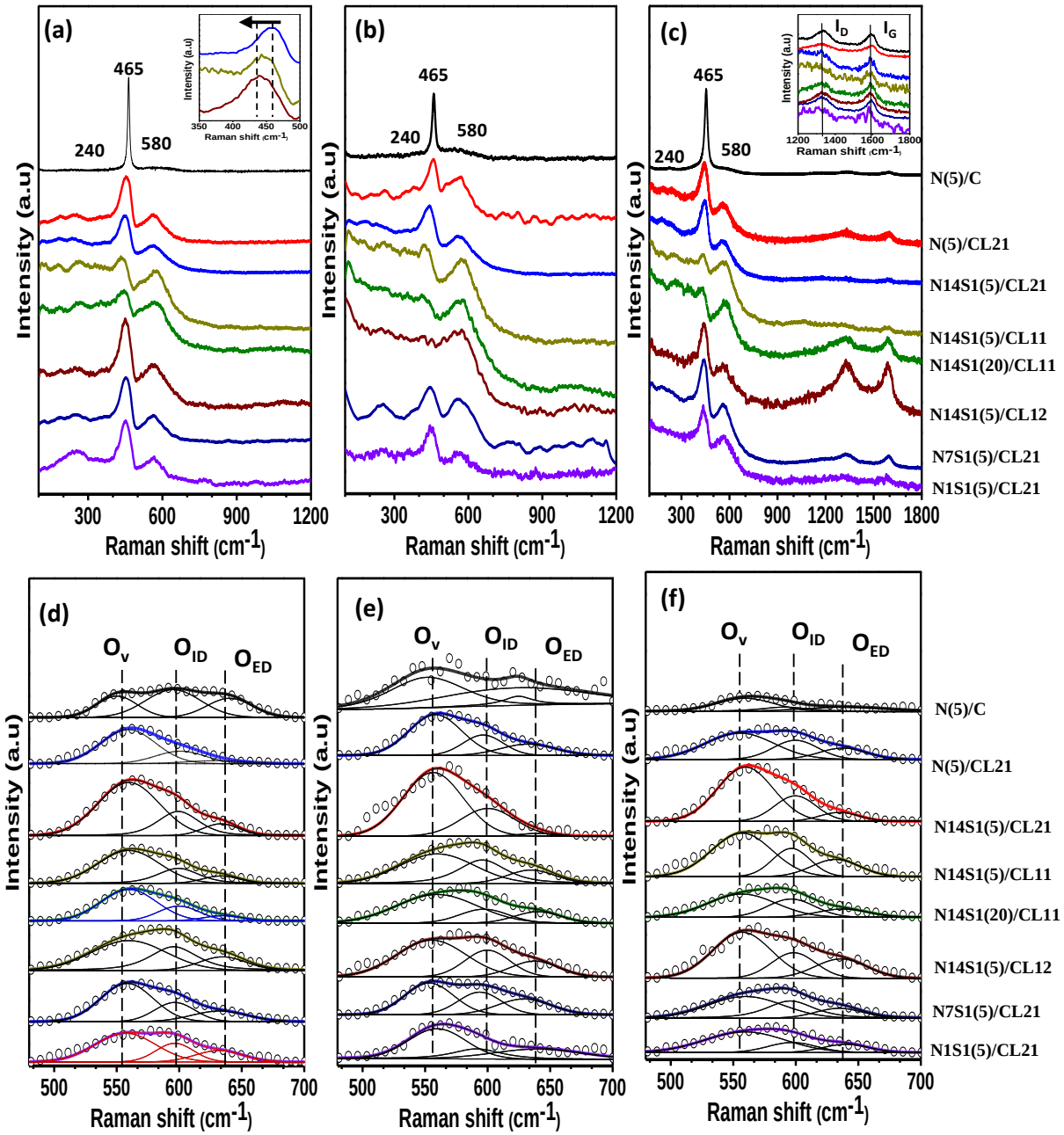

Figure 4. 34: Raman spectra for (a) fresh, (b) reduced, and (c) spent catalysts. Spectra within 480-700 cm^{-1} are de-convoluted to show the peaks corresponding to the oxygen vacancy (O_V), & defective oxygen vacancy of intrinsic (O_{ID}) and extrinsic (O_{ED}) nature present in (d) fresh, (e) reduced, (f) spent catalysts.

Grabcheno et al. [426] studied on Ni(10 wt.%)/$Ce_{1-x}La_xO_2$ (x = 0, 0.25, 0.5, 0.75 at.%) catalyst (at 650 °C, TOS=24h) and found that the decreasing order of I_D/I_G ratio on the spent catalyst is 2.23 (Ni(10 wt.%)/CeO_2) > 2.22 (Ni(10 wt.%)/$Ce_{0.75}La_{0.25}O_2$) > 1.39 (Ni(10 wt.%)/$Ce_{0.25}La_{0.75}O_2$) > 1.23 (Ni(10 wt.%)/$Ce_{0.5}La_{0.5}O_2$). It is also reported that the amount of graphite carbon deposited on Ni(10 wt.%)/$Ce_{0.75}La_{0.25}O_2$ & Ni(10 wt.%)/$Ce_{0.25}La_{0.75}O_2$ catalysts are significantly less compared with the Ni(10 wt.%)/$Ce_{0.5}La_{0.5}O_2$.

Relative oxygen vacancy concentrations (ROVC: $O_V/(O_V+O_{ID}+O_{ED})$) are calculated for fresh (**Fig. 4.34 (d)**), reduced (**Fig. 4.34 (e)**), spent (**Fig. 4.35(f)**) samples and tabulated in **Table 4.9**. In fresh catalysts, the ROVC of Ni(5)/C catalyst increases from 0.4 to 0.58 with the addition of 33 at% La^{3+} (Ce:La 2:1 mole ratio) and Sn (Ni:Sn 14:1 atomic ratio). However, increasing the La^{3+} concentration to 50 atomic% ROVC decreases to 0.45 and again increases to 0.48 at La^{3+} concentration of 67 atomic%. Changing the Sn concentration from Ni:Sn = 14:1 to 1:1 atomic ratio results in a decrease in the ROVC from 0.58 to 0.37. The decreasing order of the ROVCs is N14S1(5)/CL21 > N14S1(5)/CL12 > N(5)/CL21 > N14S1(5)/CL11 > N7S1(5)/CL21 > N14S1(20)/CL11 > N1S1(5)/CL21 > N(5)/C. For the reduced samples the ROVCs increase and then in spent samples those are decreased, however the order of decreasing trend remain the same as the fresh catalysts. High ROVC N14Sn1(5)/CL21 catalyst shows maximum catalyst activity of H_2 selectivity 60% with lowest carbon deposition, ~ 5 wt.%. Xiao et al. [227] investigate ESR over Ni(10 wt.%)/$Ce_{1-x}Pr_xO_2$ (X=0, 0.05, 0.1, 0.2, 0.3) catalysts synthesized by a citric acid assisted sol-gel method and observe that addition of Pr increases the ROVC in the samples. Ni(10 wt.%)/$Ce_{0.8}Pr_{0.2}O_2$ catalyst is found to have highest ROVC of 0.535, resulting the lowest coke deposition 0.56 $mg_{coke}/g_{cat.}$ h with high H_2 selectivity 68% and 100% EtOH conversion at 600 ℃.

Table 4. 9: Relative oxygen vacancy concentration calculated from Raman spectra for fresh, reduced, and spent catalysts.

Name of the catalyst	Relative oxygen vacancy concentration $O_V/(O_V+O_{ID}+O_{ED})$		
	Fresh	Reduced	Spent
N(5)/C	0.35	0.45	0.32
N(5)/CL21	0.46	0.6	0.41
N14S1(5)/CL21	0.58	0.71	0.6
N14S1(5)CL11	0.45	0.56	0.39
N14S1(20)/CL11	0.38	0.51	0.34
N14S1(5)CL12	0.48	0.66	0.42
N7S1(5)/CL21	0.42	0.52	0.37
N1S1(5)/CL21	0.37	0.46	0.33

Electron microscopy (FESEM & TEM) set-ups were used to study the microstructural change along with elemental analysis for the best (N14S1(5)/CL21) and worst (N14S1(20)/CL11) catalyst samples, based on the activity results, shown in **Figs. 4.35 & 4.36.** In general, interconnected particles with three-dimensional porous network were observed for all catalysts in SEM image (**Fig. 4.35**), which is common for the materials prepared by the SCS method. In fresh, reduced, & spent N14S1(5)/CL21 & N14S1(20)/CL11 catalysts (**Fig. 4.35**), the particle size calculated to be 30 & 52 nm, 33 & 504 nm, and 38 & 57 nm, respectively [427,437]. The particle sizes calculated from the plan view TEM (**Fig. 4.36**) images of the catalyst were smaller compared to that obtained from the FESEM images of the corresponding samples, but trend remain same.

More importantly carbon nano tube (CNT) growths were observed on the surface of the spent N14S1(20)/CL11 catalyst **Fig. 4.35(f)**. The CNT formation is probably governed by the tip-growth mechanism, as nickel particles were noticed on the tip of the CNT's (**Fig. 4.36**) [251]. Supplementary

Table 4.12 shows the elemental weight percentage obtained through EDS analysis for different catalysts. The lowest coke deposition was observed for the best spent N14S1(5)/CL21 catalyst.

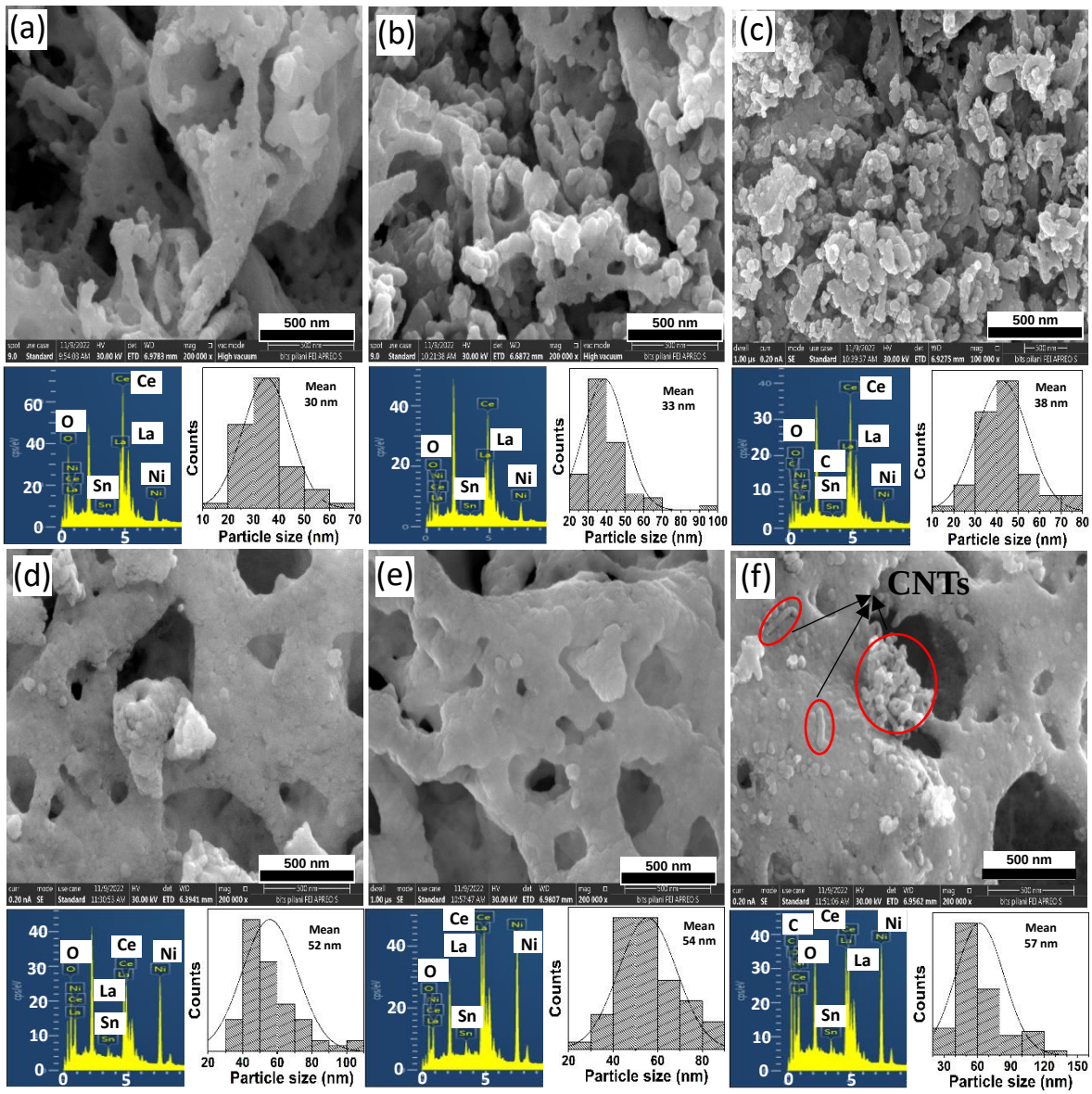

Figure 4. 35:FESEM images with particle size distribution and EDS spectrum for N14S1(5)/CL21 [(a) fresh, (b) reduce, (c) spent] and N14S1(20)/CL11 [(d) fresh, (e) reduce, (f) spent] catalysts .

Carbon nano tube deposition is a very common phenomena and widely reported in literature. Grabcheno et al. [426] reported the formation of carbon fibers with nickel metal particle at the tip on Ni(10 wt.%)/$Ce_{0.5}La_{0.5}O_2$ catalyst after 24 h of SRE at 550 °C. According to Greluk et al. [243] found that carbon nano tubes are more likely to accumulate on bigger nickel particles of the Ni(10 wt.%)-La(2 wt.%)/CeO_2 & Ni((10 wt.%)/CeO_2 catalysts during ethanol steam reforming. Xiao et al. [224] compared Ni(10 wt.%)/CeO_2 and Ni(10 wt.%)/$Ce_{0.8}La_{0.2}O_2$ catalysts for SRE and reported that the generation of carbon nanotubes were significantly reduced with addition of 20 atomic% La.

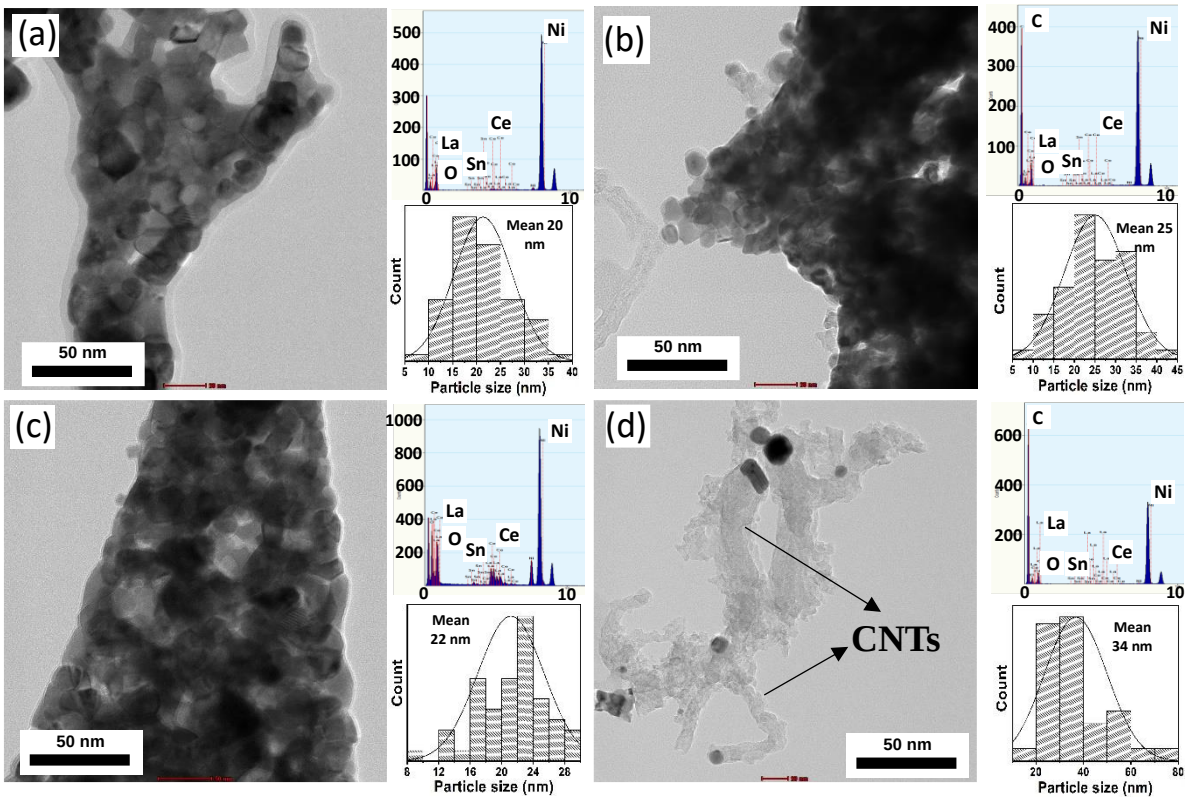

Figure 4. 36: TEM images with particle size distribution and EDX spectrum for N14S1(5)/C21 [a. reduced, b. spent], and N14S1(20)/CL11 [c. reduced, d. spent] catalysts.

XPS studies were performed to understand the oxidation state of the elements on the reduce and spent catalyst's surface. The wide scan XPS spectra of the catalysts confirmed the existence of the key components Ni, Sn, Ce, La, O, and C (Supplementary data **Fig. 4.43**). The elemental analysis calculated from XPS data for the reduced catalysts and spent samples, and metal content measured by ICP-OES (**Table 4.10**) for fresh catalysts show good agreement within ±5% error. For the best (N14S1(5)/CL21) and worst (N14S1(20)/CL11) catalysts, the elemental analysis from FESEM and TEM EDS match well with the results obtained from XPS and ICP-OES.

The high resolution XPS spectra (**Fig. 4.37(a)** & Supplementary data **Fig. 4.44 (a)**) of nickel shows three oxidation states. Peak at 850 ± 0.5 eV related to metallic nickel (Ni^0). Peaks at 854±0.5 eV & 856±0.5 eV corresponding to Ni^{2+} & Ni^{3+} oxidative states, respectively [252,438].

In reduced catalyst, $Ni^0/(Ni^0+Ni^{2+}+Ni^{3+})$ peak intensity ratio (**Fig. 4.37(a)**) increased from 0.09 to 0.16 (**Table 4.11**), with La 33 atomic% was incorporated into N(5)/C catalyst. Further, $Ni^0/(Ni^0+Ni^{2+}+Ni^{3+})$ ratio increased from 0.16 to 0.34, with addition of tin (Ni:Sn atomic ratio 14:1) in N(5)/CL21 [395]. However, increasing La to 50 atomic%, the $Ni^0/(Ni^0+Ni^{2+}+Ni^{3+})$ ratio decreased from 0.34 to 0.15 in N14S1(5)/CL21 catalyst and further $Ni^0/(Ni^0+Ni^{2+}+Ni^{3+})$ ratio increased from 0.15 to 0.24 with increasing La to 67% in N14S1(5)/CL11 catalyst. Increasing metal loading from 5 to 20 wt.% reduced the $Ni^0/(Ni^0+Ni^{2+}+Ni^{3+})$ ratio from 0.15 to 0.11 in N14S1(5)/CL11 catalyst, whereas increasing

the Ni:Sn atomic ratio 14:1 to 1:1 in N14S1(5)/CL21 catalyst, cut down the $Ni^0/(Ni^0+Ni^{2+}+Ni^{3+})$ intensity ratio from 0.34 to 0.17.

In spent catalysts, the $Ni^0/(Ni^0+Ni^{2+}+Ni^{3+})$ ratio decreased compared to the corresponding reduced samples, but similar trend was followed. The decreasing order of $Ni^0/(Ni^0+Ni^{2+}+Ni^{3+})$ peak ratio commonly for reduced and spent samples as N14S1(5)/CL21 > N14S1(5)/CL12 > N7S1(5)/CL21 > N(5)/CL21 > N1S1(5)/CL21 > N14S1(5)/CL11 > N14S1(20)/CL11 > N(5)/C.

Figure 4.37(b) & supplementary data **Fig. 4.44 (b)** of tin (Sn $3d_{5/2}$) shows three oxidation states, Sn^0, Sn^{2+}, and Sn^{4+} corresponding to peaks at 484 ± 0.5, 486.5 ± 0.5, and 488.1 ± 0.5 eV, respectively [252,296]. In reduced N14S1(5)/CL21 catalyst the $Sn^{4+}/(Sn^0+Sn^{2+}+Sn^{4+})$ ratio is calculated to be 0.51 and it bring down to 0.21 for N14S1(5)/CL11 catalyst. Further, it increased to 0.5 for N14S1(5)/CL11 catalyst [378].

The $Sn^{4+}/(Sn^0+Sn^{2+}+Sn^{4+})$ ratio decreased from 0.21 to 0.10 with increasing metal loading from 5 to 20 wt.% in N14S1(5)/CL11 catalyst. Similarly, the $Sn^{4+}/(Sn^0+Sn^{2+}+Sn^{4+})$ ratio decrease from 0.51 to 0.06 with increasing Ni:Sn atomic ratio 14:1 to 1:1 in N14S1(5)/CL21 catalyst [251]. Comparing with the reduced samples the $Sn^{4+}/(Sn^0+Sn^{2+}+Sn^{4+})$ ratio decreased for the corresponding spent sample [251]. Decreasing order of $Sn^{4+}/(Sn^{2+}+Sn^{4+})$ ratio commonly noticed in both reduced and spent samples as N14S1(5)/CL21 > N14S1(5)/CL12 > N7S1(5)/CL21 > N14S1(5)/CL11 > N14S1(20)/CL11 > N1S1(5)/CL21.

Table 4. 10: Elemental analysis from XPS and ICP-OES.

Name of the catalyst	XPS elemental analysis (wt.%)											Fresh samples metal content (wt.%) by ICP-OES			
	Reduced					Spent									
	Ni	Sn	Ce	La	O	Ni	Sn	Ce	La	O	C	Ni	Sn	Ce	La
N(5)/C	4.8	0	70	0	25	3.3	0	44.7	0	18	34	4.9	0	95.1	0
N(5)/CL21	4.9	0	46	23	27	4.1	0	30.1	14	19	33	4.8	0	48.9	46.3
N14S1(5)/CL21	4.9	0.6	46	21	28	4.7	0.5	33.5	17	22	22	4.4	0.5	49	46.1
N14S1(20)/CL21	-	-	-	-	-	-	-	-	-	-	-	17.2	2.3	41.5	39
N14S1(5)CL11	4.6	0.7	36	35	24	4.2	0.2	21.6	20	18	36	4.1	0.4	33	62.5
N14S1(20)/CL11	18	2.1	29	29	22	13	1.2	15.5	16	14	40	16.3	2.1	27.6	54
N14S1(5)CL12	4.7	0.5	23	45	28	4.5	0.4	16.8	35	19	24	4.2	0.5	20	75.3
N14S1(20)CL12	-	-	-	-	-	-	-	-	-	-	-	16.8	2	17.2	64
N7S1(5)/CL21	4.6	1.1	47	21	27	4.3	0.9	36.7	14	17	27	3.8	1.1	50	46.1
N1S1(5)/CL21	3.3	2.7	44	24	25	3.3	2.7	28.9	14	13	38	1.3	3.6	48.8	46.3

Fig. 4.37(c) & Supplementary data **Fig. 4.44 (c)** shows that CeO_2 exists in both Ce^{3+} and Ce^{4+} oxidation states. All the catalysts contained Ce^{3+} (peaks at 885 ± 0.2, 898± 0.2 eV corresponding Ce $3d_{3/2}$ and peak at 903± 0.2 eV corresponding to Ce $3d_{5/2}$) and Ce^{4+} (peaks at 883± 0.2, 890± 0.2 eV corresponding to Ce $3d_{3/2}$ and peaks at 900 ± 0.2, 907 ± 0.2, & 917 ± 0.2 eV corresponding to $3d_{5/2}$).

In reduced catalysts, adding 33 atomic% of La to N(5)/C catalyst increased $Ce^{3+}/(Ce^{3+}+Ce^{4+})$ ratio from 0.31 to 0.41 at constant metal loading. Further, this ratio increased from 0.41 to 0.77, with addition of tin (Ni:Sn atomic ratio 14:1) in N(5)/CL21 catalyst. However, increasing La to 50 atomic%, this number decreased from 0.77 to 0.32 in N14S1(5)/CL21 catalyst and further it increased from 0.32 to

0.58 with increasing La to 67 atomic% in N14S1(5)/CL11 catalyst (**Table 4.11**) [415]. The $Ce^{3+}/(Ce^{3+}+Ce^{4+})$ ratio decreased from 0.32 to 0.30 with increasing metal loading from 5 to 20 wt.% in N14S1(5)/CL11 catalyst. Similarly, the $Ce^{3+}/(Ce^{3+}+Ce^{4+})$ ratio decreased from 0.77 to 0.40 with increasing Ni:Sn atomic ratio 14:1 to 1:1 in N14S1(5)/CL21 catalyst.

During reforming reaction the Ce^{3+} converted to Ce^{4+} by absorbing oxygen and as a result $Ce^{3+}/(Ce^{3+}+Ce^{4+})$ ratio decreased compared to the corresponding reduced samples, but similar trend of the ratio was followed [251]. The common trend of $Ce^{3+}/(Ce^{3+}+Ce^{4+})$ ratio followed as N14S1(5)/CL21 > N14S1(5)/CL12 > N(5)/CL21 > N7S1(5)/CL21 > N14S1(5)/CL11 > N(5)/C > N14S1(20)/CL11.

Fig. 4.37(d) & Supplementary data **Fig. 4.44 (d)** shows oxygen (1S) high resolution XPS spectra. The peak at 529 ± 0.5 eV is attributed to the lattice oxygen (O_L), and the peak at 531 ± 1 eV is associated with oxygen vacancies (O_V) and the peak at 533 ± 0.2 eV denoted by hydroxyl species (O_{OH}) on the surface [227,252].

At constant metal loading, addition of 33 atomic% La to N(5)/C catalyst increased $O_V/(O_L+O_V+O_{OH})$ ratio. Further, enhancement of the $O_V/(O_L+O_V+O_{OH})$ ratio was observed in N(5)/CL21 catalyst due to addition of tin (Ni:Sn atomic ratio 14:1). In N14S1(5)/CL21 catalyst the $O_V/(O_L+O_V+O_{OH})$ ratio decreased due to increase La to 50 atomic%, however, the $O_V/(O_L+O_V+O_{OH})$ ratio enhanced with increasing La to 67% in N14S1(5)/CL11 catalyst [415].

Increasing metal loading from 5 to 20 wt.% in N14S1(5)/CL11 catalyst and increasing Ni:Sn atomic ratio 14:1 to 1:1 in N14S1(5)/CL21 catalyst, the $O_V/(O_L+O_V+O_{OH})$ ratio decreased. The common trend of $O_V/(O_L+O_V+O_{OH})$ concentration followed as N14S1(5)/CL21 > N14S1(5)/CL12 > N7S1(5)/CL21 > N14S1(5)/CL11 > N(5)/CL21 > N1S1(5)/CL21 > N(5)/C > N14S1(20)/CL11. Zhu et al. [415] reported that the formation of oxygen vacancies on CeO_2 surface happened, when two Ce^{4+} ions replaced by two La^{3+} ions in the CeO_2 lattice in order to maintain the charge balance. Xue et al. [429] reported that incorporation of 30 atomic% La into Rh(1 wt.%)/$Ce_{1-x}La_xO_2$ catalyst increased the oxygen vacancy by 48%. Xiao et al. [224] reported that the addition of small amount La in Ni(10 wt.%)/$Ce_{0.8}La_{0.2}O_2$ catalyst generated abundant oxygen vacancies. Lima et al. [425] reported the increase of oxygen vacancies with increasing La content in $Ce_{1-x-y}La_xNi_yO_2$ catalyst (x= 0.2, 0.4, 0.5 & y= x/2). Wang et al. [430] reported that optimum amount (~ 25 at%) of La content in Au/$La_xCe_{1-x}O_2$ (x=0.1, 0.25, 0.5, 0.75, 1 at.%) catalyst improved oxygen mobility due to formation of oxygen vacancies.

Three carbon related peaks were observed in high resolution XPS spectra of the spent catalysts (**Fig. 4.37(e)**). The peak at 284.8 ± 0.2 eV correspond to sp^2 C=C (C_C), peaks at 286 ± 0.2 eV correspond to sp^3 C-OH (C_{OH}), and peak 289 ± 0.2 eV correspond to O-C=O (C_O) [296,314].

At constant metal loading, adding 33 atomic% La to N(5)/C catalyst decreased the C=C peak area and increased the $C_{OH}/(C_C+C_{OH}+C_O)$ ratio from 0.07 to 0.14, indicating improved ability of the N(5)/CL21 catalyst to oxidize carbonaceous species compared to N(5)/C catalyst. Adding a small amount of Sn

(Ni:Sn 14:1) in N(5)/CL21 catalyst increased $C_{OH}/(C_C+C_{OH}+C_O)$ ratio from 0.14 to 0.44 by promoting the WGS reaction (**Fig. 4.37(e)**).

Table 4. 11: Oxidative state ratio for Ni^0, Sn^{4+}, Ce^{3+}, O_V, and C_{OH} calculated from XPS data for reduce (R) and spent (S) catalysts.

Catalyst Name	$Ni^0/(Ni^0+Ni^{2+}+Ni^{3+})$		$Sn^{4+}/(Sn^0+Sn^{2+}+Sn^{4+})$		$Ce^{3+}/(Ce^{3+}+Ce^{4+})$		$O_V/(O_L+O_V+O_{OH})$		$C_{OH}/(C_C+C_{OH}+C_O)$
	Reduce	Spent	Reduce	Spent	Reduce	Spent	Reduce	Spent	
N(5)/C	0.09	0.08			0.31	0.25	0.31	0.31	0.07
N(5)/CL21	0.16	0.11			0.41	0.39	0.43	0.37	0.14
N14S1(5)/CL21	0.34	0.31	0.51	0.39	0.77	0.51	0.56	0.47	0.44
N14S1(5)CL11	0.15	0.11	0.21	0.18	0.32	0.3	0.44	0.37	0.36
N14S1(20)/CL11	0.11	0.1	0.10	0.07	0.3	0.24	0.3	0.25	0.06
N14S1(5)CL12	0.24	0.19	0.5	0.26	0.58	0.45	0.53	0.44	0.42
N7S1(5)/CL21	0.21	0.17	0.47	0.27	0.42	0.39	0.5	0.43	0.28
N1S1(5)/CL21	0.16	0.12	0.06	0.05	0.4	0.34	0.33	0.33	0.09

*** R = Reduced, and S = Spent catalysts.

However, further increasing La concentration to 50 atomic% decreased the $C_{OH}/(C_C+C_{OH}+C_O)$ ratio in N14S1(5)/CL11 catalyst. At constant support composition, increasing metal loading decreased the C_{OH} peak area for N14S(20)/CL11 catalyst, suggesting that higher metal loading is not favorable for oxidizing deposited carbon. Further, increasing Ni:Sn atomic ratio from 14:1 to 1:1 reduced the $C_{OH}/(C_C+C_{OH}+C_O)$ ratio from 0.44 to 0.09 in N14S1(5)/CL21 catalyst [321,382,439]. **Table 4.11** shows the oxidation ratio of the elements.

N_2 adsorption-desorption isotherm was performed to determine the surface area, pore volume, and pore size distribution of the reduced and spent catalysts (**Fig. 4.38**). The N_2 adsorption-desorption (vs) relative pressure isotherm (probably classified as type-IV(a) hysteresis according to IUPAC) suggest a mesoporous structure for the catalyst samples [389,440].

At constant metal loading 5 wt.%, the reduced N14S1(5)/CL21 catalyst, with La 33 atomic%, revealed the higher surface area 138.7 m^2/g compare to 82 m^2/g obtained for the N14S1(5)/CL11 catalyst (**Table 4.8**), with La 50 atomic% [424]. The surface area increased to 87 m^2/g with increasing La to 67 atomic% for the N14S1(5)/CL12 catalyst . Increasing total metal loading from 5 to 20 wt.% at constant support composition reduced the surface area from 82 for N14S1(5)/CL11 to 31 m^2/g for N14S1(20)/CL11 catalyst [424].

After reforming reaction, the surface area of the catalyst decreased compared with the corresponding reduced samples, but basic trend was the same. The following equation (4.14) was used to calculate average particle size using surface area, and bulk density (mass of the material divided by volume) by assuming particles are spherical shape.

The lowest avg. particle size calculated for the N14S1(5)/CL21 catalyst is 6 nm, which is matching with the surface area [243]. Common order followed for reduced and spent samples in terms of decreasing particle size surface as N14S1(5)/CL21 > N14S1(5)/CL12 > N14S1(5)/CL11 > N14S1(20)/CL11. Xue et al. [424] found that increasing La from y= 0.5 to 1 at x = 1 the specific surface area increased from 33 to 47 m^2/g for Ni_xLa_y(10 wt.%)/CeO_2 (x & y = 0.5, 1, 2) catalyst, whereas for increasing Ni from x=0.5 to 1 at y=1 surface area drastically decreased from 41 to 33 m^2/g. Greluk et

al. [243] reported that the incorporation of small amount La in Ni-0.1La/CeO_2 catalyst, significantly increases the sample surface area.

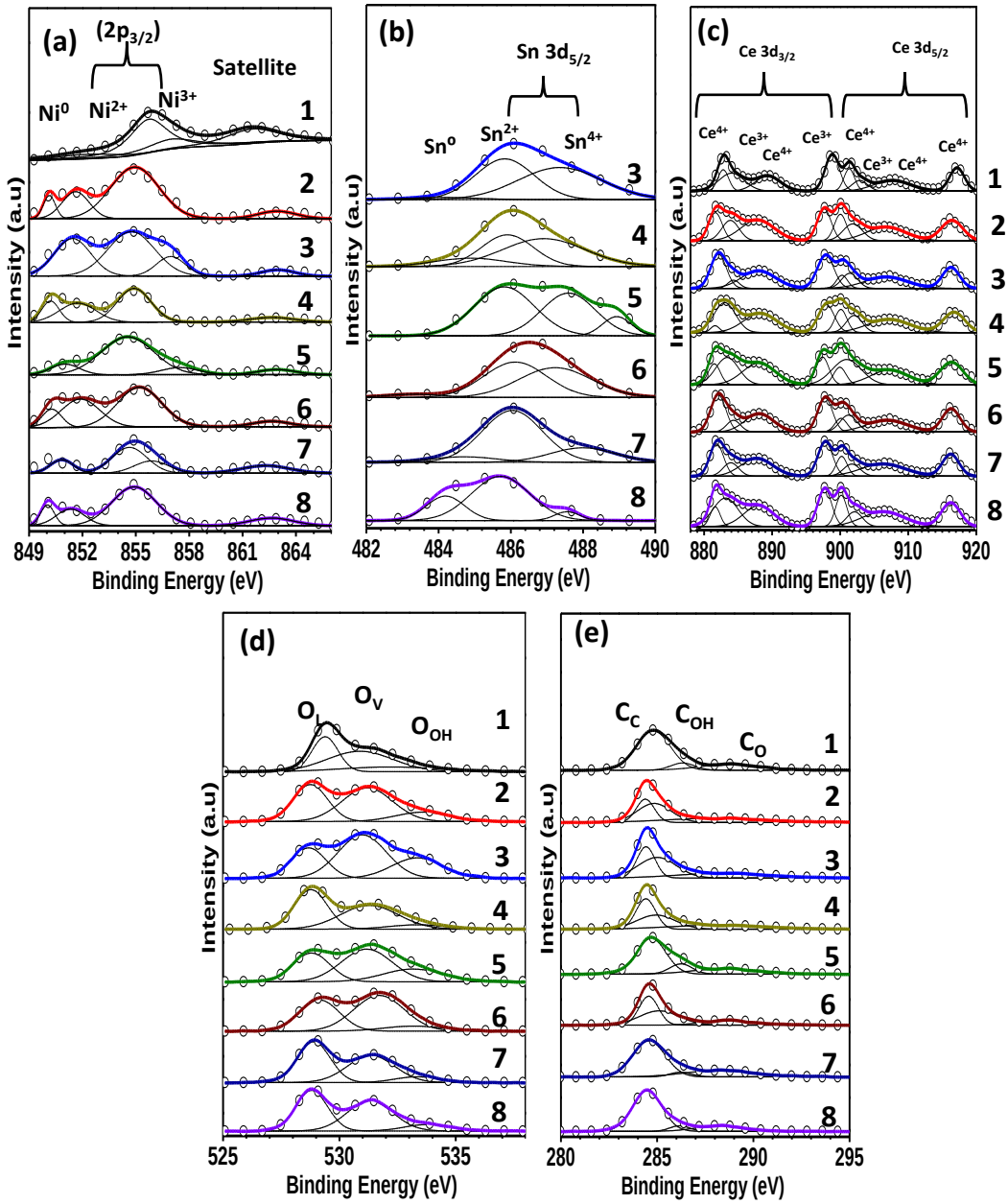

Figure 4. 37: High resolution XPS spectra for reduced catalysts (a) Nickel (2p), (b) Tin (3d), (c) Cerium (3d), and (d) oxygen (1s). Graph (e) carbon on the spent catalysts for 1.N(5)/C, 2.N(5)/CL21, 3.N14S1(5)/CL21, 4.N14S1(5)/CL11, 5.N14S1(20)/CL11, 6.N14S1(5)/CL12, 7.N7S1(5)/CL21 and 8.N1S1(5)/CL21 catalysts.

DTA/TGA analysis was used to analyse the carbon deposition on the spent catalysts shown in **Fig. 4.39** and supplementary **Fig. 4.45**. Two exothermic peaks were noticed for all catalysts. The first one observed in between 290 to 370 °C correspond to decomposition of nickel hydroxide, and the second peak in between 370 to 600 °C corresponding to vaporization of amorphous carbon [369,392].

The addition of 33 atomic% La into N(5)/C catalyst, reduced the weight loss from 54.1 to 34.2 % in N(5)/CL21 catalyst. When tiny amount of tin (NiSn 14:1) was added to the N(5)/CL21 catalyst, the

carbon weight loss greatly dropped from 34.2 to 5%, and the intensity of the peak at 580 ℃ reduced significantly in N14S1(5)/CL21 catalyst.

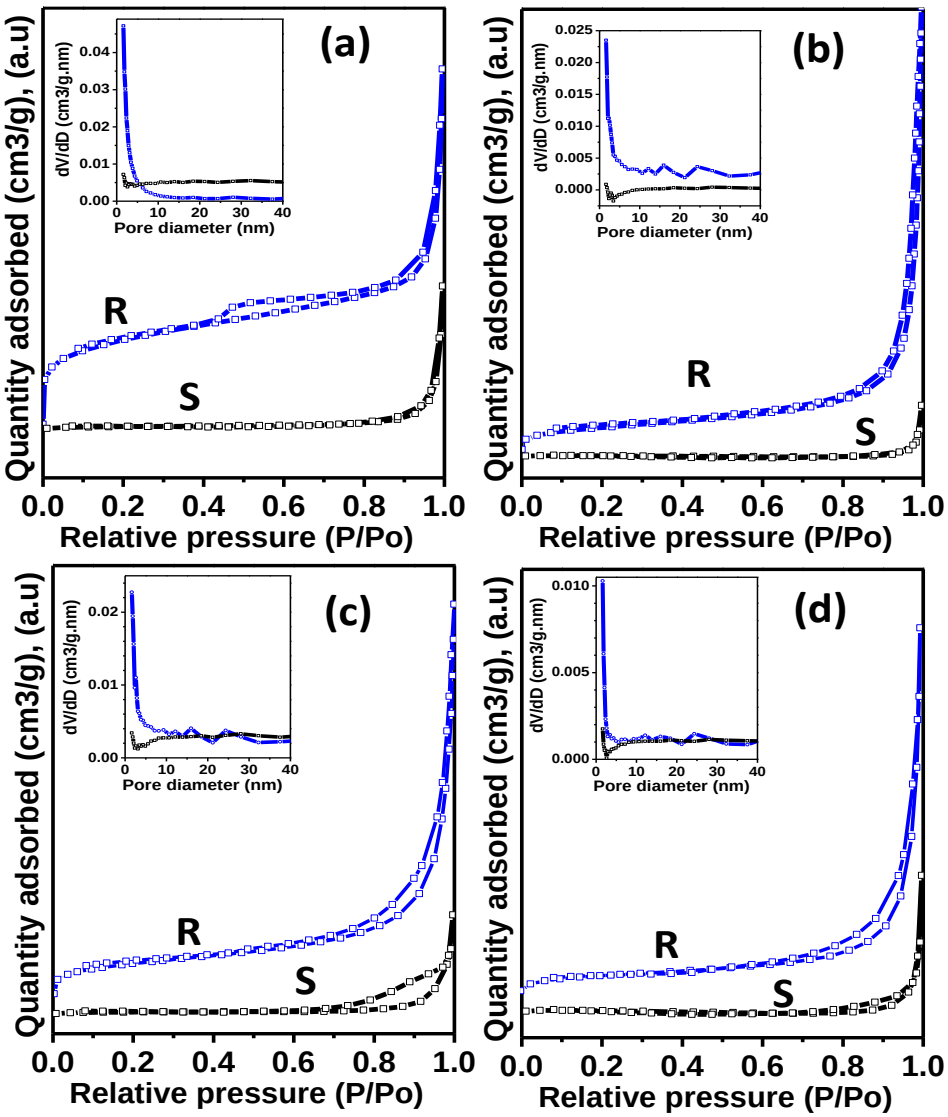

Figure 4. 38: N_2 adsorption-desorption isotherms along with pore diameter distribution for (a) N14S1(5)/CL21, (b) N14S1(5)/CL11, (c) N14S1(20)/CL11 and (d) N14S1(5)/CL12 catalysts, reduced (R) and spent (S) samples.

However, further increasing both tin and La concentration increased carbon weight loss percentage. The decreasing order of TGA weight loss showed as N14S1(5)/CL21 (5 %) > N14S1(20)/CL21 (5.9 %) > N14S1(5)/CL12 (6.46 %) > N14S1(20)/CL12 (9.21 %) > N7S1(5)/CL21 (12 %) > N14S1(5)/CL11 (23.15 %) > N14S1(20)/CL11 (29.0 %) > N1S1(5)/CL21 (32.81 %) > N(5)/CL21 (34.24 %) > N(5)/C (54.14 %). By considering the possibility of the oxidation of the leftover Ni (XPS analysis results) in the spent catalysts, ± 5% error could be considered in the calculation. Grabcheno et al. [426] develop Ni(10 wt.%)/$Ce_{1-x}La_xO_2$ (x= 0.25, 0.5, 0.75) catalysts by using wet-impregnation method and apply for ESR. The increasing order of carbon deposition (TGA weight loss) on the spent

catalysts is Ni(10 wt.%)/$Ce_{0.75}La_{0.25}O_2$ (21 %) < Ni(10 wt.%)/$Ce_{0.25}La_{0.75}O_2$ (29%) < Ni(10 wt.%)/$Ce_{0.5}La_{0.5}O_2$ (46 %).

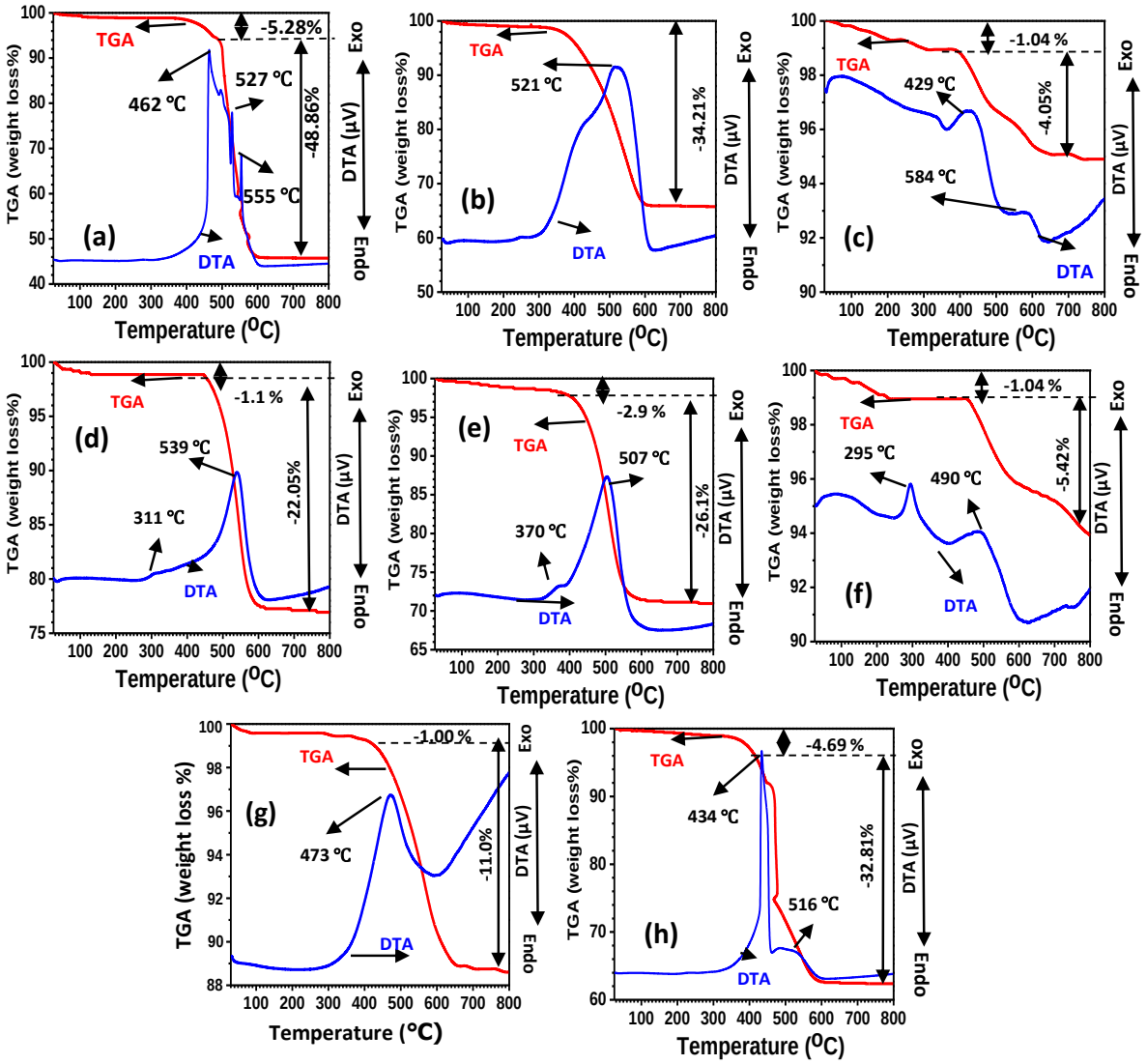

Figure 4. 39: DTA-TGA analysis for spent catalysts (a).N(5)/C, (b).N(5)/CL21, (c). N14S1(5)/CL21, (d). N14S1(5)/CL11, (e) N14S1(20)/CL11, (f) N14S1(5)/CL12, (g) N7S1(5)/CL21, and (h). N1S1(5)/CL21.

4.3.5 Discussion

This work demonstrates the combined effect of La and tin addition on Ni/CeO_2 catalyst, as well as the effect of changing total metal loading. N14S1(5)/CL21 catalyst with low metal loading (5 wt.%), optimum concentration of Sn in Ni (Ni:Sn atomic ratio 14:1) and modification of CeO_2 with La_2O_3 (Ce:La mole ratio 2:1) demonstrated the best catalytic activity in terms of H_2 & CO_2 selectivity, EtOH conversion and coke deposition during steam reforming. These could be explained by the synergistic effects between the elements revealed by a series of physico-chemical characterizations. Based on the

understanding of catalytic activity results and the previous literature study basic possible reaction pathways for NiSn/$Ce_{1-x}La_xO_2$ catalyst systems are showen in supplementary **Fig. 4.46**.

XRD analysis showed that incorporation of La (atomic ratio of 0.33, 0.5, and 0.67) into CeO_2 lattice created homogeneous solid solutions $Ce_{1-x}La_xO_2$ (variable x values) in all catalysts which remain stable under all treatment conditions; fresh, reduced and spent. The close ionic radius of La^{3+} (0.106 nm) and Ce^{4+} (0.101 nm) are considered to be responsible for it, which also observed and reported by other researchers [415,429]. The incorporation of 33 atomic% La to N(5)/C catalyst, while maintaining a constant metal loading, resulted a solid solution formation ($Ce_{0.8}La_{0.2}O_2$) and the interaction between metal and support increased according to the H_2-TPR results. Thus, the metal and support particle sizes decreased. Raman and XPS analysis show an increase in oxygen vacancy in the reduced N(5)/CL21 which could be explained by the Kröger–Vink notation as:

$$La_2O_3 \overset{CeO_2}{\longleftrightarrow} 2La'_{Ce} + V_o^{\cdot\cdot} + 3O_o^x \quad (4.18)$$

La addition helps to reduce acidity of the support too. Interestingly, at constant metal loading (5 & 20 wt.%) and Ni:Sn atomic ratio 14:1, increasing La to 50 atomic% increased the particle sizes of both metal & $Ce_{0.5}La_{0.5}O_2$ support, decrease the active surface area & oxygen vacancy concentration as revealed by XRD, XPS, Raman and N_2 absorption- desorption analysis [415,429]. H_2-TPR data demonstrated a decrease in NiO reduction temperature, specifying a weak MSI. As a result, the H_2 selectivity significantly reduced. Apparently, this seems anomalous, however similar behavior of La-Ce-O system is reported in literature. Wang et al. [430] studied the water gas shift over Au-mixed lanthanum/cerium oxide catalysts and reported that the upto 25 atomic % La addition enhance the reducibility of CeO_2 and with further La addition reducibility drops steeply. Similarly, the maximum oxygen vacancies are formed upon 25% La substitution and addition of more La decrease the available lattice oxygen and the catalytic activity declined. It is explained that the oxygen is much more strongly bound to La than to Ce.

However, further increasing La to 67 atomic% produces $Ce_{0.5}La_{0.5}O_2$ and secondary oxide phase $LaNiO_3$ in fresh N14S1(5)/CL12 catalyst. In the reduced and spent N14S1(5)/CL12 catalyst samples La_2O_3 could reveal by XRD with $LaNiO_3$. $LaNiO_3$, a member of perovskite-type oxide (ABO_3) material group, is known for high MSI (observed in H_2-TPR analysis) and produces small active metal particles during reduction as: .

$$2LaNiO_3 + H_2 \rightarrow La_2Ni_2O_5 + H_2O \quad (4.19)$$

$$La_2Ni_2O_5 + 2H_2 \rightarrow La_2O_3 + 2Ni^0 + 2H_2O \quad (4.20)$$

Thus, the metal & $Ce_{0.5}La_{0.5}O_2$ support particle size decreased, active surface area and the oxygen vacancy increased as demonstrated by XRD, XPS, Raman, H_2-TPR and N_2 absorption & desorption. XPS revealed more metallic Ni^0 in reduced and spent N14S1(5)/CL12 catalyst compared to N14S1(5)/CL11 catalyst. In terms of possible reaction pathways (Supplementary **Fig. 4.46**) it could be inferred that addition of certain amount of La to CeO_2 (Ce:La mole ratio of 2:1) enhances WGS reaction

(Supplementary Eq. (4.31)) [45] and coke gasification. However, a higher amount of La results in an increased acidity of the support. This acidity can lead to additional reactions, such as the formation of acetone and methanol (Supplementary Eq. (4.35) & (4.36)) and ethylene through dehydration (Supplementary Eq. (4.37)) [71,434], which can further polymerize to form coke [109].

With increasing total metal loading from 5 to 20 wt.% at constant support composition and Ni:Sn atomic ratio 14:1, the active surface area and MSI decreased, and particle sizes increased (H_2-TPR, XRD and N_2 absorption & desorption) for all the catalysts, as expected. Accordingly, the oxygen vacancies decreased leading to the formation of higher amount graphitic nature carbon in the spent samples compared to the 5wt% metal loaded catalysts revealed by Raman, XPS, and DTA-TGA characterizations. Important to mention that for the N14S1(x)/CL21 and N14S1(x)/CL11 catalysts no change in phases were observed during the change of x from 5 to 20 wt.%. However, for the N14S1(x)/CL12 catalyst no $LaNiO_3$ phase could be noticed and a unknown $Ce_{1-x}La_xO_3$ solid solution showing lower angle peak shifting compared to $Ce_{0.5}La_{0.5}O_2$ phase peaks is observed at x =20 wt%. At 20 wt.% total metal loading the absolute amount Ni increased. According to Cao et al. [441] and Sellam et al. [427] high Ni with La_2O_3 may produce $LaNiO_3$ during catalyst preparation as shown in Eq. 4.21. However, this phase probably decomposes to La_2O_3 & NiO (Eq. 4.22 & 4.23) due to high temperature attend during SCS. Further these La_2O_3 reacting with $Ce_{0.5}La_{0.5}O_2$ and synthesizing the unknown solid solution.

$$2Ni + La_2O_3 + 2H_2O + 1/2O_2 \rightarrow 2LaNiO_3 + 2H_2 \quad (4.21)$$

Decomposition steps of $LaNiO_3$ phase

$$2LaNiO_3 \rightarrow La_2NiO_4 + Ni^{2+} + O_2 \quad (4.22)$$

$$La_2NiO_4 \rightarrow NiO + La_2O_3 \quad (4.23)$$

Considering the reaction pathways it could be implied that methane reforming (Supplementary Eq. 4.29 & (4.30)) and WGS reaction (Supplementary Eq. (4.31)) are more favorable [107,108] at lower metal loading while methane decomposition (Supplementary Eq. (4.39)) may not occur effectively [113,114] leading to decreased carbon formation [442] compared to higher metal loading. Moreover, lower metal loading promotes acetaldehyde decomposition reaction (Supplementary Eq. (4.28)). At 5 wt.% metal loading and Ce:La = 2:1 atomic ratio, adding small amount of tin (Ni:Sn atomic ratio 14:1) in N(5)/CL21 catalyst significantly reduced the metal & $Ce_{0.8}La_{0.2}O_2$ support particle sizes and enhanced the oxygen vacancies as demonstrated by XRD, Raman, and XPS. XPS analysis revealed the highest ratio of $Sn^{4+}/(Sn^{2+}+Sn^{4+})$ for the N14S1(5)/CL21 catalyst, which is more advantageous for increasing oxygen mobility and decreasing carbon formation during SRE via water gas shift reaction [251]:

$$CO + H_2O \rightarrow CO_2 + 2H^+ + 2e^- \quad (4.24)$$

$$Sn^{4+} + 2e^- \rightarrow Sn^{2+} \quad (4.25)$$

Addition of Sn (Ni:Sn 14:1 atomic ratio) increased the reduction temperature for N14S1(5)/CL21 catalyst and maximum amount of H_2 consumption is obtained for this catalyst which indicate the reduction in metal particle size and improvement of MSI. Reportedly, some amount of Sn with Ni may help to reduce methane formation by increasing methane reforming and water gas shift reactions [395]. This increases the H_2 selectivity significantly while reducing the coke deposition during reforming.

However, increasing Ni:Sn atomic ratio from 14:1 to 1:1 in N14S1(5)/CL21 catalyst decrease the NiO reduction temperature, due to weaker MSI [395]. This is in the same line as the observations of the other researchers. Henge et al. [395] reported that addition of too much tin actually increase the reduction of NiO to Ni phase. Pastor et al. [360] detected through XPS that presence of high amount of tin (Ni:Sn atomic ratio 10:1) enhance the Ni reducibility leading to increase in the particle size of metallic Ni. XRD analysis showed the increase of both active metal and $Ce_{0.8}La_{0.2}O_2$ support particle size indicating agglomeration of the catalyst. N_2 adsorption- desorption characterization confirmed the decrease in the surface area. According to Shabaker et al. & Dumesic et al. [382] increasing the Sn concentration weakens CO adsorption and reduces catalytic performance during reforming reaction. Small amount of Sn in Ni facilitates the dehydrogenation of ethanol (supplementary Eq.(4.27)) and the water-gas shift (WGS) reaction (supplementary Eq. (4.31)) [380,443]. However less favorable for the formation of methanol (supplementary Eq. (4.32, & 4.33)) and carbon deposition through methane decomposition (supplementary Eq.(4.39)) [251,382], & ethanol decomposition (supplementary Eq.(4.37, & 4.38)) compared with the higher Ni:Sn atomic ratios of 7:1 and 1:1 [410,444].

Stroud et al. [439] reported that Sn in Ni could make Ni_3Sn or some other form of Ni-Sn alloy. But, if a high amount of Sn is present in CeO_2 then it can react with CeO_2 and create complex compounds. Thus, the bond between the nickel and the support gets weaken and rapid sintering of the particles occur. Eventually, bigger particles and also block the active sites of nickel [360], reduce the activity of the catalyst, and enhance coke deposition.

4.3.6 Conclusion

Lanthanum (as support modifier) and tin (as Ni promoter) are perceived to enhance stability and activity of the Ni/CeO_2 catalyst for low temperature ethanol steam reforming. XRD, XPS, Raman, TPR, and TPD analysis show that 33 at.% La addition reduces particle sizes and enhances oxygen vacancies, metal-support interaction, and basicity of the catalyst, which lead to the maximum H_2 selectivity of 60% with 100 % EtOH conversion and low coke deposition for the N14S1(5)/CL21 catalyst. 50 at.% La loading affects the performance of the catalyst negatively, whereas agglomeration of active metal and support particles are noticed in case of the high Sn concentration (NiSn 1:1 atomic ratio) and the high metal (20 wt.%). As a result, N14S1(20)/CL11 obtains 43% H_2 selectivity and 93% EtOH conversion and promotes coke deposition. 67 at.% La loading creates the perovskite $LaNiO_3$

phase (XRD shows) during syntheses of the fresh catalysts, which reduces the active Ni particle during reduction and leads to better activity and stability for the N14S1(5)/CL12 catalyst.

4.3.7 Supplementary data

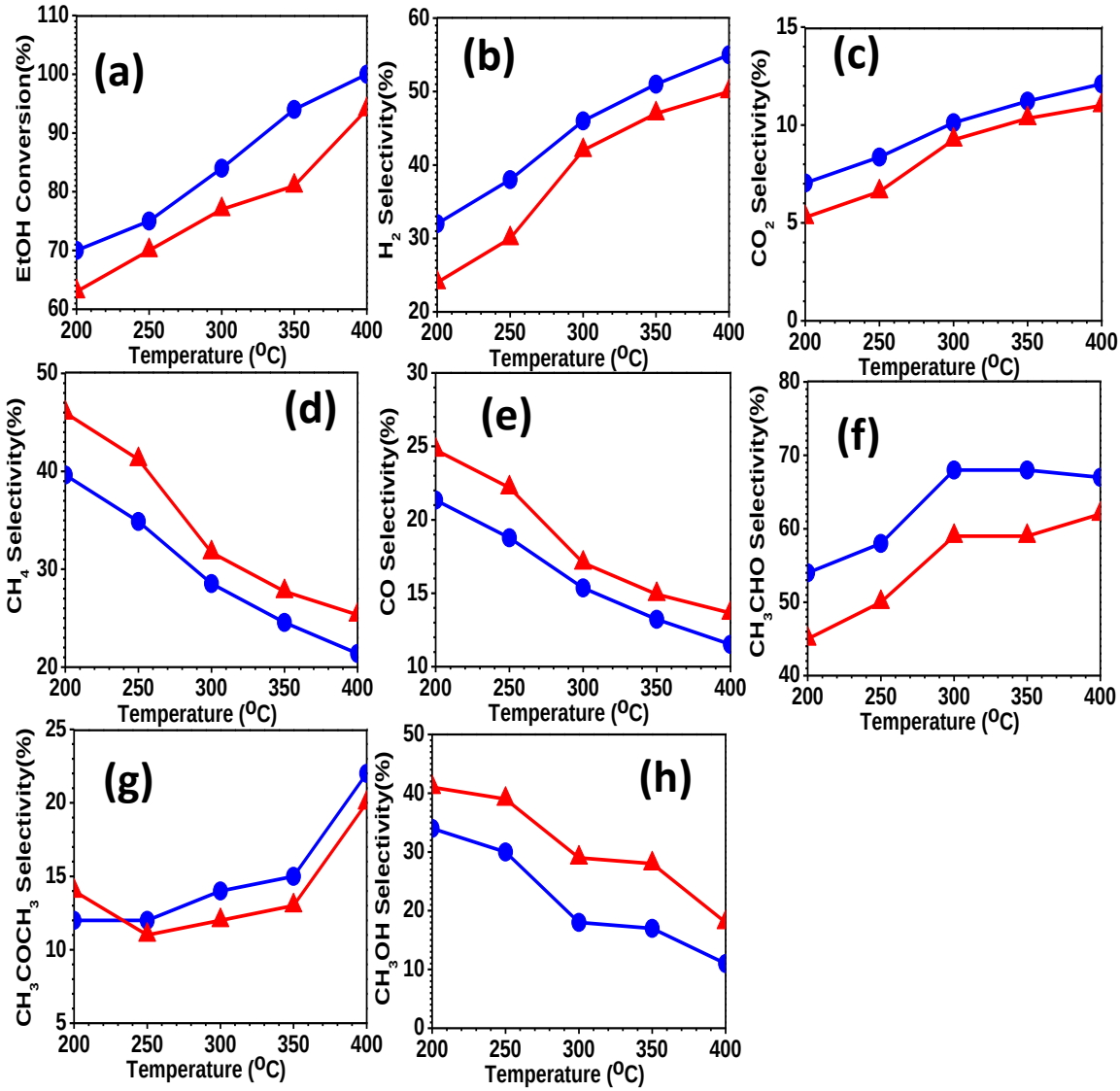

Figure 4. 40: Steady state variation of (a) EtOH conversion, selectivity of gaseous products (b) hydrogen, (c) carbon dioxide, (d) methane, (e) carbon monoxide, and liquid products (f) acetaldehyde, (g) acetone, (h) methanol as a function of temperature (200-400 °C), EtOH : H_2O 1:12 mole ratio and feed flow rate 0.1 ml/min over N14S1(20)/CL21 (●), N14S1(20)/CL12 (▲) catalysts.

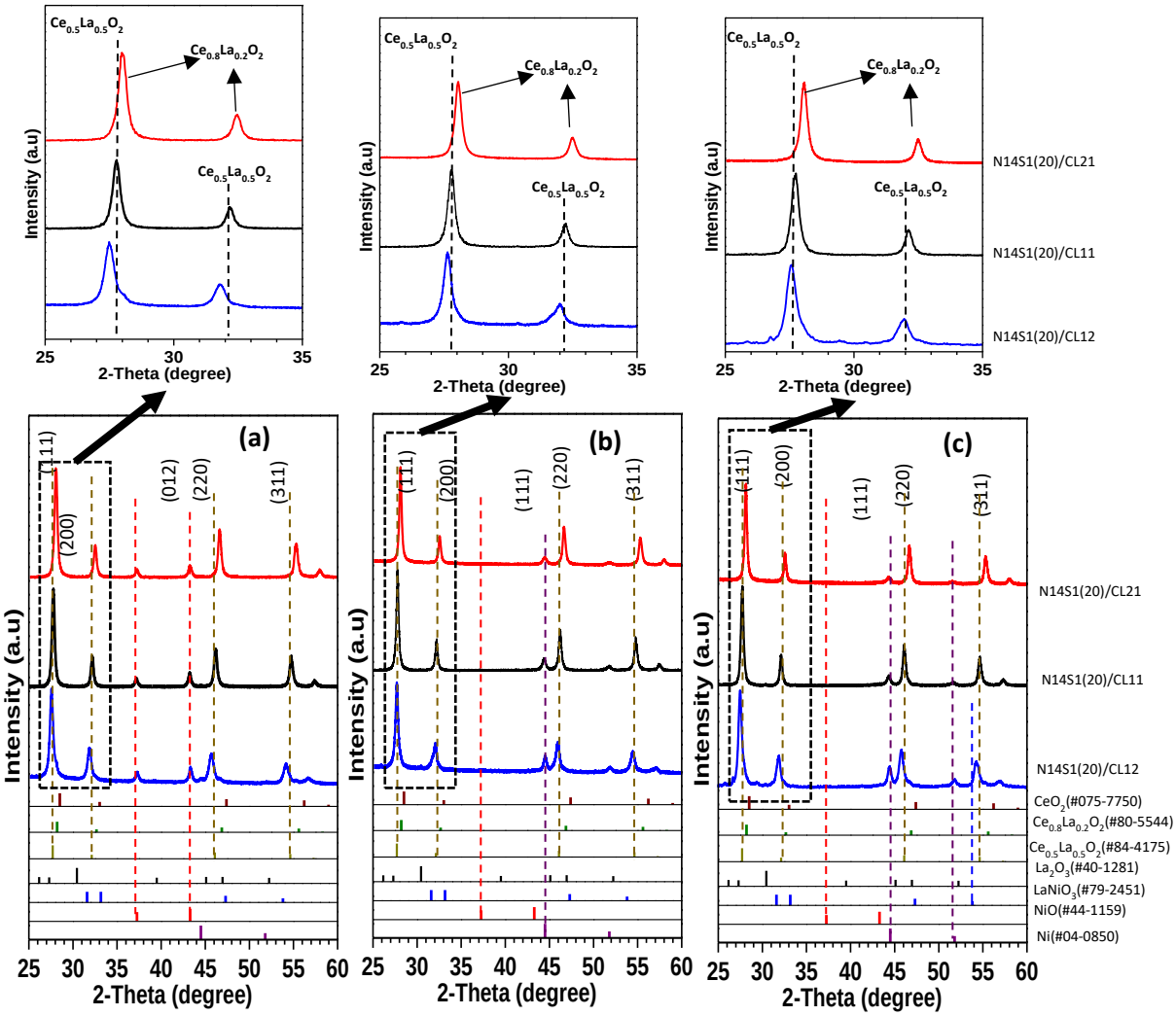

Figure 4. 41: XRD spectra for (a) Fresh, (b).Reduced, (c) Spent of phases identified with the reference powder diffraction file (PDF) of Ni(PDF# 04-0850), CeO_2(PDF#75-7750), NiO(PDF#44-1159), $Ce_{0.5}La_{0.5}O_2$(PDF#84-4175), $Ce_{0.8}La_{0.2}O_2$(PDF#80-5544), $NiLaO_3$(PDF#79-2451), La_2O_3(PDF#40-1281).

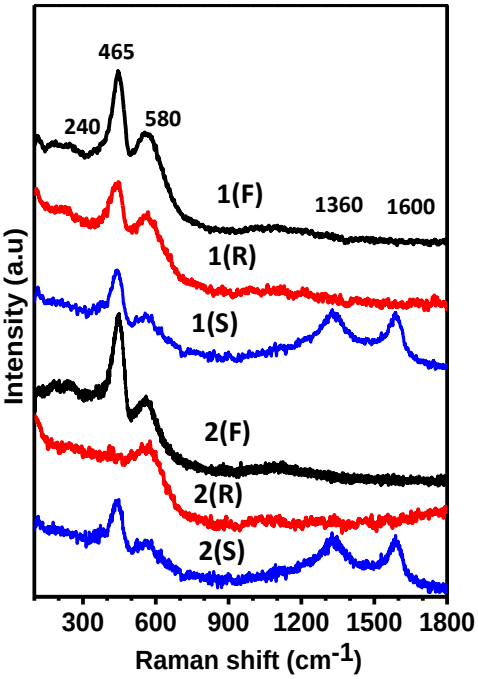

Figure 4. 42: Raman spectra for (1) N14S1(20)/CL21 and (2) N14S1(20)/CL12 catalysts of fresh (F), reduced (R), spent (S) samples.

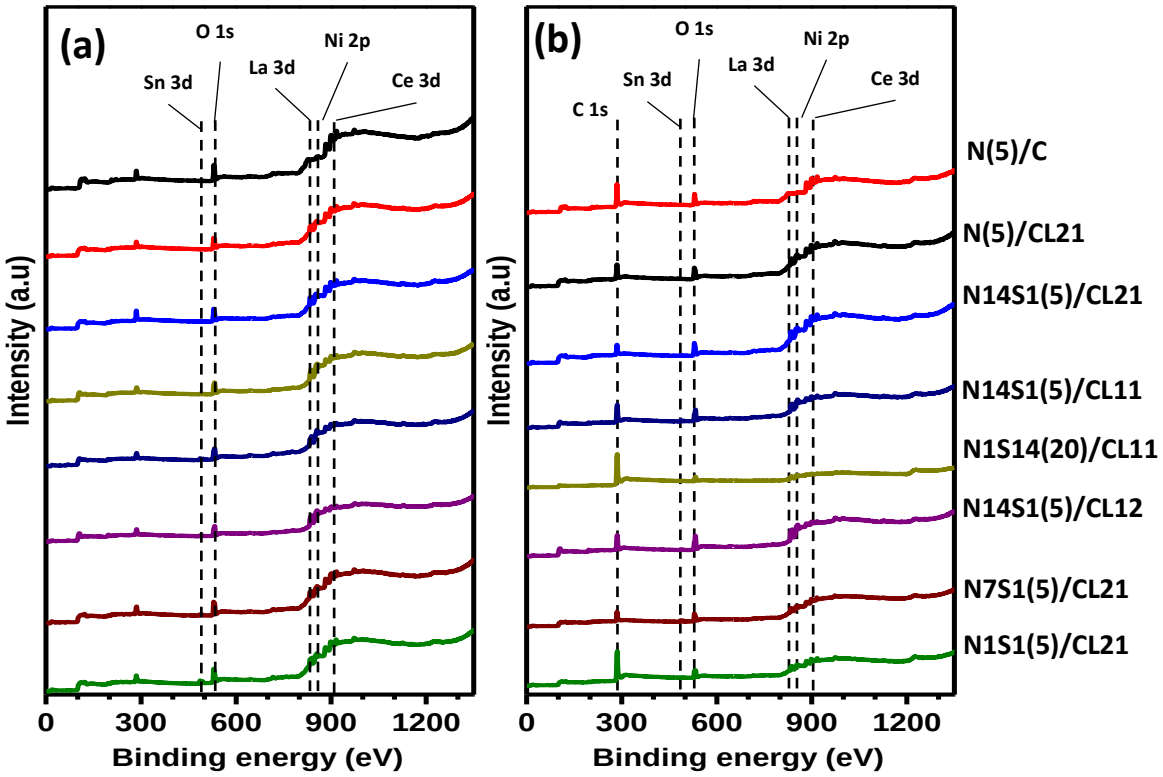

Figure 4. 43: Wide scan XPS spectra of a) Reduce and b) Spent samples.

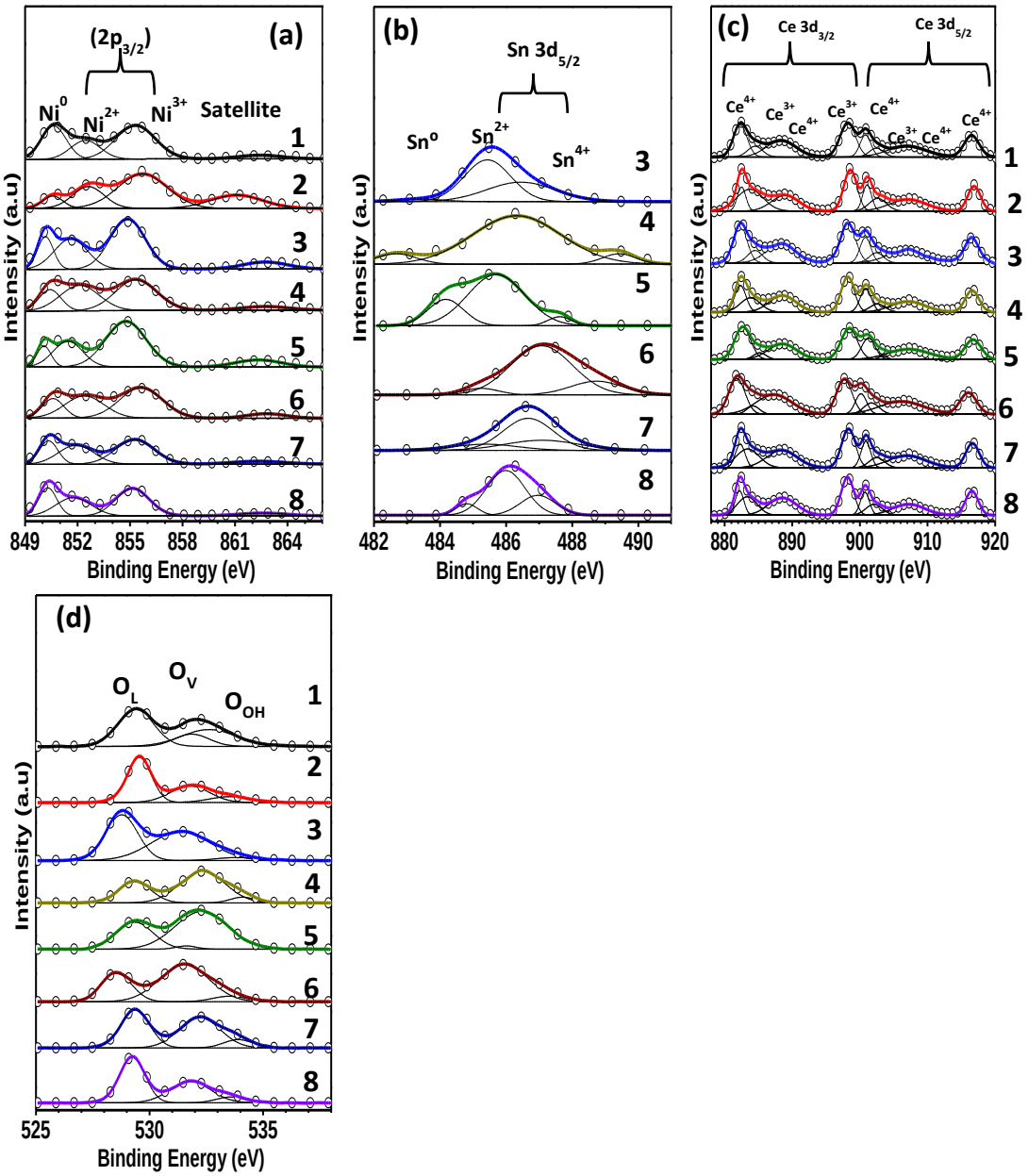

Figure 4. 44: High resolution XPS spectra for spent catalyst samples of (a) Nickel (2p), (b) Tin (3d), (c) Cerium (3d), and (d) oxygen (1s) for 1.N(5)/C, 2.N(5)/CL21, 3.N14S1(5)/CL21, 4.N14S1(5)/CL11, 5.N14S1(20)/ CL11, 6.N14S1(5)/CL12, 7.N7S1(5)/CL21 and 8.N1S1(5)/CL21 catalyst.

Table 4. 12: Elemental analysis obtained from EDS analysis.

Name of the catalyst	FESEM elemental analysis (wt.%)																TEM elemental analysis (wt.%)										
	Fresh					Reduced					Spent						Reduced					Spent					
	Ni	Sn	Ce	La	O	Ni	Sn	Ce	La	O	Ni	Sn	Ce	La	O	C	Ni	Sn	Ce	La	O	Ni	Sn	Ce	La	O	C
N14S1(5)/CL21	4.8	0.6	45	23	27	5	0.8	48	24	22	4.5	0.5	34	17	19	26	4.6	0.7	48.7	25	21	4	0.4	32.6	18	17	28
N14S1(20)/CL11	17.8	2.1	26.9	26	27	20.4	2.3	31	31	16	12.5	1.5	15	15	16	39	18.6	2.4	32	31	16	12	0.7	11.3	16	18	42

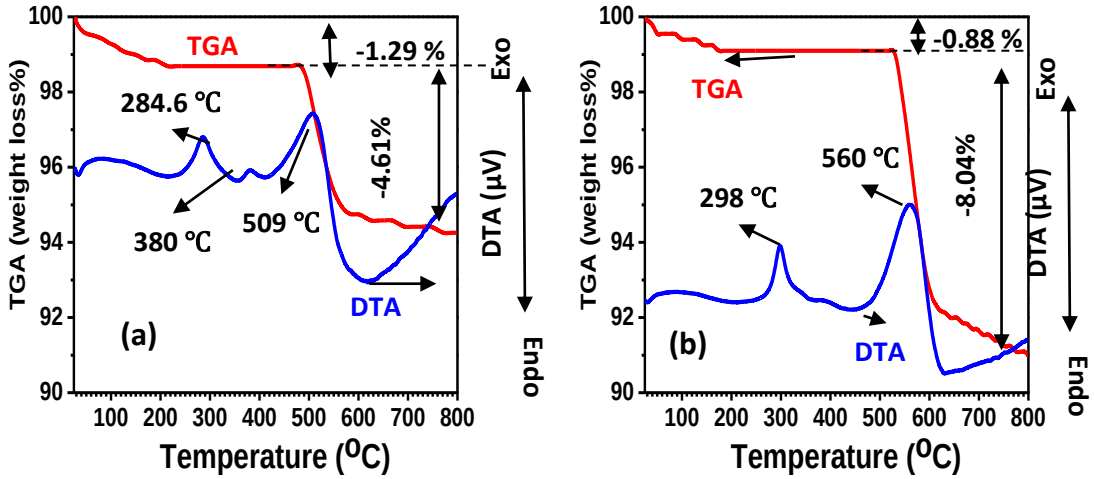

Figure 4. 45: DTA-TGA analysis for spent (a) N14S1(20)/CLL21 and (b) N14S1(20)/CL21 catalysts.

Basic Reaction Pathways

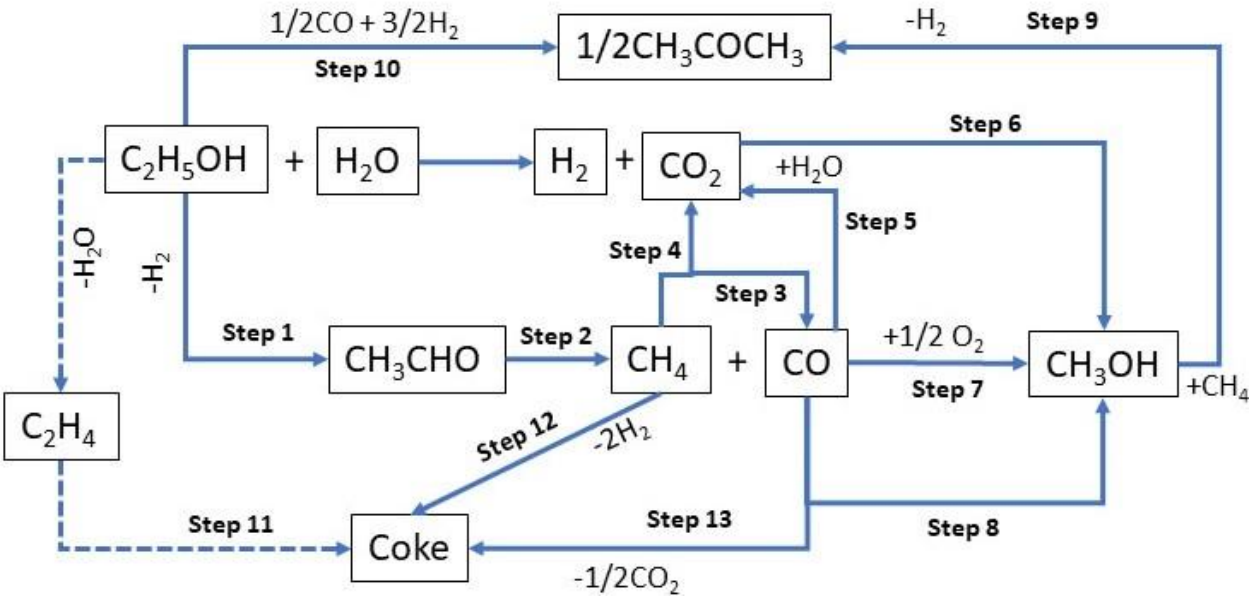

Figure 4. 46 : Possible reaction pathways for SRE on NiSn/$Ce_{1-x}La_xO_2$ catalysts [45,92,95].

"The ideal ethanol steam reforming reaction (Eq. (4.26)), for formation of H_2 and CO_2 as major products [45].

$C_2H_5OH\ (g) + 3H_2O(g) \leftrightarrow 2CO_2\ (g) + 6H_2\ (g)$ $\Delta H^o_{25} = +173$ kJ/mol (4.26)

However, during the SRE, other carbon-containing compounds such as CO, CH_4, CH_3CHO, and CH_3OH are also produced. A possible reaction pathways schematic based on the products formation and previous literatures [45,92,95] is shown in **Fig. 4.46** and could be explained as follows:

Step 1: Dehydrogenation of ethanol leading to formation of acetaldehyde [92,252]

$C_2H_5OH\ (g) \leftrightarrow CH_3CHO\ (g) + H_2\ (g)$ $\Delta H^o_{25} = +68.9$ kJ/mol (4.27)

Step 2: Acetaldehyde decomposition

$CH_3CHO\ (g) \leftrightarrow CH_4\ (g) + CO\ (g)$ $\Delta H^o_{25} = -55.8$ kJ/mol (4.28)

Steps 3 & 4: Methane steam reforming

$CH_4 (g) + H_2O (g) \leftrightarrow CO (g) + 3H_2 (g)$ $\Delta H^o_{25} = +206.2$ kJ/mol (4.29)

$CH_4 (g) + 2H_2O (g) \leftrightarrow CO_2 (g) + 4H_2 (g)$ $\Delta H^o_{25} = +186.2$ kJ/mol (4.30)

Step 5: Formation of CO_2 & H_2 through water gas shift reaction [45]

$CO(g) + H_2O (g) \leftrightarrow CO_2 (g) + H_2 (g)$ $\Delta H^o_{25} = -41$ kJ/mol (4.31)

Step 6, 7, & 8: Possible routes for formation of CH_3OH

$2H_2O (g) + CO_2 (g) \leftrightarrow CH_3OH (g) + 3/2\ O_2$ $\Delta H^o_{25} = 28$ kJ/mol (4.32)

$2H_2O (g) + CO (g) \leftrightarrow CH_3OH (g) + 1/2\ O_2$ $\Delta H^o_{25} = 24$ kJ/mol (4.33)

$2H_2 (g) + CO (g) \leftrightarrow CH_3OH (g)$ $\Delta H^o_{25} = 49$ kJ/mol (4.34)

Steps 9 & 10: Formation of CH_3COCH_3 through ethanol condensation [92,95]

$CH_3OH (g) + 2CH_4 (g) \leftrightarrow CH_3COCH_3 (g) + 3H_2 (g)$ $\Delta H^o_{25} = 141.5$ kJ/mol (4.35)

$2C_2H_5OH (g) \leftrightarrow CH_3COCH_3 (g) + CH_4 (g) + H_2O (g)$ $\Delta H^o_{25} = 183.5$ kJ/mol (4.36)

Steps 11 & 12: Possible routes for carbon formation through decomposition of ethanol and methane.

$C_2H_5OH (g) \leftrightarrow C_2H_4 (g) + H_2O (g)$ $\Delta H^o_{25} = 45$ kJ/mol (4.37)

$nC_2H_4 \rightarrow \text{polymer} \rightarrow C (s)$ $\Delta H^o_{25} = -171.5$ kJ/mol (4.38)

$CH_4 \rightarrow C + 2H_2$ $\Delta H^o_{25} = -141.5$ kJ/mol (4.39)

However, we did not see C_2H_4 as a product. So, it is shown as a dotted line.

Steps 13: Moreover, the Boudouard reaction (Eq. (4.40)) is favored at low temperatures, which is favorable for formation of carbon from CO.

$2CO (g) \leftrightarrow C(s) + CO_2 (g)$ $\Delta H^o_{25} = -171.5$ kJ/mol (4.40)

Chapter 5: Concluding remarks

5.1 Conclusions

The following conclusions are drawn based on the results obtain in the present study:

1. The promotion of Ni with tin and the modification of the CeO_2 support by MgO, ZrO_2, and La_2O_3 could be beneficial to produce hydrogen by low temperature steam reforming of ethanol; between 200 and 400 ℃.
2. Increase in reactor temperature leads to an increase in EtOH conversion, as well as H_2, CO_2, CH_3CHO and CH_3COCH_3 selectivity. On the other hand, the selectivity of CO, CH_4 and CH_3OH demonstrates an opposite trend with increasing the temperature.
3. The gas and liquid phase product distribution explains that EtOH is probably dehydrogenated to the aldehyde as a primary step, followed by the decarbonylation of the aldehyde to CH_4 and CO. Then methane reforming and WGS reaction occur, as expected in the temperature range of our experiments.
4. **Effect of Sn:** Tin addition in Ni/CeO_2 enhances the catalytic properties and the optimal quantity of tin (Ni: Sn =14:1 atomic ratio) demonstrates the maximum activity performance by increasing the H_2 selectivity. The oxygen vacancy increases with inter ionic exchange between Sn^{2+} and Ce^{3+} during reduction, as shown by Raman and XPS studies. The formation of carbon on the catalyst surface during the ethanol steam reforming reaction has been shown to decrease by DTA/TGA, Raman, and XPS analysis. Sn facilitates the water gas shift process to oxidation of the carbon, since both carbon and Sn are group-IV elements. Further increase in the Sn concentration led to the formation of graphitic carbon on the surface of the catalyst due to the geometric effect (a high concentration of larger ionic radii). This led to a agglomeration of active metal and lowering in H_2 selectivity.
5. **Effect of total metal loading:** The best activity is realized at 5 wt.% metal loading, probably due to smallest metal particle/crystallite sizes and active surface area as deduce from XRD, FESEM, and N_2-adsorption desorption results. H_2-TPR shows that the metal-support interaction (MSI) gets weaker as the amount of metal in the system increases. This might be the cause of the increasing metal particle size seen by XRD, which in turn caused the active metal surface area to decrease, as confirmed by N_2-adsorption desorption. XPS and Raman spectroscopy both revealed a decrease in oxygen vacancies for higher metal loading, which in turn led to an increase in carbon formation and a subsequent reduction in H_2 selectivity.
6. **Effect of Zr:** An increase in thermal stability due to formation of a more stable $Ce_{1-x}Zr_xO_2$ solid solution is a benefit of zirconium's incorporation into the ceria lattice. This $Ce_{1-x}Zr_xO_2$ solid solution improves the contact between the metal and the support and could be responsible for the decreasing Ni particle size. As a consequence of this, the $Ni_{0.93}Sn_{0.07}(20)/Ce_{0.33}Zr_{0.67}O_{1.33}$ catalyst displays excellent ethanol conversion, good hydrogen selectivity, and minimal coke

deposition. Technically, the replacement of Zr^{4+} (0.086 nm) by Ce^{4+} (0.101 nm) with a substantial size difference between the ions may be responsible for the development of extra oxygen vacancies in the lattice confirmed by XPS and Raman.

7. **Effect of Mg**: Adding MgO as a CeO_2 support modifier improves the catalytic performance by reducing the size of Ni and CeO_2 particle/crystallite sizes as demonstrated by XRD, Raman, FESEM, and TEM. This cause the metal's active surface area increases, which was proven by N_2-adsorption desorption. Addition of Mg^{2+} ions significantly increase OSC of the support lattice and decreases carbon formation, as shown by XPS, Raman, and DTA/TGA. Basic nature MgO reduces the acidic nature of the confirmed by NH_3-TPD. Furthermore, Mg^{2+} creates the $NiMgO_2$ solid solution, which results in an increase in MSI and prevents the sintering of nickel particles during the reduction process confirmed by XRD and H_2-TPR.
8. **Effect of La**: Incorporation of La_2O_3 into ceria supports observes the formation of $Ce_{1-x}La_xO_2$ solid solution phase. It is demonstrated by XRD and N_2-adsorption desorption that the particle size of Ni and $Ce_{1-x}La_xO_2$ drastically reduce when Ce: La = 2:1 mole ratio is maintained in catalyst and changes the surface morphology observed by FESEM. Whereas the particle size increased with further increasing La^{3+} concentration. The formation of $Ce_{1-x}La_xO_2$ solid phase leads to enhance the OSC and changes in redox property observed by XPS, Raman, H_2-TPR. DTA/TGA and Raman demonstrated that lower (5 wt.%) metal loading decrease the carbon formation on the catalyst surface, whereas increasing La^{3+} concentration increase the carbon formation.
9. Catalysts with Ce:Zr = 1:2, Ce:Mg = 1:2, and Ce:La = 2:1 show the best catalytic properties and activity results (**Table 5.1**). At 400 °C reaction temperature the maximum H_2 selectivity report to be 68%, 72%, 60% with 100% EtOH conversion, feed concertation EtOH:H_2O 1:12 mole ratio and feed flow rate 0.1 ml/min and also the maximum oxygen vacancy 68%, 81%, 56% and low carbon weight loss 2.4 wt.%, 3.2 wt.%, 5 wt.% for $Ni_{0.93}Sn_{0.07}(5)/Ce_{0.33}Zr_{0.67}O_{1.33}$, $Ni_{0.93}Sn_{0.07}(5)/Ce_{0.33}Mg_{0.67}O_{1.33}$, $Ni_{0.93}Sn_{0.07}(5)/Ce_{0.67}La_{0.33}O_2$, respectively.

Table 5. 1: List of the catalysts studied on LTSRE along with their properties and activity results.

S.No	Catalyst name		Catalyst properties				Activity results			C (%)
		D_s	D_{Ni}	TOS (h)	S_{BET}	O_V (%)	EtOH conversion (%)	H_2 (S%)	CO (S%)	
1	$Ni(5)/Ce_{0.5}Zr_{0.5}O_2$	21	14	20	-	-	90	59	5	20
2	$Ni(20)/Ce_{0.5}Zr_{0.5}O_2$	28	33		-	44	64	45	14	44
3	$Ni(5)/Ce_{0.33}Zr_{0.67}O_{1.33}$	17	14		-	-	95	62	2.5	16
4	$Ni(20)/Ce_{0.33}Zr_{0.67}O_{1.33}$	24	28		-	-	72	49	12	31
5	$Ni_{0.93}Sn_{0.07}(5)/Ce_{0.5}Zr_{0.5}O_2$	18	14		-	-	100	65	1	14
6	$Ni_{0.93}Sn_{0.07}(20)/Ce_{0.5}Zr_{0.5}O_2$	21	18		-	-	76	52	9	30
7	$Ni_{0.93}Sn_{0.07}(5)/Ce_{0.33}Zr_{0.67}O_{1.33}$	14	12		-	68	100	68	0	2.4
8	$Ni_{0.93}Sn_{0.07}(20)/Ce_{0.33}Zr_{0.67}O_{1.33}$	21	18		-	-	82	56	7	27
9	$Ni_{0.93}Sn_{0.07}(5)/CeO_2$	15	13	10	-	55	85	45	14	11
10	$Ni_{0.93}Sn_{0.07}(10)/CeO_2$	21	21		-	54	80	41	16	18

11	$Ni_{0.93}Sn_{0.07}(20)/CeO_2$	24	22		7.5	49	70	32	20	27
12	$Ni_{0.93}Sn_{0.07}(5)/Ce_{0.5}Mg_{0.5}O_2$	7	-		-	80	100	65	6	4.9
13	$Ni_{0.93}Sn_{0.07}(10)/Ce_{0.5}Mg_{0.5}O_2$	10	10		-	64	98	57	9	7.4
14	$Ni_{0.93}Sn_{0.07}(20)/Ce_{0.5}Mg_{0.5}O_2$	12	22		-	50	95	50	12	7.41
15	$Ni_{0.93}Sn_{0.07}(5)/Ce_{0.33}Mg_{0.67}O_{1.33}$	6	-		62.6	81	100	72	4	3.2
16	$Ni_{0.93}Sn_{0.07}(10)/Ce_{0.33}Mg_{0.67}O_{1.33}$	9	20		-	72	100	59	8	5.6
17	$Ni_{0.93}Sn_{0.07}(20)/Ce_{0.33}Mg_{0.67}O_{1.33}$	1	21		-	65	99	57	10	7
18	$Ni(5)/Ce_{0.33}Mg_{0.67}O_{1.33}$	8	-		-	68	98	51	11	13
19	$Ni_{0.88}Sn_{0.11}(5)/Ce_{0.33}Mg_{0.67}O_{1.33}$	7	-		-	74	84	40	16	6.6
20	$Ni(5)/CeO_2$	37	27	20	-	31	68	32	21	54
21	$Ni(5)/Ce_{0.67}La_{0.33}O_2$	36	24		-	43	88	36	20	34
22	$Ni_{0.93}Sn_{0.07}(5)/Ce_{0.67}La_{0.33}O_2$	27	17		138.7	56	100	60	9	5
23	$Ni_{0.93}Sn_{0.07}(20)/Ce_{0.67}La_{0.33}O_2$	18	19		-	-	100	55	12	5.9
24	$Ni_{0.93}Sn_{0.07}(5)/Ce_{0.5}La_{0.5}O_2$	35	23		81.8	50	88	48	15	23
25	$Ni_{0.93}Sn_{0.07}(20)/Ce_{0.5}La_{0.5}O_2$	29	25		30.6	30	96	43	17	29
26	$Ni_{0.93}Sn_{0.07}(5)/Ce_{0.33}La_{0.67}O_2$	23	19		87.2	53	100	58	10	6.5
27	$Ni_{0.93}Sn_{0.07}(20)/Ce_{0.33}La_{0.67}O_2$	20	19		-	-	94	50	14	9.2
28	$Ni_{0.87}Sn_{0.13}(5)/Ce_{0.67}La_{0.33}O_2$	33	20		-	44	90	54	12	12
29	$Ni_{0.5}Sn_{0.5}(5)/Ce_{0.67}La_{0.33}O_2$	36	23		-	33	85	40	17	33

****** D_{Ni} = nickel particle size (nm), D_s = support particle size (nm), S_{BET}= surface area (m^2/g), %S = selectivity percentage, C(%)= carbon deposition on spent catalyst percentage, TOS = time on stream (hours), O_V = oxygen vacancy.

5.2 Major contributions

1. $NiSn/CeO_2$ catalysts modified with MgO is prepared by a SCS route and ZrO_2 and La_2O_3 modified $NiSn/CeO_2$ catalysts are prepared by an ultrasonic assisted SCS route. Both processes could be beneficial for saving energy and obtaining comparatively smaller particle size that may be desirable not only for obtaining higher surface area.
2. Successful demonstration of low-temperature (200-400°C) steam reforming of ethanol over $NiSn/CeO_2$ catalyst modified by MgO, ZrO_2, La_2O_3 with different metal loading and support ratio.
3. Effect of variable tin composition in $NiSn/CeO_2$ (CeO_2 modified) catalyst for hydrogen production by low temperature steam reforming of ethanol.
4. In this project ethanol present in the water is used as feed, which might be produced from waste product after the extraction and refining of sugar from sugar cane and agro-industrial wastes. Therefore, in future, this process will help to clean the wastes at the same time producing hydrogen from it, which is one of the future goals of energy ministry.

5.3 Future work

1. Extended kinetic analysis of the catalytic activity results obtained by low temperature steam reforming of ethanol over modified $NiSn/CeO_2$ catalysts.
2. Stability and deactivation study of the modified $NiSn/CeO_2$ catalysts during reforming reactions is an important aspect. Rietveld refinement analysis of the XRD data need to be performed to examine the changes in phase, lattice strain, atomic occupancy factor and structure of the catalysts before and after catalytic reforming.

3. Preparation of catalyst by different synthesis method and comparison study with the catalyst prepared by SCS method. Examining the catalyst reduction conditions (temperature, time, hydrogen flow rate) and reforming reaction parameters (feed concentration, flow rate) on LTSER could be important.
4. Studying LTSR of other feeds (such as glycerol, methanol) over these NiSn/CeO_2 (CeO_2 modified) catalysts.
5. Exhaustive experimental studies on the regeneration or recycling of these catalyst and to see its effect on environment.
6. Techno-economic analysis of the whole process, including catalyst development, catalytic activity and regeneration or disposal of the catalyst can be performed.

References

[1] Gaigbe-Togbe V, Bassarsky L, Gu D, Spoorenberg T, Zeifman L. World Population Prospects 2022. 2022.

[2] IEA. International Energy Agency (IEA) World Energy Outlook 2022. Https://WwwIeaOrg/Reports/World-Energy-Outlook-2022/Executive-Summary 2022.

[3] Energy-2030. Energy 2030: Backgrounder. Brookings India 2014.

[4] Dudley B. BP Statistical Review of World Energy. 68th ed. London: 2019.

[5] IEO. International Energy Outlook 2021. Int Energy Outlook 2021:1–202.

[6] Energyy-India. Energy Statistics India 2022 | Ministry of Statistics and Program Implementation | Government Of India 2022:10–2.

[7] India I. Renewable Energy in India n.d. https://www.investindia.gov.in/sector/renewable-energy (accessed January 4, 2023).

[8] Hydrogen-Market. Hydrogen Generation Market Size, Share | Industry Report, 2022-2030 2027. https://www.marketsandmarkets.com/Market-Reports/hydrogen-generation-market-494.html?gclid=CjwKCAiAk--dBhABEiwAchIwkZ_lIZWSzKB8fivrDqIDcjYI6Gm9RC5EseIWwKnPGKT6R0X0ry0IsxoCnIcQAvD_BwE (accessed January 10, 2023).

[9] Hydrogen-market. Hydrogen Generation Market Size to Hit US$ 219.2 Bn by 2030 2030. https://www.precedenceresearch.com/hydrogen-generation-market (accessed January 10, 2023).

[10] Dou Y, Sun L, Ren J, Dong L. Opportunities and Future Challenges in Hydrogen Economy for Sustainable Development. Elsevier Ltd; 2017. https://doi.org/10.1016/B978-0-12-811132-1.00010-9.

[11] Global-Hydrogen. Global Hydrogen Review 2022. Global-Hydrogen-Review 2022. https://doi.org/10.1787/a15b8442-en.

[12] Kothari R, Kumar V, Pathak V V., Ahmad S, Aoyi O, Tyagi V V. A critical review on factors influencing fermentative hydrogen production. Front Biosci - Landmark 2017;22:1195–220. https://doi.org/10.2741/4542.

[13] Shah S. Hydrogen Production Processes From Biomass 2015.

[14] Shiva Kumar S, Lim H. An overview of water electrolysis technologies for green hydrogen production. Energy Reports 2022;8:13793–813. https://doi.org/10.1016/j.egyr.2022.10.127.

[15] Maru BT. Sustainable Production of Hydrogen and Chemical Commodities from Biodiesel Waste Crude Glycerol and Cellulose by Biological and Catalytic Processes 2013:1–283.

[16] ARAT HT, SÜRER MG. State of art of hydrogen usage as a fuel on aviation. Eur Mech Sci 2017;2:20–30. https://doi.org/10.26701/ems.364286.

[17] Al M, Co R, Co C, Catalysts A, Homsi D, Murr E. University of Balamand 2017:2–3.

[18] Stauffer JE. Ethanol [1]. Cereal Foods World 2007;52:100. https://doi.org/10.1094/CFW-52-3-0100.

[19] Ni M, Leung DYC, Leung MKH. A review on reforming bio-ethanol for hydrogen production. Int J Hydrogen Energy 2007;32:3238–47. https://doi.org/10.1016/j.ijhydene.2007.04.038.

[20] Tokarev A V., Kirilin A V., Murzina E V., Eränen K, Kustov LM, Murzin DY, et al. The role of bio-ethanol in aqueous phase reforming to sustainable hydrogen. Int J Hydrogen Energy 2010;35:12642–9. https://doi.org/10.1016/j.ijhydene.2010.07.118.

[21] Bion N, Epron F, Duprez D. Bioethanol reforming for H_2 production. A comparison with hydrocarbon reforming. 2010. https://doi.org/10.1039/9781847559630-00001.

[22] Muktham R, K. Bhargava S, Bankupalli S, S. Ball A. A Review on 1st and 2nd Generation Bioethanol Production-Recent Progress. J Sustain Bioenergy Syst 2016;06:72–92. https://doi.org/10.4236/jsbs.2016.63008.

[23] Ethanol. Fuel ethanol production in major countries 2021 | Statista 2022. https://www.statista.com/statistics/281606/ethanol-production-in-selected-countries/ (accessed January 10, 2023).

[24] Energy D of. DOE Explains...Catalysts | Department of Energy n.d.

https://www.energy.gov/science/doe-explainscatalysts (accessed February 5, 2023).
[25] Modak JM. Haber process for ammonia synthesis. 2011.
[26] Catalysts. CatalysisScheme.png - Wikimedia Commons n.d. https://commons.wikimedia.org/wiki/File:CatalysisScheme.png (accessed February 5, 2023).
[27] Singha RK, Yadav A, Shukla A, Iqbal Z, Pendem C, Sivakumar K, et al. Promoting Effect of CeO2and MgO for CO2Reforming of Methane over Ni-ZnO Catalyst. ChemistrySelect 2016;1:3075–85. https://doi.org/10.1002/slct.201600685.
[28] Julkapli NM, Bagheri S. Magnesium oxide as a heterogeneous catalyst support. Rev Inorg Chem 2016;36:1–41. https://doi.org/10.1515/revic-2015-0010.
[29] De Oliveira-Vigier K, Abatzoglou N, Gitzhofer F. Dry-reforming of ethanol in the presence of a 316 stainless steel catalyst. Can J Chem Eng 2005;83:978–84. https://doi.org/10.1002/cjce.5450830607.
[30] Azizan MT. Steam reforming of oxygenated hydrocarbons for hydrogen production. Dep Chem Eng 2014;Ph.D.
[31] Roy PB. BIMEVOX Catalyst Systems for Low Temperature Steam Reforming of Ethanol with the Aim of Hydrogen Production Under the Supervision of. Shwetha Thesis 2019.
[32] Kraleva E, Sokolov S, Schneider M, Ehrich H. Support effects on the properties of Co and Ni catalysts for the hydrogen production from bio-ethanol partial oxidation. Int J Hydrogen Energy 2013;38:4380–8. https://doi.org/10.1016/j.ijhydene.2013.01.190.
[33] Wang W, Wang Y. Thermodynamic analysis of hydrogen production via partial oxidation of ethanol. Int J Hydrogen Energy 2008;33:5035–44. https://doi.org/10.1016/j.ijhydene.2008.07.086.
[34] Ismaila A, Chen X, Gao X, Fan X. Thermodynamic analysis of steam reforming of glycerol for hydrogen production at atmospheric pressure. Front Chem Sci Eng 2021;15:60–71. https://doi.org/10.1007/s11705-020-1975-0.
[35] Wang W. Thermodynamic analysis of glycerol partial oxidation for hydrogen production. Fuel Process Technol 2010;91:1401–8. https://doi.org/10.1016/j.fuproc.2010.05.013.
[36] Liu N, Yuan Z, Wang C, Wang S, Zhang C, Wang S. The role of CeO2-ZrO2 as support in the ZnO-ZnCr2O4 catalysts for autothermal reforming of methanol. Fuel Process Technol 2008;89:574–81. https://doi.org/10.1016/j.fuproc.2007.11.029.
[37] Aartun I, Gjervan T, Venvik H, Görke O, Pfeifer P, Fathi M, et al. Catalytic conversion of propane to hydrogen in microstructured reactors. Chem Eng J 2004;101:93–9. https://doi.org/10.1016/j.cej.2004.01.006.
[38] Chen H, Yu H, Tang Y, Pan M, Yang G, Peng F, et al. Hydrogen production via autothermal reforming of ethanol over noble metal catalysts supported on oxides. J Nat Gas Chem 2009;18:191–8. https://doi.org/10.1016/S1003-9953(08)60106-1.
[39] Baerns M. Basic principles in applied catalysis: Preface. Springer Ser Chem Phys 2004;75. https://doi.org/10.1007/978-3-662-05981-4.
[40] Casas-Ledón Y, Arteaga-Perez LE, Morales-Perez MC, Peralta-Suárez LM. Thermodynamic Analysis of the Hydrogen Production from Ethanol: First and Second Laws Approaches. ISRN Thermodyn 2012;2012:1–8. https://doi.org/10.5402/2012/672691.
[41] Song H, Zhang L, Ozkan US. Investigation of the reaction network in ethanol steam reforming over supported cobalt catalystsv. Ind Eng Chem Res 2010;49:8984–9. https://doi.org/10.1021/ie100006z.
[42] Karim AM, Su Y, Sun J, Yang C, Strohm JJ, King DL, et al. A comparative study between Co and Rh for steam reforming of ethanol. Appl Catal B Environ 2010;96:441–8. https://doi.org/10.1016/j.apcatb.2010.02.041.
[43] Mariño FJ, Cerrella EG, Duhalde S, Jobbagy M, Laborde MA. Hydrogen from steam reforming of ethanol. characterization and performance of copper-nickel supported catalysts. Int J Hydrogen Energy 1998;23:1095–101. https://doi.org/10.1016/S0360-3199(97)00173-0.
[44] Zhang L, Li W, Liu J, Guo C, Wang Y, Zhang J. Ethanol steam reforming reactions over Al2O3 · SiO2-supported Ni-La catalysts. Fuel 2009;88:511–8. https://doi.org/10.1016/j.fuel.2008.09.030.
[45] Anil S, Indraja S, Singh R, Appari S, Roy B. A review on ethanol steam reforming for hydrogen production over Ni/Al2O3 and Ni/CeO2 based catalyst powders. Int J Hydrogen

Energy 2022;47:8177–213. https://doi.org/10.1016/j.ijhydene.2021.12.183.
[46] Cai W, Wang F, van Veen A, Descorme C, Schuurman Y, Shen W, et al. Hydrogen production from ethanol steam reforming in a micro-channel reactor. Int J Hydrogen Energy 2010;35:1152–9. https://doi.org/10.1016/j.ijhydene.2009.11.104.
[47] Haryanto A, Fernando S, Murali N, Adhikari S. Current status of hydrogen production techniques by steam reforming of ethanol: A review. Energy and Fuels 2005;19:2098–106. https://doi.org/10.1021/ef0500538.
[48] Sinfelt JH, Yates DJC. Catalytic hydrogenolysis of ethane over the noble metals of Group VIII. J Catal 1967;8:82–90. https://doi.org/10.1016/0021-9517(67)90284-9.
[49] Grenoble DC, Estadt MM, Ollis DF. The chemistry and catalysis of the water gas shift reaction. 1. The kinetics over supported metal catalysts. J Catal 1981;67:90–102. https://doi.org/10.1016/0021-9517(81)90263-3.
[50] Takoudis CG. The catalytic synthesis of hydrocarbons from H2/CO mixtures over the group VIII metals: Comments on methanation kinetics. J Catal 1982;78:265. https://doi.org/10.1016/0021-9517(82)90309-8.
[51] Taylor K. Nitric oxide catalysis in automotive exhaust systems. Catal Rev 1993;35:457–81. https://doi.org/10.1080/01614949308013915.
[52] Yao HC, Yao YFY. Ceria in automotive exhaust catalysts. I. Oxygen storage. J Catal 1984;86:254–65. https://doi.org/10.1016/0021-9517(84)90371-3.
[53] Kumar JT. Use of noble metals in automobile exhaust catalysts. J Phys Chem 1986;90:4747–52.
[54] Oh SH, Eickel CC. Effects of cerium addition on CO oxidation kinetics over alumina-supported rhodium catalysts. J Catal 1988;112:543–55. https://doi.org/10.1016/0021-9517(88)90169-8.
[55] Lööf P, Kasemo B, Keck KE. Oxygen storage capacity of noble metal car exhaust catalysts containing nickel and cerium. J Catal 1989;118:339–48. https://doi.org/10.1016/0021-9517(89)90322-9.
[56] Bera P, Patil KC, Jayaram V, Subbanna GN, Hegde MS. Ionic dispersion of Pt and Pd on CeO2 by combustion method: Effect of metal-ceria interaction on catalytic activities for NO reduction and CO and hydrocarbon oxidation. J Catal 2000;196:293–301. https://doi.org/10.1006/jcat.2000.3048.
[57] ONU. World Population Prospects 2019: Highlights. Futuribles 2019:1–39.
[58] Energy Information Administration U. International Energy Outlook 2019. 2019.
[59] Global E, Division M, Greenhouse G, Reference G. Global Monitoring Division (/ gmd /) Monthly Average Mauna Loa CO 2 2019:1–4.
[60] Outlook-2050. THE OECD ENVIRONMENTAL OUTLOOK TO 2050 - Key Findings on Climate Change n.d.:1.
[61] 2020 W. Climate change and health n.d. https://www.who.int/news-room/fact-sheets/detail/climate-change-and-health (accessed January 10, 2020).
[62] Lai AT, Lin IC, Yang YW, Wu MF. Climate change and human health. J Intern Med Taiwan 2012;23:343–50. https://doi.org/10.3329/jssmc.v8i1.31495.
[63] Schlapbach L, Züttel A. for Mobile Applications. Nature 2001;414:353–8. https://doi.org/10.1038/35104634.
[64] India plans to produce 175 GW of renewable energy by 2022 - United Nations Partnerships for SDGs platform n.d. https://sustainabledevelopment.un.org/partnership/?p=34566 (accessed October 3, 2021).
[65] R K Singh: India to invest Rs 4 lakh crore to meet 175 GW renewable energy target by 2022: R K Singh, Energy News, ET EnergyWorld n.d. https://energy.economictimes.indiatimes.com/news/renewable/india-to-invest-rs-4-lakh-cr-to-meet-175-gw-renewable-energy-target-by-2022-r-k-singh/72475254 (accessed October 3, 2021).
[66] Deloitte. Australian and Global Hydrogen Demand Growth Scenario Analysis COAG Energy Council – National Hydrogen Strategy Taskforce 2019.
[67] national hydrogen mission: National Hydrogen Mission: Leapfrogging towards India's cleaner future, Energy News, ET EnergyWorld n.d.

https://energy.economictimes.indiatimes.com/news/renewable/national-hydrogen-mission-leapfrogging-towards-indias-cleaner-future/80991679 (accessed October 3, 2021).
[68] Solution G. Our Solutions | Alset GmbH n.d. http://alset.at/our-solutions/ (accessed January 10, 2020).
[69] toyota. Toyota FC Bus | Photos, Details, Specs | Digital Trends n.d. https://www.digitaltrends.com/cars/toyota-fc-bus/#ixzz4RC3TCMNj (accessed January 10, 2020).
[70] Dal Santo V, Gallo A, Naldoni A, Guidotti M, Psaro R. Bimetallic heterogeneous catalysts for hydrogen production. Catal Today 2012;197:190–205. https://doi.org/10.1016/j.cattod.2012.07.037.
[71] Chen M, Liang D, Wang Y, Wang C, Tang Z, Li C, et al. Hydrogen production by ethanol steam reforming over M-Ni/sepiolite (M = La, Mg or Ca) catalysts. Int J Hydrogen Energy 2021;46:21796–811. https://doi.org/10.1016/j.ijhydene.2021.04.012.
[72] Chen M, Wang C, Wang Y, Tang Z, Yang Z, Zhang H, et al. Hydrogen production from ethanol steam reforming: Effect of Ce content on catalytic performance of Co/Sepiolite catalyst. Fuel 2019;247:344–55. https://doi.org/10.1016/j.fuel.2019.03.059.
[73] Wang Y, Wang C, Chen M, Hu J, Tang Z, Liang D, et al. Influence of CoAl2O4 spinel and Co-phyllosilicate structures derived from Co/sepiolite catalysts on steam reforming of bio-oil for hydrogen production. Fuel 2020;279:118449. https://doi.org/10.1016/j.fuel.2020.118449.
[74] Wang Y, Wang C, Chen M, Tang Z, Yang Z, Hu J, et al. Hydrogen production from steam reforming ethanol over Ni/attapulgite catalysts - Part I: Effect of nickel content. Fuel Process Technol 2019;192:227–38. https://doi.org/10.1016/j.fuproc.2019.04.031.
[75] Rostrup-Nielsen JR, Sehested J. Steam Reforming for Hydrogen. The Process and the Mechanism. ACS Div Fuel Chem Prepr 2003;48:218–9.
[76] Wang C, Wang Y, Chen M, Hu J, Yang Z, Zhang H, et al. Hydrogen production from ethanol steam reforming over Co–Ce/sepiolite catalysts prepared by a surfactant assisted coprecipitation method. Int J Hydrogen Energy 2019;44:26888–904. https://doi.org/10.1016/j.ijhydene.2019.08.058.
[77] Koizumi T, Ohga K. Biofuels policies in asian countries: Impact of the expanded biofuels programs on world agricultural markets. J Agric Food Ind Organ 2007;5. https://doi.org/10.2202/1542-0485.1190.
[78] Reddy GK, Smirniotis PG. Low-Temperature WGS Reaction. 2015. https://doi.org/10.1016/b978-0-12-420154-5.00003-6.
[79] Palma V, Castaldo F, Ciambelli P, Iaquaniello G. CeO2-supported Pt/Ni catalyst for the renewable and clean H2 production via ethanol steam reforming. Appl Catal B Environ 2014;145:73–84. https://doi.org/10.1016/j.apcatb.2013.01.053.
[80] Shtyka O, Dimitrova Z, Ciesielski R, Kedziora A, Mitukiewicz G, Leyko J, et al. Steam reforming of ethanol for hydrogen production: influence of catalyst composition (Ni/Al2O3, Ni/Al2O3–CeO2, Ni/Al2O3–ZnO) and process conditions. React Kinet Mech Catal 2021;132:907–19. https://doi.org/10.1007/s11144-021-01945-6.
[81] Sharma YC, Kumar A, Prasad R, Upadhyay SN. Ethanol steam reforming for hydrogen production: Latest and effective catalyst modification strategies to minimize carbonaceous deactivation. Renew Sustain Energy Rev 2017;74:89–103. https://doi.org/10.1016/j.rser.2017.02.049.
[82] Pant KK, Mohanty P, Agarwal S, Dalai AK. Steam reforming of acetic acid for hydrogen production over bifunctional Ni-Co catalysts. Catal Today 2013;207:36–43. https://doi.org/10.1016/j.cattod.2012.06.021.
[83] Matras J, Niewiadomski M, Ruppert A, Grams J. Activity of Ni catalysts for hydrogen production via biomass pyrolysis. Kinet Catal 2012;53:565–9. https://doi.org/10.1134/S0023158412050096.
[84] Davda RR, Shabaker JW, Huber GW, Cortright RD, Dumesic JA. A review of catalytic issues and process conditions for renewable hydrogen and alkanes by aqueous-phase reforming of oxygenated hydrocarbons over supported metal catalysts. Appl Catal B Environ 2005;56:171–86. https://doi.org/10.1016/j.apcatb.2004.04.027.
[85] Pizzolitto C, Menegazzo F, Ghedini E, Innocenti G, Di Michele A, Cruciani G, et al. Increase

of Ceria Redox Ability by Lanthanum Addition on Ni Based Catalysts for Hydrogen Production. ACS Sustain Chem Eng 2018;6:13867–76. https://doi.org/10.1021/acssuschemeng.8b02103.
[86] Hou T, Zhang S, Chen Y, Wang D, Cai W. Hydrogen production from ethanol reforming: Catalysts and reaction mechanism. Renew Sustain Energy Rev 2015;44:132–48. https://doi.org/10.1016/j.rser.2014.12.023.
[87] Contreras JL, Salmones J, Colín-Luna JA, Nuño L, Quintana B, Córdova I, et al. Catalysts for H2 production using the ethanol steam reforming (a review). Int J Hydrogen Energy 2014;39:18835–53. https://doi.org/10.1016/j.ijhydene.2014.08.072.
[88] Zanchet D, Santos JBO, Damyanova S, Gallo JMR, Bueno JMC. Toward understanding metal-catalyzed ethanol reforming. ACS Catal 2015;5:3841–63. https://doi.org/10.1021/cs5020755.
[89] Guerrero L, Castilla S, Cobo M. Advances in ethanol reforming for the production of hydrogen. Quim Nova 2014;37:850–6. https://doi.org/10.5935/0100-4042.20140137.
[90] Nahar G, Dupont V. Hydrogen via steam reforming of liquid biofeedstock. Biofuels 2012;3:167–91. https://doi.org/10.4155/BFS.12.8.
[91] Mattos L V., Jacobs G, Davis BH, Noronha FB. Production of hydrogen from ethanol: Review of reaction mechanism and catalyst deactivation. Chem Rev 2012;112:4094–123. https://doi.org/10.1021/cr2000114.
[92] Bshish A, Yaakob Z, Narayanan B, Ramakrishnan R, Ebshish A. Steam-reforming of ethanol for hydrogen production. Chem Pap 2011;65:251–66. https://doi.org/10.2478/s11696-010-0100-0.
[93] Phung TK, Pham TLM, Nguyen ANT, Vu KB, Giang HN, Nguyen TA, et al. Effect of Supports and Promoters on the Performance of Ni-Based Catalysts in Ethanol Steam Reforming. Chem Eng Technol 2020;43:672–88. https://doi.org/10.1002/ceat.201900445.
[94] Ogo S, Sekine Y. Recent progress in ethanol steam reforming using non-noble transition metal catalysts: A review. Fuel Process Technol 2020;199:106238. https://doi.org/10.1016/j.fuproc.2019.106238.
[95] Bepari S, Kuila D. Steam reforming of methanol, ethanol and glycerol over nickel-based catalysts-A review. Int J Hydrogen Energy 2020;45:18090–113. https://doi.org/10.1016/j.ijhydene.2019.08.003.
[96] Bineli ARR, Tasić MB, Filho RM. CATALYTIC STEAM REFORMING OF ETHANOL FOR HYDROGEN PRODUCTION: BRIEF STATUS. Chem Ind Chem Eng Q 2016;22:327–32. https://doi.org/10.2298/CICEQ160216017B.
[97] Bion N, Duprez D, Epron F. Design of nanocatalysts for green hydrogen production from bioethanol. ChemSusChem 2012;5:76–84. https://doi.org/10.1002/cssc.201100400.
[98] Wisniak J. The History of Catalysis. From the Beginning to Nobel Prizes. Educ Quim 2010;21:60–9. https://doi.org/10.1016/S0187-893X(18)30074-0.
[99] Eimert RAR, Universit LE Der. Gas Production, 2. Processes 2012. https://doi.org/10.1002/14356007.o12.
[100] Lindström B, Pettersson L. A brief history of catalysis - Ref not input correctly. CatTech 2003;7:130–8.
[101] Ross JRH. Steam Reforming of Hydrocarbons. Surf Defect Prop Solids 1975;4:34–67. https://doi.org/10.1016/s1464-2859(03)00551-0.
[102] Shi K, An X, Wu X, Xie X. Modification strategies for enhancing anti-coking of Ni-, Co-based catalysts during ethanol steam reforming: A review. Int J Hydrogen Energy 2022;47:39404–28. https://doi.org/10.1016/j.ijhydene.2022.09.097.
[103] Choong CKS, Huang L, Zhong Z, Lin J, Hong L, Chen L. Effect of calcium addition on catalytic ethanol steam reforming of Ni/Al2O3: II. Acidity/basicity, water adsorption and catalytic activity. Appl Catal A Gen 2011;407:155–62. https://doi.org/10.1016/j.apcata.2011.08.038.
[104] Vaidya PD, Wu YJ, Rodrigues AE. Kinetics of ethanol steam reforming for hydrogen production. Elsevier Inc.; 2018. https://doi.org/10.1016/B978-0-12-811458-2.00013-4.
[105] Akpan E, Akande A, Aboudheir A, Ibrahim H, Idem R. Experimental, kinetic and 2-D reactor modeling for simulation of the production of hydrogen by the catalytic reforming of concentrated crude ethanol (CRCCE) over a Ni-based commercial catalyst in a packed-bed

tubular reactor. Chem Eng Sci 2007;62:3112–26. https://doi.org/10.1016/j.ces.2007.03.006.
[106] Christiansen MA, Mpourmpakis G, Vlachos DG. DFT-driven multi-site microkinetic modeling of ethanol conversion to ethylene and diethyl ether on γ-Al2O3(1 1 1). J Catal 2015;323:121–31. https://doi.org/10.1016/j.jcat.2014.12.024.
[107] Llera I, Mas V, Bergamini ML, Laborde M, Amadeo N. Bio-ethanol steam reforming on Ni based catalyst. Kinetic study. Chem Eng Sci 2012;71:356–66. https://doi.org/10.1016/j.ces.2011.12.018.
[108] Lin YZ, Sun J, Lin JD, Chen HB, Liao DW, Yi J, et al. Energetics of chemisorption and conversion of methane on transition metal surfaces. J Mol Struct THEOCHEM 2002;587:63–71. https://doi.org/10.1016/S0166-1280(02)00097-0.
[109] Bengaard HS, Nørskov JK, Sehested J, Clausen BS, Nielsen LP, Molenbroek AM, et al. Steam reforming and graphite formation on Ni catalysts. J Catal 2002;209:365–84. https://doi.org/10.1006/jcat.2002.3579.
[110] Afolabi ATF, Li CZ, Kechagiopoulos PN. Microkinetic modelling and reaction pathway analysis of the steam reforming of ethanol over Ni/SiO2. Int J Hydrogen Energy 2019;44:22816–30. https://doi.org/10.1016/j.ijhydene.2019.07.040.
[111] Xu W, Liu Z, Johnston-Peck AC, Senanayake SD, Zhou G, Stacchiola D, et al. Steam reforming of ethanol on Ni/CeO2: Reaction pathway and interaction between Ni and the CeO2 support. ACS Catal 2013;3:975–84. https://doi.org/10.1021/cs4000969.
[112] Wang S, Guo W, Guo L, Li X, Wang Q. Experimental and subsequent mechanism research on the steam reforming of ethanol over a Ni/CeO 2 catalyst. Int J Green Energy 2015;12:694–701. https://doi.org/10.1080/15435075.2013.834821.
[113] Greluk M, Gac W, Rotko M, Słowik G, Turczyniak-Surdacka S. Co/CeO2 and Ni/CeO2 catalysts for ethanol steam reforming: Effect of the cobalt/nickel dispersion on catalysts properties. J Catal 2021;393:159–78. https://doi.org/10.1016/j.jcat.2020.11.009.
[114] Liu Z, Senanayake SD, Rodriguez JA. Elucidating the interaction between Ni and CeOx in ethanol steam reforming catalysts: A perspective of recent studies over model and powder systems. Appl Catal B Environ 2016;197:184–97. https://doi.org/10.1016/j.apcatb.2016.03.013.
[115] Patel M, Jindal TK, Pant KK. Kinetic study of steam reforming of ethanol on Ni-based ceria-zirconia catalyst. Ind Eng Chem Res 2013;52:15763–71. https://doi.org/10.1021/ie401570s.
[116] Zanchet D, Santos JBO, Damyanova S, Gallo JMR, Bueno JMC. Toward understanding metal-catalyzed ethanol reforming. ACS Catal 2015;5:3841–63. https://doi.org/10.1021/cs5020755.
[117] Ran YX, Du ZY, Guo YP, Feng J, Li WY. Density functional theory study of acetic acid steam reforming on Ni(111). Appl Surf Sci 2017;400:97–109. https://doi.org/10.1016/j.apsusc.2016.12.148.
[118] Liu Z, Senanayake SD, Rodriguez JA. Elucidating the interaction between Ni and CeOx in ethanol steam reforming catalysts: A perspective of recent studies over model and powder systems. Appl Catal B Environ 2016;197:184–97. https://doi.org/10.1016/j.apcatb.2016.03.013.
[119] Boudadi K, Bellifa A, Márquez-Álvarez C, Cortés Corberán V. Nickel catalysts promoted with lanthanum for ethanol steam reforming: Influence of support and treatment on activity. Appl Catal A Gen 2021;619. https://doi.org/10.1016/j.apcata.2021.118141.
[120] Guo Z, Wang S, Guo L, Li X. Catalytic steam reforming of ethanol for hydrogen production over Ni/CeO 2-ZrO 2 catalysts. BioResources 2011;6:4092–102. https://doi.org/10.15376/biores.6.4.4092-4102.
[121] Mondal T, Pant KK, Dalai AK. Oxidative and non-oxidative steam reforming of crude bio-ethanol for hydrogen production over Rh promoted Ni/CeO<inf>2</inf>-ZrO<inf>2</inf> catalyst. Appl Catal A Gen 2015;499:19–31. https://doi.org/10.1016/j.apcata.2015.04.004.
[122] Frusteri F, Freni S, Chiodo V, Donato S, Bonura G, Cavallaro S. Steam and auto-thermal reforming of bio-ethanol over MgO and CeO2 Ni supported catalysts. Int J Hydrogen Energy 2006;31:2193–9. https://doi.org/10.1016/j.ijhydene.2006.02.024.
[123] Moraes TS, Rabelo Neto RC, Ribeiro MC, Mattos LV, Kourtelesis M, Ladas S, et al. Ethanol conversion at low temperature over CeO2-Supported Ni-based catalysts. Effect of Pt addition to Ni catalyst. Appl Catal B Environ 2016;181:754–68.

https://doi.org/10.1016/j.apcatb.2015.08.044.
[124] Manukyan K V., Yeghishyan A V., Danghyan V, Rouvimov S, Mukasyan AS, Wolf EE. Structural transformations of highly porous nickel catalysts during ethanol conversion towards hydrogen. Int J Hydrogen Energy 2018;43:13225–36. https://doi.org/10.1016/j.ijhydene.2018.04.242.
[125] Moraes TS, Neto RCR, Ribeiro MC, Mattos LV, Kourtelesis M, Ladas S, et al. The study of the performance of PtNi/CeO2-nanocube catalysts for low temperature steam reforming of ethanol. Catal Today 2015;242:35–49. https://doi.org/10.1016/j.cattod.2014.05.045.
[126] Charisiou ND, Tzounis L, Sebastian V, Hinder SJ, Baker MA, Polychronopoulou K, et al. Investigating the correlation between deactivation and the carbon deposited on the surface of Ni/Al2O3 and Ni/La2O3-Al2O3 catalysts during the biogas reforming reaction. Appl Surf Sci 2019;474:42–56. https://doi.org/10.1016/j.apsusc.2018.05.177.
[127] Trimm DL. Coke formation and minimisation during steam reforming reactions. Catal Today 1997;37:233–8. https://doi.org/10.1016/S0920-5861(97)00014-X.
[128] Roh H-S, Platon A, Wang Y, King DL. Catalyst deactivation and regeneration in low temperature ethanol steam reforming with Rh/CeO2–ZrO2 catalysts. Catal Letters 2006;110:1–6. https://doi.org/10.1007/s10562-006-0082-2.
[129] Erdőhelyi A, Raskó J, Kecskés T, Tóth M, Dömök M, Baán K. Hydrogen formation in ethanol reforming on supported noble metal catalysts. Catal Today 2006;116:367–76. https://doi.org/10.1016/j.cattod.2006.05.073.
[130] Platon A, Roh H-S, King DL, Wang Y. Deactivation Studies of Rh/Ce0.8Zr0.2O2 Catalysts in Low Temperature Ethanol Steam Reforming. Top Catal 2007;46:374–9. https://doi.org/10.1007/s11244-007-9007-6.
[131] Vaidya PD, Rodrigues AE. Insight into steam reforming of ethanol to produce hydrogen for fuel cells. Chem Eng J 2006;117:39–49. https://doi.org/10.1016/j.cej.2005.12.008.
[132] Auprêtre F, Descorme C, Duprez D. Bio-ethanol catalytic steam reforming over supported metal catalysts. Catal Commun 2002;3:263–7. https://doi.org/10.1016/S1566-7367(02)00118-8.
[133] Charisiou ND, Polychronopoulou K, Asif A, Goula MA. The potential of glycerol and phenol towards H2 production using steam reforming reaction: A review. Surf Coatings Technol 2018;352:92–111. https://doi.org/10.1016/j.surfcoat.2018.08.008.
[134] Montero C, Remiro A, Arandia A, Benito PL, Bilbao J, Gayubo AG. Reproducible performance of a Ni/La2O3–αAl2O3 catalyst in ethanol steam reforming under reaction–regeneration cycles. Fuel Process Technol 2016;152:215–22. https://doi.org/10.1016/j.fuproc.2016.07.002.
[135] Nichele V, Signoretto M, Menegazzo F, Rossetti I, Cruciani G. Hydrogen production by ethanol steam reforming: Effect of the synthesis parameters on the activity of Ni/TiO2 catalysts. Int J Hydrogen Energy 2014;39:4252–8. https://doi.org/10.1016/j.ijhydene.2013.12.178.
[136] Chen H, Yu H, Peng F, Wang H, Yang J, Pan M. Efficient and stable oxidative steam reforming of ethanol for hydrogen production: Effect of in situ dispersion of Ir over Ir/La2O3. J Catal 2010;269:281–90. https://doi.org/10.1016/j.jcat.2009.11.010.
[137] Guo Y, Zhou L, Kameyama H. Steam reforming reactions over a metal-monolithic anodic alumina-supported Ni catalyst with trace amounts of noble metal. Int J Hydrogen Energy 2011;36:5321–33. https://doi.org/10.1016/j.ijhydene.2011.02.069.
[138] Le Valant A, Garron A, Bion N, Duprez D, Epron F. Effect of higher alcohols on the performances of a 1%Rh/MgAl2O4/Al2O3 catalyst for hydrogen production by crude bioethanol steam reforming. Int J Hydrogen Energy 2011;36:311–8. https://doi.org/10.1016/j.ijhydene.2010.09.039.
[139] Devianto H, Li ZL, Yoon SP, Han J, Nam SW, Lim T-H, et al. The effect of Al addition on the prevention of Ni sintering in bio-ethanol steam reforming for molten carbonate fuel cells. Int J Hydrogen Energy 2010;35:2591–6. https://doi.org/10.1016/j.ijhydene.2009.04.001.
[140] Sanchez N, Ruiz R, Hacker V, Cobo M. Impact of bioethanol impurities on steam reforming for hydrogen production: A review. Int J Hydrogen Energy 2020;45:11923–42. https://doi.org/10.1016/j.ijhydene.2020.02.159.

[141] Haryanto A, Fernando SD, Filip To SD, Steele PH, Pordesimo L. High Temperature Water Gas Shift Reaction over Nickel Catalysts for Hydrogen Production: Effect of Supports, GHSV, Metal Loading, and Dopant Materials. J Thermodyn Catal 2011;02. https://doi.org/10.4172/2157-7544.1000106.
[142] Hung CC, Chen SL, Liao YK, Chen CH, Wang JH. Oxidative steam reforming of ethanol for hydrogen production on M/Al 2O 3. Int J Hydrogen Energy 2012;37:4955–66. https://doi.org/10.1016/j.ijhydene.2011.12.060.
[143] Polychronopoulou K, Fierro JLG, Efstathiou AM. The phenol steam reforming reaction over MgO-based supported Rh catalysts. J Catal 2004;228:417–32. https://doi.org/10.1016/j.jcat.2004.09.016.
[144] Polychronopoulou K, Bakandritsos A, Tzitzios V, Fierro JLG, Efstathiou AM. Absorption-enhanced reforming of phenol by steam over supported Fe catalysts. J Catal 2006;241:132–48. https://doi.org/10.1016/j.jcat.2006.04.015.
[145] Canepa F, Riani P, Busca G, Lucchini MA, Garbarino G. Unsupported versus alumina-supported Ni nanoparticles as catalysts for steam/ethanol conversion and CO2 methanation. J Mol Catal A Chem 2013;383–384:10–6. https://doi.org/10.1016/j.molcata.2013.11.006.
[146] Murkin C, Brightling J. Eighty Years of Steam Reforming. Johnson Matthey Technol Rev 2016;60:263–9. https://doi.org/10.1595/205651316X692923.
[147] Alberton AL, Souza MMVM, Schmal M. Carbon formation and its influence on ethanol steam reforming over Ni/Al2O3 catalysts. Catal Today 2007;123:257–64. https://doi.org/10.1016/j.cattod.2007.01.062.
[148] Wang T, Gong J, Xiao S, Tian H, Zeng L, Li D, et al. Highly loaded Ni-based catalysts for low temperature ethanol steam reforming. Nanoscale 2016;8:10177–87. https://doi.org/10.1039/c6nr02586b.
[149] Wang K, Dou B, Jiang B, Zhang Q, Li M, Chen H, et al. Effect of support on hydrogen production from chemical looping steam reforming of ethanol over Ni-based oxygen carriers. Int J Hydrogen Energy 2016;41:17334–47. https://doi.org/10.1016/j.ijhydene.2016.07.261.
[150] Akande AJ, Idem RO, Dalai AK. Synthesis, characterization and performance evaluation of Ni/Al 2O3 catalysts for reforming of crude ethanol for hydrogen production. Appl Catal A Gen 2005;287:159–75. https://doi.org/10.1016/j.apcata.2005.03.046.
[151] Fajardo HV, Probst LFD. Production of hydrogen by steam reforming of ethanol over Ni/Al2O3 spherical catalysts. Appl Catal A Gen 2006;306:134–41. https://doi.org/10.1016/j.apcata.2006.03.043.
[152] Fajardo H V., Longo E, Mezalira DZ, Nuernberg GB, Almerindo GI, Collasiol A, et al. Influence of support on catalytic behavior of nickel catalysts in the steam reforming of ethanol for hydrogen production. Environ Chem Lett 2010;8:79–85. https://doi.org/10.1007/s10311-008-0195-5.
[153] Sehested J. Four challenges for nickel steam-reforming catalysts. Catal Today 2006;111:103–10. https://doi.org/10.1016/j.cattod.2005.10.002.
[154] Wu YW, Chung WC, Chang MB. Modification of Ni/γ-Al<inf>2</inf>O<inf>3</inf> catalyst with plasma for steam reforming of ethanol to generate hydrogen. Int J Hydrogen Energy 2015;40:8071–80. https://doi.org/10.1016/j.ijhydene.2015.04.053.
[155] Kang KH, Park S, Yoo J, Han SJ, Song JH, Bang Y, et al. Hydrogen production by steam reforming of ethanol over dual-templated Ni–Al 2 O 3 catalyst. Catal Today 2015;265:103–10. https://doi.org/10.1016/j.cattod.2015.07.041.
[156] Gil-Calvo M, Jiménez-González C, de Rivas B, Gutiérrez-Ortiz JI, López-Fonseca R. Effect of Ni/Al molar ratio on the performance of substoichiometric NiAl 2 O 4 spinel-based catalysts for partial oxidation of methane. Appl Catal B Environ 2017;209:128–38. https://doi.org/10.1016/j.apcatb.2017.02.063.
[157] Salhi N, Boulahouache A, Petit C, Kiennemann A, Rabia C. Steam reforming of methane to syngas over NiAl2O4 spinel catalysts. Int J Hydrogen Energy 2011;36:11433–9. https://doi.org/10.1016/j.ijhydene.2010.11.071.
[158] Zygmuntowicz J, Wiecińska P, Miazga A, Konopka K. Characterization of composites containing NiAl2O4 spinel phase from Al2O3/NiO and Al2O3/Ni systems. J Therm Anal Calorim 2016;125:1079–86. https://doi.org/10.1007/s10973-016-5357-2.

[159] Suffredini DFP, Thyssen V V., de Almeida PMM, Gomes RS, Borges MC, Duarte de Farias AM, et al. Renewable hydrogen from glycerol reforming over nickel aluminate-based catalysts. Catal Today 2017;289:96–104. https://doi.org/10.1016/j.cattod.2016.07.027.
[160] Pan CJ, Tsai MC, Su WN, Rick J, Akalework NG, Agegnehu AK, et al. Tuning/exploiting Strong Metal-Support Interaction (SMSI) in Heterogeneous Catalysis. J Taiwan Inst Chem Eng 2017;74:154–86. https://doi.org/10.1016/j.jtice.2017.02.012.
[161] van Deelen TW, Hernández Mejía C, de Jong KP. Control of metal-support interactions in heterogeneous catalysts to enhance activity and selectivity. Nat Catal 2019;2:955–70. https://doi.org/10.1038/s41929-019-0364-x.
[162] Lou Y, Xu J, Zhang Y, Pan C, Dong Y, Zhu Y. Metal-support interaction for heterogeneous catalysis: from nanoparticles to single atoms. Mater Today Nano 2020;12:100093. https://doi.org/10.1016/j.mtnano.2020.100093.
[163] Uchijima T. SMSI effect in some reducible oxides including niobia. Catal Today 1996;28:105–17. https://doi.org/10.1016/0920-5861(95)00235-9.
[164] Di Michele A, Dell'Angelo A, Tripodi A, Bahadori E, Sànchez F, Motta D, et al. Steam reforming of ethanol over Ni/MgAl 2 O 4 catalysts. Int J Hydrogen Energy 2019;44:952–64. https://doi.org/10.1016/j.ijhydene.2018.11.048.
[165] Barattini L, Ramis G, Resini C, Busca G, Sisani M, Costantino U. Reaction path of ethanol and acetic acid steam reforming over Ni-Zn-Al catalysts. Flow reactor studies. Chem Eng J 2009;153:43–9. https://doi.org/10.1016/j.cej.2009.06.002.
[166] Zeng G, Liu Q, Gu R, Zhang L, Li Y. Synergy effect of MgO and ZnO in a Ni/Mg-Zn-Al catalyst during ethanol steam reforming for H2-rich gas production. Catal Today 2011;178:206–13. https://doi.org/10.1016/j.cattod.2011.07.036.
[167] Denis A, Grzegorczyk W, Gac W, Machocki A. Steam reforming of ethanol over Ni/support catalysts for generation of hydrogen for fuel cell applications. Catal Today 2008;137:453–9. https://doi.org/10.1016/j.cattod.2008.03.006.
[168] Anjaneyulu C, Costa LOOD, Ribeiro MC, Rabelo-Neto RC, Mattos L V., Venugopal A, et al. Effect of Zn addition on the performance of Ni/Al2O3 catalyst for steam reforming of ethanol. Appl Catal A Gen 2016;519:85–98. https://doi.org/10.1016/j.apcata.2016.03.008.
[169] Chitsazan S, Finocchio E, Garbarino G, Flytzani-Stephanopoulos M, Busca G, Valsamakis I, et al. A study of Ni/Al 2 O 3 and Ni–La/Al 2 O 3 catalysts for the steam reforming of ethanol and phenol. Appl Catal B Environ 2015;174–175:21–34. https://doi.org/10.1016/j.apcatb.2015.02.024.
[170] Ma H, Zeng L, Tian H, Li D, Wang X, Li X, et al. Efficient hydrogen production from ethanol steam reforming over La-modified ordered mesoporous Ni-based catalysts. Appl Catal B Environ 2016;181:321–31. https://doi.org/10.1016/j.apcatb.2015.08.019.
[171] Ramírez-Hernández GY, Viveros-García T, Fuentes-Ramírez R, Galindo-Esquivel IR. Promoting behavior of yttrium over nickel supported on alumina-yttria catalysts in the ethanol steam reforming reaction. Int J Hydrogen Energy 2016;41:9332–43. https://doi.org/10.1016/j.ijhydene.2016.04.080.
[172] Han SJ, Bang Y, Yoo J, Seo JG, Song IK. Hydrogen production by steam reforming of ethanol over mesoporous Ni-Al2O3-ZrO2 xerogel catalysts: Effect of nickel content. Int J Hydrogen Energy 2013;38:8285–92. https://doi.org/10.1016/j.ijhydene.2013.04.141.
[173] Bang Y, Yoo J, Kang KH, Song JH, Song IK, Park S, et al. Hydrogen production by steam reforming of ethanol over P123-assisted mesoporous Ni–Al2O3–ZrO2 xerogel catalysts. Int J Hydrogen Energy 2014;39:10445–53. https://doi.org/10.1016/j.ijhydene.2014.05.014.
[174] Song JH, Song IK, Seo JG, Yoo J, Kang KH, Bang Y, et al. Hydrogen production by steam reforming of ethanol over mesoporous Ni–Al2O3–ZrO2 xerogel catalyst. Int J Hydrogen Energy 2013;38:15119–27. https://doi.org/10.1016/j.ijhydene.2013.09.114.
[175] Han SJ, Bang Y, Seo JG, Yoo J, Song IK. Hydrogen production by steam reforming of ethanol over mesoporous Ni-Al2O3-ZrO2 xerogel catalysts: Effect of Zr/Al molar ratio. Int J Hydrogen Energy 2013;38:1376–83. https://doi.org/10.1016/j.ijhydene.2012.11.057.
[176] Choong CKS, Zhong Z, Huang L, Wang Z, Ang TP, Borgna A, et al. Effect of calcium addition on catalytic ethanol steam reforming of Ni/Al2O3: I. Catalytic stability, electronic properties and coking mechanism. Appl Catal A Gen 2011;407:145–54.

https://doi.org/10.1016/j.apcata.2011.08.037.
[177] Srisiriwat N, Therdthianwong S, Therdthianwong A. Oxidative steam reforming of ethanol over Ni/Al2O3 catalysts promoted by CeO2, ZrO2 and CeO2-ZrO2. Int J Hydrogen Energy 2009;34:2224–34. https://doi.org/10.1016/j.ijhydene.2008.12.058.
[178] Dantas SC, Resende KA, Ávila-Neto CN, Noronha FB, Bueno JMC, Hori CE. Nickel supported catalysts for hydrogen production by reforming of ethanol as addressed by in situ temperature and spatial resolved XANES analysis. Int J Hydrogen Energy 2016;41:3399–413. https://doi.org/10.1016/j.ijhydene.2015.12.164.
[179] Vacharapong P, Arayawate S, Katanyutanon S, Toochinda P, Lawtrakul L, Charojrochkul S. Enhancement of ni catalyst using ceo2–al2o3 support prepared with magnetic inducement for esr. Catalysts 2020;10:1–13. https://doi.org/10.3390/catal10111357.
[180] Ma H, Zhang R, Huang S, Chen W, Shi Q. Ni/Y2O3-Al2O3 catalysts for hydrogen production from steam reforming of ethanol at low temperature. J Rare Earths 2012;30:683–90. https://doi.org/10.1016/S1002-0721(12)60112-4.
[181] Vicente J, Montero C, Ereña J, Azkoiti MJ, Bilbao J, Gayubo AG. Coke deactivation of Ni and Co catalysts in ethanol steam reforming at mild temperatures in a fluidized bed reactor. Int J Hydrogen Energy 2014;39:12586–96. https://doi.org/10.1016/j.ijhydene.2014.06.093.
[182] Song JH, Yoo S, Yoo J, Park S, Gim MY, Kim TH, et al. Hydrogen production by steam reforming of ethanol over Ni/Al2O3-La2O3 xerogel catalysts. Mol Catal 2017;434:123–33. https://doi.org/10.1016/j.mcat.2017.03.009.
[183] Melchor-Hernández C, Gómez-Cortés A, Díaz G. Hydrogen production by steam reforming of ethanol over nickel supported on La-modified alumina catalysts prepared by sol-gel. Fuel 2013;107:828–35. https://doi.org/10.1016/j.fuel.2013.01.047.
[184] Salvadó J, Torres JA, Montané D, Domínguez M, Casanovas A, Llorca J. Steam reforming of ethanol at moderate temperature: Multifactorial design analysis of Ni/La2O3-Al2O3, and Fe- and Mn-promoted Co/ZnO catalysts. J Power Sources 2007;169:158–66. https://doi.org/10.1016/j.jpowsour.2007.01.057.
[185] Valle B, Aramburu B, Remiro A, Bilbao J, Gayubo AG. Effect of calcination/reduction conditions of Ni/La2O3-αAl2O3 catalyst on its activity and stability for hydrogen production by steam reforming of raw bio-oil/ethanol. Appl Catal B Environ 2014;147:402–10. https://doi.org/10.1016/j.apcatb.2013.09.022.
[186] Osorio-Vargas P, Flores-González NA, Navarro RM, Fierro JLG, Campos CH, Reyes P. Improved stability of Ni/Al2O3 catalysts by effect of promoters (La2O3, CeO2) for ethanol steam-reforming reaction. Catal Today 2016;259:27–38. https://doi.org/10.1016/j.cattod.2015.04.037.
[187] Örücü E, Gökaliler F, Aksoylu AE, Önsan ZI. Ethanol steam reforming for hydrogen production over bimetallic Pt-Ni/Al2O3. Catal Letters 2008;120:198–203. https://doi.org/10.1007/s10562-007-9269-4.
[188] Soyal-Baltacioğlu F, Aksoylu AE, Önsan ZI. Steam reforming of ethanol over Pt-Ni Catalysts. Catal Today 2008;138:183–6. https://doi.org/10.1016/j.cattod.2008.05.035.
[189] González-Gil R, Herrera C, Larrubia MA, Mariño F, Laborde M, Alemany LJ. Hydrogen production by ethanol steam reforming over multimetallic RhCeNi/Al2O3structured catalyst. Pilot-scale study. Int J Hydrogen Energy 2016;41:16786–96. https://doi.org/10.1016/j.ijhydene.2016.06.234.
[190] Mariño F, Laborde M, Alemany LJ, Herrera C, Chamorro-Burgos I, Larrubia MA, et al. Production of hydrogen by catalytic steam reforming of oxygenated model compounds on Ni-modified supported catalysts. Simulation and experimental study. Int J Hydrogen Energy 2015;40:11217–27. https://doi.org/10.1016/j.ijhydene.2015.05.167.
[191] Rogatis L De, Montini T, Lorenzut B, Fornasiero P. NixCuy/Al2O3 based catalysts for hydrogen production. Energy Environ Sci 2008;1:501–9. https://doi.org/10.1039/b805426f.
[192] Mariño F, Baronetti G, Jobbagy M, Laborde M. Cu-Ni-K/γ-Al2O3 supported catalysts for ethanol steam reforming: Formation of hydrotalcite-type compounds as a result of metal-support interaction. Appl Catal A Gen 2003;238:41–54. https://doi.org/10.1016/S0926-860X(02)00113-8.
[193] Zhao X, Lu G. Modulating and controlling active species dispersion over Ni-Co bimetallic

catalysts for enhancement of hydrogen production of ethanol steam reforming. Int J Hydrogen Energy 2016;41:3349–62. https://doi.org/10.1016/j.ijhydene.2015.09.063.
[194] Campos CH, Pecchi G, Fierro JLG, Osorio-Vargas P. Enhanced bimetallic Rh-Ni supported catalysts on alumina doped with mixed lanthanum-cerium oxides for ethanol steam reforming. Mol Catal 2019;469:87–97. https://doi.org/10.1016/j.mcat.2019.03.007.
[195] Profeti LPR, Dias JAC, Assaf JM, Assaf EM. Hydrogen production by steam reforming of ethanol over Ni-based catalysts promoted with noble metals. J Power Sources 2009;190:525–33. https://doi.org/10.1016/j.jpowsour.2008.12.104.
[196] Navarro RM, Sanchez-Sanchez MC, Fierro JLG. Structure and Activity of Pt–Ni Catalysts Supported on Modified Al 2 O 3 for Ethanol Steam Reforming . J Nanosci Nanotechnol 2015;15:6592–603. https://doi.org/10.1166/jnn.2015.10875.
[197] Yue Y, Liu F, Zhao L, Zhang L, Liu Y. Loading oxide nano sheet supported Ni-Co alloy nanoparticles on the macroporous walls of monolithic alumina and their catalytic performance for ethanol steam reforming. Int J Hydrogen Energy 2015;40:7052–63. https://doi.org/10.1016/j.ijhydene.2015.04.036.
[198] Le Valant A, Bion N, Can F, Duprez D, Epron F. Preparation and characterization of bimetallic Rh-Ni/Y2O3-Al2O3 for hydrogen production by raw bioethanol steam reforming: influence of the addition of nickel on the catalyst performances and stability. Appl Catal B Environ 2010;97:72–81. https://doi.org/10.1016/j.apcatb.2010.03.025.
[199] Gayubo AG, Vicente J, Ereña J, Montero C, Olazar M, Bilbao J. Comparison of Ni and Co catalysts for ethanol steam reforming in a fluidized bed reactor. Catal Letters 2014;144:1134–43. https://doi.org/10.1007/s10562-014-1265-x.
[200] Liberatori JWC, Ribeiro RU, Zanchet D, Noronha FB, Bueno JMC. Steam reforming of ethanol on supported nickel catalysts. Appl Catal A Gen 2007;327:197–204. https://doi.org/10.1016/j.apcata.2007.05.010.
[201] Peela NR, Mubayi A, Kunzru D. Steam reforming of ethanol over Rh/CeO2/Al2O3 catalysts in a microchannel reactor. Chem Eng J 2011;167:578–87. https://doi.org/10.1016/j.cej.2010.09.081.
[202] Profeti LPR, Ticianelli EA, Assaf EM. Production of hydrogen via steam reforming of biofuels on Ni/CeO2-Al2O3 catalysts promoted by noble metals. Int J Hydrogen Energy 2009;34:5049–60. https://doi.org/10.1016/j.ijhydene.2009.03.050.
[203] Wang W. Production of hydrogen by steam reforming of bio-ethanol over nickel-copper bimetallic catalysts. Int J Green Energy 2009;6:92–103. https://doi.org/10.1080/15435070802701876.
[204] Zhang L, Liu J, Li W, Guo C, Zhang J. Ethanol steam reforming over Ni-Cu/Al 2 O 3 -M y O z (M = Si, La, Mg, and Zn) catalysts. J Nat Gas Chem 2009;18:55–65. https://doi.org/10.1016/S1003-9953(08)60078-X.
[205] Song JH, Han SJ, Yoo J, Park S, Kim DH, Song IK. Hydrogen production by steam reforming of ethanol over Ni-X/Al2O3-ZrO2 (X = Mg, Ca, Sr, and Ba) xerogel catalysts: Effect of alkaline earth metal addition. J Mol Catal A Chem 2016;415:151–9. https://doi.org/10.1016/j.molcata.2016.02.010.
[206] Huang L, Lin J, Wang Z, Choong CKS, Chen L, Zhong Z. Support and alloy effects on activity and product selectivity for ethanol steam reforming over supported nickel cobalt catalysts. Int J Hydrogen Energy 2012;37:16321–32. https://doi.org/10.1016/j.ijhydene.2012.02.119.
[207] Contreras JL, Figueroa A, Zeifert B, Salmones J, Fuentes GA, Vázquez T, et al. Production of hydrogen by ethanol steam reforming using Ni–Co-ex-hydrotalcite catalysts stabilized with tungsten oxides. Int J Hydrogen Energy 2021;46:6474–93. https://doi.org/10.1016/j.ijhydene.2020.11.143.
[208] Wang M, Kim SY, Men Y, Shin EW. Influence of metal-support interactions on reaction pathways over Ni/CeZrOx–Al2O3 catalysts for ethanol steam reforming. Int J Hydrogen Energy 2022;47:33765–80. https://doi.org/10.1016/j.ijhydene.2022.07.274.
[209] Rose HJ, Murat KJ, Carr MK. A chemical-spectrochemical method for the determination of rare earth elements and thorium in cerium minerals * minerals is under way in the U . S . Geological Survey in connection with studies of newly discovered deposits of these minerals

in California 1954;6:161–8.
[210] Di Monte R, Kašpar J. Heterogeneous environmental catalysis - A gentle art: CeO 2-ZrO2 mixed oxides as a case history. Catal Today 2005;100:27–35. https://doi.org/10.1016/j.cattod.2004.11.005.
[211] Montini T, Melchionna M, Monai M, Fornasiero P. Fundamentals and Catalytic Applications of CeO2-Based Materials. Chem Rev 2016;116:5987–6041. https://doi.org/10.1021/acs.chemrev.5b00603.
[212] Peterson EJ, Onstott EI, Johnson MR, Bowman MG. Hydrogen evolving reactions: The thermal decompositions of cerous carbonates. J Inorg Nucl Chem 1978;40:1357–63. https://doi.org/10.1016/0022-1902(78)80050-5.
[213] Polychronopoulou K, Alkhoori AA, Efstathiou AM, Jaoude MA, Damaskinos CM, Baker MA, et al. Design Aspects of Doped CeO2for Low-Temperature Catalytic CO Oxidation: Transient Kinetics and DFT Approach. ACS Appl Mater Interfaces 2021;13:22391–415. https://doi.org/10.1021/acsami.1c02934.
[214] AlKhoori AA, Polychronopoulou K, Belabbes A, Jaoude MA, Vega LF, Sebastian V, et al. Cu, Sm co-doping effect on the CO oxidation activity of CeO2. A combined experimental and density functional study. Appl Surf Sci 2020;521. https://doi.org/10.1016/j.apsusc.2020.146305.
[215] Wang F, Zhang L, Deng J, Zhang J, Han B, Wang Y, et al. Embedded Ni catalysts in Ni-O-Ce solid solution for stable hydrogen production from ethanol steam reforming reaction. Fuel Process Technol 2019;193:94–101. https://doi.org/10.1016/j.fuproc.2019.05.004.
[216] Araiza DG, Gómez-Cortés A, Díaz G. Effect of ceria morphology on the carbon deposition during steam reforming of ethanol over Ni/CeO2 catalysts. Catal Today 2020;349:235–43. https://doi.org/10.1016/j.cattod.2018.03.016.
[217] Jalowiecki-Duhamel L, Pirez C, Capron M, Dumeignil F, Payen E. Hydrogen production from ethanol steam reforming over cerium and nickel based oxyhydrides. Int J Hydrogen Energy 2010;35:12741–50. https://doi.org/10.1016/j.ijhydene.2009.08.080.
[218] Greluk M, Rotko M, Turczyniak-Surdacka S. Comparison of catalytic performance and coking resistant behaviors of cobalt- and nickel based catalyst with different Co/Ce and Ni/Ce molar ratio under SRE conditions. Appl Catal A Gen 2020;590:117334. https://doi.org/10.1016/j.apcata.2019.117334.
[219] Zhang C, Li S, Wu G, Gong J. Synthesis of stable Ni-CeO2 catalysts via ball-milling for ethanol steam reforming. Catal Today 2014;233:53–60. https://doi.org/10.1016/j.cattod.2013.08.013.
[220] Fajardo H V., Probst LFD, Carreño NLV, Garcia ITS, Valentini A. Hydrogen production from ethanol steam reforming over Ni/CeO2 nanocomposite catalysts. Catal Letters 2007;119:228–36. https://doi.org/10.1007/s10562-007-9222-6.
[221] Moraes TS, Neto RCR, Ribeiro MC, Mattos LV, Kourtelesis M, Verykios X, et al. Effects of Ceria Morphology on Catalytic Performance of Ni/CeO2 Catalysts for Low Temperature Steam Reforming of Ethanol. Top Catal 2015;58:281–94. https://doi.org/10.1007/s11244-015-0369-x.
[222] Zhurka MD, Lemonidou AA, Kechagiopoulos PN. Elucidation of metal and support effects during ethanol steam reforming over Ni and Rh based catalysts supported on (CeO2)-ZrO2-La2O3. Catal Today 2021;368:161–72. https://doi.org/10.1016/j.cattod.2020.03.020.
[223] Liu F, Zhao L, Wang H, Bai X, Liu Y. Study on the preparation of Ni-La-Ce oxide catalyst for steam reforming of ethanol. Int J Hydrogen Energy 2014;39:10454–66. https://doi.org/10.1016/j.ijhydene.2014.05.036.
[224] Xiao Z, Wu C, Wang L, Xu J, Zheng Q, Pan L, et al. Boosting hydrogen production from steam reforming of ethanol on nickel by lanthanum doped ceria. Appl Catal B Environ 2021;286:119884. https://doi.org/10.1016/j.apcatb.2021.119884.
[225] SHI Q, LIU C, CHEN W. Hydrogen production from steam reforming of ethanol over Ni/MgO-CeO2catalyst at low temperature. J Rare Earths 2009;27:948–54. https://doi.org/10.1016/S1002-0721(08)60368-3.
[226] Ye JL, Wang YQ, Liu Y, Wang H. Steam reforming of ethanol over Ni/CexTi1-xO2 catalysts. Int J Hydrogen Energy 2008;33:6602–11. https://doi.org/10.1016/j.ijhydene.2008.08.036.

[227] Xiao Z, Li Y, Hou F, Wu C, Pan L, Zou J, et al. Engineering oxygen vacancies and nickel dispersion on CeO2 by Pr doping for highly stable ethanol steam reforming. Appl Catal B Environ 2019;258:117940. https://doi.org/10.1016/j.apcatb.2019.117940.
[228] Wang H, Zhang L, Yuan M, Xu T, Liu Y. Steam reforming of ethanol over Ni/Ce0.7Pr0.3O 2 catalyst. J Rare Earths 2012;30:670–5. https://doi.org/10.1016/S1002-0721(12)60110-0.
[229] Augusto BL, Costa LOO, Noronha FB, Colman RC, Mattos L V. Ethanol reforming over Ni/CeGd catalysts with low Ni content. Int J Hydrogen Energy 2012;37:12258–70. https://doi.org/10.1016/j.ijhydene.2012.05.127.
[230] Biswas P, Kunzru D. Steam reforming of ethanol for production of hydrogen over Ni/CeO2-ZrO2 catalyst: Effect of support and metal loading. Int J Hydrogen Energy 2007;32:969–80. https://doi.org/10.1016/j.ijhydene.2006.09.031.
[231] Ebiad MA, Abd El-Hafiz DR, Elsalamony RA, Mohamed LS. Ni supported high surface area CeO2-ZrO2 catalysts for hydrogen production from ethanol steam reforming. RSC Adv 2012;2:8145–56. https://doi.org/10.1039/c2ra20258a.
[232] Andrade-Gamboa JJ, Bengió S, Carbajal-Ramos IA, Gennari FC, Abello MC, Gomez MF, et al. Catalytic behavior of Ru supported on Ce0.8Zr0.2O2 for hydrogen production. Appl Catal B Environ 2015;181:58–70. https://doi.org/10.1016/j.apcatb.2015.07.025.
[233] Santander JA, Tonetto GM, Pedernera MN, López E. Ni/CeO2–MgO catalysts supported on stainless steel plates for ethanol steam reforming. Int J Hydrogen Energy 2017;42:9482–92. https://doi.org/10.1016/j.ijhydene.2017.03.169.
[234] Trane-Restrup R, Dahl S, Jensen AD. Steam reforming of ethanol: Effects of support and additives on Ni-based catalysts. Int J Hydrogen Energy 2013;38:15105–18. https://doi.org/10.1016/j.ijhydene.2013.09.027.
[235] Arslan A, Doğu T. Effect of calcination/reduction temperature of Ni impregnated CeO2–ZrO2 catalysts on hydrogen yield and coke minimization in low temperature reforming of ethanol. Int J Hydrogen Energy 2016;41:16752–61. https://doi.org/10.1016/j.ijhydene.2016.07.082.
[236] Li N, Pu J, Chi B, Li J. Ethanol steam reforming with a Ni–BaZr 0.1 Ce 0.7 Y 0.1 Yb 0.1 O 3–δ catalyst. Mater Today Energy 2019;12:371–8. https://doi.org/10.1016/j.mtener.2019.04.002.
[237] Niazi Z, Irankhah A, Wang Y, Arandiyan H. Cu, Mg and Co effect on nickel-ceria supported catalysts for ethanol steam reforming reaction. Int J Hydrogen Energy 2020:1–11. https://doi.org/10.1016/j.ijhydene.2020.06.001.
[238] Liu Q, Liu Z, Zhou X, Li C, Ding J. Hydrogen production by steam reforming of ethanol over copper doped Ni/CeO2 catalysts. J Rare Earths 2011;29:872–7. https://doi.org/10.1016/S1002-0721(10)60558-3.
[239] SAEKI T, OHKITA H, KAKUTA N, MIZUSHIMA T. Synergistic effects of CeO_2-supported bimetallic Ni–Cu, Co–Cu, and Ni–Fe catalysts on steam reforming of ethanol. J Ceram Soc Japan 2015;123:955–60. https://doi.org/10.2109/jcersj2.123.955.
[240] Słowik G, Greluk M, Rotko M, Machocki A. Influence of composition and morphology of the active phase on the catalytic properties of cobalt-nickel catalysts in the steam reforming of ethanol. Mater Chem Phys 2021;258:123970. https://doi.org/10.1016/j.matchemphys.2020.123970.
[241] Pinton N, Vidal M V., Signoretto M, Martínez-Arias A, Cortés Corberán V. Ethanol steam reforming on nanostructured catalysts of Ni, Co and CeO2: Influence of synthesis method on activity, deactivation and regenerability. Catal Today 2017;296:135–43. https://doi.org/10.1016/j.cattod.2017.06.022.
[242] Tian H, Li X, Chen S, Zeng L, Gong J. Role of Sn in Ni-Sn/CeO2 Catalysts for Ethanol Steam Reforming. Chinese J Chem 2017;35:651–8. https://doi.org/10.1002/cjoc.201600569.
[243] Greluk M, Rotko M, Turczyniak-Surdacka S. Enhanced catalytic performance of La2O3 promoted Co/CeO2 and Ni/CeO2 catalysts for effective hydrogen production by ethanol steam reforming: La2O3 promoted Co(Ni)/CeO2 catalysts in SRE. Renew Energy 2020;155:378–95. https://doi.org/10.1016/j.renene.2020.03.117.
[244] Huang HH, Yu SW, Chuang CL, Wang C Bin. Application of boron-modified nickel catalysts on the steam reforming of ethanol. Int J Hydrogen Energy 2014;39:20712–21. https://doi.org/10.1016/j.ijhydene.2014.07.033.
[245] Słowik G, Greluk M, Rotko M, Machocki A. Evolution of the structure of unpromoted and

potassium-promoted ceria-supported nickel catalysts in the steam reforming of ethanol. Appl Catal B Environ 2018;221:490–509. https://doi.org/10.1016/j.apcatb.2017.09.052.
[246] Palma V, Ruocco C, Meloni E, Ricca A. Highly active and stable Pt-Ni/CeO2-SiO2 catalysts for ethanol reforming. J Clean Prod 2017;166:263–72. https://doi.org/10.1016/j.jclepro.2017.08.036.
[247] Palma V, Ruocco C, Meloni E, Gallucci F, Ricca A. Enhancing Pt-Ni/CeO2 performances for ethanol reforming by catalyst supporting on high surface silica. Catal Today 2018;307:175–88. https://doi.org/10.1016/j.cattod.2017.05.034.
[248] Palma V, Ruocco C, Castaldo F, Ricca A, Boettge D. Ethanol steam reforming over bimetallic coated ceramic foams: Effect of reactor configuration and catalytic support. Int J Hydrogen Energy 2015;40:12650–62. https://doi.org/10.1016/j.ijhydene.2015.07.138.
[249] Palma V, Ruocco C, Meloni E, Ricca A. Influence of catalytic formulation and operative conditions on coke deposition over CeO2-SiO2 based catalysts for ethanol reforming. Energies 2017;10. https://doi.org/10.3390/en10071030.
[250] Huang H-H, Chiou JYZ, Chuang C-L, Lai CL, Wang C-B, Yu S-W. Effect of Co, Fe and Rh addition on coke deposition over Ni/Ce 0.5 Zr 0.5 O 2 catalysts for steam reforming of ethanol. Int J Hydrogen Energy 2014;39:20689–99. https://doi.org/10.1016/j.ijhydene.2014.07.141.
[251] Seriyala AK, Rao A, Leclerc C, Appari S, Roy B. Effects of metal loading and support modification on the low-temperature steam reforming of ethanol (LTSRE) over the Ni–Sn/CeO2 catalysts. Int J Hydrogen Energy 2023:1–22. https://doi.org/10.1016/j.ijhydene.2023.01.039.
[252] Kumar Seriyala A, Appari S, Roy B. Steam reforming of ethanol for hydrogen production by low-temperature steam reforming using modified Ni-Sn/CeO2 catalyst. Mater Today Proc 2023;76:279–88. https://doi.org/10.1016/j.matpr.2022.11.231.
[253] Wang M, Yang J, Chi B, Pu J, Li J. High performance Ni exsolved and Cu added La0.8Ce0.2Mn0.6Ni0.4O3-based perovskites for ethanol steam reforming. Int J Hydrogen Energy 2020;45:16458–68. https://doi.org/10.1016/j.ijhydene.2020.04.108.
[254] Furtado AC, Alonso CG, Cantão MP, Fernandes-Machado NRC. Bimetallic catalysts performance during ethanol steam reforming: Influence of support materials. Int J Hydrogen Energy 2009;34:7189–96. https://doi.org/10.1016/j.ijhydene.2009.06.060.
[255] Muñoz M, Moreno S, Molina R. The effect of the absence of Ni, Co, and Ni-Co catalyst pretreatment on catalytic activity for hydrogen production via oxidative steam reforming of ethanol. Int J Hydrogen Energy 2014;39:10074–89. https://doi.org/10.1016/j.ijhydene.2014.04.131.
[256] Nanoscience. Metallic Nanoparticles: Top-Down and Bottom-up Approaches - Nanografi Nano Technology 2022. https://nanografi.com/blog/metallic-nanoparticles-topdown-and-bottomup-approaches/ (accessed January 14, 2023).
[257] Pal Singh J, Kumar M, Sharma A, Pandey G, Chae KH, Lee S. Bottom-Up and Top-Down Approaches for MgO. Sonochemical React 2020:1–19. https://doi.org/10.5772/intechopen.91182.
[258] Hutchings GJ, Védrine JC. Heterogeneous catalyst preparation. Springer Ser Chem Phys 2004;75:215–58. https://doi.org/10.1007/978-3-662-05981-4_6.
[259] Gan YX, Jayatissa AH, Yu Z, Chen X, Li M. Hydrothermal Synthesis of Nanomaterials. J Nanomater 2020;2020. https://doi.org/10.1155/2020/8917013.
[260] Byrappa K, Adschiri T. Hydrothermal technology for nanotechnology. Prog Cryst Growth Charact Mater 2007;53:117–66. https://doi.org/10.1016/j.pcrysgrow.2007.04.001.
[261] Roy R. Accelerating the Kinetics of Low-Temperature Inorganic Syntheses. J Solid State Chem 1994;111:11–7. https://doi.org/10.1006/jssc.1994.1192.
[262] Byrappa. Hydrothermal growth of crystals, vol. 21: Edited by K. Byrappa. P 1991. https://fdocuments.in/document/hydrothermal-growth-of-crystals-vol-21-edited-by-k-byrappa-pergamon-press.html?page=1 (accessed January 14, 2023).
[263] Yoshimura M, Suda H. Hydrothermal Processing of Hydroxyapatite: Past, Present, and Future. Hydroxyapatite Relat Mater 2019:45–72. https://doi.org/10.1201/9780203751367-3/HYDROTHERMAL-PROCESSING-HYDROXYAPATITE-PAST-PRESENT-FUTURE-MASAHIRO-YOSHIMURA-HIROYUKI-SUDA.

[264] Bustamante-Torres M, Romero-Fierro D, Estrella-Nuñez J, Arcentales-Vera B, Chichande-Proaño E, Bucio E. Polymeric Composite of Magnetite Iron Oxide Nanoparticles and Their Application in Biomedicine: A Review. Polymers (Basel) 2022;14. https://doi.org/10.3390/polym14040752.
[265] Bokov D, Turki Jalil A, Chupradit S, Suksatan W, Javed Ansari M, Shewael IH, et al. Nanomaterial by Sol-Gel Method: Synthesis and Application. Adv Mater Sci Eng 2021;2021. https://doi.org/10.1155/2021/5102014.
[266] Gonçalves RA, Toledo RP, Joshi N, Berengue OM. Green synthesis and applications of zno and tio2 nanostructures. Molecules 2021;26. https://doi.org/10.3390/molecules26082236.
[267] Rosa R, Veronesi P, Leonelli C. A review on combustion synthesis intensification by means of microwave energy. Chem Eng Process Process Intensif 2013;71:2–18. https://doi.org/10.1016/j.cep.2013.02.007.
[268] Carlos E, Martins R, Fortunato E, Branquinho R. Solution Combustion Synthesis: Towards a Sustainable Approach for Metal Oxides. Chem - A Eur J 2020;26:9099–125. https://doi.org/10.1002/chem.202000678.
[269] Tharun J, Kim DW, Roshan R, Hwang Y, Park DW. Microwave assisted preparation of quaternized chitosan catalyst for the cycloaddition of CO2 and epoxides. Catal Commun 2013;31:62–5. https://doi.org/10.1016/j.catcom.2012.11.018.
[270] Chen Q, Liu Q, Chu X, Zhang Y, Yan Y, Xue L, et al. Ultrasonic-assisted solution combustion synthesis of porous Na3V2(PO4)3/C: formation mechanism and sodium storage performance. J Nanoparticle Res 2017;19. https://doi.org/10.1007/s11051-017-3828-4.
[271] Varma A, Mukasyan AS, Rogachev AS, Manukyan K V. Solution Combustion Synthesis of Nanoscale Materials. Chem Rev 2016;116:14493–586. https://doi.org/10.1021/acs.chemrev.6b00279.
[272] Boffito DC, Crocellà V, Pirola C, Neppolian B, Cerrato G, Ashokkumar M, et al. Ultrasonic enhancement of the acidity, surface area and free fatty acids esterification catalytic activity of sulphated ZrO2-TiO2 systems. J Catal 2013;297:17–26. https://doi.org/10.1016/j.jcat.2012.09.013.
[273] Sancheti S V., Saini C, Ambati R, Gogate PR. Synthesis of ultrasound assisted nanostuctured photocatalyst (NiO supported over CeO2) and its application for photocatalytic as well as sonocatalytic dye degradation. Catal Today 2018;300:50–7. https://doi.org/10.1016/j.cattod.2017.02.047.
[274] Aruna ST, Mukasyan AS. Combustion synthesis and nanomaterials. Curr Opin Solid State Mater Sci 2008;12:44–50. https://doi.org/10.1016/j.cossms.2008.12.002.
[275] Galembeck A, Alves OL. BiVO4 thin film preparation by metalorganic decomposition. Thin Solid Films 2000;365:90–3. https://doi.org/10.1016/S0040-6090(99)01079-2.
[276] Haines PJ. Thermal Methods of Analysis. Therm Methods Anal 1995. https://doi.org/10.1007/978-94-011-1324-3.
[277] Grob RL, Barry EF. Modern Practice of Gas Chromatography, 4th Edition. Wiley 2004:1064.
[278] Patent. US Patent for Thermal conductivity detector and gas chromatograph Patent (Patent # 10,330,651 issued June 25, 2019) - Justia Patents Search 2019. https://patents.justia.com/patent/10330651 (accessed January 17, 2023).
[279] Feng D, Wang J, Ji XJ, Min WX, Yan WJ. Analysis of Volatile Organic Compounds by HS-GC-IMS in Powdered Yak Milk Processed under Different Sterilization Conditions. J Food Qual 2021;2021. https://doi.org/10.1155/2021/5536645.
[280] Yamamoto M, Narahara H. The measurement of vapor-Liquid equilibrium data by headspace gas chromatography. Sumitomo Kagaku 2004:1–10.
[281] Bicchi CP, Binello AE, Legovich MM, Pellegrino GM, Vanni AC. Characterization of Roasted Coffee by S-HSGC and HPLC-UV and Principal Component Analysis. J Agric Food Chem 1993;41:2324–8. https://doi.org/10.1021/jf00036a020.
[282] S MABS, Chuang C, Balakos MW. Automatic online fermentation headspace gas analysis using a compter controlled gas chromatograph 1900;XXV:129–32.
[283] Production A, Production M. Hydrogen Generation Market 7500+ 2020;2023:1–11.
[284] Razzaq R, Zhu H, Jiang L, Muhammad U, Li C, Zhang S. Catalytic methanation of CO and CO2 in coke oven gas over Ni-Co/ZrO2-CeO2. Ind Eng Chem Res 2013;52:2247–56.

https://doi.org/10.1021/ie301399z.
[285] Wu RC, Tang CW, Huang HH, Wang CC, Chang MB, Wang C Bin. Effect of boron doping and preparation method of Ni/Ce0.5Zr0.5O2 catalysts on the performance for steam reforming of ethanol. Int J Hydrogen Energy 2019;44:14279–89. https://doi.org/10.1016/j.ijhydene.2019.02.065.
[286] Kalamaras CM, Efstathiou AM. Hydrogen Production Technologies: Current State and Future Developments. Conf Pap Energy 2013;2013:1–9. https://doi.org/10.1155/2013/690627.
[287] Roy B, Fuierer PA. Influence of Sodium Chloride and Dibasic Sodium Phosphate Salt Matrices on the Anatase–Rutile Phase Transformation and Particle Size of Titanium Dioxide Powder. J Am Ceram Soc 2010;93:436–44. https://doi.org/10.1111/j.1551-2916.2009.03415.x.
[288] Sharma S, Patil B, Pathak A, Ghosalkar S, Mohanta HK, Roy B. Application of BICOVOX catalyst for hydrogen production from ethanol. Clean Technol Environ Policy 2018;20:695–701. https://doi.org/10.1007/s10098-017-1394-1.
[289] Sharma S, Aich S, Roy B. Low temperature steam reforming of ethanol over cobalt doped bismuth vanadate [Bi4(V0.90Co0.10)2O11-δ (BICOVOX)] catalysts for hydrogen production. J Phys Chem Solids 2021;148. https://doi.org/10.1016/j.jpcs.2020.109754.
[290] Yang F, Ma X, Cai W Bin, Song P, Xu W. Nature of Oxygen-Containing Groups on Carbon for High-Efficiency Electrocatalytic CO2 Reduction Reaction. J Am Chem Soc 2019;141:20451–9. https://doi.org/10.1021/jacs.9b11123.
[291] Lu M, Jiang Y, Sun Y, Zhang P, Zhu J, Li M, et al. Hydrodeoxygenation of Guaiacol Catalyzed by ZrO2-CeO2-Supported Nickel Catalysts with High Loading. Energy and Fuels 2020;34:4685–92. https://doi.org/10.1021/acs.energyfuels.0c00445.
[292] Kun-udom R, Jantarang S, Du Z, Kitiyanan B, Rirksomboon T, Meeyoo V. Morphology dependent? Elucidating the catalyst structures of Ni/Ce0.75Zr0.25O2 in the steam reforming of acetic acid. Green Chem Eng 2022;3:44–54. https://doi.org/10.1016/j.gce.2021.08.004.
[293] Hernández Martínez A, Lopez E, Larrégola S, Furlong O, Nazzarro MS, Cadús LE, et al. Perovskites as precursors of bimetallic Rh–Ni catalysts for ethanol steam reforming: effect of Rh inclusion on catalyst structure and behavior. Mater Today Chem 2022;26:101077. https://doi.org/10.1016/j.mtchem.2022.101077.
[294] Sohrabi S, Irankhah A. Synthesis, characterization, and catalytic activity of Ni/CeMnO2 catalysts promoted by copper, cobalt, potassium and iron for ethanol steam reforming. Int J Hydrogen Energy 2021;46:12846–56. https://doi.org/10.1016/j.ijhydene.2021.01.057.
[295] Campos CH, Pecchi G, Fierro JLG, Osorio-Vargas P. Enhanced bimetallic Rh-Ni supported catalysts on alumina doped with mixed lanthanum-cerium oxides for ethanol steam reforming. Mol Catal 2019;469:87–97. https://doi.org/10.1016/j.mcat.2019.03.007.
[296] Bobadilla LF, Romero-Sarria F, Centeno MA, Odriozola JA. Promoting effect of Sn on supported Ni catalyst during steam reforming of glycerol. Int J Hydrogen Energy 2016;41:9234–44. https://doi.org/10.1016/j.ijhydene.2016.04.119.
[297] Paresh H. Rana PAP. Role of Oxygen Storage/Supply Capacity of Mixed Oxides of Ce and Zr in Ethanol Oxidation. Chem Eng Res Des 2018. https://doi.org/10.1038/338514a0.
[298] Arandia A, Remiro A, García V, Castaño P, Bilbao J, Gayubo AG. Oxidative steam reforming of raw bio-oil over supported and bulk Ni catalysts for hydrogen production. Catalysts 2018;8. https://doi.org/10.3390/catal8080322.
[299] Parvas M, Haghighi M, Allahyari S. Catalytic wet air oxidation of phenol over ultrasound-assisted synthesized Ni/CeO2–ZrO2 nanocatalyst used in wastewater treatment. Arab J Chem 2019;12:1298–307. https://doi.org/10.1016/j.arabjc.2014.10.043.
[300] Bastan F, Kazemeini M, Larimi AS. Aqueous-phase reforming of glycerol for production of alkanes over Ni/CexZr1-xO2 nano-catalyst: Effects of the support's composition. Renew Energy 2017;108:417–24. https://doi.org/10.1016/j.renene.2017.02.076.
[301] Maia TA, Assaf EM. Catalytic features of Ni supported on CeO2-ZrO2 solid solution in the steam reforming of glycerol for syngas production. RSC Adv 2014;4:31142–54. https://doi.org/10.1039/c4ra02886d.
[302] Dhanapal K, Narayanan V, Stephen A. Influence of Sn on the magnetic ordering of Ni-Sn alloy synthesized using chemical reduction method. J Magn Magn Mater 2016;406:103–9. https://doi.org/10.1016/j.jmmm.2015.12.058.

[303] Siddqui N, Sarkar B, Pendem C, Khatun R, Sivakumar Konthala LN, Sasaki T, et al. Highly selective transfer hydrogenation of α,β-unsaturated carbonyl compounds using Cu-based nanocatalysts. Catal Sci Technol 2017;7:2828–37. https://doi.org/10.1039/c7cy00989e.
[304] Saranya PE, Selladurai S. Mesoporous 3D network Ce-doped NiO nanoflakes as high performance electrodes for supercapacitor applications. New J Chem 2019;43:7441–56. https://doi.org/10.1039/c9nj00097f.
[305] Jang WJ, Kim HM, Shim JO, Yoo SY, Jeon KW, Na HS, et al. Key properties of Ni-MgO-CeO2, Ni-MgO-ZrO2, and Ni-MgO-Ce(1-x)Zr(x)O2catalysts for the reforming of methane with carbon dioxide. Green Chem 2018;20:1621–33. https://doi.org/10.1039/c7gc03605a.
[306] Kaliyappan periyasamy, venugopalan aswathy, venugopal ashok kumar T raja. An efficient robust fluorite CeZrO4-d oxide catalyst for the eco-benign synthesis of styrene. R Soc Chem 2015;5:3619–26. https://doi.org/10.1039/C4RA12355G.
[307] Fang W, Pirez C, Paul S, Capron M, Jobic H, Dumeignil F, et al. Room temperature hydrogen production from ethanol over CeNiXHZOY nano-oxyhydride catalysts. ChemCatChem 2013;5:2207–16. https://doi.org/10.1002/cctc.201300087.
[308] Chava R, Bhaskar AVD, Roy B, Appari S. Reforming of model biogas using Ni/CeO2/γ-Al2O3 monolith catalyst. Mater Today Proc 2022. https://doi.org/10.1016/j.matpr.2022.06.234.
[309] Gouadec G, Colomban P. Raman Spectroscopy of nanomaterials: How spectra relate to disorder, particle size and mechanical properties. Prog Cryst Growth Charact Mater 2007;53:1–56. https://doi.org/10.1016/j.pcrysgrow.2007.01.001.
[310] Kosacki I, Suzuki T, Anderson HU, Colomban P. Raman scattering and lattice defects in nanocrystalline CeO2 thin films. Solid State Ionics 2002;149:99–105. https://doi.org/10.1016/S0167-2738(02)00104-2.
[311] Yu Q, Wu X, Tang C, Qi L, Liu B, Gao F, et al. Textural, structural, and morphological characterizations and catalytic activity of nanosized CeO2-MOx (M=Mg2+, Al3+, Si4+) mixed oxides for CO oxidation. J Colloid Interface Sci 2011;354:341–52. https://doi.org/10.1016/j.jcis.2010.10.043.
[312] Li L, Jiang B, Tang D, Zheng Z, Zhao C. Hydrogen Production from Chemical Looping Reforming of Ethanol Using Ni/CeO2 Nanorod Oxygen Carrier. Catalysts 2018;8:257. https://doi.org/10.3390/catal8070257.
[313] Chen YS, Kang JF, Chen B, Gao B, Liu LF, Liu XY, et al. Microscopic mechanism for unipolar resistive switching behaviour of nickel oxides. J Phys D Appl Phys 2012;45:065303. https://doi.org/10.1088/0022-3727/45/6/065303.
[314] Dwivedi N, Yeo RJ, Satyanarayana N, Kundu S, Tripathy S, Bhatia CS. Understanding the Role of Nitrogen in Plasma-Assisted Surface Modification of Magnetic Recording Media with and without Ultrathin Carbon Overcoats. Sci Rep 2015;5:7772. https://doi.org/10.1038/srep07772.
[315] Singha RK, Das S, Pandey M, Kumar S, Bal R, Bordoloi A. Ni nanocluster on modified CeO2-ZrO2 nanoporous composite for tri-reforming of methane. Catal Sci Technol 2016;6:7122–36. https://doi.org/10.1039/c5cy01323b.
[316] Mondal T, Pant KK, Dalai AK. Catalytic oxidative steam reforming of bio-ethanol for hydrogen production over Rh promoted Ni/CeO2-ZrO2 catalyst. Int J Hydrogen Energy 2015;40:2529–44. https://doi.org/10.1016/j.ijhydene.2014.12.070.
[317] Arslan A, Doğu T. Effect of calcination/reduction temperature of Ni impregnated CeO2–ZrO2catalysts on hydrogen yield and coke minimization in low temperature reforming of ethanol. Int J Hydrogen Energy 2016;41:16752–61. https://doi.org/10.1016/j.ijhydene.2016.07.082.
[318] Ramesh S, Upender G, Raju KCJ, Padmaja G, Reddy SM, Reddy C V. Effect of Ca on the Properties of Gd-Doped Ceria for IT-SOFC. J Mod Phys 2013;04:859–63. https://doi.org/10.4236/jmp.2013.46116.
[319] Lee J, Yoon SM, Kim B, Kim J, Lee H, Song H. Electrical conductivity and defect structure of yttria-doped ceria-stabilized zirconia 2001:175–84.
[320] chemguide. chemguide: Understand Chemistry n.d. https://www.chemguide.co.uk/ (accessed October 28, 2020).

[321] Xie FZ, Chu XW, Hu HR, Qiao MH, Yan SR, Zhu YL, et al. Characterization and catalytic properties of Sn-modified rapidly quenched skeletal Ni catalysts in aqueous-phase reforming of ethylene glycol. J Catal 2006;241:211–20. https://doi.org/10.1016/j.jcat.2006.05.001.
[322] Stephens E, Ross IL, Mussgnug JH, Wagner LD, Borowitzka MA, Posten C, et al. Future prospects of microalgal biofuel production systems. Trends Plant Sci 2019;15:554–64. https://doi.org/10.1016/j.tplants.2010.06.003.
[323] Ritchie, Hannah; Roser M. Fossil Fuels; Our world in data. Our World Data 2018. https://ourworldindata.org/fossil-fuels (accessed September 16, 2020).
[324] Knoema. BP: World Reserves of Fossil Fuels. Knoema 2018. https://knoema.com/smsfgud/bp-world-reserves-of-fossil-fuels (accessed September 16, 2020).
[325] UNEP. UN Environment Programme 2019. https://www.unenvironment.org/news-and-stories/press-release/cut-global-emissions-76-percent-every-year-next-decade-meet-15degc (accessed September 16, 2020).
[326] Michael Le. New Scientist 2020. https://www.newscientist.com/article/2191881-carbon-dioxide-levels-will-soar-past-the-410-ppm-milestone-in-2019/ (accessed September 16, 2020).
[327] European environment Agency. Trends in atmospheric concentrations 2020. https://www.eea.europa.eu/data-and-maps/daviz/atmospheric-concentration-of-carbon-dioxide-5#tab-chart_5_filters=%7B%22rowFilters%22%3A%7B%7D%3B%22columnFilters%22%3A%7B%22pre_config_polutant%22%3A%5B%22N2O (ppb)%22%5D%7D%7D (accessed September 16, 2020).
[328] Natural resources council of maine. Clean, Renewable Energy n.d. https://www.nrcm.org/programs/climate/clean-energy/ (accessed September 16, 2020).
[329] Al-Swai BM, Osman N, Alnarabiji MS, Adesina AA, Abdullah B. Syngas Production via Methane Dry Reforming over Ceria-Magnesia Mixed Oxide-Supported Nickel Catalysts. Ind Eng Chem Res 2019;58:539–52. https://doi.org/10.1021/acs.iecr.8b03671.
[330] Ismagilov ZR, Matus E V., Ismagilov IZ, Sukhova OB, Yashnik SA, Ushakov VA, et al. Hydrogen production through hydrocarbon fuel reforming processes over Ni based catalysts. Catal Today 2019:166–82. https://doi.org/10.1016/j.cattod.2018.06.035.
[331] Pirez C, Fang W, Capron M, Paul S, Jobic H, Dumeignil F, et al. Steam reforming, partial oxidation and oxidative steam reforming for hydrogen production from ethanol over cerium nickel based oxyhydride catalyst. Appl Catal A Gen 2016;518:78–86. https://doi.org/10.1016/j.apcata.2015.10.035.
[332] Wang W, Wang Y. Dry reforming of ethanol for hydrogen production: Thermodynamic investigation. Int J Hydrogen Energy 2009;34:5382–9. https://doi.org/10.1016/j.ijhydene.2009.04.054.
[333] Deng Y, Feng C, Tang L, Zeng G, Chen Z, Zhang M. Nanohybrid Photocatalysts for Heavy Metal Pollutant Control. vol. 2. Elsevier Inc.; 2019. https://doi.org/10.1016/B978-0-12-814154-0.00005-0.
[334] What are the Pros and Cons of Hydrogen Fuel Cells? - TWI n.d. https://www.twi-global.com/technical-knowledge/faqs/what-are-the-pros-and-cons-of-hydrogen-fuel-cells (accessed December 2, 2022).
[335] Santamaria AL, Lopez G, Arregi A. stability of different Ni supported catalysts in the in-line steam reforming of biomass fast pyrolysis volatiles. Appl Catal B Environ 2018;242:109–20. https://doi.org/https://doi.org/10.1016/j.apcatb.2018.09.081.
[336] Hanley ES, Deane JP, Gallachóir BPÓ. The role of hydrogen in low carbon energy futures–A review of existing perspectives. Renew Sustain Energy Rev 2018;82:3027–45. https://doi.org/10.1016/j.rser.2017.10.034.
[337] Liu Z, Yao S, Johnston-Peck A, Xu W, Rodriguez JA, Senanayake SD. Methanol steam reforming over Ni-CeO2 model and powder catalysts: Pathways to high stability and selectivity for H2/CO2 production. Catal Today 2018;311:74–80. https://doi.org/10.1016/j.cattod.2017.08.041.
[338] Bepari S, Pradhan NC, Dalai AK. Selective production of hydrogen by steam reforming of glycerol over Ni/Fly ash catalyst. Catal Today 2017;291:36–46. https://doi.org/10.1016/j.cattod.2017.01.015.

[339] Xiao Z, Li Y, Hou F, Wu C, Pan L, Zou J, et al. Engineering oxygen vacancies and nickel dispersion on CeO2 by Pr doping for highly stable ethanol steam reforming. Appl Catal B Environ 2019;258. https://doi.org/10.1016/j.apcatb.2019.117940.
[340] Koehler N, Mccaherty J, Wilson C, Cooper G, Baker R, Markham S, et al. 2019 ETHANOL INDUSTRY OUTLOOK RFA Board of Directors 2019.
[341] Yan X, Hu T, Liu P, Li S, Zhao B, Zhang Q, et al. Highly efficient and stable Ni/CeO2-SiO2 catalyst for dry reforming of methane: Effect of interfacial structure of Ni/CeO2 on SiO2. Appl Catal B Environ 2019;246:221–31. https://doi.org/10.1016/j.apcatb.2019.01.070.
[342] Alla SK, Mandal RK, Prasad NK. Optical and magnetic properties of Mg2+ doped CeO2 nanoparticles. RSC Adv 2016;6:103491–8. https://doi.org/10.1039/c6ra23063f.
[343] Shabaker JW, Dumesic JA. Kinetics of aqueous-phase reforming of oxygenated hydrocarbons: Pt/Al 2O3 and Sn-modified Ni catalysts. Ind Eng Chem Res 2004;43:3105–12. https://doi.org/10.1021/ie049852o.
[344] Sohrabi S, Irankhah A. Synthesis, characterization, and catalytic activity of Ni/CeMnO2 catalysts promoted by copper, cobalt, potassium and iron for ethanol steam reforming. Int J Hydrogen Energy 2021;46:12846–56. https://doi.org/10.1016/j.ijhydene.2021.01.057.
[345] Ishihara A, Andou A, Hashimoto T, Nasu H. Steam reforming of ethanol using novel carbon-oxide composite-supported Ni, Co and Fe catalysts. Fuel Process Technol 2020;197:106203. https://doi.org/10.1016/j.fuproc.2019.106203.
[346] Rodrigues TS, de Moura ABL, e Silva FA, Candido EG, da Silva AGM, de Oliveira DC, et al. Ni supported Ce0.9Sm0.1O2-Δ nanowires: An efficient catalyst for ethanol steam reforming for hydrogen production. Fuel 2019;237:1244–53. https://doi.org/10.1016/j.fuel.2018.10.053.
[347] Matus E V., Okhlopkova LB, Sukhova OB, Ismagilov IZ, Kerzhentsev MA, Ismagilov ZR. Effects of preparation mode and doping on the genesis and properties of Ni/Ce1-xMxOy nanocrystallites (M = Gd, La, Mg) for catalytic applications. J Nanoparticle Res 2019;21:11. https://doi.org/10.1007/s11051-018-4454-5.
[348] Luo X, Hong Y, Zhang H, Shi K, Yang G, Wu T. Highly efficient steam reforming of ethanol (SRE) over CeOx grown on the nano NixMgyO matrix: H2 production under a high GHSV condition. Int J Energy Res 2019;43:3823–36. https://doi.org/10.1002/er.4549.
[349] Bepari S, Basu S, Pradhan NC, Dalai AK. Steam reforming of ethanol over cerium-promoted Ni-Mg-Al hydrotalcite catalysts. Catal Today 2017;291:47–57. https://doi.org/10.1016/j.cattod.2017.01.027.
[350] Roy B, Fuierer PA. Synthesis of cobalt-doped bismuth vanadate by combustion-synthesis : Influence of fuel on phase content and morphology 2009. https://doi.org/10.1557/JMR.2009.0392.
[351] Roy B, Loganathan K, Pham HN, Datye AK, Leclerc CA. Surface modification of solution combustion synthesized Ni / Al 2 O 3 catalyst for aqueous-phase reforming of ethanol. Int J Hydrogen Energy 2010;35:11700–8. https://doi.org/10.1016/j.ijhydene.2010.07.167.
[352] Patil B, Sharma S, Mohanta HK, Roy B. BINIVOX catalyst for hydrogen production from ethanol by low temperature steam reforming (LTSR). J Chem Sci 2017;129:1741–6. https://doi.org/10.1007/s12039-017-1388-x.
[353] Sharma S, Patil B, Pathak A, Ghosalkar S, Mohanta HK, Roy B. Application of BICOVOX catalyst for hydrogen production from ethanol 2018:695–701.
[354] Roy B, Martinez U, Loganathan K, Datye AK, Leclerc CA. Effect of preparation methods on the performance of Ni/Al2O3 catalysts for aqueous-phase reforming of ethanol: Part I-catalytic activity. Int J Hydrogen Energy 2012;37:8143–53. https://doi.org/10.1016/j.ijhydene.2012.02.056.
[355] Sharma S, Yashwanth PK, Roy B. Deactivation study of the BICOVOX catalysts used in low temperature steam reforming of ethanol for H2 production. J Phys Chem Solids 2021;156. https://doi.org/10.1016/j.jpcs.2021.110138.
[356] Roy B, Artyushkova K, Pham HN, Li L, Datye AK, Leclerc CA. Effect of preparation method on the performance of the Ni / Al 2 O 3 catalysts for aqueous-phase reforming of ethanol : Part II-characterization. Interational J Hydrog Energy 2012;37:18815–26. https://doi.org/http://dx.doi.org/10.1016/j.ijhydene.2012.09.098.
[357] Roy B, Leclerc CA. Study of preparation method and oxidization/reduction effect on the

performance of nickel-cerium oxide catalysts for aqueous-phase reforming of ethanol. J Power Sources 2015;299:114–24. https://doi.org/10.1016/j.jpowsour.2015.08.069.
[358] Roy B, Sullivan H, Leclerc CA. Effect of variable conditions on steam reforming and aqueous phase reforming of n-butanol over Ni/CeO2 and Ni/Al2O 3 catalysts. J Power Sources 2014;267:280–7. https://doi.org/10.1016/j.jpowsour.2014.05.090.
[359] Zhang Y, Wang P, Zhang W, Bu W, Qi Y, Guo S. Structure and electrochemical hydrogen storage behaviors of Mg–Ce–Ni–Al-based alloys prepared by mechanical milling. J Rare Earths 2020;38:1093–102. https://doi.org/10.1016/j.jre.2019.08.002.
[360] Pastor-Pérez L, Sepúlveda-Escribano A. Multicomponent NiSnCeO2/C catalysts for the low-temperature glycerol steam reforming. Appl Catal A Gen 2017;529:118–26. https://doi.org/10.1016/j.apcata.2016.10.022.
[361] Roy B, Sullivan H, Leclerc CA. Aqueous-phase reforming of n-BuOH over Ni/Al2O3 and Ni/CeO2 catalysts. J Power Sources 2011;196:10652–7. https://doi.org/10.1016/j.jpowsour.2011.08.093.
[362] Roy B, Fuierer PA, Aich S. Photovoltaic performance of dye sensitized solar cell based on rutile TiO 2 scaffold electrode prepared by a 2 step bi-layer process using molten salt matrices. Mater Lett 2011;65:2473–5. https://doi.org/10.1016/j.matlet.2011.05.050.
[363] Tchouank Tekou Carol T, Mohammed J, Srivastava AK. Effect of calcination temperature on the structural, dielectric and optical properties of nano-sized M-type barium hexaferrites. Mater Today Proc 2014;18:566–74. https://doi.org/10.1016/j.matpr.2019.06.449.
[364] Delir Kheyrollahi Nezhad P, Haghighi M, Rahmani F. CO2/O2-enhanced ethane dehydrogenation over a sol–gel synthesized Ni/ZrO2–MgO nanocatalyst: Effects of Mgo, ZrO2,and NiO on the catalytic performance. Part Sci Technol 2018;36:1017–28. https://doi.org/10.1080/02726351.2017.1340376.
[365] Smith B. Infrared Spectral Interpretation. CRC Press; 2018. https://doi.org/10.1201/9780203750841.
[366] Heriot watt university. Group of Alcohol. UK n.d. http://www.che.hw.ac.uk/teaching/cheak2/B18OA1/Webtest/Alcohol.html (accessed September 17, 2020).
[367] Bobadilla LF, Penkova A, Álvarez A, Domínguez MI, Romero-Sarria F, Centeno MA, et al. Glycerol steam reforming on bimetallic NiSn/CeO2-MgO-Al2O3 catalysts: Influence of the support, reaction parameters and deactivation/regeneration processes. Appl Catal A Gen 2015;492:38–47. https://doi.org/10.1016/j.apcata.2014.12.029.
[368] Du X, Zhang D, Shi L, Gao R, Zhang J. Morphology dependence of catalytic properties of Ni/CeO 2 nanostructures for carbon dioxide reforming of methane. J Phys Chem C 2012;116:10009–16. https://doi.org/10.1021/jp300543r.
[369] Fang X, Zhang J, Liu J, Wang C, Huang Q, Xu X, et al. Methane dry reforming over Ni/Mg-Al-O: On the significant promotional effects of rare earth Ce and Nd metal oxides. J CO2 Util 2018;25:242–53. https://doi.org/10.1016/j.jcou.2018.04.011.
[370] Zhang Z, Hu X, Zhang L, Yang Y, Li Q, Fan H, et al. Steam reforming of guaiacol over Ni/Al2O3 and Ni/SBA-15: Impacts of support on catalytic behaviors of nickel and properties of coke. Fuel Process Technol 2019;191:138–51. https://doi.org/10.1016/j.fuproc.2019.04.001.
[371] Helveg S, Sehested J, Rostrup-Nielsen JR. Whisker carbon in perspective. Catal Today 2011;178:42–6. https://doi.org/10.1016/j.cattod.2011.06.023.
[372] Chava R, Bhaskar Anurag Varma D, Roy B, Appari S. Recent advances and perspectives of perovskite-derived Ni-based catalysts for CO2reforming of biogas. J CO2 Util 2022;65:102206. https://doi.org/10.1016/j.jcou.2022.102206.
[373] Singha RK, Shukla A, Yadav A, Sivakumar Konathala LN, Bal R. Effect of metal-support interaction on activity and stability of Ni-CeO2 catalyst for partial oxidation of methane. Appl Catal B Environ 2017;202:473–88. https://doi.org/10.1016/j.apcatb.2016.09.060.
[374] Zhang F, Liu Z, Chen X, Rui N, Betancourt LE, Lin L, et al. Effects of Zr Doping into Ceria for the Dry Reforming of Methane over Ni/CeZrO2 Catalysts: In Situ Studies with XRD, XAFS, and AP-XPS. ACS Catal 2020;10:3274–84. https://doi.org/10.1021/acscatal.9b04451.
[375] Iglesias I, Baronetti G, Alemany L, Mariño F. Insight into Ni/Ce1−xZrxO2−δ support interplay for enhanced methane steam reforming. Int J Hydrogen Energy 2019;44:3668–80.

https://doi.org/10.1016/j.ijhydene.2018.12.112.
[376] Montoya JA, Romero-pascual E, Gimon C, Angel P Del, Monzón A. Methane reforming with CO 2 over Ni / ZrO 2 – CeO 2 catalysts prepared by sol – gel. Catal Today 2000;63:71–85. https://doi.org/10.1016/S0920-5861(00)00447-8.
[377] Fan J, Zhang J, Solsona P, Suriñach S, Baró MD, Sort J, et al. Nanocasting synthesis of mesoporous SnO2 with a tunable ferromagnetic response through Ni loading. RSC Adv 2016;6:104799–807. https://doi.org/10.1039/c6ra23918h.
[378] Yerkes DC. University of illinois at Urbana n.d. http://butane.chem.uiuc.edu/cyerkes/chem102aefa07/Lecture_Notes_102/lecture 8.htm (accessed October 28, 2020).
[379] Onda A, Komatsuz.ast T, Yashima T. Characterization and catalytic properties of Ni-Sn intermetallic compounds in acetylene hydrogenation. Phys Chem Chem Phys 2000;2:2999–3005. https://doi.org/10.1039/b001381l.
[380] Min P, Zhang S, Xu Y, Li R. Enhanced oxygen storage capacity of CeO 2 with doping-induced unstable crystal structure. Appl Surf Sci 2018;448:435–43. https://doi.org/10.1016/j.apsusc.2018.04.103.
[381] Grieshammer S, Nakayama M, Martin M. Association of defects in doped non-stoichiometric ceria from first principles. Phys Chem Chem Phys 2016;18:3804–11. https://doi.org/10.1039/C5CP07537H.
[382] Shabaker JW, Simonetti DA, Cortright RD, Dumesic JA. Sn-modified Ni catalysts for aqueous-phase reforming: Characterization and deactivation studies. J Catal 2005;231:67–76. https://doi.org/10.1016/j.jcat.2005.01.019.
[383] Stroud T, Smith TJ, Le Saché E, Santos JL, Centeno MA, Arellano-Garcia H, et al. Chemical CO2 recycling via dry and bi reforming of methane using Ni-Sn/Al2O3 and Ni-Sn/CeO2-Al2O3 catalysts. Appl Catal B Environ 2018;224:125–35. https://doi.org/10.1016/j.apcatb.2017.10.047.
[384] Silva OC V, Silveira EB, Rabelo-Neto RC, Borges LEP, Noronha FB. Hydrogen Production Through Steam Reforming of Toluene Over Ni Supported on MgAl Mixed Oxides Derived from Hydrotalcite-Like Compounds. Catal Letters 2018;148:1622–33. https://doi.org/10.1007/s10562-018-2390-8.
[385] Villagran-Olivares AC, Barroso MN, López CA, Llorca J, Abello MC. Chelating agent effects in the synthesis of supported Ni nanoparticles as catalysts for hydrogen production. Appl Catal A Gen 2021;622:118219. https://doi.org/10.1016/j.apcata.2021.118219.
[386] Bendieb Aberkane A, Yeste MP, Fayçal D, Goma D, Cauqui MÁ. Catalytic Soot Oxidation Activity of NiO–CeO2 Catalysts Prepared by a Coprecipitation Method: Influence of the Preparation pH on the Catalytic Performance. Materials (Basel) 2019;12:3436. https://doi.org/10.3390/ma12203436.
[387] Lino AVP, Assaf EM, Assaf JM. NiMgAlCe Catalysts Applied to Reforming of a Model Biogas for Syngas Production. Catal Letters 2018;148:979–91. https://doi.org/10.1007/s10562-018-2304-9.
[388] Nagu A, Vasikerappa K, Gidyonu P, Prathap C, Venkata Rao M, Rama Rao KS, et al. Additive-free vapour-phase hydrogenation of benzonitrile over MgO-supported Ni catalysts. Res Chem Intermed 2020;46:2669–81. https://doi.org/10.1007/s11164-020-04113-y.
[389] Ambroz F, Macdonald TJ, Martis V, Parkin IP. Evaluation of the BET theory for the characterization of meso and microporous MOFs. Small Methods 2018;2:1–17. https://doi.org/10.1002/smtd.201800173.
[390] Bacani R, Toscani LM, Martins TS, Fantini MCA, Lamas DG, Larrondo SA. Synthesis and characterization of mesoporous NiO2/ZrO2-CeO2 catalysts for total methane conversion. Ceram Int 2017;43:7851–60. https://doi.org/10.1016/j.ceramint.2017.03.101.
[391] Nizamuddin S, Baloch HA, Griffin GJ, Mubarak NM, Bhutto AW, Abro R, et al. An overview of effect of process parameters on hydrothermal carbonization of biomass. Renew Sustain Energy Rev 2017;73:1289–99. https://doi.org/10.1016/j.rser.2016.12.122.
[392] Chava R, Purbia D, Roy B, Janardhanan VM, Bahurudeen A, Appari S. Effect of Calcination Time on the Catalytic Activity of Ni/γ-Al2O3 Cordierite Monolith for Dry Reforming of Biogas. Int J Hydrogen Energy 2021;46:6341–57.

https://doi.org/10.1016/j.ijhydene.2020.11.125.
[393] Helveg S, Sehested J, Rostrup-Nielsen JR. Whisker carbon in perspective. Catal Today 2011;178:42–6. https://doi.org/10.1016/j.cattod.2011.06.023.
[394] Zhang C, Li S, Li M, Wang S, Ma X, Gong J. Enhanced oxygen mobility and reactivity for ethanol steam reforming. AIChE J 2012;58:516–25. https://doi.org/10.1002/aic.12599.
[395] Hengne AM, Samal AK, Enakonda LR, Harb M, Gevers LE, Anjum DH, et al. Ni-Sn-supported ZrO2 catalysts modified by indium for selective CO2 hydrogenation to methanol. ACS Omega 2018;3:3688–701. https://doi.org/10.1021/acsomega.8b00211.
[396] Kumar D, Singh M, Singh AK. Crystallite size effect on lattice strain and crystal structure of Ba1/4Sr3/4MnO3 layered perovskite manganite. AIP Conf Proc 2018;1953:2–6. https://doi.org/10.1063/1.5032520.
[397] UN-Environment. Unitited nations environemtal emissions gap report 2022. vol. 20. 2022.
[398] IEA. Global Energy and Climate Model 2022.
[399] Energy. Hydrogen drives | Overview - SFC Energy 2022. https://www.sfc.com/en/glossar/heating-value-of-hydrogen/ (accessed January 11, 2023).
[400] Sanchez N, Ruiz R, Hacker V, Cobo M. Impact of bioethanol impurities on steam reforming for hydrogen production: A review. Int J Hydrogen Energy 2020;45:11923–42. https://doi.org/10.1016/j.ijhydene.2020.02.159.
[401] Shirazi M, Neyts EC, Bogaerts A. DFT study of Ni-catalyzed plasma dry reforming of methane. Appl Catal B Environ 2017;205:605–14. https://doi.org/10.1016/j.apcatb.2017.01.004.
[402] Demsash HD, Mohan R. Steam reforming of glycerol to hydrogen over ceria promoted nickel–alumina catalysts. Int J Hydrogen Energy 2016;41:22732–42. https://doi.org/10.1016/j.ijhydene.2016.10.082.
[403] Di Michele A, Dell'Angelo A, Tripodi A, Bahadori E, Sànchez F, Motta D, et al. Steam reforming of ethanol over Ni/MgAl2O4 catalysts. Int J Hydrogen Energy 2019;44:952–64. https://doi.org/10.1016/j.ijhydene.2018.11.048.
[404] Chava R, Seriyala AK, D BAV, Yeluvu K, Roy B, Appari S. Investigation of Ba doping in A-site deficient perovskite Ni-exsolved catalysts for biogas dry reforming. Int J Hydrogen Energy 2023. https://doi.org/10.1016/j.ijhydene.2023.03.464.
[405] Charisiou ND, Sebastian V, Hinder SJ, Baker MA, Polychronopoulou K, Goula MA. Ni catalysts based on attapulgite for hydrogen production through the glycerol steam reforming reaction. Catalysts 2019;9. https://doi.org/10.3390/catal9080650.
[406] Siahvashi A, Adesina AA. Hydrogen production via propane dry reforming: Carbon deposition and reaction-deactivation study. Int J Hydrogen Energy 2018;43:17195–204. https://doi.org/10.1016/j.ijhydene.2018.07.118.
[407] Cui T, Chen Q, Zhang Y, Nie B, Yang B. Understanding the mechanism of carbon deposition of Ni3Co catalysts for methane dry reforming. Appl Surf Sci 2022;599:154002. https://doi.org/10.1016/j.apsusc.2022.154002.
[408] Charisiou ND, Siakavelas G, Papageridis KN, Baklavaridis A, Tzounis L, Polychronopoulou K, et al. Hydrogen production via the glycerol steam reforming reaction over nickel supported on alumina and lanthana-alumina catalysts. Int J Hydrogen Energy 2017;42:13039–60. https://doi.org/10.1016/j.ijhydene.2017.04.048.
[409] Hengne AM, Samal AK, Enakonda LR, Harb M, Gevers LE, Anjum DH, et al. Ni-Sn-supported ZrO2 catalysts modified by indium for selective CO2 hydrogenation to methanol. ACS Omega 2018;3:3688–701. https://doi.org/10.1021/acsomega.8b00211.
[410] Shabaker JW, Huber GW, Dumesic JA. Aqueous-phase reforming of oxygenated hydrocarbons over Sn-modified Ni catalysts. J Catal 2004;222:180–91. https://doi.org/10.1016/j.jcat.2003.10.022.
[411] Salaev MA, Liotta LF, Vodyankina O V. Lanthanoid-containing Ni-based catalysts for dry reforming of methane: A review. Int J Hydrogen Energy 2022;47:4489–535. https://doi.org/10.1016/j.ijhydene.2021.11.086.
[412] Lopez G, Santamaria L, Lemonidou A, Zhang S, Wu C, Sipra AT, et al. Hydrogen generation from biomass by pyrolysis. Nat Rev Methods Prim 2022 21 2022;2:1–13. https://doi.org/10.1038/s43586-022-00097-8.

[413] Cortazar M, Sun S, Wu C, Santamaria L, Olazar L, Fernandez E, et al. Sorption enhanced ethanol steam reforming on a bifunctional Ni/CaO catalyst for H2 production. J Environ Chem Eng 2021;9:106725. https://doi.org/10.1016/j.jece.2021.106725.
[414] Wang B, Xiong Y, Han Y, Hong J, Zhang Y, Li J, et al. Preparation of stable and highly active Ni/CeO2 catalysts by glow discharge plasma technique for glycerol steam reforming. Appl Catal B Environ 2019;249:257–65. https://doi.org/10.1016/j.apcatb.2019.02.074.
[415] Zhu W, Jin J, Chen X, Li C, Wang T, Tsang CW, et al. Enhanced activity and stability of La-doped CeO2 monolithic catalysts for lean-oxygen methane combustion. Environ Sci Pollut Res 2018;25:5643–54. https://doi.org/10.1007/s11356-017-0934-x.
[416] Sun YM, Liang DF, Wang YS, Chen MQ, Hu JX, Sun GW, et al. Producing Hydrogen from Steam Reforming of Bio-oil Derived Oxygenated Model Compounds by Utilizing Ce-Modified Ni/Attapulgite Catalysts. Catal Letters 2022;152:324–39. https://doi.org/10.1007/s10562-021-03584-x.
[417] Chen M, Feng X, Wang Y, Liang D, Li C, Yang Z, et al. Ethanol steam reforming over attapulgite-based MCM-41 supported Ni-Ce-Zr catalyst for hydrogen production. Fuel 2023;346:128373. https://doi.org/10.1016/j.fuel.2023.128373.
[418] Wang Y, Lu Z, Chen M, Liang D, Wang J. Hydrogen production from catalytic steam reforming of toluene over trace of Fe and Mn doping Ni / Attapulgite. J Anal Appl Pyrolysis 2022;165:105584. https://doi.org/10.1016/j.jaap.2022.105584.
[419] Siakavelas GI, Charisiou ND, AlKhoori A, AlKhoori S, Sebastian V, Hinder SJ, et al. Highly selective and stable Ni/La-M (M=Sm, Pr, and Mg)-CeO2 catalysts for CO2 methanation. J CO2 Util 2021;51:101618. https://doi.org/10.1016/j.jcou.2021.101618.
[420] Pastor-Pérez L, Saché E Le, Jones C, Gu S, Arellano-Garcia H, Reina TR. Synthetic natural gas production from CO2 over Ni-x/CeO2-ZrO2 (x = Fe, Co) catalysts: Influence of promoters and space velocity. Catal Today 2018;317:108–13. https://doi.org/10.1016/j.cattod.2017.11.035.
[421] Bilal M, Jackson SD. Ethanol steam reforming over Rh and Pt catalysts: Effect of temperature and catalyst deactivation. Catal Sci Technol 2013;3:754–66. https://doi.org/10.1039/c2cy20703f.
[422] Greluk M, Rotko M, Słowik G, Turczyniak-Surdacka S. Hydrogen production by steam reforming of ethanol over Co/CeO 2 catalysts: Effect of cobalt content. J Energy Inst 2019;92:222–38. https://doi.org/10.1016/j.joei.2018.01.013.
[423] Moogi S, Lee IG, Park JY. Effect of La2O3 and CeO2 loadings on formation of nickel-phyllosilicate precursor during preparation of Ni/SBA-15 for hydrogen-rich gas production from ethanol steam reforming. Int J Hydrogen Energy 2019;44:29537–46. https://doi.org/10.1016/j.ijhydene.2019.03.053.
[424] Xue Z, Shen Y, Li P, Pan Y, Li J, Feng Z, et al. Promoting effects of lanthanum oxide on the NiO/CeO2 catalyst for hydrogen production by autothermal reforming of ethanol. Catal Commun 2018;108:12–6. https://doi.org/10.1016/j.catcom.2018.01.024.
[425] Pino L, Vita A, Laganà M, Recupero V. Hydrogen from biogas: Catalytic tri-reforming process with Ni/LaCeO mixed oxides. Appl Catal B Environ 2014;148–149:91–105. https://doi.org/10.1016/j.apcatb.2013.10.043.
[426] Grabchenko M, Pantaleo G, Puleo F, Kharlamova TS, Zaikovskii VI, Vodyankina O, et al. Design of Ni-based catalysts supported over binary La-Ce oxides: Influence of La/Ce ratio on the catalytic performances in DRM. Catal Today 2021;382:71–81. https://doi.org/10.1016/j.cattod.2021.07.012.
[427] Sellam D, Ikkour K, Dekkar S, Messaoudi H, Belaid T, Roger AC. CO2 reforming of methane over LaNiO3 perovskite supported catalysts: Influence of silica support. Bull Chem React Eng &Catalysis 2019;14:568–78. https://doi.org/10.9767/bcrec.14.3.3472.568-578.
[428] De Lima SM, Da Silva AM, Da Costa LOO, Assaf JM, Mattos L V, Sarkari R, et al. Hydrogen production through oxidative steam reforming of ethanol over Ni-based catalysts derived from La 1-xCe xNiO 3 perovskite-type oxides. Appl Catal B Environ 2012;121–122:1–9. https://doi.org/10.1016/j.apcatb.2012.03.017.
[429] Han X, Yu Y, He H, Shan W. Hydrogen production from oxidative steam reforming of ethanol over rhodium catalysts supported on Ce-La solid solution. Int J Hydrogen Energy

2013;38:10293–304. https://doi.org/10.1016/j.ijhydene.2013.05.137.
[430] Wang Y, Liang S, Cao A, Thompson RL, Veser G. Au-mixed lanthanum/cerium oxide catalysts for water gas shift. Appl Catal B Environ 2010;99:89–95. https://doi.org/10.1016/j.apcatb.2010.06.004.
[431] Wang C, Bai H. Catalytic Incineration of Acetone on Mesoporous Silica Supported Metal Oxides Prepared by One-Step Aerosol Method 2011:3842–8.
[432] Zheng A, Liu S Bin, Deng F. Acidity characterization of heterogeneous catalysts by solid-state NMR spectroscopy using probe molecules. Solid State Nucl Magn Reson 2013;55–56:12–27. https://doi.org/10.1016/j.ssnmr.2013.09.001.
[433] Pang C, Han R, Su Y, Zheng Y, Peng M, Liu Q. Effect of the acid site in the catalytic degradation of volatile organic compounds : A review. Chem Eng J 2023;454:140125. https://doi.org/10.1016/j.cej.2022.140125.
[434] Jiang B, Xi Z, Lu F, Huang Z, Yang Y, Sun J, et al. Ce/MgAl mixed oxides derived from hydrotalcite LDH precursors as highly efficient catalysts for ketonization of carboxylic acid. Catal Sci Technol 2019;9:6335–44. https://doi.org/10.1039/c9cy01323g.
[435] Sartoretti E, Novara C, Giorgis F, Piumetti M, Bensaid S, Russo N, et al. In situ Raman analyses of the soot oxidation reaction over nanostructured ceria-based catalysts. Sci Rep 2019:1–15. https://doi.org/10.1038/s41598-019-39105-5.
[436] Liu L, Wang X, Guo M, Zhang M. Kinetics investigation of oxygen storage capacity in La 2O 3-CeO 2 solid solution. J Nanosci Nanotechnol 2011;11:2155–62. https://doi.org/10.1166/jnn.2011.3131.
[437] Nguyen Tri. High activity and stability of nano-nickel catalyst based on LaNiO3 perovskite for methane bireforming. Vietnam J Chem 2022;60:784–97. https://doi.org/10.1002/vjch.202200060.
[438] Zhao Y, Nishida T, Minami E, Saka S, Kawamoto H. TiO2-supported Ni-Sn as an effective hydrogenation catalyst for aqueous acetic acid to ethanol. Energy Reports 2020;6:2249–55. https://doi.org/10.1016/j.egyr.2020.08.007.
[439] Stroud T, Smith TJ, Le Saché E, Santos JL, Centeno MA, Arellano-Garcia H, et al. Chemical CO2 recycling via dry and bi reforming of methane using Ni-Sn/Al2O3 and Ni-Sn/CeO2-Al2O3 catalysts. Appl Catal B Environ 2018;224:125–35. https://doi.org/10.1016/j.apcatb.2017.10.047.
[440] K. S. W. Sing, D. H. Everett, R. A. W. Haul, L. Moscou, R. A. Pierotti, J. Rouquerol and T. Siemieniewska, “Reporting Physisorption Data for Gas/Solid Systems with Special Reference to the Determination of Surface Area and Porosity,” Pure and Applied Chemistry, Vol. 57, No. 4, 1985, pp. 603-619. - References - Scientific Research Publishing n.d. https://www.scirp.org/(S(vtj3fa45qm1ean45vvffcz55))/reference/ReferencesPapers.aspx?ReferenceID=201243 (accessed December 4, 2022).
[441] Cao P, Tang P, Bekheet MF, Du H, Yang L, Haug L, et al. Atomic-Scale Insights into Nickel Exsolution on LaNiO3 Catalysts via In Situ Electron Microscopy. J Phys Chem C 2022;126:786–96. https://doi.org/10.1021/acs.jpcc.1c09257.
[442] Solsona B, Concepción P, Hernández S, Demicol B, Nieto JML. Oxidative dehydrogenation of ethane over NiO-CeO 2 mixed oxides catalysts. Catal Today 2012;180:51–8. https://doi.org/10.1016/j.cattod.2011.03.056.
[443] Kardash TY, Derevyannikova EA, Slavinskaya EM, Stadnichenko AI, Maltsev VA, Zaikovskii A V., et al. Pt/CeO 2 and Pt/CeSnO x catalysts for low-temperature CO oxidation prepared by plasma-arc technique. Front Chem 2019;7. https://doi.org/10.3389/fchem.2019.00114.
[444] da Silva F de AR, dos Santos RCR, Nunes RS, Valentini A. Role of tin on the electronic properties of Ni/Al2O3 catalyst and its effect over the methane dry reforming reaction. Appl Catal A Gen 2021;618:118129. https://doi.org/10.1016/j.apcata.2021.118129.
[445] Hung-Ting Chen, Seong Huh, Victor S.-Y. Lin. Fine-Tuning the Functionalization of Mesoporous Silica. Catal Prep 2006:46–71.

List of publications

Peer-Reviewed International Journal (On Research Area)

1. **Anil Kumar, S.**, Indraja, S., Singh, R., Appari, S., & Roy, B. (2022). A review on ethanol steam reforming for hydrogen production over Ni/Al_2O_3 and Ni/CeO_2 based catalyst powders. *International Journal of Hydrogen Energy*, *47*(13), 8177–8213. https://doi.org/10.1016/j.ijhydene.2021.12.183
2. **Anil Kumar, S.**, Rao, A., Appari, S., Leclerc, C., & Roy, B. (2022). Effects of Metal Loading and Support Modification on the Low-Temperature Steam Reforming of Ethanol (LTSRE) Over the Ni-Sn/CeO_2 Catalysts. *International Journal of Hydrogen Energy*, 1–22. https://doi.org/10.2139/ssrn.4216553.
3. **Anil Kumar, S.,** Chava, R., Baffoe, Pham, Leclerc, C., Appari, S., Roy, B. (2023). Tin and Lanthanum Modified Ni/CeO_2 Catalyst Systems for Low Temperature Steam Reforming of Ethanol (LTSRE). *International Journal of Hydrogen Energy*. (Accepted 13th August, 2023).
4. **Anil Kumar et al.** Experimental deactivation study of Ni-Sn/ $Ce_xM_{1-x}O_y$ (M=Mg, Zr, La) catalyst from low temperature steam reforming of ethanol. (Under preparation)
5. **Anil Kumar et al.,** Global kinetics study over Ni-Sn/ $Ce_xM_{1-x}O_y$ (M=Mg, Zr, La) catalyst using Langmuir Hinshelwood model for hydrogen production by low temperature steam reforming of ethanol. (Under preparation)

Peer-Reviewed international journal (Other Areas)

1. Chava, R., **Anil Kumar, S.**, Varma D, B. A., Yeluvu, K., Roy, B., & Appari, S. (2023). Investigation of Ba doping in A-site deficient perovskite Ni-exsolved catalysts for biogas dry reforming. *International Journal of Hydrogen Energy*, *48*(71), 27652–27670. https://doi.org/10.1016/j.ijhydene.2023.03.464
2. Reddy, A., **Anil Kumar, S.**, Yogin, C., Navjot, Chattopadhyay, P., Roy, B. (2023). Carbonaceous catalysts (biochar and activated carbon) from agricultural residues and their application in production of biodiesel: A review. *Chemical Engineering Research and Design*. (Under review)

Conference Publications (On Research Area)

1. **Anil Kumar, S.**, Appari, S., & Roy, B. (2022). Steam reforming of ethanol for hydrogen production by low- temperature steam reforming using modified Ni-Sn/CeO_2 catalyst. *Materials Today: Proceedings*. https://doi.org/10.1016/j.matpr.2022.11.231.

Conference Publications (Other Areas)

1. Reddy, A., **Anil Kumar, S.**, Yogin, C., Navjot, Roy, B. (2023). Synthesis of graphene type materials from agricultural residues. In recent Trends in Nanotechnology for sustainable Environment, Proceedings of ICON-NSLE 2022 published by *Springer*.

List of Conference Attended

1. **Anil Kumar, S.**, Appari, S., & Roy, B. Steam reforming of ethanol for hydrogen production by low- temperature steam reforming using modified Ni-Sn/CeO_2 catalyst. *ICON-NSLE 2022* held at BITS-Pilani during April 14-16, 2022, International.
2. **Anil Kumar, S.**, Appari, S., & Roy, B. "Hydrogen Production from Ethanol by Low Temperature Steam Reforming Using Modified Ni-Sn/CeO_2 Catalyst." International Hydrogen & Fuel Cell Conference (IHFC-2019) Organized by Hydrogen association of India during 8-10^{th} December 2019, International.
3. **Anil Kumar, S.**, Appari, S., & Roy, B. "Ni-Sn/CeO_2 modified with MgO for production of hydrogen through catalytic low temperature steam reforming of ethanol." 72^{nd} annual session of Indian institute of chemical engineers "CHEMCON-2019" held on 16-19^{th} December,2019 at IIT Delhi, National.

Biography of the candidate

Seriyala Anil Kumar completed his B.Tech in chemical engineering from Acharya Nagarjuna University in India. He got a 526 rank in chemical engineering, GATE-2011. In 2013, he was awarded master's in chemical engineering from BITS-Pilani. During his master's degree, he worked for one year as a project researcher at ITW India limited (R&D center) in Hyderabad. Currently, he is presently pursuing Ph.D. in Chemical Engineering at the Birla Institute of Technology and Science (BITS), Pilani campus, Rajasthan, India, under the supervision of Prof. Banasri Roy and Dr. Srinivas Appari.

After completion of his master's, he worked as a project manager at Kumar Organic Products Limited in Bangalore from January 2014 to June 2015. He then started working as an assistant professor in the chemical engineering department at the BV Raju Instituted of Technology and Science in Hyderabad from June 2015 to December 2017, where he taught courses heat transfer and thermodynamics, and he was in-charge for campus placements. In addition, he also teaches online courses (Mass transfer, Heat transfer and Thermodynamics) for the GATE exam at the Vaishnavi Gate Academy in Hyderabad from April 2013 to December 2017. During his Ph.D, he also contributed tutorials for subjects such as Material Science, Engineering Chemistry, Materials and Characterization Lab during his Ph.D.

His research interests include green technology, renewable energy sources, smart materials, and the manufacture of catalysts. He received third place in best academic research from the Royal Society of Chemistry in 2020 and best poster presentation at the International Hydrogen & Fuel Cell Conference (IHFC-2019) Organized by the Hydrogen Association of India on 8-10 December 2019. He published two peer-reviewed papers in the international journal of hydrogen energy and one conference paper in material today proceedings. He presented research work at the International Hydrogen & Fuel Cell Conference (IHFC-2019) and CHEMCON-2019 national level conference.

- Google scholar: https://scholar.google.com/citations?user=-L7gZRkAAAAJ&hl=en&oi=ao

Biography of Supervisor

Dr. Banasri Roy by training is a materials scientist. She completed Ph.D. in materials engineering from Colorado School of Mines & National Renewable Energy Laboratory (NREL), USA, M. Tech in materials engineering from IIT-Kanpur, M.Sc. in applied physics from University of Puerto Rico, USA, B. Tech in chemical technology & B. Sc. (with honor) in chemistry from Calcutta University. The exercise in multidisciplinary research fields helps her to understand the advance theory of the characterization and data analysis. Dr. Roy has vast expertise in materials synthesis, analytical characterization (regarding SEM/TEM, XRD, TGA, RAMAN, XPS, DTA-TGA, UV-Vis spectroscopy, etc.), and data analysis.

She has extensively worked on the development of Nano catalyst systems for renewable energy production from ethanol and biomasses. Her current focus is on the utilization of waste (agricultural and others) to convert to energy sources and other value added chemicals. She also works on the development of nanoparticles for environmental pollution control applications. Her research interest includes surface modification of different biomaterials to improve biocompatibility.

She is one of the SERB-POWER fellowship recipients of 2021 and awarded ULAM-NAWA fellowship by the Polish National Agency for Academic Exchange. Two Ph. D and 14 ME students completed their thesis successfully under her guidance and currently she is supervising four Ph. D and two ME students. She authored and co-authored 45 peer reviewed papers in different international journals, achieved around 1250 citations, 28 i-index and 19 h-index. Currently she is affiliated in the chemical engineering department at BITS- Pilani, Pilani campus.

- Institute Website: https://universe.bits-pilani.ac.in/pilani/broy/profile
- Google Scholar: https://scholar.google.com/citations?hl=en&user=HF4Inh8AAAAJ&view_op=list_works&sortby=pubdate.
- ORCID ID: 0000-0001-6365-2282
- Web of Science Researcher ID: AAQ-6273-2021

Biography of Co-Supervisor

Dr. Srinivas Appari has expertise in heterogeneous catalysis and detailed surface kinetic modelling. He completed Ph.D from IIT Hyderabad, M.Tech from JNTU Hyderabad, and B. Tech from Osmania University. After his Ph.D, he worked as Postdoctoral Research Fellow in Institute for Materials Chemistry and Engineering, Kyushu University, Japan.

Currently, he is working on the hydrogen production and value-added chemicals from alternative feedstocks like biomass and biogas via catalytic routes. He also explores the methanol and dimethyl ether from CO_2 hydrogenation on various catalysts. His research interest also includes machine learning approaches for catalyst design, and process modelling and simulation. His work has received two prestigious awards from the Japan Institute of Energy consecutively in 2015 and 2016.

Presently, he is supervising three PhD students and two ME students, and 10 ME students completed their thesis successfully. He and his group published more than 30 peer reviewed journals that significantly contribute to heterogeneous catalysis and biomass conversion. His group research work cited more than 690 citations with h-index 14 and i-10 index 17. Currently he is working as an Assistant professor in the chemical engineering department at BITS- Pilani, Pilani campus.

- Institute Website: https://www.bits-pilani.ac.in/pilani/srinivasappari/Profile
- Google Scholar: https://scholar.google.com/citations?user=ceTKjfoAAAAJ&hl=en
- ORCID ID: 0000-0001-5253-1266
- Web of Science Researcher ID: C-3389-2018

APPENDIX-I

Crystallography open database

1. Powder diffraction data of nickel

Origin entry (PDF)	96-901-3035
Crystal System	Cubic
Cell parameter(a)	3.6150 A

2 Theta	Intensity (I)	D spacing	H	K	L
44.35	100.00	2.09	1	1	1
50.49	45.06	1.81	2	0	0
74.20	22.11	1.28	2	0	2

2. Powder diffraction data of nickel oxide

Origin entry (PDF)	96-101-0096
Crystal System	Cubic
Cell parameter(a)	4.1800 A

2 Theta	Intensity (I)	D spacing	H	K	L
37.26	77.62	2.41	1	1	1
43.29	100.00	2.09	2	0	0
62.89	51.39	1.48	2	0	2
75.43	23.40	1.26	3	1	1
79.42	14.18	1.21	2	2	2

3. Powder diffraction data of CeO_2

Origin entry (PDF)	96-434-3162
Crystal System	Cubic
Cell parameter(a)	a = 5.4097 A

2 Theta	Intensity (I)	D spacing	H	K	L
28.58	100.00	3.12	1	1	1
33.12	28.78	2.70	2	0	0
47.54	51.87	1.91	2	0	2
56.41	40.99	1.63	3	1	1
59.16	7.71	1.56	2	2	2
69.51	7.21	1.35	4	0	0
76.81	15.61	1.24	3	1	3
79.18	10.19	1.21	4	0	2

4. Powder diffraction data of $Ce_{0.5}Zr_{0.5}O_2$

Origin entry (PDF)	96-210-2840
Crystal System	Tetragonal
Cell parameter(a)	3.7191A
(c)	5.305 A

2 Theta	Intensity (I)	D spacing	H	K	L
29.33	100.00	3.05	0	1	1

33.79	9.13	2.65	0	0	2
34.09	16.82	2.63	1	1	0
41.83	0.38	2.16	0	1	2
48.76	34.60	1.87	1	1	2
48.99	17.55	1.86	0	2	0
57.72	13.27	1.60	0	1	3
58.12	25.94	1.59	1	2	1
60.83	7.12	1.52	0	2	2
71.07	2.19	1.33	0	0	4
71.79	4.66	1.31	2	2	0
76.21	0.09	1.25	0	1	4
79.03	9.80	1.21	1	2	3
79.38	4.84	1.21	0	3	1

5. Powder diffraction data of ZrO_2

Origin entry (PDF)	96-152-1754
Crystal System	Cubic
Cell parameter(a)	5.0900 A

2 Theta	**Intensity (I)**	**D spacing**	**H**	**K**	**L**
30.42	100.00	2.94	1	1	1
35.27	20.23	2.55	2	0	0
50.73	55.33	2.80	2	0	2
60.31	35.58	1.53	3	1	1
63.29	5.18	1.47	2	2	2
74.58	6.82	1.27	4	0	0

6. Powder diffraction data of NiMgO2

Origin entry (PDF)	24-0712
Crystal System	Cubic
Cell parameter(a)	4.1926 A

2 Theta	**Intensity (I)**	**D spacing**	**H**	**K**	**L**
37.10	45.00	2.42	1	1	1
43.10	100.00	2.10	2	0	0
62.60	50.00	1.48	2	2	0
75.09	14.00	1.26	3	1	1
79.05	15.00	1.21	2	2	2

7. Powder diffraction data of La_2O_3

Origin entry (PDF)	00-040-1281
Crystal System	Hexagonal
Cell parameter(a)	4.257 (2)
(c)	6.43 (3)

2 Theta	**Intensity (I)**	**D spacing**	**H**	**K**	**L**
26.16	29.4	3.51	1	0	0
27.3	27.9	3.22	0	0	2

30.45	100	3.80	1	0	-1
39.5	25.6	2.37	1	0	-2
45.1	31	2.03	1	1	0
46.96	31	1.83	1	0	-3
52.24	24.3	1.76	2	0	0
54.07	86.00	1.69	2	0	-1
59.96	20.00	1.54	2	0	-2

8. Powder diffraction data of LaNiO3

Origin entry (PDF)	01-079-2451
Crystal System	Rhombohedral
Cell parameter(a)	5.457
(c)	13.14

2 Theta	**Intensity (I)**	**D spacing**	**H**	**K**	**L**
32.79	100.00	2.73	1	1	0
33.17	99.80	2.70	1	0	4
40.53	25.70	2.22	2	0	2
47.34	58.40	1.92	0	2	4
53.60	6.40	1.71	1	1	6
59.51	15.90	1.55	0	1	8
68.75	13.90	1.36	2	2	0
69.63	14.10	1.35	2	0	8
73.63	2.60	1.29	3	1	2
74.06	3.20	1.28	0	3	6
78.49	11.60	1.22	1	3	4
79.13	12.00	1.21	1	2	8

9. Powder diffraction data of $Ce_{0.5}La_{0.5}O_2$

Origin entry (PDF)	01-084-4175
Crystal System	Cubic
Cell parameter(a)	5.566

2 Theta	**Intensity (I)**	**D spacing**	**H**	**K**	**L**
27.73	100.00	3.21	1	1	1
32.13	30.20	2.78	2	0	0
46.08	47.10	1.97	2	2	0
54.64	36.30	1.68	3	1	1
57.29	6.90	1.61	2	2	2
67.22	5.70	1.39	4	0	0
74.19	11.60	1.28	3	3	1
76.46	7.60	1.24	4	2	0

Sample catalyst calculation and amounts of catalysts used for preparation.

- **Sample calculation for $Ni_{0.93}Sn_{0.07}$(10 wt.%)/CeO_2 catalyst preparation**

Basis: Considering batch size 20 g

Calc:

Amount of the Ni-Sn metal required for 20 g of batch can be = 10 wt.% x 20 g

$$= \frac{10}{100} \times 20$$

Amount of Ni-Sn = 2 gm,

So, amount of CeO_2 support = 20 gm – 2gm = 18 gm

Ni-Sn bimetal considered 14:1 atomic ratio, then

Weight fraction of Ni could be = $\frac{(14 \times Mol.\ wt.\ of\ Ni)}{(14 \times Mol.\ wt.\ of\ Ni) + (1 \times Mol.\ wt.\ of\ Sn)}$

$$= \frac{(14 \times 58.693)}{(14 \times 58.69) + (1 \times 118.71)}$$

Weight fraction of Ni = 0.8738

Amount of Ni (gm) = Amount of Ni-Sn x Weight fraction of Ni

= 2 x 0.8738

= 1.7475 gm

Moles of Ni = $\frac{1.7475}{M.W\ of\ Ni}$

Moles of Ni = 0.0298 moles

Similarly, Moles of Sn = 0.0021 moles

Moles of CeO_2 = 0.1046 moles

Precursors:

$Ni(NO_3)_2.6H_2O$ = 290.79 Mol wt.

$SnCl_2.2H_2O$ = 225.63 Mol wt.

$Ce(NO_3)_3.6H_2O$ = 434.22 Mol wt.

Amount of precursors required,

$Ni(NO_3)_2.6H_2O$ = Mol wt. x Moles of Ni

= 290.79 x 0.0298

= 8.65 gm

Similarly,

$SnCl_2.2H_2O$ = 0.479 gm

$Ce(NO_3)_3.6H_2O$ = 45.41 gm

The Oxidizer to fuel ratio considered O:F 1:1

Thus, we have O:F given by Chen et al. [445]

$$\frac{O}{F} = \frac{[\Sigma(\text{Coefficient of the elements in nitrates}) * (\text{Oxidation state})]}{(-1)\,[\Sigma(\text{Coefficient of the elements in fuel}) * (\text{Oxidation state})]}$$

Oxidation number of N=0, H = +1, C = +4, O = -2,

Then valency/oxidation state of glycine (NH_2-CH_2-COOH) = (0 x 1) + (1x 5) + (4 x 2) + (2 x -2)

= 9

Similarly, valency of

$Ni(NO_3)_2.6H_2O$ = -10

$SnCl_2.2H_2O$ = 0

$Ce(NO_3)_3.6H_2O$ = -15

Then moles of glycine required, as per stoichiometry.

$= \frac{(-10 \times Mol.\ wt.\ of\ Ni) + (0 \times Mol.\ wt.\ of\ Sn) + (-15 \times Mol.\ wt.\ of\ CeO_2)}{(-1)\,(9)}$ = 0.2073 moles

Amount of glycine required = moles x M.W

= 0.2073 x 75.07 = 15.568

Total amount of precursors required for $Ni_{0.93}Sn_{0.07}$(10 wt.%)/CeO_2 catalyst preparation

$Ni(NO_3)_2.6H_2O$ = 8.65 gm

$SnCl_2.2H_2O$ = 0.479 gm

$Ce(NO_3)_3.6H_2O$ = 45.41 gm

NH_2-CH_2-COOH = 15.56 gm

Table (i): Precursors amount for $NiSn/CeO_2$-ZrO_2 catalyst preparation.

Precursors	Amount of precursor and glycine (g)							
	$Ni(X)/Ce_{0.5}Zr_{0.5}O_2$		$Ni/Ce_{0.33}Zr_{0.67}O_2$		$Ni_{0.93}Sn_{0.07}(X)/Ce_{0.5}Zr_{0.5}O_2$		$Ni_{0.93}Sn_{0.07}(X)/Ce_{0.33}Zr_{0.67}O_2$	
	5 wt.%	20 wt.%	5 wt.%	20 wt.%	5 wt.%	20 wt.%	5 wt.%	20 wt.%
$ZrO(NO_3)_2.H_2O$	14.9	12.5	21.0	17.7	14.9	12.5	21.0	17.7
$Ce(NO_3)_3.6H_2O$	27.9	23.5	19.7	16.6	27.9	23.5	19.7	16.6
$Ni(NO_3)_2.6H_2O$	5.0	19.8	5.0	19.8	4.3	17.3	4.3	17.3
$SnCl_2.2H_2O$	0.0	0.0	0.0	0.0	0.2	1.0	0.2	1.0
NH_2-CH_2-COOH	14.8	17.0	14.7	16.8	14.7	16.3	14.5	16.1

Table (ii): Precursors amount for $NiSn/CeO_2$-MgO catalyst preparation.

Precursors	Amount of precursor and glycine (g)										
	$Ni_{0.93}Sn_{0.07}(X)/CeO_2$			$Ni_{0.93}Sn_{0.07}(X)/Ce_{0.5}Mg_{0.5}O_2$			$Ni_{0.93}Sn_{0.07}(X)/Ce_{0.33}Mg_{0.67}O_2$			$Ni(5)/Ce_{0.33}Mg_{0.67}O_2$	$Ni_{0.88}Sn_{0.11}(5)/Ce_{0.33}Mg_{0.67}O_2$
	5 wt.%	10 wt.%	20 wt.%	5 wt.%	10 wt.%	20 wt.%	5 wt.%	10 wt.%	20 wt.%		
$Mg(NO_3)_2.6H_2O$	-	-	-	22.9	21.7	19.3	38.6	36.5	32.5	38.6	38.6
$Ce(NO_3)_3.6H_2O$	47.9	45.4	40.4	38.8	36.8	32.7	32.6	30.9	27.5	32.6	32.6
$Ni(NO_3)_2.6H_2O$	4.3	8.7	17.3	4.3	8.7	17.3	4.3	8.7	17.3	5	4
$SnCl_2.2H_2O$	0.2	0.5	1	0.2	0.5	1	0.2	0.5	1	0	0.4
NH_2-CH_2-COOH	15.1	15.6	16.6	19.9	20.2	20.7	23.2	23.3	23.4	23.4	23.1

Table (iii): Precursors amount for $NiSn/CeO_2$-La_2O_3 catalyst preparation.

Precursors	Amount of precursor and glycine (g)							
	$Ni_{0.93}Sn_{0.07}(X)/Ce_{0.67}La_{0.33}O_2$		$Ni_{0.93}Sn_{0.07}(X)/Ce_{0.5}La_{0.5}O_2$		$Ni_{0.93}Sn_{0.07}(X)/Ce_{0.33}La_{0.67}O_2$		$Ni_{0.87}Sn_{0.13}(5)/Ce_{0.67}La_{0.33}O_2$	$Ni_{0.5}Sn_{0.5}(5)/Ce_{0.67}La_{0.33}O_2$
	5 wt.%	20 wt.%	5 wt.%	20 wt.%	5 wt.%	20 wt.%		
$La(NO_3)_3.6H_2O$	9.21	7.7	12.4	10.4	14.9	12.6	9.2	9.2
$Ce(NO_3)_3.6H_2O$	18.5	15.6	12.4	10.5	7.5	6.3	18.5	18.5
$Ni(NO_3)_2.6H_2O$	3.2	13	3.2	13	3.2	12.9	2.8	1.2
$SnCl_2.2H_2O$	0.2	0.7	0.2	0.7	0.2	0.7	0.3	0.9
NH_2-CH_2-COOH	8.9	10.4	8.09	9.76	7.4	9.2	8.8	8.3